DOCTORAATSPROEFSCHRIFT

2007 | Faculteit Wetenschappen

Green's Function and Dyson Orbital Studies of the Electronic Structure of Cage Compounds and Flexible Molecules: A Confrontation of Many-Body Quantum Mechanics with Electron Momentum, Photo-Electron and Penning Ionization Electron Spectroscopies

Proefschrift voorgelegd tot het behalen van de graad van
Doctor in de Wetenschappen, richting natuurkunde, te verdedigen door:

Stefan KNIPPENBERG

Promotor: prof. dr. M. S. Deleuze
Copromotor: prof. dr. J.-P. François

D/2007/2451/44

universiteit
hasselt

Bij het begin van deze dissertatie zou ik graag mijn dankbaarheid willen uitdrukken tegenover al wie op één of andere wijze aan dit werk heeft bijgedragen.

De eerste regels wil ik wijden aan mijn promotor, Prof. Dr. Michael Deleuze, en mijn copromotor, Prof. Dr. Jean-Pierre François, die vier jaren geleden de beslissing namen gelden van het Bijzonder OnderzoeksFonds (BOF) voor mijn doctoraatsonderzoek vrij te maken. Michael, je gedreven onderzoeksmethode was steeds een inspiratiebron. Ze maakte onze werkplek aan de Universiteit Hasselt tot een plaats van kennen en kunnen. Kwantitatieve resultaten gingen er hand in hand met bijzonder, kwalitatief inzicht. Prof. François, u kwam vaak aankloppen om even te praten over de dagelijkse gang van het onderzoek. Hierbij bewonderde ik meer dan eens uw gave om op een bevattelijke wijze de finesses van vele theorieën en achtergronden duidelijk te stellen.

Balázs, with your arrival in Limburg, I discovered the big advantage of having a post-doc in the group. I am happy that I had the opportunity to learn so much from you, about science as well as about life beside the campus. Filippo, you started your Ph.D. in the autumn of 2006. I wish you great insights and interesting findings. Enjoy your time at our university, and do not forget to visit nice and remarkable places here in Belgium!

For fruitful collaborations, I am extremely grateful to the groups of Prof. Dr. M. J. Brunger (Flinders University, Adelaide, Australia), Prof. Dr. K. Ohno and Dr. N. Kishimoto (Tohoku University, Sendai, Japan) and Prof. L. S. Cederbaum (Heidelberg University, Germany), and I would like to express my gratitude to Prof. Dr. Em. J. H. D. Eland (Oxford University, United Kingdom).

I would also like to thank the collaborators of Prof. Dr. J. K. Deng at Tsinghua University (Beijing, P. R. China) for the scientific support, as well as for their kind hospitality during the fortnight I stayed at their campus. A special "Hi" goes to Yanru, who came to Hasselt University to join our research group for nine pleasant months.

Magda, mijn doctoraatsthesis staat vol figuren en grafieken. Zelf zou ik er nooit in geslaagd zijn om deze klus zo kwaliteitsvol te klaren. Bedankt voor je moeite!

Adam en Sylvia, ik vond het geweldig leuk dat we tijdens mijn vier doctoraatsjaren samen het één en het ander konden bespreken, bespelen en beleven. Ook aan de mensen van de gang waar mijn bureau zich binnen de Universiteit Hasselt bevond, alsook aan de medewerkers van de departementen WNI en SBG, bedankt!

Papa, mama, Veerle en Guy, de ondersteuning die ik van jullie kreeg valt niet samen te vatten in concrete woorden. Het omvat veel meer dan wassen op vrijdag en potjes vullen op zondag. Steeds wist ik dat ik met mijn verhalen ergens te recht kon, steeds was ik er zeker van dat ik op raad en daad kon rekenen. Bedankt, jullie hebben me al het mogelijke gegeven om door te groeien naar wat bereikbaar was!

Dank ook aan de leiding en oud-leiding van JVS-Descartes. Dank voor het wekken van de wetenschappelijke interesse, dank voor de steun tijdens studies en aanverwante, dank voor de vele grappige ogenblikken die ideaal waren om na studies en werk even af te schakelen!

Aan mijn leeftijdsgenoten die na de humaniora-tijd naar Leuven trokken en aan hen die ik als vrienden daar leerde kennen, het was tof dat ik tot op het einde van mijn doctoraatstijd nog kon sporen naar de plaats waar ik verwacht werd.

En dan is er nog iedereen die ik hier niet heb kunnen noemen, maar wiens hulp en vriendschap in het kader van mijn vorming meer dan aangenaam en nuttig was. Dan gaat het over grotere en over kleinere dingen, over hele gesprekken en over eenvoudige, maar veelzeggende blikken,... Een doctoraat leg je niet alléén af, je hebt een hele ploeg nodig. En die hele bende promoveert samen met de kandidaat. Bedankt!

Ultreia, ultreia et sus eia!

Table of contents

3.1 Norbornane: An investigation into its valence electronic structure using electron momentum spectroscopy, density functional theory and one-particle Green's function theory.

3.1.6 Molecular property information

3.4 Investigation into the valence electronic structure of norbornene using electron momentum spectroscopy, Green's function and density functional theories.

3.4.6 Molecular properties of norbornene

3.5 Green's function study of the one-electron and shake-up ionization spectra of unsaturated hydrocarbon cage compounds

3.5.3 Results and discussion

4.3 Probing molecular conformations in momentum space: the case of *n*-pentane

4.4 Probing the shape and stereochemistry of molecular orbitals in locally flexible aromatic chains: a Penning ionization electron spectroscopy and Green's function study of the electronic structure of biphenyl.

Part I: General introduction

Orbitals are ubiquitous [1] in the quantum theory of matter, and are nowadays introduced in most elementary courses or textbooks of physics [2], chemistry [3], material sciences [4] or even biology [5]. It is well-known that, at the molecular level, because of the uncertainty principle of Heisenberg, motions of electrons can only be statistically described through one-electron waves – the orbitals. The picture is clear and unambiguous for simple systems containing one or two electrons (hydrogenoid atoms, the H_2^+ and H_2 molecules,…), as in this case the square of the occupied orbital can be directly related to the measurable electron density. The relationship with electron densities is not so straightforward for systems containing more than two electrons, because of the correlation of electronic motions. For many-electron systems, the wavefunctions are, in a first approximation, obtained as Slater determinants [6] of orbitals that are always formally obtained as eigenfunctions of effective (e.g. tight binding, semi-empirical, Hartree-Fock,…) one-electron Hamiltonians [6]. In practice, the consistency of the orbital formalism can only be assessed by comparing various predictions drawn from quantum mechanics with a large set of experimental observations (spectroscopic measurements, chemical reactivity, etc.). In this context, Electron Momentum Spectroscopy (EMS) [7] has triggered a revolution in our perception of the electronic structure of matter. This technique indeed affords *direct measurements* in momentum space (**p**) of the electron density associated to a single ionization channel (i.e. an orbital in a one-electron picture) in electron impact (e,2e) ionization experiments, through detailed investigations of the angular dependence of ionization intensities. The obtained momentum distributions are equivalent to structure factors derived as the square of the Fourier Transform of suited orbitals, namely Dyson orbitals [$g_n(\mathbf{x})$], defined as partial overlaps between the initial (neutral) and final (cationic) wavefunctions in an ionization process. EMS enables us therefore to directly assess the intimate relationships that prevail between the configuration (**r**) and momentum (**p**) spaces for specific ionization channels related to well-defined electron energy levels and distributions. In the outlook of material research for which a detailed control and tuning of the electronic structure is most often essential, this is a very remarkable feature since all known structural analysis techniques (X-ray diffraction, scanning-tunneling microscopy,...) can only deliver direct information on the total electron densities.

The results of EMS measurements are most often compared with data obtained by Photo-Electron Spectroscopies, more specifically X-ray and Ultra-violet Photo-electron Spectroscopies (XPS and UPS, respectively), which are more traditionally used to obtain information on the chemical composition, bonding characteristics, electronic and molecular structures of molecules in the gas phase and the top layers of solid materials. UPS experiments enable a much higher resolution than EMS but do not enable so straightforward experimental reconstructions of orbitals. Another technique suitable for studying individual orbital densities is Penning Ionization Electron Spectroscopy (PIES) [8]. With this technique, the shape of molecular orbitals, as well as their stereochemistry towards an approaching electrophilic species, are experimentally amenable through detailed studies of the collision energy dependence of partial ionization cross sections upon impact with a rare-gas atom in a metastable excited state.

Valence electron spectra are often qualitatively interpreted according to orbital energies and with the help of familiar one-electron concepts, such as Hartree-Fock molecular orbital theory and Koopmans' theorem [9]. As this approach does not take into account electron relaxation and correlation effects resulting from the ionization process, it is known to yield qualitatively and quantitatively significant errors in the assignment of spectral bands as well as to large deviations in the apparent shape of orbitals compared with EMS measurements. Standard many-body approaches such as Many-Body Perturbation Theory (MBPT), Coupled Cluster (CC) or Configuration Interaction (CI) would be here of little use as these approaches do not enable direct, i.e. one shot, calculations of the many ionization energies and of the related transition moments or Dyson orbitals that characterize a complex ionization spectrum. Assuming an extension of Koopmans' theorem, a commonly used alternative in the EMS community for coping with electron correlation in the initial ground state wavefunction (shortly, initial state correlation) is Density Functional Theory (DFT). Despite the fact that they are known to provide very poor estimates of ionization energies, Kohn-Sham orbitals have been almost systematically used over the last twenty years to analyze the experimental momentum distributions, which they most often remarkably reproduce.

The main drawback of a description of ionization events at the level of Koopmans' theorem is that electronic correlation and relaxation in the final state (Figure 1) are not accounted for. More specifically, these approaches neglect final state configuration interactions and the dispersion thereby of the ionization intensity over excited electronic (shake-up) configurations of the cation. In a one-electron picture of ionization, the main spectral bands (1-4 in Figure 1) are assumed to be in a one-to-one correspondence with the occupied orbital levels. Koopmans' theorem and its DFT extension may however fail to provide the right energy order for the main ionization bands, due to the neglect of electronic relaxation and, if Hartree-Fock orbitals are used, initial state correlation. Furthermore, provided the relaxation energy is large enough, a second electron can be excited into an unoccupied level. As a result, an additional "shake-up" (satellite) band can be seen at an excitation energy E_I above the main band. Note that shake-up bands may borrow a very high fraction of the total ionization intensity [10-14].

Another issue worth some discussion in the framework of experiments relying on electron scattering such as EMS is the suitability of the electronic potential underlying the employed model. For example, it is known that, with DFT, most currently used gradient corrected functionals decay too fast at large distance compared with the right Coulomb asymptotics, due to the unavoidable self-interaction error, which is known to yield systematic underestimations of ionization energies by several eV.

A main difficulty impeding widespread applications of EMS is that most molecules, oligomers or polymers are flexible entities which, at a given temperature, can freely change between a number of different conformational states. As variations of the molecular conformation may induce considerable changes in the electronic densities, robust enough computations of conformer abundances are essential for decent analyzing the results of EMS experiments on such systems. Also, one has to cope with the often very strong influence of the molecular conformation on the orbital energies, and, thus, ionization spectra [15, 16]. On the other hand, a pioneering study on *n*-butane has demonstrated the suitability of EMS for tracing molecular conformations [15], provided this influence is correctly accounted for in the modeling. It is clear that the interpretation of EMS experiments is most often very difficult and requires extensive theoretical work if the analysis is to have any value at all.

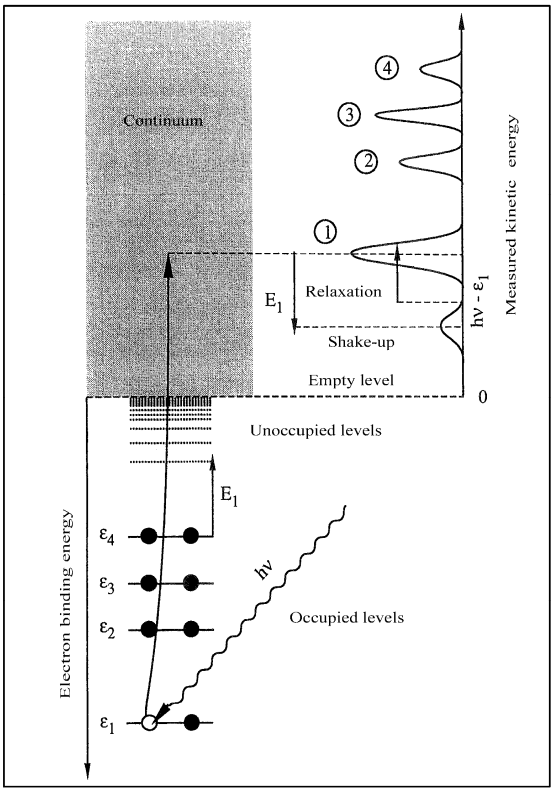

Figure 1. Sketch of the one-electron and two hole – one particle excited states (shake-up) in an ionization spectrum.

An other difficult issue that can still be hardly handled nowadays pertain to the role played by vibronic coupling interactions and ultrafast nuclear dynamical effects, which may culminate in the form of Coulomb explosion processes when multiple electron vacancies are created. We refer here in particular to the Intermolecular Coulomb Decay (ICD) mechanism, which was proposed by Cederbaum *et al.* for predicting the fate of deep inner vacancies in H_2O, HF and Ne clusters [17], and which has been recently confirmed through band width measurements in synchrotron experiments [18]. According to this mechanism, an outer-valence electron of the ionized monomer quenches into a deep inner vacancy and the released energy is transferred via photon exchange to a neighboring monomer, which results into an ionization of the second monomer within a very short timescale. This electronic decay is then followed by a Coulomb explosion of the doubly ionized cluster, which is bound by weak dispersion forces. As shall be seen, electrostatic repulsions in doubly ionized and cyclically strained molecules can also be strong enough to analogously result into an ultrafast Coulomb explosion of these compounds, which may lead to specific fingerprints in EMS experiments.

In the present thesis, we will rely extensively on the so-called third-order algebraic diagrammatic construction scheme [ADC(3)] [19] derived within the framework of one-particle Green's function (1p-GF) theory [20] for calculating valence one-electron and shake-up ionization states. The efficiency and accuracy of this approach has been amply illustrated by applications on large systems, such as carbon clusters [11, 18e, 21], or polycyclic aromatic hydrocarbons [22]. Within this scheme, the scattering potential is described with the right asymptotics and Dyson orbitals are computed through third order in correlation. ADC(3) enables therefore calculations of ionization energies and Dyson orbitals at a level of accuracy comparable to that of the benchmark multireference single-double configuration-interaction (MR-SDCI) scheme [23] with the advantages of size consistency [24] and of a greater compactness of the secular matrices to diagonalize.

In order to correctly pinpoint the lowest stationary points of conformationally versatile molecules within the confines of non-relativistic quantum mechanics, the convergence of the conformational energy differences towards the exact solution of the Schrödinger equation can be exploited by pairing increasingly complex levels of theory with basis sets of improving quality in a Focal Point Analysis (FPA) similar to that used by Allinger *et al.* for *n*-butane [25]. More specifically, highly reliable predictions will be achieved within an estimated accuracy of ~0.1 kcal mol^{-1} by means of well-suited extrapolations of results of single point calculations using CCSD(T) theory (Coupled Cluster Ansatz including single and double electronic excitations and supplemented by a perturbative treatment of triple excitations) to the limit of an asymptotically complete basis set.

The relative conformer abundances at different temperatures will be calculated according to Boltzmann thermostatistics by means of Gibbs' free energy differences derived from our best (FPA) estimates for the conformational energy differences, and statistical partition functions computed beyond the Rigid-Rotor/Harmonic-Oscillator (RRHO) approximation, taking into account the influence of hindered rotations.

Besides all these physico-chemical effects, the limited energy and momentum resolutions of the (e,2e) spectrometers must also be taken into account using appropriate convolution procedures. More specifically, in order to deal with the limited resolution in momentum space, the conversion of orbital densities to momentum space will be carried out by means of the Gaussian Weighted Planar Grid (GW-PG) method of Duffy *et al.* [26], whereas Gaussian spread functions with a width that account both for vibrational broadening as well as the experimentally achieved energy resolution will be used to convolute the theoretical one-electron and shake-up ionization spectra.

In the present thesis, we will specifically focus on EMS studies of two very opposite kinds of molecular species, namely rigid cage compounds (norbornane, norbornene, stella-2,6-diene, stella-2,6-dione, bicyclo [2.2.2] octane-2,5-dione and bicyclo [2.2.1] heptane-2,5-dione) and conformationally flexible molecules (1,3-butadiene, *n*-pentane, dimethoxymethane, biphenyl). For the former ones, the main focus lies essentially on the identification of spectral fingerprints for through-bond π-conjugation, cyclic strains and distortions of the molecular structure using the standard Kohn-Sham orbital depiction for the experimentally observed momentum distributions. For the latter ones, the computed electron binding energies and momentum distributions will be exploited to "image", i.e. experimentally reconstruct, the topological changes that molecular orbitals undergo due to torsion of the molecular backbone. Our main purpose here is to provide benchmark results for assessing the potential of EMS in probing the molecular conformation and its interplay with the molecular architecture, using the best methods that are available nowadays for computing (1) molecular structures, (2) relative energy differences, (3) conformational abundances, (4) ionization spectra, and (5) momentum space orbital densities. In line with this, a detailed study of the electronic structure of biphenyl is also presented using Penning Ionization Electron Spectroscopy and one-particle Green's function theory. As a byproduct, we will emphasize through studies of test molecules (difluoromethane, water) the limitations of the Hartree-Fock and DFT approaches in the theoretical analysis of EMS experiments, and demonstrate that ADC(3) Dyson orbitals provide a very robust alternative for computing electron momentum distributions. For these species, comparison will be made with results obtained by multi-reference methods and the Symmetry Adapted Cluster Configuration Interaction (SAC-CI) theory [27].

References

[1] Löwdin, P. O.; Bullman, P. (Eds.), *Molecular orbitals in chemistry, physics, and biology, a tribute to R. S. Mulliken*, Academic Press, New York, 1964.

[2] Young, H. D.; Freedman, R. A., *University Physics*, Addison-Wesley, Reading, Massachusetts,1996.

[3] (a) Silberberg, M. S., *Chemistry, The molecular nature of matter and change*, McGraw Hill, Boston, 2000. (b) March, J.; *Organic Chemistry*, J. Wiley & Sons, New-York, 1985. (c) Huhey, J. E.; *Inorganic Chemistry*, Harper international SI Edition, Cambridge, 1983. (d) Atkins, P. W.; *Physical Chemistry*, Oxford University Press, 1986.

[4] Kurz, W.; Mercier, J. P.; Zambelli, G.; *Introduction à la science des materiaux*, Presses Polytechniques Romandes, Lausanne, 1987.

[5] Villee, C. A.; Salomon, E. P.; Martin, C. E.; Davis, P. W.; *Biology*, Saunders College Publishing, Philadelphia, 1989.

[6] (a) Szabo, A.; Ostlund, N. S. *Modern Quantum Chemistry. Introduction to Advanced Electronic Structure Theory*; Dover: New York, 1996. (b) McWeeny, R.; *Methods of molecular quantum mechanics*; Academic Press, London, 1989.

[7] (a) McCarthy, I. E.; Weigold, E. *Rep. Prog. Phys.* 1988, *51*, 299. (b) McCarthy, I. E.; Weigold, E. *Rep. Prog. Phys.* 1991, *54*, 789. (c) Coplan, M.A.; Moore, J.H.; Doering, J.P. *Rev. Mod. Phys.* 1994, 66, 985. (d) Weigold, E.; McCarthy, I. E. *Electron Momentum Spectroscopy*; Kluwer Academic/Plenum Publishers: New York, 1999.

[8] (a) Čermák, V. *J. Chem. Phys.* 1966, 44, 3781. (b) Niehaus, A.; *Adv. Chem. Phys.* 1981, 45, 399. (c) Yencha, A. J. *Electron Spectroscopy: Theory, Technique, and Applications*, Vol. 5, Brundle, C. R.; Baker, A. D.; Eds.; Academic, New York, 1984.

[9] Koopmans, T. A. Physica (Amsterdam) 1933, 1, 104.

[10] Deleuze, M. S.; Cederbaum, L. S. *Int. J. Quantum Chem.* 1997, 63, 465.

[11] Deleuze, M. S.; Giuffreda, M. G.; François, J.-P.; Cederbaum, L. S. *J. Chem. Phys.* 2000, 112, 5325.

[12] Deleuze, M. S.; Trofimov, A. B.; Cederbaum, L. S. *J. Chem. Phys.* 2001, 115, 5859.

[13] Potts, A. W.; Holland, D. M. P.; Trofimov, A. B.; Schirmer, J. Karlsson, L.; Siegbahn, K. *J. Phys. B* 2003, 36, 3129.

[14] Deleuze, M. S. *Chem. Phys.* 2006, 329, 22.

[15] (a) Deleuze, M.; Delhalle, J.; Pickup, B. T. *Chem. Phys.* 1993, 175, 427. (b) Deleuze, M.; Delhalle, J.; Pickup, B. T.; Svensson, S. *J. Am. Chem. Soc.* 1994, 116, 10715. (c) Deleuze, M.; Denis, J.-P.; Delhalle, J.; Pickup, B. T. *J. Phys. Chem.* 1993, 97, 5115. (d) Deleuze, M.; Delhalle, J.; Mosley, D. H.; André, J. M. *Physica Scripta* 1995, 51, 111. (e) Deleuze, M. S.; Cederbaum, L. S. *J. Chem. Phys.* 1996, 105, 7583.

[16] Deleuze, M. S.; Pang, W. N.; Salam, A.; Shang, R. C. *J. Am. Chem. Soc.* 2001, 123, 4049.

[17] (a) Cederbaum, L.S.; Zobeley, J., Tarantelli, F.; *Phys. Rev. Lett.* 1997, *79*, 4778. (b) Zobeley, J.; Cederbaum, L.S.; Tarantelli, F.; *J. Chem. Phys.* 1998, *108*, 9737. (c) Santra, R.; Zobeley, J.; Cederbaum, L.S.; Moiseyev, N.; *Phys. Rev. Lett.* 2000, 85, 4490.

[18] Jahnke, T.; Czasch, A.; Schöffler, M. S.; Schössler, S.; Knapp, A.; Käsz, M.; Titze, J.; Wimmer, C.; Kreidi, K.; Grisenti, R. E.; Staudte, A.; Jagutzki, O.; Hergenhahn, U.; Schmidt-Böcking, H.; Dörner, R. *Phys. Rev. Lett.* 2004, 93, 163401.

[19] (a) Schirmer, J.; Cederbaum, L. S.; Walter, O. *Phys. Rev. A* 1983, 28, 1237. (b) von Niessen, W., Schirmer, J. Cederbaum, L. S. *Comput. Phys. Rep.* 1984, 1, 57. (c) Schirmer, J.; Angonoa, G. *J. Chem. Phys.* 1989, 91, 1754. (d) Weikert, H.-G.; Meyer, H. D.; Lederbaum, L. S.; Tarantelli, F. *J. Chem. Phys.* 1996, 104, 7122. (e) Deleuze, M.S.; Deleuze, M. S.; Giuffreda, M. G.; François, J.-P.; Cederbaum, L. S. *J. Chem. Phys.* 1999, 111, 5851.

[20] (a) Linderberg, J.; Öhrn, Y. *Propagators in Quantum Chemistry*; Academic Press, London, 1973. (b) Pickup, B. T.; Goscinski, O. *Mol. Phys.* 1973, 26, 1013. (c) Cederbaum, L. S.; Hohlneicher, von Niessen, W. *Mol. Phys.* 1973, 26, 1405. (d) Cederbaum, L. S.; Domcke, W. *Adv. Chem. Phys.* 1977, 36, 205. (e) Herman, M. F.; Freed, K. F.; Yeager, D. L. *Adv. Chem. Phys.* 1981, 48, 1. (f) Öhrn, Y.; Born, G. *Adv. Quantum Chem.* 1981, 13, 1.

[21] Deleuze, M. S.; Giuffreda, M. G.; François, J.-P. *J. Phys. Chem. A* 2002, 106, 5626.

[22] (a) Deleuze, M. S. *J. Chem. Phys.* 2002, 116, 7012. (b) Deleuze, M. S. *J. Phys. Chem. A* 2004, 108, 9244. (c) Deleuze, M. S. *Chem. Phys.* 2006, 329, 22.

[23] Zheng, Y.; Pang, W. N.; Shang, R. C.; Chen, X. J.; Brion, C. E.; Ghanty, T. K.; Davidson, E. R. *J. Chem. Phys.* 1999, 111, 9526.

[24] (a) Deleuze, M.; Delhalle, J.; Pickup, B. T.; Calais, J. L. *Phys. Rev. B* 1992, 46, 15668. (b) Deleuze, M.; Delhalle, J.; Pickup, B. T.; Calais, J. L. *Adv. Quantum Chem.* 1995, 26, 35. (c) Deleuze, M.; Pickup, B. T. *J. Chem. Phys.* 1995, 102, 8967.

[25] Allinger, N. L.; Fermann, J. T.; Allen, W. D.; Schaefer III, H. F. *J. Chem. Phys.* 1997, 106, 5143.

[26] Duffy, P.; Casida, M. E.; Brion, C. E.; Chong, D. P. *Chem. Phys.* 1992, 159, 347.

[27] See: Nakatsuji, H. *Chem. Phys. Lett.* 1991, 177, 331; and references therein.

Part 2: Theoretical methods

2.1 Hartree-Fock theory

The first objective of all quantum chemistry calculations is to find an approximate solution to the non-relativistic time-independent Schrödinger equation [1-5]

$$\hat{H}\Psi = E\Psi, \tag{1a}$$

where $\hat{H}$ is the Hamiltonian operator for a system of nuclei and electrons described by their position vectors $\mathbf{R}_A$ and $\mathbf{r}_i$, respectively. In atomic units, it is given by

$$\hat{H} = -\frac{1}{2}\sum_{i}^{electrons}\nabla_i^2 - \frac{1}{2}\sum_{A}^{nuclei}\frac{1}{M_A}\nabla_A^2 - \sum_i\sum_A\frac{Z_A}{r_{iA}} + \sum_{i>j}\frac{1}{r_{ij}} + \sum_{A<B}\frac{Z_A Z_B}{R_{AB}}. \tag{1b}$$

Ψ is the total wave function and depends on the Cartesian coordinates of the particles of the given system and on the spin coordinates. E is the total energy of the system. By solving this equation, a variety of molecular properties can be calculated such as equilibrium structures, vibrational spectra, atomic charges, dipole moments, relative stabilities of the states,…

For a many-electron system the Hamiltonian $\hat{H}$ is a sum of terms. The first two are operators of the kinetic energy of electrons and nuclei, respectively. The third term represents the Coulomb attraction between electrons and nuclei and the last two terms represent the repulsion between electrons and between nuclei, respectively.

In order to solve the Schrödinger equation (1), a number of approximations are needed. The first of these is the Born-Oppenheimer approximation [6]. By considering the fact that the mass of a proton in the atomic nucleus is 1836 times larger than the mass of an electron, Born and Oppenheimer were able to show that an approximate solution of eq. (1) can be written as a product of the so-called electronic and nuclear wave functions. The electronic wave function and the corresponding electronic energy can be obtained by solving the Schrödinger equation assuming the nuclei in a fixed position. The nuclear Schrödinger equation, describing the motion of nuclei, is then solved using as potential function the electronic energy.

In the Born-Oppenheimer approximation, the terms of kinetic energy and the repulsion of the nuclei can be neglected, as they are considered as constant, which means that they affect only the operator and not the operator eigenfunctions. So, the remaining terms build up the so-called electronic Hamiltonian of the *N*-electron system

$$\hat{H}_{elec} = -\sum_{i=1}^{N}\frac{1}{2}\nabla_i^2 - \sum_{i=1}^{N}\sum_{A=1}^{M}\frac{Z_A}{r_{iA}} + \sum_{i=1}^{N}\sum_{j>i}^{N}\frac{1}{r_{ij}}, \tag{2.a}$$

where

$$-\sum_{A=1}^{M}\frac{Z_A}{r_{iA}} = v(\mathbf{r}_i) \tag{2.b}$$

defines an "external" potential acting on electron *i*, and is due to the charges z_A of the *M* nuclei. Furthermore, ∇_i^2 is the Laplacian operator for the *i-th* electron, r_{iA} is the distance between the electron *i* and the nucleus *A*, while r_{ij} is the distance between the *i-th* and *j-th* electrons.

The solution of the electronic Schrödinger equation

$$\hat{H}_{elec}\Psi_{elec} = E_{elec}\Psi_{elec} \tag{3}$$

yields the electronic wave function

$$\Psi_{elec} = \Psi_{elec}\left\{(\mathbf{r}_i);(\mathbf{R}_A)\right\}, \tag{4}$$

describing the motion of the electrons. It depends explicitly on the electron coordinates and parametrically on the nuclear coordinates. As a consequence, the electronic energy depends parametrically on the nuclear coordinates $E_{elec} = E_{elec}(\{\mathbf{R}_A\})$.

The total energy for a fixed set of nuclei must also include the constant nuclear repulsion

$$E_{tot} = E_{elec} + \sum_{A=1}^{M}\sum_{B>A}^{M}\frac{z_A z_B}{R_{AB}}. \tag{5}$$

The above energy provides a potential for nuclear motions. More specifically, within the framework of the Born-Oppenheimer approximation, the nuclei move on a potential energy surface obtained by solving the electronic problem [eq. (3)] and by adding to the electronic energy the nuclear energy repulsion term [eq. (5)].

The solution of the nuclear Schrödinger equation

$$\hat{H}_{nucl}\Psi_{nucl} = E\Psi_{nucl}, \tag{6a}$$

with

$$\hat{H} = -\frac{1}{2}\sum_{A=1}^{M}\frac{1}{M_A}\nabla^2 + E_{tot}(\{\mathbf{R}_A\}) \tag{6b}$$

is important because Ψ_{nucl} describes the translation and internal motions of a molecule, i.e. rotations and vibrations (see also section 2.11). Ψ_{nucl} is a function of the nuclear coordinates $\mathbf{R}_A$ and *E* is the Born-Oppenheimer approximation of the total energy in eq. (1), which includes the electronic, vibrational, rotational and translational energy of the system. The total wave function of the system is approximated as:

$$\Psi(\{\mathbf{r}_i\};\{\mathbf{R}_\mathbf{A}\}) = \Psi_{elec}(\{\mathbf{r}_i\};\{\mathbf{R}_\mathbf{A}\})\Psi_{nucl}(\{\mathbf{R}_\mathbf{A}\}). \tag{7}$$

The Hamiltonians defined so far correspond to point particles interacting in a non-relativistic way through forces which have a purely Coulomb character. In reality, nuclei have a finite size and the electronic motion is relativistic. It is known that relativistic effects start to become significant with molecules containing atoms of the size equal to or larger than that of the sodium atom $(z = 11)$.

The electronic Hamiltonian, defined by eq. (2a), depends only on the spatial coordinates of the electrons of the system. In order to complete the description of an electron, it is necessary to specify its spin angular momentum or, more shortly, its spin. Experiments have shown that, in atomic units, the eigenvalue of the projector operator onto a priviledged axis (for instance that of an external magnetic field) of the spin angular momentum can be either +1/2 or -1/2. The corresponding eigenstates are usually called spin up (α) and spin down (β), respectively..

At this point, in order to obtain physically acceptable solutions of the electronic Schrödinger equation [eq. (2a)], one has to impose a restriction on the wave functions. Due to the indistinguishability of identical particles, any pair of particles can be described either by symmetric or antisymmetric wave functions, depending on the nature of the particles themselves. In other words, the wave functions must have the appropriate symmetry under the interchange of pairs of identical particles. The first category of wave functions describes the so-called boson particles, whereas the latter one describes the fermion particles. Relativistic quantum mechanics shows that such a property of the particles is unambiguously connected with their spin: particles with half-integer spin are fermions, whereas bosons, having integer spin, follow the Bose-Einstein statistics. As electrons are fermions, the wave functions ψ must be antisymmetric with respect to the interchange of the coordinates of any pair of electrons, which is known as Pauli's exclusion principle or as the antisymmetry principle.

The main aim of theoretical studies on electronic structure is to solve the electronic Schrödinger equation in an approximate way, and hence finding the electronic energy $E_{elec}\{\mathbf{R}_A\}$ as a function of the coordinates of the nuclei. In this purpose, another approximation in the electronic wave function Ψ is usually introduced. For a system containing N independent and non-interacting electrons, Ψ is written as a normalized antisymmetric product function of N orthonormalized one-electron wave functions χ_i, known as spin orbitals. The wave function Ψ can be written in determinantal form as

$$\Psi = \frac{1}{\sqrt{N!}} \begin{vmatrix} \chi_1(1) & \chi_2(2) & \cdots & \chi_N(1) \\ \chi_1(2) & \chi_2(2) & \cdots & \chi_N(2) \\ \vdots & \vdots & & \vdots \\ \chi_1(N) & \chi_2(N) & \cdots & \chi_N(N) \end{vmatrix}. \tag{8}$$

The spin orbitals $\chi_j(i) \equiv \chi_j(\mathbf{x}_i)$ depend on both the spatial (x_i, y_i, z_i) and spin (ω_i) coordinates of the electrons and are defined as the product of a space function and a spin function: $\chi_j(\mathbf{x}_i) = \psi_j(x_i, y_i, z_i)\sigma(\omega_i)$. In eq. (8), Ψ is known as the normalized Slater determinant wave function.

As no mathematical method can be found to deliver the exact solution of the electronic Schrödinger equation for most of the systems under study, approximate methods are needed for obtaining the eigenfunctions and corresponding eigenvalues. Approximate solutions can be obtained using the variation theorem. This theorem states that if E_0 is the eigenvalue of the Hamiltonian operator $\hat{H}$ corresponding to the ground state energy of a given system, then for any wave function Ψ depending on the same coordinates in which the Hamiltonian is expressed, the following holds

$$E[\Psi] = \frac{\int_\tau \Psi^* \hat{H} \Psi d\tau}{\int_\tau \Psi^* \Psi d\tau} \geq E_0, \tag{9}$$

which means that the expectation value of the Hamiltonian is an upper bound to the exact ground state energy. The equality is valid only when $\Psi = \Psi_0$, which is solution of the Schrödinger equation $\hat{H}\Psi_0 = E_0\Psi_0$ for the ground state of an N-electron system. It should be noted that $E : \Psi \to E[\Psi]$ is a functional of the wave function.

The Hartree-Fock approximation [7, 8] allows to find a set of spin orbitals $\{\chi_i\}$ such that the single determinant Ψ, build up from these spin orbitals, is the best possible approximation to the ground state of the N-electron system described by the electronic Hamiltonian $\hat{H}$. This means that it is necessary to find the set of orthonormal spin orbitals which minimizes the electronic energy of the system. Optimizing the spin-orbitals according to a variational procedure and under the constraint of orthonormality leads to a set of coupled integro-differential equations known as the Hartree-Fock equations [1-5]:

$$\hat{f}(1)\chi_i(1) = \varepsilon_i \chi_i(1), \tag{10}$$

where ε_i is the total energy for spin orbital χ_i. $\hat{f}(1)$ is the Fock operator given by

$$\hat{f}(1) = \hat{h}(1) + \sum_j [\hat{J}_j(1) - \hat{K}_j(1)]. \tag{11}$$

In eq. (11) the term $\hat{h}(1)$ is the one electron operator

$$\hat{h}(1) = -\frac{1}{2}\nabla_i^2 - \sum_{\alpha=1}^{N} \frac{z_A}{r_{1\alpha}} \tag{12}$$

The two terms in eq. (12) account for the kinetic energy and the nuclear-electronic attraction, respectively.

$\hat{J}_j(1)$ is a local operator, referred to as the Coulomb operator

$$\hat{J}_j(1) = \int \chi_j^*(2) \frac{1}{r_{12}} \chi_j(2) d\tau_2 . \tag{13}$$

$\hat{K}_j(1)$ is a non-local operator known as the exchange, operator defined by its effect when operating on a spin orbital $\chi_j(1)$ as

$$\hat{K}_j(1)\chi_i(1) = \left[\int \chi_j^*(2) \frac{1}{r_{12}} \chi_i(2) d\tau_2\right] \chi_j(1). \tag{14}$$

Since these operators depend on the spin-orbitals, the Hartree-Fock equations can only be solved iteratively. The solution of the Hartree-Fock eigenvalue problem [eq. (10)] yields a set $\{\chi_i\}$ of orthonormal Hartree-Fock spin orbitals with orbital energies $\{\varepsilon_i\}$. The N spin orbitals with the lowest energies and "carrying" the electrons are called the occupied orbitals. Throughout this thesis, these orbitals are labelled by the indices $i, j, k, \ldots$ The remaining members of the set $\{\chi_i\}$ are called virtual or unoccupied spin orbitals, which will be labelled by the indices $r, s, t\ldots$

In order to understand the physical meaning of the orbital energies ε_i and ε_r, it is useful to consider their expansion in a set of spin orbitals. The final expressions are:

$$\varepsilon_i = \langle i|\hat{h}|i\rangle + \sum_{j\neq i}\left(\langle ij|ij\rangle - \langle ij|ji\rangle\right), \tag{15}$$

$$\varepsilon_r = \langle r|\hat{h}|r\rangle + \sum_{j}\left(\langle rj|rj\rangle - \langle rj|jr\rangle\right). \tag{16}$$

Here ε_i represents the energy of the i^{th} electron in the spin orbital $|\chi_i\rangle$. The first term on the right hand-side of eq. (15) refers to the kinetic energy of the i^{th} electron and the electronic-nuclear attraction, while the $\langle ij|ij\rangle$ and $\langle ij|ji\rangle$ terms are coulomb and exchange interactions with each of the remaining $N-1$ electrons located in the $N-1$ orbitals $|\chi_j\rangle$ with $j \neq i$, respectively. The expression for ε_r is almost the same, but it must be noted that it includes the coulomb and exchange interactions with all N electrons of the Hartree-Fock ground state $|\Psi_0\rangle$. Taking the sum of the orbital energies ε_i for each of the N electrons in the ground state $|\Psi_0\rangle$, the following expression is obtained:

$$\sum_i^N \varepsilon_i = \sum_i^N \langle i|\hat{h}|i\rangle + \sum_i^N\sum_j^N \langle ij||ij\rangle, \tag{17}$$

with $\langle ij||ij\rangle \equiv \langle ij|ij\rangle - \langle ij|ji\rangle$.

Knowing that the energy for the Hartree-Fock ground state is

$$E_0 = \sum_i^N \langle i|\hat{h}|i\rangle + \frac{1}{2}\sum_i^N\sum_j^N \langle ij||ij\rangle, \tag{18}$$

it is clear that

$$E_0 \neq \sum_i^N \varepsilon_i, \tag{19}$$

which means that the total energy of the ground state $|\Psi_0\rangle$ is not simply the sum of the orbital energies. In this respect, two different processes have to be considered: the first one consisting in adding one electron to an N-electron state $|\Psi_0\rangle = |{}^N\Psi_0\rangle = |\chi_1\chi_2\cdots\chi_\kappa\cdots\chi_N\rangle$ and the other one consisting in subtracting one electron from the same system. In the first case, when one electron is removed from a given orbital χ_k, a $(N-1)$-electron single determinant state $|{}^{N-1}\Psi_k\rangle = |\chi_1\chi_2\cdots\chi_{k-1}\chi_{k+1}\cdots\chi_N\rangle$ is obtained, with the remaining spin orbitals being identical to those in

$\left|{}^{N}\Psi_0\right\rangle$. The ionization potential, which is the energy required to remove one electron from the state $\left|{}^{N}\Psi_0\right\rangle$ is

$$IP = {}^{N-1}E_k - {}^{N}E_0 . \tag{20}$$

${}^{N-1}E_k$ and ${}^{N}E_0$ are the expectation energy values for the two single determinants describing the systems; their expressions are

$${}^{N}E_0 = \sum_i \langle i|\hat{h}|i\rangle + \frac{1}{2}\sum_i\sum_j \langle ij||ij\rangle , \tag{21}$$

$${}^{N-1}E_k = \sum_{i\neq k} \langle i|\hat{h}|i\rangle + \frac{1}{2}\sum_{i\neq k}\sum_{j\neq k} \langle ij||ij\rangle . \tag{22}$$

Assuming that the spin orbitals of the two considered states are identical, the energy difference, which is precisely the ionization potential, can be calculated as

$$\begin{aligned} IP &= {}^{N-1}E_k - {}^{N}E_0 \\ &= -\langle k|\hat{h}|k\rangle - \sum_j \langle kj||kj\rangle \end{aligned} . \tag{23}$$

Comparing this result with eq. (15) for an occupied spin orbital energy, it is easy to show that the ionization potential for removing one electron from the orbital χ_k is simply the negative of the orbital energy ε_k:

$$\begin{aligned} IP &= {}^{N-1}E_k - {}^{N}E_0 \\ &= -\varepsilon_k \end{aligned} . \tag{24}$$

Following the previous procedure for the process of adding one electron to a virtual spin orbital χ_r of the state $\left|{}^{N}\Psi_0\right\rangle$ and knowing already that the expression of the electron affinity is

$$EA = {}^{N}E_0 - {}^{N+1}E_r , \tag{25}$$

where ${}^{N+1}E_r$ is the energy of a single determinant $\left|{}^{N+1}\Psi_0\right\rangle$, the following similar result is obtained

$$\begin{aligned} EA &= {}^{N}E_0 - {}^{N+1}E_r \\ &= -\varepsilon_r \end{aligned} . \tag{26}$$

Thus, after a change of sign, the energy ε_k of an occupied spin-orbital χ_k in the single determinant approximation is the energy needed to remove one electron from χ_k, whereas the energy ε_r of an unoccupied spin orbital χ_r is the energy required to add one electron to χ_r (Koopmans' theorem) [1, 9].

2.1.1. Restricted closed-shell Hartree-Fock theory: the Roothaan-Hall equations

The restricted closed-shell formalism is basically introduced to describe systems with an even number of N-electrons. The restricted spin orbitals are constrained to have the same spatial function for the α ("spin up") and the β ("spin down") spin functions. The contributions of Hall [10], and independently, of Roothaan [11] to this formalism consisted in showing how, by introducing a set of known spatial basis functions, the spatial integro-differential equation can be converted into a set of algebraic equations which can be solved by standard matrix techniques.

Shortly, the application of this theory to molecular systems consists in expressing the unknown molecular orbitals $\psi_i(\mathbf{r})$ as a linear combination of a finite set of K known basis functions $\{\phi_\mu(\mathbf{r})|\mu=1,2,\ldots K\}$:

$$\psi_i = \sum_{\mu=1}^{K} c_{\mu i}\phi_\mu , \qquad i=1,2,\ldots K , \qquad (27)$$

with $c_{\mu i}$ the molecular orbital expansion coefficients. The more complete the basis set $\{\phi_\mu\}$ becomes, the more accurate is the representation of the "exact" molecular orbitals. In simple versions of molecular orbital theory, atomic orbitals of the atoms involved in the system under study are used as basis functions. These treatments are usually referred to as Linear Combination of Atomic Orbitals (LCAO) theories. In practice, any set of functions described in an appropriate way can be used for a basis expansion. At this point, the problem of calculating the Hartree-Fock molecular orbitals is reduced to the calculation of the set of the molecular orbital expansion coefficients $c_{\mu i}$.

Expressing the Hartree-Fock equations in matrix form, the so-called Roothaan-Hall equations are obtained:

$$\mathbf{FC} = \mathbf{SC}\varepsilon . \qquad (28)$$

$\mathbf{F}$ is the Fock matrix whose elements are

$$F_{\mu\nu} = \int \phi_\mu^*(1)\hat{f}(1)\phi_\nu(1)dr_1 . \qquad \mu,\nu = 1,2\ldots K \qquad (29)$$

This matrix can also be expressed in terms of the core-Hamiltonian matrix, two electron repulsion integrals and in the one-electron density matrix as described in detail by Szabo and Ostlund [1].

$\mathbf{S}$ is the overlap matrix with elements

$$S_{\mu\nu} = \int \phi_\mu^*(1)\phi_\nu(1)dr_1 , \qquad \mu,\nu = 1,2\ldots K . \qquad (30)$$

$\mathbf{C}$ is a $K \times K$ square matrix of the expansion coefficients $c_{\mu i}$ and ε is a diagonal matrix of the orbital energies ε_i. It is clear therefore that the problem of finding the Hartree-Fock molecular orbitals $\{\psi_i\}$ and orbital energies ε_i inevitably involves solving the Roothaan-Hall matrix equation eq. (28).

It should be remarked that the basis, introduced in practical calculations, is not orthogonal. The first important step is the orthogonalization of the basis so that the transformed Roothaan-Hall equations

$$\mathbf{F}'\mathbf{C}' = \mathbf{C}'\varepsilon \tag{31}$$

have the form of a matrix eigenvalue problem. A full description of the transformation is presented in [1].

In order to solve the transformed equation in an efficient way, an iterative procedure is set up. The first step is to make an initial guess of the expansion coefficients and a transformed Fock matrix $\mathbf{F}'$ is constructed. By diagonalizing this matrix new coefficients and orbital energies are obtained. The new coefficients are then used to build a new Fock matrix and this procedure is repeated until the orbital energies or the coefficients are smaller than a certain threshold. This procedure constitutes the so-called Self Consistent Field (SCF) procedure.

There are two types of basis functions in widespread use. The first type are Slater-type orbitals (STO's) and the second one are Gaussian-type orbitals (GTO's). It is practically impossible to give an exhaustive description of the large number of existing Gaussian basis sets. Detailed surveys are available in the literature [1, 3, 12-18]. The selection of a basis set is determined by the molecular system under study and by the properties on which the interest is focused.

2.1.2 Spin-unrestricted open-shell Hartree-Fock Theory: the Pople-Nesbet equations

Up to now the theory has been limited to closed-shell systems where the orbitals $\chi_i(\mathbf{x})$ have the same spatial orbitals $\psi_i(\mathbf{r})$ and differ only for the spin functions. Unfortunately, molecular species in certain electronic states cannot all be described in this way. There are cases where a molecule has one or more unpaired electrons so that the electrons cannot completely be assigned to orbitals in pairs. The Roothaan-Hall equations need to be modified therefore. In the spin-unrestricted Hartree-Fock (UHF) theory, different spatial orbitals are assigned to α and β electrons:

$$\chi_i(\mathbf{x}) = \begin{cases} \psi_i^{\alpha}(\mathbf{r})\alpha(\omega) \\ \psi_i^{\beta}(\mathbf{r})\beta(\omega) \end{cases}. \tag{32}$$

The electrons of α and β spin are thus described by two different sets ψ_i^{α} and ψ_i^{β}, respectively.

In order to solve the unrestricted Hartree-Fock (UHF) equations, a basis is introduced again to convert the integro-differential equations into matrix equations. At this point, a set of basis functions $\{\phi_\mu | \mu = 1,2,\ldots K\}$ is introduced and the unrestricted molecular orbitals are expanded in this set:

$$\psi_i^{\alpha} = \sum_{\mu=1}^{K} c_{\mu i}^{\alpha}\phi_\mu , \qquad \psi_i^{\beta} = \sum_{\mu=1}^{K} c_{\mu i}^{\beta}\phi_\mu , \qquad i = 1,2,\ldots,K . \tag{33}$$

The coefficients $c_{\mu i}^{\alpha}$ and $c_{\mu i}^{\beta}$ are varied independently, leading to the following matrix equations:

$$\left.\begin{array}{l}\mathbf{F}^{\alpha}\mathbf{C}=\mathbf{S}\mathbf{C}^{\alpha}\boldsymbol{\varepsilon}^{\alpha}\\ \mathbf{F}^{\beta}\mathbf{C}=\mathbf{S}\mathbf{C}^{\beta}\boldsymbol{\varepsilon}^{\beta}\end{array}\right\},\qquad \text{or} \tag{34}$$

$$\left.\begin{array}{l}\sum\limits_{\nu=1}^{K}\left(F_{\mu\nu}^{\alpha}-\varepsilon_i^{\alpha}S_{\mu\nu}\right)c_{\mu i}^{\alpha}=0\\ \sum\limits_{\nu=1}^{K}\left(F_{\mu\nu}^{\beta}-\varepsilon_i^{\beta}S_{\mu\nu}\right)c_{\mu i}^{\beta}=0\end{array}\right\},\qquad \mu=1,2,\ldots,K\,. \tag{35}$$

Eqs. (34) or (35) are the UHF generalization of the Roothaan-Hall equations, and are known as the Pople-Nebset equations.

The Fock matrices can be expressed in terms of the overlap matrix, the core-Hamiltonian matrix, two electron repulsion integrals and the one-electron density matrices. Moreover, the integrals $S_{\mu\nu}$, $H_{\mu\nu}^{core}$ and $\left(\mu\nu|\lambda\sigma\right)$ are the same as those of the Roothaan-Hall equations for closed-shell systems. It should be remarked that the two sets of equations [eqs. (35)] are coupled via the density matrices and can only be solved iteratively. Since the UHF wave functions are not true eigenfunctions of the total spin operator $\hat{S}^2$, they are contaminated by functions corresponding to states with higher multiplicity. This represents the main important disadvantage of the UHF theory.

2.2 Electron correlation effects

Although the Hartree-Fock theory is remarkably successful in many cases, at least from a qualitative viewpoint, it shows also serious limitations due to the fact that it does not treat adequately the correlation between the motions of the electrons. The single determinant used in the HF theory does not take into account the correlation between electrons with opposite spin. Note however that the motion of the electrons with the same spin is already partly accounted for by virtue of the determinantal form of the wave function and its antisymmetry with respect to particle interchange, which prevents two electrons with the same spin from occupying the same region of space. Since the effect of electron correlation cannot be observed, the correlation energy (Fermi correlation, see further) [19] is a purely theoretical concept. It is usually defined as the error which is made on the electronic energy in the limit of a single determinantal description and basis completeness:

$$E_{corr}=E-E_{HF}<0\,, \tag{36}$$

where E and E_{HF} are the exact nonrelativistic Born-Oppenheimer energy of the system and the HF energy, respectively.

Since some properties of atoms and molecules depend directly on the electronic energy, it is clear that they are affected also by the correlation energy and by the accuracy with which it is calculated. For example, in molecules the equilibrium geometry is determined by the energy and it has been shown that, when the correlation energy is included the agreement with the experiment is very good and systematic. Correlation energy is also important in the determination of the shape of potential energy curves and surfaces, due to the effect on the values of fundamental vibrational frequencies, and in the determination of dipole moment or of second order properties like polarizability.

Theories which describe properly electron correlation need to satisfy some important requirements:

- The calculated electronic energy must be *variational*, which means it has to be an upper bound to the energy that would be obtained from exact solution of the electronic Schrödinger equation. If the energy is calculated as an expectation value of the Hamiltonian according to the variational theorem then this requirement is satisfied.
- They must be *size-consistent*, that is the energy of a many-particle system, even when there are interactions, should become proportional to the number of particles in the infinite limit. In other words, the energy of any system should be written as the sum of the energies of its component parts if these parts are placed at an infinite distance and this result does not depends on how these parts are defined. Size consistency is very important in calculating, for instance, molecular interaction energies, ionization energies, dissociation energies etc.
- Finally, in order to study many systems of relevance in chemistry, these theories should not lead to a rapid increase of *computational demands* with molecular size.

During the last decades, quantum chemists have developed numerous methods for treating electron correlation, such as Configuration Interaction (CI), Many-Body Perturbation Theory (MBPT), Coupled Cluster theories (CC), Density Functional Theory (DFT) and Many-Body Green's Function (MBGF) theory. The latter one provides mostly information on electron affinities and the ionization potential of an N -electron system.

At this point, before continuing the description and methods which go beyond the Hartree-Fock model, it is worth to summarize the most important effects related to electron correlation:

- *Fermi Correlation.* This correlation type is due to the repulsion between two electrons with the same spin and prevents them to be found in the same point of space. When the particles are fermions, like electrons, it is accounted for with the antisymmetric wave functions. Fermi correlation is already taken in account at the HF level of theory through the exchange integrals.
- *Near-Degeneracy.* This correlation effect, also known as non-dynamic correlation, is caused by the existence of exited states very close to the ground state energy.
- *Dynamical Correlation Energy.* This is defined as the difference between the total and near-degeneracy correlation energies.
- *Core Correlation.* This is a dynamical correlation and involves excitations from at least one occupied non-valence orbital. It can be also partitioned in core-core and core-valence correlation: the first one involves only excitation from core orbitals, whereas the latter involves excitations both from core and valence orbitals.

2.3 Configuration interaction

The conceptually simplest and most straightforward method to deal with electronic correlation is the Configuration Interaction (CI) method. This method was suggested since the thirties, but due to the limited computer capabilities at that time, CI applications began to appear only in the 1960's. A review article on CI has been published by Shavitt in 1977 [20]. Important developments have been made in the following years and some of them are discussed in the book by Mcweeny [2]. A more recent review (1990) of this subject has been written by Bauschlicher *et al.* [21].

Very generally, in this method, the single determinant Hartree-Fock wave function is extended to a wave function composed of a linear combination of many determinants in which the coefficients are optimized in a variational way. In other words, the basic idea consists in the diagonalization of an N-electron Hamiltonian in a basis of N-electron functions, which are Slater determinants. These determinants are obtained by selecting occupied and virtual orbitals generated previously using the Hartree-Fock or Multiconfigurational SCF (MCSCF) calculations. The name "configuration interaction" comes from the fact that the Slater determinants involved are commonly called configurations, whereas the interaction refers to off-diagonal elements of the $\mathbf{H}$ matrix described in the next section. The main problem of this method is that the number of determinants which can be generated scale like $(2K)!/\left[N!(2K-N)!\right]$, where N is the number of electrons and $2K$ is the number of spin orbitals, so it is clearly extremely large, even when the basis set used is rather small.

2.3.1. Full configuration interaction

In 1959, Löwdin formulated [22] a theorem which is fundamental in configuraction interaction (CI) theory. This theorem states that every antisymmetric wave function which is normalizable can be expanded as a sum of an infinite series of Slater determinants constructed from a complete basis set of one-electron functions, which defines an exact solution of the many-electron problem. Similarly, diagonalizing the finite secular matrix formed from a set of $(2K)!/\left[N!(2K-N)!\right]$ determinants that can be built in a finite set of spin-orbitals $\{\chi_1,\chi_2,\ldots,\chi_{2N}\}$ leads to solutions that are exact within the one-electron subspace spanned by these *2K* spin-orbitals, and define therefore the Full Configuration Interaction (FCI) limit in this subspace. The FCI solution becomes exact provided the basis set is complete.

Consider a wave function $\Psi_{ij\ldots p}(\mathbf{x}_1,\mathbf{x}_2,\ldots,\mathbf{x}_N)$ for an independent-particle model in which $2K$ spin orbitals $\chi_i,\chi_j,\ldots,\chi_p$ are occupied by N electrons, and suppose also that the Hartree-Fock problem using these basis functions has already been solved and the single-determinant wave function ψ_0 has been obtained as

$$\Psi_0 = (N!)^{-1/2}\det\left|\chi_1(\mathbf{1})\chi_2(\mathbf{2})\ldots\chi_N(\mathbf{N})\right|. \tag{37}$$

It is worth noting that the spin orbitals used here are a subset of the total set which has been determined in the variational procedure. The unused spin orbitals are the unoccupied ones, which as usual are denoted with the labels $r,s,t,\ldots$ In addition to $|\Psi_0\rangle$, a large number of different N-electron determinants can be formed from the $2K$ spin orbitals. These new determinants can also be described by defining how they differ from $\left|\Psi_0\right\rangle$. Thus, if the occupied spin orbitals $\chi_i, \chi_j, \ldots$ are substituted by virtual ones such as $\chi_r, \chi_s, \ldots$ then the possible determinants can be further classified into singly excited determinants $\left|\Psi_i^r\right\rangle$ in which the occupied spin orbital χ_i has been substituted by the virtual one χ_r, doubly excited determinants $\left|\Psi_{ij}^{rs}\right\rangle$ where the χ_i has been replaced by χ_r and χ_j by χ_s, triply excited determinants and so on until the N-tuply excited determinants. The general substitution determinant may be written as $\left|\Psi_{ijk\ldots}^{rst\ldots}\right\rangle$ where $i < j < k$ and $r < s < t$ in order to avoid repetition of the same configuration. In the FCI method, the following trial wave function is used:

$$\left|\Phi_0\right\rangle = c_0\left|\Psi_0\right\rangle + \sum_i c_i^r\left|\Psi_i^r\right\rangle + \sum_{\substack{i<j\\ r<s}} c_{ij}^{rs}\left|\Psi_{ij}^{rs}\right\rangle + \sum_{\substack{i<j<k\\ r<s<t}} c_{ijk}^{rst}\left|\Psi_{ijk}^{rst}\right\rangle + \ldots, \tag{38}$$

and the unknown coefficients c in the linear combination are determined according to the linear variational method.

The FCI method is the most complete treatment possible within the limitations imposed by a basis set. As the basis set becomes more complete, that is as $K \to \infty$, the result of a FCI treatment will approach the exact solution of a non-relativistic Schrödinger equation. The FCI method is size consistent and is variational. Unfortunately, FCI calculations are feasible only for very small systems due to the very large number of substituted determinants that are generated.

2.3.2 Truncated configuration interaction

The most straightforward manner of limiting the length of a CI expansion is to truncate the series of a given level of substitution. Inclusion of only single substitutions, termed Configuration Interaction Singles or CIS:

$$\left|\Phi_{cis}\right\rangle = \left|\Psi_0\right\rangle + \sum_i^{occ}\sum_r^{virt} c_i^r\left|\Psi_i^r\right\rangle \tag{39}$$

leads to no improvement to the Hartree-Fock wave function or energy for the ground state, by virtue of Brillouin's theorem, which rules out the mixing of the HF ground state with singly excited electronic configurations.

Therefore, the first scheme which leads to an improvement of the calculated energy is the Configuration Interaction Doubles or CID, which includes only doubly excited configurations:

$$\left|\Phi_{CID}\right\rangle = \left|\Psi_0\right\rangle + \sum_{i<j}^{occ}\sum_{r<s}^{virt} c_{ij}^{rs}\left|\Psi_{ij}^{rs}\right\rangle. \tag{40}$$

At a slightly higher level of theory, both single and double substitutions can be included in the CI treatment. The model is termed Configuration Interaction, Singles and Doubles, or CISD. As already stated, even if singly excitated states do not mix with the HF ground state, they do contribute to the wave function, since there are non-zero coupling elements over the Hamiltonian between singly and doubly excited determinants. However, the energy lowering due to the inclusion of single substitutions is much less than that due to the doubles. The trial CISD wave function is

$$\left|\Phi_{CISD}\right\rangle = \left|\Psi_0\right\rangle + \sum_{i}^{occ}\sum_{r}^{virt} c_i^r \left|\Psi_i^r\right\rangle + \sum_{i<j}^{occ}\sum_{r<s}^{virt} c_{ij}^{rs} \left|\Psi_{ij}^{rs}\right\rangle. \tag{41}$$

Although the CID and CISD approaches can be applied to rather large molecular systems and although they are variational methods, these methods do not satisfy the important request of size consistency.

2.3.3 Multiconfigurational self-consistent field and complete active space self consistent field theories

In the beginning of section 2.3 it has been mentioned that the first step in a CI calculation is to generate occupied and virtual orbitals which define the Slater determinants using Hartree-Fock or MultiConfiguration (MC) Self Consistent Field approaches. In the Hartree-Fock model, all the required information about the electronic structure is contained in the occupied molecular orbitals (or spin orbitals) and in their occupation numbers. On the other hand, this subsection intends to give a short overview of models in which sets of orbitals can be constructed for more complicated wave functions, including correlation effects.

In the MCSCF method [23-25], one has to deal with the problem of optimizing both CI coefficients and molecular orbitals in a CI-type wave function in order to obtain the minimized electronic energy. As more unknowns are introduced in the MCSCF method with respect to the CI one, this approach becomes much more computationally demanding. Moreover, this method is also limited by the choice of the configuractions, as it can deal with only relatively small expansions and needs manual procedures to force the calculations towards the correct direction. Among all the MCSCF methods, the most commonly used one is the Complete Active Space (CAS) SCF approach developed by Roos and co-workers [26]. The CASSCF formalism yields MCSCF wave functions corresponding to full CI within a limited configuration space (active space) and a limited number of electrons. The energy in this approach is also invariant to rotations among active orbitals.

The problem with the CASSCF method, however, is that the number of configurations in the full CI increases drastically with the number of electrons. The CASSCF method is variational but not size-consistent, although an evaluation of dissociation energies is technically possible. In this sense, the usual procedure is to perform CASSCF calculations on both the molecule and the fragments at very large distances.

2.4 Many body perturbation theory

Many Body Perturbation Theory (MBPT) finds its origin in the work of Møller and Plesset [27], who gave the first general ideas of the theory in 1934. However, once again applications of the theory came a few decades after the conceptual presentation. The revision and implementation of MBPT is mainly due to Bartlett [28, 29] and the research team around Pople [3]. MBPT, as a systematic procedure to calculate correlation energy, is also referred to as Rayleigh-Schrödinger Perturbation Theory (RSPT). It turns out to be not a variational method, but more importantly, it is size consistent.

MBPT is based on a partition of the total Hamiltonian in two parts: a zeroth-order part $\hat{H}_0$, with known eigenfunctions and eigenvalues, and a perturbation $\hat{V}$. The exact energy is expressed as an infinite sum of contributions with a more and more complex structure. These contributions include eigenvalues of $\hat{H}_0$ and matrix elements of the perturbation between the eigenfunctions of $\hat{H}_0$. This zeroth order Hamiltonian must be selected with great care in order to have a "small" $\hat{V}$ leading to a perturbation expansion which converges very quickly.

Since the main scope of MBPT is the computation of the correlation energies, an adequate choice here is to consider the Hartree-Fock Hamiltonian as the zeroth-order one. As shown before, the HF Hamiltonian $\hat{H}_0$ can be expressed as the sum of Fock operators $\hat{f}(i)$ for all electrons in the molecule:

$$\hat{H}_0 = \sum_i \hat{f}(i). \tag{42}$$

Consequently, the total Hamiltonian operator reads:

$$\hat{H} = \hat{H}_0 + \hat{V} = \sum_i \hat{f}(i) + \hat{V}, \qquad \text{with} \tag{43}$$

$$\hat{V} = \hat{H} - \sum_i \hat{f}(i). \tag{44}$$

This partitioning of the Hamiltonian together with the general expression of RSPT is most commonly referred to as Møller Plesset (MP) Perturbation Theory.

The HF wave function $|\Psi_0\rangle$ is an eigenfunction of the Hamiltonian $\hat{H}_0$

$$\hat{H}_0 |\Psi_0\rangle = E_0^{(0)} |\Psi_0\rangle \tag{45}$$

with the eigenvalue

$$E_0^{(0)} = \sum_i \varepsilon_i, \tag{46}$$

which is the zeroth-order perturbation energy. The first-order energy is

$$E_0^{(1)} = \langle \Psi_0 | \hat{V} | \Psi_0 \rangle = -\frac{1}{2}\sum_{ij} \langle ij || ij \rangle . \tag{47}$$

The HF energy is the sum of the zeroth-order and first-order perturbation energies:

$$E_0 = E_0^{(0)} + E_0^{(1)} = \sum_i \varepsilon_i - \frac{1}{2}\sum_{ij} \langle ij || ij \rangle . \tag{48}$$

The second-order perturbation energy $E_0^{(2)}$, sometimes also denoted as E_{MP2}, is

$$E_0^{(2)} = \sum_{i<j}\sum_{r<s} \frac{\left| \langle ij || rs \rangle \right|^2}{\varepsilon_i + \varepsilon_j - \varepsilon_r - \varepsilon_s} \tag{49}$$

Note that in this expression only bielectron integrals over two occupied and two virtual orbitals are involved. Hence, compared with higher order methods for which the whole set of bielectron integrals is needed, MP2 is a relatively easily tractable approach, from a computational viewpoint.

Higher order expression for the energies, such as third-order (MP3) or fourth-order (MP4) are also available [30-32]. MP3, as well as MP2, requires only double substitutions (D), whereas MP4 requires singles (S), double (D), triple (T) and quadruple (Q) excitations. From the computational point of view, the steps necessary for these calculations scale as M^5 for MP2, M^6 for MP3 and MP4(SDQ), and finally M^7 for MP4(SDTQ), where M is the number of basis functions. It is worth to note that in MP4 the most demanding step is the one related to the triple contributions, whereas the other contributions form a negligible extra cost with respect to MP3. For this reason, there are two different MP4 implementations: the first one is MP4(SDQ), where the triple contributions are neglected, and the second implementation is MP4(SDTQ), which is the complete one. The triple excitation contribution seems to be generally overestimated at the MP4 level. In the 1990's, Møller-Plesset theory has also been developed to orders five and six (MP5 and MP6) [33, 34].

For the elimination of spin contamination, spin projected techniques have also been developed [35]. Furthermore, analytical gradients for MP4 [36-38] and second derivatives for MP2 [39-43] are available for both closed-shell and open-shell systems.

MBPT is size-consistent to any order but, as a perturbation theory, it is not variational. Handy and co-workers [44] have shown that the MP series converges very slowly in the presence of low-lying excited states in cases of spin contamination.

2.5 Coupled Cluster theory

Formally developed in the 1960's, coupled cluster methods started to be used only one decade later. In the following years, thanks to an easier mathematical formulation, and more importantly, to efficient computational implementations, coupled cluster methods have been widely used because of the higher accuracy obtained for molecules which are already well described qualitatively at the Hartree-Fock level.

Coupled Cluster (CC) theory is based on the exponential Ansatz of Coester and Kümmel [45, 46], which is a consequence of the so-called linked-diagram theorem [47]. Here, the excitation operator $\hat{T}$ is considered, which is defined as

$$\hat{T} = \hat{T}_1 + \hat{T}_2 + \hat{T}_3 + \ldots, \tag{50}$$

where the operator $\hat{T}_p$ simply generates p-fold excitations. According to the exponential Ansatz the CC wave function is given by

$$\Psi_{CC} = \exp\left(\hat{T}\right)\Psi_0 = \left(1 + \hat{T} + \frac{1}{2!}\hat{T}^2 + \frac{1}{3!}\hat{T}^3 + \ldots\right)\Psi_0, \tag{51}$$

where Ψ_0 is a single determinant reference function usually taken as the HF determinant, and the exponential has been expanded in a power series.

In the CC Doubles (CCD) method, only double excitations are included in the operator $\hat{T}$, i.e., $\hat{T} = \hat{T}_2$, and the wave function Ψ_{CCD} is given by

$$\Psi_{CCD} = \left(1 + \hat{T}_2 + \frac{1}{2!}\hat{T}_2^2 + \ldots\right)\Psi_0 = \Psi_0 + \sum_{\substack{i<j \\ r<s}} t_{ij}^{rs}\Psi_{ij}^{rs} + \sum_{\substack{r<j<k<l \\ r<s<t<u}} t_{ij}^{rs} t_{kl}^{tu} \Psi_{ijkl}^{rstu} + \ldots \tag{52}$$

The usual convention is adopted here: the $i, j, k, l \ldots$ are occupied orbitals and $r, s, t, u \ldots$ are the virtual ones. In expression (52), the unknown coefficients t_{ij}^{rs} are the cluster amplitudes. Now, the question arises how these coefficients have to be optimized. A variety of approaches is available to derive coupled sets of non-linear equations, which define these unknown amplitudes. The coupled cluster equations are usually obtained by inserting the wave function from eq. (51) into the electronic Schrödinger equation projected by the reference function Ψ_0 and single, double and higher excitations.

Considering the operator $\hat{W} = \hat{H} - E_0$, where E_0 is the usual Hartree-Fock energy, and using this operator, the "Schrödinger equation" can be projected as

$$\hat{H}\exp\left(\hat{T}\right)\Psi_0 = E\exp\left(\hat{T}\right)\Psi_0 \tag{53}$$

on the N-particle basis. Then, the CCD equations are

$$\left\langle \Psi_0 \middle| \hat{W} \middle| \hat{T}_2 \Psi_0 \right\rangle = \Delta E, \qquad \text{or} \tag{54}$$

$$\left\langle \Psi_{ij}^{rs} \middle| \hat{W} \middle| \left(1+\hat{T}_2+\frac{1}{2!}\hat{T}_2^2\right)\Psi_0 \right\rangle = \Delta E t_{ij}^{rs}, \qquad \forall ij;rs, \tag{55}$$

with ΔE the correlation energy. These equations give access to the amplitudes t_{ij}^{rs}. It is worth to remind that the equations for the cluster amplitudes are independent from the energy. Moreover, no higher terms than $\hat{T}_2^2$ can contribute to the CC equations; in fact $\hat{T}_2^3$ would generate sextuple excitations which would have vanishing matrix elements with Ψ_{ij}^{rs}. This can be generalized by saying that even if the exponential CC wave function consists of all terms up to n-fold excitations, the CC amplitude equations are always of lower order.

The CCSD model takes the single and double excitations into account. $\hat{T}$ is truncated at $\hat{T}_1+\hat{T}_2$ in order to obtain a practical approach. In fact a truncation at $\hat{T}_1$ would not include any dynamic correlation effect and the single excitations would not interact with the HF reference function. On the other hand, $\hat{T}_2$ certainly accounts for most of the dynamic correlation effects. In this model, equations for t_i^r and t_{ij}^{rs} can be obtained [48-55].

In the CCSDT approach also triple excitations are included. The excitation operator is $\hat{T}=\hat{T}_1+\hat{T}_2+\hat{T}_3$ and amplitude equations are given for t_i^r, t_{ij}^{rs} and t_{ijk}^{rst} [56, 57]. Higher order methods are obtained with the same procedure and up to now, CCSDTQ is the highest implemented, with $\hat{T}=\hat{T}_1+\hat{T}_2+\hat{T}_3+\hat{T}_4$ [58]. The CC model with no truncation of $\hat{T}$ is equivalent to full CI; however, contrarily to the latter, CC methods are size-extensive to any order.

At this point, it is important to give an idea of the computational effort required for these methods in order to evaluate whether widespread applications of such models are conceivable. The CCD and CCSD models scale both as $n^2N^4N_{it}$ where n and N are the numbers of unoccupied and occupied spin orbitals in the HF wave function Ψ_0, respectively. N_{it} refers to the number of iterations. As the interest is focused on quantitative or chemical accuracy, it is unavoidable to go beyond the CCSD approximation and to use large basis sets. The computational effort for CCSDT calculations is proportional to $n^3N^5N_{it}$ which clearly indicates that this approach is rather expensive and the use of large basis sets is impossible unless one is dealing with very small atoms or molecules. As on passing from CCSD to CCSDT the scaling goes from n^2N^4 to n^3N^5 in each iteration, it is immediately clear that the CCSDT level requires a large computational effort. Moreover, the CCSDTQ model is so demanding that it becomes most usually untractable except for applications on exceedingly small systems. For these reasons, new approximations have been proposed in order to reduce the computational cost of the calculations without loosing the effects of higher connected excitations.

As already pointed out, the triple excitations are the most demanding on the computational side. Then, due to the analogy between the CC and perturbation theories, an alternative approach is to include the triple excitations through perturbation theory. The most used approximations of this kind are CCSD+T(CCSD) [59] and CCSD(T) [60]. In the CCSD+T(CCSD) method, the double amplitudes

t_{ij}^{rs} from the CCSD wave function are used for the triples corrections through a formula which is similar to that used in MP4 perturbation theory. The CCSD(T) method is then CCSD+T(CCSD) plus a single and triples interaction term. This fifth-order term prevents the overestimation of the contribution from connected triple excitation and it is also an indicator of the importance of non-dynamical correlation effects; in other words, the larger is the fifth-order term, the stronger are the non-dynamical effects [61-65]. Whenever the non-dynamical correlation effects are not important, the CCSD+T(CCSD) and CCSD(T) methods give comparable results. Both these approaches have a $n^2N^4N_{it}$ computational dependence (for CCSD) per iteration with a single n^3N^4 step. Up to now, the CCSD(T) method seems to be the best single-reference correlation treatment available, and it is also the best compromise between computational effort and chemical accuracy, allowing also the use of large basis sets.

As briefly mentioned before, CC methods are size-consistent (size-extensive) to any order [28, 66, 67] but they are not variational. However, due to the high accuracy obtained with these methods for many molecular properties this last point is not considered anymore as a disadvantage [68].

In the literature, a large number of publications can be found regarding the CC methods due to their extensive success in predicting many molecular properties such as equilibrium structures, vibrational spectra, heats of formations, vertical electronic excitation energies, binding energies and dipole moments [28, 68]. The accuracy of these calculations can easily be compared with that of the best experiments.

For the sake of completeness, it is worth to mention that due to the non-linearity of the CC equations non-physical solutions can also exist. The problem of the existence and the reality of the solutions of the CC equations was already extensively studied since the late 1970's [69, 70]. In general, it is not possible to guarantee that an obtained solution is physical (e.g. see Meissner, Balková, and Bartlett [71]), but experience suggests that as long as the reference function is a reasonable approximation, the obtained solution will be the desired one.

Before concluding this section, it is necessary to discuss a final important aspect of Coupled Cluster theory. In several occasions it has been underlined that the CC model is a single-reference treatment, and that the most common reference function considered is usually the HF determinant. This means that the success of the CC methods is seriously compromised every time multireference effects become sufficiently large. In order to estimate the importance of these multireference effects, Lee and Taylor [72] introduced a quantity known as the T_1 diagnostic, which is an indicator of non-dynamical effects, i.e. near-degeneracy effects. This diagnostic is based on the following quantity

$$T_1 = \frac{\|\mathbf{t}_1\|}{\sqrt{N}}, \tag{56}$$

where $\mathbf{t}_1$ is the vector of single excitation amplitudes and N is the number of electrons. On the basis of empirical comparison, it was suggested initially that $T_1 > 0.02$ indicates significant non-dynamical effects and consequently a decrease of the reliability of the CCSD method, leading to the necessity of using a multireference CI (MRCI) approach. However, as already shown, the single-reference

CCSD(T) method properly describes the effects of the connected triple excitations and so this coupled cluster method can be used rather than a multireference approach. For this reason, the threshold of the T_1 diagnostic has been revised and increased to 0.08 [73]. In conclusion, as long as the T_1 values are lower than this crucial limit of 0.08 the description with a single determinant wave function seems to be valid.

2.6 Density Functional Theory

The methods based on Density Functional Theory (DFT) [74-79] are as old as quantum mechanics itself; in fact they find their origin in the 1920's with the Thomas-Fermi-Dirac models [80-82]. Indeed, physicists put a large effort in developing this theory in the 1950's, following an idea introduced by Slater [83]. He suggested that the complex exchange term in the Hartree-Fock method could be replaced by the Dirac potential [82], which he claimed at that time to include both exchange and correlation effects.

Only in the late 1990's, density functional theory has become one of the most frequently used approaches in computational quantum chemistry for studying ground state properties. One of the main reasons must be searched in the computational cost of this method. The advantage is even more pronounced when compared to typical post Hartree-Fock treatments of electron correlation (e.g. MPn, CCSD(T),…), the cost of which scale very unfavorable with system size.

It should be emphasized that DFT is a method which allows an exact description of a many electron system if the exact density functional is used. However, an exact expression for the density functional is not known and there is no general scheme for finding it. For practical DFT computations, use is made of approximate expressions and much work has been devoted for constructing them. Some of these approximate functionals, depending upon the gradient of the electron density, have been found to be quite successful in predicting molecular properties. The DFT approach, in which a carefully selected approximate functional is used, constitutes a method which includes electron correlation and appears to be not more expensive than a traditional Hartree-Fock calculation for large systems.

The DFT approach is based upon the idea that the energy of an electronic system can be expressed in terms of its density. If the exact electron density $\rho(\mathbf{r})$ is known, then the positions of the nuclei are also known from the cusps of $\rho(\mathbf{r})$. Furthermore, the knowledge of the magnitude of the gradients of the electron density, $|\nabla\rho(\mathbf{r})|$, at the nuclei gives their nuclear charges (Kato's theorem) [84a]. Thus the full Schrödinger Hamiltonian is known since it is completely defined once the position and the charges of the nuclei are given. Hence, in principle, the wave function as well as the energy are known, and thus the full system is known. This reasoning was made in 1965 by the theoretical spectroscopist E. Bright Wilson [84b]. In short, he understood that a knowledge of the electron density is a necessary and sufficient condition for a complete determination of all molecular properties. This simple argument constitutes the basic idea of modern density functional theory.

2.6.1 Hohenberg-Kohn theorems

The two fundamental theorems of DFT are due to Hohenberg and Kohn. In an electronic system, the number of electrons per unit volume in a given state is the electron density $\rho(\mathbf{r})$ for that state. The relationship between the electron density in a point $\mathbf{r}_1$ and the wave function Ψ is

$$\rho(\mathbf{r}_1) = N\int\ldots\int\left|\Psi(\mathbf{x}_1,\mathbf{x}_2,\ldots,\mathbf{x}_N)\right|^2 d\sigma_1 d\mathbf{x}_2\ldots d\mathbf{x}_N\,, \tag{57}$$

where $\Psi(\mathbf{x}_1,\mathbf{x}_2,\ldots,\mathbf{x}_N)$ is the electronic wave function for the given state of the system. The coordinates $\mathbf{x}_i$ for the i^{th} electron comprise both space and spin coordinates, i.e. $\mathbf{r}_i$ and σ_i, respectively. The electron density $\rho(\mathbf{r})$ is a non-negative function of the three variables x, y and z, to be integrated to the total number of electrons N:

$$\int\rho(\mathbf{r})d\mathbf{r} = N\,. \tag{58}$$

Now, it is worth to recall that for an electronic system described by the Hamiltonian of eq. (2a), both the ground-state energy and the wave function are determined by the minimization of the energy functional $E[\Psi]$ of eq. (9). For an N-electron system, the Hamiltonian is completely fixed by the external potential $v(\mathbf{r})$; hence, N and $v(\mathbf{r})$ determine all properties for the ground state. This is of course not surprising since $v(\mathbf{r})$ defines the whole nuclear frame of the molecule, which, together with the number of electrons N, determines all the electronic properties of the ground state.

Instead of N and $v(\mathbf{r})$, the first theorem of Hohenberg and Kohn legitimizes the use of the electron density $\rho(\mathbf{r})$ as basic variable. It is formulated as: "The external potential $v(\mathbf{r})$ is determined within an additive constant by the electron density $\rho(\mathbf{r})$." In fact, since ρ determines the number of electrons, $\rho(\mathbf{r})$ also determines the ground state wave function Ψ and all other electronic properties of the system. It should be noted that $v(\mathbf{r})$ is not restricted to be a Coulomb potential.

At this point, the energy of the system can be presented as a functional of the density as

$$E[\rho] = V_{ne}[\rho] + T[\rho] + V_{ee}[\rho] \tag{59a}$$

$$= \int\rho(\mathbf{r})v(\mathbf{r})d\mathbf{r} + T[\rho] + V_{ee}[\rho]\,. \tag{59b}$$

Here $\rho(\mathbf{r})$ is the exact electron density and $v(\mathbf{r})$ is the external potential defined in eq. (2b), $V_{ne}[\rho]$ is the nucleus-electron energy functional given by

$$V_{ne}[\rho] = \int\rho(\mathbf{r})v(\mathbf{r})d\mathbf{r}\,. \tag{60}$$

$T[\rho]$ is the kinetic energy functional, while $V_{ee}[\rho]$ is the electron-electron interaction energy which contains the classical Coulomb repulsion $J[\rho]$ and a non-classical term playing an important role in the exchange-correlation energy. Thus

$$V_{ee}[\rho] = J[\rho] + \text{non-classical term}, \tag{61}$$

where

$$J[\rho] = \frac{1}{2}\iint \frac{1}{r_{12}} \rho(\mathbf{r}_1)\rho(\mathbf{r}_2) d\mathbf{r}_1 d\mathbf{r}_2. \tag{62}$$

The second theorem by Hohenberg and Kohn [85] introduces the energy variational principle. It can be stated as follows:

“For a trial electron density $\tilde{\rho}(\mathbf{r})$ with $\tilde{\rho}(\mathbf{r}) \geq 0$ and $\int \tilde{\rho}(\mathbf{r}) d\mathbf{r} = N$,

$$E_0 \leq E_{\mathrm{v}}[\rho], \tag{63}$$

where $E_{\mathrm{v}}[\rho]$ is the energy functional (59).”

This theorem can be easily proved as follows. The first Hohenberg-Kohn theorem assures that the trial $\tilde{\rho}(\mathbf{r})$ determines its own $\tilde{v}(\mathbf{r})$, Hamiltonian $\tilde{H}$ and the wave function $\tilde{\Psi}$. Using this wave function in the usual variational principle gives

$$\begin{aligned} \langle \tilde{\Psi} | \hat{H} | \tilde{\Psi} \rangle &= \int \tilde{\rho}(\mathbf{r}) v(\mathbf{r}) d\mathbf{r} + T[\tilde{\rho}] + V_{ee}[\tilde{\rho}] \\ &= E[\tilde{\rho}] \\ &\geq E[\rho] = \langle \Psi | \hat{H} | \Psi \rangle. \end{aligned} \tag{64}$$

This variational principle requires that the ground state satisfies the stationary principle

$$\delta\left\{E[\rho] - \mu\left[\int \rho(\mathbf{r}) d\mathbf{r} - N\right]\right\} = 0, \tag{65}$$

giving the Euler-Lagrange equation

$$\begin{aligned} \mu &= \frac{\delta E[\rho]}{\delta \rho(\mathbf{r})} \\ &= v(\mathbf{r}) + \frac{\delta T[\rho]}{\delta \rho(\mathbf{r})} + \frac{\delta V_{ee}[\rho]}{\delta \rho(\mathbf{r})}. \end{aligned} \tag{66}$$

μ is the Lagrange multiplier associated to the constraint $\int \rho(\mathbf{r}) d\mathbf{r} = N$, and is also known as the chemical potential. If the exact $T[\rho] + V_{ee}[\rho]$ is known, eq. (65) is an exact equation for the ground state electron density. It should be remarked that $T[\rho] + V_{ee}[\rho]$ is defined independently of the external potential $v(\mathbf{r})$ and is therefore a universal functional of $\rho(\mathbf{r})$. After finding an explicit expression (either approximate or accurate) for $T[\rho] + V_{ee}[\rho]$, the method can be applied to any system.

2.6.2 The Kohn-Sham method

In 1965, Kohn and Sham [86] turned density functional theory into a practical tool for rigorous calculations, inventing an indirect approach to the kinetic-energy functional $T[\rho]$, known as the Kohn-Sham (KS) method. They proposed the idea of introducing orbitals into the problem in such a way that the kinetic energy could have been computed in a simple way, but with a good accuracy. They considered the determinantal wave function for N non-interacting electrons in N orbitals ψ_i. For such a system, the formulas for the kinetic energy and the exact electron density are respectively given by

$$T_s[\rho] = \sum_i^N \langle \psi_i | -\frac{1}{2}\nabla^2 | \psi_i \rangle, \quad \text{and} \tag{67}$$

$$\rho(\mathbf{r}) = \sum_i^N \sum_\sigma |\psi_i(\mathbf{r},\sigma)|^2 . \tag{68}$$

The corresponding non-interacting reference system is described by the Hamiltonian

$$\hat{H}_s = \sum_i^N \left(-\frac{1}{2}\nabla_i^2\right) + \sum_i^N \nu_s(\mathbf{r}), \tag{69}$$

where $v_s(\mathbf{r})$ is an external potential. In eq. (69) there are no electron-electron repulsion terms. Through a proper definition of the external potential $v_s(\mathbf{r})$, the ground-state electron density is exactly ρ. For such a system, there is also an exact determinantal ground state wave function

$$\Psi_s = \frac{1}{\sqrt{N!}} \det[\psi_1\psi_2 \ldots \psi_N], \tag{70}$$

where the orbitals ψ_i are the N lowest eigenstates of the one-electron Hamiltonian $\hat{h}_s$:

$$\hat{h}_s \psi_i = \varepsilon_i \psi_i, \quad \text{or} \tag{71a}$$

$$\left[-\frac{1}{2}\nabla^2 + \nu_s(\mathbf{r})\right]\psi_i = \varepsilon_i \psi_i . \tag{71b}$$

The electronic energy of the non-interacting system is

$$E_s[\rho] = T_s[\rho] + \int v_s(\mathbf{r})\rho(\mathbf{r})d\mathbf{r} . \tag{72}$$

Eqs. (71a-b) are the Euler equations, which are obtained when $E[\rho]$ is minimized with respect to variations in the orbitals constituting the density as defined in eq. (68). Attention has been put to the constraint that they remain normalized.

Now, as the systems of interest are those with interacting electrons, the energy functional [eq. (59)] can be rewritten as

$$E[\rho] = \int v(\mathbf{r})\rho(\mathbf{r})d\mathbf{r} + T[\rho] + V_{ee}[\rho] \tag{73a}$$

$$= \int v(\mathbf{r})\rho(\mathbf{r})d\mathbf{r} + T_s[\rho] + J[\rho] + \left(T[\rho] - T_s[\rho]\right) + \left(V_{ee}[\rho] - J[\rho]\right) \tag{73b}$$

$$= \int v(\mathbf{r}) \rho(\mathbf{r}) d\mathbf{r} + T_s[\rho] + J[\rho] + E_{xc}[\rho]. \qquad (73c)$$

Here, the first line (73a) comes from equation (59b), the second line inserts and removes the non-interacting kinetic energy and Coulomb energy, the latter line introduces the exchange-correlation energy functional defined as

$$E_{xc}[\rho] \equiv T[\rho] - T_s[\rho] + V_{ee}[\rho] - J[\rho]. \qquad (74)$$

This functional contains the difference between T and T_s, which is probably very small, and the non classical part of $V_{ee}[\rho]$. The functional derivative of $E_{xc}[\rho]$ is the exchange-correlation potential v_{xc}:

$$v_{xc}(\mathbf{r}) = \frac{\delta E_{xc}[\rho]}{\delta \rho(\mathbf{r})}. \qquad (75)$$

At this point, the Euler equation (66) becomes

$$\mu = v_{eff} + \frac{\delta T_s[\rho]}{\delta \rho(\mathbf{r})}, \qquad (76)$$

where the KS effective potential is defined by

$$\begin{aligned} v_{eff}(\mathbf{r}) &= v(\mathbf{r}) + \frac{\delta J[\rho]}{\delta \rho(\mathbf{r})} + \frac{\delta E_{xc}[\rho]}{\delta \rho(\mathbf{r})} \\ &= v(\mathbf{r}) + \int \frac{\rho(\mathbf{r}')}{|\mathbf{r}-\mathbf{r}'|} d\mathbf{r}' + v_{xc}(\mathbf{r}). \end{aligned} \qquad (77)$$

In summary, the Kohn-Sham treatment is as follows. Eq. (76) with the constraint (58) is exactly the same equation which is obtained from conventional density functional theory applied to a system of non-interacting electrons moving in an external potential $v_s(\mathbf{r}) = v_{eff}(\mathbf{r})$. Therefore, for any given $v_{eff}(\mathbf{r})$ the electron density $\rho(\mathbf{r})$, which satisfies eq. (69), is simply obtained by solving the following set of N one-electron equations

$$\left[-\frac{1}{2}\nabla^2 + v_{eff}(\mathbf{r}) \right] \psi_i(\mathbf{r}) = \varepsilon_i \psi_i(\mathbf{r}), \qquad (78)$$

and setting

$$\rho(\mathbf{r}) = \sum_i^N \sum_\sigma |\psi_i(\mathbf{r}, \sigma)|^2. \qquad (79)$$

Here, $v_{eff}(\mathbf{r})$ depends itself on $\rho(\mathbf{r})$ through the exchange-correlation potential, so this problem must be solved self-consistently. The starting point of the procedure is an initial guess for $\rho(\mathbf{r})$, from which $v_{eff}(\mathbf{r})$ is constructed through eq. (77). A new $\rho(\mathbf{r})$ is consecutively found from eqs. (78) and (79). The procedure continues until self-consistency.

The energy functional can be computed directly from eq. (73c) as

$$\begin{aligned}E[\rho] &= \int v(\mathbf{r})\rho(\mathbf{r})d\mathbf{r} + T_s[\rho] + J[\rho] + E_{xc}[\rho] \\ &= \int v(\mathbf{r})\rho(\mathbf{r})d\mathbf{r} + \sum_i^N \sum_\sigma \int \psi_i^*(\mathbf{r})\left(-\frac{1}{2}\nabla^2\right)\psi_i(\mathbf{r})d\mathbf{r} + J[\rho] + E_{xc}[\rho],\end{aligned} \tag{80}$$

or indirectly from eqs. (68) and (78) as

$$E = \sum_i^N \varepsilon_i - \frac{1}{2}\iint \frac{\rho(\mathbf{r})\rho(\mathbf{r}')}{|\mathbf{r}-\mathbf{r}'|} d\mathbf{r}d\mathbf{r}' + E_{xc}[\rho] - \int v_{xc}(\mathbf{r})\rho(\mathbf{r})d\mathbf{r}, \tag{81}$$

where

$$\begin{aligned}\sum_i^N \varepsilon_i &= \sum_i^N \langle \psi_i | -\frac{1}{2}\nabla^2 + v_{eff}(\mathbf{r}) | \psi_i \rangle \\ &= T_s[\rho] + \int v_{eff}(\mathbf{r})\rho(\mathbf{r})d\mathbf{r}.\end{aligned} \tag{82}$$

Like in Hartree-Fock theory, the total energy is not the sum of the orbital energies. Finally, once the exchange-correlation functional $E_{xc}[\rho]$ is determined, the exact electronic energy can be given through eq. (80).

2.6.3 Exchange, correlation and hybrid functionals

At this stage, it is important to notice that it is impossible to find the exact exchange-correlation functional, so approximations must be introduced. This means that DFT should be probably considered as a semi-empirical method. However, as the parameters introduced into the functionals are not molecule specific, DFT is therefore one of the best semi-empirical approaches.

In the Kohn-Sham treatment of the density functional theory, as already shown, the electronic energy is

$$E[\rho] = T_s[\rho] + J[\rho] + E_{xc}[\rho] + \int v(\mathbf{r})\rho(\mathbf{r})d\mathbf{r}. \tag{83}$$

However, the exchange-correlation functional $E_{xc}[\rho]$ is usually divided into two separated parts

$$E_{xc}[\rho] = E_x[\rho] + E_c[\rho]. \tag{84}$$

$E_x[\rho]$ in the right hand side of eq. (84) takes into account the exchange energy arising from antisymmetry of the quantum mechanical wave function, whereas $E_c[\rho]$ accounts for the dynamic correlation in the motions of the individual electrons. In general, $E_{xc}[\rho]$ is approximated as an integral involving only the spin densities and possibly their gradients

$$E_{xc}[\rho] = \int f\left(\rho_\alpha(\mathbf{r}), \rho_\beta(\mathbf{r}), \nabla\rho_\alpha(\mathbf{r}), \nabla\rho_\beta(\mathbf{r})\right)d\mathbf{r}. \tag{85}$$

ρ_α represents the α spin electron density, ρ_β the β spin electron density. ρ is the total electron density given by

$$\rho = \rho_\alpha + \rho_\beta \,. \tag{86}$$

$E_x[\rho]$ and $E_c[\rho]$ can be of two distinct types: local functionals depending only on the electron density ρ, and gradient-corrected functionals depending both on ρ and its gradient $\nabla\rho$.

The Local Density Approximation (LDA) and the Xα functional described in details in [74, 83, 87, 88] are local exchange correlation functionals, whereas the Local Spin-Density (LSD) Approximation functional, also known as the Volsko, Wilk, and Nusair (VWN) functional [87, 89] is a local correlation functional. The Becke Exchange Correction [Becke 88] [87, 88b] and Gill 96 [G96] [90] functionals are gradient corrected exchange functionals. The Lee-Yang-Parr (LYP) [87, 91-94], the 1991 Perdew-Wang (PW91) and 1992 Perdew-Wang (PW92) [95-97] contain gradient-corrected correlation functionals.

There are a number of other functionals which consider at the same time the exchange and the correlation parts, such as the Perdew-Yang 1991 exchange-correlation functional [98] and the Becke-Lee-Parr functional [99], and which have gained importance. In this series, also BP86 has to be mentioned as it is the combination of the Becke 88 gradient corrected exchange and Perdew 86 local correlation [100] functionals.

A. Hybrid functionals

The idea of hybrid functionals is due to Becke [101] who formulated functionals which include both Hartree-Fock and DFT exchange terms together with DFT correlation terms. The B3LYP exchange-correlation functional is expressed as follows:

$$E_{xc}^{B3LYP} = E_{xc}^{LDA} + c_0\left(E_x^{HF} - E_x^{LDA}\right) + c_x \Delta E_c^{B88} + E_c^{VWN} + c_c\left(E_c^{LYP} - E_c^{VWN}\right). \tag{87}$$

Here, the parameter c_0 allows any admixture of Hartee-Fock and LDA exchange. Moreover, Becke's gradient corrections to LDA exchange, ΔE_x^{B88}, is also included, scaled by the parameter c_x. Similarly the VWN (LDS) correlation functional (V in the original paper) is also used, corrected by the LYP correlation through the parameter c_c.

In the B3LYP functional the three parameters have been determined by Becke using a linear least square fit to a set of 56 atomization energies, 42 ionization potentials, 8 proton affinities, and 10 first-row total atomic energies. The optimum values are: $c_0 = 0.20$, $c_x = 0.72$, $c_c = 0.81$.

In his original work, Becke used the PW91 gradient correction for correlation, ΔE_c^{PW91} [101, 102], rather than VWN and LYP:

$$E_{xc} = E_{xc}^{LDA} + c_0\left(E_x^{HF} - E_x^{LDA}\right) + c_x \Delta E_x^{B88} + E_c^{LDA} + c_c \Delta E_c^{PW91}. \tag{88}$$

Further details are available in [87, 102, 103].

B. Kinetic functionals

The MPW1PW91 (Modified Perdew-Wang, 1991 Perdew-Wang) functional developed by Barone and Adamo [104] uses a modified version of the PW91 exchange functional in combination with the original PW91 correlation functional and a mixing ratio of exact (HF) and DFT exchange of 0.25:0.75.

The modified Perdew-Wang 1-parameter model for kinetics (MPW1K) enables an increased accuracy for the computed transition state energies [105], compared with B3LYP. The MPW1K functional is a modification of the MPW1PW91 functional where the percentage of HF exchange has been optimized for accurately investigating the energetics of well known hydrogen-atom transfer reactions of small systems in the gas phase. The development of this new MPW1K functional involved mixing various amounts of the Hartree-Fock non-local exchange operator with local DFT exchange-correlation functionals and gradient-corrected density functions. In its final form, the energy functional is expressed as follows:

$$E_{xc}^{MPW1K} = E^{HF} + XE_x^{HF} + (1-X)(E_x^S + E_x^{MPW1}) + E_c^{PW91}, \qquad (89)$$

with a mixing ratio of exact and DFT exchange energy terms of 0.428 : 0.572.

In eq. (89), E^{HF} describes the non-exchange part of the HF operator, E_x^{HF} is the HF exchange operator, X the fraction of HF exchange, E_x^S is the Slater's local density functional for exchange, E_x^{MPW1} is the gradient corrected exchange functional and E_c^{PW91} is the Perdew-Wang correlation functional. For a complete overview of the set of reactions involved in the parameterization of this 1-parameter model reference [105] should be consulted.

2.6.4 Self-interaction problem

An important problem in DFT is the so-called self-interaction of electrons. An electron interacts with other electrons in a molecular species via the Coulomb potential; it does not interact with itself. It should be remarked that in the Hartree-Fock approximation no self-interaction contribution is present. However, the situation is different in practical DFT calculations.

The electronic energy in the Kohn-Sham scheme is given by eq. (81). If an exact exchange-correlation functional is used, $E_{xc}\left[\rho\right]$ and the classical electrostatic repulsion term $\frac{1}{2}\iint\frac{\rho(\mathbf{r})\rho(\mathbf{r}')}{|\mathbf{r}-\mathbf{r}'|}d\mathbf{r}d\mathbf{r}'$ cancel exactly and no spurious self-interaction can be remarked. When approximate exchange-correlation functionals are used, this is not necessarily the case; this is the point where errors are introduced. An important consequence of the self-interaction error is that in the Kohn-Sham depiction, the electronic potential decays faster tan $1/r$ in the asymptotic region.

2.6.5 Computational implementation and limitations in DFT.

In order to conclude the section on DFT methods, it is worth to give a general introduction to the computational aspects of that theoretical method. In this section, it will be shown that the Kohn-Sham equations resemble the SCF ones.

In the spin-unrestricted formalism, the electrons of α and β spin are described by sets of orthonormal spatial orbitals $\{\psi_i^\alpha | i = 1, 2, \ldots, n_\alpha\}$ and $\{\psi_i^\beta | i = 1, 2, \ldots, n_\beta\}$, respectively. Hence, the partial and total electron densities can be defined as

$$\rho_\alpha = \sum_i^{n_\alpha} \left|\psi_i^\alpha\right|^2 , \tag{90a}$$

$$\rho_\beta = \sum_i^{n_\beta} \left|\psi_i^\beta\right|^2 , \quad \text{and} \tag{90b}$$

$$\rho = \rho_\alpha + \rho_\beta . \tag{90c}$$

As stated previously, the electronic energy is given by a particular formal expression in the Kohn-Sham formalism, namely

$$E[\rho] = T_s[\rho] + J[\rho] + E_{xc}[\rho] + \int v(\mathbf{r})\rho(\mathbf{r})d\mathbf{r} , \tag{91}$$

and the kinetic energy functional $T_s[\rho]$ is given by

$$T_s[\rho] = \sum_i^{n_\alpha} \left\langle \psi_i^\alpha \right| -\frac{1}{2}\nabla^2 \left| \psi_i^\alpha \right\rangle + \sum_i^{n_\beta} \left\langle \psi_i^\beta \right| -\frac{1}{2}\nabla^2 \left| \psi_i^\beta \right\rangle . \tag{92}$$

The external potential is

$$v(\mathbf{r}) = -\sum_A^{nuclei} \frac{Z_A}{|\mathbf{r} - \mathbf{r}_A|} . \tag{93}$$

$J[\rho]$ and $E_{xc}[\rho]$ have already been defined in eqs. (62) and (74), respectively. At this point, the Kohn-Sham integro-differential equations for the orbitals ψ_i^α and ψ_i^β are obtained by minimizing the total energy [eq. (91)], after the selection of an exchange-correlation functional. Like for the unrestricted Hartree-Fock method, a basis set is also introduced here in order to convert these integro-differential equations in matrix equations which are computationally easier to handle. Hence, a new set of basis functions $\{\phi_\mu | \mu = 1, 2, \ldots, K\}$ is introduced and the unrestricted molecular orbitals are expressed as finite expansions in such a basis:

$$\psi_i^\alpha = \sum_{\mu=1}^{K} c_{\mu i}^\alpha \phi_\mu , \quad \psi_i^\beta = \sum_{\mu=1}^{K} c_{\mu i}^\beta \phi_\mu , \qquad i = 1, 2, \ldots, K . \tag{94}$$

The partial densities and the gradients are given as

$$\begin{aligned}\rho_\alpha &= \sum_\mu^K \sum_\nu^K \sum_i^{n_\alpha} \left(c_{\mu i}^\alpha\right)^* c_{\nu i}^\alpha \phi_\mu \phi_\nu \\ &= \sum_\mu^K \sum_\nu^K P_{\mu\nu}^\alpha \phi_\mu \phi_\nu\end{aligned}, \tag{95}$$

$$\nabla\rho_\alpha = \sum_\mu^K \sum_\nu^K P_{\mu\nu}^\alpha \nabla\left(\phi_\mu \phi_\nu\right), \tag{96}$$

with similar expressions for ρ_β and $\nabla\rho_\beta$. By substituting these expressions in the total energy [eq. (91)] and minimizing this energy with respect to the unknown coefficients $c_{\mu\nu}^\alpha$ and $c_{\mu\nu}^\beta$ in the LCAO expansion of molecular orbitals, under the constraint of orthonormality, a set of algebraic equations is obtained for the canonical orbitals

$$\left.\begin{aligned}\sum_{\nu=1}^K \left(F_{\mu\nu}^\alpha - \varepsilon_i^\alpha\right) c_{\mu\nu}^\alpha = 0 \\ \sum_{\nu=1}^K \left(F_{\mu\nu}^\beta - \varepsilon_i^\beta\right) c_{\mu\nu}^\beta = 0\end{aligned}\right\}. \tag{97}$$

ε_i^α and ε_i^β are the orbital energies for the occupied orbitals. A set of Fock-like matrices can be defined as

$$F_{\mu\nu}^\alpha = H_{\mu\nu}^{core} + J_{\mu\nu} + F_{\mu\nu}^{xc,\alpha}, \quad \text{and} \tag{98}$$

$$F_{\mu\nu}^\beta = H_{\mu\nu}^{core} + J_{\mu\nu} + F_{\mu\nu}^{xc,\beta}. \tag{99}$$

Here, $S_{\mu\nu}$ and $H_{\mu\nu}^{core}$ are the overlap and bare-nucleus Hamiltonian matrices, respectively, and $J_{\mu\nu}$ is the Coulomb matrix given by

$$J_{\mu\nu} = \sum_\lambda^K \sum_\sigma^K P_{\lambda\sigma} \left(\mu\nu|\lambda\sigma\right), \tag{100}$$

with $P_{\lambda\sigma}$ the total density matrix

$$P_{\lambda\sigma} = P_{\lambda\sigma}^\alpha + P_{\lambda\sigma}^\beta. \tag{101}$$

The conventional notation is used for the two-electron repulsion integrals [1].

The innovation with respect to the HF formulation is the exchange-correlation part of the Fock-like matrices which are expressed as

$$F_{\mu\nu}^{xc,\alpha} = \int \left[\frac{\partial F}{\partial\rho_\alpha}\phi_\mu\phi_\nu + \left(2\frac{\partial F}{\partial\gamma_{\alpha\alpha}}\nabla\rho_\alpha + \frac{\partial F}{\partial\gamma_{\alpha\beta}}\nabla\rho_\beta\right).\nabla\left(\phi_\mu\phi_\nu\right)\right] d\mathbf{r}, \tag{102a}$$

$$\gamma_{\alpha\alpha} = \left|\nabla\rho_\alpha\right|^2, \quad \gamma_{\beta\beta} = \left|\nabla\rho_\beta\right|^2, \tag{102b}$$

$$\gamma_{\alpha\beta} = \nabla\rho_\alpha \cdot \nabla\rho_\beta, \tag{102c}$$

and similar equations for $F_{\mu\nu}^{xc,\beta}$. These equations are analogous to the closed-shell Roothaan-Hall equations (where $c_{\mu\nu}^{\alpha} = c_{\mu\nu}^{\beta}$) and the unrestricted open-shell equations of Pople-Nesbet, which are described in previous sections. Once the equations have been solved by an iterative self-consistent field procedure, the Kohn-Sham energy is given by

$$E = \sum_{\mu,\nu}^{K} P_{\mu\nu} H_{\mu\nu}^{core} + \frac{1}{2} \sum_{\mu,\nu,\lambda,\sigma}^{K} P_{\mu\nu} P_{\lambda\sigma} \left(\mu\nu|\lambda\sigma\right) + E_{xc} , \tag{103}$$

where E_{xc} is given by eq. (85) and depends on the density and gradient of both the α and β spin electrons.

At this point, one of the main difficulties is the evaluation of the integrals in eqs. (85) and (102) which can only be carried out by a numerical procedure. Therefore, in order to describe the procedure for evaluating such integrals, it is useful to generalize the discussion. Consider an integral where the integrand is a function $F(\mathbf{r})$, like in

$$I = \int F(\mathbf{r}) d\mathbf{r} = \int_0^{\infty} \int_0^{\pi} \int_0^{2\pi} F(r,\theta,\varphi) r^2 \sin\theta \, dr d\theta d\varphi . \tag{104}$$

The radial and angular integrations can be separated by using the following product quadrature formula

$$I = \sum_{i=1}^{N^r} \omega_i^r \sum_{j=1}^{N^{\Omega}} \omega_j^{\Omega} F\left(r_i, \theta_j, \varphi_j\right), \tag{105}$$

where N^r and N^{Ω} are the number of radial and angular points, respectively, and the ω_i^r and ω_j^{Ω} are the radial and angular weights, respectively. The inner sum in eq. (105) corresponds to a quadrature on the surface of a sphere. Detailed descriptions of the integration grids and values for the different parameters can be found in [106-111]. More information on the implementation of DFT methods have been reported in [110, 112-116].

Besides efficient numerical methods, expressions for analytical gradients and/or second derivatives can be derived in order to efficiently determine minima on a potential energy surface and to optimize the related geometries by using DFT, as well as by Hartree-Fock and post-Hartree Fock methods [1, 110, 111]. The optimization of transition states is further discussed in more detail in section 2.12.4. Although it is clear that the DFT calculations using functionals such as B3LYP are extremely useful in predicting equilibrium structures [117] and harmonic frequencies, there are some failures. B3LYP is suited for semi-quantitative calculations of reaction and activation energies (enthalpies), but DFT calculations with the latter functional seem to be unreliable for transition states energies, as in fact, the calculated energy barriers are found to be too low [118]. On the other hand, MPW1K was shown to provide improved energy barriers [119-121], but at the expense of the quality of the geometries of saddle points. A very detailed survey of the performance of DFT is presented in [110].

2.7 One-Particle Green's Function theory

2.7.1 General Overview

In this section, the general principles of the one-particle Green's function [122-126] theory of ionization and electron attachment are briefly introduced within the more general framework of propagator theory, which is one of the most solid theories of many particle systems [1, 2, 19, 123, 127]. Causal two-time propagators are defined in the time domain as auto-correlation functions, describing the probability of an observable $\langle B \rangle$ at a time t_2 when a perturbation A is switched on at an earlier time t_1, or conversely of an observable $\langle A \rangle$ at a time t_1, when a perturbation B is switched on at an earlier time t_2:

$$\langle\langle B(t_2), A(t_1)\rangle\rangle = i^{-1}\left\langle \Psi_0^N \left| T_W\{B(t_2), A(t_1)\} \right| \Psi_0^N \right\rangle, \tag{106}$$

with Ψ_0^N the exact ground state wave function of a n-particle system, and the chronological time ordering operator of Wick, which is defined as

$$T_W\left(B(t_2), A(t_1)\right) = \begin{cases} B(t_2)A(t_1) & for\, t_2 - t_1 > 0 \\ \eta B(t_2)A(t_1) & for\, t_2 - t_1 < 0 \end{cases}, \tag{107}$$

with $\eta=+1$ if *A* and *B* symbolize boson-type operators, or $\eta=-1$ when the operators have a fermion character.

In this thesis, use has been made of the simplest example of two-time propagators, which is known as the one-electron propagator [123, 125] or, equivalently, one-particle Green's Function (1p-GF) [124]. The 1p-GF, containing information about electron affinities and ionization potentials, provides a systematic framework to improve these properties which in a first approximation are obtained at the Hartree-Fock level by Koopmans' theorem.

In the time domain, the 1p-GF gives the probability amplitude of propagation in a correlated background of an extra electron or hole between two one-particle states, χ_i and χ_j, in a given time interval *(t,t')*:

$$\mathbf{G}_{ij}(t',t) = \frac{1}{i}\left\langle \Psi_0^N \left| T_W\left\{a_i(t'), a_j^+(t)\right\} \right| \Psi_0^N \right\rangle, \tag{108}$$

where a_i and a_j^+ are the annihilation and creation operators of an electron in spin-orbital χ_i or χ_j, respectively, for $\eta=-1$ in eq. (107).

This discrete set of one-particle states χ_i can be obtained from the ground state one-particle Hartree-Fock (HF) spin-orbitals. Working with atomic units and in the framework of a nonrelativistic approach, the importance of the one-particle Green's function in describing the electronic structure theory of correlated systems can be appreciated from its spectral representation in the frequency domain. For a *N*-particle system with a non-degenerate closed-shell ground state, this representation reads:

$$\mathbf{G}_{ij}(\omega) = \lim_{\substack{\alpha \to 0 \\ >}} \left[\sum_{n\in\{N+1\}} \frac{\langle \Psi_0^N | a_i | \Psi_n^{N+1} \rangle \langle \Psi_n^{N+1} | a_j^+ | \Psi_0^N \rangle}{\omega + (E_0^N - E_n^{N+1}) + i\alpha} + \sum_{n\in\{N-1\}} \frac{\langle \Psi_0^N | a_j^+ | \Psi_n^{N-1} \rangle \langle \Psi_n^{N-1} | a_i | \Psi_0^N \rangle}{\omega + (E_0^{N-1} - E_0^N) - i\alpha} \right]. \tag{109}$$

In this expression, α ensures the convergence of the Fourier transform which couples the time and energy representations of **G**. $\left|\Psi_n^{N\pm1}\right\rangle$ and $E_n^{N\pm1}$ are the exact *(N±1)*-particle states and the corresponding energies, respectively, while E_0^N is the energy of the exact neutral ground state $\left|\Psi_0^N\right\rangle$. The first term on the right hand side of eq. (109) relates to the so-called retarded part with *t' > t* in eq. (108), which bears information on electron attachment processes, while the second component describing ionization processes derives from the advanced part with *t' < t*. Specifically, the poles of **G**(ω) in the complex ω-plane give access to the vertical-electronic ionization energies and electron affinities, whereas the correspoinding residues relate to Feynman-Dyson transition amplitues

$$x_i^{(n)} = \begin{cases} \langle \Psi_0^N | a_i | \Psi_0^{N+1} \rangle & \forall n \in \{N+1\} \\ \langle \Psi_n^{N-1} | a_i | \Psi_0^N \rangle & \forall n \in \{N-1\} \end{cases}, \tag{110}$$

which provide direct information on spectroscopic intensities. The probability to observe a specific ionic state $\left|\Psi_n^{N-1}\right\rangle$ is then given by a spectroscopic *pole strength* of the form

$$\Gamma_n = \sum_i \left| x_i^{(n)} \right|^2. \tag{111}$$

By definition, therefore, the pole strength Γ_n related to a pole ($\omega_n = E_0^N - E_n^{N-1} = -IP_n$) of the 1p-GF gives an estimation of the fraction of the ionization intensity related to a one-particle process, while the remaining fraction 1-Γ_n represents the intensity dispersed in correlation and relaxation effects. In this context, pole strengths close to unity characterize one-particle processes, whereas pole strengths smaller than ~0.85, are indicative of a breakdown of the one-particle picture [128] in the form of a dispersion of the ionization intensity derived from the same level to several ionizaiton lines of low intensity, and corresponding to excited (shake-up) configurations of the ionized system.

The exact one-particle Green's function of a many-body system can be obtained through a renormalization [122-127, 129-132] of a suitable zeroth-order form $\mathbf{G}_0(\omega)$ by means of the Dyson equation [1]

$$\mathbf{G}(\omega) = \mathbf{G}_0(\omega) + \mathbf{G}_0(\omega)\boldsymbol{\Sigma}(\omega)\mathbf{G}(\omega), \tag{112}$$

where the irreducible self-energy $\boldsymbol{\Sigma}(\omega)$ represents an effective and energy-dependent potential accounting for the interactions between electrons. In principle, this equation must be solved iteratively, since $\mathbf{G}(\omega)$ appears in the correction term on the right hand side of eq. (112). Obviously, if the exact form $\boldsymbol{\Sigma}(\omega)$ could be known, solving the Dyson equation for the Green's function would provide straightforward access to the exact ionization potentials and electron affinities of the correlated *N*-particle system.

The zeroth-order GF matrix derives from an uncorrelated model which is generally taken as the Hartree-Fock level

$$\mathbf{G}_{ij}^{(0)} = \lim_{\substack{\eta \to 0 \\ >}} \delta_{ij} \left(\frac{n_i}{\omega - \varepsilon_j - i\eta} + \frac{\overline{n}_i}{\omega - \varepsilon_j + i\eta} \right), \tag{113}$$

with δ_{ij} and ε_i denoting the usual Kronecker delta and the HF spin-orbital energies, respectively. As such, $n_i = 1 - \overline{n}_i$ defines the HF ground-state occupation numbers. Because the HF model is already correct through first-order in the correlation potential, the self-energy only contains second and higher order conttributions. As such, the cancellation of $\mathbf{\Sigma}^{(1)}$ terms is a direct extension of Brillouin's theorem in Møller-Plesset theory [1].

Since the exact irreducible self-energy $\mathbf{\Sigma}(\omega)$ describing a particular system is unknown, approximations must be introduced for practical applications of the 1p-GF theory. At this stage, the methods of approximation for the self-energy can be classified in two main categories: the pure algebraic and mixed algebraic-diagrammatic methods.

In the early 1970's, Pickup and Goscinski [133] and, independently, Purvis and Öhrn [134] formulated their algebraic approaches based on the superoperator formalism by Goscinski and Lukman [135]. The equation-of-motion (EOM) formalism has, since then, led to a number of efficient secular schemes for the treatment of ionization spectra [126, 136-141]. In the same period, Cederbaum and coworkers derived comparable schemes by comparison with appropriate Feynman diagram representations of the self-energy [124, 128]. Further develepments have led to one of the most efficient and accurate schemes for the calculation of ionization spectra, which is known as the Algebraic Diagrammatic Construction [142, 143] scheme through third-order in the correlation potential [ADC(3)] which is also referred to as the extended two-particle-hole Tamm-Dancoff Approximation (extended 2ph-TDA). In the next section, some hints with respect to the derivation and implementation of this powerful approach are discussed.

2.7.2 The ADC(3) approach

The dynamic self-energy $\mathbf{\Sigma}(\omega)$ [see eq. (112)] is decomposed into two parts [123-125, 127, 129]

$$\mathbf{\Sigma}(\omega) = \mathbf{\Sigma}(\infty) + \mathbf{M}(\omega), \tag{114}$$

where $\mathbf{\Sigma}(\infty)$ denotes the static (i.e. energy-independent) self-energy, relating to instantaneous scattering processes in the time domain, whereas $\mathbf{M}(\omega)$ is the dynamic self-energy describing the energetic outcome of the long-time scale many-body effects due to the propagation of an extra electron or hole in a correlated background. In the energy domain, the static self-energy is more specifically defined as the electrostatic potential felt by an incoming or outgoing particle due to correlation corrections to the HF ground state density ρ_{lk}^{HF}. As such, it is expanded as

$$\mathbf{\Sigma}_{pq}(\infty) = \sum_{kl} \langle pk \| ql \rangle \left[\rho_{lk}^{exact} - \rho_{lk}^{HF} \right], \tag{115}$$

with ρ_{lk}^{exact} the exact ground state density and $\langle pk \| ql \rangle$ the antisymmetrized bielectron integral over the spin-orbitals *(p,q,k,l)*, defined as

$$\langle pk \| ql \rangle = \iint d\mathbf{r}_1 d\mathbf{r}_2 \chi_p^*(\mathbf{r}_1)\chi_k^*(\mathbf{r}_2)\left(\frac{1-P_{ql}}{r_{12}}\right)\chi_q(\mathbf{r}_1)\chi_l(\mathbf{r}_2), \tag{116}$$

with P_{ql} the permutation operator on the spin-orbital labels q and l.

By analogy with eq. (109), describing G in terms of retarded and advanced parts, the dynamic self-energy $\mathbf{M}(\omega)$ can be decomposed in two terms which relate to excitations of the *(N+1)* and *(N-1)*-particle systems:

$$\mathbf{M}(\omega) = \mathbf{M}^+(\omega) + \mathbf{M}^-(\omega) \tag{117}$$

This decomposition of $\mathbf{M}(\omega)$ is directly reflected in its diagrammatic perturbation expansion, order by order. According to the Hugenholtz conventions [1 and references therein], the *n-th* order self-energy is obtained as the sum of all *topologically disctinct, time-ordered, linked* (one piece) and *irreducible* (strongly connected) diagrams built from *n antisymmetrized bi-electron interaction elements*, represented as dots with two lines going in and two lines going out, and *2n-1 oriented contraction lines*, describing zeroth-order (HF) $\mathbf{G}_{jj}^{(0)}$ propagators. One in-going and one out-going line from the interaction dots are left uncontracted. These hanging lines account for the spin-orbital labels casting the self-energy matrix. In these time-ordered self-energy diagrams, upward lines are *particle* lines describing the propagation of an electron forward in time, through virtual spin-orbitals (*r*, *s*, *t*,…). In the same way, downward contraction lines describe the propagation of an electron *backward* in time. Such a process being equivalent to the propagation of a hole forward in time, these lines are therefore referred to as *hole* lines and relate to occupied spin-orbitals (*a*, *b*, *c*,…). The *n!* time-ordered diagrams for a given *n-th* order time-unordered Feynman diagram can be divided into two distinct classes according to the time ordering $t > t'$ and $t < t'$ of the external vertices. The first class ($t > t'$) contributes exclusively to $\mathbf{M}^+(\omega)$, whereas the second class ($t < t'$) contributes only to $\mathbf{M}^-(\omega)$. There are no mixed terms and $\mathbf{M}^+(\omega)$ and $\mathbf{M}^-(\omega)$ may be calculated separately from their respective diagrammatic expansions.

At second-order, the static self-energy $\mathbf{\Sigma}(\infty)$ identically cancels, and only two diagrams account for $\mathbf{M}(\omega)$ (Figure 1). The 18 time-ordered third order self-energy diagrams are displayed in Figure 2. The diagrams C_1 to C_3 and D_1 to D_3 contribute to $\mathbf{M}^+(\omega)$, whereas the C_4 to C_6 and D_4 to D_6 diagrams contribute to $\mathbf{M}^-(\omega)$. The A_1 to A_6 diagrams account for the third-order static self-energy. The mathematical expressions for the second-and third-order self-energies are given in Appendix.

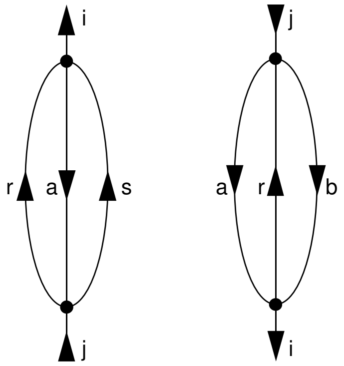

Figure 1. Time ordered diagrams of second order.

The rules for translating such self-energy diagrams into algebraic expressions can be summarized as:

1. Join the external indices *i* and *j* with a $e^{-i\omega(t'-t)}$ line, which accounts for the Fourier transform from the time to the energy domain.
2. Draw *n*-1 horizontal lines between successive pairs of $\langle ij \| kl \rangle$ points. Each of these horizontal lines *I* is associated with an energy factor A_i^{-1}.
3. Each $\mathbf{G}_{jj}^{(0)}$ line and $e^{-i\omega(t'-t)}$ line cut by an horizontal line *I* supplies an additive contribution to the factor A_i, namely $+\omega$ ($-\omega$) when the $e^{-i\omega(t'-t)}$ line points downward (upward), + ε_j ($-\varepsilon_j$) when the $\mathbf{G}_{jj}^{(0)}$ line points downward (upward).
4. Each dot in the diagram contributes a bielectron integral $\langle \text{label}-1\text{ in label}-2\text{ in} \| \text{label}-1\text{ out label}-2\text{ out}\rangle$ to the numerator.
5. The sign of the diagram is $(-1)^{\Sigma_h+\Sigma_l}$, where Σ_h is the number of hole lines, and Σ_l is the number of closed fermion loops.
6. Multiply the above contributions by 2^{-q}, where *q* is the number of permutations of two contraction lines in the diagram, leaving the diagram unchanged.
7. Sum the final expression over all particle and hole indices.

The ADC(3) scheme is based on the observation that the dynamic self-energy has the exact algebraic form [142]

$$\mathbf{M}_{pq}^{\pm}(\omega) = (\mathbf{U}_p^{\pm})^{\dagger}(\omega - \mathbf{K}^{\pm} - \mathbf{C}^{\pm})^{-1}\mathbf{U}_q^{\pm}, \tag{118}$$

where ($\mathbf{K}^{\pm}$ + $\mathbf{C}^{\pm}$) represent the effective energy interactions between excited states of the (*N* ± 1) particle system. $\mathbf{U}_q^{\pm}$ are the coupling amplitudes between these states and the state derived from ionization or electron attachment of an electron from or into spin orbital χ_q. $\mathbf{K}^{\pm}$ are diagonal matrices and correspond to a zeroth-order, i.e. HF, estimation of the shake-on and shake-up configuration spaces of the (*N* + 1)- and (*N* - 1)-particle systems.

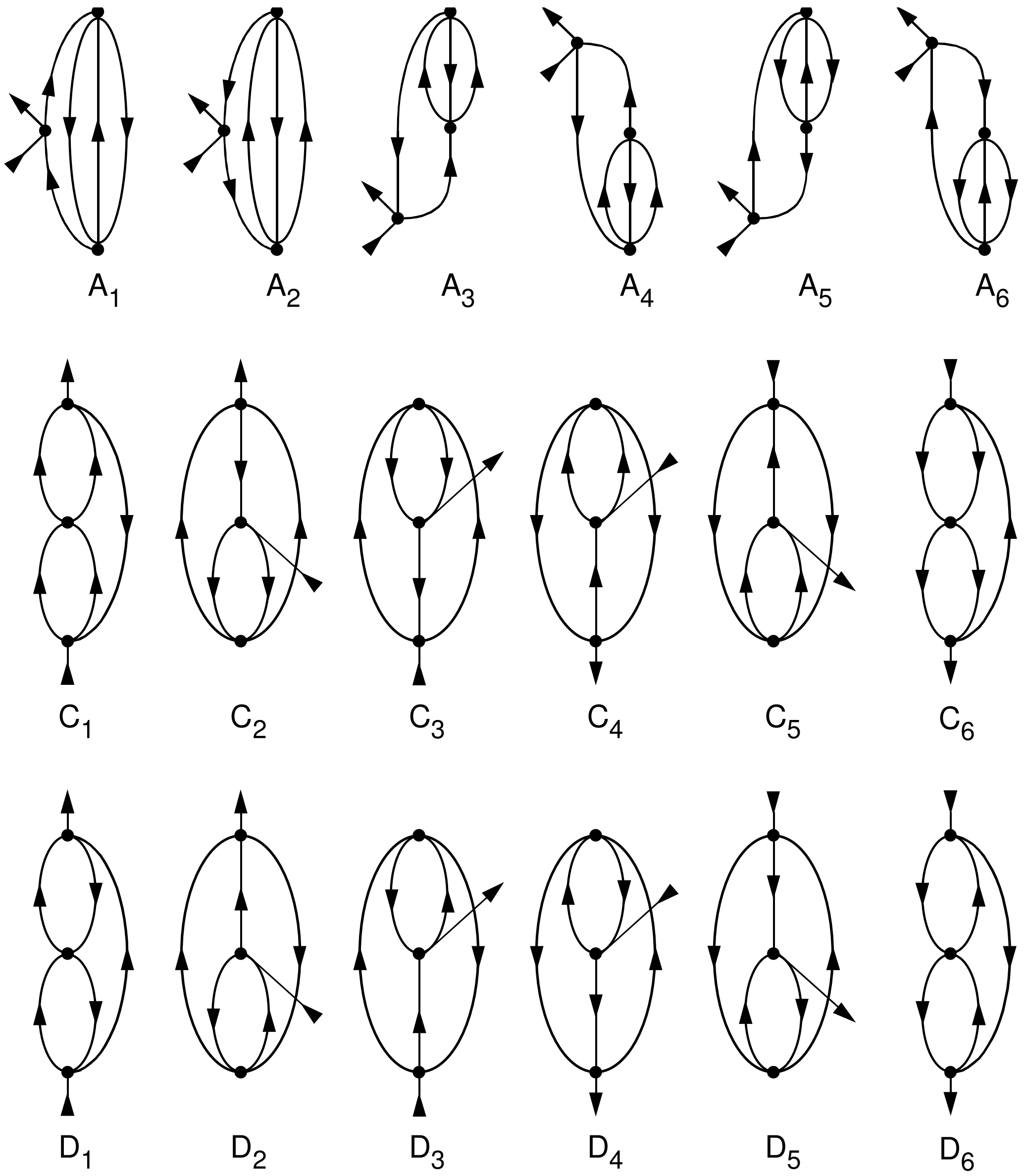

Figure 2. The 18 time-ordered third-order self-energy diagrams.

Specifically, the configuration space required to expand $\mathbf{M}^{+}(\omega)$ is determined by the 2*p*-1*h*, 3*p*-2*h*,… (two-particle/one-hole, three-particle/two-hole,…) shake-on excitations, whereas the $\mathbf{M}^{-}(\omega)$ component requires the 2*h*-1*p*, 3*h*-2*p*,… (two-hole/one-particle, three-hole/two-particle,…) shake-up excitations. In this nomenclature, the symbols *p* and *h* mean *particle* and *hole*; they describe creation of an electron in a virtual level, and the destruction of an electron in an occupied level, respectively.

In the ADC(3) scheme, appropriate expressions for the requested energy shifts $\mathbf{C}^{\pm}$ and coupling amplitudes $\mathbf{U}_q^{\pm}$ of eq. (118) have been derived by comparison with the diagrammatic perturbation expansions of $\mathbf{M}^{\pm}(\omega)$, through the required order in the correlation potential. By virtue of the matrix inverse in eq. (118), infinite but partial geometrical series in powers of the energy shifts $\mathbf{C}^{\pm}$, which take into account the effect of collective excitations, are automatically included. The ADC(3) approach also accounts for the influence of the electron correlation in the ground state on the dynamic polarization effects by means of the vectors of coupling amplitudes $\mathbf{U}_q^{\pm}$. The explicit (spin-unadapted) expressions for the $\mathbf{K}^{\pm}$, $\mathbf{C}^{\pm}$, and $\mathbf{U}^{\pm}$ matrices used in the ADC(3) scheme are the following:

$$\mathbf{U}^{+}_{ars,j} = \langle sr \| ja \rangle + \frac{1}{2}\sum_{cd} \frac{\langle sr \| cd \rangle \langle cd \| ja \rangle}{\varepsilon_c + \varepsilon_d - \varepsilon_r - \varepsilon_s} + (1 - P_{rs}) \sum_{cu} \frac{\langle rc \| ju \rangle \langle su \| ca \rangle}{\varepsilon_c + \varepsilon_a - \varepsilon_s - \varepsilon_u}, \qquad (119)$$

$$\mathbf{U}^{-}_{rab,j} = \langle ba \| jr \rangle + \frac{1}{2}\sum_{cd} \frac{\langle ba \| tu \rangle \langle tu \| jr \rangle}{\varepsilon_a + \varepsilon_b - \varepsilon_t - \varepsilon_u} + (1 - P_{ab}) \sum_{cu} \frac{\langle au \| jc \rangle \langle cb \| ru \rangle}{\varepsilon_b + \varepsilon_c - \varepsilon_r - \varepsilon_u}, \qquad (120)$$

$$\begin{aligned}(\mathbf{K}^{+} + \mathbf{C}^{+})_{ars,a'r's'} = {} & (-\varepsilon_a + \varepsilon_r + \varepsilon_s)\delta_{aa'}\delta_{rr'}\delta_{ss'} + \frac{1}{2}\langle rs \| r's' \rangle \delta_{aa'} \\ & - (1 + P_{rs}) \langle sa' \| s'a \rangle \delta_{rr'} \end{aligned}, \qquad (121)$$

$$\begin{aligned}(\mathbf{K}^{-} + \mathbf{C}^{-})_{rab,r'a'b'} = {} & (\varepsilon_a + \varepsilon_b - \varepsilon_r)\delta_{aa'}\delta_{bb'}\delta_{rr'} - \frac{1}{2}\langle ab \| a'b' \rangle \delta_{rr'} \\ & + (1 + P_{ab}) \langle br' \| b'r \rangle \delta_{aa'} \end{aligned}. \qquad (122)$$

As shown in eq. (115), the static self-energy $\mathbf{\Sigma}(\infty)$ depends also on the correlated one-electron density. In the ADC model, this quantity is expanded through Coulson contour integration over a suitable truncated form of the Dyson expansion of $\mathbf{G}(\omega)$ [144, 145]. With this approach, the determination of $\mathbf{\Sigma}(\infty)$ can in practice be reduced to a set of linear inhomogeneous equations entirely defined in the space of the one-particle and one-hole configurations, as follows

$$\mathbf{\Sigma}_{pq}(\infty) = b_{pq} + \sum_{kl} \langle pk \| ql \rangle \frac{n_l \bar{n}_k - \bar{n}_l n_k}{\varepsilon_l - \varepsilon_k} \mathbf{\Sigma}_{pq}(\infty), \qquad (123)$$

where the inhomogeneties are expanded as follows:

$$b_{pq} = \sum_{kl} \langle pk \| ql \rangle Q_{lk} . \qquad (124)$$

In the latter equation, Q_{lk} represents the correlation correction to the HF electron density matrix. It can be sorted out into six contributions as follows:

$$
\begin{aligned}
Q^{(ADC)}_{1;ml} &= -n_m n_l (\mathbf{V}^+_m)^\dagger \mathbf{V}^+_l ,\\
Q^{(ADC)}_{2;ml} &= +\bar{n}_m \bar{n}_l (\mathbf{V}^-_m)^\dagger \mathbf{V}^-_l ,\\
Q^{(ADC)}_{3;ml} &= +\bar{n}_m n_l (\varepsilon_l - \varepsilon_m)^{-1} (\mathbf{V}^+_m)^\dagger \mathbf{U}^+_l ,\\
Q^{(ADC)}_{4;ml} &= +n_m \bar{n}_l (\varepsilon_m - \varepsilon_l)^{-1} (\mathbf{V}^+_m)^\dagger \mathbf{U}^+_l ,\\
Q^{(ADC)}_{5;ml} &= -n_m \bar{n}_l (\varepsilon_l - \varepsilon_m)^{-1} (\mathbf{V}^-_m)^\dagger \mathbf{U}^-_l ,\\
Q^{(ADC)}_{6;ml} &= -\bar{n}_m n_l (\varepsilon_m - \varepsilon_l)^{-1} (\mathbf{V}^-_m)^\dagger \mathbf{U}^-_l .
\end{aligned}
\tag{125}
$$

Notice the analogy with the six A_1 to A_6 constant self-energy diagrams. The calculation of the vectors $\mathbf{V}^\pm_k$ implied in these equations requires the resolution of a system of inhomogeneous linear equations of the form

$$(\varepsilon_k - \mathbf{K}^+ - \mathbf{C}^+)\mathbf{V}^+_k = \mathbf{U}^+_k \qquad \bar{n}_k = 1, \tag{126}$$

$$(\varepsilon_k - \mathbf{K}^- - \mathbf{C}^-)\mathbf{V}^-_k = \mathbf{U}^-_k \qquad n_k = 1. \tag{127}$$

Once the static self-energy has been completely characterized through solving eq. (123), the identification of the poles of the one-particle GF becomes equivalent to solving a standard CI problem

$$\mathbf{HX} = \mathbf{XE}, \qquad \mathbf{X}^\dagger\mathbf{X} = 1, \tag{128}$$

with

$$\mathbf{H} = \begin{bmatrix} \boldsymbol{\varepsilon} + \boldsymbol{\Sigma}(\infty) & \mathbf{U}^+ & \mathbf{U}^- \\ (\mathbf{U}^+)^\dagger & \mathbf{K}^+ + \mathbf{C}^+ & \mathbf{0} \\ (\mathbf{U}^-)^\dagger & \mathbf{0} & \mathbf{K}^- + \mathbf{C}^- \end{bmatrix}, \tag{129}$$

where the block-matrices $\mathbf{K}^\pm + \mathbf{C}^\pm$ and $\mathbf{U}^\pm$ represent the effective coupling amplitudes between the excited (2*p*-1*h*, 2*h*-1*p*) configurations of the ($N \pm 1$)-particle systems, and the coupling of these excited states with the primary (1*p*, 1*h*) ionized states, respectively. $\boldsymbol{\varepsilon}$ is a diagonal matrix containing the HF orbital energies. Correspondingly, $\boldsymbol{\Sigma}(\infty)$ is the static (frequency-independent) self-energy block, as determined through eq. (123), which represents the electrostatic potential felt by an in-going or out-going electron due to correlation corrections to the zeroth-order (i.e. Hartree-Fock) density. By solving eq. (129) for ionization through diagonalization, the poles $\omega_n = E^N_0 - E^{N-1}_n$ and the residue amplitudes $x^{(n)}_i = \left\langle \Psi^{N-1}_n \middle| a_i \middle| \Psi^N_0 \right\rangle$ [see also eq. (110)] defining $\mathbf{G}(\omega)$ are immediately derived from the eigenvalues and the corresponding eigenvectors of the $\mathbf{H}$ matrix, respectively.

At this stage, it must be stressed that only the eigenvalues and eigenvectors of the ionization sector of $\mathbf{G}(\omega)$ are important and need to be explicitly extracted. For this purpose, it is advantageous to exploit the independence of the (N + 1)- and (N - 1)- particle blocks of the dynamic self-energy and the fact that these blocks are energetically located very far from each other. This allows a diagonalization in two steps, and the replacement of the (N + 1) electron attachment ($\mathbf{K}^+ + \mathbf{C}^+$) block, which is in general of very large dimensions, by a much smaller matrix which represents perfectly well the behavior of this block in the ionization region [143]. In order to overcome the problem of the truncation of the $K^{+}+C^{+}$ block by a selection of the most important configurations, which would certainly affect the accuracy of the final results, use has been made of projection methods based on a block extension [146, 147] of the Lanczos algorithm [148].

A complete diagrammatic overview of the self-energies amounting to the 1p-GF/ADC(3) scheme, in terms of time-ordered Hugenholtz diagrams is provided in Figure 3. Specifically, Figure 3 (a) represents the dynamic self-energy $\mathbf{M}(\omega)$ of eq. (118), where the 2*p*-1*h*/2*p*-1*h* and 2*h*-1*p*/2*h*-1*p* $\mathbf{K}^{\pm}$ + $\mathbf{C}^{\pm}$ kernels [see eqs. (121)-(122)] sketched in Figures 3(c,d) are iteratively expanded through first-order in correlation. The diagrams of figures 3(e,f,g,h) can be seen as *screened* bi-electronic interactions, amounting at the ADC(3) level to the second-order $(\mathbf{U}^{+})^{\dagger}$, $\mathbf{U}^{+}$, $(\mathbf{U}^{-})^{\dagger}$, and $\mathbf{U}^{-}$ coupling amplitudes of eqs. (119)-(120). At the ADC(3) level, these couplings reduce simply to first-order bielectronic interactions. Figure 3(b) amounts to the inhomogeneity, ***b***, from which the static self-energy $\mathbf{\Sigma}(\omega)$ is expanded by means of the diagrammatic equation of Figure 3(i), corresponding to eq. (123).

Compared to more traditional methods, the higher efficiency of the ADC approach is established by important properties such as the greater compactness of the employed secular matrix, and the size-consistency of the computed ionization and electron attachment energies [149, 150]. The perturbation expansions for the secular matrix elements behave regularly, i.e. like the perturbation expansions of the ground state. The configuration spaces used in this model are smaller than those of a comparable CI treatment, as the ADC(n) manifold of shake-up states extends only with each even order of n. Specifically, at the ADC(3) level, only the 2*p*-1*h* (two-particle/one-hole) and the 2*h*-1*p* (two-holes/one-particle) excitations are necessary to span the configuration spaces of the (N ± 1)-particle systems, respectively, whereas 3*h*-2*p* states would also be required in a CI treatment of ionization spectra at the same order in correlation.

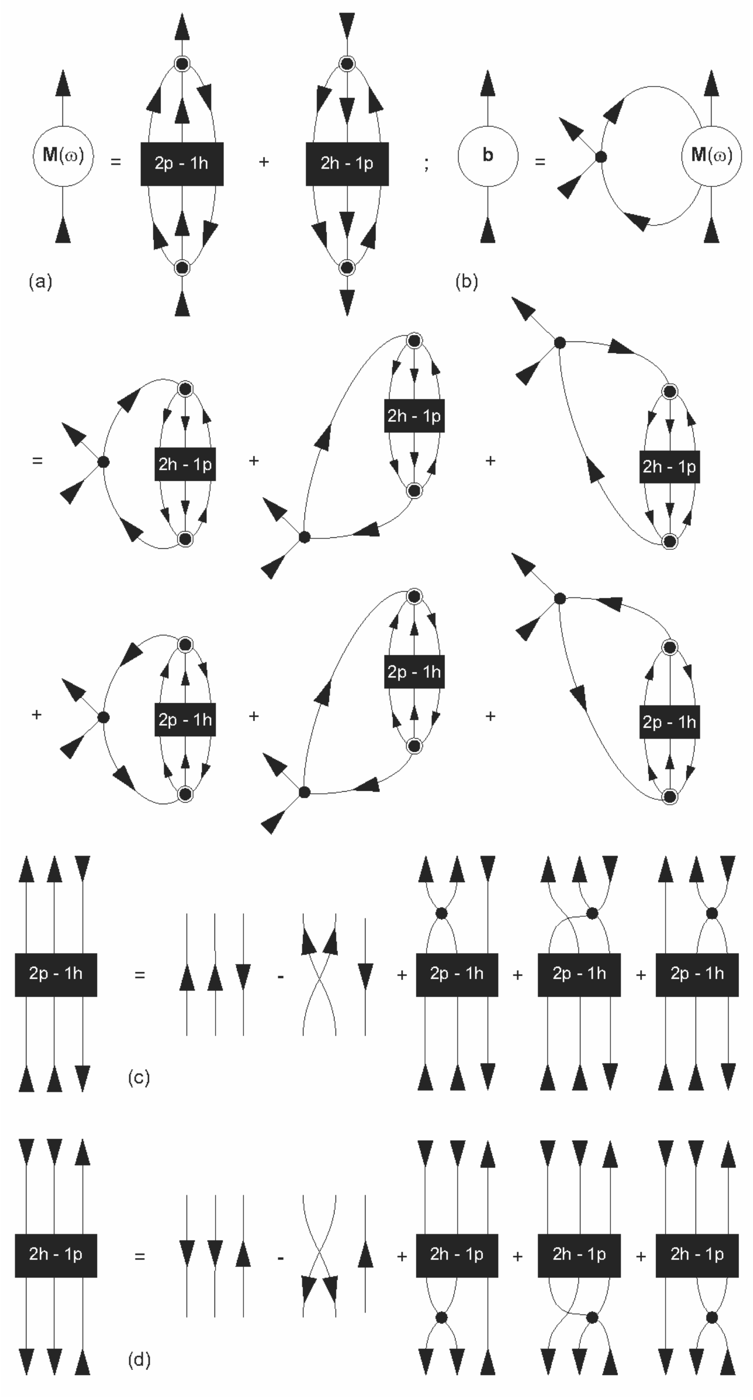
M(ω)
2p - 1h
2h - 1p
b
(a)
(b)
(c)
(d)

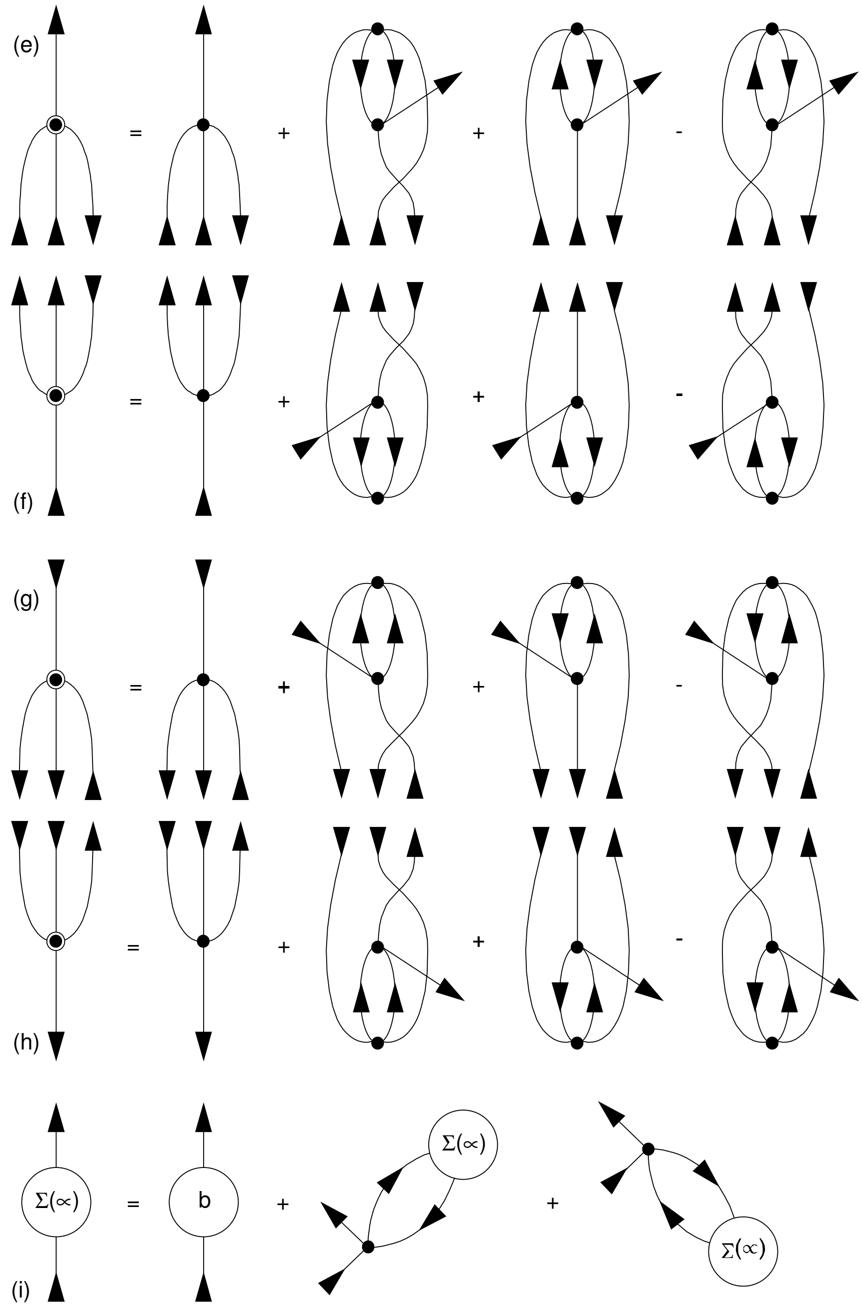

Figure 3. Complete diagrammatic overview of the self-energies amounting to the 1p-GF/ADC(3) scheme, in terms of time-ordered diagrams.

The size-consistency of the ADC model implies that for a system of identical *non-interacting* subunits or fragments, the results do not depend on whether the method is applied to the total system or to the fragments. This important requirement is ensured by the linked properties of all self-energy diagrams embodied in this treatment [150]. The size-consistency of the 1p-GF/ADC(3) method also implies a *balance* [150b] between the number of 2*h*-1*p* shake-up states and the scaling properties of bielectronic interactions. For a chain of *n* vertices, this balance can be physically traced from the size-dependence properties of shake-up bands [151]: each one-electron level (molecular orbital) gives rise [151e] to n^2 2*h*-1*p* satellites whose intensity individually scale like n^{-2}.

Note that the ADC corrections, **Q**, to the HF ground state one-electron density lead to a slight violation of the particle number [$\mathrm{tr}(\mathbf{Q}) \neq 0$], which, because of the long-range character of the Coulomb interaction [150b], results in turn into a logarithmic divergence [150c] with system size of the computed static self-energies, and hence ionization energies [150c]. Such a divergence can be prevented by substituting to **Q** in eq. (124) a suitable rescaled form [150c]:

$$\tilde{Q}_{ml} = \frac{N}{N + \mathrm{tr}(\mathbf{Q})}\left[Q_{ml} - n_m \delta_{ml} \frac{\mathrm{tr}(\mathbf{Q})}{N}\right], \qquad (130)$$

Ensuring the charge consistency of the ADC(3) ground state electron density [$\mathrm{tr}(\tilde{\mathbf{Q}}) = 0$] and the correct decay of the scattering potential described by the self-energy at large distances.

Shortly, it can be said that, prior to a rescaling of the electron densities, ADC(3) provides size-consistent results at all orders, but size-intensive results through fourth order, since the computed one electron densities are charge-consistent through third order only (as the particle number is computed exactly up to that order) [150c]. Rather fortunately, at this level, the impact of these charge violations is barely noticeable (0.02 eV) in practical applications on systems as large as pentacene [152].

2.7.3 The outer-valence Green's function

Nowadays, accurate one-hole (1*h*) ionization energies and electron affinities can be routinely obtained by means of the Outer Valence Green's Functions (OVGF) method. This approach is based on the observation that no poles of the self-energy lie in the outer-valence region, which means that in this area it is not necessary to calculate the poles of $\mathbf{\Sigma}(\omega)$ accurately. This observation can therefore be advantageously exploited to considerably simplify the calculations.

The OVGF approach also derives from the one-electron propagator formalism and relies on the quasi-particle, i.e. diagonal approximation for the self-energy $\mathbf{\Sigma}$. It consists in a diagonal renormalization scheme being exact through third-order in electron correlation. This method has been developed principally by Cederbaum and coworkers [124, 128j, 142, 153], and has been recently implemented by Ortiz and collaborators [154-156] in the Gaussian package of programs. The OVGF scheme is very simple and requires a negligible amount of computational effort, but has the limitation to be applicable only to outer-valence ionization processes, which can be correctly described as one-electron events. This approach performs poorly in obtaining accurate ionization energies and intensities in the presence of nearby shake-up states.

In the OVGF scheme, it is assumed that the Green's function matrix is diagonal for those orbital indices which are far from the poles of the self-energy. Since **G** is diagonal, the self-energy $\mathbf{\Sigma}(\omega)$ is also diagonal. The energy dependent part of the ADC(3) self-energy can be written as

$$\mathbf{M}_{pp}^{ADC(3)}(\omega) = \sum_n \frac{\left|m_p^{(n)}\right|^2}{\omega - \omega_n}, \tag{131}$$

where the superscript ± in eq. (118) has been dropped for brevity. In the ADC(3) scheme, all poles ω_n develop from poles of the second-order self-energy $\mathbf{M}^{(2)}(\omega)$. The ADC(3) self-energy can therefore be rewritten as

$$\mathbf{M}_{pp}^{ADC(3)}(\omega) = \sum_n \frac{\left|m_{pn}^{(2)}\right|^2 (1 - A_{pn})}{\omega - \omega_n^{(0)} - x_n}, \tag{132}$$

where $\omega_n^{(0)}$ is a pole of the second-order self-energy (of the form $\omega_n^{(0)} = \varepsilon_k - \varepsilon_l - \varepsilon_m$), and $\left|m_{pn}^{(2)}\right|^2$ is the second-order residue associated to this pole. The quantities x_n and A_{pn} are defined such that their inclusion in eq. (132) reproduces the ADC(3) self-energy given in eq. (131). These corrections x_n and A_{pn} are assumed to be small, i.e.

$$\left|A_{pn}\right| < 1, \qquad \left|\frac{x_n}{\varepsilon_p - \omega_n^{(0)}}\right| < 1. \tag{133}$$

At this point, $\mathbf{M}_{pp}(\omega)$ is expanded as a Taylor series

$$\mathbf{M}_{pp}^{ADC(3)}(\omega) = \sum_n \frac{\left|m_{pn}^{(2)}\right|^2}{\omega - \omega_n^{(0)}} \left\{1 + \frac{x_n}{\omega - \omega_n^{(0)}} + \ldots\right\} - \sum_n \frac{A_{pn}\left|m_{pn}^{(2)}\right|^2}{\omega - \omega_n^{(0)}} \left\{1 + \frac{x_n}{\omega - \omega_n^{(0)}} + \ldots\right\}. \tag{134}$$

Each term of this expansion can be assigned to groups of distinct diagrams [124, 153]. An average quantity A_p is defined as:

$$A_p \sum_n \frac{\left|m_{pn}^{(2)}\right|^2}{\omega - \omega_n^{(0)} - x_n} = \sum_n \frac{A_{pn}\left|m_{pn}^{(2)}\right|^2}{\omega - \omega_n^{(0)} - x_n}. \tag{135}$$

A_p actually depends on ω, but, as in this approach the energies ω of interest are far from the poles of the self-energy, A_p can be considered as a constant for $\omega \approx \varepsilon_p$, with ε_p the orbital energy of the considered orbital. To lowest (first) order, the renormalization factor A_p is determined by

$$A_p = -\sum_{i=2}^{5} \frac{(C_i + D_i)_{pp}}{\mathbf{M}_{pp}^{(2)}}, \tag{136}$$

where the diagrams C_2 to C_5 and D_2 to D_5, being the third-order self-energy contribution depicted in Figure 2, are explicitly given in Appendix. The analysis of the terms in eq. (134) leads to the final result

$$\mathbf{\Sigma}_{pp}(\omega) = \mathbf{\Sigma}_{pp}^{(2)}(\omega) + (1 + A_p)^{-1}\Sigma_{pp}^{(3)}(\omega), \tag{137}$$

which is the OVGF self-energy.

In fact, there are three versions of the OVGF method, known as versions *A*, *B*, and *C*, which differ in the corrections to the self-energy. Eq. (137) represents the version *A*. The version *B* has the following expression

$$\mathbf{\Sigma}_{pp}(\omega) = \mathbf{\Sigma}^{(2)}_{pp}(\omega) + \mathbf{\Sigma}^{(3)}_{pp}(\infty) + (1 + A^{+}_{p})^{-1}\mathbf{M}^{+(3)}_{pp} + (1 + A^{-}_{p})^{-1}\mathbf{M}^{-(3)}_{pp}, \tag{138}$$

where

$$A^{+}_{p} = -\frac{(C_2 + C_3)_{pp}}{\mathbf{M}^{+(2)}_{pp}}, \qquad A^{-}_{p} = -\frac{(C_4 + C_5)_{pp}}{\mathbf{M}^{-(2)}_{pp}}. \tag{139}$$

Finally, in version *C*, the self energy is defined as follows

$$\mathbf{\Sigma}_{pp}(\omega) = \mathbf{\Sigma}^{(2)}_{pp}(\omega)(1 + X_p)^{-1}\mathbf{\Sigma}^{(3)}_{pp}(\omega), \tag{140}$$

with

$$X_p = \frac{A^{-}_{p}\mathbf{\Sigma}^{-(3)}_{pp}(\omega) + A^{+}_{p}\mathbf{\Sigma}^{+(3)}_{pp}(\omega)}{\mathbf{\Sigma}^{(3)}_{pp}(\omega)}. \tag{141}$$

A detailed algorithm for choosing the best scaling factor has been presented in [157]. This algorithm analyses the ratios of selected second- and third-order diagrams which are introduced in each method:

- If ω_A > 15 eV and $|A_p| \le 0.85$ then
  - if $\mathbf{\Sigma}^{(2)}$ < 0.6 and $|X_p| \le 0.85$ then use *C*,
  - else, use *A*,
- else if ω_A > 15 eV and $|A_p| > 0.85$ and ω_B > 15 eV, while $|A^{+}_{p}| \le 0.85$ and $|A^{-}_{p}| \le 0.85$ then
  - if $\mathbf{\Sigma}^{(2)}$ < 0.6 use *C*,
  - else use *B*,
- else if ω_A > 15 eV and $|A_p| > 0.85$ and ω_B ≤ 15 eV, while $|A^{+}_{p}| \le 0.85$ and $|A^{-}_{p}| \le 0.85$ then
  - if $\mathbf{\Sigma}^{(2)}$ < 0.6 use *C*,
  - else use *B*,
- else if ω_A > 15 eV and $|A_p| > 0.85$ and ω_C ≤ 15 eV, while $|X_p| \le 0.85$ then
  - use *C*,
- else if $\mathbf{\Sigma}^{(2)}$ < 0.6 use *C*,
- else use *B*,

where ω_x (*x*= *A, B, C*) stands for a given method's ionization energy estimate.

In the OVGF approach, once the self-energy part has been calculated, the relevant pole of the Green's function $\mathbf{G}_{pq}(\omega)$ is determined as a root of the following Dyson equation

$$\omega = \varepsilon_p + \mathbf{\Sigma}_{pp}(\omega), \tag{142}$$

which is solved iteratively. With a diagonal Green's function matrix, the pole strength related to one-electron ionization or electron attachment processes is given by

$$\Gamma_p = \left[1 - \frac{\partial \mathbf{\Sigma}_{pp}(\varepsilon_p)}{\partial \omega}\right]^{-1}, \tag{143}$$

with ε_p the solution of eq. (142). It can be noted that $0 \le \Gamma_p \le 1$. At the OVGF level, $\Gamma_p < 0.85$ foretells a breakdown of the orbital picture of ionization at the ADC(3) level [223d, 223e].

The simplicity of the equations for determining the self-energy part and for solving the Dyson equation makes the OVGF approach, compared with ADC(3), applicable to larger molecules and/or enables the use of much larger basis sets.

Appendix: Evaluation of $\Sigma^{(2)}$ and $\Sigma^{(3)}$

$$\Sigma_{ij}^{(2)} = \frac{1}{2}\sum_{ars}\frac{\langle ia\,||\,rs\rangle\langle rs\,||\,ja\rangle}{\omega+\varepsilon_a-\varepsilon_r-\varepsilon_s} + \frac{1}{2}\sum_{abr}\frac{\langle ir\,||\,ab\rangle\langle ab\,||\,jr\rangle}{\omega+\varepsilon_r-\varepsilon_a-\varepsilon_b}$$

$$\Sigma_{ij}^{(3)}(\omega) = \sum_{k=1}^{6}(A_k + C_k + D_k)$$

with

$$A_1 = -\frac{1}{2}\sum_{abcrs}\frac{\langle ja\,||\,ib\rangle\langle rs\,||\,ac\rangle\langle rs\,||\,bc\rangle}{(\varepsilon_a+\varepsilon_c-\varepsilon_r-\varepsilon_s)(\varepsilon_b+\varepsilon_c-\varepsilon_r-\varepsilon_s)}$$

$$A_2 = +\frac{1}{2}\sum_{abrst}\frac{\langle jr\,||\,is\rangle\langle rt\,||\,ab\rangle\langle st\,||\,ab\rangle}{(\varepsilon_a+\varepsilon_b-\varepsilon_t-\varepsilon_r)(\varepsilon_a+\varepsilon_b-\varepsilon_t-\varepsilon_s)}$$

$$A_3 = +\frac{1}{2}\sum_{abcrs}\frac{\langle ja\,||\,it\rangle\langle rs\,||\,ab\rangle\langle rs\,||\,tb\rangle}{(\varepsilon_a+\varepsilon_b-\varepsilon_r-\varepsilon_s)(\varepsilon_a-\varepsilon_t)}$$

$$A_4 = +\frac{1}{2}\sum_{abcrs}\frac{\langle jt\,||\,ia\rangle\langle rs\,||\,ab\rangle\langle rs\,||\,tb\rangle}{(\varepsilon_a+\varepsilon_b-\varepsilon_r-\varepsilon_s)(\varepsilon_a-\varepsilon_t)}$$

$$A_5 = -\frac{1}{2}\sum_{abcrs}\frac{\langle jc\,||\,ir\rangle\langle rs\,||\,ab\rangle\langle cs\,||\,ab\rangle}{(\varepsilon_a+\varepsilon_b-\varepsilon_r-\varepsilon_s)(\varepsilon_c-\varepsilon_r)}$$

$$A_6 = -\frac{1}{2}\sum_{abcrs}\frac{\langle jr\,||\,ic\rangle\langle rs\,||\,ab\rangle\langle cs\,||\,ab\rangle}{(\varepsilon_a+\varepsilon_b-\varepsilon_r-\varepsilon_s)(\varepsilon_c-\varepsilon_t)}$$

$$C_1 = +\frac{1}{4}\sum_{arstu}\frac{\langle ia\,||\,rs\rangle\langle rs\,||\,tu\rangle\langle tu\,||\,ja\rangle}{(\omega+\varepsilon_a-\varepsilon_r-\varepsilon_s)(\omega+\varepsilon_a-\varepsilon_r-\varepsilon_s)}$$

$$C_2 = +\frac{1}{4}\sum_{abcrs}\frac{\langle ia\,||\,rs\rangle\langle rs\,||\,bc\rangle\langle bc\,||\,ja\rangle}{(\omega+\varepsilon_a-\varepsilon_r-\varepsilon_s)(\varepsilon_b+\varepsilon_c-\varepsilon_r-\varepsilon_s)}$$

$$C_3 = +\frac{1}{4}\sum_{abcrs}\frac{\langle ia\,||\,bc\rangle\langle bc\,||\,rs\rangle\langle rs\,||\,ja\rangle}{(\omega+\varepsilon_a-\varepsilon_r-\varepsilon_s)(\varepsilon_b+\varepsilon_c-\varepsilon_r-\varepsilon_s)}$$

$$C_4 = +\frac{1}{4}\sum_{abrst}\frac{\langle ir\,||\,ab\rangle\langle ab\,||\,st\rangle\langle st\,||\,jr\rangle}{(\omega+\varepsilon_r-\varepsilon_a-\varepsilon_b)(\varepsilon_a+\varepsilon_b-\varepsilon_s-\varepsilon_t)}$$

$$C_5 = +\frac{1}{4}\sum_{abrst}\frac{\langle ir\,||\,st\rangle\langle st\,||\,ab\rangle\langle ab\,||\,jr\rangle}{(\omega+\varepsilon_r-\varepsilon_a-\varepsilon_b)(\varepsilon_a+\varepsilon_b-\varepsilon_s-\varepsilon_t)}$$

$$C_6 = -\frac{1}{4}\sum_{abcdr} \frac{\langle ir \| cd\rangle\langle cd \| ab\rangle\langle ab \| jr\rangle}{(\omega+\varepsilon_r-\varepsilon_a-\varepsilon_b)(\omega+\varepsilon_r-\varepsilon_c-\varepsilon_d)}$$

$$D_1 = +\sum_{abrst} \frac{\langle ia \| rs\rangle\langle rb \| at\rangle\langle st \| jb\rangle}{(\omega+\varepsilon_a-\varepsilon_r-\varepsilon_s)(\omega+\varepsilon_b-\varepsilon_s-\varepsilon_t)}$$

$$D_2 = +\sum_{abrst} \frac{\langle ia \| rt\rangle\langle ts \| ab\rangle\langle rb \| js\rangle}{(\omega+\varepsilon_a-\varepsilon_r-\varepsilon_s)(\varepsilon_a+\varepsilon_b-\varepsilon_t-\varepsilon_s)}$$

$$D_3 = +\sum_{abrst} \frac{\langle it \| br\rangle\langle ab \| ts\rangle\langle sr \| ja\rangle}{(\omega+\varepsilon_a-\varepsilon_r-\varepsilon_s)(\varepsilon_a+\varepsilon_b-\varepsilon_s-\varepsilon_t)}$$

$$D_4 = +\frac{1}{4}\sum_{abcrs} \frac{\langle ir \| cb\rangle\langle ba \| rs\rangle\langle cs \| ja\rangle}{(\omega+\varepsilon_r-\varepsilon_b-\varepsilon_c)(\varepsilon_a+\varepsilon_b-\varepsilon_r-\varepsilon_s)}$$

$$D_5 = +\sum_{abcrs} \frac{\langle ia \| cs\rangle\langle rs \| ba\rangle\langle cb \| jr\rangle}{(\omega+\varepsilon_r-\varepsilon_b-\varepsilon_c)(\varepsilon_a+\varepsilon_b-\varepsilon_r-\varepsilon_s)}$$

$$D_6 = -\sum_{abcrs} \frac{\langle ir \| ab\rangle\langle as \| rc\rangle\langle bc \| js\rangle}{(\omega+\varepsilon_r-\varepsilon_a-\varepsilon_b)(\omega+\varepsilon_s-\varepsilon_b-\varepsilon_c)}$$

In these expressions, the indices (a, b, c,…) and (r, s, t,…) describe the occupied and virtual spin-orbitals, respectively.

2.8 Electron Momentum Spectroscopy

Electron momentum spectroscopy (EMS) [158], also known as binary (e,2e) spectroscopy, provides information on the electronic structure and permits the reconstruction in momentum space of spherically averaged electron density distributions for different ionization channels, i.e. orbitals, of atoms [159-162] and molecules, in the gas [163-190] as well as in the solid phases [191-194]. This powerful spectroscopy is therefore often somehow abusively referred to as an "orbital imaging" technique. This technique is based on binary (e,2e) electron impact ionization experiments in which the kinematics of the two outgoing electrons are fully determined using angular resolved electron spectroscopy and coincidence techniques. Such experiments provide ionization spectra at valence electron binding energies typically ranging from ~0 to ~30 eV, as a function of the relative azimuthal angle ϕ between the outgoing electrons. The electron momentum distribution for the target electron, in the initial neutral ground state wave function can be obtained by measuring the EMS cross-sections as a function of ϕ at a specific electron binding energy defining the ionization channel (i.e. orbital) of interest.

In this thesis, experimental data for gas phase molecular species have been provided by the groups of Prof. M. J. Brunger (School of Chemistry, Physics and Earth sciences, Flinders University, Adelaide, Australia) and of Prof. J. K. Deng (Department of Physics, Laboratory of Nanosciences, Tsinghua University, Beijing, P. R. China).

EMS is based on electron impact ionization experiments focusing on reactions

$$M + e^- \rightarrow M^+ + 2e^- . \tag{144}$$

As is depicted in Figure 4, these experiments employ a non-coplanar symmetric kinematical set up: the outgoing electrons have equal kinetic energies ($E_A = E_B = 750\,\text{eV}$) and make equal polar angles ($\theta_A = \theta_B = \theta = 45°$) with respect to the direction of the incident electron, which ensures a clean knock-out ionization process, initiated by electrons of energy so high that the target structure is determined independently of the incident energy. The target electron momentum p prior to ionization is monitored by scanning the azimuthal angle ϕ under which the outgoing electrons are selected at a given kinetic energy for the impinging electrons, according to basic conservation laws on momenta and energies:

$$p = \sqrt{\left(2\,p_A \cos\theta - p_0\right)^2 + \left(2\,p_A \sin\theta \sin(\phi/2)\right)^2} \quad \text{and} \tag{145}$$

$$E_A + E_B = E_0 - E_f\,, \tag{146}$$

with E_0 the impact energy and E_f the binding energy under investigation, which generally ranges from ~0 to ~30 eV. The total kinetic energy [E_A+E_B, eq. (146)] for the two outgoing electrons typically amounts to 1200 eV (Tsinghua University, Beijing) or 1500 eV (Flinders University, Adelaide).

Generally, in atomic units ($\hbar = e = m_0 = 1$), the differential cross section for ionization is [195]

$$\frac{d^5\sigma}{d\vec{p}_A d\vec{p}_B dE_A} = (2\pi)^4 \left(\frac{p_A p_B}{p_0}\right) \sum_{av} \left| \left\langle \vec{p}_A \vec{p}_B I \left| T \right| G \vec{p}_0 \right\rangle \right|^2 , \tag{147}$$

with the operator T governing the transition from the entrance channel to the exit channel. A formal discussion of this T-matrix can furthermore be found in [196]. I and G point at the state of the residual ion and at the initial ground state of the sample, respectively. $\sum_{av}$ denotes the sum required for averaging the contributions from all rotational, vibrational and electronic states (both initial and final) that are not resolved in the experiment. In the matrix element, $\vec{p}_0$ and $\{\vec{p}_A, \vec{p}_B\}$ represent the wave functions of the impinging and of the two outgoing electrons, respectively, with the corresponding momenta p_0, and $\{p_A, p_B\}$.

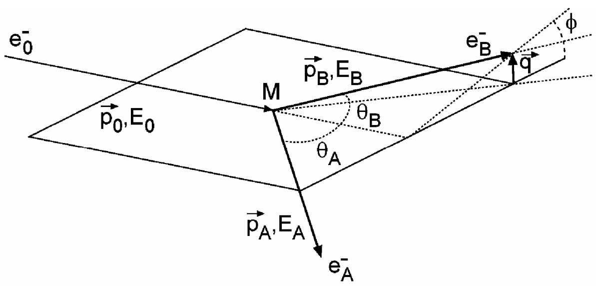

Figure 4: Schematic diagram illustrating the kinematics of a (e,2e) ionization reaction. The subscripts 0, A and B refer to the incident, scattered and ejected electrons (e^-), while $\vec{p}$ and E respectively denote their momenta and energy. The plane in the figure denotes the scattering plane. θ_A and θ_B are the in plane polar angles for the scattered and ejected electrons, while ϕ is the out-of-plane azimuthal angle for the ejected electron. $\vec{q}$ is the ion recoil momentum.

For molecular gases, the above eq. (147) can be simplified by invoking the Born-Oppenheimer approximation, in which the coordinate-space representations of the initial and final states are products of separate electronic, vibrational and rotational functions. At normal temperatures, the target is in its vibrational ground state, while the final rotational and vibrational states are not resolved and can be discarded by closure. Assuming that the collision operator T only depends on the electronic degrees of freedom, the differential cross section can be simplified to

$$\frac{d^5\sigma}{d\vec{p}_A d\vec{p}_B dE_A} = 4\pi^3\left(\frac{p_A p_B}{p_0}\right)\sum_{av}\int d\Omega \left|\left\langle \vec{p}_A \vec{p}_B \Psi_n^{N-1}\right| T \left|\Psi_0^N \vec{p}_0\right\rangle\right|^2, \qquad (148)$$

where the integration over the whole solid angle Ω of molecular orientations counts for the initial state rotational averaging. In eq. (148), $\sum_{av}$ thus only refers to an averaging over all rotational, vibrational and electronic degeneracies of the final ionized state. $\left|\Psi_0^N\right\rangle$ and $\left|\Psi_n^{N-1}\right\rangle$ represent the electronic neutral ground and ionized states of the target, respectively. For this equation (148), it has been supposed that the vibrational average gives the same result as taking the electronic functions at their equilibrium nuclear positions. In practice, the final vibrational and rotational states induced by an ionization event are usually not resolvable experimentally. These can be regarded therefore as degenerate within the energy resolution of the experiment. In this form, an explicit expression for the T-operator can be found in a study by Stia *et al.* [197] on the ionization of hydrogen molecules by fast electron impact:

$$T \sim \frac{1}{r_{1p}} + \frac{1}{r_{2p}} - \frac{1}{R_a} - \frac{1}{R_b}, \qquad (149)$$

with r_{1p} and r_{2p} denoting the distance between the projectile and the two electrons of the system. R_a and R_b point at the distance between the projectile and the two nuclei. Note therefore that the collision operator explicitely depends on nuclear and electronic coordinates.

Invoking the binary encounter approximation, it is assumed that the momentum lost by the incident electron is transferred to the ejected ones. The operator T depends on the coordinates of only three electrons: the projectile and the ejected electrons. Note that the two outgoing electrons, which have equal energies and momenta in the kinematic set-up under consideration, are measured in coincidence and cannot be distinguished. In this respect, $\vec{p}_A$ and $\vec{p}_B$ should always be considered together.

Furthermore, according to the Born or sudden approximation, a vertical depiction for ionization is assumed (i.e. geometrical relaxation and nuclear dynamical effects are neglected). When the incident electron only interacts with the ejected electrons and neither affects the target nor is affected by the target, the impulse approximation is considered. Modelling the incident and outgoing electrons as plane waves yields ultimately the Plane Wave Impulse Approximation (PWIA). Consequently, the momentum $\vec{p}$ of the target electrons prior to ionization satisfies

$$\vec{p} = -\vec{q} \qquad (150)$$

with $\vec{q} = \vec{p}_0 - \vec{p}_A - \vec{p}_B$, the recoil momentum of the target. As a consequence, the structure factor in eq. (148) fulfils

$$\left|\left\langle \vec{p}_A \vec{p}_B \Psi_n^{N-1} \middle| T \middle| \Psi_0^N \vec{p}_0 \right\rangle\right|^2 = \sigma_{\text{Mott}} \left|\left\langle \nu_{\vec{p}} \Psi_n^{N-1} \middle| \Psi_0^N \right\rangle\right|^2, \qquad (151)$$

with $\nu_{\vec{p}}(\vec{r}) = e^{i\vec{p}\cdot\vec{r}}$. In this equation, the Mott scattering cross section σ_{Mott} satisfies [196]

$$\sigma_{\text{Mott}} = \frac{1}{4\pi^4} \frac{2\pi\eta}{e^{2\pi\eta} - 1} \left[\frac{1}{|\vec{p}_0 - \vec{p}_A|^4} + \frac{1}{|\vec{p}_0 - \vec{p}_B|^4} - \frac{1}{|\vec{p}_0 - \vec{p}_A|^2} \frac{1}{|\vec{p}_0 - \vec{p}_B|^2} \cos\left(\eta \ln \frac{|\vec{p}_0 - \vec{p}_B|^2}{|\vec{p}_0 - \vec{p}_A|^2} \right) \right], \qquad (152)$$

with $\eta = \dfrac{1}{|\vec{p}_A - \vec{p}_B|}$. This kinematic factor is practically constant under the employed experimental setup.

As such, the differential cross-section for the electron impact ionization process displayed in Figure 4 is given by [198]

$$\frac{d^5\sigma}{d\vec{p}_A d\vec{p}_B dE_A} = 4\pi^3 \left(\frac{p_A p_B}{p_0} \right) \sigma_{Mott} \sum_{av} \int d\Omega \left|\left\langle \nu_{\vec{q}} \Psi_n^{N-1} \middle| \Psi_0^N \right\rangle\right|^2 . \qquad (153)$$

As all employed approximations become more accurate with increasing incident energy E_0, the structure factor in eq. (153) is assumed to be independent of the energy under the PWIA. Recently, it has been shown that its validity for polyatomic molecules may be substantially different, as convincingly illustrated for biacetyl [199] and ethylene [200]. These results are in contrast with earlier impact energy dependence studies on momentum distributions for outer valence orbitals of simple targets such as Ar [201], H_2 [199, 202] and HF [203], for which thresholds of only a few hundred electron volts have been noted. As the influence of distorted waves decreases with an increase of the impact energy [200], experiments at different values of E_0 are needed to prove whether the PWIA is valid or not under the employed experimental conditions. Unfortunately, theoretical calculations using a distorted wave impulse approximation (DWIA) in molecules cannot be achieved until now due to the multicenter nature of molecular targets.

Within a vertical depiction for ionization and in the limit of high kinetic energies, the transition amplitude in eq. (153) is simply [151c, 204, 205]

$$\left\langle \nu_{\vec{q}} \Psi_n^{N-1} \middle| \Psi_0^N \right\rangle = \left\langle \nu_{\vec{q}} \middle| g_n(\mathbf{x}) \right\rangle , \tag{154}$$

where $g_n(\mathbf{x})$ is the Dyson spin-orbital [124, 133] associated to the ionized state Ψ_n^{N-1}, which accounts for correlation and relaxation effects on ionization intensities. The overlap matrix in (153) reduces to the Fourier transforms in momentum space ($\vec{p}$) of Dyson spin-orbitals $g_n(\mathbf{x}) = g_n(\omega, \vec{r})$, with ω the spin variable. This (spin-) orbital is defined as the partial overlap between the neutral ground state and the final cationic state [2, 125, 204]:

$$g_n(\mathbf{x}) = \sqrt{N} \int \Psi_n^{N-1}(\mathbf{x}_1, \mathbf{x}_2, \ldots, \mathbf{x}_{N-1})\, \Psi_0^N(\mathbf{x}_1, \mathbf{x}_2, \ldots, \mathbf{x}_{N-1}; \mathbf{x})\, d\mathbf{x}_1\, d\mathbf{x}_2 \cdots d\mathbf{x}_{N-1} , \tag{155}$$

with N the number of electrons in the target molecule.

Upon introducing a parameter

$$K = 4\pi^3 \left(\frac{p_A p_B}{p_0} \right) \sigma_{Mott} , \tag{156}$$

and incorporating the prefactors in eq. (153), one finds therefore:

$$\frac{d^5\sigma}{d\vec{p}_A d\vec{p}_B dE_A} = K \int d\Omega \left| g_n(\omega, \vec{p}) \right|^2 . \tag{157}$$

For closed-shell systems, the operation $\sum_{av}$, which stems from eq. (153), is discarded by considering the degeneracies of the electronic ion as different and distinct states characterized by different Dyson orbitals. The analysis of the angular dependence of the (e,2e) cross sections at large impact energies enable us to experimentally infer momentum distributions. As such, EMS can be regarded as a powerful orbital-imaging technique, although, even for systems containing only one electron, orbitals derived as eigenfunctions of one-electron hamiltonians do not represent true molecular observables [206].

Using a canonical molecular orbital basis, Dyson orbitals can be expanded as linear combinations of Hartree-Fock (HF) orbitals χ_i, as follows:

$$g_n(\mathbf{x}) = \sum_i x_{in} \chi_i(\mathbf{x}) , \tag{158}$$

where $x_{in} = \left\langle \Psi_n^{N-1} \middle| a_i \middle| \Psi_0^N \right\rangle$ defines the Feynman-Dyson transition amplitude for ion state *n*, orbital *i* and the initial ground state. Note that second quantization [1] has been employed in the latter equation for describing the annihilation of an electron in orbital *i* by means of the operator a_i. From section 2.7 about the one-particle Green's Function, it is clear that the norm of a Dyson orbital defines the spectroscopic strength $\Gamma_n = \sum_i \left| x_{in} \right|^2$ of the corresponding ionic state $\left| \Psi_n^{N-1} \right\rangle$. Provided all ionization channels can be identified, the spectroscopic strengths satisfy the sum rules

$$\sum_n x_{in} = 1, \qquad \text{as well as} \tag{159}$$

$$\sum_n \Gamma_n = N. \tag{160}$$

Consequently, the most exact treatment for fully interpreting momentum distributions inferred from an analysis of the angular dependence of EMS spectra is the *Target-Dyson* approximation, which amounts to substituting the structure factor of eq. (157) for expression (158). We recall that this model is formally exact with regards to a many-body treatment of ionization processes, within the framework of the binary encounter approximation for electronic scattering, the Born assumption of a sudden (vertical) ionization event, and the plane wave impulse approximation for the ingoing and outgoing electrons.

Dropping spin for simplicity, this results into

$$\frac{d^5\sigma}{d\vec{p}_A d\vec{p}_B dE_A} = K \sum_i x_{in}^2 \int d\Omega \left| \chi_i(\vec{p}) \right|^2. \tag{161}$$

Following the discussion from section 2.7 concerning one-particle Green's Function theory, the Feynman-Dyson coefficients x_{in} in eq. (161) are computed by means of the third order Algebraic Diagrammatic Construction scheme [ADC(3)].

Assuming that the most important *1h* contribution to the ionization channel *n* is due to one specifical HF molecular orbital χ_j^{HF} and that all other contributions can be neglected, eq. (161) reduces to

$$\frac{d^5\sigma}{d\vec{p}_A d\vec{p}_B dE_A} \approx K\,\Gamma_n \int d\Omega \left| \chi_j^{HF}(\vec{p}) \right|^2, \tag{162}$$

which defines the so-called *Target Hartree-Fock Approximation.*

In the same way, by replacing the Dyson orbital in eq. (157) by the relevant Kohn-Sham (KS) orbital χ_j^{KS} [207, 208], we may empirically introduce the *Target Kohn-Sham Approximation*:

$$\frac{d^5\sigma}{d\vec{p}_A d\vec{p}_B dE_A} \approx K\,\Gamma_n \int d\Omega \left| \chi_j^{KS}(\vec{p}) \right|^2, \tag{163}$$

which amounts to stating that Kohn-Sham orbitals are equal to normalized Dyson orbitals. One may argue that KS orbitals used to expand the electron density of a *N*-electron interacting system can be mapped onto the Dyson orbitals of an (hypothetical) non-interacting system [209]. This does not imply however that KS orbitals coincide with the Dyson orbitals of the interacting system. No theory so far ever proved that a formal relationship exists between the Kohn-Sham and Dyson orbitals of a correlated system in its neutral ground state. Even DFT calculations employing an exact functional would not provide the Dyson orbitals of such a system! Also, Janak's theorem [210] equating ionization energies to KS eigenvalues is only strictly valid for the highest occupied molecular orbital (HOMO). Note that a more recent development referred to the meta-Koopmans theorem [211] relates Kohn-Sham orbital energies to *relaxed* ionization energies for one-electron events. Standard functionals for ground state calculations were however certainly not explicitely parametrized for accounting with electronic relaxation. Even upon a reparametrization of functionals in this purpose, the DFT formalism remains unsuited for coping with final-state configuration interactions, leading to the dispersion of the ionization intensity into shake-up processes. Due to the self-interaction error (section 2.6.4), the most widely used gradient corrected and hybrid functionals like B3LYP and BP do not have the correct Coulomb asymptotic behavior ($-1/r$) [110]. Nevertheless, KS orbitals have been extensively used as an empirical tool for rather accurately simulating electron momentum distributions. The generally excellent agreement between theory and experiment is probably the outcome of fortuitous error cancellations (neglect of final state correlation versus a too rapid falloff of the DFT exchange correlation potential at large distances due to the self-interaction error). In the sequel of this thesis, it is demonstrated that, in contrast with Green's function theory, it is impossible to assign highly congested (e,2e) ionization spectra by resorting only to Hartree-Fock or Kohn-Sham orbital energies and their related electron momentum distributions.

In practice, prior to any further analysis, ionization spectra obtained by EMS have to be deconvolved with a set of gaussians whose number and positions are traditionally taken from available UPS spectra, which is a rather essential and critical step in the interpretation of EMS experiments. Electron Momentum Distributions (MDs) for the selected and/or properly identified ionization channels are then inferred from an angular analysis of the related (e,2e) cross sections. Shortly, in view of the target-Dyson, target-HF and target-KS approximations, orbital densities for specific sets of ionization channels are imaged in momentum space. In our computations, spherically averaged Dyson orbital momentum distributions have been correspondingly generated from the output of 1p-GF/ADC(3) calculations using the MOMAP program by Brion and co-workers [212] and homemade interfaces. Traditionally, two types of momentum distributions (MDs) are discriminated. Orbitals characterized by MDs with a non-vanishing contribution at $\phi \sim 0°$ are described as being of the *s*-type, while orbitals of the *p*-type have MDs with vanishing intensity at the origin of momentum space.

To compare experimental MDs with theoretical ones, the latter have to be convolved with weight functions that take into account the limited angular resolution of the spectrometer. For a particular theoretical cross section Π [see eq. (161)], the intensity s at a particular momentum p_0 is thus calculated according to

$$s(p_0) = \int \Pi[f(\phi,\theta)] R(\phi,\phi_0) R(\theta,\theta_0)\, d\phi\, d\theta\,, \qquad (164)$$

with $f(\varphi,\theta)$ expressing the equivalence between the momentum p of the target electron prior to ionization and the angles φ and θ [see eq. (145)]. In this thesis, the Gaussian weighted planar grid (GW-PG) method of Duffy *et al.* [213, 214] has been used to define the functions $R(\phi,\phi_0)$ and $R(\theta,\theta_0)$, which are given by Gaussians with deviations $\Delta\theta$ and $\Delta\phi$ of ~0.7° and ~1.9°, respectively, [215-217] for the experimental apparatus in Beijing and with $\Delta\theta$ and $\Delta\phi$ of ~0.6° and ~1.2° [158d, 218], respectively, for the one in Australia. The resolution on momenta Δp amount correspondingly to ~0.20 a.u. and ~0.16 a.u.

Currently, the Full-Width-at-Half-Maximum (FWHM) for the experimental set-up in Adelaide amounts to 0.6 eV in energy domain [158d, 218], measured on helium, compared with 1.2 eV for the apparatus in Beijing [215, 216]. Note that, due to natural and vibrational line widths of the various electronic transitions and to dispersion of the ionization intensity into shake-up states, these values are enlarged. Consequently, the orbital imaging capability of EMS is lowered when it is applied to large molecules and compounds with a low bandgap and/or a limited symmetry point group.

In the near future, it will be possible to reach improved resolutions with the (e,2e) spectrometer at Tsinghua University. In test studies, an energy resolution of ~0.68 eV (FWHM) has already been achieved, as well as angular resolutions of $\Delta\theta$~0.53° and $\Delta\phi$~0.84°. Referring to the resulting resolution of 0.16 a.u. on momenta, the latter apparatus is then comparable to that one used by the group of Prof. X. J. Chen (University of Science and Technology, Hefei, P. R. China), with a momentum resolution of 0.15 au [219].

2.9 Penning ionization electron spectroscopy

Penning Ionization Electron Spectra (PIES) are obtained by measuring the kinetic energy distribution of electrons that are ejected upon collision between a molecular target, *M*, and a rare gas atom in a metastable excited state, *A**, as a result of chemi-ionization processes for various ionization channels [220]

$$A^{*}+M \rightarrow A+M_{i}^{+}+e^{-}. \qquad (165)$$

These spectra are very similar to photon-impact ionization spectra, with the essential advantage that the obtained ionization intensities represent a direct measure of the extent of the molecular orbitals outside the molecular surface and of their relative reactivity towards an approaching electrophilic agent. Therefore like EMS, Penning ionization electron spectroscopy is also known as an efficient method for probing the shape and spread of molecular orbitals.

In the electron exchange mechanism proposed for Penning ionization [221], an electron in a molecular orbital φ_i of the molecular target *M* is transferred to the lowest unoccupied orbital of *A**, whereas the excited electron in *A** is ejected into the continuum, provided *A** has a larger excitation energy than the energy required for ionizing an electron in orbital φ_i. Upon neglecting through-space interactions between *A** and *M* (see further), the excess kinetic energy of the ejected electron (in short the electron energy) is equal, in a molecular orbital (or quasi-particle) picture of ionization, to the difference between the excitation energy of the rare gas atom and the electron-binding energy (or ionization energy, IE_i) of an electron in orbital φ_i. According to Hartree-Fock (HF) theory and Koopmans's theorem [1], the latter binding energy is simply minus the energy of the ionized HF orbital ($-\varepsilon_i$). At such level, the predicted order of ionized states is very uncertain due to the neglect of many-electron interactions. A number of quasi-particle schemes exist for improving this approximation by accounting for the removal of electronic correlation induced by the annihilation of a single electron in an occupied orbital, and for the relaxation energy released by the creation of an electron hole [1]. We refer in particular to the Outer Valence Green's Function scheme [124, 153-155] (see also section 2.7), an approach that describes ionization within a quasi-particle picture through third-order in the correlation potential, and ensures therefore accuracies of about 0.1 - 0.2 eV on *vertical* one-electron ionization energies of large and low band-gap systems in the limit of an asymptotically complete basis set [222]. However, the energy released by electronic relaxation is most often largely sufficient to induce numerous electronic excitation processes within the cation, yielding to a very significant dispersion of the ionization intensity over many shake-up states with comparable intensities. This is particularly true for large π-conjugated systems [151b, 151e, 152, 223]. With these systems, the dispersion of intensity into many-body processes is such that for many ionization bands, both in the inner- and outer-valence regions, it is impossible to discriminate the shake-up states and the one-electron ionization states from which they originate. In such situations where the orbital picture of ionization so severely breaks down, one must resort to theoretical approaches which consistently account both for initial and final state electron correlation, as well as configuration interactions in the cation.

2.9.1 Ionization cross sections

In a hard-sphere depiction, the probability of the electron transfer in Penning ionization experiments, and, thus, the related cross sections mainly depend on the overlaps during the collision between the lowest unoccupied orbital of A^* and the ionized molecular orbital φ_i of M, outside the collision boundary surface [224]. On the basis of the electron-exchange mechanism, branching ratios of Penning ionization probabilities can be reliably studied by means of the exterior electron density (EED) model [224-226]. In this model, the exterior electron density ρ_i is calculated for individual canonical (Hartree-Fock) MOs, by means of

$$\rho_i = \int_{\Omega} \left|\varphi_i(r)\right|^2 dr, \tag{166}$$

where Ω is the subspace outside the repulsive molecular surface. EED values calculated with *ab initio* MOs and using as repulsive molecular surface the envelope defined by rigid van der Waals spheres are known [225, 226] to provide consistent insights into the relative intensities of bands in PIES. As a result of their greater extension outside the molecular van der Waals (vdW) surface, the Penning ionization cross sections of the π bands of conjugated hydrocarbons are naturally much larger than those measured for the σ bands, which the EED model easily explains [224-226].

2.9.2 Interaction potentials and collision-energy dependence of partial ionization cross sections

According to a two-potential curve model of Penning ionization processes, the electron energy (more precisely, the kinetic energy of the ejected electron, E_e^i) is equal to the energy difference, at the interdistance (R) at which the excitation transfer and chemi-ionization arise, between the incoming potential curve $V^*(R)$ for the entrance channel ($A^* + M$) and the outgoing potential curve $V^+(R)$ for the exit channel ($A + M_i^+$), provided that the relative translational energy is conserved during the transfer of electronic excitation [226, 227] The position of peaks measured in PIES can be therefore analyzed as follows

$$\begin{aligned} E_e^i(R) &= V^*(R) - V_i^+(R) \\ &= E_{A^*} - \left[IP_i(\infty) + \Delta IP_i(R)\right] \end{aligned}, \qquad (167)$$

where E_{A^*} is the excitation energy of the atomic probe, A* (19.82 eV for He*[2^3S]), IP_i (∞) is the ionization potential for the i^{th} ionization channel of the *isolated* molecule, and is most commonly determined by means of UPS. At last, $\Delta IP_i(R)$ accounts for the shift in the ionization potential due to the interactions between the molecular target and the probe. It has been found that

$$\Delta IP_i = V^*(\infty) - V_i^+(\infty) - \left[V^*(R) - V_i^+(R)\right]. \qquad (168)$$

The interaction potential curves V^* describing the approach of the He*(2^3S) probe toward the molecular target along various directions have been calculated on the basis of the well-known resemblance [220b] between the He*(2^3S) and Li(2^2S) species in collision processes. It has indeed been shown that the velocity dependence of the total scattering cross section of He*(2^3S) by He, Ar, and Kr very closely matches that of Li (2^2S) [228], and that the He*(2^3S) and Li(2^2S) probes exhibit very similar interaction potentials with various targets [229, 230], both in terms of the location and depth of the interaction well. With regards to these findings and the difficulties arising with calculations of potential energy surfaces for excited states, the Li(2^2S) atom is most commonly used in place of the He*(2^3S) atom.

Such calculations of interaction potentials are essential for qualitatively unraveling the dependence upon the collision energies of the partial ionization cross section (CEDPICS) measured from collision-energy-resolved Penning ionization electron spectra (CERPIES). Indeed, the collision energy dependence of these cross sections [$\sigma(E_c)$] can be expressed [220b, 231-233] as

$$\log \sigma(E_c) \propto (-2/s)\log E_c \qquad (169)$$

when the long-range attractive part of the interaction potential V^* is dominant and of the form

$$V^*(R) \propto R^{-s}. \qquad (170)$$

In equation (170), the s parameter relates to the collision energy dependence of the partial ionization cross sections in PIES via $s = -2/m$ for atomic targets, with m the slope parameter characterizing the linear regression of $\sigma(E_c)$ as a function of log (E_c). These equations show that, when the interaction potential for the entrance channel is attractive, the measured cross sections decrease as the collision energy increases: the higher the kinetic energy of the impinging metastable He* atoms, the lower the extent of the deflections of the trajectories of these species within an attractive potential well. On the contrary, if the entrance interaction potential is repulsive, the measured cross section $\sigma(E_c)$ increases with the collision energy E_c. This is because in such a situation faster He* atoms can more deeply poke into the target molecular orbital. From a more quantitative viewpoint, it is known [220b, 232, 233] that in this case the slope parameter m relates to the effective decay parameter d for the repulsive interaction potential [$V^*(R) = B \exp(-dR)$], where R represents the distance between the metastable atomic probe and a target molecule, and the effective parameter b for the transition probability [$W(R) = C \exp(-bR)$] through the relation

$$m = (b/d) - 1/2. \qquad (171)$$

Here, the effective parameter b derives from the first ionization potential [234, 235] [$I(M)$] via

$$b = 2\{2I(M)\}^{1/2}. \qquad (172)$$

Thus, the slope of the correlation of log $\sigma(E_c)$ vs log (E_c) provides an effective measure of the attractivity ($m < 0$) or repulsivity ($m > 0$) of a specific MO region of the target molecule towards an electrophilic He(2^3S) species.

2.10 Photo-electron spectroscopy

In the traditional technique of photo-electron spectroscopy, of which more information can be found in [236], a sample is irradiated by high-energy photons, which, for the purposes in this thesis, fall in the X-ray (XPS) or ultraviolet (UPS) range. With XPS, photons with an energy of 1486.6 eV (Al K_α radiation) are typically used, while, for UPS, energies of 21.22 eV (He I) or 40.82 eV (He II) are applied. During the measurement, the kinetic energy (KE) of the ejected electron is analyzed. In a one-electron picture of ionization, the ionization energy (I) of the target electron is estimated from $I = h\nu - KE$. A plot of the number of electrons reaching the detector versus the electron kinetic energy gives a spectrum of the various ionic states that are produced during the process.

The resolution of ultraviolet photo-electron spectroscopy is clearly superior to that of EMS [158d]. Measured on the rare gases helium and argon, the parameter for EMS indicating the full width at half of maximum amounts to 0.6 eV [218], while for UPS this parameter is as small as 0.03 eV [236b]. With XPS, the resolution is comparable to that of the best EMS set-ups nowadays.

2.11 Quantum mechanical description of nuclear motions

In the next sections we present an overview of the approximations and models used to describe the nuclear motions (translation, vibrations and rotations) in polyatomic molecules on quantum mechanical grounds. In section 2.12 the quantum mechanical energy levels of molecules, related to the nuclear motions, are then connected to macroscopically measured thermodynamic quantities such as the entropy (S), the enthalpy (H), ….

2.11.1 Translations

The motions of any mechanical system can always be decomposed into independent motions, namely a translational part and an internal part, related to the vibrational and rotational motions. Correspondingly, the Hamiltonian and the energy can be decomposed and written as the sum of independent terms:

$$\hat{H} = \hat{H}_{trans} + \hat{H}_{rot,vib}\,, \tag{173}$$

$$E = \varepsilon_{trans} + \varepsilon_{rot,vib}\,. \tag{174}$$

The translational motion is described by the motion of a freely translating point of mass $M = \sum_i^N m_i$ situated at the center of mass (center of mass motion) of the system. By definition the coordinates of the center of mass (cm) are given by:

$$x_{cm} = \frac{\sum_i^N m_i x_i}{\sum_i^N m_i},\; y_{cm} = \frac{\sum_i^N m_i y_i}{\sum_i^N m_i} \quad \text{and} \quad z_{cm} = \frac{\sum_i^N m_i z_i}{\sum_i^N m_i}. \tag{175}$$

Thus, the position of the center of mass can be calculated if the mass m_i and the location (x_i, y_i, z_i) of each component is known.

The translational energies of a molecule can be calculated by modelling the molecule as a dimensionless particle of mass *M* confined to a three-dimensional box with lengths *a* [237]. The quantum energy levels associated with the translational motions are then given by

$$\varepsilon_{trans} = \frac{h^2}{8Ma^2}(n_x^2 + n_y^2 + n_z^2)\,, \tag{176}$$

where n_x, n_y, n_z = 1, 2, 3 … represent the translational quantum numbers, and *h* is Planck's constant ($h = 6.62608 \cdot 10^{-34}$ J s).

The location of each of the *N* atoms in a polyatomic molecule is defined in terms of three coordinates; hence, 3*N* coordinates are required to completely describe the molecule. Of these, three coordinates are required to specify the center of mass (x_{cm}, y_{cm}, z_{cm}) of the molecule (translational degrees of freedom).

2.11.2 Rotations

The internal motions of the nuclei consist of rotational motions about the center of mass and of vibrational motions of the nuclei. In the rigid-rotor approximation, the rotational and vibrational motions are decoupled i.e. it is assumed that rotation occurs for a fixed value of interatomic distance. This allows rewriting the Hamiltonian related to the internal motions as follows:

$$\hat{H}_{rot,vib} = \hat{H}_{rot} + \hat{H}_{vib}\,. \tag{177}$$

The eigenstates can then be quantified according to the rotational and vibrational energy of the system:

$$\varepsilon_{rot,vib} = \varepsilon_{rot} + \varepsilon_{vib}\,. \tag{178}$$

The classical energy of a rigid rotor E_{rot} is all kinetic energy and is given by

$$E_{rot} = \frac{1}{2} I\omega^2 , \tag{179}$$

where $\omega = 2\pi\nu$ is the angular velocity and I the moment of inertia defined by

$$I = \mu R_0^2 , \tag{180}$$

with μ the reduced mass ($\mu = \frac{m_1 m_2}{m_1 + m_2}$) and R_0 the bond length.

The classical angular momentum is

$$J = I\omega . \tag{181}$$

Consequently, the energy can be written as

$$E_{rot} = \frac{J^2}{2I} . \tag{182}$$

The Hamiltonian operator is the kinetic energy operator

$$\hat{H} = -\frac{h^2}{8\pi^2 I}\nabla^2 = \frac{\hat{J}^2}{2I} , \tag{183}$$

where

$$\hat{J}^2 = -\frac{h^2}{4\pi^2}\left[\frac{1}{\sin\theta}\frac{\partial}{\partial\theta}(\sin\theta\frac{\partial}{\partial\theta}) + \frac{1}{\sin^2\theta}\frac{\partial^2}{\partial\phi^2}\right] . \tag{184}$$

The eigenvalues of $\hat{H}$ are

$$\varepsilon_{rot} = \frac{h^2}{8\pi^2 I} J(J+1) \quad \text{with} \quad J = 0,1,2,\ldots \tag{185}$$

For a linear molecule, two angular coordinates are required to specify its orientation in space (the molecule has only two axes where rotations can take place into physical distinguishable positions as the third possible axis is the molecular backbone), whereas for a non-linear molecule three coordinates are needed (the molecule as a whole can rotate around the *X*, *Y* and *Z* directions).

For a polyatomic molecule, $I = \sum_i^N m_i R_i^2$ where m_i is the atomic mass and R_i the distance of the i^{th} atom from the molecular center of mass. The moments of inertia of a rigid body characterize the rotational properties of the body. The moments of inertia about any set of Cartesian axes (with origin at the center of mass) are:

$$I_{xx} = \sum_{i=1}^{n} m_i \left[\left(y_i - y_{cm} \right)^2 + \left(z_i - z_{cm} \right)^2 \right], \tag{186}$$

$$I_{yy} = \sum_{i=1}^{n} m_i \left[\left(x_i - x_{cm} \right)^2 + \left(z_i - z_{cm} \right)^2 \right], \tag{187}$$

$$I_{zz} = \sum_{i=1}^{n} m_i \left[\left(x_i - x_{cm} \right)^2 + \left(y_i - y_{cm} \right)^2 \right]. \tag{188}$$

In addition there are also products of inertia such as:

$$I_{xy} = \sum_{i=1}^{n} m_i \left(x_i - x_{cm} \right) \left(y_i - y_{cm} \right). \tag{189}$$

The angular momentum J can be written in matrix notation as

$$\begin{pmatrix} J_x \\ J_y \\ J_z \end{pmatrix} = \begin{bmatrix} I_{xx} & I_{xy} & I_{xz} \\ I_{yx} & I_{yy} & I_{yz} \\ I_{zx} & I_{zy} & I_{zz} \end{bmatrix} \begin{pmatrix} \omega_x \\ \omega_y \\ \omega_z \end{pmatrix}, \tag{190}$$

with ω_x, ω_y and ω_z the angular velocity related to the angular rotations about the X, Y and Z axes, respectively.

It is always possible to find a particular set of Cartesian axes X, Y, Z called the principal axes such that all the products of inertia (I_{xy},…) vanish. The moments of inertia about the axes are called the principal moments of inertia I_{XX}, I_{YY}, I_{ZZ} (later also referred to as I_A, I_B, I_C) and can be obtained through diagonalization of the moment of inertia tensor I:

$$\begin{pmatrix} J_A \\ J_B \\ J_C \end{pmatrix} = \begin{pmatrix} I_A & 0 & 0 \\ 0 & I_B & 0 \\ 0 & 0 & I_C \end{pmatrix} \begin{pmatrix} \omega_A \\ \omega_B \\ \omega_C \end{pmatrix}. \tag{191}$$

For polyatomic molecules, separate principal moments of inertia are considered as the molecule rotates around the principal axes depending on the shape of the molecule. If $I_A = I_B = I_C$, the rigid body is called a "spherical top", while if $I_A = I_B \neq I_C$ then it is called a "symmetric top" and if $I_A \neq I_B \neq I_C$, the body is called an "asymmetric top".

For a spherical top the energy levels are given by

$$\varepsilon_{rot} = \frac{h^2 J(J+1)}{8\pi^2 I}, \tag{192}$$

with $J = 0, 1, 2, 3, \ldots$

The expression for the energy levels of a symmetric top is:

$$\varepsilon_{rot} = \frac{h}{8\pi}\left[\frac{J(J+1)}{I_A} + K^2\left(\frac{1}{I_C} - \frac{1}{I_A}\right)\right]. \tag{193}$$

For a symmetric top, J+1 sublevels of different energy can be found for each value of J, namely those with $K = J, J\text{-}1, J\text{-}2, ..., \text{-}J$. The quantum number K is a measure of the component of the rotational angular momentum along the unique Z axis of the symmetric top.

The energy levels of the asymmetric top cannot be represented by an explicit formula analogous to that for the spherical or symmetric top. The energy levels of an asymmetric top can be compared with two limiting cases, one in which $I_A < I_B = I_C$ (prolate symmetric top) and the other in which $I_B = I_A < I_C$ (oblate symmetric top) (Figure 5). By gradually decreasing I_B from $I_B=I_C$ to $I_B=I_A$, we can expect a continuous change of the energy levels. In a rough approximation, the energy levels of the asymmetric top are obtained simply by connecting (by smooth curves) the levels of a given J. For a more detailed description, the book "Infrared and Raman spectra" by Herzberg should be consulted [237]. For each value of J there are $2J+1$ different energy levels. There is no "good" quantum number having a physical meaning that distinguishes the $2J+1$ different levels with equal J. Therefore they are distinguished by adding a subscript τ to J such that τ takes the values $\tau = \text{-}J, \text{-}J\text{+}1, \ldots J$.

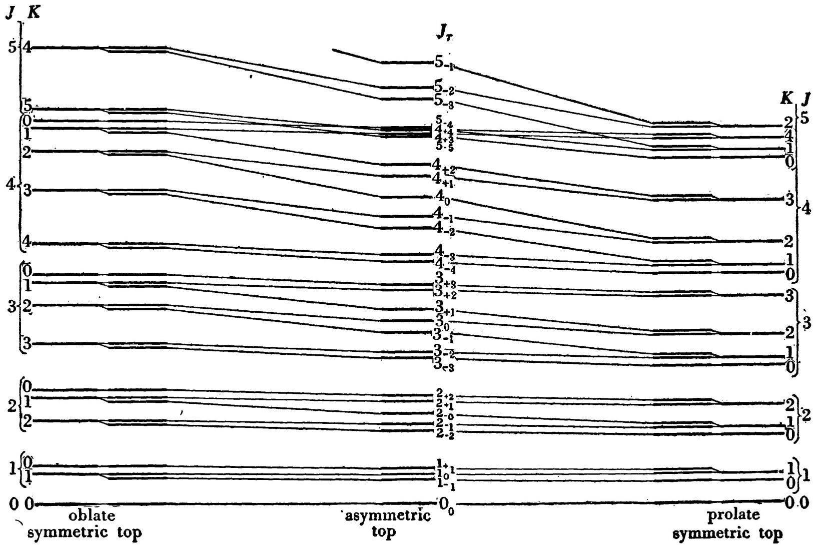

Figure 5. Energy levels of the asymmetric top; correlation to those of symmetric tops.

2.11.3 Vibrations

The remaining *3N-5* (for linear molecules) or *3N-6* (for non-linear molecules) relative coordinates (vibrational degrees of freedom) determine the potential in which the nuclei vibrate. In the harmonic approximation, the anharmonic terms of the potential are dropped and a vibration is described as an harmonic oscillator. An harmonic oscillator is defined by the potential energy being proportional to the square of the distance displaced from the equilibrium position:

$$V(x) = \frac{1}{2}kx^2 = \frac{1}{2}(m\omega^2)x^2, \quad \text{with} \tag{194}$$

$$\omega = \sqrt{\frac{k}{\mu}} \qquad \text{and} \qquad \mu = \frac{m_1 m_2}{m_1 + m_2}.$$

ω is the angular frequency, k the force constant, and μ the reduced mass.

A solution of the Schrödinger equation with this form of potential leads to a sequence of evenly spaced energy levels characterized by a quantum number n (Figure 6), as

$$\varepsilon_{vib} = (n + \frac{1}{2})\hbar\omega \quad \text{with} \quad n = 0, 1, 2, 3\ldots \tag{195}$$

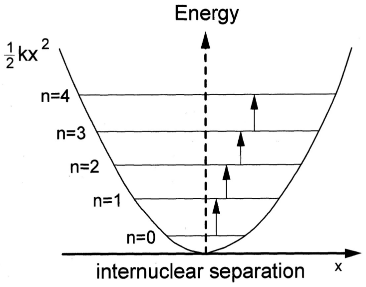

Figure 6. Potential energy form of an harmonic oscillator.

Eq. (195) shows that in the lowest vibrational state, $n = 0$, vibrations contribute in a non-vanishing way to the energy. This so-called "zero-point vibration energy" of the ground state (defined by $n = 0$) implies that molecules are not completely at rest, even at absolute zero temperature. The ground state energy for the quantum harmonic oscillator can be shown to be the minimum energy allowed by the uncertainty principle by Heisenberg:

$$\Delta x \Delta p \geq \frac{\hbar}{2}. \tag{196}$$

Indeed, the energy of the quantum harmonic oscillator must be at least

$$E = \frac{(\Delta p)^2}{2m} + \frac{1}{2}m\omega^2(\Delta x)^2, \tag{197}$$

where Δx and Δp describe the uncertainty on the position and on the momentum, respectively.

Taking the lower limit allowed by the uncertainty principle,

$$\Delta x \Delta p = \frac{\hbar}{2}, \tag{198}$$

the energy expressed in terms of the position uncertainty can then be written as

$$E = \frac{\hbar^2}{8m(\Delta x)^2} + \frac{1}{2} m\omega^2 (\Delta x)^2 . \tag{199}$$

Minimizing this energy by taking the derivative with respect to Δx and searching for a local minimum leads to

$$-\frac{\hbar^2}{4m(\Delta x)^3} + m\omega^2 \Delta x = 0 . \tag{200}$$

Solving for the position uncertainty gives finally

$$\Delta x = \sqrt{\frac{\hbar}{2m\omega}} . \tag{201}$$

Substitution of eq. (201) into eq. (199) gives the allowed minimum value of energy:

$$E_0 = \frac{1}{2}\hbar\omega . \tag{202}$$

Polyatomic molecules can be considered as a set of coupled harmonic oscillators. The collective motions of the atoms in a molecule can be decomposed into a set of independent harmonic oscillators by introducing normal modes of vibration and normal coordinates (q_j). With the normal coordinates, the cross terms in the potential of polyatomic molecules can be eliminated and the Hamiltonian can be written as a sum of independent harmonic oscillators:

$$\hat{H} = -\sum_{j=1}^{\infty} \frac{-\hbar^2}{2\mu} \frac{\partial^2}{\partial q_j^2} + \sum_{j=1}^{\infty} \frac{1}{2} k_j q_j^2 , \tag{203}$$

with eigenvalues

$$\varepsilon_{vib} = \sum_{j=1}^{\alpha} (n_j + \frac{1}{2}) h\nu_j \text{ with} \tag{204}$$

$$\nu_j = \frac{1}{2\pi}\sqrt{\frac{k_j}{\mu_j}} \quad \text{and} \quad n_j = 0,1,2,\ldots \tag{205}$$

The summation over *j* runs over the α = 3*N*-6 vibrational normal modes of non-linear molecules or over 3*N*-5 vibrational normal modes of linear molecules.

In practice, the Hessian matrix (*f*), which holds the second partial derivatives of the potential *V* with respect to the displacement of the atoms in Cartesian coordinates is first converted to mass-weighted coordinates:

$$f_{ij} = \left(\frac{\partial^2 V}{\partial q_i \partial q_j} \right) \quad \text{with} \tag{206}$$

$$q_i = \sqrt{m_i} \Delta x_i . \tag{207}$$

After diagonalization, a set of 3*N* eigenvectors (normal modes) and 3*N* eigenvalues are obtained. In the next step, the center of mass is translated to the origin and the principal axes are determined. After finding the matrix that diagonalizes the moments of the inertia tensor, the normal modes or vectors corresponding to the rotations and translations can be obtained. An orthogonalization is used to generate the 3*N*-6 (or 3*N*-5) remaining vectors which are orthogonal to the six (or five) rotational and translational vectors. The mass-weighted Cartesian coordinates are transformed to internal coordinates and the Hessian matrix is transformed to these internal coordinates. Diagonalization of this matrix yields eigenvalues ε_j which represent the quantities $\sqrt{\frac{k_j}{\mu_j}}$ from which the vibrational frequencies ν_j can be obtained using eq. (205).

2.12 Elements of statistical thermodynamics

The essence of statistical mechanics is to connect the quantum mechanical energy levels of molecules to macroscopically measured thermodynamic quantities. In this section, important macroscopic observables such as the entropy *S*, the enthalpy *H*, … are expanded in terms of the partition function derived from molecular properties. Up till here, the widely used Rigid Rotor Harmonic Oscillator (RRHO) approximation is used. A quantum chemistry package like *Gaussian* uses the RRHO scheme to search for example for transition states via a variety of methods. However, for conformationally versatile molecules, it will further be shown that an improved analysis is needed, based on hindered rotors. Therefore, in the last section, light will be shed on the influence of hindered rotations on the partition functions and on the associated thermodynamic statefunctions.

2.12.1 Partition functions

The (canonical) partition function Q contains all information concerning the thermodynamics of a system of independent molecules (ideal gas) at thermal equilibrium. It is defined as the mean number of quantum energy levels which are thermally accessible at a given temperature, or, formally,

$$Q = \sum_j e^{\frac{-E_j}{k_B T}} = \sum_i e^{\frac{-\varepsilon_i^a}{k_B T}} \sum_j e^{\frac{-\varepsilon_j^b}{k_B T}} \ldots = q_a q_b \ldots, \tag{208}$$

where E_j describes the energy of the *j*th level, respectively. k_B is Boltzmann's constant (1.3807 10^{-23} J K^{-1}). The superscript denotes the particle (in case of distinguishable particles) and the subscript the state. The partition function of the entire system (Q) can be written in terms of individual molecular partition functions $q_{molecule}$, reducing the *N*-body problem to a more tractable one-body problem. In turn $q_{molecule}$ can be further decomposed into irreducible degrees of freedom (translation, rotation …) of the single particles:

$$q_{molecule} = q_{trans} q_{vib} q_{rot} q_{elec} q_{nucl} \, . \tag{209}$$

The relation between the molecular partition function and the partition function of a set of N independent indistinguishable particles in the gas phase is given by:

$$Q = \frac{(q_{trans} q_{vib} q_{rot} q_{elec} q_{nucl})^N}{N!} \, . \tag{210}$$

The electronic partition function is defined as

$$q_{elec} = \sum_i g_i e^{\frac{-\varepsilon_{elec}}{k_B T}} = g_0 e^{\frac{-\varepsilon_0}{k_B T}} + g_1 e^{\frac{-\varepsilon_1}{k_B T}} + \ldots , \tag{211}$$

where g_i and ε_i describe the degeneracy and the electronic energy of the i^{th} level, respectively. Mostly, an arbitrary zero of energy is fixed such that $\varepsilon_0 = 0$. The higher electronic energies are then determined relative to this ground state. When the first electronic excitation is much greater than $k_B T$ the first and higher excited states are inaccessible at the temperature upon consideration. In such a case, the electronic partition function, simply becomes $q_{elec} = g_0$.

The translational partition function can be obtained by substitution of ε_{trans} [eq. (176)] into

$$q_{trans} = \sum_{n_x, n_y, n_z = 1} e^{-\frac{\varepsilon_{trans}}{k_B T}} \, , \text{ which results into} \tag{212}$$

$$q_{trans} = \sum_{n_x = 1} e^{\frac{-\beta h^2 n_x^2}{8Ma^2}} \sum_{n_y = 1} e^{\frac{-\beta h^2 n_y^2}{8Ma^2}} \sum_{n_z = 1} e^{\frac{-\beta h^2 n_z^2}{8Ma^2}} \text{ or} \tag{213}$$

$$\mathrm{q}_{trans} = \left(\sum_{n=1} e^{\frac{-\beta h^2 n^2}{8Ma^2}} \right)^3 \tag{214}$$

with $\beta = \frac{1}{k_B T}$. The successive terms in these summations differ so little from each other that it can be considered that such terms vary continuously. Thus, in a good approximation, the summation can be replaced by an integration:

$$q_{trans} = \left(\int e^{-\frac{\beta h^2 n^2}{8Ma^2}} dn \right)^3 = \left(\frac{2\pi M k_B T}{h^2} \right)^{\frac{3}{2}} V \, . \tag{215}$$

The rotational partition function is given by

- Spherical top:

$$q_{rot} = \frac{\pi^{\frac{1}{2}}}{\sigma}\left(\frac{8\pi^2 I k_B T}{h^2}\right)^{\frac{3}{2}}. \tag{216}$$

- Symmetric top:

$$q_{rot} = \frac{\pi^{\frac{1}{2}}}{\sigma}\left(\frac{8\pi^2 I_A k_B T}{h^2}\right)\left(\frac{8\pi^2 I_C k_B T}{h^2}\right)^{\frac{1}{2}}. \tag{217}$$

- Asymmetric top:

$$q_{rot} = \frac{\pi^{\frac{1}{2}}}{\sigma}\left(\frac{8\pi^2 I_A k_B T}{h^2}\right)^{\frac{1}{2}}\left(\frac{8\pi^2 I_B k_B T}{h^2}\right)^{\frac{1}{2}}\left(\frac{8\pi^2 I_C k_B T}{h^2}\right)^{\frac{1}{2}}. \tag{218}$$

It should be noticed that for an asymmetric top molecule no closed expression can be derived for q_{rot} on the quantum mechanical level. For sufficiently high temperatures the classical expression [eq. (218)] is used [237, 238]. σ is the symmetry number, giving the number of rotations which leave the molecule invariant. This number avoids overcounting indistinguishable configurations.

At last, the vibrational partition function for polyatomic molecules reads:

$$q_{vib} = \prod_{j=1}^{\alpha}\left(\frac{e^{\frac{-h\nu_j}{2k_B T}}}{1-e^{\frac{-h\nu_j}{k_B T}}}\right), \tag{219}$$

where the summation over *j* runs over the α = 3*N*-6 vibrational normal modes of non-linear molecules or over 3*N*-5 vibrational normal modes of linear molecules.

The influence of the identity of nuclei and of the nuclear spin is not treated in the present thesis. A discussion can be found in reference [237]. As such, the nuclear partition function, q_{nucl}, is set equal to 1.

Finally, for non-linear polyatomic molecules, the total partition function is given by

$$q_{molecule} = \left(\frac{2\pi M k_B T}{h^2}\right)^{\frac{3}{2}} V.\frac{\pi^{\frac{1}{2}}}{\sigma}\left(\frac{8\pi^2 I_A k_B T}{h^2}\right)^{\frac{1}{2}}\left(\frac{8\pi^2 I_B k_B T}{h^2}\right)^{\frac{1}{2}}\left(\frac{8\pi^2 I_C k_B T}{h^2}\right)^{\frac{1}{2}}.\prod_{j=1}^{\alpha}\left(\frac{e^{\frac{-h\nu_j}{2k_B T}}}{1-e^{\frac{-h\nu_j}{k_B T}}}\right).g_0. \tag{220}$$

2.12.2 Formal derivation of thermodynamical quantities

After determination of the canonical partition function Q one can formally calculate thermodynamic state functions such as the internal energy *U*, the entropy *S*,…[237] By differentiating Q with respect to the temperature at constant volume, the following equation is obtained:

$$(\frac{\partial Q}{\partial T})_V = \frac{1}{k_B T^2}\sum_i E_i e^{\frac{-E_i}{k_B T}} . \qquad (221)$$

Since $e^{\frac{-E_i}{k_B T}} = P_i Q$ where P_i is the fraction of the system with energy E_i and since $U = \sum_i P_i E_i$, it follows immediately that the internal energy U relates to the partition function Q via

$$U = \frac{k_B T^2}{Q}(\frac{\partial Q}{\partial T})_V = k_B T^2(\frac{\partial \ln Q}{\partial T})_V . \qquad (222)$$

According to Boltzmann's hypothesis, the entropy *S* is defined as

$$S = -k_B \sum_i P_i \ln P_i . \qquad (223)$$

Substituting $P_i = \frac{e^{\frac{-E_i}{k_B T}}}{Q}$ or $\ln P_i = -\frac{E_i}{k_B T} - \ln Q$ into eq. (223) gives

$$S = -k_B \left[-\frac{1}{k_B T}\sum_i P_i E_i - \ln Q \sum_i P_i \right]. \qquad (224)$$

Since $U = \sum_i P_i E_i$ and $\sum_i P_i = 1$, it follows that

$$S = \frac{U}{T} + k_B \ln Q . \qquad (225)$$

Upon substituting eq. (222) for U into eq. (225), the entropy becomes

$$S = k_B T(\frac{\partial \ln Q}{\partial T})_V + k_B \ln Q . \qquad (226)$$

Next, the Helmholtz function ($F = U - TS$) is now easily obtained from a combination of eqs. (222) and (226):

$$F = -k_B T \ln Q . \qquad (227)$$

At constant temperature, the pressure is given by

$$P = -(\frac{\partial F}{\partial V})_T , \qquad (228)$$

which gives rise to

$$P = k_B T(\frac{\partial \ln Q}{\partial V})_T . \qquad (229)$$

From the definition of the enthalpy ($H = U + PV$) and the Gibbs free energy ($G = H\text{-}TS$), it is found that

$$H = k_B T^2 (\frac{\partial \ln Q}{\partial T})_V + k_B T V (\frac{\partial \ln Q}{\partial V})_T \qquad (230)$$

and

$$G = -k_B T \left[\ln Q - V(\frac{\partial \ln Q}{\partial V})_T \right]. \qquad (231)$$

2.12.3 Practical calculation of thermodynamical quantities

In practice, Q is too large to use formulas (222), (226), (227), (230) and (231). The purpose of this section is to explain how thermodynamical values such as the entropy and the internal energy are computed. Mostly molar values are used, so that the above expressions can be divided by $n = N / N_A$, while $N_A k_B$ can be substituted by R with N_A and k_B Avogadro's and Boltzmann's constants, respectively. By using the Stirling approximation

$$\ln(N!) \approx N \ln N - N , \qquad (232)$$

the resulting relation between the partition function and the entropy can then be written as

$$S = R + R \ln\big(q(V,T)\big) + RT \left(\frac{\partial \ln q}{\partial T} \right)_V . \qquad (233)$$

We can also move the first term into the natural logarithm as e, which gives

$$S = R \ln\big(q(V,T)\ e\big) + RT \left(\frac{\partial \ln q}{\partial T} \right)_V , \qquad \text{or also} \qquad (234)$$

$$S = R \left(\ln\big(q_{trans} q_{elec} q_{rot} q_{vib} e\big) + T \left(\frac{\partial \ln(q_{trans} q_{elec} q_{rot} q_{vib})}{\partial T} \right)_V \right). \qquad (235)$$

The internal energy U can also be obtained from the partition function via

$$U = RT^2 \left(\frac{\partial \ln(q_{trans} q_{elec} q_{rot} q_{vib})}{\partial T} \right)_V . \qquad (236)$$

The contributions to the entropy and the internal energy resulting from the translational, the electronic, rotational and vibrational motions are individually calculated. The starting point of the calculations is the partition function for each individual contribution.

Contribution from the translational motion

The translational partition function is given by

$$q_{trans} = \left(\frac{2\pi M k_B T}{h^2} \right)^{\frac{3}{2}} V \qquad (237)$$

For an ideal gas $pV = Nk_BT$ (*N* is the number of particles) so that $V = \frac{Nk_BT}{p}$. The translation partition function then becomes:

$$q_{trans} = \left(\frac{2\pi M k_B T}{h^2}\right)^{\frac{3}{2}} \frac{Nk_BT}{p} \tag{238}$$

The translational entropy is then calculated via

$$S_{trans} = R\left(\ln\left(q_{trans}e\right) + T\left(\frac{5}{2T}\right)\right) = R\left(\ln q_{trans} + 1 + \frac{5}{2}\right), \tag{239}$$

with $\left(\frac{\partial \ln q_{trans}}{\partial T}\right)_V = \frac{5}{2T}$.

and the contribution to the internal energy due to translation is

$$U_{trans} = RT^2\left(\frac{\partial \ln q_{trans}}{\partial T}\right)_V = RT^2\left(\frac{5}{2T}\right) = \frac{5}{2}RT. \tag{240}$$

Contribution from the electronic motion

Using the electronic partition function $q_{elec} = g_0$ the corresponding electronic entropy is expressed by

$$S_{elec} = R\left(\ln q_{elec} + T\left(\frac{\partial \ln q_{elec}}{\partial T}\right)_V\right) = R \ln q_{elec}. \tag{241}$$

The internal energy due to the electronic motions is zero ($U_{elec} = 0$) since there are no temperature dependent terms in the partition function.

Contribution from the rotational motion

For the discussion of molecular rotation we will restrict ourselves to an asymmetric top. For such a molecule the rotational partition function is

$$q_{rot} = \frac{\pi^{\frac{1}{2}}}{\sigma}\left(\frac{8\pi^2 I_A k_B T}{h^2}\right)^{\frac{1}{2}}\left(\frac{8\pi^2 I_B k_B T}{h^2}\right)^{\frac{1}{2}}\left(\frac{8\pi^2 I_C k_B T}{h^2}\right)^{\frac{1}{2}}, \tag{242}$$

which gives rise to

$$S_{rot} = R\left(\ln q_{rot} + T\left(\frac{\partial \ln q_{rot}}{\partial T}\right)_V\right) = R\left(\ln q_{rot} + \frac{3}{2}\right) \quad \text{and} \tag{243}$$

$$U_{rot} = RT^2\left(\frac{\partial \ln q_{rot}}{\partial T}\right)_V = \frac{3}{2}RT. \tag{244}$$

Contribution from the vibrational motion

The contribution from vibrational motions is composed of the contributions from each vibrational mode. Only the real modes are considered, modes with imaginary frequencies are ignored. As shown before, the vibrational partition function is

$$q_{vib}=\prod_{j=1}^{\alpha}\left(\frac{e^{\frac{-h\nu_j}{2k_BT}}}{1-e^{\frac{-h\nu_j}{k_BT}}}\right). \tag{245}$$

We will now introduce the characteristic vibrational temperature of each vibrational mode: $\Theta_{v,j}=\dfrac{h\nu_j}{k_B}$, by rewriting the vibrational partition function as

$$q_{vib}=\prod_{j=1}^{\alpha}\left(\frac{e^{\frac{-\Theta_{v,j}}{2T}}}{1-e^{\frac{-\Theta_{v,j}}{T}}}\right). \tag{246}$$

The entropy contribution from the vibrational partition function is consequently

$$\begin{aligned}
S_{vib} &= R\left(\ln q_{vib}+T\left(\frac{\partial \ln q_{vib}}{\partial T}\right)_V\right)\\
&= R\left(\ln q_{vib}+T\left(\sum_K\frac{\Theta_{v,K}}{2T^2}+\sum_K\frac{\left(\Theta_{v,K}/T^2\right)e^{\frac{-\Theta_{v,K}}{T}}}{1-e^{\frac{-\Theta_{v,K}}{T}}}\right)\right)\\
&= R\left(-\sum_K\left(\frac{\Theta_{v,K}}{2T}+\ln\left(1-e^{\frac{-\Theta_{v,K}}{T}}\right)\right)+T\left(\sum_K\frac{\Theta_{v,K}}{2T^2}+\sum_K\frac{\left(\Theta_{v,K}/T^2\right)e^{\frac{-\Theta_{v,K}}{T}}}{1-e^{\frac{-\Theta_{v,K}}{T}}}\right)\right)\\
&= R\left(-\sum_K\ln\left(1-e^{\frac{-\Theta_{v,K}}{T}}\right)+\left(\sum_K\frac{\left(\Theta_{v,K}/T\right)e^{\frac{-\Theta_{v,K}}{T}}}{1-e^{\frac{-\Theta_{v,K}}{T}}}\right)\right)\\
&= R\sum_j\left(\frac{\Theta_{v,j}/T}{e^{\Theta v,j/T}-1}-\ln\left(1-e^{-\Theta_{v,j}/T}\right)\right).
\end{aligned} \tag{247}$$

The contribution to the internal energy from molecular vibration is:

$$E_{vib} = RT^2\left(\frac{\partial \ln q_{vib}}{\partial T}\right)_V$$

$$= R\sum_j \Theta_{v,j}\left(\frac{1}{2}+\frac{1}{e^{\frac{\Theta_{v,j}}{T}}-1}\right). \tag{248}$$

2.12.4 Location of transition states

Reactant, product, and transition states are all stationary points on the potential energy surface, meaning that at these points the derivative of the energy with respect to the reaction coordinate is zero. Minima (reactant, product) are points where the second derivative is greater than zero, and first-order saddle points (transition states) have one second derivative less than zero.

Gaussian uses the Synchronous Transit-Guided Quasi-Newton (STQN) method, developed by Schlegel and co-workers, for locating transition structures [239]. A linear synchronous transit or quadratic synchronous transit (QST) approach is used to get closer to the quadratic region around the transition state and then uses a quasi-Newton or eigenvector following algorithm to complete the optimization. This method is requested with the QST2 and/or QST3 options to the Opt keyword. QST2 requires two molecule specifications as input, namely the reactant and the product, while QST3 requires three molecule specifications: the reactant, the product, and an initial structure for the transition state.

In the QST2-guided search, the method of linear synchronous transit (LST) locates an initial transition state along the path connecting the reactant and the product. For each of the first few steps of a QST2-guided search, the optimizer is restricted to search along the circular curve connecting the reactant, transition state guess, and product structures. This restriction prevents the optimizer from being led far astray by the inaccuracies of the guessed Hessian, and prevents it from exploring transition states that do not correspond to the reaction of interest. During these steps, the optimizer approaches the maximum-energy structure (total energy gradient is zero) along the reactant-to-product curve, and also greatly improves the Hessian. Once it has obtained the improved Hessian and transition state guess, the optimizer removes the strict requirement that the search must be along the circular curve between the structures. For all subsequent steps in the search, the optimizer follows the Hessian eigenvector that is most similar to the tangent of the circular curve.

In a QST3-guided search an approximate transition state is provided. For best results, the reactant and product structures should not be radically different from the transition state. For instance, to find the transition state in a bond-breaking reaction, it would be better to provide a product structure in which the breaking bond was fairly long and weak than a true minimum-energy structure in which the bond had completely dissociated.

Transition states for dissociation or for proton transfers can also be identified by iteratively stretching the bonds of interest via a scan of the potential energy surface. At maximal energy, a suited geometry can be selected. By means of the Rational Function Optimization (RFO) method [240] or by using one of the methods mentioned above, a relaxation to a first order saddle point is then finally performed.

2.12.5 Treatment of Hindered Rotations

Significant errors can be made if the Rigid Rotor Harmonic Oscillator (RRHO) approximation [237] described in the preceding sections is used to calculate the partition function for low frequency modes that represent hindered internal rotation, as illustrated in Figure 7. Ayala and Schlegel [241] developed in 1998 a procedure that identifies internal rotation modes and rotating groups and proposed an improved approximation to the corrections for the partition functions. As shown later in this thesis, the hindered rotations are found to have an important influence on the computed thermodynamic state functions and partition functions.

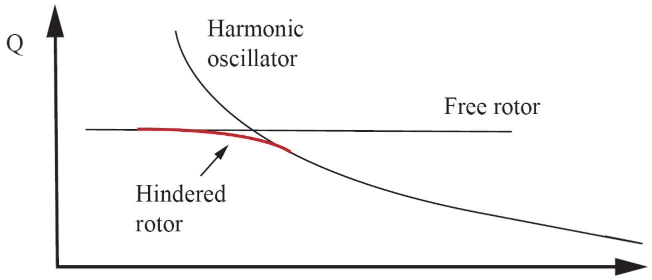

Figure 7. A representation of the partition function Q for a free rotor, hindered rotor, and harmonic oscillator as a function of $u = \frac{h\nu}{k_B T}$, where ν is the vibrational frequency and T is the temperature.

Working in internal coordinates, the internal rotations can be identified before the normal mode problem is solved by constructing a projector that removes all the stretches, bends and out-of-plane motions, leaving only the bond torsions. The internal rotations are determined by considering the greatest overlap between the actual normal modes and the projected ones. The symmetry number of the rotational top follows from the redundant internal coordinates. The periodicity of the torsional potential is defined by using the hybridization of the bond atom, as these are implemented in the force field DREIDING by Mayo, Olafson, and Goddard [242]. Once the rotating groups have been identified, the reduced moments of inertia $I_{r,i}$ can be obtained using Kilpatrick and Pitzer's protocol [243]:

$$I_{r,i} = I_i^0 \left[1 - I_i^0 \left(\frac{\lambda_A^{\ 2}}{I_A} + \frac{\lambda_B^{\ 2}}{I_B} + \frac{\lambda_C^{\ 2}}{I_C} \right) \right], \qquad (249)$$

with I_i^0 the moment of inertia of the i^{th} group and λ_A (λ_B, λ_C) the cosine of the angle between the axis of the group and the axis of the moment of inertia I_A (I_B, I_C) of the whole molecule.

Assuming a weak energy coupling between *n* hindered rotors in one species, and considering a single cosine function for each torsion, the potential energy can be expressed as

$$V = \sum_{i=1}^{n} \frac{V_i}{2}(1 - \cos(\sigma_i \tau_i)), \tag{250}$$

with σ_i, τ_i and V_i being the periodicity, the twist angle and the internal rotational barrier height of the i^{th} rotor, respectively. The approximation to the hindered rotor partition function suggested by Ayala and Schlegel [241] is then given by

$$\begin{aligned} Q^{\text{hin.}} = \prod_{i=1}^{n} \left(\frac{Q_i^{\text{h.o.q}}}{Q_i^{\text{h.o.cl}}}\right) Q_i^{\text{free rot}} \frac{1 + P_{2,i} \exp[-V_i/(2k_B T)]}{1 + P_{1,i} \exp[-V_i/(2k_B T)]}, \\ \times \exp[-V_i/(2k_B T)] J_0(iV_i/(2k_B T)) \end{aligned} \tag{251}$$

with $Q_i^{\text{h.o.q}}$ and $Q_i^{\text{h.o.cl}}$ the quantum and classical partition functions, respectively, for the harmonic oscillator *i* with a vibrational frequency ν_i given by

$$Q_i^{\text{h.o.q}} = \frac{e^{-u_i/2}}{1 - e^{-u_i}}; \quad Q_i^{\text{h.o.cl}} = \frac{1}{u_i} \quad \text{with} \quad u_i = \frac{h\nu_i}{k_B T}. \tag{252}$$

In eq. (251), $Q_i^{\text{free rot}}$ is the classical partition function for the i^{th} free rotor

$$Q_i^{\text{free rot}} \approx \left(\frac{8\pi^3 k_B T}{\sigma^2 h^2}\right)^{1/2} I_{r,i}^{1/2}, \tag{253}$$

while $J_0(iV_i/(2k_B T))$ denotes the zeroth order Bessel function [244]

$$\begin{aligned} J_0(z) &= \frac{1}{\pi}\int_0^{\pi} e^{iz\cos\theta} d\theta \\ &= \sum_{k=0}^{\infty} (-1)^k \frac{(z^2/4)^k}{(k!)^2} \end{aligned}. \tag{254}$$

$P_{1,i}$ and $P_{2,i}$ are two polynomials which amount to

$$\begin{aligned} P_{1,i} = {} & 0.003235x_i - 0.026252x_i^2 + 0.110460x_i^3 - 0.203340x_i^4 + 0.130633x_i^5 \\ & -0.010112y_i^{0.5} + 0.650122x_i y_i^{0.5} + 0.067112x_i^2 y_i^{0.5} + 0.088807x_i^3 y_i^{0.5} \\ & -0.114290x_i^4 y_i^{0.5} - 0.364852y_i + 0.913073x_i y_i - 0.021116x_i^2 y_i \\ & -0.092086x_i^3 y_i - 0.415689y_i^{1.5} - 1.128961x_i y_i^{1.5} + 0.233009x_i^2 y_i^{1.5} \\ & +0.421344y_i^2 + 0.505139x_i y_i^2 - 0.215088y_i^{2.5}, \end{aligned} \tag{255}$$

$$\begin{aligned} P_{2,i} = {} & 0.067113x_i + 0.772485x_i^2 - 3.0674131x_i^3 + 4.595051x_i^4 \\ & -2.101341x_i^5 + 0.015800y_i^{0.5} + 0.102119x_i y_i^{0.5} - 0.555270x_i^2 y_i^{0.5} \\ & -1.125261x_i^3 y_i^{0.5} + 0.071884x_i^4 y_i^{0.5} - 0.397330y_i + 2.284956x_i y_i \\ & +0.850046x_i^2 y_i - 0.174240x_i^3 y_i - 0.451875y_i^{1.5} - 2.136226x_i y_i^{1.5} \\ & +0.303469x_i^2 y_i^{1.5} + 0.470837y_i^2 + 0.675898x_i y_i^2 \\ & -0.226287y_i^{2.5}, \end{aligned} \tag{256}$$

with $x_i = \dfrac{1}{Q_i^{\text{free rot}}}$ and $y_i = \dfrac{V_i}{k_B T}$.

With eq. (251) and $Q = Q^{hin.}$, *Gaussian98* calculates the internal energy U and the entropy S for hindered rotations using eqs. (222) and (226), respectively. For 1 mol particles, the enthalpy and the Gibbs' free energy can then correspondingly be calculated by using $H^{hin} = U^{hin} + RT$, with R the universal gas constant, and $G^{hin} = H^{hin} - TS^{hin}$.

2.13 Basis sets

Two types of basis functions are commonly used in practical calculations: Slater type functions [12] and Gaussian type functions [245]. Their properties have been extensively reviewed in textbooks and will not be repeated here.

One series of basis sets are based on Pople's double zeta 6-31G basis set which contains s- and p-type functions. The 6-31G* basis [14, 246] adds d-type functions to heavy atoms (Li till F). The 6-31G** basis adds, in addition to d-type functions, p-type functions to hydrogen. In the 6-311G** basis set [14, 32, 247], a set of polarization d-functions has been added to heavy atoms (H to F); however, it is not of triple zeta quality [247]. In addition, diffuse s- and p-functions can be added, denoted by a '+', in for example 6-311++G**. The second '+' indicates that a set of diffuse s-functions has been added to each hydrogen atom.

Another series of basis sets, the correlation consistent basis sets (cc-pVXZ sets with X=D, T, and Q), has been developed by Dunning and co-workers [18]. The smallest set in this series is cc-pVDZ or the correlation consistent polarized valence double-zeta basis set. It has been observed that properties computed using successively larger basis sets of this series – like cc-pVTZ (correlation consistent polarized valence triple-zeta basis set), cc-pVQZ (correlation consistent polarized valence quadruple-zeta basis set), … – appear to converge exponentially at the Hartree-Fock level [248] or converge according to polynomial expressions at the correlated level [249]. Indeed, well-suited extrapolations of the HF total electronic energies E_∞ obtained for the neutral molecules and their cations using Dunning's series of cc-pVXZ basis sets are suggested by Feller [248], who proposed a fit of the form

$$E(l) = E_\infty + Ae^{-Bl}, \tag{257}$$

where the cardinal number l equals 2, 3, 4,... when X=D, T, Q,... respectively. In turn, correlated total energies are extrapolated to an asymptotically complete basis set, indicated by E_∞, by means of a three-point extension (named Schwartz 6(*lmn*) [250]) of Schwartz' extrapolation formula [249], which is based on inverse powers of (l + ½) :

$$E(l) = E_\infty + \frac{B}{\left(l+\frac{1}{2}\right)^4} + \frac{C}{\left(l+\frac{1}{2}\right)^6}. \tag{258}$$

In the present thesis, basis sets with increasing size have been used for accurately calculating energy differences between different conformers of a non-rigid molecule and to calculate activation barriers of cage fragmentation reactions in order to select the most appropriate set and to gain some insight into the size and characteristics of a basis set needed to obtain a given level of calculational accuracy.

Other basis sets which have been used are Dunning's double-zeta basis set with polarization and diffuse functions (DZP+) [251] and Roos's augmented double-zeta basis set of atomic natural orbitals (aug-ANO) [252].

2.14 Software and hardware

The programs and computer systems listed below have been used to perform the present work.

The Gaussian package can perform a variety of *ab initio* calculations. In this work, Gaussian98 [253] and Gaussian03 [254] has been used to optimize geometries, calculate frequencies, investigate basis set convergences and energy differences, charge distributions, perform DFT calculations,… An overview of the capabilities of the Gaussian package has been given in [255].

Molpro [256] also contains a number of *ab initio* techniques for molecular electronic structure calculations. It has been used to perform highly accurate coupled cluster [CCSD(T)] computations since it uses integral direct local electron correlation methods, which significantly reduce the increase of the computational cost with molecular size.

Use has been made of an augmented version of the ADC approach [143, 257] incorporating in a first diagonalization step a Block-Lanczos [146-148] reduction in the 1p/2p-1h and 2p-1h/2p-1h blocks pertaining to electron attachment. The ionization energies and the related spectroscopic (pole) strengths are extracted in the final diagonalization step, using the block-Davidson [258, 259] procedure and considering a threshold on the pole strength depending on the given system. The spatial symmetry is exploited to the extent of the largest one-dimensional Abelian subgroup of the full molecular point group, to construct symmetry-adapted configurations and decouple the eigenvalue problem into lower-dimensional problems for each irreducible representation. This package has been used to study the valence one-electron and shake-up ionization bands.

All spherically averaged Kohn-Sham and Dyson orbital MDs have been obtained using MOMAP, which is an adaptation of the HEMS program, produced by the group of Brion at the University of British Columbia [212].

All calculations have been performed at Hasselt University on the following computers:

- DEC ALPHA DIGITAL 533au2
  2Gb RAM, 36Gb disk space
  Digital UNIX V4.0E (Rev. 1091)
- COMPAQ SRM V5.8-43
  4Gb RAM, 510 Gb disk space
  Compaq Tru64 UNIX V5.1 (Rev. 732)
- COMPAQ ES-47
  20Gb core memory, 680 Gb disk
  Compaq Tru64 UNIX V5.1B (Rev. 2650)

References

[1] Szabo, A.; Ostlund, N.S. *Modern Quantum Chemistry* (Revised first edition), McGraw-Hill, New York, 1989.

[2] Mcweeny, R. *Methods of Molecular Quantum Mechanics*, Second Edition, Academic Press, London, 1989

[3] Hehre, W. J.; Radom, L.; von Ragué Scheyler, Pople, J.A. *Ab Initio molecular orbital theory*, John Wiley, New York, 1986.

[4] Amlöf, J. *Notes on Hartree-Fock Theory and Related Topics* In Lecture Notes in Quantum Chemistry II, B.O. Roos (Ed.), Springer- Verlag, Berlin 1994.

[5] Jensen, F. *Introduction to computational chemistry*, Wiley, 1999.

[6] Born, M.; Oppenheimer, J.R. *Ann. Physik* 1927, 84, 457.

[7] Hartree, D. R. *Proc. Cambridge Phil. Soc*. 1928, 24, 89, 111, 426.

[8] Fock, V. Z. *Physik* 1930, 61, 126.

[9] Koopmans, T. A. Physica (Amsterdam) 1933, 1, 104.

[10] Hall, G. G.; *Proc. Roy. Soc. London*. 1951, A205, 541.

[11] Roothaan, C. C. J. *Rev. Mod. Phys*. 1951, 23, 69.

[12] Slater, J. C. *Phys. Rev*. 1930, 36, 57.

[13] Poirier, R. A.; Kari, R.; Czismadia, I.G. *Handbook of Gaussian Basis Sets*, Elsevier, Amsterdam, 1985.

[14] Huzinaga,S. *Computer Phys. Rep.* 1985, 2, 279.

[15] Helgaker, T.; Taylor, P.R. *Gaussian Basis Sets and Molecular Integrals in Modern Electronic Structure Theory*, Edited by D. R. Yarkony, World Scientific Publishing, Singapore, 1995.

[16] Gill, P. M. W. *Adv. Quant. Chem*. 1994, 25, 142.

[17] Almlöf, J.; Taylor, P. R. *J. Chem. Phys*. 1987, 86, 4070.

[18] Dunning, T. H. Jr *J. Chem. Phys*. 1989, 90, 1007.

[19] Wilson, S. *Electron Correlation in Molecules*, Clerendon Press, Oxford, 1984.

[20] Shavitt, I. in *Modern theoretical Chemistry* (Ed. H. F. Schaefer III), Plenum Press, New York, London, 1977, p.189.

[21] Baushlicher, C. W. Jr; Langhoff, S. R.; Taylor, P. R. *Adv. Chem. Phys.* 1990, 77, 103.

[22] Löwdin, P. O. *Adv. Chem. Phys.* 1959, 2, 207.

[23] Roos, B.O. *The multiconfigurational (MC) Self-Consistent Field (SCF) Theory* in Lecture Notes in Quantum Chemistry I, B. O. Roos (Ed.), Springer-Verlag, Berlin, 1992.

[24] Werner, H. J. *Matrix-Formulated Direct Multiconfiguration Self-Consistent Field and Multiconfigurational Reference Configuration-interaction Methods* in Advances in chemical Physics LXIX, John Wiley, New York, 1987.

[25] Shepard, R. *The Multiconfigurational Self-Consistent Field Method* in Advances in Chemical Physics LXIX, John Wiley, New York, 1987.

[26] Roos, B.O. *The Complete Active Space Self-Consistent Field Method and its Applications in Electronic Structure Calculations* in Advance in Chemical Physics LXIX, John Wiley, New York, 1987.

[27] Møller, C.; Plesset, M. S. *Phys. Rev*. 1934, 46, 618.

[28] Bartlett, R. J.; Stanton, J. F. *Applications of Post-Hartree-Fock Methods: A tutorial* in Reviews in Computational Chemistry (K.B. Lipkowitz and D.B. Boyd Eds.), Vol.5, VCH Publisher, New York, 1994.

[29] Bartlett, R. J. *Ann. Rev. Phys. Chem*. 1981, 32, 359.

[30] Pople, J. A.; Binkley, J. S.; Seeger, R. *Int. J. Quantum Chem*. 1976, 10, 1.

[31] Krishnan, R.; Pople, J. A. Int. *J. Quantum Chem*. 1978, 14, 91.

[32] Krishnan, R.; Binkley, J.S.; Seeger, R.; Pople, J. A. *J. Chem. Phys*. 1980, 72, 650.

[33] Kucharski, S. A.; Noga, J.; Bartlett, R. J. *J. Chem. Phys*. 1989, 90, 7282.

[34] Cremer, D.; He, Z. J. *Phys. Chem*. 1996, 100, 6173.

[35] Schlegel, H. B. *J. Chem. Phys*. 1986, 84, 4530.

[36] Gauss, J.; Cremer, D. *Chem. Phys. Lett*. 1987, 138, 131; *ibid*. 1988, 153, 303.

[37] Trucks, G. W.; Watts, J. D.; Salter, E. A.; Bartlett, R.J. *Chem. Phys. Lett*. 1988, 153, 490.

[38] Watts, J. D.; Trucks, G. W.; Bartlett, R.J. *Chem. Phys. Lett*. 1989, 164, 502.

[39] Handy, N. C.; Amos, R. D.; Gaw, J. F.; Rice, J. E.; Simandiras, E. D.; Lee, T. J.; Harrison, R. J.; Laidig, W. D.; Fitzgerald, G. B. ; Bartlett, R. J. in Geometrical Derivatives of Energy Surfaces and Molecular Properties, edited by P. Jørgesen and J. Simons (Reidel, Dordrecht, 1986).

[40] Handy, N. C.; Amos, R. D.; Gaw, J. F.; Rice, J. E.; Simandiras, E.D. *Chem. Phys. Lett*. 1985, 120, 151.

[41] Harrison, R. J.; Fitzgerald, G. B.; Laidig, W.D.; Bartlett, R. J. *Chem. Phys. Lett*. 1986, 124, 291.

[42] Stanton, J. F.; Gauss J.; Bartlett, R. J. *Chem. Phys. Lett*. 1992, 194, 195.

[43] Gauss, J.; Stanton, J. F.; Bartlett, R. J. *J. Chem. Phys*. 1992, 97, 7825.

[44] Handy, N. C. ; Knowles, P. J.; Somasundram, K. *Theor. Chim. Acta* 1985, 68, 87; Knowles, P. J.; Somasundram, K. ; Handy, N. C.; Hirao, K. *Chem. Phys. Lett.* 1985, 113, 8.

[45] Coester, F. *Nucl. Phys.* 1958, 17, 477.

[46] Coester, F.; Kümmel, H. *Nucl. Phys.*, 1975, 9, 105.

[47] Paldus, J.; Cízek, J. *Adv. Quantum Chem*. 1975, 9, 105.

[48] Purvis, G. D.; Bartlett, R. J. *J. Chem. Phys.* 1982, 76, 1910.

[49] Scuseria, G.; Scheiner, A.C.; Lee, T.J.; Rice, J. E.; Shaefer, H.F. *J. Chem. Phys.* 1987, 86, 2881.

[50] Lee, T. J.; Rice, J. E. *Chem. Phys. Lett*. 1988, 150, 406.

[51] Scuseria, G.; Jansen, C. L.; Schaefer, H. F. *J. Chem. Phys.* 1988, 89, 7382.

[52] Piecuch, P.; Paldus, J. *Int. J. Quantum. Chem.* 1989, 36, 429.

[53] Stanton, J. F.; Gauss, J.; Watts, J. D.; Bartlett, R. D. *J. Chem. Phys.* 1991, 94, 4334.

[54] Geertsen, J.; Eriksen, S.; Oddershede, J. *Adv. Quantum Chem.* 1991, 22, 168.

[55] Jayatilaka, D.; Lee, T. J. *Chem. Phys. Lett.* 1992, 199, 211.

[56] Noga, J.; Bartlett, R. J. *J. Chem. Phys.* 1987, 86, 7041; erratum *J. Chem. Phys.* 1988, 89, 4031.

[57] Scuseria, G.; Schaefer, H. F. *Chem. Phys. Lett.* 1988, 152, 382.

[58] Kucharski, S. A.; Bartlett, R. J. J. Chem. Phys. 1992, 97, 4282.

[59] Urban, M.; Noga, J.; Cole, S. J.; Bartlett, R. J. J. Chem. Phys. 1985, 83, 4041.

[60] Raghavachari, K.; Trucks, G. W.; Pople, J. A.; Head-Gordon, M. *Chem. Phys. Lett.* 1989, 157, 479.

[61] Lee, T.J.; Rendell, A. P.; Taylor, P. R. *J. Chem. Phys.* 1990, 92, 489.

[62] Rendell, A. P.; Lee, T. J.; Taylor, P. R. *J. Chem. Phys.* 1990, 92, 7050.

[63] Lee, T. J.; Rendell, A. P.; Taylor, P. R. *J. Chem. Phys.* 1990, 93, 6636.

[64] Lee, T. J.; Rendell, A. P.; Taylor, P.R. *Theor. Chim. Acta* 1992, 83, 165.

[65] Lee, T. J.; Scuseria, G. E. *J. Chem. Phys.* 1990, 93, 489.

[66] Bartlett, R. J. *Ann. Rev. Phys. Chem.* 1981, 32, 359.

[67] Bartlett, R. J. *J. Phys. Chem.* 1989, 93, 1697.

[68] Lee, T. J.; Scuseria, G. E. *Achieving Chemical Accuracy with Coupled-Cluster theory* in S.R. Langhoff (Ed.), *Quantum Mechanical Electronic Structure Calculations with Chemical Accuracy*, Kluwer, Dordrecht, 1995.

[69] Zivkovic, T. P. *Int. J. Quantum. Chem. Symp.* 1977, 11, 413.

[70] Zivkovic, T. P.; Mokhorst, H. J. *J. Math. Phys.* 1978, 19, 1007.

[71] Meissner, L.; Balkovà, A.; Bartlett, R. J. *Chem. Phys. Lett.* 1993, 212, 177.

[72] Lee, T. J.; Taylor, P. R. *Int. J. Quantum Chem. Symp.* 1989, 23, 199.

[73] Martin, J. M. L.; Lee, T. J.; Scuseria, G. E.; Taylor, P. R. *J. Chem. Phys.* 1992, 97, 6549.

[74] Parr, R.G.; Yang, W. *Density Functional Theory of Atoms and Molecules*, Oxford University Press, Oxford, 1989.

[75] Kryachko, E. S.; Ludeña, E.V. *Energy Density Functional Theory of Many-Electron Systems*, Kluwer, Dordrecht, 1990.

[76] Labanowski, J. K.; Andzelm, J. W. (Eds.), *Density Functional Methods in Chemistry*, Springer-Verlag, New York, 1991.

[77] March, N. H.; *Electron Density Theory of Atoms and Molecules*. Academic Press, New York, 1992.

[78] Handy, N.C. *Density Functional Theory* in *Lecture Notes in Quantum Chemistry II*, B.O. Roos (Ed.), Springer-Verlag, Berlin, 1994.

[79] Chong, D. P. (Ed.), *Recent Advances in Density Functional Methods*, Part I, World Scientific, Singapore, 1995.

[80] Thomas, L. H. *Proc. Camb. Phil. Soc.* 1927, 23, 542.

[81] Fermi, E. *Rend. Accad., Lincei* 1927, 6, 602; ibid. *Z. Phys*. 1928, 48, 73; ibid. *Rend. Accad., Lincei* 1928, 7, 342.

[82] Dirac, P. A. M. *Proc. Cambridge Philos. Soc.* 1930, 26, 376.

[83] Slater, J. C. *Phys. Rev*. 1951, 81, 385.

[84] (a) Kato, T. *Commun. Pure Appl. Math.* 1957, 10, 151. (b) Bright Wilson, E. *"Structural Chemistry and Biology",* eds. A. Rich and N. Davidson, W. H. Freeman, San Francisco, 1968, pp. 753-760.

[85] Hohenberg, P.; Kohn, W. *Phys. Rev. B* 1964, 136, 864.

[86] Kohn, W.; Sham, L. J. *Phys. Rev. A* 1965, 140, 1133.

[87] Dunning, T. H., Jr. *J. Phys. Chem. A* 2000, 104, 9062; Dunning, T. H., Jr.; Peterson, K. A.; Woon, D. E. *Basis Sets: Correlation Consistent Sets* in *Encyclopedia of Computational Chemistry*, P.v.R. Schleyer, Editor, John Wiley, New York, 1998.

[88] (a) Gáspár, R. *Acta Phys. Acad. Sci. Hung*. 1954, 3, 263. (b) Becke, A. D. *J. Chem. Phys.* 1988, 88, 2547.

[89] Vosko, S. J.; Wilk, L.; Nusair, M. *Can. J. Phys.* 1980, 58, 1200.

[90] Gill, P. M. W. *Molec. Phys*. 1996, 89, 433.

[91] Ceperley, D. M.; Alder, B. *J. Phys. Rev. Lett*. 1980, 45, 566.

[92] Colle, R.; Salvetti, O. *Theor. Chim. Acta* 1975, 37, 329.

[93] Lee, C.; Yang, W.; Parr, R. G. *Phys. Rev. B* 1988, 37, 385.

[94] Miehelich, B.; Savin, A.; Stoll, H.; Preuss, H. *Chem. Phys. Lett*. 1989, 157, 200.

[95] Perdew, J. P. in *Electronic Structure of Solids,* P. Ziesche and H. Eschrig (Eds.), Akademic Verlag, Berlin, 1991.

[96] Perdew, J. P. *Physics B 1991*, 172, 1.

[97] Perdew, J. P.; Wang, Y. *Phys. Rev. B* 1992, 45, 13244.

[98] Perdew, J. P.; Chevary, J. A.; Vosko, S. H.; Jackson, K. A.; Pederson, M. R.; Singh, D. J.; Fiolhais, C. *Phys. Rev. B* 1996, 46, 6671.

[99] Gill, P. M. W.; Johnson, B. G.; Pople, J. A.; Frisch, M. J. *Int. J. Quantum Chem. Symp.* 1992, 26, 319.

[100] Perdew, J. P., *Phys. Rev. B* 1986, 33, 8822.

[101] Becke, A. D. *J. Chem. Phys.* 1993, 98, 5648.

[102] (a) Harris, J.; Jones, R. O. *J. Phys. F* 1974, 4, 1170. (b) Gunnarson, O.; Lundquist, B. T. *Phys. Rev. B* 1976, 13, 4274. (c) Harris, J. *Phys. Rev. A* 1984, 29, 1648. (d) Becke, A. D. *J. Chem. Phys.* 1988, 88, 1053.

[103] Becke, A. D. *J. Chem. Phys.* 1993, 98, 1372.

[104] Adamo, C.; Barone, V. *J. Chem. Phys.* 1998, 108, 664

[105] (a) Lynch, B. J.; Fast, P. L.; Harris, M.; Truhlar, D. G. *J. Phys. Chem. A* 2000, 104, 4811. (b) Lynch, B. J.; Truhlar, D. G. *J. Phys. Chem. A* 2001, 105, 2936.

[106] Lebedev, V. J. *Zh. Vychisl. Mat. Fiz.* 1975, 15, 48; ibid. 1976, 16, 293; ibid. *Sibirsk. Mat. Zh.* 1977, 18, 132; ibid. *Proc. Conf. Novosibirsk* (1978), ed S. L. Sobolev (Nauka Sibisk. Otdel, Novosibirsk, 1980).

[107] Konyaev, S. I. *Mat. Zametki* 1979, 25, 629.

[108] Gill, P. M. W.; Johnson, B. G.; Pople, J. A. *Chem. Phys. Lett.* 1993, 209, 506.

[109] Murray, C. W.; Handy, N. C.; Laming, G. *J. Molec. Phys.* 1993, 78, 997.

[110] Koch, W.; Holthausen, M. C. *A Chemist's Guide to Density Functional Theory*, Second Edition, Wiley-VCH, Weinheim, 2001.

[111] Press, W. H.; Teukolsky, S. A.; Vetterling, W. T.; Flannery, B. P. *Numerical Recipes in Fortran 77: The Art of Scientific Computing*, Ed Prentice Hall: Harlow, UK, 2001.

[112] Pople, J. A.; Gill, P. M. W.; Johnson, B. G. *Chem. Phys. Lett.* 1992, 199, 557.

[113] Johnson, B. G.; Gill, P. M. W.; Pople, J. A. *J. Chem. Phys.* 1993, 98, 5612.

[114] Handy, N. C.; Tozer, D. J.; Laming, G. J.; Murray, C. W.; Amos, R. D. *Israel. J. Chem.* 1993, 33, 331.

[115] Johnson, B. G.; Frisch, M. J. *Chem. Phys. Lett.* 1993, 216, 133.

[116] Johnson, B. G.; Frisch, M. J. *J. Chem. Phys.* 1994, 100, 7429.

[117] Martin, J. M. L.; El-Yazal, J.; François J-P. *Chem. Phys. Lett.* 1996, 248, 345.

[118] Johnson, B. G.; Gonzales, C. A.; Gill, P. M. W.; Pople, J. A. *Chem. Phys. Lett.* 1994, 221, 100.

[119] Claes, L.; François, J.-P.; Deleuze, M. S. *J. Am. Chem. Soc.* 2003, 125, 7129.

[120] Claes, L.; François, J.-P.; Deleuze, M. S. *J. Comp. Chem.* 2003, 24, 2023.

[121] Zhao, Y.; Truhlar, D. G. *J. Phys. Chem. A* 2004, 108, 6908.

[122] Fetter, A. L.; Walecka, J. D. *Quantum Theory of Many Particle Systems*, McGaw-Hill, New York, 1971.

[123] Linderberg, J.; Öhrn, Y. Propagators in Quantum Chemistry, Wiley: Hoboken, New-Jersey, 2004.

[124] Cederbaum, L. S.; Domcke, W. *Adv. Chem. Phys.* 1977, 36, 205.

[125] Öhrn, Y., Born, G. *Adv. Quantum Chem.* 1981, 13, 1.

[126] Herman, M. F.; Freed, K. F.; Yeager, D. L. *Adv. Chem. Phys.* 1981, 48, 1.

[127] Pickup, B. T. *Methods in Computational Chemistry*, 5, S.J. Wilson (Ed.), Plenum, London, 1993, p. 157

[128] (a) Cederbaum, L. S.; Hohlneicher, G.; Peyerimhoff, S. *Chem. Phys. Lett.* 1971, 11, 421. (b) Cederbaum, L. S.; Hohlneicher, G.; von Niessen, W. *Chem. Phys. Lett.* 1973, 18, 503. (c) Cederbaum, L. S *Chem. Phys. Lett.* 1974, 25, 562. (d) Cederbaum, L. S. *Mol. Phys.* 1974, 28, 479. (e) Cederbaum, L. S.; Schirmer, J.; Domcke, W.; von Niessen, W. *Int. J. Quant. Chem.* 1978, 14, 593. (f) Cederbaum, L. S.; Domcke, W.; Schirmer, J.; von Niessen, W.; Diercksen, G. H. F.; Kraemer, W. P. *J. Phys. B* 1978, 69, 1591. (g) Schirmer, J.; Domcke, W.; Cederbaum, L. S ; von Niessen, W. *J. Phys. B* 1978, 11, 1901. (h) Domcke, W.; Cederbaum, L. S.; Schirmer, J.; von Niessen, W. *Chem. Phys.* 1979, 40, 171. (i) Schirmer, J. ; Domcke, W.; Cederbaum, L. S.; von Niessen, W.; Åsbrink, L. *Chem. Phys. Lett.* 1979, 61, 30. (j) von Niessen, W.; Diercksen, G.

H. F. *J. Electr. Spectr. Rel. Phen.* 1980, 20, 95. (k) Cederbaum, L. S.; Schirmer, J.; Domcke, W.; von Niessen, W. *Adv. Chem. Phys.* 1986, 65, 115.

[129] (a) Öhrn, Y. *Lectures on theory of spectroscopy in terms of propagators,* 1988. (b) Öhrn, Y. *Propagators for molecular electronic spectra* in Lecture notes in Chemistry, Vol. 50, p. 185, D. Muckerjee (Ed.), Springer-Verlag, 1988.

[130] Harris, F. R.; Monkhorst, H. J.; Freeman, D. L. *Algebraic and diagrammatic methods in many-fermion theory*, Oxford Press University, Oxford, 1992.

[131] March, N. H.; Young, W. H.; Samanthar, S. *The Many-Body Problem in Quantum Mechanics*, Cambridge University Press, Cambridge, 1967.

[132] Mattuck, A. D. *A Guide to Feynman Diagrams in the Many-Body Problem*, McGraw-Hill, New York, 1967.

[133] Pickup, B. T.; Goscinski, O. *Mol. Phys.* 1973, 26, 1013.

[134] Purvis, G. D.; Öhrn, Y. *J. Chem. Phys.* 1974, 60, 4063.

[135] Goscinski, O.; Lukman, B. *Chem. Phys. Lett.* 1970, 7, 573.

[136] Simons, J.; Smith, W. D. *J. Chem. Phys.* 1973, 63, 4899.

[137] Purvis, G. D.; Öhrn, Y. *J. Chem. Phys.* 1975, 33, 396.

[138] Jørgensen, P.; Simons, J. *J. Chem. Phys.* 1975, 63, 5302.

[139] (a) Herman, M. F.; Yeager, D. L. *Chem. Phys. Lett.* 1977, 46, 1. (b) Freed, K. F.; Yeager, D. L. *Chem. Phys.* 1977, 22, 401. (c) Herman, M. F.; Yeager, D. L. ; Freed, K. F. *Chem. Phys.* 1978, 29, 77. (d) Herman, M. F.; Freed, K. F.; Yeager, D. L. *Chem. Phys.* 1978, 32, 437. (e) Herman, M. F.; Freed, K. F. *Chem. Phys.* 1979, 36, 383. (f) Herman, M. F.; Freed, K. F.; Yeager, D. L. *J. Chem. Phys.* 1980, 72, 602. (g) Herman, M. F.; Freed, K. F.; Yeager, D. L. *J. Chem. Phys.* 1980, 72, 611.

[140] (a) Baker, J.; Pickup, B. T. *Chem. Phys. Lett.* 1980, 56, 537. (b) Baker, J.; Pickup, B. T. *Mol. Phys.* 1983, 49, 651. (c) Baker, J. *Chem. Phys. Lett.* 1983, 101, 136; (d) Baker, J. *Chem. Phys.* 1983, 79, 117. (e)Baker, J. *Chem. Phys.* 1984, 79, 2693; (f) Baker, J. *J. Chem. Phys.* 1985, 80, 117. (g) Baker, J. *Int. J. Quant. Chem.* 1985, 27, 145.

[141] (a) Ortiz, J. V.; Basy, R.; Öhrn, Y. *Chem. Phys. Lett.* 1983, 103, 29. (b) Ortiz, J. V. *Int. J. Quantum Chem.* 1989, S23, 321. (c) Ortiz, J. V. *EPT90, An ab ionitio electron propagator program*, University of New Mexico, 1990. (d) Ortiz, J. V. *Int. J. Quantum Chem.* 1991, S25, 35. (e) Ortiz, J. V. *Chem. Phys. Lett.* 1992, 199, 530.

[142] Schirmer, J.; Cederbaum, L. S.; Walter, O. *Phys. Rev. A* 1983, 28, 1237.

[143] Weikert, H.-G.; Meyer, H.-D.; Cederbaum, L. S.; Tarantelli, F. *J. Chem. Phys.* 1996, 104, 7122.

[144] von Niessen, W.; Schirmer, J; Cederbaum, L. S. *Comput. Phys. Rep.* 1984, 1, 59.

[145] Schirmer, J.; Angonoa, G. *J. Chem. Phys.* 1989, 91, 1754.

[146] Ruthe, A. *Math. Comput.* 1979, 33, 680.

[147] Meyer, H. D.; Pal, S. *J. Chem. Phys.* 1989, 91, 6195.

[148] (a) Lanczos, G. *J. Res. Natl. Bur. Stand.* 1950, 45, 255. (b) Parlett, B. N. *The Symmetric Eigenvalue Problem*, Prentice-Hall, Englewood Cliffs, N. J., 1980. (c) Cullum, J. K.; Wiloughby,

R. A. *Lanczos Algorithms for Large Symmetric Eigenvalue Computations*, Birkhuser, Boston, 1985.

[149] (a) Tarantelli, A.; Cederbaum, L. S. *Phys. Rev. A* 1994, 49, 3407. (b) Schirmer, J.; Mertins, F. *Int. J. Quantum Chem.* 1996, 58, 329. (c) Mertins, F.; Schirmer, J.; Tarantelli, A. *Phys. Rev. A*, 1996, 53, 2153.

[150] (a) Deleuze, M.; Delhalle, J.; Pickup, B. T.; Calais, J.-L. *Phys. Rev. B* 1992, 46, 15668. (b) Deleuze, M.; Delhalle, J.; Pickup, B. T.; Calais, J.-L. *Adv Quantum Chem.* 1995, 26, 35. (c) Deleuze, M.; Scheller, M. K.; Cederbaum, L. S. *J. Chem. Phys.* 1995, 103, 3578.

[151] (a) Deleuze, M. S.; Cederbaum, L. S. *Phys. Rev. B* 1996, 53, 13326. (b) Deleuze, M. S.; Cederbaum, L. S. *J. Chem. Phys.* 1996, 105, 7583. (c) Deleuze, M. S.; Cederbaum, L. S. *Int. J. Quantum Chem.* 1997, 63, 465. (d) Golod, A.; Deleuze, M. S.; Cederbaum, L. S. *J. Chem. Phys.* 1999, 110, 6014. (e) Deleuze, M. S.; Cederbaum, L. S. *Adv. Quantum Chem.* 1999, 35, 77.

[152] Deleuze, M. S.; Trofimov, A. B.; Cederbaum, L. S. *J. Chem. Phys.* 2001, 115, 5859.

[153] Cederbaum, L. S. *J. Phys. B* 1975, 8, 290.

[154] Ortiz, J. V. in *Computational Chemistry: Reviews of Current Trends*, Vol. 2, 1, edited by J. Leszczynski, World Scientific, Singapore, 1997.

[155] (a) Ortiz, J. V. *J. Chem. Phys.* 1988, 89, 6348; (b) ibid. 1998, 108, 1008.

[156] Ortiz, J. V.; Zakrzewski, V. G.; Dolgounitcheva, O. in *Conceptual Perspectives in Quantum Chemistry*, Edited by J. L. Calais and E. Kryachko, Kluwer, The Netherlands, 1997, p. 465.

[157] Zakrzewski, V. G.; Ortiz, J. V.; Nichols, J. A.; Heryadi, D.; Yeager, D. L.; Golab, J. T. *Int. J. Quantum Chem.* 1996, 60, 29.

[158] (a) McCarthy, I. E.; Weigold, E. *Rep. Prog. Phys.* 1988, 51, 299. (b) McCarthy, I. E.; Weigold, E. *Rep. Prog. Phys.* 1991, 54, 789. (c) M.A. Coplan, J.H. Moore and J.P. Doering, Rev. Mod. Phys. 66, 985 (1994). (d) Weigold, E.; McCarthy, I. E. *Electron Momentum Spectroscopy*; Kluwer Academic/Plenum Publishers: New York, 1999.

[159] Miyake, Y.; Takahashi, M.; Watanabe, N.; Khajuria, Y.; Udagawa, Y.; Sakai, Y.; Mukoyama, T. *Phys. Chem. Chem. Phys.* 2006, 8, 3022.

[160] Watanabe, N.; Khajuria, Y.; Takahashi, M.; Udagawa, Y. *J. Electron. Spectr. Rel. Phen.* 2005, 142, 325.

[161] Nicholson, R. J. F.; Braidwood, S. W.; McCarthy, I. E.; Weigold, E.; Brunger, M. J. *Phys. Rev. A* 1996, 53, 4205.

[162] Nicholson, R. J. F.; McCarthy, I. E.; Weigold, E.; Brunger, M. J. *Chem. Phys. Lett.* 1996, 255, 105.

[163] Subramaniam, C. K.; Coplan, M. A.; Tossell, J. A.; Moore, J. H.; Leung, K. T., *Chem. Phys.* 1994, 185, 237.

[164] Zheng, Y.; Neville, J. J.; Brion, C. E.; Wang, Y.; Davidson, E. R. *Chem. Phys.* 1994, 188, 109.

[165] Hollebone, B. P.; Neville, J. J.; Zheng, Y.; Brion, C. E.; Wang, Y.; Davidson, E. R. *Chem. Phys.* 1995, 196, 13.

[166] Rolke, J.; Cann, N.; Zheng, Y.; Hollebone, B. P.; Brion, C. E.; Wang, Y. A.; Davidson, E. R. *Chem. Phys.* 1995, 1.

[167] Zheng, Y.; Neville, J. J.; Brion, C. E. *Science* 1995, 270, 786.

[168] Davidson, E. R. *Can. J. Phys.* 1996, 74, 757.

[169] Rioual, S.; Nguyen Vien, G.; Pochat, A. *Phys. Rev. A* 1996, 54, 4968.

[170] Zheng, Y.; Brion, C. E.; Brunger, M. J.; Zhao, K.; Grisogono, A. M.; Braidwood, S.; Weigold, E.; Chakravorty, S. J.; Davison, E. R.; Sgamellotti, A.; von Niessen, W. *Chem. Phys.* 1996, 212, 269.

[171] Rolke, J.; Zheng, Y., Brion, C. E.; Chakravorty, S. J.; Davidson, E. R.; McCarthy, I. E. *Chem. Phys.* 1997, 215, 191.

[172] Adcock, W.; M. J. Brunger, Michalewicz, M. T.; Winkler, D. A. *Aust. J. Phys.* 1998, 51, 707.

[173] Brunger, M. J.; Winkler, D.A.; Michalewicz, M. T.; Weigold, E. *J. Chem. Phys.* 1998, 108, 1859.

[174] Takahashi, M.; Ogino, R.; Udagawa, Y. *Chem. Phys. Lett.* 1998, 288, 714.

[175] Winkler, D. A.; Michalewicz, M. T.; Wang, F.; Brunger, M. J. *J. Phys. B.: At. Mol. Opt. Phys.* 1999, 32, 3239.

[176] Zheng, Y.; Pang, W. N.; Shang, R. C.; Chen, X. J.; Brion, C. E.; Ghanty, T. K.; Davidson, E. R. *J. Chem. Phys.* 1999, 111, 9526.

[177] Adcock, W.; M. J. Brunger, McCarthy, I. E.; Michalewicz, M. T.; von Niessen, W.; Wang, F.; Weigold, E.; Winkler, D. A. *J. Am. Chem. Soc.* 2000, 122, 3892.

[178] Litvinyuk, I. V.; Zheng, Y.; Brion, C. E. *Chem. Phys.* 2000, 253, 41.

[179] Deng, J. K.; Li, G. Q.; He, Y.; Huang, J. D.; Deng, H.; Wang, X. D.; Wang, F.; Zhang, Y. A.; Ning, C. G.; Gao, N. F.; Wang, Y.; Chen, X. J.; Zheng, Y. *J. Chem. Phys.* 2001, 114, 882.

[180] Deleuze, M. S.; Pang, W. N.; Salam, A.; Shang, R. C. *J. Am. Chem. Soc.* 2001, 123, 4049.

[181] Wang, F.; Mackenzie-Ross, H.; Winkler, D. A.; McCarthy, I. E.; Campbell, L.; Brunger, M. J. *J. Comput. Chem.* 2001, 22, 1321.

[182] Tixier, S.; Shapley, W. A.; Zheng, Y.; Chong, D. P.; Brion, C. E.; Shi, Z.; Wolfe, S. *Chem. Phys.* 2001, 270, 263.

[183] Deng, J. K.; Li, G. Q.; Wang, X. D.; Huang, J. D.; Deng, H.; Ning, C. G.; Wang, Y.; Zheng, Y. *J. Chem. Phys.* 2002, 117, 4839.

[184] Mackenzie-Ross, H.; Brunger, M. J.; Wang, F.; Adcock, W.; Trout, N.; McCarthy, I. E.; Winkler, D. A. *J. Electron Spectr. Rel. Phen.* 2002, 123, 389.

[185] Mackenzie-Ross, H.; Brunger, M. J.; Wang, F.; Adcock, W.; Maddern, T.; Campbell, L.; Newell, W. R.; McCarthy, I. E.; Weigold, E.; Appelbe, B.; Winkler, D. A. *J. Phys. Chem. A* 2002, 106, 9573.

[186] Nixon, K. L.; Wang, F.; Campbell, Maddern, T.; Winkler, D.; Gleiter, R.; Loeb, P.; Weigold, E.; Brunger, M. J. *J. Phys. B: At. Mol. Opt. Phys.* 2003, 36, 3155.

[187] Takahashi, M.; Saito, T.; Hiraka, J.; Udagawa, Y. *J. Phys. B: At. Mol. Opt. Phys.* 2003, 36, 2539.

[188] Wang, F.; Brunger, M. J.; McCarthy, I. E.; Winkler, D. A. *Chem. Phys. Lett.* 2003, 382, 217.

[189] Wang, F.; Brunger, M. J.; Winkler, D. A. *J. Phys. Chem. Sol.* 2004, 65, 2041.

[190] Jones, D. B.; Bolorizadeh, M. A.; Brunger, M. J.; Saha, S.; Wang, F.; Gleiter, R.; Bueber, J.; Winkler, D. A. *J. Phys. B: At. Mol. Opt. Phys.* 2006, 39, 2411.

[191] Dennison, J. R.; Ritter, A. L. *J. Electron. Spectrosc. Relat. Phenom.* 1996, 77, 99.

[192] Vos, M.; McCarthy, I. *Am. J. Phys.* 1997, 65, 544.

[193] McCarthy, I. E.; Vos, M. *Aust. J. Phys.* 1999, 52, 363.

[194] Vos, M.; Bowles, C.; Kheifets, A. S.; Sashin, V. A.; Weigold, E.; Aryasetiawan, F. *J. Electr. Spectr. Rel. Phen.* 2004, 137-140, 629.

[195] McCarthy, I. E.; Weigold, E. *Electron-Atom Collisions*, Cambridge University Press: Cambridge, 1995.

[196] Ford, W. F. *Phys. Rev. B* 1964, 133, 1616.

[197] Stia, C. R.; Fojon, O. A.; Rivarola, R. D.; Hanssen, J.; Kamalou, O.; Martina, D.; Chesnel, J.-Y.; Frémont, F. *Inst. Phys. Conf. Ser. No. 183*, 2005.

[198] Pang, W. N.; Gao, J. F.; Ruan, C. J.; Shang, R. C.; Trofimov, A. B.; Deleuze, M. S. *J. Chem. Phys.* 2000, 112, 8043.

[199] Takahashi, M.; Udagawa, Y. *J. Electron. Spectrosc.* 2004, 137, 387.

[200] Ren, X. G.; Ning, C. G.; Deng, J. K.; Zhang, S. F.; Su, G. L.; Huang, F.; Li, G. Q. *Phys. Rev. Lett.* 2005, 94, 163201.

[201] Brunger, M.J.; McCarthy, I. E.; Weigold, E. *Phys. Rev. A* 1999, 59, 1245.

[202] Dey, S.; McCarthy, I. E.; Teubner, P. J. O.; Weigold, E. *Phys. Rev. Lett.* 1975, 34, 782.

[203] Braidwood, S. W.; Brunger, M. J.; Konovalov, D. A.; Weigold, E. *J. Phys. B* 1993, 26, 1655.

[204] Pickup, B. T. *Chem. Phys.* 1977, 19, 193.

[205] Deleuze, M.; Pickup, B. T.; Delhalle, J. *Mol. Phys.* 1994, 83, 655.

[206] Schwarz, W. H. E. *Ang. Chem.* 2006, 45, 1508.

[207] Duffy, P.; Chong, D.P.; Casida, M.E.; Salahub, D.R. *Phys. Rev. A* 1994, 50, 4704.

[208] Casida, M. E. *Phys. Rev. A* 1995, 51, 2005.

[209] Gritsenko, O.V.; Braïda, B.; Baerends, E.J. *J. Chem. Phys.* 2003, 119, 1937.

[210] Janak, J. F. *Phys. Rev. B* 1978, 18, 7165.

[211] Gritsenko, O.V.; Baerends, E.J.; *J. Chem. Phys.* 2002, 117, 9154.

[212] See various contributions to the original HEMS program as recorded by Bawagan [Bawagan, A. O. *Ph. D. Thesis*; University of British Columbia (UBC), 1987]. The HEMS (now known as MOMAP) program has been extensively revised and extended at UBC by Cann, N. M.; and Cooper, G.

[213] Duffy, P.; Casida, M. E.; Brion, C. E.; Chong, D. P. *Chem. Phys.* 1992, 159, 347.

[214] Bawagan, A. O.; Brion, C. E. *Chem. Phys.* 1990, 144, 167.

[215] Ning, C. G.; Ren, X. G.; Deng, J. K.; Zhang, S. F.; Su, L.; Huang, F.; Li, G. Q. *J. Chem. Phys.* 2005, 122, 224302.

[216] Ren, X. G.; Ning, C. G.; Deng, J. K.; Zhang, S. F.; Su, L.; Huang, F.; Li, G. *Rev. Sci. Instr.* 2005, 76, 063103.

[217] Ning, C. G.; Deng, J. K.; Su, G. L.; Zhou, H.; Ren, X. G. *Rev. Sci. Instr.* 2004, 75, 3062.

[218] Brunger, M. J.; Adcock, W. *J. Chem. Soc., Perkin Trans. 2* 2002, 1.

[219] (a) Zhou, L. X.; Shan, X.; Chen, X. J.; Yin, X. F.; Zhang, X. H.; Xu, C. K.; Wei, Z.; Xu, K. Z. *J. Electron Spectrosc. Rel. Phen.* 2006, 153, 58. (b) Shan, X.; Chen, X. J.; Xu, C.; Zhou, L. Xu, K. *Chem. Phys. Lett.* 2006, 422, 246.

[220] (a) Čermák, V. *J. Chem. Phys.* 1966, 44, 3781. (b) Niehaus, A.; *Adv. Chem. Phys.* 1981, 45, 399. (c) Yencha, A. J. *Electron Spectroscopy: Theory, Technique, and Applications*, Vol. 5, Brundle, C. R.; Baker, A. D.; Eds.; Academic, New York, 1984.

[221] Hotop, H.; Niehaus, A. *Z. Phys.* 1969, 228, 68.

[222] Deleuze, M. S.; Claes, L.; Kryachko, E.G.; Francois, J.-P. *J. Chem. Phys.* 2003, 119, 3106.

[223] (a) Deleuze, M. S.; Giuffreda, M. G.; Francois, J.-P.; Cederbaum, L. S. *J. Chem. Phys.* 1999, 111, 5851. (b) Deleuze, M. S.; Giuffreda, M.G.; Francois, J.-P.; Cederbaum, L. S.; *J. Chem. Phys.* 2000, 112, 5325. (c) Deleuze, M. S.; Giuffreda, M. G.; Francois, J.-P. *J. Phys. Chem. A* 2002, 106, 5626. (d) Deleuze, M. S. *J. Chem. Phys.*, 2002, 116, 7012. (e) Deleuze, M. S. *J. Phys. Chem. A* 2004, 108, 9244.

[224] Ohno, K.; Mutoh, H.; Harada, Y. *J. Am. Chem. Soc.* 1983, 105, 4555.

[225] Ohno, K.; Matsumoto, S.; Harada, Y. *J. Chem. Phys.* 1984, 81, 4447.

[226] Ohno, K.; Harada, Y. *Penning Ionization : the Outer Shape of Molecule,* pp-199-233 in *Theoretical Models of Chemical Bonding* (*Vol. Part 3)*; Z.B. Maksić, Ed.; Springer-Verlag, Berlin, 1991.

[227] Niehaus, A. *Ber. Bunsenges. Phys. Chem.* 1973, 77, 632.

[228] Rothe, E.W.; Neynaber, R. H.; Trujillo, S. M. *J. Chem. Phys.* 1965, 42, 3310.

[229] Hotop, H. *Radiat. Res.* 1974, 59, 379.

[230] Haberland, H.; Lee, Y. T.; Siska, P. E. *Adv. Chem. Phys.* 1981, 45, 487.

[231] Mitsuke, K.; Takami, T.; Ohno, K. *J. Chem. Phys.* 1989, 91, 1618.

[232] Ohno, K.; Yamakado, H.; Ogawa, T.; Yamata, T. *J. Chem. Phys.* 1996, 105, 7536.

[233] Ohno, K.; Takami, T.; Mitsuke, K.; Ishida, T. *J. Chem. Phys.* 1991, 95, 918

[234] Handy, N.C.; Marron, M. T.; Silverstone, H. J. *Phys. Rev.* 1969, 180, 45.

[235] Morrell, M.M.; Parr, R.G.; Levy, M. *J. Chem. Phys.* 1975, 62, 549.

[236] (a) Banwell, C. N.; *Fundamentals of molecular spectroscopy*, Mc Graw Hill, Maidenhead, U. K., 1972. (b) Kimura, K.; Katsumata, S.; Achiba, Y.; Yamazaki, T.; Iwata, S. *Handbook of HeI Photoelectron Spectra of Fundamental Organic Molecules*; Japan Scientific Society: Tokyo, 1981. (c) Eland, J. H. D. *Photoelectron Spectroscopy. Second English edition*; Butterworths, 1984.

[237] (a) Herzberg, G.; *"Infrared and Raman Spectra"*; Van Nostrand Reinhold Compagny, New York, 1945. (b) McQuarrie, D. A. *Statistical Mechanics*; Harper and Row: New York, 1976. (c) McQuarrie, D.A.; Simon, J.D.; *Physical Chemistry, A Molecular Approach*, University Science Approach, Sausalits, 1997. (d) McQuarrie, D. A. *Statistical Mechanics*; University Science Books, Sausalito, California, 2000.

[238] Martin, J. M. L.; François, J. P.; Gijbels, R. *J. Chem. Phys.* 1991, *95*, 8374.

[239] (a) Peng, C.; Ayala, P. Y.; Schlegel, H. B.; Frisch, M. J. *J. Comp. Chem.* 1996, 17, 49. (b) Peng, C.; Schlegel, H. B. *Israel J. Chem.* 1994, 33, 449.

[240] Simons, J.; Jorgensen, P.; Taylor, H.; Ozment, J. *J. Phys. Chem.* 1983, *87*, 2745.

[241] Ayala, P. Y.; Schlegel, H. B. *J. Chem. Phys.* 1998, 108, 2314.

[242] Mayo, S. L.; Olafson, B. D.; Goddard, W. A. *J. Phys. Chem.* 1990, *94*, 8897.

[243] Kilpatrick, J. E.; Pitzer, K. S. *J. Chem. Phys.* 1949, 17, 1064.

[244] Abramowitz, M.; Stegun, I. A. *Handbook of Mathematical Functions*; Dover Publications inc., New-York, 1972, p. 360.

[245] Boys, S. F. *Proc. Roy. Soc. (London) A* 1950, 200, 542.

[246] Hariharan, P. C.; Pople, J. A. *Theor. Chim. Acta* 1973, 28, 213.

[247] Grev, R. S.; Schaeffer III, H. F. *J. Chem. Phys.* 1989, 91, 7305.

[248] (a) Feller, D. *J. Chem. Phys.* 1992, 96, 6104. (b) Feller, D. *J. Chem. Phys.* 1993, 98, 7059.

[249] Schwartz, C. in *Methods in Computational Physics 2*; Alder, B. J., Ed.; Academic: New York, 1963.

[250] Martin, J. M. L.; *Ab Initio Thermochemistry Beyond Chemical Accuracy for First- and Second-Row Compounds*, in NATO ASI Symposium volume *Energetics of Stable Molecules and Reactive Intermediates*; Mirrasda Piedade, M. E. and Irikura, K. K, Eds.; Kluwer: Dordrecht, The Netherlands, 1999.

[251] Dunning, T. H., Jr.; Hay, P. J. in *Methods of Electronic Structure Theory*; Schaefer, H. F., Ed.; Plenum Press: New York, 1977; Vol. 2.

[252] Widmark, P. O.; Malmqvist, P. A.; Roos, B. O. *Theor. Chim. Acta* 1990, 77, 291.

[253] Frisch, M. J.; Trucks, G. W.; Schlegel, H. B.; Scuseria, G. E.; Robb, M. A.; Cheeseman, J. R.; Zakrzewski, V. G.; Montgomery, J. A.; Stratmann, R. E.; Burant, J. C.; Dapprich, S.; Millam, J. M.; Daniels, A. D.; Kudin, K. N.; Strain, M. C.; Farkas, O.; Tomasi, J.; Barone, V.; Cossi, M.; Cammi, R.; Mennucci, B.; Pomelli, C.; Adamo, C.; Clifford, S.; Ochterski, J.; Petersson, G. A.; Ayala, P. Y.; Cui, Q.; Morokuma, K.; Malick, D. K.; Rabuck, A. D.; Raghavachari, K.; Foresman, J. B.; Cioslowski, J.; Ortiz, J. V.; Stefanov, B. B.; Liu, G.; Liashenko, A.; Piskorz, P.; Komaromi, I.; Gomberts, R.; Martin, R. L.; Fox, D. J.; Keith, T.; Al-Laham, M. A.; Peng, C. Y.; Nanayakkara, A.; Gonsalez, C.; Challacombe, M.; Gill, P. M. W.; Johnson, B. G.; Chen, W.; Wong, M. W.; Andres, J. L.; Head-Gordon, M.; Replogle, E. S.; Pople, J. A. *GAUSSIAN 98* (Revision A.7); Gaussian, Inc., Pittsburgh, PA, 1998.

[254] Gaussian 03, Revision D.01, Frisch, M. J.; Trucks, G. W.; Schlegel, H. B.; Scuseria, G. E.; Robb, M. A.; Cheeseman, J. R.; Montgomery, Jr., J. A.; Vreven, T.; Kudin, K. N.; Burant, J. C.; Millam, J. M.; Iyengar, S. S.; Tomasi, J.; Barone, V.; Mennucci, B.; Cossi, M.; Scalmani, G.; Rega, N.; Petersson, G. A.; Nakatsuji, H.; Hada, M.; Ehara, M.; Toyota, K.; Fukuda, R.; Hasegawa, J.; Ishida, M.; Nakajima, T.; Honda, Y.; Kitao, O.; Nakai, H.; Klene, M.; Li, X.; Knox, J. E.; Hratchian, H. P.; Cross, J. B.; Bakken, V.; Adamo, C.; Jaramillo, J.; Gomperts, R.; Stratmann, R. E.; Yazyev, O.; Austin, A. J.; Cammi, R.; Pomelli, C.; Ochterski, J. W.; Ayala, P. Y.; Morokuma, K.; Voth, G. A.; Salvador, P.; Dannenberg, J. J.; Zakrzewski, V. G.; Dapprich, S.; Daniels, A. D.; Strain, M. C.; Farkas, O.; Malick, D. K.; Rabuck, A. D.; Raghavachari, K.; Foresman, J. B.; Ortiz, J. V.; Cui, Q.; Baboul, A. G.; Clifford, S.; Cioslowski, J.; Stefanov, B. B.; Liu, G.; Liashenko, A.; Piskorz, P.; Komaromi, I.; Martin, R. L.; Fox, D. J.; Keith, T.; Al-Laham, M. A.; Peng, C. Y.;

Nanayakkara, A.; Challacombe, M.; Gill, P. M. W.; Johnson, B.; Chen, W.; Wong, M. W.; Gonzalez, C.; and Pople, J. A.; Gaussian, Inc., Wallingford CT, 2004.

[255] Frisch, A.; Frisch, M. J. Gaussian 98, User's reference Gaussian Inc., Pittsburgh, PA 15106, 1998.

[256] MOLPRO is an *ab initio* MO package by Werner, H.-J.; Knowles, P.J., with contributions from Almlöf, J.; Amos, R.D.; Berning, A.; Cooper, D.L.; Deegan, M.J.O; Dobbyn, A.J.; Eckert, F.; Elbert, S.T.; Hampel, C.; Lindh, R.; Lloyd, A.W.; Meyer, W.; Nicklass, A.; Peterson, K.; Pitzer, R.; Stone, A.J.; Taylor, P.R.; Mura, M.E.; Pulay, P.; Schütz, M.; Stoll, H. and Thorsteinsson, T. (University of Birmingham 1996).

[257] The ADC(3) code developed by Scheller, M. K.; Angonoa, G.; Walter, O.; Schirmer, J.; contributions due to Trofimov, A. B.

[258] (a) Davidson, E. R. *J. Comput. Phys.* 1975, 17, 87. (b) Butscher, W.; Kammer, W. E. *Ibid.* 1975, 17, 87.

[259] Tarantelli, F. (unpublished)

Part 3: Cage compounds

3.1 Norbornane: An investigation into its valence electronic structure using electron momentum spectroscopy, density functional theory and one-particle Green's function theory.

3.1.1 Introduction

In spite of the importance of norbornane (NBA) to chemistry and pharmaceutical research [1, 2], the experimental determination of its structure has been problematic. The molecule has an extremely small dipole moment (~ 0.09D [3]) making structural determination by microwave spectroscopy very difficult. Choplin [3] studied the microwave response of norbornane but was unable to determine its structure because of the weak intensity of rotational transitions, due to the low dipole moment, as well as difficulties in preparing isotopically enriched samples. There have been a number of structural studies by electron diffraction [4] but the norbornane molecule is problematic due to strong correlations between parameters used to determine the similar carbon-carbon bond lengths in the molecule. The use of x-ray crystallography to determine an unambiguous structure was complicated by the fact that norbornane, like many globular molecules, is orientationally disordered at ambient temperatures, transforming from cubic to hexagonal at 306 K. Single crystals of norbornane have not been available and Fitch and Jobic [5] only recently solved the structure by powder x-ray diffraction methods using a synchrotron radiation source. However this structure was for solid norbornane, and structures from x-ray diffraction are subject to substantial deformation because of crystal lattice interactions.

Consequently, a precise gas phase structure of norbornane has not been determined experimentally and computational approaches have been valuable in interpreting the available experimental data in a consensus fashion. van Alsenoy and coworkers [6] employed *ab initio* Hartree Fock (HF) calculations to assist in the interpretation of the microwave structure model [6], and Allinger's group [7] used molecular mechanics methods to analyze the x-ray diffraction and electron diffraction data to give a consistent structure for norbornane.

An experimental calibration of the model employed (i.e. theoretical approach and basis set) using electron momentum spectroscopy (EMS) provides a way to select a wave function which is reliable enough for accurately predicting the molecular structure of norbornane, as well as calculating other important molecular properties such as the dipole moment, bond orders, charge distributions, NMR and vibrational spectra. Previous studies [7, 8] have used a variety of molecular mechanics and molecular orbital approaches to determine structural and electronic properties of norbornane. Here we use the unique orbital imaging capability [9, 10] of EMS to determine which of the employed density functional theory exchange correlation functionals and basis sets best describes the experimental momentum distributions. This optimum basis and exchange correlation functional is then used to derive the structure and molecular properties of norbornane. These data are next compared with independent experimentally determined values, and those from other MO calculations, to determine how well the optimum model was able to reproduce norbornane's molecular properties.

While conducting our study, it became quite clear that existing investigations into the outer- and inner-valence electronic structure of norbornane are rather scarce. Previous photoelectron spectroscopy (PES) studies include the He(I) measurements from Bischof *et al.* [11] and Getzlaff and Schönhense [12] and the He(II) measurement from Bieri *et al.* [13]. Theoretical interpretation of these spectra has been even more limited with only the modified intermediate neglect of differential overlap, version 2 (MINDO/2) result from Bodor *et al.* [14] currently being available in the literature. Hence the present Hartree-Fock (HF), Density Functional Theory (DFT) and one-particle Greens Function (1p-GF) calculations significantly expand the available theoretical knowledge of the electronic structure of norbornane. In addition we believe that the present EMS measurements are the first to be made on this molecule, thus further expanding our understanding of its electronic structure through our original momentum space images of its MOs.

Finally we note that norbornane is the second molecule in the chemically similar series norbornadiene(I) [15, 16], norbornene(II) and norbornane(III), which are interesting to be studied using EMS, HF and DFT techniques. In going from (I) to (III) the C=C double bonds in these highly strained bicyclic hydrocarbons are progressively saturated. It is our thesis that by unravelling the electronic structure of norbornane using EMS in conjunction with DFT calculations and the one-particle Greens Function (1p-GF) theory of ionization, we may probe the influence of substantial cyclic strains on chemical bonds. In this respect we note a preliminary study [17] on all three molecules [(I) - (III)].

In the following section of this paper we briefly discuss our EMS measurements, including our ionization spectra. Details of our HF, DFT and 1p-GF calculations, and some of the electronic structure information we can extract from them are presented in sections 3 and 4, while in section 5 we compare and discuss the experimental and theoretical momentum distributions associated to all bands in the EMS ionization spectra. In section 6 the molecular property information derived from our optimum basis set and exchange correlation functional is detailed, while in section 7 some of the conclusions drawn from the current study are presented.

3.1.2. Experimental details and preliminary analysis

A sample of high-purity norbornane was synthesized ``in-house" using commercially purchased (Aldrich Chemical Company) norbornene in the following manner. To a thick-walled flask we added norbornene (5g, 52 mmol), AR methanol (100 ml) and a spatula amount of 10% Pd on carbon. The resulting mixture was hydrogenated under 40 psi of H_2 for 12 hours with rocking. There was an instantaneous uptake of H_2. More H_2 was introduced and left overnight. Water was added and then extracted with $CFCl_3$ (2 × 20 ml). The bottom organic layer was collected and allowed to evaporate at room temperature. The crude norbornane (~1g) was pure according to gas chromatographic (GC) and ^{13}C and ^{1}H NMR analysis agreed with previously reported data [18]. This material was then distilled into a U-tube immersed in liquid nitrogen and under vacuum and then transferred into the reaction vessel. The reaction vessel was in turn connected to the gas handling system of the EMS spectrometer. In addition, it was degased *in situ* by repeated freeze-pump-thaw cycles before being introduced into the interaction region. Comparing our $\phi = 0° + 10°$ ionization spectrum with the PES result of Bischof *et al.* [11] shows that the level of qualitative agreement between them is very good. This gives further evidence for the purity of our NBA sample, an important consideration given the high sensitivity of EMS to the presence of any impurities.

All the 20 MO's of the complete valence region of NBA, namely the $3a_2$, $5b_2$, $7a_1$, $5b_1$, $6a_1$, $4b_2$, $2a_2$, $4b_1$, $3b_2$, $3b_1$, $5a_1$, $2b_1$, $4a_1$, $2b_2$, $3a_1$, $1a_2$, $2a_1$, $1b_2$, $1b_1$ and $1a_1$ MO's, were then investigated in several experimental runs using the Flinders symmetric noncoplanar EMS spectrometer [9]. Details of this coincidence spectrometer and the method of taking the data can be found in Brunger and Adcock [10], and Weigold and McCarthy [9], and so we do not repeat them again here.

The high-purity NBA is admitted into the target chamber through a capillary tube, the flow rate being controlled by a variable leak value. Possible clustering, due to supersonic expansion, was avoided by maintaining a low NBA driving pressure throughout data collection. The collision region is differentially pumped by a 700 l s^{-1} diffusion pump. Apertures and slits are cut in the collision chamber for the incident electron beam and the scattered and ejected electrons. The differentially pumped collision region makes it possible to increase the target gas density by a factor ~3 while keeping the background pressure below 10^{-5} Torr. This was important as it enabled us to maintain workable coincidence count rates, even with the smaller electron beam current output from the (e,2e) monochromator (typically 30 μA in this work) compared to that of a normal electron gun [19]. The coincident energy resolution of the present measurements was ~ 0.55 eV full-width-at-half-maximum (FWHM) as determined from measurements of the binding-energy (ε_f) spectrum of helium. Note that the profile of the helium spectrum was found to be well represented by a Gaussian function.

However, due to the natural and vibrational line widths (sometimes also known as the Franck-Condon widths) of the various electronic transitions and a quite strong dispersion of the ionization intensity into many-electron processes at the bottom of the carbon-2s region, the fitted resolutions of the spectral peaks for NBA varied from ~0.88 to 2.31 eV (FWHM). It is precisely this limitation which forces us to combine our measured highest occupied molecular orbital (HOMO) and next-highest occupied molecular orbital (NHOMO) ($3a_2$ and $5b_2$) momentum distributions (MDs), $5b_1$ and $6a_1$ orbital MDs, $4b_2$, $2a_2$ and $4b_1$ orbital MDs, $3b_2$ and $3b_1$ orbital MDs, $5a_1$ and $2b_1$ orbital MDs and $2a_1$, $1b_2$ and $1b_1$ orbital MDs, respectively. While there is no doubt one loses some physical information in combining these MDs, to not do so would have raised serious question as to the uniqueness of the MDs derived in the fits to our binding energy spectra (see below). The angular resolution, which determines the momentum resolution, was typically 1.2° (FWHM), as determined from the electron optics and apertures and from a consideration of the argon $3p$ angular correlation.

Ionization spectra of norbornane measured at representative angles ϕ in the region 7-29 eV and at E = 1500 eV are displayed in Figure 1. The solid curve in each panel represents the envelope of the 13 fitted Gaussians (various dashed curves) whose positions below ε_f ~ 23 eV are taken from the available PES data [11-13]. A summary of the available orbital binding-energies from PES data, the present EMS binding-energies and our tentative orbital assignments are given in Table I. The fact that we use only 13 Gaussians to analyze spectra containing 20 valence MOs simply reflects our earlier point that our energy resolution was insufficient to uniquely deconvolve all the orbitals, so that some were combined (summed). Notwithstanding this it is clear from Figure 1 that the fits to the measured binding-energy spectra are excellent. The least-squares-fit deconvolution technique used in the analysis of these spectra is based on the work of Bevington and Robinson [20], to whom readers are referred for more detail. Above ε_f ~ 23 eV there are no PES data available to guide us in our fitting of the binding-energy spectra. Under these circumstances the positions and widths of the Gaussian peaks, and the number of Gaussians, used in the spectral deconvolution were simply determined by their utility in best fitting the observed data for all ϕ. The fact that the inner valence $2a_1$, $1b_2$, $1b_1$ and $1a_1$ orbitals need 3 very broad Gaussians (peaks 11 - 13) to incorporate the measured coincidence intensity into the fit, is undoubtedly indicative of a severe dispersion of ionization intensity over many satellite states, an observation which led us to undertake thorough 1p-GF calculations of the valence one-electron and shake-up ionization spectrum of norbornane (see section 4).

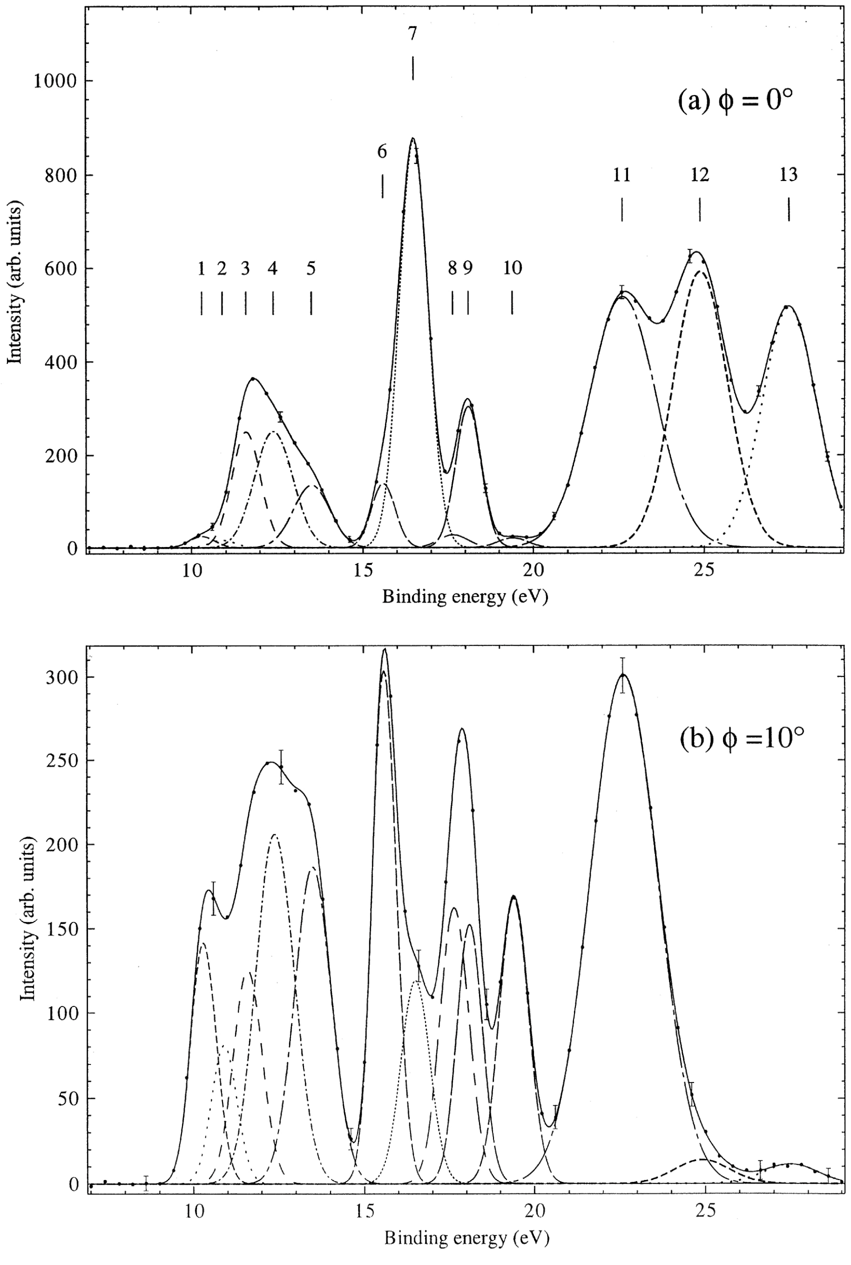

Figure 1. Typical binding-energy spectra from our 1500 eV noncoplanar symmetric EMS investigation into norbornane. The curves show the fits to the spectra at (a) $\phi = 0°$ ($p \approx 0.03$ a.u.) and (b) $\phi = 10°$ ($p \approx 0.92$ a.u.) using the known energy resolution. The peak positions of the Gaussians used in the fit (see also Table I) are indicated. Note that indicative error bars are shown on this figure.

The EMS ionization spectra of Figure 1 clearly reflect the respective symmetries [9] of the valence orbitals of norbornane. For instance the unresolved HOMO and NHOMO (peak 1) show significantly more intensity at $\phi = 10°$ compared to that at $\phi = 0°$. This is consistent with the "*p*-type" symmetry of these orbitals. On the other hand the $4a_1$ orbital (peak 7) has a much greater intensity at $\phi = 0°$ compared to that found at $\phi = 10°$, an angular dependence which corroborates its "*s*-type" symmetry. On the basis of the symmetry indicated by the EMS binding-energy spectra and the results of our calculations in Table II (see sections 3 and 4 for more details) tentative orbital assignments were made and are given in Table I.

In general these orbital assignments are consistent with those found from our 1p-GF calculations, with the exception of band 12 in the inner-valence region. The angular dependence of the EMS cross sections indicate that bands 12 and 13 have similar "*s*-type" MDs, so that both bands at first glance could be ascribed to originating from the $1a_1$ orbital. Our 1p-GF calculations support the notion that band 13 relates essentially to satellites originating from ionization of the $1a_1$ orbital. In addition, the EMS and 1p-GF interpretations of band 11 are largely consistent in assigning that flux as mainly being due to a set of lines related to ionization of the $2a_1$, $1b_2$ and $1b_1$ orbitals. Band 12, however, appears to be a far more complicated issue than was originally anticipated (see section 4).

TABLE I. Norbornane—electronic structure (experimental).

Orbital number	Present Classification	ϵ_f (eV) Experimental				Natural width (eV) (Refs. 11–13)
		PES (Ref. 11)	PES (Ref. 12)	PES (Ref. 13)	Present EMS	
1	$3a_2$	~10.2	~10.3	~10.3	10.3	0.72
2	$5b_2$					
3	$7a_1$	~10.7	~10.9	~10.9	10.9	0.72
4	$5b_1$	~11.4–12.12	~11.6	~11.6	11.6	0.86
5	$6a_1$					
6	$4b_2$		~12.4	~12.4	12.4	1.20
7	$2a_2$					
8	$4b_1$					
9	$3b_2$	~13.4	~13.6	~13.5	13.5	1.14
10	$3b_1$					
11	$5a_1$	~15.5	~15.6	~15.6	15.6	0.64
12	$2b_1$					
13	$4a_1$	~16.4	~16.5	~16.5	16.5	0.86
14	$2b_2$	~17.5	~17.5–17.8	~17.65	17.65	0.86
15	$3a_1$	···	~18.1	~18.1	18.1	0.72
16	$1a_2$	···	~19.4	~19.4	19.4	0.86
17	$2a_1$	···	···	~22.62	~22.6	2.25
18	$1b_2$	···	···			
19	$1b_1$	···	···			
20	$1a_1$ [a]	···	···	···	24.9	1.80
					27.5	1.80

[a] This assignment is controversial. See text.

3.1.3 Theoretical analysis of EMS cross sections

The plane wave impulse approximation (PWIA) [21] is used to analyze the measured cross sections for high-momentum transfer (e,2e) collisions. Using the Born-Oppenheimer approximation for the target and ion wave functions as well as the weak coupling approximation, the EMS differential cross section σ, for randomly oriented molecules and unresolved rotational and vibrational states, can be reduced to [9] an expression explicitly depending on the relevant orbital of the Hartree-Fock (Target Hartree-Fock approximation) or Kohn-Sham ground state (Target Kohn-Sham approximation).

The Kohn-Sham equation of DFT may be considered as an approximate quasi-particle equation, with the potential operator approximated by the exchange-correlation potential [22, 23]. Often this is done at the local spin density (LSD) approximation level, although in this study we concentrate on approximating the exchange-correlation (XC) functional with functionals that depend on the electron density and its gradients [24-27] (i.e., the generalized gradient approximation (GGA)). Specifically, here we employed two different approximations to the XC energy functional due to Becke and Perdew (BP) [24-26] and Becke, Lee, Yang and Parr (BLYP) [24, 25, 27].

TABLE II. Norbornane–electronic structure (theory).

		ϵ_f (eV) Basis sets		
Orbital number	Present Classification	Present HF/TZVP	Present HF/ cc-pVDZ	Present DFT BP/TZVP
1	$3a_2$	11.332	11.328	6.88
2	$5b_2$	11.666	11.641	7.24
3	$7a_1$	12.033	12.006	7.54
4	$5b_1$	12.585	12.531	7.90
5	$6a_1$	12.659	12.607	7.98
6	$4b_2$	13.140	13.108	8.19
7	$2a_2$	13.439	13.384	8.41
8	$4b_1$	13.695	13.634	8.65
9	$3b_2$	14.767	14.734	9.41
10	$3b_1$	14.887	14.831	9.46
11	$5a_1$	17.079	16.999	11.16
12	$2b_1$	17.332	17.232	11.43
13	$4a_1$	18.474	18.360	12.26
14	$2b_2$	19.793	19.772	12.82
15	$3a_1$	20.547	20.500	13.42
16	$1a_2$	22.372	22.328	14.64
17	$2a_1$	25.576	25.542	16.94
18	$1b_2$	26.593	26.570	17.68
19	$1b_1$	27.135	27.067	18.10
20	$1a_1$	31.606	31.532	21.48

To compute the coordinate space Kohn-Sham orbitals ψ_j, we employed DGauss, a program package originally developed at CRAY Research by Andzelm and colleagues [28, 29]. It has been known for a number of years [30] that HF theory provides momentum distributions of lower quality than DFT, therefore we do not assess HF momentum distributions again here. DGauss is itself a part of UniChem [30]. The molecular structure of norbornane has been optimized through energy minimization with various gradient-corrected functionals and basis sets, employing the UniChem user interface. Note that a geometry optimization was performed in DGauss with each basis set used. The electronic structural calculations using restricted Hartree-Fock (RHF) and second-order Moller-Plesset (MP2) approaches along with a polarized valence basis set of triple zeta (TZVP) quality are based on GAMESS [31]. A subset of our calculated orbital energies from both our DFT and SCF calculations is given in Table II. Clearly none of these results give particularly good agreement with the corresponding experimental values of Table I. Despite Koopmans' theorem, all HF orbital energies overestimate the measured ionization energies by ~1 to ~3 eV, which indicates that these energies are substantially influenced by electron-correlation effects and, more importantly, electron relaxation effects. On the other hand our BLYP- and BP- DFT computations all underestimate the respective experimental binding energies by ~ 3.5 - 4.7 eV. Such a result was, however, not entirely unexpected. It is known ([32] and references therein) that XC functionals, whether at LSD or GGA levels, fail to give the correct dispersion interaction in the large *r* region. This error in the asymptotic limit of the XC functionals leads to ionization energies that underestimate those determined by experiment by as much as 5 eV.

Information of the molecular structure and the molecular orbital wave functions for the ground electronic state of NBA, obtained from the DGauss DFT calculations, were next treated as input to the Flinders-developed program AMOLD [19], which computes the momentum space spherically averaged molecular-structure factor [21] and the (e,2e) cross section or MD. Note that all the theoretical MDs we report in this paper have had the experimental angular resolution folded in using the method of Frost and Weigold [33].

The comparisons of calculated MDs with experiment (see section 5) may be viewed as an exceptionally detailed test of the quality of the XC energy and basis set. From our previous experience [34, 35], the GGA-DFT methods using the BP and BLYP XC functionals give best agreement with the experimental MDs, compared to the LSD method. As a result, GGA-BP and GGA-BLYP are used in combination with three basis sets to examine the behavior of the XC functionals and basis sets. These basis sets are denoted by the acronyms DZVP, DZVP2 and TZVP. The notations DZ and TZ denote basis sets of double - or triple - zeta quality. V denotes a calculation in which such a basis is used only for the valence orbitals and a minimal basis is used for the less chemically reactive core orbitals. The inclusion of long-range polarisation functions is denoted by *P*. We note, in particular, that the basis sets of DGauss was specially designed for DFT calculations [28, 36]. The TZVP basis set has a contraction scheme [7111/411/1] for carbon and [3111/1] for hydrogen. The auxiliary basis set corresponding to the TZVP basis is called *A*1 [37], in which the *s*-, *p*- and *d*-orbital exponents were determined separately from an optimization that reproduces, as accurately as possible, the energy from an atomic DFT calculation. The contraction schemes of the *A*1 basis sets for H are [4/1] and for C [8/4/4].

The DFT DGauss calculations were performed on a Silicon Graphics 02 (R5200) workstation as the UniChem client and a CRAY *J*90*se*/82048 computer as the DFT computational engine. Further Hartree-Fock (RHF) and second-order Møller-Plesset (MP2) calculations using the TZVP basis set and a GAMESS02 suite of programs [31], were carried out on the Compaq Alpha Server SC cluster at the Australian Partnership for Advanced Computing National Facilities.

In light of the marginal agreement between the DFT and experimental ionization energies, that we described earlier, further calculations employing more sophisticated Greens Function techniques were undertaken. These calculations are all based on geometries that have been optimized using Density Functional Theory by means of the GAMESS02 program [31] employing the TZVP basis set and the non-local hybrid Becke three-parameter Lee-Yang-Parr functional (B3LYP) [27, 38].

3.1.4 Theoretical analysis of valence ionization spectra

Vertical ionization spectra have been computed using one-particle Greens Function [1p-GF] theory at the level of the third-order algebraic diagrammatic construction [ADC(3)] scheme [39-42], in conjunction with Dunnings' correlation consistent polarized valence basis set of double zeta quality (cc-pVDZ [43]), and with the original code interfaced to the GAMESS92 package [31]. With the 1p-

GF/ADC(3) approach, the primary one-hole (1h) and the shake-up two-hole-one-particle (2h-1p) ionization energies are recovered through third- and first-order in correlation, respectively. Constant self-energy diagrams have been computed through fourth-order in correlation, using charge-consistent [44] one-electron densities. A threshold on pole strengths of 0.005 has been retained for solving the ADC(3) secular equation, using a Block-Davidson diagonalization procedure [45] in the final diagonalisation step. The assumption of frozen core electrons has been used throughout and symmetry has been exploited to the extent of the C_{2v} point group.

Our results from these calculations are presented in Table III. For comparison purposes, more specifically to evaluate the sensitivity of the computed ionization energies to the quality of the basis set, a few results obtained from Outer-Valence Greens Function (OVGF [46, 47]) calculations, performed with the GAUSSIAN98 package [48], are also presented in Table III. For these benchmark computations of one-electron ionization energies, specifically, we will consider basis sets such as Dunning's correlation consistent polarized valence basis set of triple zeta quality (cc-pVTZ [43]), and the cc-pVDZ basis augmented by a set of diffuse $\{s,p\}$-functions on hydrogens, and a set of diffuse $\{s,p,d\}$ functions on carbons (aug-cc-pVDZ [43, 49]). With the cc-pVDZ, aug-cc-pVDZ and cc-pVTZ basis sets, 158, 269, and 378 basis functions in total are incorporated in the OVGF computations on norbornane, respectively.

Because of the complexity of the outermost valence bands, encompassing the contributions of many and strongly overlapping ionization lines, it is preferable to resort to theoretical simulations for analyzing the available PES measurements. As a guide to the eye, the identified solutions of the secular ADC(3)/cc-pVDZ eigenvalue problem are therefore displayed as a spike spectrum and in the form of a convoluted density of states, along with the ultra-violet photoionization spectra by Getzlaff *et al.* [12] and Bieri *et al.* [13] (see figure 2 and Table III). The convolution has been performed using as a spread function a combination of a Gaussian and a Lorentzian with equal weight, a FWHM parameter of 0.6 eV, and by simply scaling the line intensities according to the computed ADC(3) pole (spectroscopic) strengths. Despite the neglect of cross section effects, the shape, position and the relative intensities of bands in the He(I) and He(II) spectra are overall very finely reproduced in the simulation. In particular, in line with the convoluted spectrum, three substructures are seen with the outermost He(II) ionization band, namely a shoulder at ~ 10.9 eV, and two maxima at ~ 11.7 and ~ 12.1 eV.

There are several points we would like to highlight from the results in Table III: First, the current Greens Function results for ε_f, of each respective orbital, are in satisfactory agreement with those correspondingly found in the previous PES work [11-13] (see Figure 2) and present EMS study (see Table I), particularly for the outer valence orbitals. Second, our ADC(3) results predict that the ionization intensity resulting from the inner valence $2a_1$, $1b_2$, $1b_1$ and $1a_1$ orbitals is severely split due to final state electron correlation effects. For these orbitals, the fractions of intensity recovered under the form of lines with a spectroscopic strength larger than 0.005 amount to 0.765, 0.697, 0.725 and 0.481, respectively. This observation is entirely consistent with previous one-particle Green's Function [50-53] or MR-SDCI [54] studies of the ionization spectra of saturated hydrocarbons larger than ethane. As has been noted earlier [50, 51], the dispersion of ionization intensity over many shake-up lines at energies larger than 22 eV correlates well with significant band broadening on the experimental side [see the FWHM values reported in Table I for peaks 11-13].

TABLE III. Norbornane—electronic structure (theory). Binding energies are given in eV, along with the OVGF and ADC(3) spectroscopic factors in parentheses. Results obtained using (I) B3-YP/TZVP, (II) B3LYP/cc-pVTZ, and MP2/aug-cc-pVDZ geometries.

			ϵ_f (eV) Basis sets					
Symbol	Orbital number	Present classification	Present ADC(3)/ cc-pVDZ (I)	Present OVGF/ cc-pVDZ (I)	Present OVGF/ aug-cc-pVDZ (I)	Present OVGF/ cc-pVTZ (I)	Present OVGF/ cc-pVTZ (II)	Present OVGF/ cc-pVTZ (III)
u	1	$3a_2$	10.513 (0.91)	10.390 (0.91)	10.467 (0.91)	10.443 (0.91)	10.392 (0.91)	10.359 (0.91)
t	2	$5b_2$	10.863 (0.91)	10.746 (0.91)	10.830 (0.91)	10.793 (0.91)	10.758 (0.91)	10.734 (0.91)
s	3	$7a_1$	11.189 (0.91)	11.063 (0.91)	11.154 (0.91)	11.121 (0.91)	11.075 (0.91)	11.055 (0.91)
r	4	$5b_1$	11.657 (0.90)	11.513 (0.91)	11.607 (0.91)	11.555 (0.91)	11.534 (0.91)	11.507 (0.91)
q	5	$6a_1$	11.670 (0.91)	11.529 (0.91)	11.615 (0.91)	11.557 (0.91)	11.554 (0.91)	11.507 (0.91)
p	6	$4b_2$	12.102 (0.91)	11.986 (0.91)	12.072 (0.91)	12.043 (0.91)	11.995 (0.91)	11.975 (0.91)
n	7	$2a_2$	12.445 (0.91)	12.390 (0.91)	12.453 (0.91)	12.452 (0.91)	12.406 (0.91)	12.353 (0.91)
m	8	$4b_1$	12.645 (0.90)	12.545 (0.91)	12.629 (0.91)	12.592 (0.91)	12.569 (0.91)	12.518 (0.91)
l	9	$3b_2$	13.657 (0.90)	13.589 (0.91)	13.670 (0.91)	13.650 (0.91)	13.605 (0.91)	13.557 (0.91)
k	10	$3b_1$	13.736 (0.90)	13.687 (0.91)	13.762 (0.91)	13.755 (0.91)	13.706 (0.91)	13.635 (0.91)
j	11	$5a_1$	15.757 (0.89)	15.587 (0.91)	15.624 (0.90)	15.650 (0.90)	15.619 (0.91)	15.552 (0.91)
i	12	$2b_1$	15.948 (0.89)	15.734 (0.90)	15.771 (0.90)	15.784 (0.90)	15.772 (0.90)	15.685 (0.91)
h	13	$4a_1$	16.897 (0.88)	16.698 (0.90)	16.740 (0.89)	16.741 (0.89)	16.746 (0.90)	16.649 (0.90)
g	14	$2b_2$	17.866 (0.86)	17.817 (0.89)	17.843 (0.89)	17.872 (0.89)	17.831 (0.89)	17.741 (0.89)
f	15	$3a_1$	18.473 (0.86)	18.405 (0.88)	18.435 (0.88)	18.449 (0.88)	18.429 (0.88)	18.335 (0.88)
e	16	$1a_2$	19.926 (0.83)	19.953 (0.87)	19.979 (0.87)	19.988 (0.87)	19.980 (0.88)	19.881 (0.87)
d	17	$2a_1$	21.695 (0.02)[a]	22.560 (0.85)[b]	22.588 (0.85)[b]	22.566 (0.85)	22.595 (0.85)[b]	22.497 (0.85)[b]
			22.088 (0.09)[c]					
			22.389 (0.13)[d]					
			22.484 (0.51)					
			23.573 (0.01)					
			23.961 (0.01)					
c	18	$1b_2$	22.493 (0.01)	23.288 (0.84)[b]	⋯	23.286 (0.84)[b]	23.327 (0.84)[b]	23.256 (0.84)[b]
			22.951 (0.39)					
			22.960 (0.02)					
			23.053 (0.04)					
			23.162 (0.07)					
			23.235 (0.01)					
			23.397 (0.01)					
			23.345 (0.08)					
			23.448 (0.04)					
			23.650 (0.02)					
			23.968 (0.01)					
			24.042 (0.01)					
			24.108 (0.02)					
b	19	$1b_1$	22.327 (0.01)	23.786 (0.84)[b]	⋯	23.782 (0.83)[b]	23.834 (0.84)[b]	23.735 (0.84)[b]
			22.555 (0.01)					
			22.810 (0.01)					
			23.167 (0.02)					
			23.190 (0.02)					
			23.287 (0.04)					
			23.378 (0.08)					
			23.444 (0.05)					
			23.456 (0.01)					
			23.533 (0.01)					
			23.597 (0.17)					
			23.663 (0.24)					
			23.708 (0.01)					
			24.091 (0.01)					
			24.177 (0.01)					
			24.263 (0.01)					
			24.452 (0.01)					
			24.514 (0.01)					
a	20	$1a_1$	25.318 (0.01)	⋯	⋯	⋯	⋯	⋯
			25.410 (0.01)					
			25.676 (0.01)					
			26.104 (0.01)					
			26.350 (0.01)					
			26.411 (0.01)					
			26.445 (0.01)					
			26.459 (0.01)					
			26.493 (0.01)					

TABLE III. (*Continued.*)

			ϵ_f (eV) Basis sets					
Symbol	Orbital number	Present classification	Present ADC(3)/ cc-pVDZ (I)	Present OVGF/ cc-pVDZ (I)	Present OVGF/ aug-cc-pVDZ (I)	Present OVGF/ cc-pVTZ (I)	Present OVGF/ cc-pVTZ (II)	Present OVGF/ cc-pVTZ (III)
a	20	$1a_1$	26.581 (0.01)	⋯	⋯	⋯	⋯	⋯
			26.655 (0.01)					
			26.669 (0.01)					
			26.685 (0.01)					
			26.729 (0.02)					
			26.804 (0.03)					
			26.917 (0.02)					
			26.930 (0.03)					
			27.012 (0.01)					
			27.099 (0.01)					
			27.163 (0.01)					
			27.183 (0.02)					
			27.208 (0.01)					
			27.228 (0.01)					
			27.279 (0.04)					
			27.287 (0.01)					
			27.331 (0.03)					
			27.352 (0.01)					
			27.368 (0.01)					
			27.385 (0.01)					
			27.393 (0.01)					
			27.402 (0.01)					
			27.432 (0.02)					
			27.437 (0.01)					
			27.469 (0.02)					
			27.518 (0.01)					
			27.679 (0.01)					
			27.784 (0.01)					
			27.993 (0.01)					

[a] Dominant electronic configuration: $3a_2^{-2}8a_1^{+1}$ (HOMO^{-2} LUMO^{+1}).

[b] Breakdown of the MO picture of ionization; see J. Chem. Phys. **116**, 7012 (2002).

[c] Dominant electronic configuration: $5b_2^{-2}8a_1^{+1}$ [(HOMO-1)$^{-2}$ LUMO^{+1}].

[d] Dominant electronic configuration: $3a_2^{-1}5b_2^{-1}6b_1^{+1}$.

Finally, the present calculations confirm the empirical rule [55] (and references therein) that OVGF pole strengths smaller than 0.85 very consistently foretell a breakdown of the MO picture of ionization at the ADC(3) level. In other words, the quasi-particle approach that has been somewhat unfortunately referred to over the last two decades as the OVGF approach, can also be reliably used for inner-valence states as long as the OVGF spectroscopic strengths remain larger than 0.85. Within that part of the spectrum that can be reliably described by one-hole states, i.e. up to binding energies of 20 eV, the OVGF and ADC(3) ionization energies do not differ by more than ~ 0.13 eV. For the $2a_1$ orbital the MO picture still holds to some extent, since among the identified satellites one of them emerges at 22.5 eV, in the ADC(3) ionization spectrum, with rather dominant intensity ($\Gamma_n = 0.51$) and a rather clear $2a_1^{-1}$ one-hole character. At higher binding-energies, however, the breakdown of the MO picture intensifies and the OVGF approach can no longer be applied. Note that the impact of diffuse functions on the 1 hole ionization energies is very limited (< 0.1 eV) - see Table III.

Convergence, within ~ 0.1 eV accuracy, of the OVGF/cc-pVDZ and, by extension, ADC(3)/cc-pVDZ ionization energies (with regards to further improvements of the basis set) is also confirmed by comparison with the OVGF/cc-pVTZ results. Finally, the last two columns of Table III, obtained using geometries optimized at the B3LYP/cc-pVDZ and MP2/aug-cc-pVDZ levels, demonstrate the very limited dependence of the computed ionization spectra on details of the molecular structures. All in all, at the ADC(3)/cc-pVDZ level, we thus expect accuracies of ± 0.2 eV on the computed *vertical* one-electron ionization energies. Indeed, an agreement better than 0.2 eV is found upon comparing the theoretical one-electron binding energies reported in Table III with the He(I), He(II) and EMS experimental values of Table I.

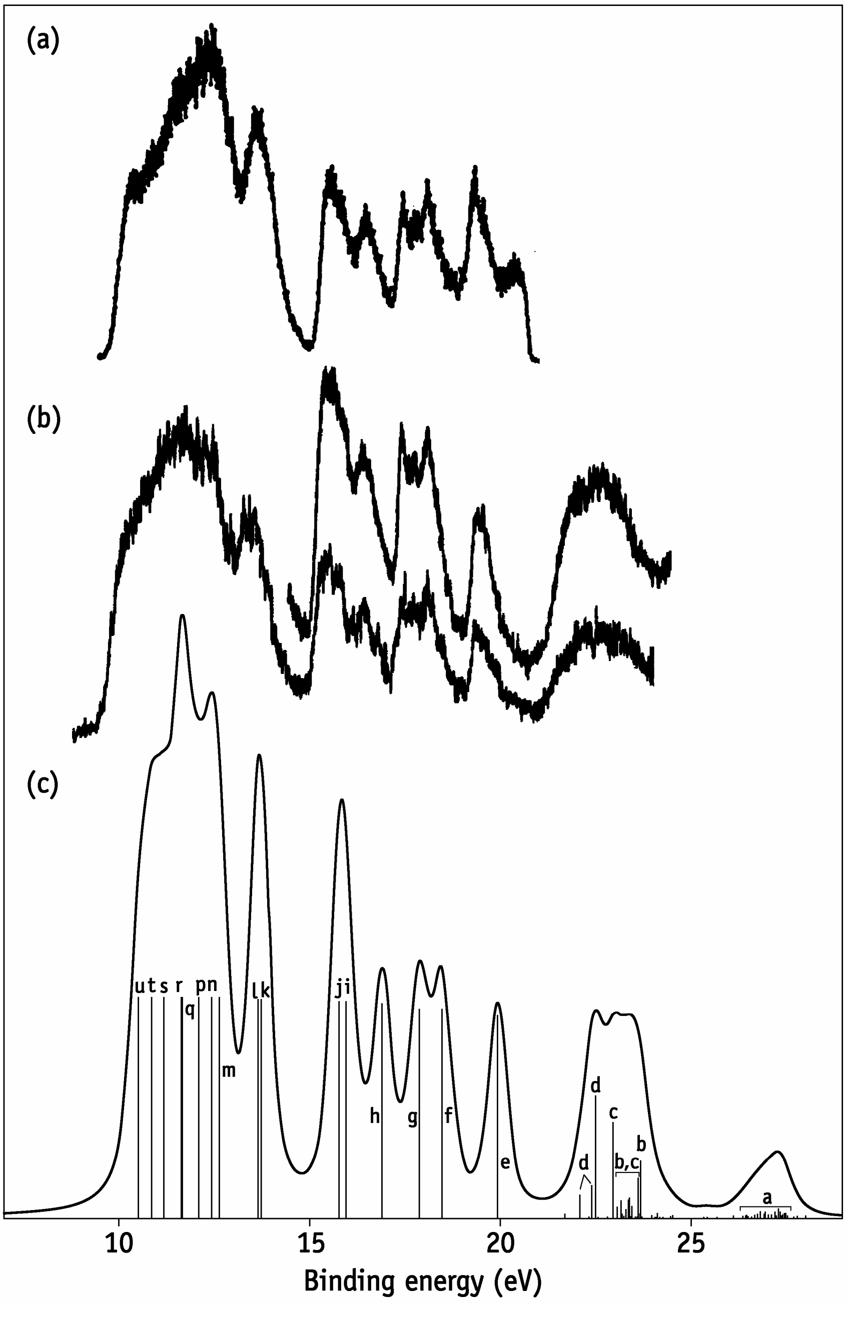

Figure 2. Comparison between the measured (a) He(I) (Ref. 12), (b) He(II) (Ref. 13), and (c) ADC(3)/cc-pVDZ theoretical ionization spectrum of norbornane.

Nonetheless, a discrepancy of ~ 0.6 eV is noticed for the $1a_2^{-1}$ ionization line. Although one can never exclude some calibration problems on the experimental side (the He(I) and He(II) ionization energies reported in [13] can be in error by approximately ± 0.2 eV), this unusually large discrepancy most presumably relates to strong geometry relaxation effects and vibronic interactions in a molecule characterized by pronounced cyclic strains. It can in particular be noticed that the corresponding band in the He(I) and He(II) spectra [12, 13], reproduced in Figure 2, has a very asymmetric shape, which is a quite typical feature for such effects. Further studies of the Franck-Condon vibrational profiles associated to this one-electron ionization line would be necessary for quantitatively clarifying this issue.

The most striking discrepancy between the EMS measurements displayed in Figure 1 and the ADC(3)/cc-pVDZ spectrum of Figure 2c is the band (12) seen at 24.9 eV in the experimental spectrum, which does not correlate to any set of ionization lines with appreciable enough intensity on the theoretical side. At this point, it is worth recalling that, because of the rather weakly correlated nature of wide band-gap compounds like saturated hydrocarbons, the expected accuracies of *vertical* one-electron and shake-up ionization energies at the ADC(3)/cc-pVDZ level are around 0.2 (see above) and 0.6 eV, respectively. On the basis of the angular dependence of band 12 (Figure 1), and of the related MD, which appear to be very similar to that of band 13 (see section 5), it would be very tempting to assign both bands to orbital $1a_1$. However, upon examining the ADC(3)/cc-pVDZ simulation of Figure 2c and the corresponding data in Table III, it is immediately apparent that the shake-up lines ascribed to ionization of orbital $1a_1$ concentrate only around 27.5 eV. By analogy with a band-Lanczos study [52] of the valence ionization spectra of *n*-alkanes, the missing fraction (52%) of the $1a_1$ ionization intensity should normally be recovered under the form of an extremely long correlation tail, extending from ~ 27 eV up to binding energies of 60 eV, and possibly beyond.

Upon performing further MP2/cc-pVDZ calculations of the total energy of norbornane in its neutral and dicationic ground ($^1A_1$) states, including full geometry optimization for both species, it was found that the vertical and adiabatic double ionization potentials of norbornane amount to 25.9 and 23.5 eV, respectively. Further studies, based on two-particle Green's Function calculations of doubly ionized states, or highly challenging one-particle Green's Function calculations incorporating very diffuse functions, Coulomb and distorted plane waves in the basis set, might thus be necessary for identifying with certainty the origin of band 12. Note that, as the $1a_1$ ionization intensity falls clearly much above the double ionization threshold, the shake-up lines which have been identified for that orbital should most correctly be regarded as discrete (bound and excited) cationic states embedded in a continuum of unbound (resonance and shake-off) dicationic states.

Finally, we note that all the MP2, OVGF, and ADC(3) calculations described in section 4 were carried out on a DEC-Compaq ES-40 workstation at the University of Hasselt.

3.1.5 Comparison between experimental and theoretical momentum distributions

Deconvolving the ionization spectra measured at each of a chosen set of angles ϕ by means of a least squares fit technique [20] allows us to derive the MDs associated to each of the bands identified in Figures 1a and 1b. Although the measured MDs are not absolute, relative magnitudes for the different transitions are obtained [19]. In the current EMS investigation of the valence states of NBA, the experimental MDs are placed on an absolute scale by summing the experimental flux for each measured ϕ for the first ten outer-valence orbitals, and then normalizing this to the corresponding sum for our PWIA-BP/TZVP calculation.

The results from this process for the unresolved HOMO ($3a_2$) and NHOMO ($5b_2$) orbitals are shown in Figure 3. In this case we find very good agreement between all the calculated PWIA-XC/DFT momentum distributions and our corresponding EMS data taken in two independent runs (Run A and Run B). Note that the error bars on all the MD data represent one standard deviation uncertainty. Further note that the experimental MD data from independent runs A and B are in very good agreement with one another, a feature that is repeated for all the measured MDs. The results in Figure 3 strongly suggest that the EMS spectroscopic factors for both the respective $3a_2$ and $5b_2$ orbitals are ~ 1. This observation is entirely consistent with our calculated ADC(3) and OVGF spectroscopic factors for these orbitals (see Table III). Although not shown, a similar level of agreement between the experimental and theoretical MDs is found for the $7a_1$ orbital. This result implies $\Gamma_{7a_1}^{EMS}(\varepsilon_f = 10.9\,\text{eV}) \sim 1$, which is also in good accord with our calculated ADC(3) and OVGF pole strengths (see again Table III).

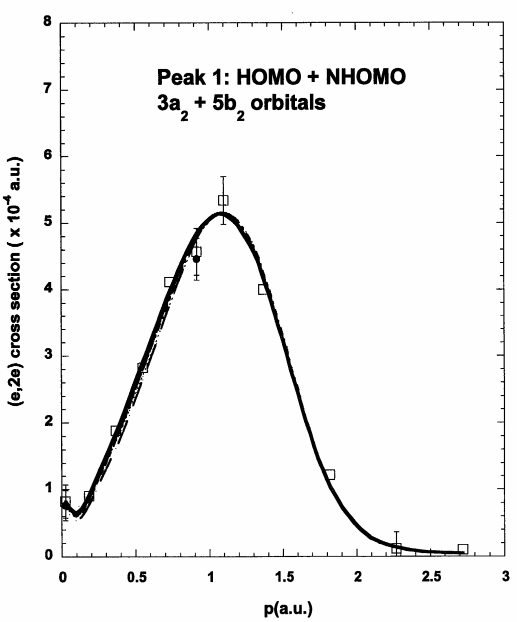

Figure 3. 1500 eV symmetric noncoplanar MD for the $3a_2$ + $5b_2$ orbitals or norbornane (ε_f ~10.3 eV). The present data for run A (•) and run B (□) are compared against the results of our PWIA-DFT calculations: (---) BP/DZVP, (— —) BLYP/DZVP, (·—·—) BP/DZVP2, (····) BLYP/DZVP2, (——) BP/TZVP, and (- —) BLYP/TZVP.

In Figure 4 we show the measured and calculated MDs for the $5b_1$ + $6a_1$ orbitals of norbornane. In this case we find that the momentum distributions calculated at the BLYP/DZVP level, within the plane wave impulse approximation (PWIA), significantly overestimates the magnitude of the experimental cross section for all *p*. This indicates that the combination of the BLYP exchange correlation functional and DZVP basis set is not providing a very good representation of these orbitals. While it is a less striking effect, Figure 4 also appears to indicate, for momenta in the region 0.1 au $\leq p \leq$ 0.6 au, that the PWIA-BLYP/DZVP2 MD somewhat underestimates the magnitude of the experimental MD. Nonetheless, the good level of agreement between theory and experiment for the remaining XC/DFT basis set results indicates the EMS spectroscopic factors of both the $5b_1$ and $6a_1$ orbitals are respectively ~ 1. This finding is consistent with the MO picture of ionization being valid here for these outer-valence orbitals, a result in good agreement with our ADC(3) and OVGF calculations of Table III.

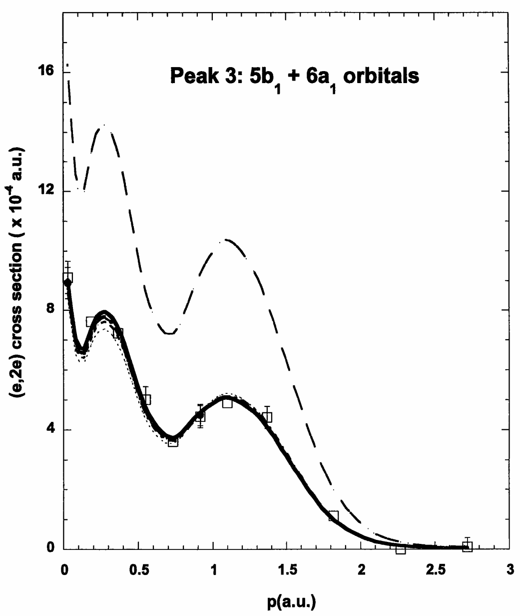

Figure 4. 1500 eV symmetric non-coplanar MD for the $5b_1$+$6a_1$ orbitals of norbornane (ε_f ~ 11.6 eV). The legend is the same as that for Figure 3.

The present MDs for the $4b_2$ + $2a_2$ + $4b_1$ orbitals of norbornane are shown in Figure 5. In this case there is a very interesting trend for momenta in the range 0.1 au $\leq p \leq$ 0.55 au. Specifically, in this region all the PWIA-BLYP/DFT MDs predict a somewhat higher cross section magnitude compared to all the corresponding PWIA-BP/DFT MDs, with the experimental cross sections favoring the PWIA-BP/DFT results. This is quite unusual in our experience [10, 15, 16] as typically we have found that our experimental MDs are more discriminating in terms of the types of basis sets employed, rather than the type of XC functional used. We would characterize the overall level of agreement between our PWIA-BP/DFT momentum distribution results and the experimental momentum distributions as being good, suggesting EMS spectroscopic factors for each of these orbitals lying somewhere in the range 0.9 - 1.0. Such EMS spectroscopic factors for the $4b_2$, $2a_2$ and $4b_1$ orbitals are found again to be in good agreement with the predictions from our ADC(3) and OVGF calculations, as can be seen in Table III.

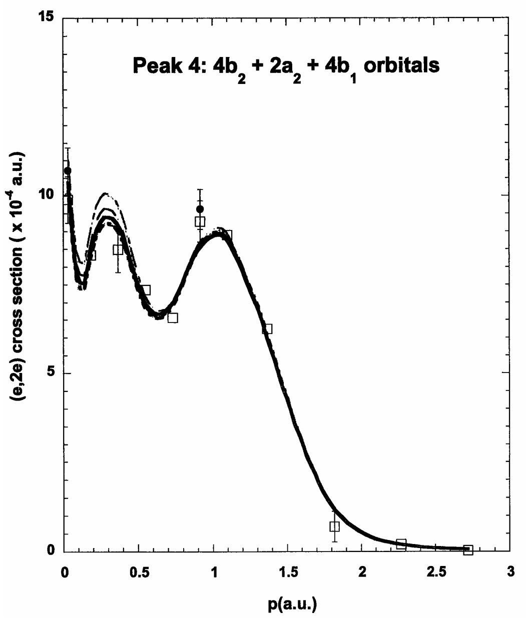

Figure 5. 1500 eV symmetric non-coplanar MD for the $4b_2$+$2a_2$+$4b_1$ orbitals of norbornane ($\varepsilon_f \sim$ 12.4 eV). The legend is the same as that for figure 3.

The $4a_1$ orbital momentum distributions are illustrated in Figure 6. In this case we see that all the MDs are strongly peaked (large cross section) as $p \to 0$ au, indicating an "*s*-type" symmetry [9] which is probably due to strong C(2*s*) contributions. For $p \geq 0.2$ au all the theoretical MD's are in good agreement with each other and with the experimental MD results. For $p < 0.2$ au, however, only the BP/TZVP, BLYP/TZVP and, to a lesser extent, the BP/DZVP models are providing a good description of the measurements. When we combine this observation with what we have previously discussed from Figures 4 and 5, we start to see a trend emerging. Namely, in the one-electron ionization part of the spectrum, the BP/TZVP model gives overall the most accurate description for each of the experimental MDs. Note that this observation also holds for all the MDs we do not specifically plot. Hence, from the results obtained for the one-electron ionization lines, the BP/TZVP wave function appears to be one of the best suited wave functions for studying further structural, vibrational and electronic properties of norbornane - see section 6.

Let us now consider the most challenging part of the ionization spectrum, namely the inner-valence region beyond the shake-up threshold at ~ 22 eV. In Figure 7a we plot the experimental MD for the sum of peaks 11-13 of Figure 1, and the corresponding theoretical MDs from the models considered. Here all the theoretical MDs do a fair job in predicting the shape of the experimental result, although they all underestimate the magnitude of the experimental cross section across most of the measured momentum range. This result might reflect a break-down in the inner valence region for the PWIA description of the reaction mechanism. There certainly exists a large body of evidence that shows that for certain atomic systems [9] the PWIA breaks down for inner valence orbitals. In these cases the (e,2e) ionization process has to be described within a distorted wave framework [9].

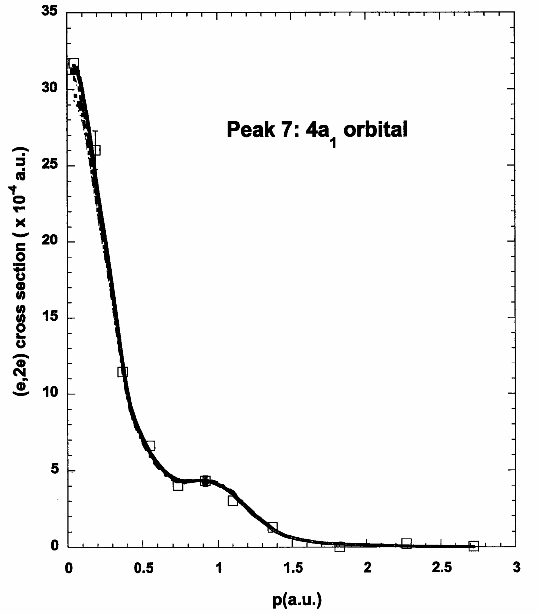

Figure 6. 1500 eV symmetric noncoplanar MD for the 4a_1 orbital of norbornane (ε_f ~ 16.5 eV). The legend is the same as that for Figure 3.

The ADC(3) calculation suggests that peak 11 originates mainly from the 2a_1, 1b_2 and 1b_1 orbitals and the present EMS experimental MD for this peak supports such a notion. As can be seen from Figure 7b, the experimental MD for 2a_1 + 1b_2 + 1b_1 orbitals has very good shape agreement with the corresponding theoretical MDs, although as it might be expected from Figure 7a there is a mismatch in the magnitude of these cross sections. Nonetheless, the present experimental momentum profile exhibits clearly a minimum at p ~ 0.2 au, in fair agreement with the theoretical predictions for the summed 2a_1 + 1b_2 + 1b_1 orbital set, and thus nicely reflects the fact that band 11 consists of a mixture of ionization lines with "s-type" and "p-type" symmetries.

If we consider the experimental momentum distribution for peak 13, compared to 0.5 × 1a$_1$ for PWIA-BP/TZVP (see Figure 8), then we see the level of agreement between them is quite good. This is strong evidence that peak 13 largely originates from the innermost valence 1a_1 orbital, a result which is consistent with our ADC(3) findings. We would like to recall that the missing experimental flux (~ 50 %) is expected to be found at binding energies beyond the range sampled in the present study. There is evidence in Figure 1 that supports the idea that there is additional 1a_1 flux at ε_f > 29 eV. As peak 12 has a similar (although by no means identical) MD to that of peak 13 (see Figure 9), it is tempting to conclude that it too might originate from the 1a_1 orbital. However, as noted earlier, our ADC(3) calculation does not support such an assignment.

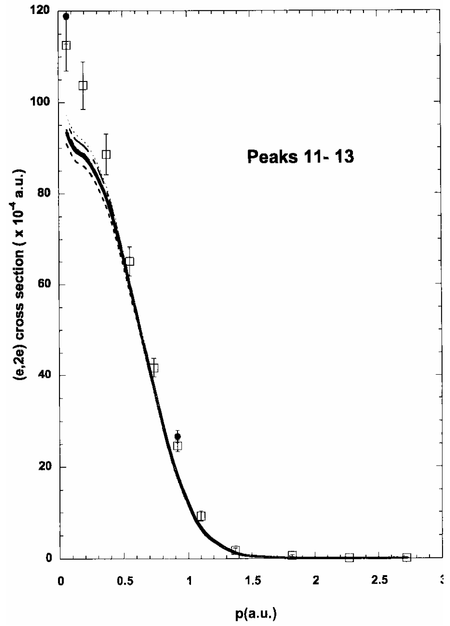

Figure 7 (a). 1500 eV symmetric noncoplanar MD for peaks 11-13 in the ionization spectrum of norbornane. The legend is the same as that for Figure 3.

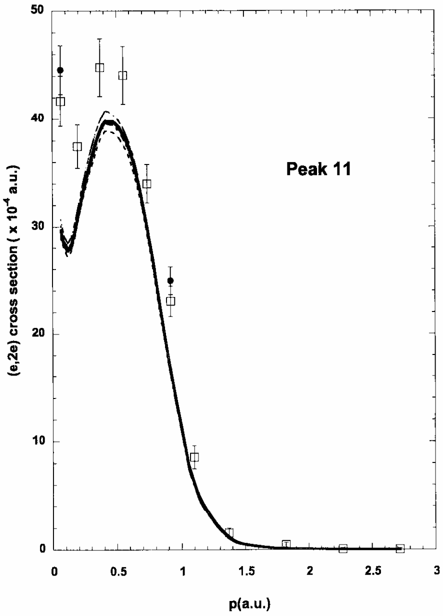

Figure 7 (b). 1500 eV symmetric noncoplanar MD for the shake-up band 11 and the $2a_1+1b_1+1b_2$ orbitals of norbornane. The legend is the same as that of Figure 3.

It is possible that peak 12 partly originates from the $2a_1$ orbital with some additional $1b_1$ and $1b_2$ contributions. Such a scenario is allowed by our ADC(3)/cc-pVDZ results (Table III) which suggest that up to 23.5 %, 30.3 % and 27.5 % of the $2a_1$, $1b_1$ and $1b_2$ fluxes might reside under peak 12, respectively, in the form of long correlation tails [52] consisting of shake-up lines with a spectroscopic strength smaller than 0.005. However, even upon admitting that this missing fraction of the $2a_1$ shake-up intensity would be entirely recovered under peak 12, it would still be far too small to explain the intensity of this peak in the spectrum recorded at the azimuthal angle $\phi = 0°$, relative to that of band 11 [Figure 1a]. This, the fact that the 1p-GF/ADC(3) and density functional theories of ionization and (e,2e) cross sections provide very consistent insights into the shape, energy location and into the momentum distributions characterising the neighboring peaks 11 and 13, and the vast experience accumulated over the last 25 years with 1p-GF calculations of the shake-up transitions of saturated hydrocarbons [51-53] and many other molecules (see for instance [40, 42, 55-57] and references therein), lead us to believe that band 12 does not belong to the vertical one-electron and 2h-1p shake-up ionization spectrum of norbornane in its ground electronic state, as described by the ADC(3) model of ionization. A band - Lanczos study of the correlation tails in the ionization spectrum of NBA is, however, necessary to fully confirm this assertion.

Finally, we note that there are still quite a few orbital MDs that we have not specifically discussed or plotted in this section. These MDs reinforce the argument for the utility of BP/TZVP that we have made in this section, but do not add any further insight.

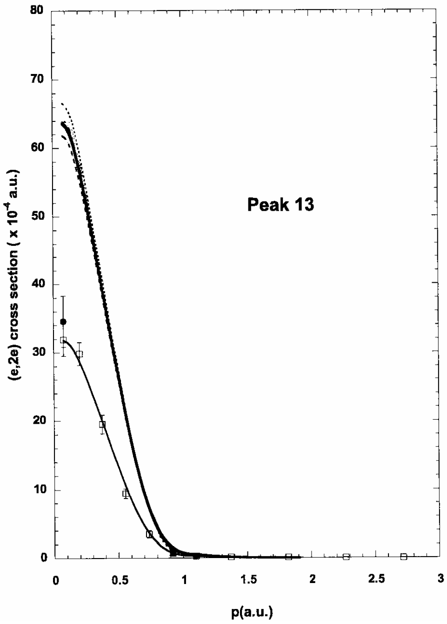

Figure 8. 1500 eV symmetric noncoplanar MD for the shake-up band 13 and the $1a_1$ orbital of norbornane. The legend is the same as that of Figure 3, except 0.5* BP/TZVP (–) is also shown.

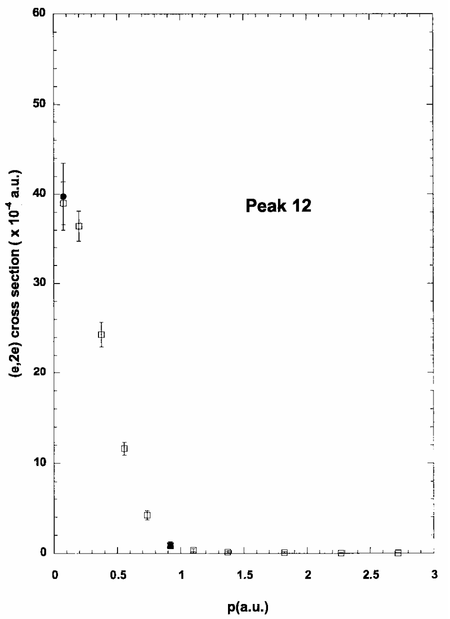

Figure 9. 1500 eV symmetric noncoplanar MD for band 12 of the EMS binding energy spectra. The present data for run A (•) and run B (□) are shown.

3.1.6 Molecular property information

We now use the BP/TZVP model which best described the experimental MDs to derive the structure and a selection of the molecular properties of norbornane. These are compared in detail with independent experimentally determined values and those from other MO calculations, to determine how well the BP/TZVP model was able to reproduce these molecular properties.

A. Molecular geometries

In general, our calculations of molecular geometries using the BP/TZVP model are in very good agreement with experimentally determined molecular geometries (given the experimental uncertainties), and compare favorably with the results from other MO calculations. The results are summarized in Table IV. Note that in Table IV we have also included relevant data from our B3LYP/cc-pVTZ and MP2/aug-cc-pVDZ calculations. While these basis sets were not prevalidated using our EMS MDs, we have included them for completeness and in general their results appear to compare well with those from BP/TZVP. Further note that to assist the reader in the discussion that follows, a structural representation and atom numbering of the norbornane molecule is given in Figure 10.

TABLE IV. Experimental and theoretical molecular geometry and dipole moment of norbornane.

Parameter	ED Doms *et al.* (Ref. 6)	x-ray Fitch and Jobic (Ref. 5)	BP/TZVP This work	HF/STO-3G Castro *et al.* (Ref. 58)	HF/3-21G Castro *et al.* (Ref. 58)	HF/4-21G Castro *et al.* (Ref. 58)	HF/4-31G Castro *et al.* (Ref. 58)	MNDO Walklmar *et al.* (Ref. 8)	B3LYP/cc-pVTZ This work	MP2/aug-cc-pVDZ This work
r(C1-C2) (Å)	1.536(15)	1.548	1.549	1.550	1.550	1.551	1.545	1.561	1.543	1.547
r(C1-C7) (Å)	1.546(24)	1.551	1.548	1.544	1.549	1.549	1.544	1.562	1.540	1.546
r(C2-C3) (Å)	1.573(15)	1.578	1.571	1.669	1.571	1.572	1.560	1.558	1.562	1.568
r(C1-H) (Å)	1.113(3)	1.091	1.101	1.087	1.083	1.079	1.084	1.102	1.089	1.101
r(C2-H) (Å)	1.113(3)	1.086, 1.090	1.102	1.087	1.083	1.082	1.084	1.109	1.091	1.102
r(C7-H) (Å)	1.113(3)	1.090	1.102	1.087	1.083	1.082	1.084	1.106	1.091	1.103
∠C1C2C3 (deg)	102.7	106.9	103.11	103.2	103.2	103.1	103.2	103.04	103.08	103.1
∠C1C7C4 (deg)	93.4(1)	93.12	94.52	94.4	94.6	94.6	94.4	93.07	94.42	94.5
∠C2C1C6 (deg)	109.0	110.41	108.82	108.3	107.7	108.0	108.3	109.35	108.47	108.22
∠C2C1C7 (deg)	102.0(1)	99.3	101.35	101.6	101.6	101.6	101.5	101.57	101.54	101.54
∠C7C1H (deg)			116.02	116.4	116.3	116.2	116.3		116.17	116.11
∠HC3H (deg)	107.2	107.64	109.15	112.0, 112.3	110.7, 112.3	110.8, 112.3	110.8, 112.1	106.10	107.33	107.71
∠HC7H′ (deg)	107.2, 110	106.97	109.05	109.4	109.9	109.7	108.9		108.95	109.43
d(C2⋯C6) (Å)		2.542	2.520						2.504	2.506
μ (D)	0.091(8) MW[a] Choplin (Ref. 3)		0.076						0.089	0.085

[a] MW stands for microwave.

The two single bonds (C_2-C_3 and C_5-C_6) involving the four methylene carbon-carbon have bond distances of 1.571 Å from our calculations in excellent agreement with the two experimental values of 1.573 Å from an electron diffraction study [4, 6], and 1.578 Å from Fitch and Jobic's powder x-ray diffraction study [5]. The remaining carbon-carbon bonds involving the bridge or bridgehead carbon atoms are also in excellent agreement with experiment. The agreement with experiment is better than for the small basis set *ab initio* and semiempirical MO-derived geometries in Table IV [8, 58]. The distance between the two single bonds involving the four methylene carbon atoms (C_2-C_3 and C_5-C_6) was particularly well reproduced with the $C_2 \cdots C_6$ distance from BP/TZVP of 2.520 Å compared with the experimental distance of 2.542 Å from powder x-ray diffraction studies.

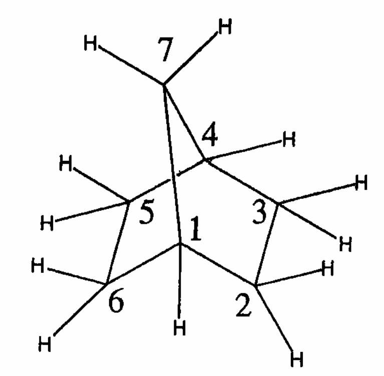

Figure 10. Structural representation of norbornane and the atom numbering.

Bond angles were also well reproduced, especially the bridge and bridgehead angles. The bridge angle (e.g. $\angle C_1C_7C_4$) of 94.5° from our DFT calculations compares well with 93.1° from the x-ray structure and 93.4° from electron diffraction. The bridgehead angles (e.g. $\angle C_2C_1C_7$) were calculated to be 101.4° by our DFT calculation, compared with 102.0° from electron diffraction studies, and 99.3° from the x-ray diffraction studies. There was some evidence of lattice perturbations in the x-ray structure when compared with the electron diffraction structure and the structures predicted by MO methods, as illustrated in Table IV. For example the bridgehead bond angle $\angle C_2C_1C_6$ is substantially larger in the x-ray structure than in the other experimental and theoretical structures, as is the angle $\angle C_1C_2C_3$, which is approximately 4° larger than in the other structures.

B. Dipole moment

Like all saturated hydrocarbons, norbornane has a small dipole moment which has been well reproduced by our BP/TZVP DFT calculations. We obtain a value of 0.076 D from our calculations compared with a very accurate value of 0.091(8)D inferred from the Stark effect in the microwave spectrum of norbornane [3]. Wilcox and colleagues had earlier estimated the dipole moment as 0.03(2) from dielectric measurements [59], which appears to be too low.

C. NMR properties

There have been many measurements of the chemical shifts [60-62] of carbon and protons in norbornane, examples of which are the work of Abraham and coworkers [60] and Lippmaa *et al.* [61]. We used the localized orbital/local origin (LORG) [63], individual gauge localized orbitals (IGLO) [64] and gauge-independent atomic orbital (GIAO) methods [65] to calculate ^{13}C chemical shifts from our BP/TZVP calculations. Chemical shifts were determined by comparisons with the ^{1}H and ^{13}C isotropic shifts computed for tetramethylsilane at the BP/TZVP level. Our chemical shift values are compared in Tables V and VI with those determined by Sauers [66] from a GIAO calculation using Hartree-Fock theory. As in many previous computations of NMR chemical shifts (see [67] and references therein), these HF results systematically underestimate the experimental values whereas the opposite is seen with our BP/TZVP results.

TABLE V. ^{13}C NMR chemical shifts (in ppm).

Carbon	Experimental	BP/TZVP LORG	BP/TZVP IGLO	HF/6-31+G* GIAO (Ref. 66)	BP/TZVP GIAO[a]
1	36.8	46.5	47.8	33.2	43.0
2	30.1	35.0	36.3	27.4	34.6
3	30.1	35.0	36.3	27.4	34.6
7	38.7	43.5	45.2	34.4	41.9
6	30.1	35.0	36.3	27.4	34.6
5	30.1	35.0	36.3	27.4	34.6
4	36.8	46.5	47.8	33.2	43.0

[a] Results obtained using a B3LYP/6-31G* geometry.

TABLE VI. ^{1}H NMR chemical shifts (in ppm).

Proton	Experimental	BP/TZVP LORG	BP/TZVP IGLO	HF/6-31+G* GIAO (Ref. 66)	BP/TZVP GIAO[a]
1	2.19	2.36	4.56	1.91	2.28
2	1.16	1.27	3.32	1.12[b]	1.28
2′	1.47	1.49	3.68	1.37[b]	1.62
3	1.16	1.27	3.32	1.12[b]	1.28
3′	1.47	1.49	3.68	1.37[b]	1.62
4	2.19	2.36	4.56	1.92[b]	2.28
5	1.16	1.27	3.32	1.12[b]	1.28
5′	1.47	1.49	3.68	1.37[b]	1.62
6	1.16	1.27	3.32	1.12[b]	1.28
6′	1.47	1.49	3.68	1.37[b]	1.62
7	1.18	1.23	3.08	1.13	1.25

[a] Results obtained using a B3LYP/6-31G* geometry.
[b] This work.

The LORG method produced better agreement with the experimental ^{1}H and ^{13}C chemical shifts than the IGLO method, particularly for the proton spectrum. However, it appears that when a correlated wavefunction is used the GIAO approach provides the best agreement with experiment. At this level, the chemical shifts for carbon predicted by our DFT calculations are overall in good agreement with the experimental shifts, although the bridgehead (methine) carbons had a larger error (~ 7 ppm) than the other (methylene) carbons (error ~ 3 ppm). The proton chemical shifts were in excellent agreement with experiment with an average error of 0.09 ppm. Put another way, at the GIAO level the BP/TZVP approach yields overestimates of between 4 to 10 %, in the experimental proton shifts.

The well-known differences in the chemical shifts between the *endo* and *exo* protons in norbornane are very nicely reproduced by our BP/TZVP calculations. At this level, and using the GIAO approach, we calculate a difference of 0.34 ppm compared with the experimental difference of 0.31 ppm.

TABLE VII. Infrared vibrational frequencies and intensities.

Symmetry label	Mode	BP/TZVP spectrum		Experimental spectrum [Levin and Harris (Ref. 70)]		
		TZVP (cm^{-1})	Intensity (km mol^{-1})	Frequency (cm^{-1})	Intensity	Assignment
a_2	7	164.82	0.0			
b_2	8	332.85	0.2	344	*w*	$\upsilon 26,\upsilon 39,\upsilon 51$
a_1	9	392.74	0.0	407	*w*	$\upsilon 15$
b_1	10	437.64	0.0	485	*w*	$\upsilon 35$
a_2	11	532.85	0.0	542	*vw*	$\upsilon 14$
a_1	12	738.32	0.8	755	*s*	$\upsilon 13,\upsilon 99$
b_2	13	744.02	0.1			
b_1	14	776.35	0.4	787	*ms*	$\upsilon 24,\upsilon 37$
a_1	15	797.49	0.0			
b_2	16	804.12	2.7	814	*s*	
a_1	17	857.80	1.4	874	*s*	$\upsilon 13$
b_1	18	873.00	1.3	889	*s*	$\upsilon 48$
a_1	19	908.14	1.6	925	*s*	$\upsilon 11$
a_2	20	926.69	0.0			
b_1	21	927.12	0.5	949	*m*	$\upsilon 36,\upsilon 47$
a_2	22	937.65	0.0			
b_2	23	937.94	0.6	958	*w*	$\upsilon 23$
a_1	24	973.06	0.1	990	*w*	$\upsilon 10$
b_1	25	1004.32	0.4	1031	*m*	$\upsilon 35,\upsilon 46$
b_2	26	1054.78	0.2	1069	*w*	$\upsilon 31$
b_1	27	1092.25	0.1	1091	*w*	$\upsilon 22$
a_2	28	1103.68	0.0	1103	*w*	$\upsilon 34$
a_1	29	1125.17	1.0	1120	*m*	$\upsilon 9$
b_2	30	1136.82	0.3	1140	*m*	$\upsilon 33$
b_1	31	1186.00	3.2	1160	*w*	
a_2	32	1195.51	0.0	1207	*m*	$\upsilon 8,\upsilon 45$
b_2	33	1225.65	1.2	1217	*mw*	$\upsilon 30$
a_1	34	1236.83	1.0	1242	*w*	$\upsilon 32$
b_2	35	1242.20	0.0	1259	*mw*	$\upsilon 7$
a_2	36	1253.65	0.0			
a_2	37	1276.66	0.0			
a_1	38	1293.44	1.8	1274	*w*	
b_2	39	1293.70	2.6	1301	*m*	$\upsilon 44$
b_1	40	1297.16	0.0	1317	*m*	$\upsilon 19$
a_2	41	1433.85	0.0	1400	*w*	$\upsilon 31$
a_1	42	1439.98	7.3			
b_2	43	1446.88	2.1	1442	*m*	$\upsilon 18$
b_1	44	1452.03	5.9	1455	*s*	$\upsilon 6,\upsilon 30,\upsilon 43$
a_1	45	1475.76	0.5	1465		$\upsilon 5$
b_2	46	2962.27	59.9			
a_2	47	2963.18	0.0			
a_1	48	2964.46	51.4			
b_1	49	2973.15	95.4			
a_1	50	2973.44	15.6			
a_2	51	2996.72	0.0			
b_2	52	2998.48	10.8			
b_1	53	3012.16	91.4	2866	*m*	
b_2	54	3012.82	4.2	2912	*m*	
a_1	55	3016.85	1.9	2928	*m*	
b_1	56	3017.78	62.8	2954	*vs*	
a_1	57	3022.19	94.0	2964	*vs*	

D. Vibrational spectra

The DFT calculations were able to calculate the frequencies of the vibrational modes of norbornane with reasonable accuracy. Table VII shows the vibrational frequencies calculated at the BP/TZVP level in the present work. The calculated intensities of the transitions are also in reasonable agreement with the observed [68] experimental IR spectrum of norbornane, as Table VII also illustrates. The level of agreement between our (unscaled) BP/TZVP frequencies and experiment is similar to that of the work of Shaw *et al.* [69], who studied the norbornane infrared spectrum using a rescaled HF/3-21G *ab initio* force field. The assignment of the norbornane vibrational modes follows from the work of Levin and Harris [70]. For completeness we note that according to the dipole selection rules for IR spectroscopy, transitions from the zero-point level to the excited vibrational levels belonging to the a_2 irreducible representation of the C_{2v} point group are forbidden by symmetry [71]. One of these transitions is nonetheless detected in the IR spectrum of norbornane, in the form of an extremely weak line at 542 cm^{-1}. This line must thus be described as a hot band.

3.1.7 Conclusions

We have reported on the first comprehensive EMS study into the complete valence electronic structure of norbornane, in conjunction with DFT calculations of orbital MDs, and 1p-GF [OVGF and ADC(3)] calculations of the one-electron and shake-up ionization spectrum. Excellent agreement is generally found between the experimental PES and EMS binding energies, on the one hand, and the 1p-GF results, on the other hand. Where a comparison is possible, pole strengths calculated by our 1p-GF procedures, certainly for the outer valence orbitals, were found to be largely consistent with those determined from our EMS MD data. Strong final state configuration interaction effects are predicted in our ADC(3) calculation for the inner valence $2a_1$, $1b_2$, $1b_1$ and $1a_1$ orbitals, and this prediction is consistent with the very significant band broadening observed at binding energies beyond ~ 22 eV. A striking discrepancy between one-particle Greens Function theory and experiment has been noted, however. It takes the form of a very intense band at ~ 25 eV in the EMS spectrum recorded at an azimuthal angle $\phi = 0°$, which could not be reproduced by the large scale ADC(3) calculations presented in this work. According to the related momentum distribution, this band has apparently "*s*-type" symmetry. Further theoretical studies will be needed to establish whether it relates, for instance, to shake-up transitions to particularly diffuse bound states, to double ionization processes, or to autoionization via electronically excited and dissociating states [72]. The latter suggestion is in particular worthy of consideration, in light of the extent of the cyclic strains in a compound like norbornane. On the experimental side, further He(II), Penning ionization and XPS studies of the innermost valence levels of norbornane are also clearly necessary.

Momentum distributions for the $3a_2 + 5b_2$, $7a_1$, $5b_1 + 6a_1$, $4b_2 + 2a_2 + 4b_1$, $3b_2 + 3b_1$, $5a_1 + 2b_1$, $4a_1$, $2b_2$, $3a_1$, $1a_2$, $2a_1 + 1b_2 + 1b_1$ and $1a_1$ orbitals were measured and compared against a series of PWIA-based calculations using DFT DGauss basis sets. Our calculations, for each of the three basis sets (DZVP, DZVP2, TZVP), were performed using both BP and BLYP exchange correlation corrections to the DFT functional. On the basis of this comparison between the experimental and theoretical MDs, we found that BP/TZVP provided the most physically reasonable representation of the NBA wave function. Molecular property information derived from this "optimum" BP/TZVP wave function was seen to be in generally good agreement with the results from independent measurements. This provides compelling evidence for the pedigree of EMS in *a priori* evaluation of a quantum chemical wave function. For a molecule such as NBA, where unambiguous molecular geometry information is not readily available from traditional methods, this can be particularly useful.

Finally, the present work highlights the need for implementing more efficient diagonalization approaches, that preserve the total spectral moments, for exhaustively studying, with larger basis sets, the innermost correlation tails in the 1p-GF/ADC(3) ionization spectra. Also, we note that an improvement in the (e,2e) reaction mechanism description, particularly for the inner valence and core orbitals, by the development of a distorted wave framework [9] for multicentred targets (i.e. molecules) is still desirable. While this is a very difficult task, a clear need for its implementation exists.

References

[1] Zhao, C.-Y.; Zhang, Y.; You, X.-Z. *J. Phys. Chem. A* 1997, 101, 5174.

[2] Morino, Y.; Kutchitsu, K.; Yokozeki, A. *Bull Chem Soc Jpn* 1967, 40, 1552.

[3] Choplin, A *Chem Phys Letts* 1980, 71, 503.

[4] Chiang, J. F.; Wilcox, C. F.; Bauer, S. H. *J Am Chem Soc* 1968, 90, 3149.

[5] Fitch, A. N.; Jobic, H. *J Chem Soc Chem Commun* 1993, 1516.

[6] Doms, L.; van den Enden, L.; Geise, H. J.; van Alsenoy, C. *J. Am. Chem. Soc.* 1983, 105, 158.

[7] Allinger, N. L.; Geise, H. J.; Pyckhout, W.; Paquette, L. A.; Gallucci, J. C. *J Am Chem Soc* 1989, 111, 1106.

[8] Walkimar, J.; Carneiro, J. W.; Seidl, P. R.; Tostes, G. R.; Taft, C. A. *J. Mol. Struct. (Theochem)* 1987, 152, 281.

[9] Weigold, E.; McCarthy, I. E. *Electron Momentum Spectroscopy*; Kluwer Academic/Plenum Publishers: New York, 1999.

[10] Brunger, M. J.; Adcock, W. *J. Chem. Soc., Perkin Trans 2*, 2002, 1.

[11] Bischof, P.; Hashmall, J. A.; Heilbronner, E.; Harnung, V. *Helv Chim Acta* 1969, 52, 1745.

[12] Getzlaff, M.; Schönhense, G. *J. Electron Spectrosc. Relat. Phen.* 1998, 95, 225.

[13] Bieri, G; Burger, F.; Heilbronner, E.; Maier, J. P. *Helv. Chim. Acta* 1977, 60, 2213.

[14] Bodor, N.; Dewar, M. J. S.; Worley, S. D. *J Am Chem Soc* 1970, 92, 19.

[15] Mackenzie-Ross, H.; Brunger, M. J.; Wang, F.; Adcock, W.; Trout, N.; McCarthy, I. E.; Winkler, D. A. *J. Electron Spectrosc. Relat. Phen.* 2002, 123, 389.

[16] Mackenzie-Ross, H.; Brunger, M. J.; Wang, F.; Adcock, W.; Maddern, T.; Campbell, L.; Newell, W. R.; McCarthy, I. E.; Weigold, E.; Appelbe, B.; Winkler, D. A. *J. Phys. Chem. A* 2002, 106, 9573.

[17] Wang, F.; Brunger, M. J.; Winkler, D. A. *J. Phys. Chem. Sol.*, 2004, 65, 2041.

[18] Bicker, R.; Kessler, H.; Zimmermann, G. *Chem. Ber.* 1978, 111, 3200.

[19] McCarthy, I. E.; Weigold, E. *Rep. Prog. Phys.* 1991, 54, 789.

[20] Bevington, P. R.; Robinson, D. K. *Data Reduction and Error Analysis for the Physical Sciences*; McGraw-Hill Inc: New York, 1990.

[21] McCarthy, I. E.; Weigold, E. *Rep. Prog. Phys.* 1988, 51, 299.

[22] Casida, M. *Phys. Rev. A* 1995, 51, 2005.

[23] Kohn, W.; Sham, L. J. *Phys. Rev.* 1965, 140, A1133.

[24] Becke, A. D. *Phys Rev A* 1988, 38, 3098.

[25] Becke, A. D. *J. Chem. Phys.* 1988, 88, 2547.

[26] Perdew, J. P. *Phys. Rev. B* 1986, 33, 8822.

[27] Lee, C.; Yang, W.; Parr, R. G. *Phys Rev B* 1988, 37, 785.

[28] Andzelm, J.; Wimmer, E. *J. Chem. Phys.* 1992, 96, 1290.

[29] Komornicki, A.; Fitzgerald, G. J. *J. Chem. Phys.* 1993, 98, 1398.

[30] Michalewicz, M. T.; Brunger, M. J.; McCarthy, I. E.; Norling, V. M. *CRAY Users Group 1995 Fall Proceedings*; Shaginaw, R., Ed.; 1995; pp 37-41.

[31] Schmidt, M. W.; Baldridge, K. K.; Boatz, J. A.; Elbert, S. T.; Gordon, M. S.; Jensen, J. J.; Koseki, S.; Matsunaga, N.; Nguyen, K. A.; Su, S.; Windus, T. L.; Dupuis, M.; Montgomery, J. A. *J. Comput. Chem.* 1993, 14, 1347.

[32] Hamel, S.; Duffy, P.; Casida, M.; Salahub, D. R. *J. Electron Spectrosc. Relat. Phenom.* 2002, 123, 345.

[33] Frost, L.; Weigold, E. *J. Phys. B* 1982, 15, 2531.

[34] Adcock, W.; Brunger, M. J.; Clark, C. I.; McCarthy, I. E.; Michalewicz, M. T.; von Niessen, W.; Weigold, E.; Winkler, D. A. *J. Am. Chem. Soc.* 1997, 119, 2896.

[35] Adcock, W.; Brunger, M. J.; McCarthy, I. E.; Michalewicz, M. T.; von Niessen, W.; Wang, F.; Weigold, E. *J. Am. Chem. Soc.* 2000, 122, 3892.

[36] Godbout, N.; Salahub, D. R.; Andzelm, J.; Wimmer, E. *Can. J. Chem.* 1992, 70, 560.

[37] Dunlap, B. I.; Conolly, J. W. D.; Sabin, J. R. *J. Chem. Phys.* 1979, 71, 4993.

[38] Becke, A. D. *J. Chem. Phys.* 1993, 98, 5648.

[39] Schirmer, J.; Cederbaum, L. S.; Walter, O. *Phys. Rev. A* 1983, 28, 1237.

[40] von Niessen, W.; Schirmer, J.; Cederbaum, L. S. *Comput. Phys. Rep.* 1984, 1, 57.

[41] Schirmer, J.; Angonoa, G. *J. Chem. Phys.* 1989, 91, 1754.

[42] Weikert, H.-G.; Meyer, H.-D.; Cederbaum, L. S.; Tarantelli, F. *J. Chem. Phys.* 1996, 104, 7122.

[43] Dunning, T. H., Jr. *J. Chem. Phys.* 1989, 90, 1007.

[44] Deleuze, M. S. *Int. J. Quantum. Chem.* 2003, 93, 191.

[45] Tarantelli, F.; Sgamellotti, A.; Cederbaum, L. S.; Schirmer, J. *J. Chem. Phys.* 1987, 86, 2201.

[46] Cederbaum, L. S.; Domcke, W. *Adv. Chem. Phys.* 1977, 36, 205.

[47] Zakrewski, V. G.; von Niessen, W. *J. Comput. Chem.* 1993, 14, 13.

[48] Frisch, M. J.; Trucks, G. W.; Schlegel, H. B., *et al. GAUSSIAN 98* (Revision A.7); Gaussian, Inc., Pittsburgh, PA, 1998.

[49] Kendall, R. A.; Dunning, T. H., Jr; Harrison, R. J. *J. Chem. Phys.* 1992, 96, 6796.

[50] Deleuze, M. S.; Delhalle, J.; Pickup, B. T.; Svensson, S. *J. Am. Chem. Soc.* 1994, 116, 10715.

[51] Deleuze, M. S.; Cederbaum, L. S. *J. Chem. Phys.* 1996, 105, 7583.

[52] Golod, A.; Deleuze, M. S.; Cederbaum, L. S. *J. Chem. Phys.* 1999, 110, 6014.

[53] Deleuze, M. S.; Pang, W. N.; Salam, A.; Shang, R. C. *J. Am. Chem. Soc*. 2001, 123, 4049.

[54] Zheng, Y.; Pang, W N; Shang, R. C.; Chen, X. J., Brion, C. E.; Ghanty, T. K.; Davidson, E. R. *J. Chem. Phys.* 1999, 111, 9526.

[55] Deleuze, M. S. *J. Chem. Phys*. 2002, 116, 7012.

[56] Cederbaum, L. S.; Domcke, W.; Schirmer, J.; von Niessen, W. *Adv. Chem. Phys*. 1986, 65, 115.

[57] Deleuze, M. S.; Trofimov, A. B.; Cederbaum, L. S. *J. Chem. Phys*. 2001, 115, 5859.

[58] Castro, C. R.; Dutler, R.; Rauk, A.; Wieser, H. *J. Mol. Struct. (THEOCHEM)* 1987, 152, 241.

[59] Wilcox, C. F.; Zajacek, J. G.; Wilcox, M. F. *J. Org. Chem*. 1965, 30, 2621.

[60] Abraham, R. J.; Fisher, J. *THEOCHEM* 1985, 25, 25.

[61] Lippmaa, E.; Bobyleva, A. A.; Kalinichenko, A. N.; Ordubadi, M. D.; Platé, A F. *Org. Magn. Res.* 1976, 8, 74.

[62] Seidl, P. R.; Leal, K. Z.; Costa, V. E. J.; Poli, N. D. *Magn. Res. Chem.* 1990, 28, 869.

[63] Kutzelnigg, W. *Isr. J. Chem.* 1980, 19, 193.

[64] Malkin, V. G.; Malkina, O. L.; Salahub, D. R. *Chem. Phys. Lett.* 1993, 204, 80.

[65] Wolinski, K.; Hilton, J. F.; Pulay, P. *J. Am. Chem. Soc*. 1990, 112, 8251.

[66] Sauers, R. R. *Tetrahedron* 1998, 54, 337.

[67] Chestnut, D. B. in *Reviews in Computational Chemistry Vol 8*; Lipkowitz, K. B.; Boyd, D. B., Eds; VCH: New York, 1996; pp 245-297.

[68] NIST Chemistry WebBook (see http://webbook.nist.gov/chemistry).

[69] Shaw, R. A.; Castro, C. R.; Dutler, R.; Rauk, A.; Weiser, H. *J. Chem. Phys.* 1988, 89, 716.

[70] Levin, I. W.; Harris, W. C. *Spectrochim. Acta* 1973, Part A 29, 1815.

[71] Herzberg, G. *Infrared and Raman Spectra*; van Nostrand Reinhold Company: New York, 1945.

[72] Kishimoto, N.; Matsumara, E.; Ohno, K.; Deleuze, M. S. *J. Chem. Phys*. 2004, 121, 3074.

3.2 The band 12 issue in the electron momentum spectra of norbornane: a comparison with additional Green's function calculations and ultraviolet photoemission measurements.

3.2.1 Introduction

Norbornane (C_7H_{12}, C_{2v}-symmetry) is known to be an important compound in pharmaceutical research – it is useful in the therapy of cardiac infarcts or apoplectic fits [1] as well as asthma, bronchitis and thromboses. Its outer-valence electronic structure has been early (1969) studied by Bishof *et al.* [2] and, more recently (1998), by Getzlaff and Schönhense [3], using Ultra-violet [He(I)] Photoemission Spectroscopy (Figure 1a). Bieri *et al.* also investigated the inner valence ionization bands of this compound, up to binding energies of ~24 eV, by means of an He(II) photon beam [4] (Figure 1b).

Of primary relevance to the present work is a recent theoretical study [5] of the ionization spectrum of norbornane, within the framework of one-particle Green's Function theory (1p-GF) [6,7] and resorting to the so-called third-order algebraic diagrammatic construction scheme [ADC(3)] [8-12] as well as Dunning's correlation-consistent polarized valence basis set of double-zeta quality [cc-pVDZ] [13]. These ADC(3)/cc-pVDZ calculations were performed in support to an EMS (Electron Momentum Spectroscopy [14]) study of the ionization spectrum of this compound, at electron impact energies of 1.5 keV, and down to binding energies of 29 eV (Figure 1c,d). This is much beyond the shake-up and double ionization thresholds, which theory locates at ~22 and ~26 eV, respectively [5].

The agreement between the theoretical and experimentally available [He(I), He(II), EMS] ionization spectra was within the usual expectations, with discrepancies on binding energies which most generally do not exceed ~0.2 eV, except for the $1a_2^{-1}$ ionization line at ~20 eV. The 1p-GF calculations overestimate the experimentally apparent ionization potential for this line by ~0.6 eV, which presumably reflects particularly strong geometrical relaxation effects as well as vibronic interactions. The most striking disagreement noted between theory and experiment is a strongly protruding band at ~25 eV in the EMS spectrum recorded at an azimuthal angle of 0°, which the ADC(3) calculations completely failed to reproduce: the ADC(3)/cc-pVDZ spectrum of norbornane does not show any dense enough set of shake-up lines that could explain the band (12) seen around 25 eV in this EMS spectrum (Figure 1d).

This failure is extremely puzzling, considering the prevalence and successes of the ADC(3) approach in studies of ionization spectra of all kind [see refs. 10, 12, 15, 16 and references therein]. This, and the fact that the momentum profiles inferred for all other bands from the angular dependence of the (e,2e) ionization intensities of norbornane are entirely consistent with the ADC(3) assignment [5], led us to tentatively conclude [5] that this band at ~25 eV does not belong to the vertical one-electron and shake-up ionization spectrum of this compound and could relate to transitions to diffuse (Rydberg-like) electronically excited states of the cation or to auto-ionization processes. The purpose of the present work is to verify the first of these assumptions by studying the basis set dependence of the ADC(3) ionization spectrum and by comparing these new computations with further He(II) measurements extended up to binding energies of 40 eV.

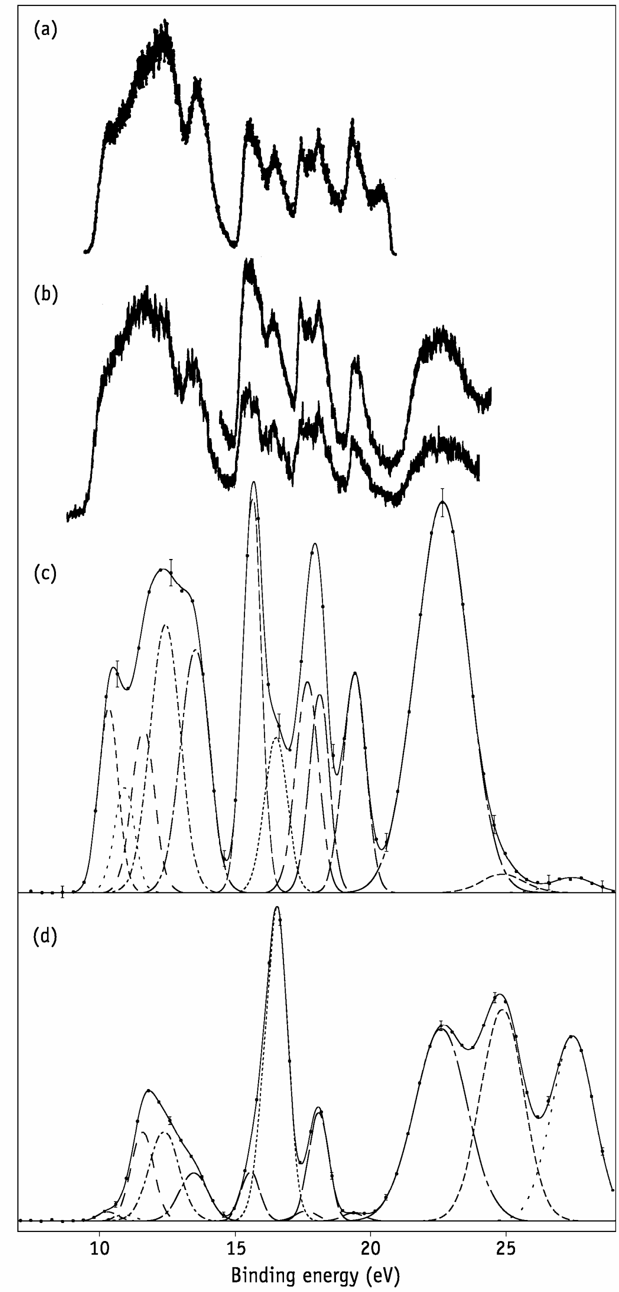

Figure 1. Experimental ionization spectra of norbornane obtained using (a) He(I) [3] and (b) He (II) [4] ultra-violet photoemission spectroscopy, or Electron Momentum Spectroscopy at azimuthal angles of (c) $\varphi = 10°$ and (d) $\varphi = 0°$, respectively (adapted from [5]).

3.2.2 Computations

The ADC(3) calculations, presented in [5], and which were carried out with a cc-pVDZ basis set incorporating on total 165 contracted atomic functions, have been in the present work supplemented by calculations of the vertical ionization spectrum of norbornane performed using the standard 6-31G basis set [17], as well as Dunning's DZP+ basis set [namely, a double zeta basis set with polarization and diffuse functions] [18]. The latter two basis sets include 87 and 205 basis functions, respectively. As in [5], the original code interfaced to the GAMESS package of programs [19] has been employed to complete these 1p-GF calculations. At the SCF level, the requested convergence on each of the elements of the density matrix were fixed to 10^{-10}. With the 1p-GF/ADC(3) approach, the one-hole (1*h*) and shake-up two-hole-one-particle (2*h*-1*p*) ionization energies are recovered through third- and first-order in correlation, respectively, which implies accuracies of ~0.2 [20] and ~0.6 eV, respectively with a basis set approaching completeness. Constant self-energy diagrams have been computed through fourth-order in correlation, using charge-consistent [21] one-electron densities. The spectra have been calculated up to binding energies of 29 eV, retaining all eigenvalues of the ADC(3) secular matrix with a pole strength equal or larger than 0.005. This matrix has been diagonalized using the Block-Davidson diagonalization procedure [22, 23] in the final diagonalization step [12].

The assumption of frozen core electrons has been used throughout and symmetry has been exploited to the extent of the largest abelian subgroup of the full molecular symmetry point group. All ADC(3) calculations discussed in the present study are based on molecular geometries that have been optimized by means of the GAUSSIAN98 [24] quantum chemistry package, using Dunning's basis set of triple zeta quality [25] with polarized valence functions (TZVP), Density Functional Theory (DFT) in conjunction with the non-local hybrid and gradient corrected Becke three-parameter Lee-Yang-Parr functional (B3LYP) [26, 27], an approach which is known to deliver excellent results for equilibrium geometries and related properties (such as vibrational frequenties) [28].

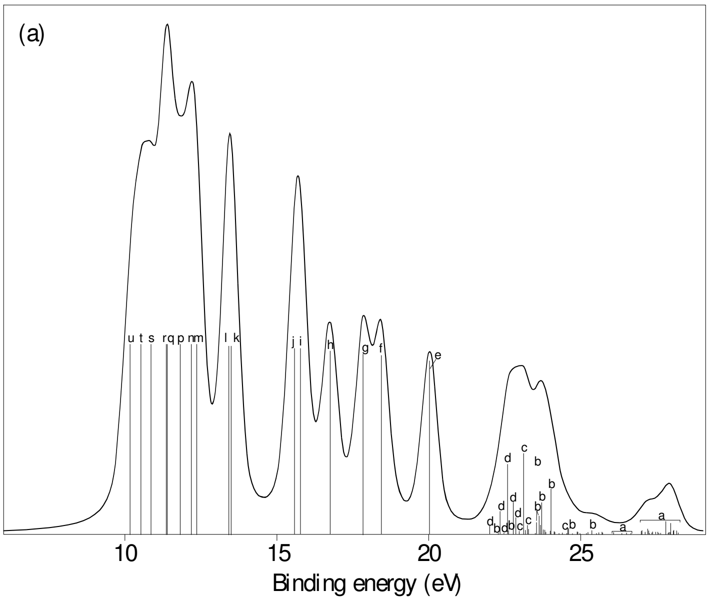

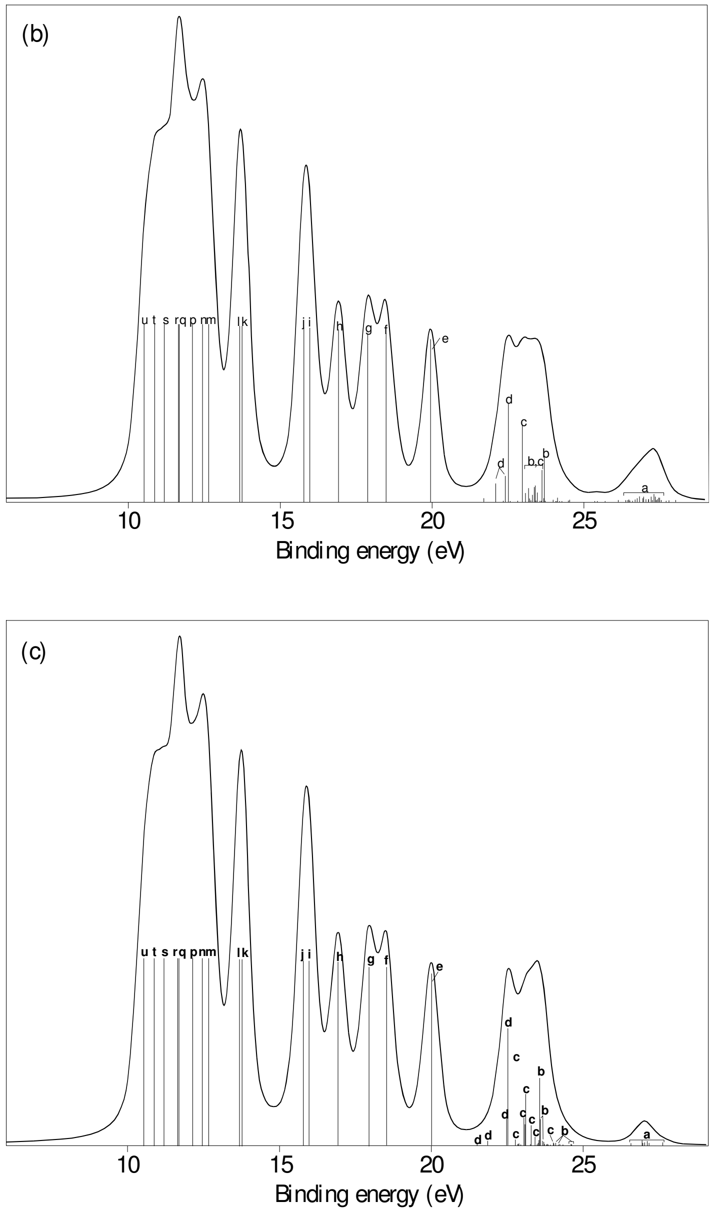

Figure 2. Theoretical ADC(3) ionization spectra of norbornane obtained using the (a) 6-31G, (b) cc-pVDZ and (c) Dunning's DZP+ basis sets. The orbital labels are given as follows: *u*: $3a_2$; *t*: $5b_2$; *s*: $7a_1$; *r*: $5b_1$; *q*: $6a_1$; *p*: $4b_2$; *n*: $2a_2$; *m*: $4b_1$; *l*: $3b_2$; *k:* $3b_1$; *j*: $5a_1$; *i*: $2b_1$; *h*: $4a_1$; *g*: $2b_2$; *f*: $3a_1$; *e:* $1a_2$; *d*: $2a_1$; *c*: $1b_2$; *b*: $1b_1$; *a*: $1a_1$.

As a guide to the eye, the identified solutions of the secular ADC(3) eigenvalue problems are displayed in Figure 2 as spike spectra and in the form of convoluted densities of states. The convolution has been performed using as a spread function a combination of a Gaussian and a Lorenzian with equal weight with an FWHM parameter of 0.6 eV and by simply scaling the line intensities according to the computed ADC(3) pole strength, neglecting thereby the varying influence of molecular orbital cross sections.

3.2.3 Experiment

Norbornane was purchased from Aldrich. Initial purification of the crude material was performed *in vacuo* to remove any volatile contaminations. Subsequently, the norbornane sample was subjected to sublimation in a Kugelrohr distillation apparatus. The fraction subliming at a heating temperature of 80-100 °C was collected. A white crystalline solid was obtained and stored under inert atmosphere. For analysis, the ^{1}H-NMR spectrum was recorded with a Varian Inova Spectrometer at 300 MHz using a 5 mm probe and the GC-MS data were obtained with a Varian TSQ 3400 Gas Chromatograph and a TSQ 700 Finnigan Mat mass spectrometer. ^{1}H-NMR (300 MHz, $CDCl_3$): $\delta =$ 2.17 (m, 2H), 1.44 (m, 4H), 1.14 (m, 6H). Details of the recorded Mass Spectrum are given in Table 1, along with assignments of the main lines. It is already worth noting at this stage that, in the mass spectrum of norbornane, the intensities of lines relative to the molecular peak indicate that this compound is very prone to fragmentation into five- or six-membered rings upon ionization by electron impact at a kinetic energy of 70 eV in this case.

Photoelectron spectra were measured using the time-of-flight photoelectron- photoelectron coincidence (TOF-PEPECO) apparatus which has been described before [29]. Briefly, ionizing light from a pulsed discharge in He is wavelength-selected by a toroidal grating monochromator and refocused to intersect an effusive jet of target gas in the source of a magnetic bottle TOF electron spectrometer. The time between a light pulse and the detection of an electron at the 5.5 m distant detector is used to determine the electron energy. The energy resolution is strongly dependent on the electron energy and thus, for a given band, on the photon energy. Because individual atomic lines are selected by the monochromator, complete photoelectron spectra can be measured at any available wavelength. The spectrum of dication states populated by double electron ejection is acquired at the same time as the simple photoelectron spectra.

TABLE 1: GC-Mass Spectrum of Norbornane

peak	rel abs (%)	process	remarks
96.2	6.95	M^+ ($C_7H_{12}^+$)	
82.3	5.28	$(M^+)^* - CH_3 \rightarrow C_6H_9^+$	
81.2	77.11	$M^+ - CH_3 \rightarrow C_6H_9^+$	results possibly in six-membered closed shell cyclic species, with a double bond and a positive charge
79.2	6.82	$C_6H_9^+ - H_2 \rightarrow C_6H_7^+$	additional H-loss from the ring system
77.2	4.24	$C_6H_7^+ - H_2 \rightarrow C_6H_5^+$	additional H-loss form the ring system
68.2	65.97	$C_7H_{12}^+ - C_2H_4 \rightarrow C_5H_8^+$	bridge breaks, resulting in an opening of the ring and loss of C_2H_4
67.2	100	$C_7H_{12}^+ - C_2H_5 \rightarrow C_5H_7^+$	bridge breaks, resulting in an opening of the ring and loss of C_2H_5
66.2	11.88		additional H-loss
65.2	6.66		additional H-loss
55.2	17.73	$C_7H_{12}^+ - C_3H_5 \rightarrow C_4H_7^+$	bridge breaks, resulting in an opening of the ring and loss of C_3H_5
54.1	43.00	$C_7H_{12}^+ - C_3H_6 \rightarrow C_4H_6^+$	bridge breaks, resulting in an opening of the ring and loss of C_3H_6
53.2	15.78	$C_7H_{12}^+ - C_3H_7 \rightarrow C_4H_5^+$ or $C_5H_8^+ - CH_3 \rightarrow C_4H_5^+$	bridge breaks, resulting in an opening of the ring and loss of C_3H_7

3.2.4 Discussion of theoretical results

The theoretical ADC(3)/6-31G, ADC(3)/cc-pVDZ and ADC(3)/DZP+ ionization spectra of norbornane are compared in Figure 2. It is immediately apparent that all three basis sets give essentially the same distribution of ionization lines. With all three basis sets, the energy threshold for shake-up ionization processes, leading to excited configurations of the cation, is located at a binding energy of ~22.0 eV. At electron binding energies below that threshold, enlarging the basis set has virtually no effect on the shape of the convoluted bands: therefore, even a 6-31G basis set would be reliable enough to correctly assign most bands in the ionization spectrum of norbornane. These bands have already been analyzed in detail in [5], and this analysis will not be repeated here. Above the shake-up threshold, enlarging the basis set yields a redistribution of the ionization intensity over different sets of shake-up lines, but without very drastic changes in convoluted bands. Nonetheless, compared with ADC(3) calculations performed using the larger cc-pVDZ and DZP+ basis sets, the ADC(3)/6-31G results seem to overemphasize the dispersion of ionization intensity over shake-up lines for orbital $2a_1$: with the cc-pVDZ and DZP+ basis sets, the idea of a one-electron ionization process can be partly retained for that orbital, in the form of line at a binding energy of ~22.4 eV with a pole strength larger than 0.5. All three basis sets indicate on the other hand that the orbital picture of ionization breaks down completely for the three innermost orbitals, namely $1b_2$, $1b_1$ and $1a_1$. This breakdown is particularly acute for the last orbital $1a_1$, and as a result only a very small fraction of the $1a_1$ ionization intensity could be recovered (Table 2).

Some slight but significant differences between the three simulated ionization spectra can be observed with the relative intensities of the correlation tail of orbital $1b_1$, at about 25 eV, and of the innermost band at 28 eV and relating to shake-up lines originating from orbital $1a_1$. It appears that both spectral features tend to disappear upon enlarging the basis set and, in particular, including diffuse functions (Figure 2c). The explanation to this observation is that enlarging the basis set implies that more shake-up states are allowed to borrow ionization intensity, thus yielding more lines with on average lower ionization intensity. The effect is more striking above the vertical double ionization threshold, which the benchmark CCSD[T] theoretical approach [30] locates at 26.5 eV [Table 3], in qualitatively good agreement with the results of lesser accurate approaches such as second, third and fourth order Moller-Plesset Theory (MP2, MP3, MP4SDQ). On total, a more substantial fraction of ionization intensity is lost above that energy threshold when larger basis sets are used because of the required threshold (0.005) on pole strengths. To avoid such computational artefacts, the shake-up ionization spectra should be computed by means of more sophisticated diagonalization approaches that preserve the first spectral moments, such as the block- or band-Lanczos approaches (see [8] and references therein). Assuming nonetheless that the limit of an infinitely complete basis set including very diffuse and continuum functions could be reached, and that the ionization intensity calculated under such a basis set could be entirely recovered for all orbitals, there is no doubt, however, that the $1a_1$ band at ~28 eV should dilute into a very broad signal relating to a continuum of resonance and shake-off states at binding energies above ~26.5 eV, confirming our earlier statement [5] that the shake-up states computed for orbital $1a_1$ are subject to decay [by ionization of a second-electron] into the continuum.

Importantly, it is clear also from Figures 2a-c that improving the basis set will not provide any satisfactory solution to the puzzling issue of band 12, at 25 eV in the (e,2e) electron impact (or EMS) ionization spectrum of norbornane [Figure 2c-d]. Whereas the ionization spectrum recorded in an EMS experiment at electron impact energies of 1.5 keV, using a non-coplanar symmetric kinematics, and under an azimuthal angle of 0 degrees by Michael Brunger and co-workers [5] exhibit a very strongly protruding band at *25* eV, our ADC(3) spectra do not show any significantly dense and intense enough set of shake-up lines in this region. It has been conjectured [5] that this band might partly relate to the correlation tail of orbitals $2a_1$, $1b_2$ or $1b_1$ which has not been recovered because of the finite threshold on pole strengths (see recovered fraction of ionization intensity in Table 2). However, whatever the basis set, the missing fraction of ionization intensity would be clearly far too small to fit well with that of band 12. Also, by analogy with a band-Lanczos study of the ionization spectra of *n*-alkanes [8], the missing ionization intensity for orbital $1a_1$ is expected to be found in a very long correlation tail extending from the onset at ~26.9 eV up to much higher binding energies, for instance 60 eV, and possibly beyond. Thus, the present comparison of ADC(3)/6-31G, ADC(3)/cc-pVDZ and ADC(3)/DZP+ results confirm our earlier suggestion that band 12 in the EMS ionization spectrum of norbornane does not belong to the vertical one-electron and $2h$-$1p$ shake-up ionization spectrum of norbornane in its ground electronic state and equilibrium geometry, as described by the ADC(3) model of ionization.

TABLE 2: Present ADC(3) and Experimental UPS Results for the Ionization Spectrum of Norbornane[a]

symbol	level	HF/cc-pVDZ	ADC(3)/6-31G		ADC(3)/cc-pVDZ		ADC(3)/DZP+		experimental			
									He I[3]	He II 304 Å	He II 256 Å	EMS[5]
u	$3a_2$	11.328	10.183	(0.917)	10.513	(0.908)	10.515	(0.908)	~10.3	~11.2	~11.2	10.3 [1]
t	$5b_2$	11.641	10.544	(0.917)	10.863	(0.908)	10.852	(0.908)				10.9 [2]
s	$7a_1$	12.006	10.865	(0.916)	11.189	(0.906)	11.178	(0.907)	~10.9			10.9 [2]
r	$5b_1$	12.531	11.363	(0.914)	11.657	(0.905)	11.640	(0.905)	~11.6			11.6 [3]
q	$6a_1$	12.607	11.372	(0.915)	11.670	(0.906)	11.670	(0.906)				11.6 [3]
p	$4b_2$	13.108	11.816	(0.914)	12.102	(0.905)	12.111	(0.905)				12.4 [4]
n	$2a_2$	13.384	12.178	(0.915)	12.445	(0.905)	12.445	(0.906)	~12.4			12.4 [4]
m	$4b_1$	13.634	12.355	(0.914)	12.645	(0.904)	12.643	(0.905)				12.4 [4]
l	$3b_2$	14.734	13.426	(0.910)	13.657	(0.901)	13.657	(0.901)	~13.6	~13.3 (j)	~13.3	13.5 [5]
k	$3b_1$	14.831	13.479	(0.911)	13.736	(0.901)	13.735	(0.902)				13.5 [5]
j	$5a_1$	16.999	15.569	(0.901)	15.757	(0.892)	15.752	(0.893)	~15.6	~15.6	~15.5	15.6 [6]
i	$2b_1$	17.232	15.764	(0.898)	15.948	(0.890)	15.936	(0.890)				15.6 [6]
h	$4a_1$	18.360	16.722	(0.890)	16.897	(0.882)	16.887	(0.883)	~16.5	~16.6	~16.4	16.5 [7]
g	$2b_2$	19.772	17.814	(0.872)	17.866	(0.863)	17.877	(0.864)	~17.7	~17.6	~17.5	17.65 [8]
f	$3a_1$	20.500	18.423	(0.865)	18.473	(0.856)	18.475	(0.858)	~18.1		~18.0 (j)	18.1 [9]
e	$1a_2$	22.328	19.999	(0.838)	19.926	(0.832)	19.943	(0.833)	~19.4	~19.4	~19.4	19.4 [10]
d	$2a_1$	25.542	21.976	(0.042) (c)	22.088	(0.094) (a)	21.788	(0.025) (e)		~22.2	~22.1	~22.6 [11]
			22.320	(0.112)	22.389	(0.132) (b)	22.413	(0.135) (f)				
			22.565	(0.341)	22.484	(0.507)	22.443	(0.571)				
			22.758	(0.157)								
			22.834	(0.078)								
				(**0.789**) (+)		(**0.764**) (+)		(**0.731**) (+)				
c	$1b_2$	26.570	23.096	(0.390)	22.951	(0.392)	22.701	(0.031)				~22.6 [11]
			23.213	(0.046)	23.053	(0.044)	22.980	(0.137)				
			23.258	(0.025) (d)	23.162	(0.071)	23.022	(0.032)				
			23.528	(0.025)	23.345	(0.077)	23.029	(0.250)				
			23.626	(0.050)	23.448	(0.037)	23.219	(0.100)				
			23.683	(0.050)	24.108	(0.020)	23.349	(0.044)				
			23.744	(0.023)			23.466	(0.031)				
			23.796	(0.023)								
			24.533	(0.029)								
				(**0.720**) (+)		(**0.725**) (+)		(**0.702**) (+)				
b	$1b_1$	27.067	23.156	(0.023)	23.167)	(0.021	23.500	(0.031)				~23.6 [11]
			23.530	(0.059)	23.287	(0.036)	23.505	(0.328)				
			23.611	(0.087)	23.378	(0.084)	23.536	(0.129)				
			23.689	(0.154)	23.444	(0.049)	23.602	(0.025)				
			24.012	(0.222)	23.597	(0.165)	23.641	(0.022)				
			24.559	(0.031)	23.663	(0.236)						
				(0.737) (+)		**(0.697)** (+)		(**0.662**) (+)				
a	$1a_1$ (g)	31.532	26.991	(0.020)	26.804	(0.028)	26.504	(0.015)			25.8 (h)	
			27.18	(0.028)	26.930	(0.027)	26.866	(0.029)		25.9 (h)		
			27.773	(0.064)	27.183	(0.025)	26.891	(0.014)				
			27.933	(0.021)	27.279	(0.038)	26.899	(0.011)				
			28.012	(0.023)	27.331	(0.026)	26.956	(0.018)			28.5 (i)	27.5 [13]
			28.037	(0.021)	27.432	(0.020)	27.032	(0.022)				
			28.127	(0.021)			27.093	(0.016)				
							27.531	(0.020)				
				(**0.452**) (+)		(**0.481**) (+)		(**0.145**) (+)				

[a] Binding energies are given in eV, along with the ADC(3) spectroscopic factors, which are given in parentheses. (Only lines with a pole strength larger than 0.02 are listed.) The results are compared with the EMS ionization energies of ref 5, and the corresponding band numbers of Figure 1c,d are given in square brackets. Dominant electronic configurations: (a) $5b_2^{-2}\ 8a_1^{+1}$ [(HOMO$-$1)$^{-2}$ LUMO^{+1}]; (b) $3a_2^{-1}\ 5b_2^{-1}\ 6b_1^{+1}$ [HOMO^{-1} (HOMO$-$1)$^{-1}$ (LUMO+2)$^{+1}$]; (c) $3a_2^{-2}\ 8a_1^{+1}$ [HOMO^{-2} LUMO^{+1}]; (d) $7a_1^{-1}\ 3a_2^{-1}\ 6b_1^{+1}$ [(HOMO$-$2)$^{-1}$ HOMO^{-1} (LUMO+2)$^{+1}$]; (e) $5b_2^{-2}\ Xa_1^{+1}$ (X = 9, 13, 15, 17 ...); (f) $3a_2^{-2}\ Xa_1^{+1}$ (X = 11, 14, 17, 20 ...). g: beyond the double ionization threshold. h: experimental threshold for double ionization. i: position of maximum in the shake-off bands. j: shoulder. (+) fraction of ionization intensity recovered on total, from ***all*** lines with a pole strength larger than ***0.005***.

TABLE 3: Determination of the Vertical and Adiabatic Double Ionization Potentials (VDIP and ADIP, Respectively) of Norbornane Associated with the Lowest Singlet (S) and Triplet (T) States of the Dication[a]

	VDIP (eV)[b]		VDIP (eV)[c]		ADIP (eV)[d]	
theoretical level	S	T	S	T	S	T
HF/cc-pVDZ	27.246	26.073	27.168	26.018	24.334	24.969
MP2/cc-pVDZ	26.015	26.524	25.931	26.460	24.714	26.739
MP3/cc-pVDZ	26.943	26.834	26.867	26.775	23.662	25.146
MP4/cc-pVDZ	27.063	26.830	26.987	26.772	23.481	24.891
CCSD/cc-pVDZ	27.033	26.728	26.959	26.672	23.472	24.871
CCSD(T)/cc-pVDZ	26.571	26.475	26.496	26.419	22.131	23.715
MP2/aug-cc-pVDZ	26.052	26.587	25.968	26.524	23.507	25.561

[a] Results were obtained by means of single-point calculations upon B3LYP/TZVP or MP2/aug-cc-pVDZ geometries, within the constraint of a C_{2v} point group. [b] Single-point calculations, using the B3LYP/TZVP geometry of the neutral in its singlet ground state. [c] Single-point calculations, using the MP2/aug-cc-pVDZ geometry of the neutral in its singlet ground state. [d] From the results of single-point calculations upon MP2/aug-cc-pVDZ geometries for the neutral and adiabatically relaxed doubly ionized forms of norbornane.

3.2.5 Discussion of experimental results

The newly performed UPS measurements on norbornane (Figure 3) also fully confirm these theoretical predictions. They are fully consistent with the earlier He(I) and He(II) spectra of Getzlaff and Schönhense [3] or Bieri *et al.* [4] up to binding energies of 21 and 24 eV, respectively, as well as with all our ADC(3) calculations, taking into account the fact that the innermost orbital lies much above the first two-electron ionization potential. The onset of double ionization is indeed located experimentally [Figure 3] at 25±0.5 eV, a value which is much closer to that of our most accurate [CCSD(T)/cc-pVDZ/MP2/aug-cc-pVDZ] evaluation of the vertical (~26.6 eV) double ionization threshold than to the value (~22.13 eV) obtained at the same level for the adiabatic double ionization threshold (Table 3). This seems to indicate that with double ionization, geometrical relaxation effects are such in a strained species like norbornane that the time required for a complete geometrical relaxation of the dication strongly exceeds the timescale characterizing UPS upon a 40 eV photon beam ($\sim 10^{-13}$ s, see further), and rules out therefore the scenario that band 12 in the EMS record of Figures 1c and d would relate to transitions from the electronic ground state of norbornane in equilibrium geometry to the lowest adiabatically relaxed singlet or triplet doubly ionized state. Note also that the experimentally observed shake-off band shows a slight extremum at ~29 eV, as a reminiscence of the densest sets of the vertical shake-up states found for the $1a_1$ orbital at the ADC(3) level.

The measurements performed using wavelengths of 304 and 256 Å show also some very long and weak signal extending between 24 and 27 eV, which should be related to the correlation tail of band 11 and, more specifically, of orbitals $1b_2$ and $1b_1$. This tail is more strongly apparent in the ADC(3)/6-31G spectrum of Figure 2a, and tends to disappear in the ADC(3) spectra obtained with larger basis set, as a result of enhanced shake-up fragmentations and the limitation of the search to the solutions of the ADC(3) secular equation to lines with a pole strength larger than 0.005. Since it is a well established principle that shake-up lines originating from the same orbital have relative intensities proportional to their pole strength, this tail, and the missing ionization intensity for orbitals $1b_2$ and $1b_1$ in the ADC(3) simulations of Figure 2, are far too weak to be related to such an intense and striking feature as band 12 in the EMS measurement of Figure 1d.

Also, it is worth reminding that the momentum distribution inferred from band 12 is of *s*-type and is therefore completely incompatible with the *p*-type profile that is expected for antisymmetric orbitals such as $1b_2$ and $1b_1$. This also rules out the scenario that band 12 could be the outcome of exceptionally strong vibronic coupling interactions between states produced by ionization of these two orbitals.

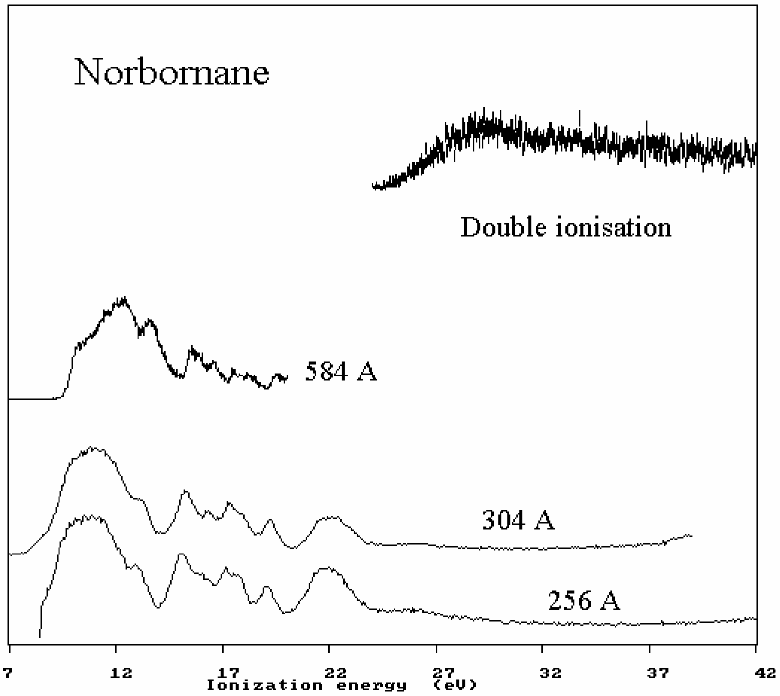

Figure 3. Newly recorded ultra-violet photoemission [He(I), He(II)] spectra at incident photon energies of 21.25 eV (λ = 584 Å), 40.82 eV (λ = *304* Å) and 48.47 eV (λ = 256 Å). At the right top, the experimental double ionization spectrum is given.

Since band 12 has a very similar *s*-type momentum distribution to that inferred from band 13, it would be very tempting from a topological viewpoint to relate both bands to ionization of orbital $1a_1$. We would like to emphasize once more that, from an energy viewpoint, such an assertion is completely incompatible with a vertical depiction of the $1a_1$ ionization process of norbornane in its ground state wavefunction and C_{2v} equilibrium geometry. A number of GF [31-39] or MR-SDCI [40] studies on *n*-alkanes and cyclolkanes, and the present ADC(3) results for the $1a_1$, $1b_1$, $1b_2$ and $2a_1$ orbitals of norbornane show that, compared with the HF level, the electronic relaxation effects induced by ionization of an electron out of the innermost C_{2s} orbitals are always comprised within 3.0 and 3.5 eV. Even when invoking configuration interactions in the cation and dispersion of the $1a_1$ ionization intensity into shake-up lines (and by extension, shake-off bands in the limit of an asymptotically complete basis set), it seems therefore impossible that a band at 25 eV, thus at ~1.5 eV below the vertical double ionization threshold, relates via a vertical single or double ionization process to an orbital ($1a_1$) which is characterized by a one-electron binding energy of 31.5 eV at the HF level. Also, if bands 12 and 13 would both relate to shake-up and/or shake-off states derived from the innermost C_{2s} orbital, $1a_1$, and since molecular orbitals having similar atomic compositions normally display comparable UPS cross sections, these bands would both have intensities in the same range than those seen for the other inner-valence orbitals encompassed in band 11 ($1b_1$, $1b_2$ and $2a_1$).

It is worth noting that very significant discrepancies, up to 4 eV, have already been noted previously between the appearance potentials for double ionization in electron and photon impact experiment [41, 42]. The reasons for these discrepancies can be instrumental, i.e. due to inherent differences in the determination of the onset of the appearance potentials for double ionization, and (or) related to intrinsic molecular properties and different behaviors under electron and photon impact. Wannier theory [43] and its extension by Geltman [44] indicate that, for an electron as compared with photon impact, the (total) cross section for direct double ionization should rise less steeply, at threshold, as a function of the energy of the impinging particle. Higher appearance potentials for double ionization processes are thus normally expected in electron impact experiments, as compared with photon impact, and it seems therefore unlikely that the presence of an additional band at 25 eV in the EMS measurements on norbornane as compared with the newly presented UPS ones can be explained on such grounds. In the experimental set up employed for these EMS experiments, the impinging electron has a kinetic energy of 1.5 keV, which also rules out the possibility of a breakdown of the Born (sudden, or knocked-out) approximation, and thus the excitation of optically forbidden triplet states because of electron exchange in the target molecule (this energy is much above the 200 eV limit beyond which the Born approximation is usually considered to be valid).

The duration of interaction of a photon with an energy in the 20-40 eV range and incident on a molecule of a few Angstroms in dimension is much longer than for an electron with an energy of 1.5 keV. This interaction time depends on the specific physical processes involved in energy transfer in each case. The photoionization process requires typically about 500 cycles of the radiation field (according to [41]) to fully manifest its harmonic character during the perturbation time. For a photon of 40 eV, this corresponds to an interaction time of the order of 0.05 ps. For an electron, the duration of interaction with the molecule depends on the distance over which direct momentum transfer can occur between the incident electron and the molecular electrons. This range, limited to the close collision region, can be taken to be about 3 Å. Since the velocity of a 1.5 keV electron is about 2.28×10^9 cm s^{-1}, it will traverse 3 Å in about 0.01 fs. Thus, the effective interaction time of a molecule with a 1.5 keV electron should be about four order of magnitudes smaller than with a 40 eV photon. An electron which collides with a molecular target in the EMS experiment with an energy of ~1.5 keV has a collision time of $\sim 10^{-17}$ s, whereas with UPS the interaction time is around 10^{-13} s. Ultra-violet photon ionization tends therefore to be an adiabatic process, whereas with EMS, ionization remains normally nonadiabatic as far as geometry relaxation and nuclear motions are concerned. From a timescale viewpoint, the presence of an additional peak at 25 eV in EMS as compared with UPS seems therefore highly paradoxical. Since this band is clearly missing in UPS, and has a momentum distribution very similar to that of orbital $1a_1$, band 12 in Figures 1c and d might therefore be indicative of ultrafast and unidentified electronic or nuclear dynamical processes, at timescales comprised between 0.1 ps and 0.01 fs, that are initiated by double ionization of the norbornane compound.

The most attractive scenario is an indirect ionization process in which highly electronically superexcited singlet and triplet states of the neutral target molecule are initially formed, followed by single-electron, shake-up or double autoionization, with possibly as ultimate consequence a charge separation or covalent molecular fragmentation of the carbon cage. Assuming that the autoionization scenario is valid, the latter complications are quite likely to occur with regards to the extent of cyclic strains within a cage structure such as norbornane, and which single and almost double ionization events should clearly intensify. It is worth noting that single-electron ionization processes following molecular dissociation events are known to result into additional bands at fixed electron kinetic energies and relatively high apparent electron binding energies in [Penning] ionization experiments upon collision with metastable excited atoms [see ref. 45 and references therein]. Note also that, if autoionization processes would indeed occur upon molecular dissociation, the final states observed by means of EMS or UPS would clearly be completely different, considering the very different timescales of the two spectroscopies.

3.2.6 Conclusions

In extension to a recent study of the electronic structure of norbornane using Electron Momentum Spectroscopy in conjunction with calculations of orbital momentum distributions by means of Density Functional Theory as well as Green's Function calculations of the ionization spectrum, we made use again of the ADC(3) approach to compare spectra obtained using basis sets of improving quality (6-31G, cc-pVDZ, DZP+) with newly performed high-resolution He(I) and He(II) measurements, up to binding energies of ~40 eV. The present work fully confirms the former suggestion [5] that a band observed at 25 eV in the (e,2e) ionization spectrum of norbornane upon impact with a 1.5 keV electron does not belong to the vertical one-electron and shake-up ionization spectrum of this compound in its ground state and equilibrium geometry. Furthermore, extrapolating to the asymptotic limit the dependence of the computed sets of shake-up lines on the basis set also show that, in a vertical depiction, this band cannot relate to vertical double ionization processes. This finding is in line with further benchmark quantum mechanical results for the vertical and adiabatic double ionization thresholds, which are located at 26.5 eV and 22.1 eV, and with newly presented ultra-violet photoelectron measurements, in which this band is entirely missing (in UPS, the onset of double ionization is located at ~25 eV, and the extremum of intensities in shake-off bands is not reached before 29 eV).

Considerations on relative timescales, on the extent of geometrical relaxation effects, as well as on the *s*-type symmetry characterizing the momentum distributions inferred in EMS from the innermost valence bands rule out the scenarios that band 12 is the result of exceptionally strong vibronic coupling interactions between states originating from ionization of the $1b_1$ and $1b_2$ orbitals, or of double adiabatic ionization processes starting from the ground state electronic wavefunction of norbornane in its equilibrium geometry. It would thus be worth redoing further EMS measurements on norbornane at varying energies for the incoming electron, in order to test the remaining hypothesis [5] of single or double autoionization processes via electronically highly excited and possibly dissociating states [45]. The absence of such a spectral feature in ultra-violet photoemission spectroscopy suggests indeed that the band seen at 25 eV in the (e,2e) electron impact ionization spectra of norbornane [5] relates to ultra-fast autoionization and/or coulomb fragmentation processes, at time scales comprised between 10^{-14} and 10^{-17} s, that are induced specifically by double ionization. Measurements of electron energy loss spectra at large deflection angles, and of mass spectra at varying electron kinetic energies, would for this reason also be most welcome. On the side of theory, detailed quantum chemical investigations of the potential energy surfaces of norbornane^{2+} in its singlet form, is necessary for elucidating the present enigma, and will be presented in a separate study [46].

References

[1] Buchbauer, G.; Pauzenberger, I. *Pharmazie* 1999, 54, 5.

[2] Bischof, P.; Hashmall, J. A.; Heilbronner, E; Hornung, V *Helv. Chim. Acta* 1969, 52, 1745.

[3] Getzlaff, M.; Schönhense, G. *J. Electr. Spectr. & Rel. Phen.* 1998, 95, 225.

[4] Bieri, G.; Burger, F.; Heilbronner, E.; Maier, J. P. *Helv. Chim. Acta* 1977, 60, 2213.

[5] Knippenberg, S.; Nixon, K. L.; Brunger, M. J.; Maddern, T.; Campbell, L.; Trout, N.; Wang, F.; Newell, W. R.; Deleuze, M. S.; François, J.-P.; Winkler, D. A. *J. Chem. Phys.* 2004, 121, 10525.

[6] Cederbaum, L. S.; Domcke, W. *Adv. Chem. Phys.* 1977, 36, 205.

[7] Ortiz, J. V. In *Computational Chemistry: Reviews of Current Trends*; Leszczyinski, J.; World Scientific; Singapore, 1997; Vol. 2, p. 1-61.

[8] Golod, A.; Deleuze, M. S.; Cederbaum, L. S. *J. Chem. Phys.* 1999, 110, 6014.

[9] Schirmer, J.; Cederbaum, L. S.; Walter, O. *Phys. Rev. A* 1983, 28, 1237.

[10] von Niessen, W.; Schirmer, J.; Cederbaum, L. S. *Comput. Phys. Rep.* 1984, 1, 57.

[11] Schirmer J.; Angonoa, G. *J. Chem. Phys.* 1989, 91, 1754.

[12] Weikert, H.-G.; Meyer, H.-D.; Cederbaum, L. S.; Tarantelli, F. *J. Chem. Phys.* 1996, 104, 7122.

[13] Dunning Jr., T. H. *J. Chem. Phys.* 1989, 90, 1007.

[14] McCarthy, I. E.; Weigold, E. *Rep. Prog. Phys.* 1991, 54, 789.

[15] Deleuze, M. S.; Trofimov, A. B.; Cederbaum, L. S. *J. Chem. Phys.* 2001, 115, 5859.

[16] Deleuze, M. S. *J. Phys. Chem. A* 2004, 108, 9244.

[17] Hehre, W. J.; Ditchfield, R.; Pople, J. A. *J. Chem. Phys.* 1972, 56, 2257.

[18] Dunning Jr., T. H.; Hay, P. J. In *Methods of Electronic Structure Theory*; Schaefer, H. F.; Plenum Press: New York, 1977; Vol. 2.

[19] Schmidt, M. W.; Baldridge, K. K.; Jensen, J. H.; Koseki, S.; Gordon, M. S.; Nguyen, K. A.; Windus, T. L.; Elbert, S. T. *QCPE Bull.* 1990, 10.

[20] Deleuze, M. S.; Claes, L.; Kryachko, E. S.; François, J.-P. *J. Chem. Phys.* 2003, 119, 3106.

[21] Deleuze, M. S. *Int. J. Quantum Chem.* 2003, 93.

[22] Liu, B. In *Numerical Algorithms in Chemistry, Algebraic Methods*; LBL-8158; Lawrence Berkely Laboratory.

[23] Tarantelli, F.; Sgamellotti, A.; Cederbaum, L. S.; Schirmer, J. *J. Chem. Phys.* 1987, 86, 2201.

[24] Frisch, M. J.; Trucks, G.W.; Schlegel, H.B, *et al.* Gaussian98, revision A.7; Gaussian Inc, Pittsburg, PA 1998.

[25] Dunning Jr., T. H. *J. Chem. Phys.* 1971, 55, 716.

[26] Becke, A. D. *J. Chem. Phys.* 1993, 98, 5648.

[27] Lee, C.; Yang, W.; Parr, R. G. *Phys. Rev. B* 1988, 37, 785.

[28] Boese, A. D.; Martin, J. M. L. *J. Chem. Phys.* 2004, 121, 3405.

[29] Eland, J. H. D. *Chem. Phys.* 2003, 294, 171.

[30] Coupled cluster theory with single and double excitations, along with a perturbative treatment of triple excitations; Raghavachari, K.; Trucks, G. W.; Pople, J. A.; Head-Gordon, M. *Chem. Phys. Lett.* 1989, 157, 479.

[31] Deleuze, M.; J.-P. Denis, Delhalle, J.; Pickup, B.T. *J. Phys. Chem.* 1993, 97, 5115.

[32] Deleuze, M.; Delhalle, J.; Pickup, B.T. *J. Phys. Chem.* 1994, 98, 2382.

[33] Deleuze, M.; Delhalle, J.; Pickup, B.T.; Svensson, S. *J. Am. Chem. Soc.* 1994, 116, 10715.

[34] Deleuze, M. S.; Cederbaum, L. S. *J. Chem. Phys.* 1996, 105, 7583.

[35] Deleuze, M. S., Di Paolo, S.; Gijsen, J.; Riga, J.; Deleuze, M.; Delhalle, J. *J. Phys. Chem. B* 1997, 101, 884.

[36] Pang, W. N.; Shang, R. C.; Gao, J. F.; Gao, N. F.; Chen, X. J.; Deleuze, M. S.*; Chem. Phys. Lett.* 1998, 296, 605.

[37] Pang, W. N.; Gao, J. F.; Ruan, C. J.; Shang, R. C.; Trofimov, A. B.; Deleuze, M. S.*; J. Chem. Phys.* 2000, 112, 8043.

[38] Deleuze, M. S.; Pang, W. N.; Salam, A.; Shang, R. C. *J. Am. Chem. Soc.* 2001, 123, 4049.

[39] Deleuze, M. S.; Delhalle, J. *J. Phys. Chem. A* 2001, 105, 6695.

[40] Zheng, Y.; Pang, W. N.; Shang, R. C.; Chen, X. J.; Brion, C. E.; Ghanty, T. K.; Davidson, E. R. *J. Chem. Phys.* 1999, 111, 9526.

[41] Tobita, S.; Leach, S.; Jochims, H. W.; Rühl, E.; Illenberger, E.; Baumgärtel, H. *Can. J. Phys.* 2004, 72, 1060.

[42] Rülf, E.; Price, S.D.; Leach, S. *J. Phys. Chem.* 1989, 93, 6312.

[43] Wannier, G.H. *Phys. Rev.* 1953, 90, 817.

[44] Geltman, S. *Phys. Rev.* 1956, 102, 171.

[45] Kishimoto, N.; Matsumura, E.; Ohno, K.; Deleuze, M. S. *J. Chem. Phys.* 2004, 121, 3074.

[46] Knippenberg, S.; Hajgató, B.; François, J.-P.; Deleuze, M. S.; accepted for publication in *J. Phys. Chem. A*

3.3 Theoretical study of the fragmentation pathways of norbornane in its doubly ionized ground state.

3.3.1 Introduction

Gas-phase dications [1-7] have received considerably less attention, both from experimental and theoretical viewpoints, than has been accorded to their monocationic counterparts. This is a consequence of the somewhat greater difficulties inherent in studies of doubly charged versus singly charged species. Molecular dications are subject to sizeable electrostatic strains due to intra-molecular Coulomb repulsions, as well as to important electronic or multi-reference correlation effects due to the more limited energy gap between occupied and unoccupied orbital levels. Clearly, their formation necessitates larger ionization energies than monocations. In the condensed phase (either in solution or in the solid state), dications are stabilized by interactions with counter-ions, solvent molecules [8] or appropriate ligands [9] that can accommodate the positive charges. In the gas phase, these stabilizing factors are missing and the majority of small molecular dications (e.g. CF_2^{2+} or CF_3^{2+} [10]) are thermodynamically prone to Coulomb fragmentation processes, in order to release excessively strong electrostatic repulsions. Very few diatomic dications are thermodynamically stable in the gas phase [5]. In contrast to this, large cage compounds such as fullerenes [11] are known to exhibit exceptional stability [12] against charge fragmentation processes, due to their special structure and size. Multiply charged C_{60} ions can therefore be rather easily produced and characterized [13].

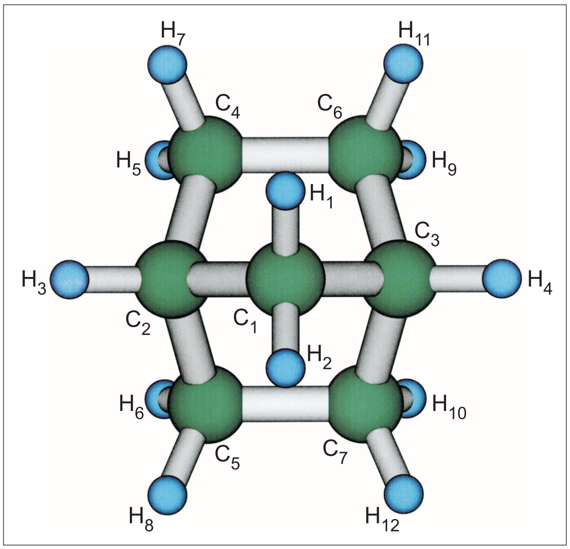

Figure 1: Norbornane in its neutral ground state. The non-redundant internal coordinates of this compound within its C_{2v} symmetry point group are as follows: $R(C_1\text{-}C_2) = 1.54$ Å; $R(C_2\text{-}C_4) = 1.55$ Å; $R(C_4\text{-}C_6) = 1.56$ Å; $R(C_1\text{-}H_1) = 1.10$ Å; $R(C_2\text{-}H_3) = 1.10$ Å; $R(C_4\text{-}H_5) = 1.10$ Å; $R(C_4\text{-}H_7) = 1.10$ Å; $\theta(C_3\text{-}C_1\text{-}C_2) = 94.4°$; $\theta(C_1\text{-}C_2\text{-}C_4) = 101.5°$; $\theta(C_2\text{-}C_4\text{-}C_6) = 103.1°$; $\theta(H_1\text{-}C_1\text{-}C_2) = 113.3°$; $\theta(H_3\text{-}C_2\text{-}C_4) = 113.8°$; $\theta(H_5\text{-}C_4\text{-}C_6) = 112.8°$; $\theta(H_7\text{-}C_4\text{-}C_6) = 111.1°$; $\tau(H_5\text{-}C_4\text{-}C_6\text{-}C_3) = -120.9°$; $\tau(H_7\text{-}C_4\text{-}C_6\text{-}C_3) = 118.7°$ (B3LYP/cc-pVDZ geometry).

Most gas phase molecular dications are *kinetically* metastable [5, 6]. More specifically, these molecular dications exist in long-lived states that are separated from the energy asymptotes for the dissociation products by sizeable enough energy barriers on the potential energy surface. These barriers are the consequence of the fact that chemical bonding can be strong enough to overcome the electrostatic repulsions between charge centers [5, 6]. Somewhat counter-intuitively, two-electron ionization events in weakly bound clusters of aromatic molecules were for instance found to lead to the formation of large kinetically metastable assemblies [14] tightened by additional covalent bonds. In view of the combination of high kinetic stability and exceptional thermodynamic instability, many molecular dications can be regarded as "energy rich" or "volcanic" systems that could represent a possible source of propulsion energy [15].

Studies of carbenium dications are especially motivated by the fact that these species are produced exclusively by the removal of electrons from bonding electrons in the neutrals. In the absence of conjugation with π- or lone-pair donating substituents, the observed systems owe their existence to delocalizing interactions anchored to π-conjugation, hyperconjugation, and aromaticity. Examples of experimentally known dicarbenium dications comprise the dications of ethylene [16], cyclobutadiene [17], norbornadiene [18] and pagodanes [19]. An exceptionally stable dication is the 1,3-dehydro-5,7-adamantanediyl dication [20] that exhibits three-dimensional aromaticity due to the overlap of four C_{2p} orbitals in a tetrahedral fashion.

Bimolecular reactions of dications with neutral molecules are, furthermore, often merely dominated by electron transfer. The few known bond-forming reactions of molecular dications [21, 22] are limited to processes with concomitant electron transfer [23]. Fragmentation reactions of some arene dications [24-26] suggest, however, that medium-sized organic dications may react with neutral compounds, such as acetylene, without the occurrence of electron transfer [27].

The cage compound under investigation in this study is norbornane (C_7H_{12}). This molecule is a highly strained, bicyclic hydrocarbon possessing C_{2v} symmetry (Figure 1), which has proved useful in the therapy of cardiac infarcts as well as asthma, bronchitis and thromboses [28]. Its molecular and electronic structures were already studied in the sixties [29, 30]. The outer-valence ionization spectrum of norbornane has been recorded by Bishof *et al.* [31] and Getzlaff and Schönhense [32] by means of ultraviolet (He I) photoemission (UPS) spectroscopy. Bieri *et al.* [33] investigated further the inner valence ionization bands up to ~24 eV, using a He II photon beam.

Very recently, our group has been involved in an exhaustive study of the valence wave function of norbornane employing Electron Momentum Spectroscopy (EMS) [34]. The EMS spectrum and related momentum distributions were found to corroborate the available UPS measurements and 1p-GF calculations employing the benchmark third order Algebraic Diagrammatic Construction scheme [ADC(3)] [35-38], except for a particularly broad and intense band at 25 eV in the EMS spectrum which the 1p-GF/ADC(3) calculations failed to reproduce [39]. This striking discrepancy between theory and experiment was thereafter referred to as the "band 12 issue" [40]. It has led us to undertake further ADC(3) calculations with various basis sets [40] and to compare these with updated UPS measurements [40] by J. H. D. Eland (Oxford University) employing a 256 Å photon beam up to binding energies of 40 eV. Except for a barely visible increase of the spectral background at ~26 eV that has been ascribed to the double ionization threshold, the agreement between all theoretical ADC(3) and the new experimental UPS data was here almost perfect. Therefore, with regards to the characteristic time scales of ionization processes in EMS and UPS (10^{-17} versus 10^{-13} s, respectively), it has been suggested that ultrafast nuclear dynamical effects and coulomb fragmentation processes induced by double ionization might be at the origin of the band at 25 eV in the EMS ionization spectrum. More specifically, shake-up states above the double ionization threshold are expected to decay into dissociative shake-off states within time scales of the order of 1 to a few ten femtoseconds [41, 42], through relaxation of the excited electron into the inner-valence vacancy and auto-ionization of a second electron into the continuum (Figure 2).

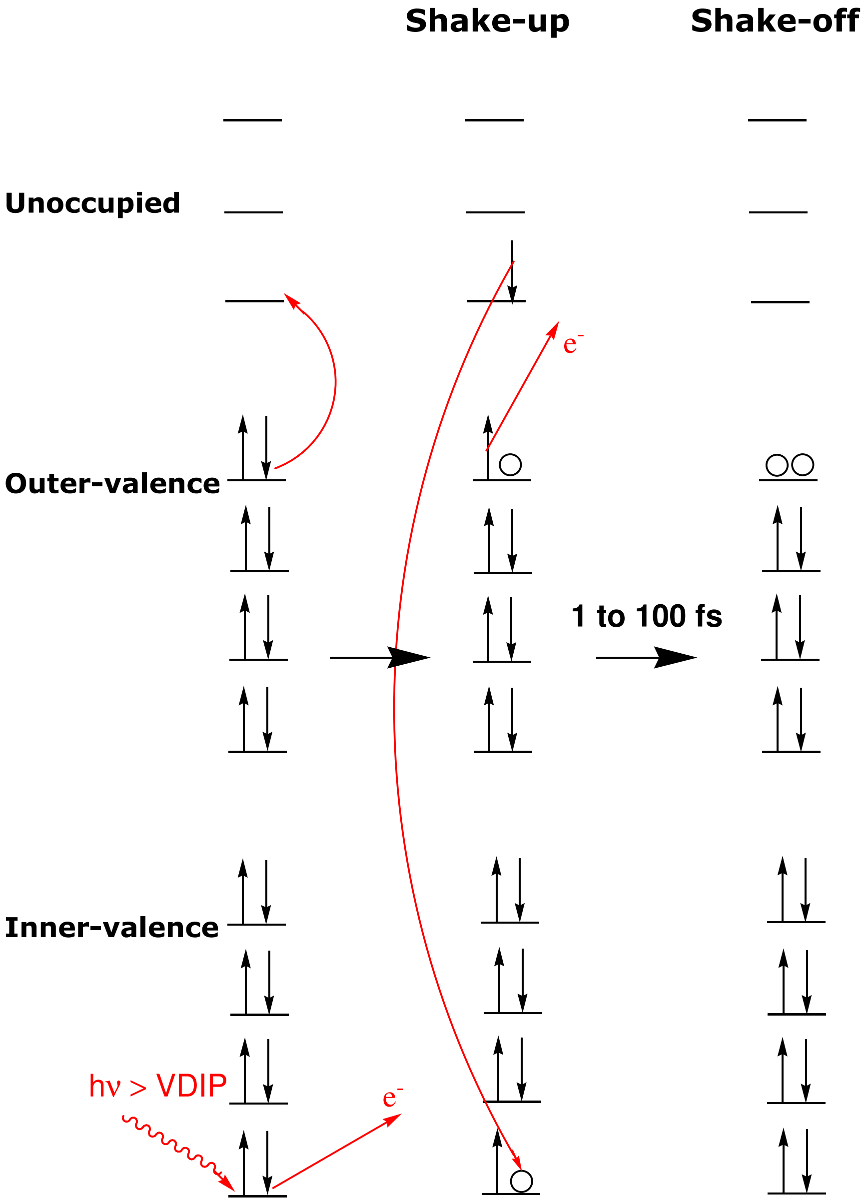

Figure 2. Intramolecular Coulomb decay of electronically excited shake-up states of norbornane^{2+} at the vertical double ionization threshold of the neutral.

In straightforward analogy with the intermolecular Coulomb decay (ICD) mechanism, electric charges in dicationic species are expected to localize on separate fragments in order to minimize the extent of Coulomb repulsions. The ICD mechanism was proposed by Cederbaum *et al.* [41] for weakly bound clusters of molecules or noble gas atoms, and has been confirmed experimentally for neon clusters [43]. Within a fully saturated hydrocarbon cage compound like norbornane, all chemical bonds derive, according to a basic Lewis depiction, from the pairing of two electrons with opposite spin. In view of the importance of cyclic strains in the cage, the most important contribution of which arise from the C_2-C_1-C_3 bridge (Figure 1), it is therefore natural to expect on intuitive chemical grounds that a double ionization event would induce the breaking of a single C-C bond. In other words, a purely electronic *intra*molecular Coulomb Decay mechanism is expected to precede with severe intramolecular rearrangements, once nuclear dynamics comes into play. The purpose of the present work is thus to test this hypothesis by studying in details the Potential Energy Surface (PES) of the dication of norbornane in its singlet ground state. In this work we invoke the standard Born-Oppenheimer approximation, which enables us to compute the potential energy $U(\{R_X\})$ of a fixed configuration of nuclei as the sum of the electronic energy obtained through solving the exact electronic Schrodinger equation ($H^{elec}\ \Psi^{elec} = E^{elec}\ \Psi^{elec}$) or, at least, an approximation to it, and of the nuclear repulsion energy ($\sum_{A,B} Z_A Z_B \left|R_A - R_B\right|^{-1}$).

3.3.2 Methodology section

All geometry and frequency calculations presented in this work have been performed by means of the GAUSSIAN98 [44] quantum chemistry package. Density Functional Theory (DFT) in conjunction with the non-local hybrid and gradient corrected Becke three-parameter Lee-Yang-Parr functional (B3LYP) [45], along with Dunning's correlation-consistent polarized valence basis set of double-ζ quality (cc-pVDZ) [46]. The default pruned integration grid with 75 radial shells per atom and 302 angular points per shell has been used. The convergence of the results obtained with this grid was checked through comparisons with a few calculations of stationary points on the investigated potential surface, using an ultrafine pruned integration grid containing 99 radial shells per atom and 590 angular points.

Relaxation of the vertical double ionized state under the constraints of a C_{2v} point group was found to result into a second order saddle point, referred to as S_2 (C_{2v}). This molecular structure has thereafter been systematically distorted according to the normal vibrational modes characterized by imaginary frequencies, until first order saddle points or energy minima could be reached. Transition states (TS) for proton transfers have been similarly identified by iteratively stretching the C-H bonds of interest via a scan of the potential energy surface, using the Molden graphical interface in order to construct suited Z-matrices, and letting geometries relax to first order saddle points, by means of the Rational Function Optimization (RFO) method [47]. Enlarging the bridge of the C_{2v} structure of norbornane in its dicationic singlet ground state gave rise to a third order saddle point S_3 (C_s), whose geometry has been optimized using the Synchronous Transit-Guided Quasi-Newton Method [48-49]. The expectation value of the $\mathbf{S}^2$ operator was found to be zero. The stability of the spin-restricted wave function has also been checked [50-51] for all identified stationary points through calculations of electronic excited states using Configuration Interaction approach with singly excited determinants (CIS). In all cases, the wave functions were found to be electronically stable (i.e. all electronic excitation energies were of positive sign). Besides this stability test, the single-reference nature of the wave function at the CCSD (Coupled Cluster with Single and Double excitations) level [52-55] of theory has also been checked according to the T1 diagnostic [56], by means of the Molpro package [57]. All T_1 values were found to be less than 3.0% for each of the structures of interest, which typically reflects limited multi-reference effects. At last, a few single-point calculations on test cases have been performed at the Complete Active Space Self Consistent Field (CASSCF) [58] level, using 6 active electrons in 8 orbitals, in conjunction with the cc-pVDZ basis set, in order to evaluate the outcome of multi-reference effects. The weights of the main configurations were found to be over 90%, which justifies again a single-reference depiction for the wave function.

Harmonic vibrational frequencies and the related zero-point vibrational energies (ZPVEs) have been analytically calculated throughout this work, in order to verify whether the identified stationary structures correspond to energy minima or to saddle-points on the potential energy surfaces. Thermodynamical state functions (enthalpies, entropies and Gibbs' free energies) were obtained from Boltzmann's thermodynamical partition functions [59] calculated at the B3LYP/cc-pVDZ level at 298.15 K using the Rigid Rotor-Harmonic Oscillator (RRHO) approximation. Furthermore, natural bond orbital (NBO) analyses [60-67] have been performed on all identified stationary points on the potential surface in order to investigate charge distributions.

Adiabatic ionization energies have been computed as energy differences between the structurally optimized doubly ionized states and the neutral singlet ground state, at the B3LYP/cc-pVDZ level and using various many-body treatments of electron correlation upon the corresponding B3LYP/cc-pVDZ geometries. The employed post-SCF treatments comprise MP2, MP3 and MP4SDQ (second, third and partial fourth order Møller-Plesset theory, respectively [68-72]), CCSD and CCSD(T) [Coupled Cluster (CC) calculations employing the coupled cluster Ansatz for single (S) and double (D) electronic excitations, and supplemented by a perturbative estimate [73] of triple (T) excitations).

Energy differences among the identified stationary points on the potential energy surface were accurately evaluated by a Focal Point Analysis [FPA] similar to those carried out by Allinger *et al.* [74], Salam *et al.* [75], Kwasniewski *et al.* [76] and Huang *et al.* [77], to determine the conformational energy differences or barriers of *n*-butane, *n*-pentane, stilbene and dimethoxymethane, respectively. The main feature of such an analysis is to determine by pairing different levels of theory and basis sets how the energy differences converge to the exact solution of the Schrödinger equation. To be more specific, one exploits in this purpose the faster convergence with respect to the basis set of the higher-order correlation corrections to the calculated energy differences in well-suited extrapolations of results of single-point calculations performed upon the B3LYP/cc-pVDZ geometries using *ab initio* (HF and many-body) approaches and basis sets of improving quality. Reliable estimations of CCSD(T) energy differences in the limit of an exceedingly large basis set can then be made by adding almost converged high-level correlation corrections, obtained at the MP3, CCSD, and CCSD(T) levels with rather limited basis sets, to lower-level HF and MP2 results which are calculated in conjunction with the largest basis sets, along with suited extrapolation procedures.

In the analysis, the employed basis sets were Dunning's correlation consistent polarized valence double-, triple-, and quadruple-ζ basis sets, namely cc-pVDZ, cc-pVTZ and cc-pVQZ [46], incorporating on total 158, 378 and 745 atomic functions, respectively. These even-tempered basis sets enable an extrapolation of the HF/cc-pVXZ (X = D, T, Q) energies to the limit of an asymptotically complete (cc-pV∞Z) basis set with an exponential fit as was suggested by Feller [78-79]. The MP2/cc-pVXZ energies can be similarly extrapolated to the asymptotic limit of basis set completeness using a three-point version [known as Schwartz 6(lmn) [80]] of Schwartz' extrapolation [81].

The key point in a Focal Point Analysis [FPA] is to determine at which basis set each of the successive corrections evaluated by the various *ab initio* methods has converged within a satisfactory enough threshold. With such a procedure, it is then possible to extrapolate benchmark CCSD(T) results to the asymptotically complete cc-pV∞Z basis set, which enables a determination of conformational energy differences within an accuracy of ~0.05 kcal/mol [75-77], or ionization energies within an accuracy of ~0.04 eV [82].

Many thorough studies have shown that DFT, in conjunction with standard hybrid and gradient corrected (GGA) functionals such as B3LYP, is suited for semi-quantitative calculations of reaction and activation energies (enthalpies), i.e. within relative accuracies of ~10% on energy differences [83-86]. The B3LYP functional is nonetheless known to substantially underestimate energy barriers for unimolecular rearrangement reactions. As an alternative, use has also been made of the modified Perdew-Wang 1-parameter model for kinetics (MPW1K) [83, 87] for exploring the potential energy surface of norbornane^{2+} in its singlet ground state. This hybrid functional is characterized by a higher fraction of Hartree-Fock exchange than B3LYP, which normally helps describing the electron delocalization induced by bond stretching in a more reliable way. MPW1K was thus shown to provide improved energy barriers [84, 88, 89], but at the expense of the quality of the geometries of saddle points. For the sake of completeness, we have thus been willing to calibrate the two functionals from a comparison of the results of B3LYP/cc-pVDZ and MPW1K/cc-pVDZ calculations with benchmark CCSD(T) and FPA data, considering both single-point calculations on B3LYP/cc-pVDZ geometries as well full optimization runs at the MPW1K/cc-pVDZ level, in order to assess the influence of the geometry of the identified stationary points on the quality of the computed energy differences.

3.3.3 Results and discussion

3.3.3.1 Potential energy surface

A. Relaxation of doubly ionized norbornane to five membered monocyclic intermediates (C5-Min$_x$, x=1, 2, 3)

Adiabatic ionization energies corresponding to the most important stationary points identified on the potential energy surface of norbornane^{2+} in its singlet ground state are given in Table 1 (included at the end of this chapter), and compared with the vertical double ionization potential. At the B3LYP/cc-pVDZ level, under the constraint of C_{2v} symmetry, geometrical relaxation of this singlet dicationic species was found to yield a second order saddle point, referred to as S_2 (C_{2v}). This stationary point defines the central entry on our conformational energy map displayed in Figure 3, obtained by sketching the evolution of the potential energy $U(\{R_X\})$ of the doubly ionized molecule as a function of molecular distortions measured by the two vibrational modes $\mathbf{q_1}$ and $\mathbf{q_2}$ that are characterized by imaginary frequencies (426*i* and 365*i* cm^{-1}). Compared with the vertical double ionized state, geometry relaxation was found at the same level (Table 2 – included at the end of this chapter) to release an energy of 2.41 eV or 55.57 kcal/mol. From this point, vibrations along the $\mathbf{q_1}$ and $\mathbf{q_2}$ modes and subsequent geometry optimization under the constraints of C_s symmetry point groups enable energy relaxation (i.e. a lowering of the potential energy $U(\{R_X\})$ into four directions, which divide the conformational energy map into four symmetry equivalent quartants (Figure 3). Figure 4 is equivalent to one of these quartants. Upon analyzing the NBO charge distributions (Table 3 – included at the end of this chapter) in the S_2 (C_{2v}) species (Figure 4a), it is clear that in this highly symmetric but unstable structure the charges are merely delocalized over the outer most hydrogens {H_7, H_8, H_{11}, H_{12}}

and over the bridgehead carbons C_2 and C_3. Upon comparing the total electric charge ascribed to the carbon backbones of the S_2 (C_{2v}) structure with that for the neutral, singlet C_{2v} structure of norbornane (see Table 4 – included at the end of this chapter), it also appears that +0.48*e* or only about one-fourth of the double positive charge is effectively localized on the carbon backbone of the system.

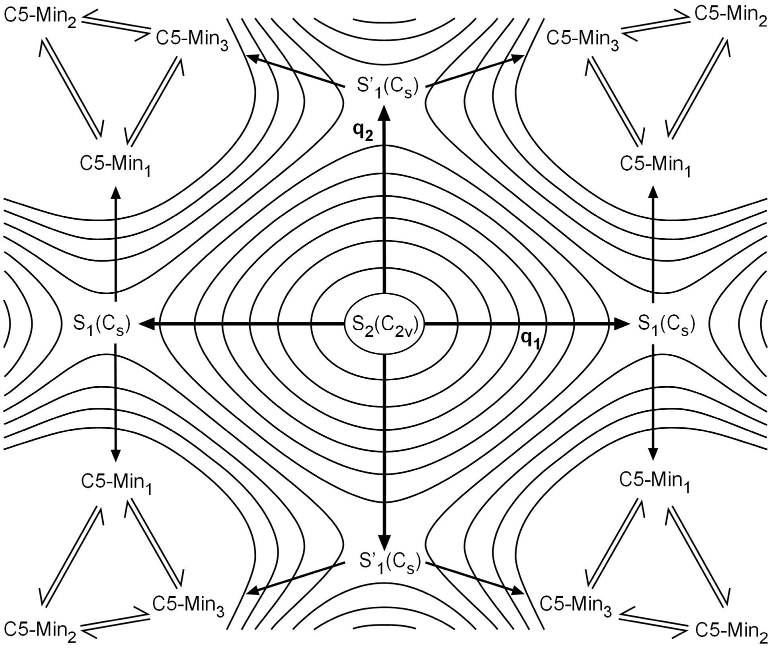

Figure 3. Sketch of the potential energy surface of norbornane^{2+} in its singlet ground state.

A potential energy lowering of 17.43 kcal/mol (Table 2) is observed when distorting and relaxing the S_2 (C_{2v}) structure upon the constraint of the C_s symmetry plane which contains the C and H atoms in the bridge methylenic group (H_1, C_1 and H_2). The obtained transition state (S'$_1$ (C_s) in Figure 4b) is a strongly stretched structure consisting of an ethylene molecule (C_2H_4) bound via charge transfer to a five-membered cyclic dicarbenium dication ($C_5H_8^{2+}$). Indeed, the covalent bond order of the C_4-C_6 bond, as defined by Wiberg [90], has been found to be equal to 1.718. The ethylene fragment borrows a substantial fraction of the double positive charge (+0.36*e*), whereas an absolute NBO charge of +1.64*e* remains localized on the five-membered ring. Comparison of the NBO charges in the S'$_1$ (C_s) species with those of norbornane in its neutral ground state indicates that in this S'$_1$ (C_s) species the double positive charge ascribed to the removal of two electrons dominantly localize on atoms C_2 and C_3 (Table 4).

This observation, as well as the almost planar configuration of substituents attached to the C_2 and C_3 atoms corroborate the idea of an sp^2 hybridization state and the presence of an empty C_{2p} orbital on these atoms. More specifically, the C_1-C_3-H_4-C_7 dihedral angle amounts to 166.7°. The inter-atomic distances C_2- C_4 and C_3- C_6 are found to be equal to 2.65 Å, a value to compare with the C_2-C_5 or C_3-C_7 bond lengths of 1.46 Å. Clearly, symmetry lowering and bond breaking at this stage can already lead to a localization of charges, which preludes the expected Coulomb fragmentation.

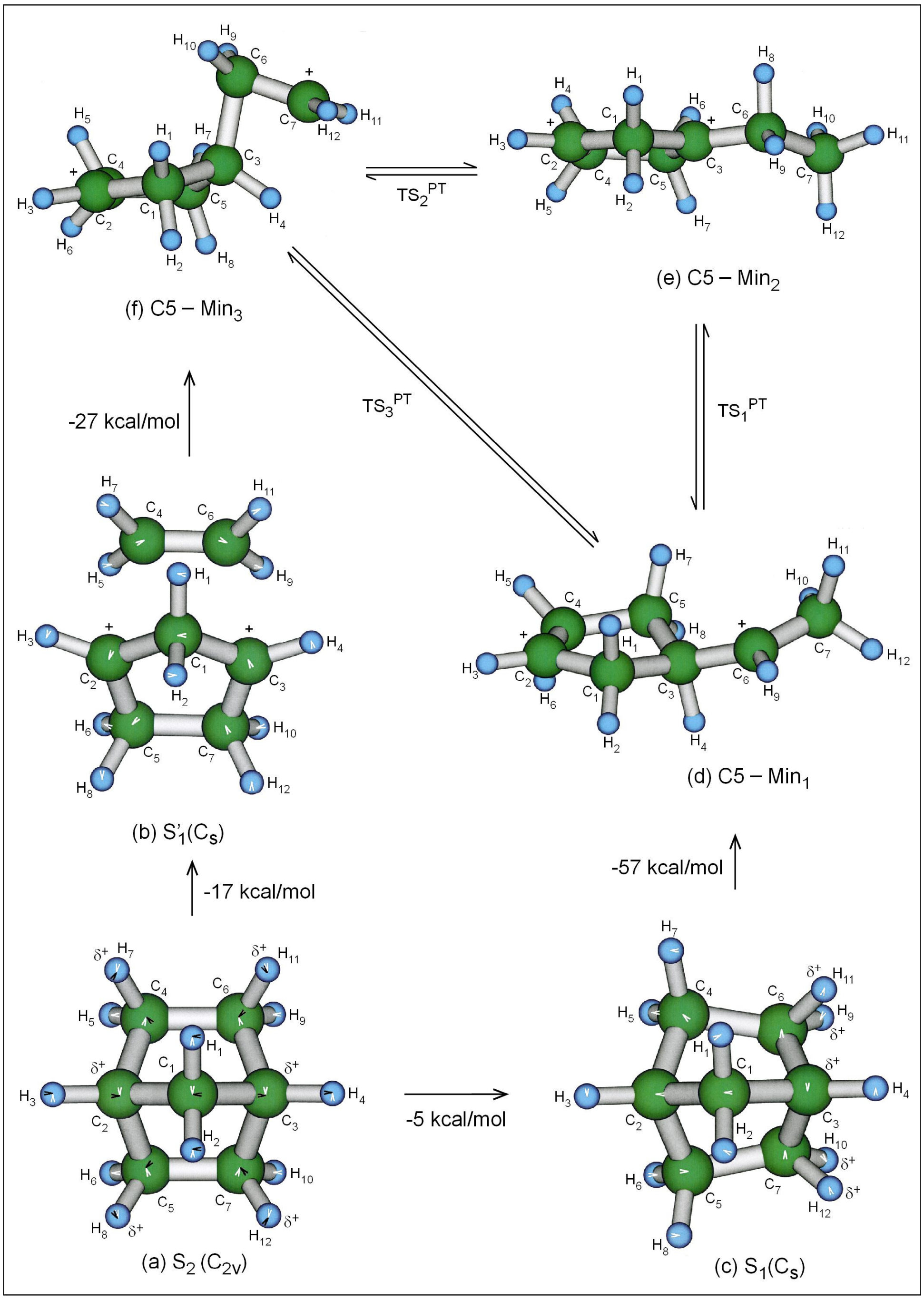
(f) C5 – Min$_3$
TS_2^{PT}
(e) C5 – Min$_2$
-27 kcal/mol
TS_3^{PT}
TS_1^{PT}
(b) S'$_1$(C$_s$)
(d) C5 – Min$_1$
-17 kcal/mol
-57 kcal/mol
-5 kcal/mol
(a) S$_2$ (C$_{2v}$)
(c) S$_1$(C$_s$)
C$_1$
C$_2$
C$_3$
C$_4$
C$_5$
C$_6$
C$_7$
H$_1$
H$_2$
H$_3$
H$_4$
H$_5$
H$_6$
H$_7$
H$_8$
H$_9$
H$_{10}$
H$_{11}$
H$_{12}$
δ+
+

Figure 4

Figure 4. B3LYP/cc-PVDZ study of a non redundant part of the potential energy surface of norbornane^{2+} in its singlet ground state. Darts provide the atomic displacements associated with the vibrational eigenmodes characterized by imaginary frequencies. The δ^+ and + signs indicate moderate and strong localization of the charges created by double ionization, in line with the values reported in boldface in Tables 3 and 4. See Figure 5 for the transition states describing proton transfers. The reported energy variations are B3LYP/cc-pVDZ results. See text for more accurate estimates.

In contrast with this first distortion, distorting and relaxing the S_2 (C_{2v}) structure under the constraint of the symmetry plane containing the {C_1, C_2, C_3} set of atoms enables a (potential) energy lowering by 4.62 kcal/mol only at the B3LYP/cc-pVDZ level (Table 2). A comparison of the charge distribution (Table 3) in the resulting species S_1 (C_s) (Figure 4c) with that of the neutral C_{2v} structure of norbornane indicates (Table 4) a rather pronounced localization of charges produced by double ionization on C_3, H_{11} and H_{12} and to a lesser extent, over H_9, H_{10}, C_6 and C_7. The overall pattern is therefore a localization of one of the two positive charges within the most strongly stretched and angularly distorted part of the molecule (on the right-hand side of Figure 4c). More specifically, the distortions in this species amount to a stretching of the C_3-C_6 (or, through symmetry, C_3-C_7) bonds from 1.63 Å in the S_2 (C_{2v}) structure to 1.66 Å for the S_1 (C_s) one, along with a decrease of the C_7-C_3-C_6 angle from 93.6° to 68.1°. In contrast, and in line with the decrease of the charge density in the region defined by the left hand-side of Figure 4c, the C_2-C_4 and C_2-C_5 bond lengths decrease from 1.67 Å to 1.55 Å, whereas the corresponding C_5-C_2-C_4 bond angle increases from 93.6° to 102.0°. For the sake of comparison, it is worth mentioning that, at the same level, norbornane in its neutral and singlet ground state is characterized by C_4-C_2-C_5 and C_3-C_6-C_7 bond angles that are equal to 108.5°, while values of 1.57 Å and 1.55 Å are found for the C_4-C_6 (C_5-C_7) and C_2-C_4 (C_2-C_5) bond lengths.

Upon distorting the S_1 (C_s) saddle-point according to the vibrational mode associated to the imaginary frequency (296*i* cm^{-1}), the C_3-C_6 bond is found to break and to release, at the B3LYP/cc-pVDZ level, an energy of 56.50 kcal/mol (Table 2) after relaxation into the C5-Min$_1$ species (Figure 4d). The latter structure defines the global energy minimum in the series of all identified structures with a five-membered (C5) ring – hence its working name. After cleavage of the C_3-C_7 bond, two proton transfers are observed during the relaxation process, the first one from C_6 to C_7, and the second one from C_2 to C_4, according to the atom labeling used in Figure 4d. The doubly positive charged product is a $C_5H_8^+$ ring bearing a 1-dehydro-ethyl cation substituent (CH^+-CH_3) in the γ-position relative to the charge center in the ring. In this structure, the largest positive partial charges are located on the C_2 and C_6 carbons. This structure and the above mentioned energy release of 56.50 kcal/mol are the result of a balance between a minimization of the electrostatic Coulomb repulsion and a maximization of stabilizing effects such as hyperconjugation interactions between C-H bonds and empty C_{2p} orbitals, as well as inductive effects which tends to favor localization of charges on carbocations bearing the maximal number of hydrogen substituents. The latter argument is consistent with Markovnikov's rule [91], which states that a highly substituted carbocation is more stable than a less substituted one. Hyperconjugation interactions are directly reflected by the values found for the C_3-C_6-H_9-C_7 and H_4-C_3-C_6-H_9 dihedral angles (176.2° and -84.4°, respectively), from which one may infer in particular that the C_3-H_4 bond lies parallel to the nearby empty C_{2p} orbital. Besides, departures from planarity for the $C_5H_8^+$ ring remain limited, which favor through-space methylenic hyperconjugation interactions [92] between approximately parallel C-H bonds: the C_1-C_2-C_4-C_5, C_2-C_4-C_5-C_3, C_1-C_3-C_5-C_4, C_2-C_1-C_3-C_5 and C_3-C_1-C_2-C_4 angles are for instance equal to -8.2°, 19.5°, -23.3°, 19.0°, and -6.9°, respectively.

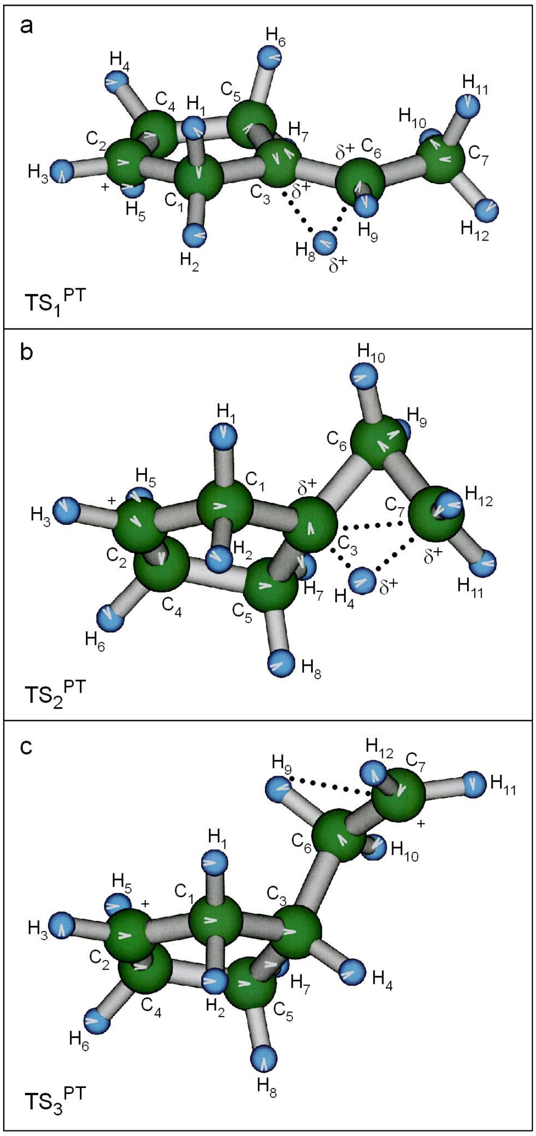

Figure 5. Transition states describing proton transfers (B3LYP/cc-pVDZ structures). Darts provide the atomic displacements associated with the vibrational eigenmodes characterized by imaginary frequencies. The δ^{+} and + signs indicate moderate and strong localization of the charges created by double ionization, in line with the values reported in boldface in Tables 3 and 4.

Enforcing a proton transfer (PT) between the C_3 and C_6 atoms in the C5-Min$_1$ species results into a second minimum referred to as C5-Min$_2$ (Figure 4e), in which an ethyl group is attached to one of the carbocationic centers of the cyclic $C_5H_7^{2+}$ structure. This structures lies at 4.05 kcal/mol above the C5-Min$_1$ species (Table 2). In the C5-Min$_2$ structure, holes are located rather closely to each other on C_2 and C_3 in an almost planar $C_5H_7^{2+}$ cyclic ring (in this ring, the largest dihedral angle [C_1-C_3-C_5-C_4] amounts to 5.8° only. This species is, according to Markovnikov's rule [91], more effectively stabilized than C5-Min$_1$ by inductive effects around the tertiary carbenium atom (C_3), but at the expense of stronger electrostatic repulsions between the charge centers. Here also, hyperconjugation between the C_6-H_8 bond and the empty C_{2p} orbital on C_3 plays an important role, as the C_1-C_3-C_6-H_8 dihedral angle amounts to 78.7°. Note in particular that the Wiberg bond index of C_3-C_6 and the corresponding bond lengths amount to 1.26 and 1.44 Å. The transition state for this proton transfer is TS_1^{PT} (Figure 5) defining an energy barrier of 1.97 kcal/mol only (Table 2) relative to the C5-Min$_2$ species. In line with this and the endothermicity of the transformation from C5-Min$_1$ to C5-Min$_2$, the structure of TS_1^{PT} is found to resemble that of C5-Min$_2$, in agreement with Hammond's principle [91]. For TS_1^{PT}, the transferred proton (H_8) is found at 1.47 Å and 1.26 Å from the C_3 and C_6 atoms. The C_3-H_8 and C_6-H_8 Wiberg bond indices correspondingly amount to 0.309 and 0.469, respectively.

The C5-Min$_3$ minimum (Figure 4f) is found upon distorting the S'$_1$ (C_s) structure according to the mode associated to the imaginary frequency (232*i* cm^{-1}). This geometry relaxation results into an energy lowering of 26.90 kcal/mol (Table 2). The S'$_1$ (C_s) structure can be described as a $C_5H_8^+$ ring bearing this time a 2-dehydro-ethyl cation substituent (CH_2-CH_2^+) in the γ-position relative to the charge center in the ring. In this structure, electrostatic repulsion between the charge centers are clearly minimized, since the interdistance between the C_2 and C_7 atoms is equal to 4.27 Å, to compare with the 3.39 Å separating the C_2 and C_6 atoms. On the other hand, the disadvantage here lies at the level of much less favourable inductive effects around a primary carbenium atom (C_7), in line with Markovnikov's rule. Despite an interdistance of 1.94 Å between the H_4 and C_7 atoms, hyperconjugation between the C_3-H_4 bond and the nearby empty C_{2p} atomic orbital on C_7 is inferred from the H_4-C_3-C_6-C_7 dihedral angle (-0.2°), from the unusually low value of 81.0 ° found for the C_3-C_6-C_7 bond angle, as well as from a Wiberg bond index of 0.794 for the C_3-H_4 bond, indicating that this bond is deprived partly of its electron density. Thus, hyperconjugation here obviously develops at the expense of much more pronounced angular strains. All in all, this energy minimum is thus found to lie at ~16.8 kcal/mol above the C5-Min$_1$ global energy minimum. From Figure 3, it is then clear that the S_2 (C_{2v}) structure defining the central second-order saddle point on the potential energy map will dominantly relax into the C_5-min$_1$ structure, when following the steepest energy gradients without any control on symmetry.

A further pathway connecting the C5-Min$_2$ and C5-Min$_3$ minima could be identified via the transition state TS_2^{PT}, which coincides with a proton transfer from C_3 to C_7 (Figure 5b). This transition state lies at 14.34 kcal/mol and 1.60 kcal/mol above C5-Min$_2$ and C5-Min$_3$, respectively. It can be noticed from Figure 5b that, as the C5-Min$_3$ species to which it closely relates by virtue of Hammond's principle, the ethyl tail of TS_2^{PT} is subject to considerable angular strains. In this structure, the C_3-H_4 and C_7-H_4 bond lengths, and the C_3-C_6-C_7 bond and C_1-C_3-C_6-C_7 torsion angles amount to 1.23 Å, 1.42 Å, 74.4° and 113.3°, respectively. In this structure, the H_4-C_3-C_6-C_7 torsion angle remains equal to 0°. The Wiberg bond indices for the C_3-H_4, C_7-H_4 and C_3-C_7 atomic pairs are correspondingly equal to 0.524, 0.286, and 0.477.

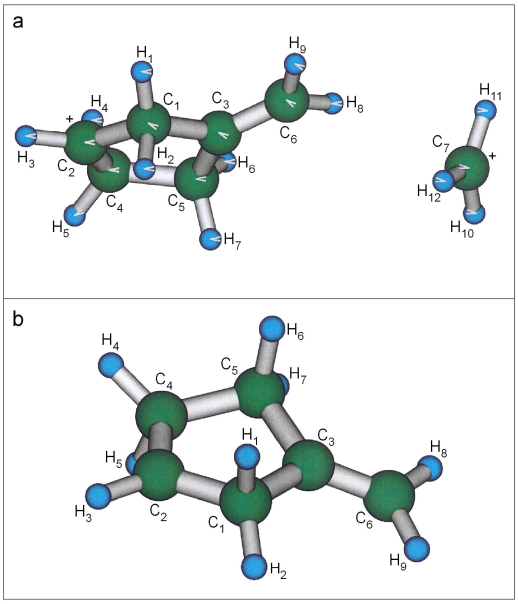

Figure 6. (a) Transition state and (b) product of the radical (homolytic) dissociation of $C_5H_8^+$-CH^+-CH_3 intermediate (the C5-Min$_1$ reference) into $C_5H_7^+$=CH_2 and CH_3^+ (B3LYP/cc-pVDZ results. Darts provide the atomic displacements associated with the vibrational eigenmodes characterized by imaginary frequencies. The + signs indicate strong localization of the charges created by double ionization, in line with the values reported in boldface in Tables 3 and 4.

The C5-Min$_3$ species transforms into the global energy minimum form (C5-Min$_1$) among five-membered cyclic species via the TS$_3^{PT}$ saddle-point structure of Figure 5c. The latter species lies at 2.54 kcal mol^{-1} above C5-Min$_3$, and essentially differs from it by an opening of the C_3-C_6-C_7 bond angle from 81.0° (C5-Min$_3$) to 111.9° (TS$_3^{PT}$). This opening implies a breaking of bonding interactions due to hyperconjugation between the C_3-H_4 bond and empty C_{2p} atomic orbital on C_7, and rotation of the end methylene group (C_7, H_{11}, H_{12}) about the C_3-C_6 bond in order to minimize electrostatic and steric repulsions: after rotation, for TS$_3^{PT}$, the C_2-C_7 inter-atomic distance and C_1-C_3-C_6-C_7 torsion angle are equal to 4.41 Å and 111.9°. In this transition state, the migrating hydrogen atom (H_9) remains closely bound to C_6; the C_6-H_9 bond length and the corresponding Wiberg index amount to 1.11 Å and 0.806, respectively. On the contrary, the bond index of C_6-C_7 is found to be 1.274.

B. Charge fragmentation of five membered monocyclic intermediates

In a next step, dissociation can occur at the B3LYP/cc-pVDZ level through an heterolytic breaking of the C_6-C_7 bond in the $C_5H_7^{2+}$-CH_2-CH_3 (C5-Min$_2$) structure (Figure 6a), giving rise to a methyl cation (CH_3^+) and to a $C_5H_7^+$=CH_2 cation with the charge center in a γ-position relative to the carbon atom bearing the methylene substituent (Figure 6b). This depiction is in line with the charge distributions reported in Table 3, with the relative orientation of substituents around the C_2, C_3 and C_6 atoms, and with a Wiberg covalent bond index of 1.911 for the C_3-C_6 bond in $C_5H_7^+$=CH_2. The transition state for this breaking has been first roughly identified by studying the potential energy curve associated to a progressive stretching of the C_6-C_7 bond in the $C_5H_8^+$-CH^+-CH_3 (C5-Min$_1$) species, using a stepsize of 0.05 Å for the scan. During the elongation, we observed an hydrogen transfer from C_3 to C_6 at C_6-C_7 bond lengths ranging from 1.68 Å to 1.73 Å. The elongation process was pursued until an energy maximum was clearly reached. Optimizing the structure characterizing this maximum under the constraint of one negative curvature led to the TS$^{\mathrm{Dis}}$ structure displayed in Figure 6a. In this structure, C_3-C_6 is already a double bond (with a Wiberg bond index of 1.778). A residual bond between C_6 and C_7 remains partially preserved with a Wiberg bond index of 0.169, while the bond length between these two carbon atoms amounts to 3.68 Å.

At the B3LYP/cc-pVDZ level, the activation enthalpy for the proton transfer from the $C_5H_8^+$-CH^+-CH_3 (C5-Min$_1$) to the $C_5H_7^{2+}$-CH_2-CH_3 (C5-Min$_2$) species is found to be 4.58 kcal/mol (zero-point vibrational energies and thermal corrections included), while the activation enthalpy for the subsequent fragmentation of $C_5H_7^{2+}$-CH_2-CH_3 (C5-Min$_2$) to $C_5H_7^+$=CH_2 + CH_3^+ correspondingly amounts to 36.14 kcal mol^{-1} (see Figure 7). Provided thermal equilibrium with the environment is reached, the $C_5H_8^+$-CH^+-CH_3 and $C_5H_7^{2+}$-CH_2-CH_3 species will be both extremely long lived with respect to charge fragmentation, whereas there will be subject to rapid interconversions via proton transfers. Typically, according to transition state theory [93], using the RRHO partition functions, the related unimolecular reaction rate constants associated to the above barriers at 298K are estimated to be around $6.7 \cdot 10^9$ s^{-1} and $5.2 \cdot 10^{-11}$ s^{-1}, respectively. The corresponding half lifetimes amount to ~0.10 nanoseconds and ~426 years. Note that on the B3LYP/cc-pVDZ energy surface (Figure 7), the $C_5H_7^{2+}$-CH_2-CH_3 (C5-Min$_2$) species corresponds to a very shallow energy minimum.

In line with the proton transfer from C_3 to C_6 induced upon stretching the C_6-C_7 bond in the C5-Min$_1$ species (see above), it is thus worth mentioning that refinement (see further) of the potential energy surface from single-point calculations on B3LYP/cc-pVDZ geometries at the benchmark CCSD(T)/cc-pVDZ level or at an extrapolated CCSD(T)/cc-pV∞Z level (see Table 2) seems to indicate that on the corresponding potential energy surfaces, the $C_5H_7^{2+}$-CH_2-CH_3 (C5-Min$_2$) species and related TS$_1^{\mathrm{PT}}$ transition would become almost iso-energetic, in which case these structures would both essentially coincide (Figure 7) with a thermodynamically insignificant shoulder on a huge energy barrier, of the order of 41 kcal/mol, associated with a straightforward fragmentation of $C_5H_8^+$-CH^+-CH_3 into $C_5H_7^+$=CH_2 and CH_3^+. With such a scenario, considering our best estimate for the activation enthalpy (ZPVE's and thermal corrections included), and a TST value of ~$2.4 \cdot 10^{-13}$ s^{-1} for the associated rate constant, the $C_5H_8^+$-CH^+-CH_3 species would then be characterized by a half-life time of ~9 10^4 years at room temperature. More detailed and costly calculations involving full geometry optimizations at the CCSD(T)/cc-pVDZ level or beyond would be needed for investigating the potential energy surface of norbornane^{2+} within sub-chemical accuracy (ΔE=0.1 kcal/mol) and discriminating which of the two scenarios displayed in Figure 7 is correct.

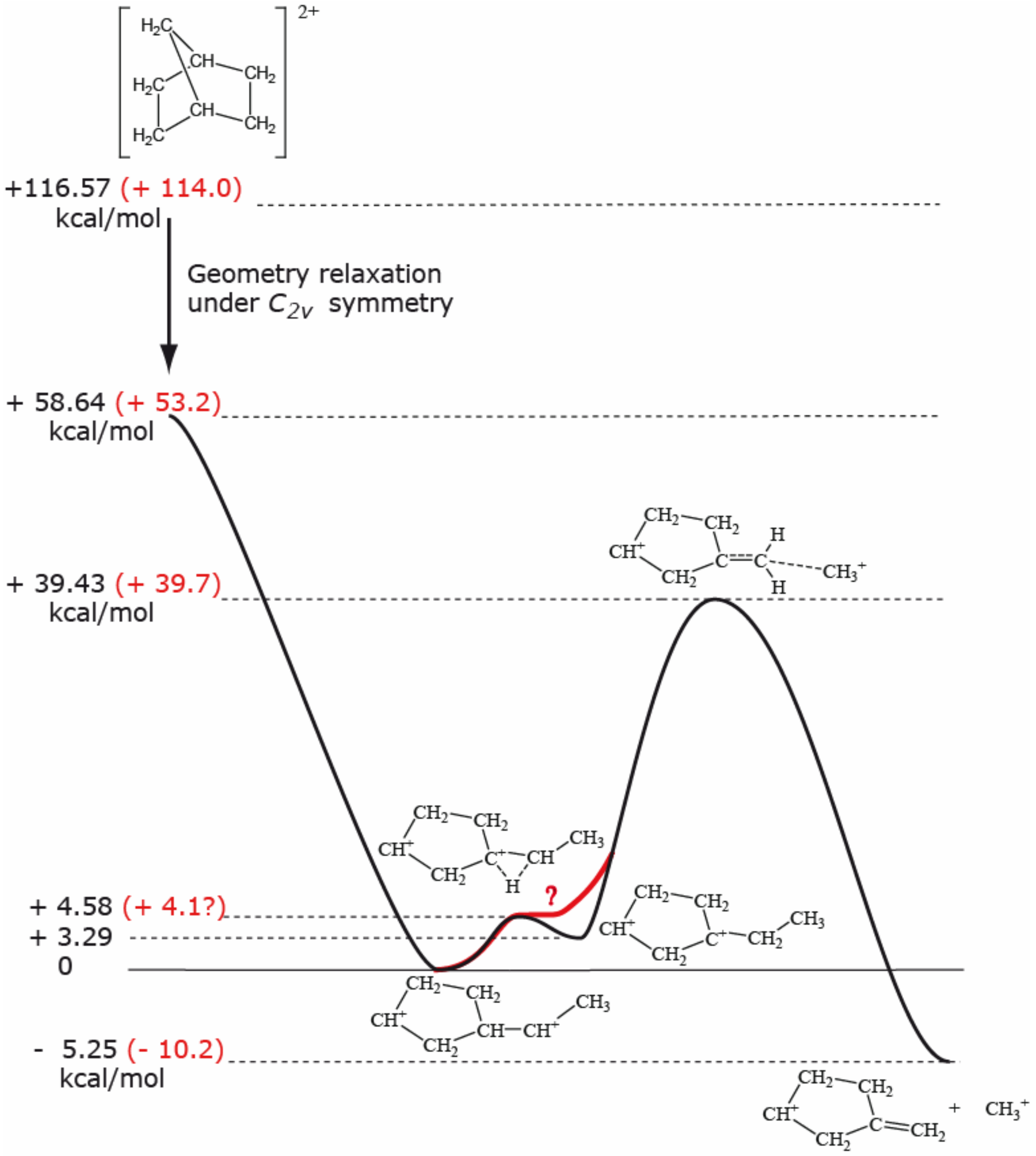

Figure 7. B3LYP/cc-pVDZ (black) and extrapolated CCSD(T)/cc-pV∞Z (red) potential energy pathways associated to relaxation of the vertical double ionized singlet ground state of norbornane^{2+} into the kinetically metastable $C_5H_8^+$-CH^+-CH_3 [C5-Min$_1$] intermediate and fragmentation of the latter into $C_5H_7^+$=CH_2 and CH_3^+ through stretching of the C_6-C_7 chemical bond. The reported values are enthalpy differences relative to the C5-Min$_1$ intermediate.

Whatever the final answer to this issue, it is clear that the initial state in the process is very far from equilibrium, considering the potential energy of ~114 kcal/mol [CCSD(T)/cc-pV∞Z estimate] that can be converted into kinetic energies (rotations, vibrations, and translations) through a relaxation of the vertically doubly ionized singlet form of norbornane into the kinetically metastable $C_5H_8^+$-CH^+-CH_3 [C5-Min$_1$] intermediate and thereafter dissociation of the cage into smaller fragments. After double ionization of norbornane, there will thus certainly be enough energy for overcoming all the energy barriers (see Tables 1 and 2) on the reaction pathways leading to charge fragmentation of this intermediate into $C_5H_7^+$=CH_2 and CH_3^+. Since the reaction is exothermic enough (ΔE = -7.8 kcal/mol, and ΔH_0 = -11.3 kcal/mol, according to our best estimates – see further), this fragmentation will be spontaneous and irreversible under high vacuum conditions. Therefore, at least one efficient and straightforward path for a fragmentation of norbornane^{2+} into two distinct mono-cationic species has been found, which provides support to the scenario invoked for tentatively explaining the origin of band 12 in the EMS ionization spectrum of norbornane (see introduction).

Another likely charge dissipation pathway implies dissociation of the C5-Min$_1$ intermediate into $C_5H_8^+$ and $C_2H_4^+$ doublet radical cations: this reaction is indeed only slightly endothermic (ΔE=3.87 kcal/mol) at the B3LYP/cc-pVDZ level. Other reaction paths have been similarly tested, but at first glance seem less interesting from a thermodynamical viewpoint. The C5-Min$_2$ singlet dicationic species can dissociate into singlet $C_5H_7^+$ and $C_2H_5^+$ radical cations, under a more substantial energy input of 23.88 kcal/mol. Also, an energy of 46.81 kcal/mol is required for dissociating the C5-Min$_3$ dication into $C_5H_8^{2+}$ and C_2H_4 in their singlet ground state.

For comparison purposes, we would like to mention that the dissociation of $C_5H_8^+$-CH^+-CH_3 (C5-Min$_1$) into doublet C_5H_7=CH_2 and CH_3^{2+} species requires more than 370 kcal/mol at the B3LYP/cc-pVDZ level. The latter dication is a loosely bound species of C_{2v} symmetry which is characterized at the same theoretical level by C-H bond lengths (bond orders) equal to 1.65 Å (0.50) and 1.16 Å (1.02). This species is thus obviously prone to a straightforward dissociation into CH_2^+ and H^+. At the B3LYP/cc-pVDZ level, the reaction energy and energy barrier for this process amount indeed to -100.63 kcal/mol and +0.88 kcal/mol, respectively.

Similarly, a dissociation of this intermediate into doublet $[C_5H_7$=$CH_2]^{2+}$ and CH_3 species is also highly unfavourable, in view of an endothermic reaction energy of more than 85 kcal/mol. Note also that, according to our calculations, further fragmentations through deprotonation of the $C_5H_7^+$=CH_2 species are energetically not favorable at all as these would require more than ~100 kcal/mol (~4 eV). Deprotonation of other dicationic species requires similar energies [14].

Considering the energies that are involved in ionization processes, in particular with (e, 2e) experiments employing electron momentum spectroscopy and a kinetic energy of ~1.2 keV for the impinging electron, it is clear that, on long enough timescales, and as with any experiments employing mass spectroscopy, the $C_5H_7^+$=CH_2 species will further decay through bond breaking and fragmentation. Since these processes require considerable energies (100 kcal/mol or more), their time scales go certainly beyond those encountered with electron- or photon-impact ionization spectroscopies such as EMS or UPS. In other words, these pathways go beyond the scope of our article.

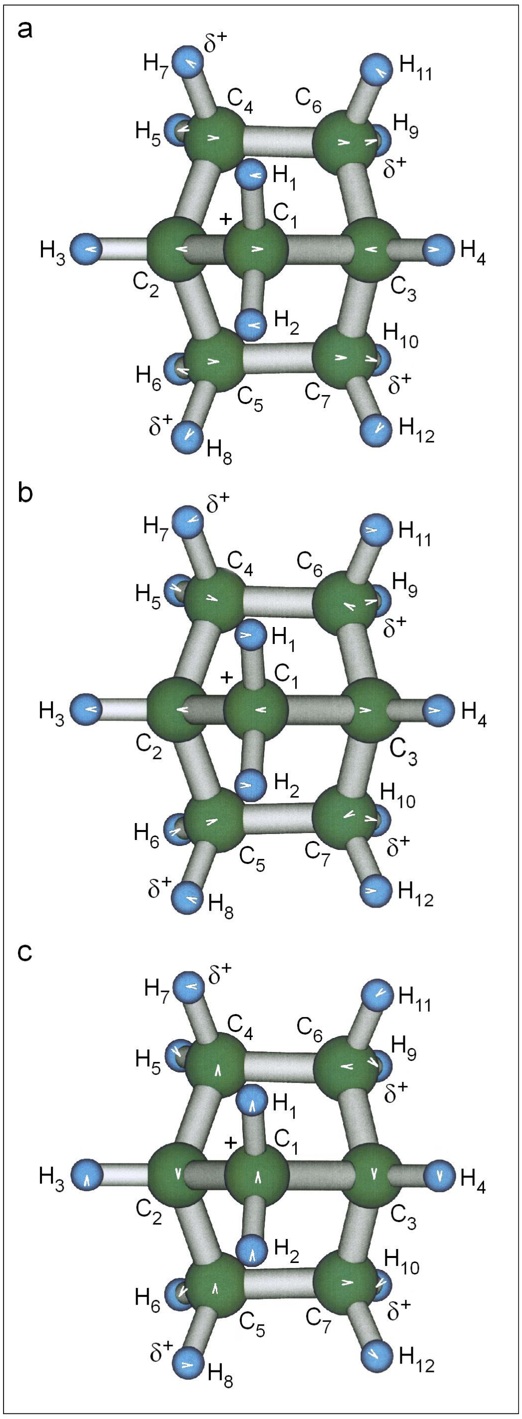

Figure 8. Structure of the third order saddle point *S_3 (C_s)*, along with the atomic displacements defining the three vibrational modes characterized by imaginary frequencies of (a) 658*i* cm^{-1}, (b) 268*i* cm^{-1} and (c) 253*i* cm^{-1} at the B3LYP/cc-pVDZ level. The δ^+ and + signs indicate moderate and strong localization of the charges created by double ionization, in line with the values reported in boldface in Tables 3 and 4.

C. Relaxation of doubly ionized norbornane to a six membered monocyclic species (C_6-Min_4)

Starting again from the S_2 (C_{2v}) structure of Figure 4a, a higher lying third order saddle point S_3 (C_s) could be obtained (Table 2, Figure 8) upon enlarging the C_1-C_2 bond and letting the structure relax under the constraint of a C_s symmetry point group. Further distorting the S_3 (C_s) structure along the antisymmetric mode (Figure 8c) associated to the imaginary frequency 253*i* cm^{-1} and letting the structure relax without symmetry constraints yields a structure that resembles the C5-Min$_1$ structure displayed in Figure 4d, with the only difference that the end CH$^+$-CH$_3$ group has undergone a rotation by ~180° around the C_3-C_6 bond. The obtained structure lies at ~0.21 kcal/mol above C5-Min$_1$, and except for a minor conformational rearrangement is thus almost equivalent to the most stable structure for the identified five membered cyclic species (C5-Min$_x$, x=1,2,3).

In contrast, distorting the above mentioned S_3 (C_s) structure along the symmetric vibrational modes associated with the other two vibrational modes (Figures 8a and b) characterized by imaginary frequencies of 268*i* and 658*i* cm^{-1} results into a breaking of the C_2-C_1-C_3 bridge. In both cases this induces an intramolecular rearrangement into the six-membered monocyclic dicationic species displayed in Figure 9. This species can be described as a 1,4-didehydro-cyclohexane dicationic ring bearing a methyl substituent attached to one of the carbocationic centers. Very interestingly, this structure, referred to as C6-Min$_4$ (C_s) in Table 2 is located 11.87 kcal/mol ***below*** C5-Min$_1$. The two carbenium atoms (C_2 and C_3) are both located in the six-membered ring, and exhibit at a relatively larger interdistance (2.92 Å) than in the C5-Min$_1$ species (3.74 Å). The increase in electrostatic repulsion between the charge centers is thus here compensated by more favorable inductive effects in a structure that contains one tertiary and one secondary carbocation. Here also, hyperconjugation between the empty C_{2p} orbital on C_2 and the adjacent C_1-H_3 bond should favourably stabilize this new dicationic structure. Deprotonation of the methyl-tail of this structure was considered but found to be energetically not favourable at all (ΔE = +105.7 kcal/mol). Also, attempts to find other minima by enforcing a proton transfer from C_1 to C_2 failed: we believe therefore that this structure can be merely regarded as a dead end in our search of suitable routes for an immediate charge fragmentation of norbornane^{2+} in its singlet ground state.

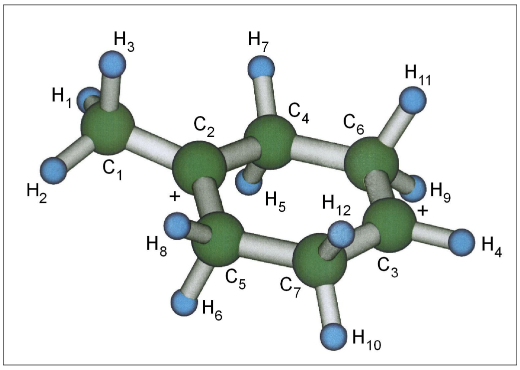

Figure 9. B3LYP/cc-pVDZ molecular structure of the C6-Min$_4$ (C_s) species. The δ^+ and + signs indicate moderate and strong localization of the charges created by double ionization, in line with the values reported in boldface in Tables 3 and 4.

3.3.3.2 Focal point and thermochemical analyses of the potential energy surface of norbornane^{2+}

The B3LYP/cc-pVDZ results that have been discussed so far are supplemented in Table 2 by the results of calculations performed using the MPW1K functional and benchmark energy differences derived from a Focal Point Analysis (FPA) of estimates obtained by means of correlation treatments and basis sets of improving quality (Table 5 – included at the end of this chapter). As can be seen from Table 2, most conclusions that have been drawn so far from calculations at a rather qualitative level resist a more robust and quantitative analysis. Considering the height of the computed barriers, B3LYP/cc-pVDZ energy differences and the results of single point MPW1K/cc-pVDZ//B3LYP/cc-pVDZ energy calculations are found to be overall in good agreement, within relative accuracies of the order of 10%. The B3LYP values tend in general to underestimate the MPW1K ones by 5-10 kcal/mol, which is consistent with former studies of intramolecular rearrangements using these functionals [82-86, 91, 92].

Reoptimizing at the MPW1K/cc-pVDZ level the structures of the identified transition states is found also in general to have only minor effects on the computed energy differences. All transition states and minima are in general correspondingly very comparable with the B3LYP/cc-pVDZ ones, both structurally and in view of the computed bond orders and charge distributions. One exception arises with the S_1 (C_s) transition state, the structure of which is found to be extremely sensitive to the employed functional. It is a 1, 5-didehydro-cyclopentane dicationic ring bearing an ethyl substituent in a γ-position relative to the first carbocationic center with, countra-intuitively, partial positive charges that are located quite close to each other, on the C_6 and C_7 atoms. All transition states and minima are in general correspondingly very comparable with the B3LYP/cc-pVDZ ones, both structurally and in view of the computed bond orders and charge distributions. Another difference arises with the C5-Min$_3$ structure, which corresponds to a rather shallow and high-lying energy minimum on the B3LYP/cc-pVDZ potential energy surface. This energy minimum, as well as the related transition states for proton transfers, could not be identified at the MPW1K/cc-pVDZ level, which presumably reflects the importance of through-space non-bonding interactions in this structure, which the MPW1K functional may underestimate due to the high proportion of Hartree-Fock exchange. All in all, and in contrast with former works employing comparatively these two functionals, it appears that, whatever the geometry, the B3LYP/cc-pVDZ results are most generally closer to results obtained at the CCSD(T)/cc-pVDZ level or from a benchmark Focal Point Analysis (FPA). This justifies *a postiori* the use of the B3LYP/cc-pVDZ approach for computing the potential energy surface of norbornane^{2+}.

We now examine in details the determination within the confines of non-relativistic quantum mechanics, i.e. via the FPA procedure, of the energies of all identified stationary points relative to the C5-Min$_1$ structure. The values reported in Table 5 under the ΔHF entries correspond to energy differences at the HF level, whereas the values reported in the +MP2, +MP3, +CCSD, +CCSD(T) entries are the corrections to these differences obtained by successively comparing the MP2 with the HF results, the MP3 with the MP2 results, the CCSD with the MP3 results, and, at last, the CCSD(T) with the CCSD results. In each column, the sum of the reported values up to a given row associated to a specific theoretical model gives thus the relative energy for that model chemistry in particular.

As a main example we consider the evaluation of the energy of the S_2 (C_{2v}) species relative to the C5-Min$_1$ reference. From Table 5, it is clear that, despite the importance of the corresponding energy difference in this case, results obtained at the HF level converge extremely fast with basis sets of increasing size, and extrapolation to the limit of an asymptotically complete basis set within an accuracy of ~0.05 kcal/mol is straightforward therefore. Corrections for electronic correlation at the second-order and, to a lesser extent, third-order level of Møller-Plesset Perturbation Theory are found to be large, and converge more slowly to basis set completeness. Nonetheless, a comparison of results obtained using the cc-pVTZ and cc-pVQZ basis sets as well as with the asymptotically complete cc-pV∞Z basis set (according to Schwartz' extrapolation procedure described in section II) indicates convergence of the MP2 energy differences within ~0.2 kcal/mol. Since in absolute value the successive correlation corrections tend to strongly decrease with the order attained in perturbation theory, it can be reasonably assumed that the +MP3/cc-pVTZ, +MP4SDQ/cc-pVDZ, +CCSD/cc-pVDZ and +CCSD(T)/cc-pVDZ corrections represent optimal estimates of results that would be obtained using larger basis sets. Despite the oscillatory behaviour of these corrections, this allows a determination of the S_2 (C_{2v}) – C5-Min$_1$ (C_1) energy difference at the CCSD(T)/cc-pV∞Z level, as follows : 102.68 – 64.59 + 23.29 + 2.78 + 0.40 – 8.85 = 55.71 kcal/mol. Note nonetheless that triple excitations have here a rather substantial influence on the final results, which is rather typical of a strongly stretched structure that is thus subject to significant electron correlation effects. Note also that in general the successive correlation corrections tend to scale proportionally to the computed energy differences and that the influence of triple excitations is comparatively much more limited for energy minima, as it should.

For the sake of completeness, a thermochemical refinement of the potential energy surface is at last provided in Table 6 (included at the end of this chapter). In this table, enthalpy differences at 0K are calculated by adding to the benchmark FPA estimates (unrescaled) B3LYP/cc-pVDZ zero-point vibrational energies. Enthalpy differences at room temperature are evaluated by adding further thermal corrections derived from statistical thermodynamical partition functions calculated at the same level for energy minima and transition states using the RRHO approximation. Contribution from mechanical work (RT) against external pressure is accounted for in the evaluation of the reaction enthalpy for the dissociation of the $C_5H_8^+$-CH^+-CH_3 intermediate (the C5-Min$_1$ reference) into $C_5H_7^+$=CH_2 and CH_3^+. These data are supplemented by entropy differences obtained from the same partition functions, which have been in turn used to calculate Gibb's free energy differences. As can be seen, all zero-point, thermal enthalpy and entropy corrections have a marginal influence on the energy barriers and reaction energies pertaining to intramolecular rearrangements and proton transfers. For instance, the C6-Min$_4$ (C_s) species is located at 11.87 kcal/mol below the C5-Min$_1$ species at the B3LYP/cc-pVDZ level. This energy difference reduces to 10.16 kcal/mol according to the focal-point analysis, yielding in turn a Gibbs' free energy difference amounts of 10.37 kcal/mol in favour of the C6-Min$_4$ species (Table 6).

In contrast, entropy effects are found to very substantially lower the reaction energy calculated for the dissociation of the $C_5H_8^+$-CH^+-CH_3 intermediate (the C5-Min$_1$ reference) into $C_5H_7^+$=CH_2 and CH_3^+, which is typical of radical dissociations [88]. Translations and rotations provide substantial positive contributions to the reaction enthalpy, whereas the vibrational contribution is negative and comparatively smaller in absolute value. These variations simply relate to the fact that, because of the cleavage of the $C_5H_8^+$-CH^+-CH_3 intermediate into smaller species, three additional rotational and three additional translation modes become available at the expense of six vibrational modes. Note that the rotational entropy of the $C_5H_7^+$=CH_2 species is only ~ 1.37 cal mol^{-1} K^{-1} below that of the $C_5H_8^+$-CH^+-CH_3 intermediate, therefore the increase in rotational entropy can be ascribed to the emission of a much smaller and rapidly spinning CH_3^+ moiety.

3.3.4 Conclusions

The main purpose of the present work was to identify at least one suitable pathway for a straightforward and ultra-fast fragmentation of norbornane^{2+} into two distinct monocationic species, in an attempt to qualitatively explain a very unusually intense band at electron binding energies around the double ionization threshold in the EMS ionization spectrum of the neutral [39, 40]. The potential surface of norbornane in its dicationic singlet ground state has been therefore investigated in details using Density Functional Theory along with the non-local hybrid and gradient corrected Becke three-parameter Lee-Yang-Parr functional (B3LYP) and the cc-pVDZ basis set. For the sake of more quantitative insights into these processes, this study was supplemented by a calculation of basic thermodynamical state functions coupled to a Focal Point Analysis of energy differences obtained using correlation treatments and basis sets of improving quality, enabling an extrapolation of these energy differences at the CCSD(T) level in the limit of an asymptotically complete (cc-pV∞Z) basis set.

Our best results indicate that geometrical relaxation of the vertical double ionized state within the C_{2v} point group leads to a lowering of the molecular potential energy by 58.3 kcal/mol. 55.7 kcal/mol can be further converted into kinetic forms of the energy by a bond breaking and straightforward rearrangement of the doubly charged norbornane cage into a five-membered cyclic $C_5H_8^+$-CH^+-CH_3 intermediate, with the ethyl cation substituent (CH^+-CH_3) in the γ-position relative to the charge center in the five-membered cyclic ring. This process and the associated proton transfers were found to enable charge localization within different parts of the molecule. They are influenced by various competitive factors such as electrostatic interactions, inductive effects, cyclic strains, and methylenic hyperconjugation interactions. The above intermediate can be regarded as a kinetically metastable species, defining the entry gate towards the dissociation pathway of norbornane^{2+} into $C_5H_7^+$=CH_2 and CH_3^+. Indeed, according to our best estimates, the corresponding reaction and activation enthalpies at 298K and 1 atm amount to -10.2 kcal/mol and + 39.7 kcal/mol, respectively. The heterolytic charge fragmentation of the $C_5H_8^+$-CH^+-CH_3 singlet species into $C_5H_7^+$=CH_2 and CH_3^+ singlet species involves possibly a transient or short-lived $C_5H_7^{2+}$-CH_2-CH_3 species at ~ 3.3 to 5.3 kcal/mol above the $C_5H_8^+$-CH^+-CH_3 intermediate: this structure corresponds to a shallow energy minimum on the B3LYP/cc-pVDZ surface, and possibly to an energy shoulder on the potential energy curve associated to the fragmentation channel at a benchmark many-body quantum mechanical level (CCSD(T)/cc-pV∞Z). In view of an estimated energy barrier of 5.0 to 6.0 kcal/mol only, this proton transfer will be certainly favoured by pronounced tunnelling effects [94], and may therefore be regarded as incommensurably faster than the charge fragmentation itself. Entropy effects were found to tremendously favour the charge fragmentation, through a contribution of -11.4 kcal mol^{-1} to the Gibbs' free reaction energy at 298K.

In our quest for additional straightforward pathways and clues for an ultra-fast Coulomb fragmentation of norbornane^{2+}, an opening of the methylene bridge led us to identify a six-membered cyclic structure [$C_6H_9^{2+}$-CH_3] in the form of 1,4-didehydro-cyclohexane dicationic ring bearing a methyl substituent attached to one of the carbocationic centers, at an energy of 10.2 kcal/mol below the $C_5H_8^+$-CH^+-CH_3 species, according to our best estimates. On the singlet ground state potential energy surface of norbornane^{2+}, this structure can be regarded as a dead end on short time scales ($< 10^{-9}$ s), since a charge fragmentation into distinct monocationic species would at least imply the breaking of two single C-C bonds.

Considering the energy released (ΔH_{298} = 114.0 kcal/mol) by molecular relaxation of norbornane^{2+} after a sudden removal of two electrons from the neutral, compared with the energy barrier ($\Delta H^{\dagger}_{298}$= 39.7 kcal/mol) to overcome for a charge fragmentation of the $C_5H_8^+$-CH^+-CH_3 intermediate, it seems more than plausible that, at ionization energies around the double ionization threshold, and following a purely electronic, and thus, straightforward *intra*molecular Coulomb decay of shake-up states into dissociative shake-off states, norbornane becomes subject to ultra-fast nuclear dynamical processes involving intramolecular rearrangements and a Coulomb explosion into mono-cationic species. Since a vertical double ionization process leads to a second-order saddle-point under relaxation within the C_{2v} point group, a breaking of the Born-Oppenheimer approximation is likely to occur, in line with the range of timescales (~10^{-15} s to ~10^{-13} s) inferred previously [40] for these rearrangement processes from a comparison of UPS (He I) and EMS (E_k=1.5 keV) measurements. Ultrafast nuclear dynamics would then explain the unusually large width of the bands observed at electron binding energies above ~25 eV [39], indicating considerable natural broadening due to very limited lifetimes. Ultra-fast nuclear dynamics might also be related to the unusually large (e, 2e) ionization intensities recorded under the EMS conditions at these electron binding energies. An argument in favor of this fairly daring hypothesis is a very severe turn-up [95] of the (e, 2e) ionization intensity associated to the fully dissociative $^2\Sigma_u(2p\sigma_u)$ shake-up state of H_2, which so far still elude all theoretical explanations, even upon considering advanced (second-order Born) treatments of distorted wave effects [96]. It is thus worth reminding that the interaction operator governing transition amplitudes in (e, 2e) ionization processes explicitly depends on the electronic *and nuclear* coordinates [97]. We have thus the feeling that the final answer to the band 12 issue in the EMS ionization spectrum of norbornane might be strongly related to the dissociative nature of the potential energy surface that has been computed for the dicationic ground state of this compound.

To be fully reliable, a complete interpretation of EMS experiments on norbornane throughout the valence region of norbornane should therefore consistently cover the four spaces underlying quantum mechanics, namely Energy, Time, Configuration and Momentum spaces. In our work, we simply studied within the framework of the Born-Oppenheimer approximation the structural consequences of a double ionization event resulting from the sudden removal of two electrons, assuming that in the initial state no residual nuclear kinetic energy remains. In other words, we have considered as initial state the shake-off state which lies precisely at an electron binding energy equal to the vertical double ionization energy of norbornane (~26.5 eV according to our best data). Note that the initial state in the geometrical process lies high above the energy barrier leading to dissociation of the cage into smaller fragments, and is thus not subject to a quantization of the vibrational and rotational energies over stationary states. On the contrary, vibrational and rotational motions for the states above the double ionization threshold that would be generated using high energy photons are by definition of transient nature, as these states are embedded in an energy continuum. Further studies employing nuclear dynamics [98] or wave packet dynamics [99] around conical intersections [100] will probably be necessary for quantitatively evaluating the effects of vibrational and rotational excitations on the dynamics that can be predicted from the computed potential energy landscape, and for investigating the influence of the identified intra-molecular rearrangement and charge dissociation processes on the innermost valence ionization spectrum of norbornane, as well as on the corresponding electron distributions in the configuration and momentum spaces.

References

[1] Shields, G.C.; Moran, T.P. *Theor. Chim. Acta* 1986, 69, 147.

[2] Lammertsma, K.; von R. Schleyer, P.; Schwarz, H. *Ang. Chem. Int. Ed.* 1989, 28, 1321.

[3] Mathur, D. *Phys. Rep.* 1993, 225, 193.

[4] See a special issue on multiply charged ions in *Int. J. Mass. Spectrom.* 1999, 192.

[5] Schröder, D.; Schwarz, H. *J. Phys. Chem. A* 1999, 103, 7385.

[6] Nenajdenko, V. C.; Shevchenko, N. E.; Balenkova, E. S.; Alabugin, I. V. *Chem. Rev.* 2003, 103, 229.

[7] Mathur, D. *Phys. Rep.* 2004, 391, 1.

[8] Basch, H.; Hoz, S.; Goldberg, M. *Isr. J. Chem.* 1993, 33, 403.

[9] Hensen, K.; Stumpf, T.; Bolte, M.; Nätscher, C.; Fleischer, H. *J. Am. Chem. Soc*. 1998, 120, 10402.

[10] Tafadar, N.; Kaltsoyanis, N.; Price, S. D. *Int. J. Mass. Spectrometry* 1999, 192, 205.

[11] Kroto, H. W.; Heath, J.R.; O'Brion, S.C.; Curl, R.F.; Smalley, R.E. *Nature* 1985, 318, 162.

[12] Cioslowski, J.; Patchovski, S.; Thiel, W. *Chem. Phys. Lett.* 1996, 248, 116.

[13] (a) Scheier, P.; Märk, T.D. *Phys. Rev. Lett.* 1994, 73, 54; (b) Jin, J.; Khemliche, H.; Prior, M. H.; Xie, Z. *Phys. Rev. A* 1996, 53, 615.

[14] Deleuze, M.S.; François, J.-P.; Kryachko, E. *J. Am. Chem. Soc.* 2005, 127, 16824.

[15] Nicolaides, C.A. *Chem. Phys. Lett.* 1989, 161, 547.

[16] (a) Benoit, C.; Horsley, J.A. *Mol. Phys.* 1975, 30, 557; (b) Lammertsma, K.; Barzaghi, M.; Olah, G.A.; Pople, J.A.; Kos, A.J.; von R. Schleyer, P. *J. Am. Chem. Soc.* 1983, 105, 5252.

[17] Maier, G. *Angew. Chem.* 1988, 100, 317.

[18] Carnadi, H.; Giordano, C.; Heldeweg, R.F.; Hogeveen, H.; E. M. G. A. van Kruchten *Isr. J. Chem.* 1981, 21, 229.

[19] Prakash, G.K.S.; Krishnamurthy, V.V.; Herges, R.; Bau, R.; Yuan, H.; Olah, G.A. *J. Am. Chem. Soc.* 1986, 108, 836; (b) Prakash, G.K.S.; Krishnamurthy, V.V.; Herges, R.; Bau, R.; Yuan, H.; Olah, G.A.; Fessner, W. D.; Prinzbach, J. *J. Am. Chem. Soc.* 1988, 110, 7764; (c) Weber, K.; Lutz, G.; Knothe, L.; Mortensen, J.; Heinze, J.; Prinzbach, H. *J. Chem. Soc. Perkin Trans. 2* 1995, 1991.

[20] (a) Bremer, M.; Schleyer, P. v. R.; Schoetz, K.; Kausch, M.; Schindler, M. *Ang. Chem., Int. Ed. Engl.* 1987, *26*, 761; (b) Fokin, A.A.; Kiran, B.; Bremer, M.; Yuang, X.M.; Jiao, H.J.; Schreiner, P.R. *Chem. Eur. J.* 2000, 6, 1615.

[21] Price, S. D.; Manning, M.; Leone, S. R. *J. Am. Chem. Soc.* 1994, *116*, 8673.

[22] Price, S. D. *Phys. Chem. Chem. Phys.* 2003, 5, 1717.

[23] Roithová, J.; Herman, Z.; Schröder, D.; Schwarz, H. *Chem.-Eur. J.* 2006, 12, 2465.

[24] Roithová, J.; Schröder, D.; Schwarz, H. *J. Phys. Chem. A* 2004, 108, 5060.

[25] Roithová, J.; Schröder, D.; Schwarz, H. *Chem.-Eur. J.* 2005, 11, 627.

[26] Roithová, J.; Schröder, D.; Loos, J.; Schwarz, H.; Jankowiak, H.-Ch.; Berger, R.; Thissen, R.; Dutuit, O. *J. Chem. Phys.* 2005, 122, 094306.

[27] Leach, S. W. *Z. Phys. Chem.* 1996, 195, 15.

[28] Buchbauer, G.; Pauzenberger, I. *Pharmazie* 1999, 54, 5.

[29] Chiang, J. F.; Wilcox, C. F.; Bauer, S. H. *J. Am. Chem. Soc.* 1968, 90, 3149.

[30] Choplin, A. *Chem. Phys. Lett.* 1980, 71, 503.

[31] Bischof, P.; Hashmall, J. A.; Heilbronner, E; Hornung, V *Helv. Chim. Acta* 1969, 52, 1745.

[32] Getzlaff, M.; Schönhense, G. *J. Electr. Spectr. & Rel. Phen.* 1998, 95, 225.

[33] Bieri, G.; Burger, F.; Heilbronner, E.; Maier, J. P. *Helv. Chim. Acta* 1977, 60, 2213.

[34] Weigold, E.; McCarthy, I. E. *Electron Momentum Spectroscopy*; Kluwer Academic/Plenum Publishers: New York, 1999.

[35] Schirmer, J.; Cederbaum, L. S.; Walter, O. *Phys. Rev. A* 1983, 28, 1237.

[36] Schirmer, J.; Angonoa, G. *J. Chem. Phys.* 1989, 91, 1754.

[37] Weikert, H. G.; Meyer, H.-D.; Cederbaum, L. S.; Tarantelli, F. *J. Chem. Phys.* 1996, 104, 7122.

[38] Deleuze, M. S.; Giuffreda, M. G.; François, J.-P.; Cederbaum, L. S. *J. Chem. Phys.* 1999, 111, 5851.

[39] Knippenberg, S.; Nixon, K. L.; Brunger, M. J.; Maddern, T.; Campbell, L.; Trout, N.; Wang, F.; Newell, W. R.; Deleuze, M. S.; François, J.-P.; Winkler, D. A. *J. Chem. Phys.* 2004, 121, 10525.

[40] Knippenberg, S.; Deleuze, M. S.; Cleij, T. J.; François, J.-P.; Cederbaum, L. S.; Eland, J. H. D. *J. Phys. Chem. A* 2005, 109, 4267.

[41] Cederbaum, L. S.; Zobeley, J.; Tarantelli, F. *Phys. Rev. Lett.* 1997, 79, 4778.

[42] Marburger, S.; Kugeler, O.; Hergenhahn, U.; Möller, T. *Phys. Rev. Lett.* 2003, 90, 203401.

[43] Jahnke, T.; Czasch, A.; Schöffler, M. S.; Schössler, S.; Knapp, A.; Käsz, M.; Titze, J.; Wimmer, C.; Kreidi, K.; Grisenti, R. E.; Staudte, A.; Jagutzki, O.; Hergenhahn, U.; Schmidt-Böcking, H.; Dörner, R. *Phys. Rev. Lett.* 2004, 93, 163401

[44] Frisch, M. J.; Trucks, G. W.; Schlegel, H. B. *et al.*, *GAUSSIAN 98* (Revision A.7); Gaussian, Inc., Pittsburgh, PA, 1998.

[45] (a) Lee, C.; Yang, W.; Parr, R. G. *Phys. Rev. B* 1988, 37, 785; (b) Becke, A. D. *J. Chem. Phys.* 1993, 98, 5648.

[46] Dunning, T. H. Jr. *J. Chem. Phys.* 1989, 90, 1007.

[47] Simons, J.; Jorgensen, P.; Taylor, H.; Ozment, J. *J. Phys. Chem.* 1983, 87, 2745.

[48] Peng, C.; Schlegel, H. B. *Israel J. Chem.* 1994, 33, 449.

[49] Peng, C.; Ayala, P. Y.; Schlegel, H. B.; Frisch, M. J. *J. Comp. Chem.* 1996, 17, 49.

[50] Seeger, R.; Pople, J. A. *J. Chem. Phys.* 1977, 66, 3045.

[51] Bauernschmitt, R.; Ahlrichs, R. *J. Chem. Phys.* 1996, 104, 9047.

[52] Cizek, J. *Adv. Chem. Phys.* 1969, 14, 35.

[53] Purvis, G. D.; Bartlett, R. J. *J. Chem. Phys.* 1982, 76, 1910.

[54] Scuseria, G. E.; Janssen, C. L.; Schaefer III, H. F. *J. Chem. Phys.* 1988, 89, 7382.

[55] Scuseria, G. E. ; Schaefer III, H. F. *J. Chem. Phys.* 1989, 90, 3700.

[56] Lee, T. J.; Taylor, P. R. *Int. J. Quantum Chem. Symp.* 1989, 23, 199.

[57] (a) Werner, H.-J.; Knowles, P. J.; Lindh, R., *et al.*, *MOLPRO*, version 2000.1, a package of ab initio programs, see http://www.molpro.net. (b) Lindh, R.; Ryu, U.; Liu, B. *J. Chem. Phys.* 1991, 95, 5889. (c) Hampel, C.; Peterson, K.; Werner, H.-J. *Chem. Phys. Lett.* 1992, 190, 1.

[58] Roos, B. O.; Taylor, P. R.; Siegbahn, P. E. M. *Chem. Phys.* 1980, 48, 157.

[59] McQuarrie, D. A. *Statistical Mechanics*; University Science Books, Sausalito, California, 2000.

[60] Glendening, E. D.; Reed, A. E.; Carpenter, J. E.; Weinhold, F *NBO Version 3.1*.

[61] Carpenter, J. E.; Weinhold, F. *J. Mol. Struct. (THEOCHEM)* 1988, 169, 41.

[62] Foster, J.P.; Weinhold, F. *J. Am. Chem. Soc.* 1980, 102, 7211.

[63] Reed, A.E.; Weinhold, F. *J. Chem. Phys.* 1983, 78, 4066.

[64] Reed, A.E.; Weinhold, F. *J. Chem. Phys.* 1983, 78, 1736.

[65] Reed, A.E.; Weinstock, R.B.; Weinhold, F. *J. Chem. Phys.* 1985, 83, 735.

[66] Reed, A.E.; Curtiss, L.A.; Weinhold, F. *Chem. Rev.* 1988, 88, 899.

[67] Weinhold, F.; Carpenter, J.E. in *The Structure of Small Molecules and Ions*; Naaman, R; Vager, Z., Eds.; Plenum: New York, 1988; pp 227-236.

[68] Szabo, A.; Ostlund, N. S. *Modern Quantum Chemistry: Introduction to Advanced Electronic Structure Theory*; Dover Publications Inc.: New York, 1996.

[69] Møller, C.; Plesset, M. S. *Phys. Rev.* 1934, 46, 618.

[70] Binkley, J. S.; Pople, J. A. *Int. J. Quant. Chem.* 1975, 9, 229.

[71] Pople, J. A.; Binkley, J. S.; Seeger, R. *Int. J. Quantum Chem. Symp.* 1976, 10, 1.

[72] Krishnan, R.; Pople, J. A. *Int. J. Quant. Chem.* 1978, 14, 91.

[73] Pople, J. A.; Head-Gordon, M.; Raghavachari, K. *J. Chem. Phys.* 1987, 87, 5968.

[74] Allinger, N. L.; Fermann, J. T.; Allen, W. D.; Schaefer III, H. F. *J. Chem. Phys.* 1997, 106, 5143.

[75] Salam A.; Deleuze, M. S. *J. Chem. Phys.* 2002, 116, 1296.

[76] Kwasniewski, S. P.; Claes, L.; François, J.-P.; Deleuze, M. S. *J. Chem. Phys.* 2003, 118, 7823.

[77] Huang, Y. R.; Knippenberg, S.; Hajgato, B.; François, J.-P.; Deng, J. K.; Deleuze, M. S. *J. Phys. Chem. A* 2007, 111, 5879.

[78] Feller, D. *J. Chem. Phys.* 1992, 96, 6104.

[79] Feller, D. *J. Chem. Phys.* 1993, 98, 7059.

[80] Martin, J. M. L.; *Ab Initio Thermochemistry Beyond Chemical Accuracy for First- and Second-Row Compounds*, in NATO ASI Symposium volume *Energetics of Stable Molecules and Reactive Intermediates*; Mirrasda Piedade, M. E. and Irikura, K. K, Eds.; Kluwer: Dordrecht, The Netherlands, 1999.

[81] Schwartz, C. in *Methods in Computational Physics 2*; Alder, B. J., Ed.; Academic: New York, 1963.

[82] Lynch, B. J.; Truhlar, D. G.; *J. Phys. Chem. A* 2001, 105, 2936.

[83] Deleuze, M.S.; Claes, L.; Kryachko, E.S.; François, J.-P.; *J. Chem. Phys.* 2003, 106, 8569.

[84] Zhao, Y.; Truhlar, D. G. *J. Phys. Chem. A* 2004, 108, 6908.

[85] Zhao, Y.; Lynch, B. J.; Truhlar, D. G. *J. Phys. Chem. A.* 2004, 108, 4786.

[86] Zhao, Y.; Pu, J.; Lynch, B. J.; Truhlar, D. G. *Phys. Chem. Chem. Phys.* 2004, 6, 673.

[87] Lynch, B. J.; Fast, P. L.; Harris, M.; Truhlar, D. G.; *J. Phys. Chem. A* 2000, 104, 4811.

[88] Claes, L.; François, J.-P.; Deleuze, M. S. *J. Am. Chem. Soc.* 2003, 125, 7129.

[89] Claes, L.; François, J.-P.; Deleuze, M. S. *J. Comp. Chem.* 2003, 24, 2023.

[90] Wiberg, K. *Tetrahedron* 1968, 24, 1083.

[91] McMurry, J. *Organic Chemistry*; Brooks/Cole: Belmont, California, 2004.

[92] Deleuze, M.; Denis, J.-P.; Delhalle, J.; Pickup, B.T. *J. Phys. Chem.* 1993, 97, 5115.

[93] Gilbert, R.G.; Smith, S. C. *Theory of Unimolecular and Recombination Reactions*, Blackwell Scientific Publications: Oxford, 1990.

[94] Cukier, R. I. *J. Phys. Chem.* 1995, 99, 16101.

[95] Takahashi, M.; Khajuria, Y.; Udagawa, Y. *Phys. Rev. A* 2003, 68, 042710; (b) M. Takahashi, M.; Watanabe, N.; Khajuria, Y.; Nakayama, K.; Udagawa, Y.; Eland, J.H.D. *J. Electron Spectr. Relat. Phenom.* 2004, 141, 83.

[96] Dal Capello, C.; Mansouri, A.; Houamer, L.S.; Joulakian, B. *J. Phys. B* 2006, 39, 2431.

[97] See a paper presented at the International Conference on Electron and Photon Impact Ionization and Related Topics, Louvain-la-Neuve, 2004 (Belgium) by Stia, C.R.; Fojon, O.A.; Rivarola, R.D.; Hanssen, J.; Kamalou, O.; Martina, D.; Chesnel, J.-Y.; Frémont, F.; *Inst. Phys. Conf. Ser.* 2005, 183, 73.

[98] See: Köppel, H. in *Quantum Dynamics of Complex molecular systems*; D. A. Micha; Burghardt, I., Eds.; Springer, Heidelberg, 2006; and references therein.

[99] See: Manz, J.; Wöste, L.; *Femtosecond Chemistry*; Weinheim: Verlag Chemie, 1995; and references therein.

[100] See: Domcke, W.; Yarkony, D. R.; Köppel, H. *Conical Intersections: Electronic Structure, Dynamics and Spectroscopy*, World Scientific: Singapore, 2004; and references therein.

Table 1. Calculations of the vertical and adiabatic double ionization potentials (VDIP and ADIP, respectively) of norbornane considering various possible energy minima on the potential energy surface of norbornane^{2+} in its singlet ground state (results in eV, using the cc-pVDZ basis set and B3LYP/cc-pVDZ geometries).

	VDIP	ADIP				
		S_2 (C_{2v})[b]	C5-Min_1	C5-Min_2	C5-Min_3	C6-Min_4 (C_s)
HF	27.178	24.021	19.548	19.842	20.240	19.125
MP2	25.941	23.516	21.726	21.998	22.225	21.314
MP3	26.873	24.214	21.493	21.768	22.086	21.069
MP4[a]	26.995	24.312	21.470	21.740	22.070	21.054
CCSD	26.965	24.301	21.442	21.714	22.047	21.034
CCSD(T)	26.503	23.963	21.487	21.748	22.066	21.084
B3LYP	26.218	23.813	21.163	21.338	21.891	20.648

[a] Fourth order Møller-Plesset perturbation theory, using the space of single, double and quadruple substitutions.

[b] Given for the sake of comparison, as a rough estimate of the adiabatic double ionization potential *prior* to bond breaking [40].

Table 2. Energies of the identified stationary points on the potential energy surface of norbornane^{2+} in its singlet ground state obtained with a variety of methods along with the cc-pVDZ basis set, relative to the $C_5H_8^+$-CH^+-CH_3 energy (C5-Min$_1$) minimum.

Structure	ΔE (kcal mol^{-1})					
	B3LYP[a]	MPW1K[a]	MPW1K[b]	CCSD(T)[a]	CCSD(T)[b]	FPA[a,c]
S_2 (C_{2v})	61.12	63.94	63.51	57.09	57.77	55.71
S'_1 (C_s)	43.69	51.61	51.37	45.04	44.43	43.37
S_1 (C_s)	56.50	49.10	41.94	47.80	41.27	45.86
C5-Min$_1$	0.00	0.00	0.00	0.00	0.00	0.00
C5-Min$_2$	4.05	4.60	4.68	6.01	6.06	5.33
TS_1^{PT}	6.02	5.09	5.33	5.54	6.10	4.99
C5-Min$_3$	16.79	15.44	-	13.34	-	11.17
TS_2^{PT}	18.39	14.20	-	13.29	-	12.56
TS_3^{PT}	19.33	19.86	-	16.46	-	16.92
TS^{Dis}	41.45	49.73	49.78	40.56	40.80	41.71
S_3 (C_s)	92.06	100.61	-	93.35	-	93.58
C6-Min$_4$ (C_s)	-11.87	-11.87	-11.77	-9.29	-9.23	-10.16
$C_5H_7^+$=CH_2 + CH_3^+	-2.82	0.91	1.06	-9.08	-8.94	-7.77

[a] Based on B3LYP/cc-pVDZ geometries.

[b] Based on MPW1K/cc-pVDZ geometries.

[c] Extrapolated CCSD(T)/cc-pV∞Z data; see Table 5 for details.

Table 3. Natural population analysis of the electronic density for all identified stationary points on the potential surface of norbornane^{2+} in its singlet ground state, compared with that of the neutral (B3LYP/cc-pVDZ results, see Figures 4, 5, 6, 8 and 9 for atom labelling).

	Neutral[a]	S_2 (C_{2v})	S'_1 (C_s)	S_1 (C_s)	C5-Min$_1$	C5-Min$_2$	TS_1^{PT}	C5-Min$_3$	TS_2^{PT}	TS_3^{PT}	TS^{Dis}	S_3 (C_s)	C6-Min$_4$ (C_s)	CH_3^+	$C_5H_7^+$=CH_2
C_1	-0.445	-0.491	-0.591	-0.493	-0.542	-0.632	-0.593	-0.546	-0.550	-0.566	-0.571	**-0.148**	-0.721	0.295	-0.537
C_2	-0.245	**-0.090**	**0.239**	-0.217	**0.329**	**0.350**	**0.341**	**0.326**	**0.333**	**0.320**	**0.316**	-0.169	**0.450**	-	**0.273**
C_3	-0.245	**-0.090**	**0.239**	**0.000**	-0.357	**0.435**	**0.146**	-0.253	**-0.145**	-0.203	0.030	-0.188	**0.319**	-	-0.078
C_4	-0.444	-0.392	-0.342	-0.470	-0.548	-0.570	-0.562	-0.555	-0.550	-0.559	-0.539	-0.387	-0.543	-	-0.524
C_5	-0.444	-0.392	-0.541	-0.470	-0.442	-0.540	-0.496	-0.430	-0.434	-0.440	-0.472	-0.387	-0.568	-	-0.454
C_6	-0.444	-0.392	-0.342	-0.332	**0.310**	-0.525	**-0.256**	-0.424	-0.413	-0.578	-0.359	-0.433	-0.568	-	-0.320
C_7	-0.444	-0.392	-0.541	-0.332	-0.746	-0.652	-0.672	**0.037**	**-0.204**	**0.258**	**0.124**	-0.433	-0.543	-	-
H_1	0.224	0.309	0.344	0.333	0.362	0.391	0.398	0.338	0.347	0.323	0.338	0.288	0.308	0.235	0.368
H_2	0.224	0.309	0.379	0.333	0.344	**0.411**	0.367	0.379	0.372	0.384	0.372	0.288	0.308	0.235	0.319
H_3	0.237	0.328	0.313	0.327	0.301	0.308	0.306	0.302	0.305	0.296	0.289	0.345	0.360	0.235	0.273
H_4	0.237	0.328	0.313	0.352	0.376	0.399	0.377	0.341	**0.388**	0.294	0.377	0.359	0.296		0.312
H_5	0.222	0.327	0.262	0.313	0.358	0.388	0.395	0.381	0.391	0.375	0.342	0.355	0.362		0.348
H_6	0.222	0.327	0.356	0.313	0.386	0.355	0.331	0.364	0.366	0.363	0.293	0.355	0.362		0.265
H_7	0.225	**0.415**	0.258	0.325	0.278	0.364	0.323	0.289	0.296	0.288	0.290	**0.370**	0.334		0.277
H_8	0.225	**0.415**	0.389	0.325	0.294	0.388	**0.418**	0.292	0.290	0.299	0.241	**0.370**	0.334		0.243
H_9	0.222	0.327	0.262	**0.387**	0.276	0.323	0.311	0.297	0.298	0.336	0.242	**0.392**	0.374		0.235
H_{10}	0.222	0.327	0.356	**0.387**	0.286	0.248	0.257	0.291	0.292	0.304	0.229	**0.392**	0.374		-
H_{11}	0.225	**0.415**	0.258	**0.461**	0.378	0.292	0.309	0.286	0.311	0.267	0.230	0.315	0.380		-
H_{12}	0.225	**0.415**	0.389	**0.461**	0.357	0.268	0.299	0.283	0.307	0.240	0.229	0.315	0.380		-

[a] B3LYP/cc-pVDZ natural population analysis of norbornane in its neutral, ground state singlet C_{2v} structure. See Figure 1 for atom labeling.

Table 4. Charge differences obtained from a natural population analysis of the electronic density of a few stationary points on the potential energy surface of doubly ionized norbornane in its singlet ground state compared with that of the neutral in its singlet ground state (B3LYP/cc-pVDZ results).

	S_2 (C_{2v})	S’$_1$ (C_s)	S_1 (C_s)	S_3 (C_s)	C6-Min$_4$ (C_s)
C_1	-0.046	-0.146	-0.048	**0.297**	-0.276
C_2	**0.155**	**0.484**	0.028	0.076	**0.695**
C_3	**0.155**	**0.484**	**0.245**	0.057	**0.564**
C_4	0.052	0.102	-0.026	0.057	-0.099
C_5	0.052	-0.097	-0.026	0.057	-0.124
C_6	0.052	0.102	0.112	0.011	-0.124
C_7	0.052	-0.097	0.112	0.011	-0.099
H_1	0.085	0.120	0.109	0.064	0.084
H_2	0.085	0.155	0.109	0.064	0.084
H_3	0.091	0.076	0.090	0.108	0.123
H_4	0.091	0.076	0.115	0.122	0.059
H_5	0.105	0.040	0.091	0.133	0.140
H_6	0.105	0.134	0.091	0.133	0.140
H_7	**0.190**	0.033	0.100	0.145	0.109
H_8	**0.190**	0.164	0.100	0.145	0.109
H_9	0.105	0.040	0.165	**0.170**	0.152
H_{10}	0.105	0.134	0.165	**0.170**	0.152
H_{11}	**0.190**	0.033	**0.236**	0.090	0.155
H_{12}	**0.190**	0.164	**0.236**	0.090	0.155

Table 5. Focal point analysis of the energies (in kcal mol^{-1}) of the identified structures relative to the $C_5H_8^+$-CH^+-CH_3 intermediate.[a]

	Basis set	cc-pVDZ	cc-pVTZ	cc-pVQZ	cc-pV∞Z
	Size[b]	*158*	*378*	*745*	
S_2 (C_{2v}) *-C5-Min_1*	ΔHF	103.14	102.58	102.61	*102.68*[c]
	+MP2	-61.87	-64.18	-64.44	*-64.59*[d]
	+MP3	21.49	*23.29*		
	+MP4[e]	*2.78*			
	+CCSD	*0.40*			
	+CCSD(T)	*-8.85*			
	Total	57.09	56.02	55.79	*55.71*
S'_1 (C_s) *-C5-Min_1*	ΔHF	49.50	47.62	47.32	*47.28*[c]
	+MP2	-2.86	-2.74	-2.58	*-2.58*[d]
	+MP3	1.15	*1.42*		
	+MP4[e]	*-0.51*			
	+CCSD	*-0.06*			
	+CCSD(T)	*-2.18*			
	Total	45.04	43.55	43.41	*43.37*
S_1 (C_s) *-C5-Min_1*	ΔHF	76.38	75.68	75.64	*75.68*[c]
	+MP2	-36.44	-38.15	-38.39	*-38.51*[d]
	+MP3	10.82	*11.65*		
	+MP4[e]	*0.26*			
	+CCSD	*0.97*			
	+CCSD(T)	*-4.19*			
	Total	47.80	46.22	45.94	*45.86*
C5-Min_2 *-C5-Min_1*	ΔHF	6.78	6.51	6.49	*6.51*[b]
	+MP2	-0.51	-0.73	-0.88	*-0.94*[c]
	+MP3	0.07	*0.09*		
	+MP4[e]	*-0.10*			
	+CCSD	*0.04*			
	+CCSD(T)	*-0.27*			
	Total	6.01	5.54	5.37	*5.33*
TS_1^{PT} *-C5-Min_1*	ΔHF	9.00	8.75	8.71	*8.70*[b]
	+MP2	-4.55	-4.87	-4.96	*-4.98*[c]
	+MP3	0.89	*1.07*		
	+MP4[e]	*0.40*			
	+CCSD	*0.25*			
	+CCSD(T)	*-0.45*			
	Total	5.54	5.15	5.02	*4.99*

Table 5 (continued).[a]

	Basis set	cc-pVDZ	cc-pVTZ	cc-pVQZ	cc-pV∞Z
	Size[b]	*158*	*378*	*745*	
C5-Min$_3$ -C5-Min$_1$	ΔHF	15.95	14.37	14.33	*14.45*[b]
	+MP2	-4.44	-5.22	-5.15	*-5.28*[c]
	+MP3	2.16	*2.33*		
	+MP4[e]	*0.17*			
	+CCSD	*0.12*			
	+CCSD(T)	*-0.62*			
	Total	13.34	11.15	11.18	*11.17*
TS$_2^{PT}$ -C5-Min$_1$	ΔHF	21.41	20.84	20.81	*20.85*[b]
	+MP2	-10.77	-11.25	-11.22	*-11.27*[c]
	+MP3	2.89	*3.22*		
	+MP4[e]	*0.37*			
	+CCSD	*0.27*			
	+CCSD(T)	*-0.88*			
	Total	13.29	12.57	12.57	*12.56*
TS$_3^{PT}$ -C5-Min$_1$	ΔHF	16.00	15.96	15.98	*16.00*[b]
	+MP2	0.99	1.18	1.33	*1.35*[c]
	+MP3	0.18	*0.28*		
	+MP4[e]	*-0.41*			
	+CCSD	*-0.21*			
	+CCSD(T)	*-0.09*			
	Total	16.46	16.71	16.88	*16.92*
TS^{Dis} -C5-Min$_1$	ΔHF	32.45	31.71	31.63	*31.65*[b]
	+MP2	10.14	11.24	11.69	*11.76*[c]
	+MP3	-1.34	*-1.01*		
	+MP4[e]	*-0.95*			
	+CCSD	*-0.48*			
	+CCSD(T)	*0.74*			
	Total	40.56	41.25	41.62	*41.71*
S$_3$ (C$_s$) -C5-Min$_1$	ΔHF	140.54	140.72	140.85	*140.93*[c]
	+MP2	-54.86	-56.35	-56.41	*-56.49*[d]
	+MP3	17.35	*18.82*		
	+MP4[e]	*0.28*			
	+CCSD	*-0.15*			
	+CCSD(T)	*-9.81*			
	Total	93.35	93.51	93.58	*93.58*

Table 5 (contintued).[a]

	Basis set	cc-pVDZ	cc-pVTZ	cc-pVQZ	cc-pV∞Z
	Size[b]	*158*	*378*	*745*	
C6-Min$_4$ (C$_s$) -C5-Min$_1$	ΔHF	-9.76	-9.83	-9.83	*-9.83*[b]
	+MP2	0.26	-0.18	-0.39	*-0.44*[c]
	+MP3	-0.28	*-0.38*		
	+MP4[e]	*0.19*			
	+CCSD	*0.18*			
	+CCSD(T)	*0.12*			
	Total	-9.29	-9.90	-10.11	*-10.16*
($C_5H_7^+$=CH$_2$ +CH_3^+) - C5-Min$_1$	ΔHF	-17.81	-18.45	-18.51	*-18.49*[b]
	+MP2	10.57	11.68	12.17	*12.25*[c]
	+MP3	-1.31	*-1.00*		
	+MP4[e]	*-0.91*			
	+CCSD	*-0.48*			
	+CCSD(T)	*0.86*			
	Total	-9.08	-8.30	-7.87	*-7.77*

[a] Calculations are based on B3LYP/cc-pVDZ geometries.

[b] Total number of atomic functions.

[c] Results obtained using the extrapolation suggested by Feller [78, 79]

[d] Results obtained using the extrapolation suggested by Schwartz [81]

[e] Fourth order Møller-Plesset perturbation theory, using an excitation manifold comprising single, double and quadruple electronic excitations.

Table 6. Thermochemical analysis of the intramolecular rearrangement and fragmentation processes induced by double ionization of norbornane. Differences in electronic energies (ΔE), zero point vibrational energies (ΔZPE), enthalpies at 0 K (ΔH_0) as well as enthalpies, entropies and Gibbs free energies at 298.15 K and a pressure of 1 atm (ΔH_{298}, ΔS_{298} and ΔG_{298}, respectively) are given relative to the kinetically metastable C5-Min$_1$ intermediate. Energies (enthalpies) and entropies are given in kcal mol^{-1} and entropies are in kcal mol^{-1}and cal mol^{-1}*K^{-1}, respectively. Imaginary frequencies (in cm^{-1}) characterizing the first-order saddle-points (Freq) are also listed.[a]

Structure	$\Delta E^{(a)}$	Freq	ΔZPE	ΔH_0	ΔH_{298}	ΔS_{298}^{trans}	ΔS_{298}^{vib}	ΔS_{298}^{rot}	ΔS_{298}^{elec}	ΔS_{298}^{tot}	ΔG_{298}
S'$_1$ (C$_s$)	43.37	232*i*	-1.26	42.11	42.12	0.000	0.451	-0.106	0.000	0.346	42.01
S$_1$ (C$_s$)	45.86	296*i*	0.55	46.41	45.36	0.000	-7.357	-0.960	0.000	-8.316	47.84
C5-Min$_1$	0.00	-	0.00	0.00	0.00	0.000	0.000	0.000	0.000	0.000	0.00
C5-Min$_2$	5.33	-	-0.91	4.42	4.57	0.000	1.279	0.001	0.000	1.280	4.19
TS$_1^{PT}$	4.99	483*i*	-1.18	3.81	3.55	0.000	-1.888	0.004	0.000	-1.884	4.11
C5-Min$_3$	11.17	-	1.65	12.82	12.61	0.000	-0.969	-0.222	0.000	-1.191	12.97
TS$_2^{PT}$	12.56	234*i*	0.70	13.26	12.57	0.000	-4.388	-0.272	0.000	-4.660	13.96
TS$_3^{PT}$	16.92	243*i*	0.44	17.36	17.06	0.000	-1.399	-0.036	0.000	-1.434	17.49
TS^{Dis}	41.71	91*i*	-3.14	38.57	39.69	0.000	12.076	1.141	0.000	13.217	35.75
C6-Min$_4$ (C$_s$)	-10.16	-	0.35	-9.81	-9.80	0.000	1.987	-0.099	0.000	1.888	-10.37
$C_5H_7^+$=CH$_2$ + CH$_3^+$	-7.77	-	-3.56	-11.33	-10.20[b]	33.562	-8.165	12.739	0.000	38.135	-21.57[b]

[a] The differences in total internal energies (ΔE) derive from the Focal Point Analyses (see Table 6); other thermochemical data were obtained upon adding to the ΔE values the B3LYP/cc-pVDZ estimates for zero-point vibrational energies (ΔH_0=ΔE +ΔZPE), thermal corrections to the entropies ($\Delta H_{298}=\Delta H_0+\Delta\Delta H_{298}$, with $\Delta\Delta H_{298}=\Delta H_{298}$ - ΔH_{298} at the B3LYP/cc-pVDZ level) and entropy corrections to Gibb's free energies ($\Delta G_{298}=\Delta H_{298}-T\Delta S_{298}^{tot}$) .

[b] Mechanical work against external pressure (*RT*=0.59 kcal/mol) included, assuming an ideal gas behavior.

3.4 Investigation into the valence electronic structure of norbornene using electron momentum spectroscopy, Green's function, and density functional theories.

3.4.1 Introduction

The bicyclo [2.2.1] seven-membered hydrocarbon cages, of which bicyclo [2.2.1]-2-heptene or norbornene (C_7H_{10}) is a member, have frequently been used to fix geometric variables in structure/reactivity studies and in the probing of the relationship between spectroscopic properties and structure [1]. The framework (see Figure 1) consists of a six-membered ring held in a "boat" conformation that serves as a model system for the transition state for "chair-chair" interconversion in the chemically important six membered ring. The additional bridgehead ("7") group subtends a less-than-ideal angle for a saturated linkage and is thus expected to exhibit (and act as a vehicle for studying) strain effects. The electronic structure of the norbornene (NBN) ring system also predisposes it towards rapid reaction on the *exo face* of the double bond [2, 3]. While several theoretical explanations exist (see for example [4, 5]), the origin of the exceptional reactivity has eluded unequivocal physical detection. More recently [6], femtosecond-resolved spectroscopic detection of intermediates in a simple retro Diels-Alder [7] reaction has created considerable excitement. The thermal unimolecular dissociation of NBN into ethylene and cyclopentadiene is a classic illustration of the retro Diels-Alder reaction [6], the mechanisms of which are still somewhat controversial [8].

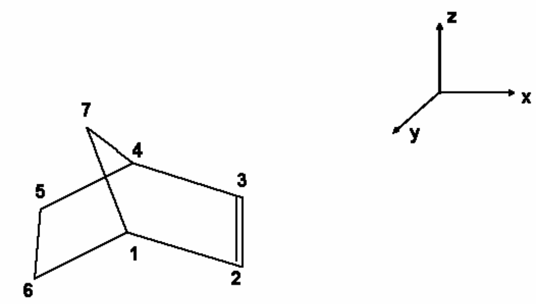

Figure 1. Structural representation of norbornene and the atom numbering.

In all of the above examples of the chemical importance of NBN, whether it be for an unambiguous determination of its structure or a mechanistic description of its role in various reactions, quantum chemical calculations play a major role in assisting our understanding [9]. However the results of these calculations are often very sensitive to the type of theory employed (including the basis set used) [6], so that a technique that validates *a priori* quantum chemical models is potentially very useful. The unique orbital imaging capability of electron momentum spectroscopy (EMS) [10, 11] can in principle fulfill just such a role and here we report on its application to NBN. Specifically, we use EMS to determine which of our employed density functional theory (DFT) exchange correlation functionals and basis sets best describe the experimental momentum distributions. This optimum basis and exchange correlation functional is then used to derive the molecular geometry of norbornene. That data are next compared with independent experimentally determined values, and those from other MO calculations, to determine how well the optimum model was able to reproduce norbornene's molecular geometry.

While conducting our study, it became quite clear that existing investigations into the outer- and inner-valence electronic structure of norbornene are rather scarce. Previous photoelectron spectroscopy (PES) studies include the He(I) measurements from Bischof *et al.* [12], Demeo and Yencha [13] and Wen *et al.* [14] and the He (II) measurement from Bieri *et al.* [15]. Theoretical interpretation of these spectra has been even more limited with only the modified intermediate neglect of differential overlap, version 2 (MINDO/2) result from Bodor *et al.* [16] being available in the literature. Hence the present Hartree-Fock (HF), Density Functional Theory (DFT) and one-particle Green's Function (1p-GF) calculations significantly expand the available theoretical knowledge of the electronic structure of norbornene. In addition we believe that the present EMS measurements are the first to be made on this molecule, thus further expanding our understanding of its electronic structure through our original momentum space images of its molecular orbitals (MO's).

In the next section of this paper we discuss briefly our EMS measurements, including our ionization spectra. Details of our HF, DFT and 1p-GF calculations, and some of the electronic structure information we can extract from them by investigating the EMS cross sections and the valence ionization spectra are presented in sections 3 and 4, respectively. In section 5 we compare and discuss the experimental and theoretical momentum distributions associated to all bands in the EMS ionization spectra. In section 6 the molecular geometry derived from our optimum basis set and exchange correlation functional is detailed, while in section 7 some of the conclusions drawn from the current study are presented.

3.4.2 Experimental details and preliminary analysis

A sample of norbornene was purchased from the Aldrich Chemical Company. As the quoted purity was greater than 99.99 %, this sample was used in our measurements without further purification. Note, however, that as EMS is highly sensitive to the presence of any impurities, our NBN sample was degassed *in situ* by repeated freeze-pump-thaw cycles of its storage vessel before being introduced into the interaction region.

All of the 19 occupied MO's of the complete valence region of NBN, namely the $12a'$, $7a''$, $6a''$, $11a'$, $10a'$, $9a'$, $5a''$, $4a''$, $8a'$, $7a'$, $6a'$, $5a'$, $3a''$, $4a'$, $2a''$, $3a'$, $1a''$, $2a'$ and $1a'$ MO's, were then investigated in several experimental runs using the Flinders symmetric noncoplanar EMS spectrometer [10]. Details of this coincidence spectrometer and the method of taking the data can be found in Brunger and Adcock [11] and Weigold and McCarthy [10], so we do not repeat them again here.

The high-purity NBN sample was admitted into the target chamber through a capillary tube, the flow rate being controlled by a variable leak valve. Possible clustering due to supersonic expansion was avoided by maintaining a low NBN driving pressure throughout data collection. The collision region was differentially pumped by a 700 l s^{-1} diffusion pump. Apertures and slits were cut in the collision chamber for the incident electron beam and the scattered and ejected electrons. Our (e,2e) monochromator [11] typically produces incident electron beam currents of the order of 30 μA into the interaction region, with the overall coincident energy resolution of the present measurements being ~ 0.6 eV full-width-at-half-maximum (FWHM). Note that the coincident energy resolution was determined from measurements of the binding-energy (ε_f) spectrum of helium, whose profile was found to be well represented by a Gaussian function. However, due to the natural and vibrational line widths (Franck-Condon widths) of the various electronic transitions and a quite strong dispersion of the ionization intensity into many-electron processes at the bottom of the carbon-2s region, the fitted resolutions of the spectral peaks for NBN varied from ~ 0.90 to 2.45 eV (FWHM).

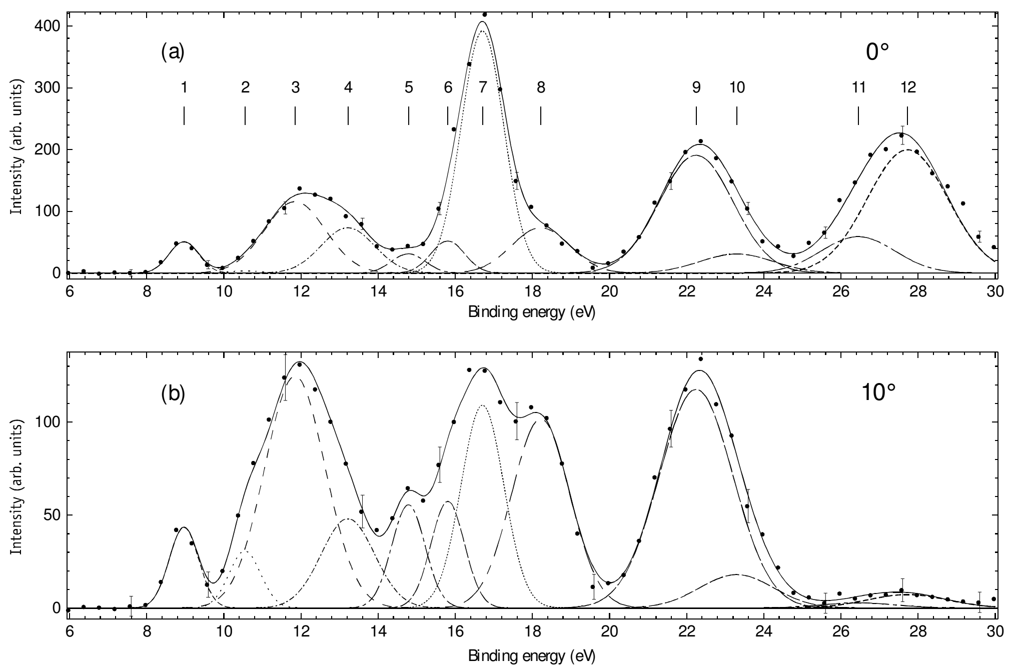

Figure 2. Typical binding-energy spectra from our 1500 eV noncoplanar symmetric EMS investigation into norbornene. The curves show the fits to the spectra at (a) $\phi = 0°$ ($p \approx 0.03$ a.u.) and (b) $\phi = 10°$ ($p \approx 0.92$ a.u.) using the known energy resolution. Note that indicative error bars are shown on this figure, and that the peak positions of the Gaussians used in the fit (see also Table 1a) are indicated.

It is precisely this limitation which forces us to combine our measured $6a''$, $11a'$, $10a'$, $9a'$ and $5a''$ orbital momentum distributions (MDs), $4a''$ and $8a'$ orbital MDs, $5a'$ and $3a''$ orbital MDs, $4a'$ and $2a''$ orbital MDs and $3a'$, $1a''$ and $2a'$ orbital momentum distributions, respectively. While there is no doubt one loses some physical information in combining these MDs, to not do so would have raised serious question as to the uniqueness of the MDs derived in the fits to our binding energy spectra (see below). The angular resolution, which determines the momentum resolution, was typically 1.2° (FWHM) as determined from the electron optics and apertures and from a consideration of the argon 3p angular correlation.

Ionization spectra of norbornene measured at representative angles ϕ [17] in the region 6-30 eV and at $E = 1500$ eV are displayed in Figure 2. The solid curve in each panel represents the envelope of the 12 fitted Gaussians (various dashed curves) whose positions below $\varepsilon_f \sim 23$ eV are taken from the available PES data [12-15]. A summary of the available orbital binding energies from PES data [12, 15], the present EMS binding energies and our tentative orbital assignments are given in Table 1a. The fact that we used only 12 Gaussians to analyze spectra containing 19 valence MOs simply reflects our earlier point that our energy resolution was insufficient to uniquely deconvolve all the orbitals, so that some were combined (summed). Notwithstanding this, it is clear from Figure 2 that the fits to the measured binding-energy spectra are excellent. The least-squares-fit deconvolution technique used in the analysis of these spectra is based on the work of Bevington and Robinson [18], to whom readers are referred for more detail. Above ε_f ~ 23 eV there are no PES data available to guide us in our fitting of the binding-energy spectra. Under these circumstances the positions and widths of the Gaussian peaks, and the number of Gaussians, used in the spectral deconvolution were simply determined by their utility in best fitting the observed data for all ϕ. The fact that the inner valence 3a', 1a'', 2a' and 1a' orbitals need 4 very broad Gaussians to incorporate the measured coincidence intensity into the fit, is undoubtedly indicative of a severe dispersion of ionization intensity over many satellite states. This observation led us to undertake thorough one-particle Green's Function (1p-GF) calculations of the valence one-electron and shake-up ionization spectrum of norbornene (see section 4).

TABLE 1

a. Experimental Electronic Structure of Norbornene[a,b]

orbital no.	classification present	ϵ_f (eV) experimental PES[12,15]	present EMS
1	12a′	8.97	8.97
2	7a″	10.55	10.55
3	6a″	11.85	11.85
4	11a′		
5	10a′		
6	9a′		
7	5a″		
8	4a″	13.22	13.22
9	8a′		
10	7a′	14.79	14.79
11	6a′	15.81	15.81
12	5a′	16.71	16.71
13	3a″		
14	4a′	18.22	18.22
15	2a″		
16	3a′	22.25	22.25, 23.30
17	1a″		
18	2a′		
19	1a′		26.45, 27.73

b. Theoretical Electronic Structure Calculations for Norbornene[b]

orbital no.	classification present	ϵ_f (eV) present SCF RHF/TZVP	present DFT LSD/TZVP	present DFT BLYP/TZVP	present DFT BP/TZVP
1	12a′	9.21	5.83	5.51	5.75
2	7a″	11.70	7.20	7.06	7.25
3	6a″	12.30	7.96	7.62	7.87
4	11a′	12.65	8.10	7.83	8.06
5	10a′	13.19	8.22	8.06	8.25
6	9a′	13.20	8.39	8.16	8.38
7	5a″	13.40	8.43	8.23	8.42
8	4a″	14.44	9.25	9.01	9.23
9	8a′	15.06	9.56	9.34	9.55
10	7a′	16.38	10.78	10.44	10.70
11	6a′	17.52	11.70	11.27	11.57
12	5a′	18.94	12.38	12.24	12.49
13	3a″	19.14	12.71	12.31	12.60
14	4a′	20.84	13.55	13.39	13.64
15	2a″	21.67	14.08	13.97	14.22
16	3a′	25.71	17.00	16.72	17.05
17	1a″	26.38	17.62	17.25	17.61
18	2a′	27.43	18.22	17.90	18.25
19	1a′	32.04	22.06	21.35	21.84

[a] Our tentative classifications for the valence orbitals are also given in this table. [b] All binding energies (ϵ_f) are given in eV.

The EMS ionization spectra of Figure 2 clearly reflect the respective symmetries [10] of the valence orbitals of norbornene. For instance the next-highest-occupied-molecular-orbital (NHOMO, peak 2 of Figure 2) exhibits significantly more intensity at $\phi = 10°$ compared to that at $\phi = 0°$. This is consistent with the "*p*-type" symmetry of this orbital. On the other hand, the unresolved 5a' and 3a'' orbitals (peak 7) have a much greater intensity at $\phi = 0°$ compared to that found at $\phi = 10°$ (almost 4:1), which corroborates the dominance of an "*s*-type" symmetry. On the basis of the symmetry indicated by the EMS binding-energy spectra and the results of our calculations in Table 1b (see section 3 for more details) tentative orbital assignments were made and are given in both Tables 1a and 1b. In general these orbital assignments are consistent with those found from our 1p-GF calculations (see Table 2). The angular dependence of the EMS cross sections indicate that peaks 11 and 12 have similar *s*-type MDs, so that both peaks at first glance could be ascribed to originating from the $1a'$ orbital. Our 1p-GF calculations, however do not find any ionization lines with a pole (spectroscopic) strength larger than 0.005 at binding energies greater than 26 eV. This latter result is due to the extreme shake-up fragmentation in this region of the binding-energy spectrum arising because of the very low symmetry of the norbornene compound, enabling many configuration interactions in the cation. Without theoretical support from our 1p-GF calculation, our assignment of peaks 11 and 12 in Figure 2 must therefore remain tentative at this time.

3.4.3 Theoretical analysis of EMS cross sections

As explained in Chapter 2.8, the EMS cross section can be expressed as a function of a structure factor [10, 19-21] derived as the Fourier transform of the relevant Hartree-Fock [22] or Kohn-Sham ground state, multiplied by a spectroscopic amplitude Γ_f defined as the norm of the Dyson orbital pertaining to the ionization channel *f*.

The Kohn-Sham equation [23-26] of DFT may be considered as an approximate quasi-particle equation, with the potential operator approximated by the exchange-correlation potential [20]. We note that there has been a long-standing and vigorous debate on the interpretation of the Kohn-Sham orbital energies as approximate vertical ionization potentials, for which the current situation is described and improved in [24]. DFT is often applied with the exchange-correlation (XC) potential represented at the local spin density (LSD) approximation level. In this study we use both the LSD and functionals that depend on the gradients of the electron density [27-30], i.e. the generalized gradient approximation (GGA). Specifically, here we employed two different approximations to the XC energy functional due to Becke and Perdew (BP) [27-29] and Becke, Lee, Yang and Parr (BLYP) [27, 28, 30]. However, none of these functionals have the correct Coulomb asymptotic behavior (-1/r). Also, Janak's theorem equating ionization energies to KS eigenvalues is only valid for the highest occupied molecular orbital (HOMO). Therefore, any agreement with experimental ionization energies should be viewed as fortuitous.

Since Kohn-Sham orbital energies have often been employed to interpret ionization spectra, and are even now used to test the accuracy of extremely sophisticated approaches which incorporate relativistic effects [31, 32], we take this opportunity to emphasize the dangers inherent in such practices. Nonetheless, these same functionals have been shown, for many molecules [10, 11] to provide a good description for the EMS momentum distributions. To further support this latter assertion we also invoke works by Duffy *et al.* [33] and Davidson and colleagues [34, 35] that demonstrate that KS orbitals most often provide excellent approximations to normalized Dyson orbitals obtained from benchmark quantum mechanical calculations, possibly as the outcome of error cancellations (neglect of final-state correlation, i.e. relaxation effects on orbitals versus the too rapid fall-off of the DFT exchange correlation potential at large distances due to the self-interaction error). Gritsenko *et al.* [25] also notes overlap larger than 0.999 between normalized Dyson orbitals and the corresponding Kohn-Sham orbital for a one electron ionization event. Thus, presently, the most thorough analyses of EMS are most commonly completed using structure factors derived from KS orbitals derived from DFT calculations employing gradient corrected functionals, along with pole strengths obtained separately from advanced MR-SDCI (multi-reference single-double configuration interactions [36]) or one-particle Green's Function calculations (1p-GF) of the ADC(3) type [37-39] (see further). For this very first analysis of EMS measurements on norbornene, we again apply this very well-established hybrid (1p-GF+DFT) procedure, prior to considering further code developments employing ADC(3) Dyson orbitals for modeling (e,2e) electron momentum distributions.

TABLE 2: Present ADC(3) and OVGF Calculation Results for the Electronic Structure of Norbornene[a]

		HF/cc-pVDZ(I)	ADC(3)/ cc-pVDZ(I)		OVGF/ cc-pVDZ(I)		OVGF/ aug-cc-pVDZ(I)		OVGF/ cc-pVTZ(I)		OVGF/ cc-pVDZ(II)		OVGF/ cc-pVDZ(III)	
symbol	label	ϵ_f (eV)	ϵ_f (eV)	Γ_f	ϵ_f (eV)	Γ_f	ϵ_f (eV)	Γ_f	ϵ_f (eV)	Γ_f	ϵ_f (eV)	Γ_f	ϵ_f (eV)	Γ_f
s	12a′	9.117	8.975	0.899	8.855	0.907	8.972	0.905	8.909	0.904	8.874	0.907	8.749	0.906
r	7a″	11.682	10.838	0.905	10.717	0.910	10.832	0.908	10.796	0.907	10.722	0.910	10.746	0.910
q	6a″	12.215	11.388	0.901	11.239	0.907	11.353	0.905	11.281	0.904	11.260	0.907	11.232	0.906
p	11a′	12.604	11.749	0.903	11.628	0.908	11.739	0.906	11.685	0.905	11.650	0.908	11.624	0.907
n	10a′	13.102	12.166	0.902	12.042	0.909	12.152	0.907	12.102	0.906	12.061	0.909	11.981	0.909
m	9a′	13.148	12.101	0.899	11.972	0.904	12.102	0.902	12.044	0.902	11.987	0.904	11.912	0.904
l	5a″	13.339	12.322	0.905	12.232	0.910	12.340	0.908	12.308	0.908	12.237	0.911	12.225	0.910
k	4a″	14.376	13.280	0.895	13.186	0.905	13.298	0.903	13.271	0.902	13.197	0.906	13.183	0.905
j	8a′	14.910	13.684	0.895	13.560	0.903	13.688	0.901	13.638	0.900	13.588	0.903	13.453	0.903
i	7a′	16.282	15.003	0.780	15.004	0.899	15.114	0.896	15.074	0.896	15.039	0.899	14.952	0.898
			15.295 (i)[b]	0.074										
h	6a′	17.390	15.945	0.503	15.829	0.894	15.890	0.891	15.893	0.890	15.857	0.894	15.769	0.893
			16.151 (ii)	0.416										
			19.478	0.011										
g	5a′	18.778	17.160	0.826	16.995	0.881	17.071	0.878	17.068	0.878	17.043	0.882	16.916	0.881
			17.954 (iii)	0.055										
f	3a″	19.097	16.765 (iv)	0.044	17.147	0.877	17.210	0.874	17.233	0.874	17.157	0.878	17.108	0.876
			17.083	0.151										
			17.268	0.647										
e	4a′	20.757	18.494	0.604	18.531	0.864			18.588	0.860	18.559	0.865	18.438	0.863
			19.122 (v)	0.223										
			20.785	0.009										
d	2a″	21.633	18.669 (vi)	0.048	19.621	0.858			19.320	0.853	19.278	0.858	19.183	0.854
			19.215	0.657										
			19.781	0.068										
			19.945	0.010										
			20.201	0.008										
			20.288	0.024										
			20.342	0.025										
			21.703	0.010										
c	3a′	25.627	20.964	0.007	22.544	0.811[c]					22.581	0.812[c]		
			21.271	0.009										
			21.631	0.006										
			21.675	0.007										
			21.866	0.015										
			22.010	0.051										
			22.090	0.021										
			22.164	0.122										
			22.176	0.008										
			22.278	0.006										
			22.294	0.060										
			22.319	0.151										
			22.407	0.040										
			22.450	0.009										
			22.484	0.009										
			22.675	0.010										
			22.764	0.059										
			22.834	0.030										
			22.856	0.040										
			22.864	0.124										
			22.931	0.059										
			22.977	0.015										
			23.106	0.007										
			23.200	0.009										
b	1a″	26.331	21.548	0.009										
			22.008	0.009										
			22.194	0.006										
			22.237	0.015										
			22.307	0.020										
			22.515	0.029										
			22.541	0.010										
			22.611	0.016										
			22.651	0.006										
			22.756	0.014										
			22.820	0.017										
			22.846	0.008										
			22.895	0.011										
			22.903	0.029										
			23.011	0.225										
			23.039	0.047										
			23.119	0.054										

TABLE 2 (Continued)

		HF/cc-pVDZ(I)	ADC(3)/ cc-pVDZ(I)		OVGF/ cc-pVDZ(I)		OVGF/ aug-cc-pVDZ(I)		OVGF/ cc-pVTZ(I)		OVGF/ cc-pVDZ(II)		OVGF/ cc-pVDZ(III)	
symbol	label	ϵ_f (eV)	ϵ_f (eV)	Γ_f	ϵ_f (eV)	Γ_f	ϵ_f (eV)	Γ_f	ϵ_f (eV)	Γ_f	ϵ_f (eV)	Γ_f	ϵ_f (eV)	Γ_f
			23.155	0.007										
			23.180	0.057										
			23.224	0.030										
			23.292	0.026										
			23.309	0.016										
			23.381	0.016										
			23.401	0.016										
			23.416	0.008										
			23.476	0.013										
			23.568	0.009										
a	2a′	27.311	23.168	0.006										
			23.261	0.010										
			23.372	0.027										
			23.420	0.014										
			23.493	0.010										
			23.555	0.011										
			23.581	0.019										
			23.609	0.010										
			23.627	0.009										
			23.658	0.007										
			23.685	0.026										
			23.694	0.064										
			23.732	0.060										
			23.792	0.007										
			23.834	0.010										
			23.901	0.031										
			23.968	0.010										
			24.000	0.084										
			24.008	0.017										
			24.046	0.027										
			24.086	0.008										
			24.255	0.006										
			24.315	0.006										

Dominant Electronic Configurations:

i	$12a'^{-1}$	$7a''^{-1}$	$8a''^{+1}$	$[(\mathrm{HOMO})^{-1}$	$(\mathrm{HOMO}\text{-}1)^{-1}$	$(\mathrm{LUMO})^{+1}]$	
ii	$12a'^{-1}$	$6a''^{-1}$	$8a''^{+1}$	$[(\mathrm{HOMO})^{-1}$	$(\mathrm{HOMO}\text{-}2)^{-1}$	$(\mathrm{LUMO})^{+1}]$	
iii	$12a'^{-1}$	$4a''^{-1}$	$8a''^{+1}$	$[(\mathrm{HOMO})^{-1}$	$(\mathrm{HOMO}\text{-}7)^{-1}$	$(\mathrm{LUMO})^{+1}]$	
iv	$12a'^{-1}$	$9a'^{-1}$	$8a''^{+1}$	&	$12a'^{-1}$	$10a'^{-1}$	$8a''^{+1}$
	$[(\mathrm{HOMO})^{-1}$	$(\mathrm{HOMO}-5)^{-1}$	$(\mathrm{LUMO})^{+1}]$	&	$[(\mathrm{HOMO})^{-1}$	$(\mathrm{HOMO}\text{-}4)^{-1}$	$(\mathrm{LUMO})^{+1}]$
v	$12a'^{-1}$	$7a''^{-1}$	$8a''^{+1}$	$[(\mathrm{HOMO})^{-1}$	$(\mathrm{HOMO}\text{-}1)^{-1}$	$(\mathrm{LUMO})^{+1}]$	
vi	$12a'^{-1}$	$8a'^{-1}$	$8a''^{+1}$	$[(\mathrm{HOMO})^{-1}$	$(\mathrm{HOMO}\text{-}8)^{-1}$	$(\mathrm{LUMO})^{+1}]$	

[a] The binding energies (ϵ_f) are given in eV, along with the OVGF and ADC(3) spectroscopic factors (Γ_f). (I) using B3LYP/TZVP geometry. (II) using B3LYP/cc-pVTZ geometry and (III) using MP2/aug-cc-pVDZ geometry. [b] Dominant electronic configurations given at bottom of table. [c] Breakdown of the MO picture of ionization (*J. Chem. Phys.* **2002**, *116*, 7012).

To compute the coordinate space Kohn-Sham orbitals ψ_j, we employed DGauss, a program package originally developed at CRAY Research by Andzelm and colleagues [40, 41]. It has been known for a number of years [42] that HF theory provides momentum distributions of lower quality than DFT due to the lack of electron correlation, therefore we do not assess HF momentum distributions again here. DGauss is itself a part of UniChem [42]. The molecular structure of norbornene has been optimized through energy minimization with various gradient-corrected functionals and basis sets, employing the UniChem user interface. Note that a geometry optimization was performed in DGauss with each basis set used. The electronic structural calculations using a restricted Hartree-Fock (RHF) approach along with a polarized valence basis set of triple zeta (TZVP) quality are based on GAMESS [43]. A subset of our calculated orbital energies from both our DFT and RHF calculations is given in Table 1b. Clearly none of these results give particularly good agreement with the corresponding experimental values of Table 1a. The reasons for these discrepancies were explored in our recent paper on norbornane [44], so we do not repeat them again here.

Information of the molecular structure and the molecular orbital wave functions for the ground electronic state of NBN, obtained from the DGauss DFT calculations, were next treated as input to the Flinders-developed program AMOLD [17], which computes the momentum space spherically averaged molecular-structure factor [19] and the (e,2e) cross section or MD. Note that all the theoretical MDs we report in this paper have had the experimental angular resolution folded in using the method of Frost and Weigold [45].

The comparisons of calculated MDs with experiment (see section 5) may be viewed as an exceptionally detailed test of the quality of the XC energy and functional and basis set. In this context our LSD, GGA-BP and GGA-BLYP are used in combination with two basis sets to examine the behavior of the XC functionals and basis sets. These basis sets are denoted by the acronyms DZVP and TZVP. The notations DZ and TZ denote basis sets of double - or triple - zeta quality. V denotes a calculation in which such a basis is used only for the valence orbitals and a minimal basis is used for the less chemically reactive core orbitals. The inclusion of long-range polarization functions is denoted by P. We note, in particular, that the basis sets of DGauss were specially designed for DFT calculations [40, 46]. The TZVP basis set has a contraction scheme [7111/411/1] for carbon and [3111/1] for hydrogen. The auxiliary basis set corresponding to the TZVP basis is called A1 [47], in which the *s*-, *p*- and *d*-orbital exponents were determined separately from an optimization that reproduces, as accurately as possible, the energy from an atomic DFT calculation. The contraction schemes of the A1 basis sets for H are [4/1] and for C [8/4/4].

The DFT DGauss calculations were performed on a Silicon Graphics 02 (R5200) workstation as the UniChem client and a CRAY J90se/82048 computer as the DFT computational engine. A further Hartree-Fock (RHF) calculation, using the TZVP basis set and a GAMESS02 suite of programs [43], was carried out on the Compaq Alpha Server SC cluster at the Australian Partnership for Advanced Computing National Facilities.

In light of the marginal agreement between the DFT and experimental ionization energies, that we described earlier, further calculations employing more sophisticated Green's Function techniques were undertaken. These calculations, described in detail in the next section, are all based on geometries [9] that have been optimized using Density Functional Theory by means of the GAMESS02 program [43] employing the TZVP basis set and the non-local hybrid Becke three-parameter Lee-Yang-Parr functional (B3LYP) [30, 48].

3.4.4 Theoretical analysis of valence ionization spectra

The valence one-electron and 2h-1p (two-hole, one-particle) shake-up ionization bands of norbornene have been calculated using the ADC(3) scheme [49-51] derived within the framework of one-particle Green's Function (or one-electron propagator) theory [52-55].

The ADC(3) calculation, presented in Table 2, was carried out with Dunning's correlation-consistent polarized valence basis set of double-zeta quality (cc-pVDZ [56]). The original code, interfaced to the GAMESS02 package of programs [43], has been employed to complete these 1p-GF calculations. At the Self Consistent Field (SCF) level, the requested convergence on each of the elements of the density matrix was fixed to 10^{-10}. With the 1p-GF/ADC(3) approach, the one-hole (1*h*) and shake-up two-hole-one-particle (2h-1p) ionization energies are recovered through third- and first-order in correlation, respectively, which implies accuracies of ~ 0.2 [57] and ~ 0.6 eV on one-electron and shake-up ionization energies, respectively, with a basis set approaching completeness. The spectra have been calculated up to binding energies of 25 eV, retaining all eigenvalues of the ADC(3) secular matrix with a pole strength equal to or larger than 0.005. This matrix has been diagonalized using the Block-Davidson diagonalization procedure [58, 59] in the final diagonalization step [60]. The assumption of frozen core electrons has been used throughout and symmetry has been exploited to the extent of the C_s point group. The ADC(3) calculation performed in the present study is based on a molecular geometry that has been optimized using the non-local hybrid and gradient corrected Becke three-parameter Lee-Yang-Parr functional (B3LYP) [30, 48] in conjunction with Dunning's basis set of triple zeta quality [61] with polarized valence functions (TZVP). It has previously been shown that this approach delivers excellent equilibrium geometries [62]. For the Density Functional Theory (DFT) computations, the GAUSSIAN98 [63] quantum chemistry package has been used.

To evaluate the sensitivity of the computed ionization energies on the quality of the basis set, a few results (Table 2) were obtained from outer-valence Green's function (OVGF [64, 65]) calculations. For these benchmark computations of one-electron ionization energies, three basis sets have been used: Dunning's correlation consistent polarized valence basis set of double zeta quality (cc-pVDZ [56]), the cc-pVDZ basis augmented by a set of diffuse *s*,*p* functions on the hydrogen atoms together with a set of diffuse *s*,*p*,*d* functions on the carbon atoms (aug-cc-pVDZ [56, 66]), and Dunning's correlation consistent polarised valence basis set of triple zeta quality (cc-pVTZ [56]). The first basis set introduces 148 basis functions for norbornene, the second one 251 and the third one 350, respectively.

The results confirm the empirical rule [67] that OVGF pole strengths smaller than 0.85 corroborate a breakdown of the orbital picture of ionization at the ADC(3) level. To examine the influence of the functional and basis set applied in the optimization of the geometry, the molecular structure of norbornene has been further optimized at the MP2/aug-cc-pVDZ theoretical level (MP2 ≡ Møller-Plesset second order perturbation theory). With respect to the very limited influence (Table 2) on *vertical* one-electron OVGF/cc-pVDZ ionization energies of further improvements of the employed (cc-pVDZ) basis set and (B3LYP/TZVP) geometry (~0.05 to ~0.1 eV and ~0.02 to ~0.03 eV, respectively), the expected accuracy for the corresponding ADC(3)/cc-pVDZ results is of the order (or better) than ~0.2 eV, which a comparison with the experimental (*adiabatic*) PES (He I, He II) vales of Table 1 confirms, except for orbital 7a'' (~0.3 eV discrepancy).

As a guide to the eye, the identified solutions of the secular ADC(3) eigenvalue problem are displayed in Figure 3 as a spike spectrum and in the form of a convoluted density of states, along with the ultraviolet photoionization spectra by Bischof *et al.* [12] and Bieri *et al.* [15]. The convolution has been performed using as a spread function a combination of a Gaussian and a Lorenzian with equal weight with a Full Width at Half Maximum (FWHM) parameter of 1.1 eV and by simply scaling the line intensities according to the computed ADC(3) pole strengths, neglecting thereby the varying influence of molecular orbital cross sections. The comparison between theory and experiment is more than satisfactory for the ionization spectra: our simulations very nicely reproduce the position, shape, width and relative intensities of bands in the He(I) and He(II) spectra. Note a very significant breakdown of the orbital picture of ionization at binding energies above 22 eV, in the form of a dispersion of the 3a', 1a'' and 2a' ionization intensity over many shake-up lines, with comparable strength ($\Gamma_f < 0.225$). No line with a pole strength larger than 0.005 could be recovered for the 1a' orbital, as a result of the extremely limited symmetry C_s of norbornene, which enables many interactions between excited configurations in the cation. By analogy with the 3a', 1a'' and 2a' orbitals, and a number of studies of the ionization spectra of n-alkanes and cycloalkanes [67-72], as well as norbornane [44], we may assume energy relaxation effects of the order of ~ 3.5 eV for ionization of an electron out of orbital 1a'. Considering that the HF/cc-pVDZ orbital energy amounts to 31.9 eV, the most important shake-up lines derived from that orbital should therefore concentrate around 28.4 eV, i.e. at ~ 4 eV above the vertical double ionization threshold of norbornene which the benchmark CCSD(T)/cc-pVDZ theoretical level locates at 24.6 eV. 1p-GF studies of ionization spectra using diagonalization approaches that preserve spectral moments, such as the band-Lanczos procedure [73, 74], should be performed to fully confirm this prediction. It is nonetheless clear that all shake-up states that would be identified from such band - Lanczos calculations for the 1a' orbital are subject to decay via emission of a second electron, and therefore should more correctly be regarded as resonances in a continuum of shake-off states.

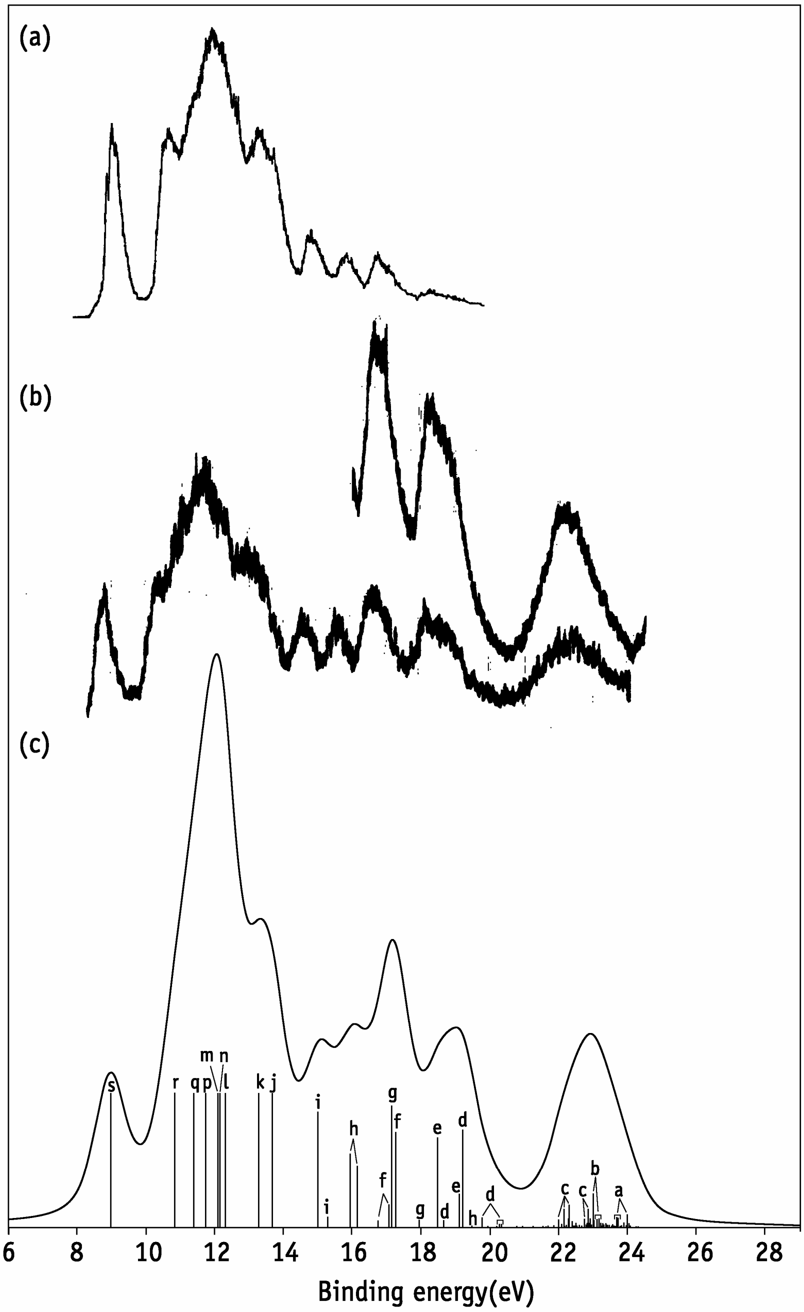

Figure 3. Comparison between the measured (a) He (I) [12], (b) He (II) [15] and (c) ADC(3)/cc-pVDZ theoretical ionization spectrum of norbornene.

3.4.5 Comparison between experimental and theoretical momentum distributions

Deconvolving the ionization spectra, measured at each of a chosen set of angles ϕ, by means of a least squares fit technique [18] allows us to derive the MDs associated to each of the peaks identified in Figures 2a and 2b. Although the measured MDs are not absolute, relative magnitudes for the different transitions are obtainable [17]. In the current EMS investigation of the valence states of NBN, the experimental MDs are placed on an absolute scale by summing the experimental flux for each measured ϕ for the first 13 outer-valence orbitals, and then normalizing this to the corresponding sum from our PWIA-BP/TZVP calculation.

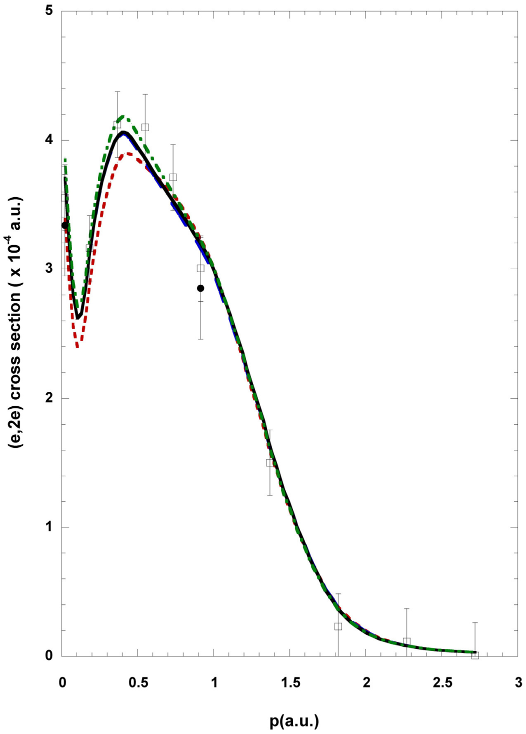

Figure 4. 1500 eV symmetric noncoplanar MD for the $12a'$ HOMO of norbornene (ε_f ~ 8.97 eV). The present data for run A (•) and run B (□) are compared against the results of our PWIA-DFT calculations: (red ---) LSD/DZVP, (blue — —) LSD/TZVP, (black·—) BP/TZVP, (green ·-·-) BLYP/TZVP. Acronyms are defined in the text.

The results from this process for the highest occupied molecular orbital (HOMO), the 12a' orbital, are shown in Figure 4. In this case we find generally good agreement between all the calculated PWIA-XC/TZVP momentum distributions and our corresponding EMS data taken in two independent runs (Runs A and B). Agreement between the data and the calculated PWIA-LSD/DZVP momentum distribution is less impressive, but still fair. A slight underestimation of the experimental results by all theoretical methods is noted for $p < 0.8$ au. Significant differences from one model to the other are observed in that momentum region. Note that the error bars on all the MD data represent one standard deviation uncertainty. Further note that the experimental MD data from independent runs A and B are also consistent with one another, a feature that is repeated for all the measured MDs. The results in Figure 4 strongly suggest that the EMS spectroscopic factor (Γ_f) for the 12a' HOMO is approximately 1. This observation is entirely consistent with our calculated ADC(3) and OVGF spectroscopic factors for this orbital (see Table 2).

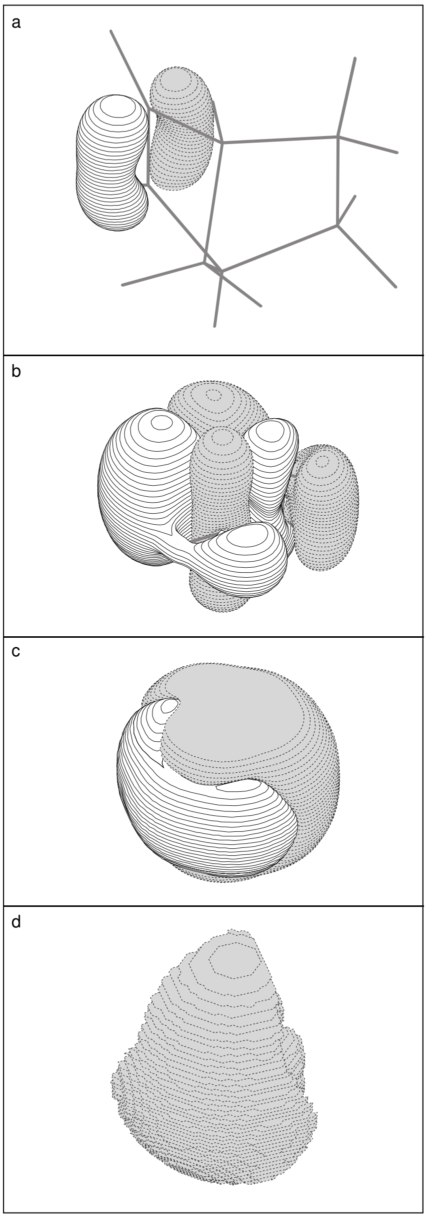

Figure 5. Density contours for the HOMO, using MOLDEN 3.8 and the following inputs: (a) contour = 0.100, edge = 7.00 Å; (b) contour= 0.800, edge = 15.00 Å; (c) contour = 1.00×10^{-8}, edge = 40.00 Å; (d) contour = 5.00×10^{-10}, edge = 200.00 Å (B3LYP/TZVP results).

The HOMO of norbornene has a' symmetry, and as such is expected to have a momentum distribution with a non-vanishing and maximal density at $p \rightarrow 0$. This is indeed what is predicted theoretically and observed experimentally (Figure 4). Also in apparently good agreement with the experimental momentum distribution for the HOMO, the peak calculated at $p \rightarrow 0$ is very narrow and followed by a deep minimum at $p \rightarrow 0.1$ a.u.. At larger momenta, the momentum density for the

HOMO rises again, to form a second broad distribution with a rather characteristic *p*-type profile, with a maximum at *p* ~ 0.4 a.u., and a slight shoulder at *p* ~ 1.0 a.u. In line with these observations, it is worth noting that, upon large contour values and at close distances (3.5 Å) in the molecular framework, the HOMO can be merely described as a π-type orbital that is strongly localized around the unique C=C bond of this molecule (Figure 5a). This is in sharp contrast with all other orbitals of norbornene (see for example Figures 6 and 7 for the NHOMO). This topology at short distances in configuration space explains the very strong resemblance of the corresponding momentum distribution to a *p*-type profile, at values of *p* larger than 0.1 a.u.. Upon selecting contour values of 0.008, we see (Figure 5b) that the π-bond starts to interact with much less important contributions from the nearby C-C and C-H bonds. Interestingly, the average radius of the electron density enclosed by this contour is around 7 Å, which corresponds to an electron momentum of 0.0076 a.u., thus very close to the location of the minimum observed in the MD profile of the HOMO! Upon looking at an extremely low contour value (10^{-8} in Figure 5c and 5×10^{-10} in Figure 5d), and correspondingly at very large distances (r = 20.0 Å and r = 100.0 Å), it appears that the topology of the HOMO reverts to an *s*-type for an external observer. Thus, it can be concluded *that EMS very reliably probes the effective topology of orbitals at varying distances from the molecular centre in configuration space, and the way the individual atomic components interact with each other.* In more specific words, the sharp but clearly apparent peak at $p \to 0$ should be regarded as the consequence at very large distances ($r \to \infty$) of interferences of the neighboring C-C bonds on the localized π-bond.

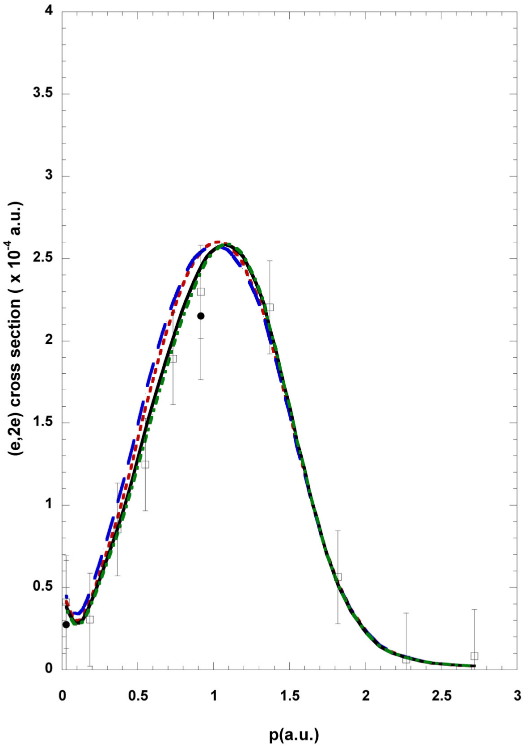

Figure 6. 1500 eV symmetric noncoplanar MD for the 7a'' NHOMO of norbornene (ε_f ~10.55 eV). The legend is the same as that for Figure 4.

Unlike the MD for the HOMO, which exhibits some structure at small *p* (see Figure 4), the measured and calculated MDs for the $7a''$ NHOMO all exhibit classic “*p*-like” symmetry [10]. This is clearly illustrated in Figure 6. For the NHOMO, however, the PWIA-LSD/DZVP and PWIA-LSD/TZVP calculations slightly overestimate the magnitude of the measured MD. We can not be more definitive in our comments because of the size of the error bars on the measurement, which largely reflect the relatively small (e,2e) cross section for this orbital. Agreement between the measured MD and the calculated PWIA-BP/TZVP and PWIA-BLYP/TZVP momentum distributions remains excellent. As was the case for the HOMO, the results in Figure 6 also strongly suggest that $\Gamma^{EMS}_{7a''} \sim 1$, which is again in good accord with our calculated ADC(3) and OVGF pole strengths (see Table 2). Finally, from inspection of the density contours drawn for the NHOMO (see Figure 7), we note that this orbital clearly contributes to the $\sigma_{C\text{-}C}$ and $\sigma_{C\text{-}H}$ bond systems of norbornene.

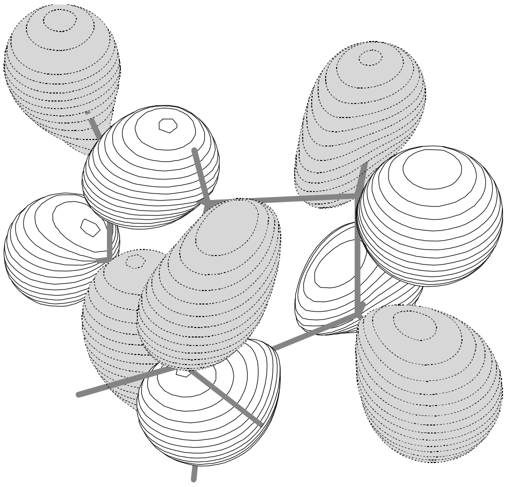

Figure 7. Density contour for the NHOMO, using MOLDEN 3.8 and the following inputs: contour = 0.05, edge = 10.00 Å.

In Figure 8 we show the measured and calculated MDs for the 6a” + $11a'$ + $10a'$ + $9a'$ + 5a” orbitals of norbornene. Recall that combining the MDs of all these orbitals was necessary due to the limited experimental energy resolution. For these orbitals we find that the momentum distribution calculated at the LSD/DZVP level, within the plane wave impulse approximation (PWIA), significantly overestimates the magnitude of the experimental cross section for all *p*. This suggests that the combination of the LSD exchange correlation functional and DZVP basis set is not providing a very good representation of these orbitals. While less striking, Figure 8 also appears to indicate for momenta in the range 0.15 au $\leq p \leq$ 0.75 au, that the PWIA-LSD/TZVP momentum distribution overestimates the magnitude of the experimental MD. Nonetheless, the very good level of agreement between theory and experiment for the remaining BP/TZVP and BLYP/TZVP results show that the EMS spectroscopic factors for all the $6a''$, $11a'$, $10a'$, $9a'$ and $5a''$ orbitals probably lie within the range 0.9-1. This finding is consistent with the MO picture of ionization being valid here for these outer-valence orbitals, a result in good agreement with our ADC(3) and OVGF calculations of Table 2. The momentum distribution shown in Figure 8 exhibits 3 maxima and 2 minima, which presumably reflects the fact that the corresponding set of orbitals contain two *p*-type (a'') and three *s*-type (a') orbitals, hence the non-vanishing contribution at *p* = 0 a.u.

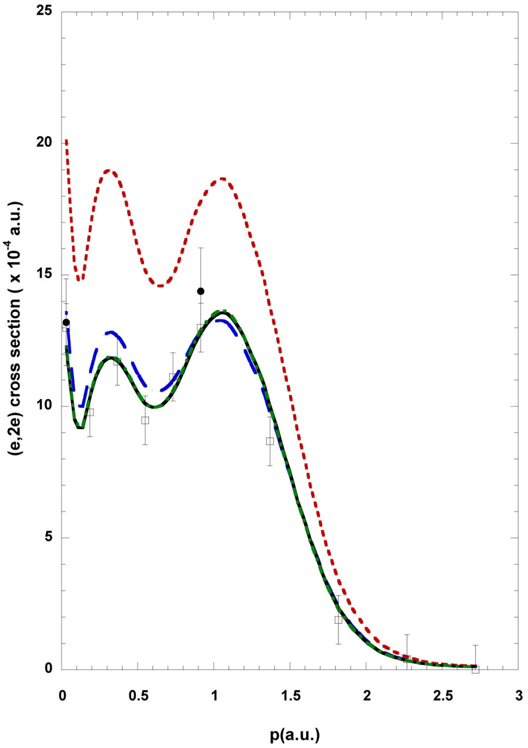

Figure 8. 1500 eV symmetric noncoplanar MD for the 6a''+11a'+10a'+9a'+5a'' orbitals of norbornene (ε_f ~11.85 eV). The legend is the same as that for Figure 4.

The 5a' + 3a'' orbital momentum distributions are illustrated in Figure 9. In this case we see that all the MDs are strongly peaked (large cross section) as $p \rightarrow 0$ au, indicating an "*s*-type" symmetry [10] probably due to strong C(2s) contributions. However, it is also clear from Figure 9 that there is an important structure in the MDs, occurring at around p ~ 0.9 au. This indicates there is also a *p*-type contribution [10] to the overall symmetry of the MDs, due to orbital 13 (3a''). In all cases we find very good agreement between the experimental and theoretical MDs for these orbitals, suggesting that the 5a' + 3a'' orbitals do not provide a very sensitive test for the quality of our various PWIA-XC/DFT calculations. From the data in Figure 9 we estimate our (total) EMS spectroscopic factors for the 5a' and 3a'' orbitals would be in the range 0.9 - 1, which is consistent with the fractions of intensity recovered under the form of lines with a spectroscopic strength larger than 0.005 and which amount to 0.881 and 0.842, respectively. Note nonetheless a shake-up satellite originating from ionization of the 3a'' orbital with a rather significant intensity Γ_f= 0.151) at 17.1 eV, which EMS can not discriminate from the main (one-electron) ionization line at 17.3 eV because of the too limited experimental resolution.

The MD shown in Figure 10 displays two maxima at p ~ 0 a.u. and p = 0.75 a.u., along with one minimum at 0.2 a.u.. This undoubtedly reflects the fact that the analyzed set of orbitals (4a'+ 2a'') contain one *s*-type (4a') orbital and one *p*-type (2a'') orbital. In this case the superiority of the PWIA-BP/TZVP and PWIA-BLYP/TZVP MDs, for p < 0.4 au, is clear. However, none of the theoretical MDs correctly reproduces the experimental MD over the entire range of p studied. The theoretical MDs seem to underestimate the magnitude of the peak in the (e,2e) cross section in the vicinity of p ~ 0.75 au, and none of the theory MDs correctly predicts the width of this peak.

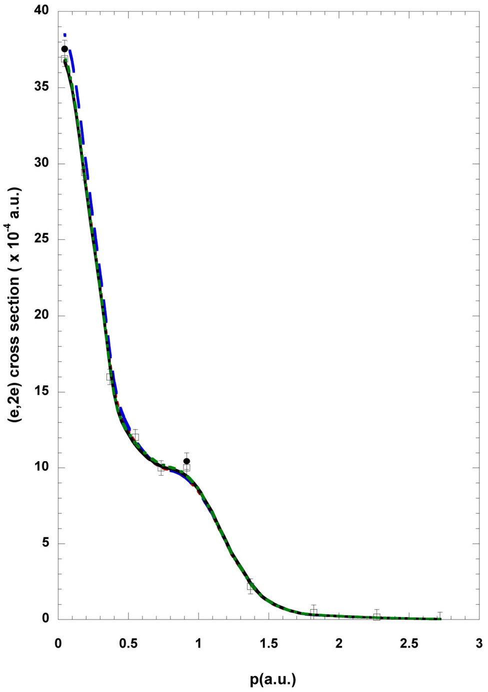

Figure 9. 1500 eV symmetric noncoplanar MD for the 5a'+3a''orbitals of norbornene (ε_f ~16.71 eV). The legend is the same as that for Figure 4.

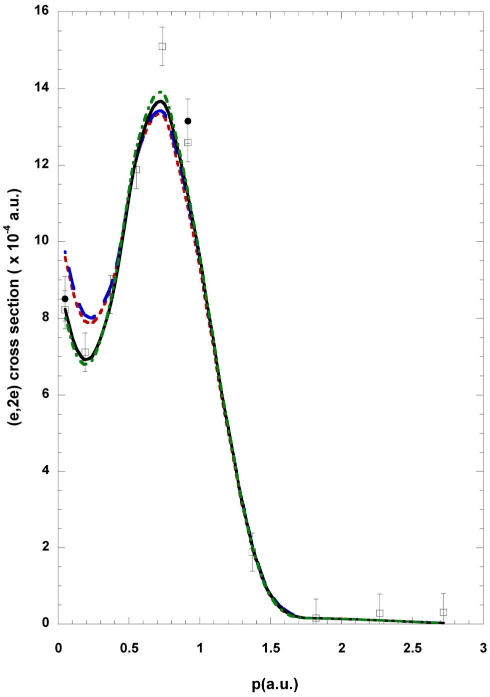

Figure 10. 1500 eV symmetric noncoplanar MD for the 4a'+2a''orbitals of norbornene (ε_f ~18.22 eV). The legend is the same as that for Figure 4.

This is precisely the reason why we seek an "optimum" wavefunction for the molecule in question. It is quite rare in EMS for theory to be able to accurately predict all the experimental MDs for all the MOs in question [10, 11]. For norbornene we have seen that both the PWIA-BP/TZVP and PWIA-BLYP/TZVP calculations do a reasonable job in reproducing the experimental MDs for most of the orbitals considered. For norbornene however, unlike some previous species [11], it is hard to state which model wavefunction works best overall. As a consequence we must rely on the experience acquired with previous studies of chemically similar species such as norbornane [44] and norbornadiene [75]. In those two cases the BP/TZVP exchange correlation functional and basis set best represented these species, and as a consequence we also choose BP/TZVP as our "optimum" model for norbornene. Before discussing the molecular geometry of norbornene, derived from BP/TZVP, let us consider the most challenging part of the ionization spectrum, namely the innermost valence region at $\varepsilon_f \geq 25$ eV.

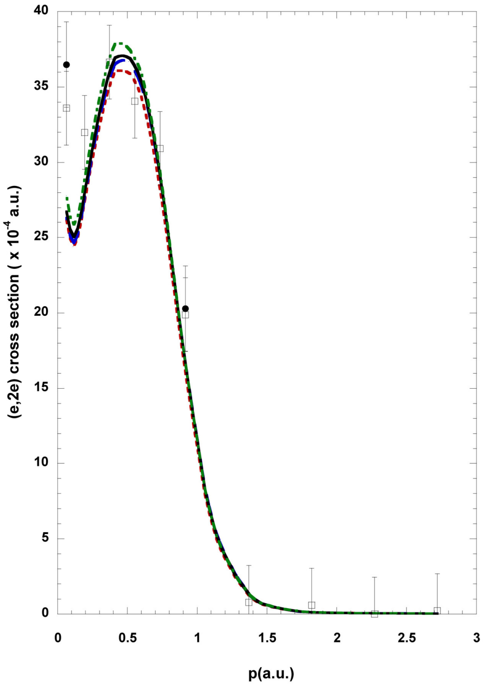

Figure 11. 1500 eV symmetric noncoplanar MD for the 3a'+1a''+2a' orbitals of norbornene. The legend is the same as that for Figure 4.

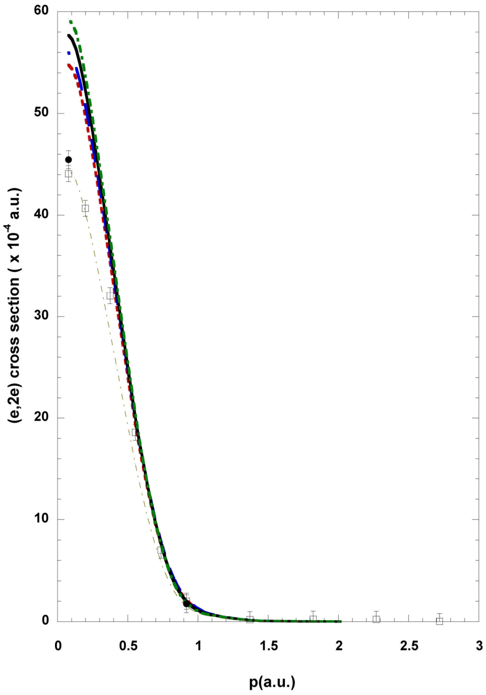

Figure 12. 1500 eV symmetric noncoplanar MD for the innermost valence orbital (1a') of norbornene. The legend is the same as that for Figure 4, except an additional MD representing 0.77 × PWIA-BP/TZVP result (thin dash-dot line) is also plotted.

The cumulative momentum distribution for orbitals 3a', 1a'' and 2a' is displayed in Figure 11. As for the $2a_1$ + $1b_2$ + $1b_1$ orbitals of norbornane [44], the theoretical momentum distributions, whatever the employed model chemistry, are somewhat lower in magnitude than the experimental ones, especially at $p < 1$ a.u. Nonetheless, the present experimental momentum profile exhibits clearly a minimum at $p \sim 0.2$ a.u., in fair agreement with theory, and thus nicely reflects the fact that bands 9 and 10 consist of a mixture of ionization lines with *s*-type and *p*-type symmetries. The underestimation by theory of the experimental EMS cross sections at low momenta can be attributed to a number of shortcomings in the employed model, among others being the well-known deficiencies of the currently used gradient corrected BP functional in the asymptotic region ($r \rightarrow \infty$), or significant departures from a vertical depiction of ionization due to ultrafast molecular relaxation and nuclear dynamical effects in a highly strained cage structure, at shake-up ionization energies approaching the double ionizable threshold (24.6 eV, see above). By analogy with [76], one may of course also always invoke a breakdown of the plane wave impulse approximation - we would like to emphasize however that it may not be appropriate to systematically and only blame failings in that approximation as soon as Kohn-Sham (BP) momentum distributions for vertical ionization events fail to quantitatively reproduce experiment. In line with this we suggest for instance that the strong dependence of the relative (e,2e) cross sections at very small momenta, on the energy of the impinging electron, that was recently observed in EMS experiments on glyoxal [77], might not (only) be due to shortcomings in the PWIA. Rather, it might also reflect changes of the timescale of the (e,2e) ionization processes (~ 10^{-17} s [78]) - in other words this energy dependence may reflect variations of the extent of the nuclear motions that are effectively probed in these experiments.

Figure 12 illustrates the experimental MD for the sum of peaks 11 and 12 of Figure 2, and the corresponding $1a^{'}$ theoretical MDs from the models considered. All the theoretical MDs do a fair job in predicting the shape of the experimental result, although they all overestimate the magnitude of the experimental cross section over most of the measured momentum range. This result is not really surprising as it is clear from Figure 2 that there is additional experimental flux at binding energies greater than 30 eV which we are not accessing in this study. When our PWIA-BP/TZVP momentum distribution for the $1a^{'}$ orbital is scaled by a factor of 0.77, fair agreement is found between the experimental MD for peaks 11 and 12 and this scaled theory result. This provides further justification for our preliminary assignment of the measured flux originating from ionization of the $1a^{'}$ orbital. However, as our ADC(3) result does not find any ionization line for the $1a^{'}$ orbital with a pole strength larger than 0.005, our assignment must remain tentative at this time. We would advocate further band - or block – Lanczos studies of the bands relating to shake-up lines with a pole strength smaller than 0.005.

Finally, we note that there are several orbital MDs that we have not specifically discussed or plotted in this section. These MDs reinforce the argument for the utility of either BP/TZVP or BLYP/TZVP that we have made in this section, but do not add any further insight.

3.4.6 Molecular properties of norbornene

A. Molecular geometry

We used the BP/TZVP model to derive the molecular structure of norbornene. This was compared in detail with experimentally determined values [79-81] and those from other MO calculations [1, 9, 81, 82] to determine how well the BP/TZVP model reproduced the structure.

In general, our calculations of molecular geometries using the BP/TZVP model are in very good agreement with the experimentally determined molecular geometries (given the experimental uncertainties), and compare favorably with the results from other MO calculations. The results are summarized in Table 3. Note that in Table 3 we have only included the highest-level calculation reported by Holthausen and Koch [82], and have omitted the recent calculations on the structural impact on the methano-ring in norbornadiene, norbornene and norbornane by Wang *et al.* [9] as they originate from our group. To assist the reader in the discussion that follows, refer to the structural representation and atom numbering of the norbornene molecule that we gave in Figure 1.

The C_5-C_6 single bond involving two of the methylene carbon atoms has a bond distance of 1.560 Å from our calculations, in excellent agreement with that from the recent synchrotron radiation powder diffraction study [81] and also in good agreement with those from the earlier electron diffraction [79] and x-ray powder diffraction [80] studies. The $C_2 = C_3$ double bonded methylene carbons have a bond length of 1.348 Å from our BP/TZVP calculation, in fair agreement with all the experimental results [79, 80] when their respective uncertainties are allowed for. The remaining carbon-carbon bonds involving the bridge or bridgehead carbon atoms are also in excellent agreement with experiment (see Table 3). The agreement with experiment for our BP/TZVP calculation is better than for the small basis set *ab initio* and semi-empirical MO-derived geometries in Table 3 [1, 81, 82], although we note that the second-order Møller/Plesset perturbation theory (MP2) result from Holthausen and Koch [82] is also doing a fair overall job.

TABLE 3: Experimental and Theoretical Molecular Geometry of Norbornene

parameter	gas phase electron diffraction[79]	X-ray powder diffraction[80]	synchrotron radiation powder diffraction[81]	BP/TZVP present	HF/STO-3G[1]	HF/6-31G* [81]	MP2/6-311G(d)
$r(C_1-C_6)$ Å	1.550	1.562	1.558	1.571	1.563	1.558	1.561
$r(C_1-C_7)$ Å	1.566	1.547	1.543	1.550	1.548	1.541	1.540
$r(C_5-C_6)$ Å	1.556	1.556	1.560	1.560	1.556	1.559	1.555
$r(C_2-C_3)$ Å	1.336	1.334	1.332	1.348	1.314	1.324	1.351
$r(C_1-C_2)$ Å	1.529	1.524	1.524	1.524	1.535	1.523	1.515
$\angle C_1C_5C_6$, deg	–	100.5	103.5	102.98	102.9	102.7	–
$\angle C_1C_7C_4$, deg	–	92.3	95.3	93.78	93.3	93.5	94.0
$\angle C_2C_1C_6$, deg	–	109.3	105.6	105.87	106.4	106.5	–
$\angle C_2C_1C_7$, deg	–	99.4	99.0	100.29	100.9	100.5	–
$\angle C_6C_1C_7$, deg	–	102.1	99.6	100.32	99.4	100.0	–
$\angle C_1C_2C_3$, deg	108.6	106.5	108.1	107.45	107.8	107.6	107.3
$d(C2-C6)$ Å	–	–	–	2.470	–	–	–

The experimental bond angles were also in general well reproduced by our BP/TZVP calculation, especially the bridge and bridgehead angles. The bridge angle ($\angle C_1C_7C_4$) of 93.78° from our DFT calculation lies comfortably within the experimental range of 92.3° - 95.3° from the X-ray and synchrotron powder diffraction studies [79, 80], respectively. A similar result can be found for nearly all the other bond angles we list in Table 3, namely our DFT result lies comfortably within the spread of angles represented by the various experimental investigations [79-81], except for the $\angle C_2C_1C_7$ which the BP/TZVP approach tends to slightly overestimate as compared with the experimental results.

B. Vibrational spectra

In the present work, we also make use of the BP/TZVP model that has been previously calibrated against experimental momentum distributions in a study of the infrared (IR) spectrum of norbornene, employing the Harmonic Oscillator approximation for computing vibrational eigenstates. Electrical harmonicity is further invoked to compute IR frequencies as functions of mixed second-order derivatives of the total energies with respect to normal displacements and to an external electric field (the so-called double harmonic approximation [83, 84]). The obtained results are provided in Figure 13, using as a spread function for convolving the spike spectrum a Gaussian of 20 cm^{-1} full width at half the maximum. Along with the experimental spectrum [85] and the BP/TZVP simulation, the most apparent vibrational eigenmodes are also displayed in Figure 13. The simulation in Figure 13b for the frequency range comprised between 2800 to 3200 cm^{-1} has been drawn using for the sake of clarity a rescaling factor of 0.985 on frequencies, whereas unrescaled frequencies have been used for Figure 13a (600 - 1700 cm^{-1}).

With the BP/TZVP model, we have been able to reproduce the position of the bands in the experimental spectrum (Figure 13, Table 4) with reasonable accuracy (about ~ 27 cm^{-1} on average). A rather noteworthy exception is band O at 2880 cm^{-1} which, whatever the level, theory systematically overestimates by 100 to 200 cm^{-1} (Table 4). It is thus worth noting that the BP/TZVP results are also in line with B3LYP/cc-pVTZ and MP2/aug-cc-pVDZ calculations (Table 4), except for an energy reordering of a few pairs of nearly degenerate lines, within energy intervals of the order of a few cm^{-1}, and which can therefore not be resolved experimentally. Relative intensities of bands are also nicely reproduced (Figure 13), taking into account the fact that rotational transitions may differently broaden bands. Rotational levels with a characteristic energy spacing of about 10 cm^{-1} are for instance very clearly apparent on the experimental side in the bands (**A**, **P**) associated to the vibrational eigenmodes **6** and **39-43**, which both relate to rather strongly localized distortions, namely the H-C=C out-of-plane bending and C-H stretching modes, respectively (Figure 13). The other modes (Figure 13) are more delocalized and quite naturally therefore exhibit a lesser IR intensity.

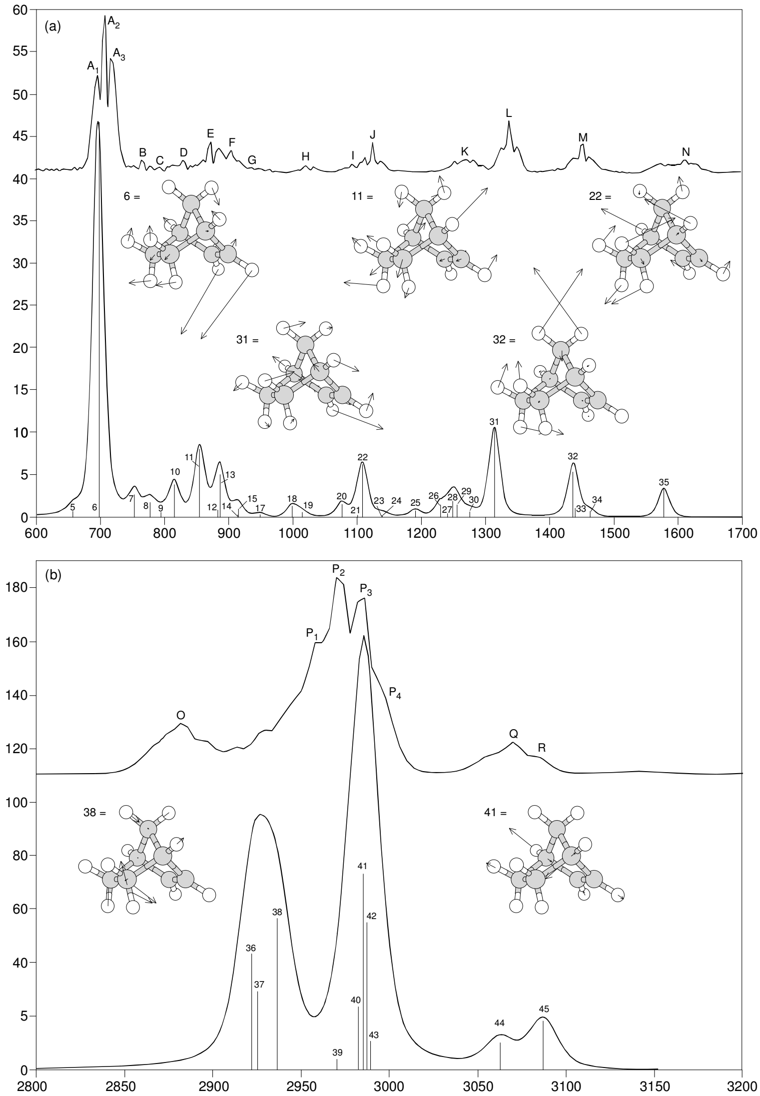

Figure 13. Experimental [85] and BP/TZVP simulation for the vibrational spectra of norbornene: (a) 600-1700 cm^{-1}, (b) 2800-3200 cm^{-1}. Note that the theory is convolved with a 20 cm^{-1} (FWHM) Gaussian. Note also that the most apparent vibrational eigenmodes are displayed in this figure (see Table 4 for label definitions).

TABLE 4: Theoretical Analysis of the IR Spectrum of Norbornene[a]

		BP/TZVP		B3LYP/TZVP		MP2/aug-cc-pVDZ		experiment[b]			
mode number	symmetry label	freq	int	freq	int	freq	int	peak	freq	max int[c]	int abs[d]
1	a″	246.8	0.0	258.8	0.0	241.5	0.0				
2	a′	366.5	3.1	382.1	2.6	372.6	3.1				
3	a′	460.8	1.3	479.2	1.1	467.9	1.2				
4	a″	471.8	0.2	487.9	0.2	471.7	0.2				
5	a″	656.7	0.7	677.9	0.6	661.8	0.6	A_1	698.0	16.25	
6	a′	697.9	46.6	730.0	41.4	713.9	45.4	A_2	710.0	26.02	16.98
								A_3	718.0	19.11	
7	a′	753.1	2.7	775.7	2.5	773.3	4.9	B	766.0	2.680	0.625
8	a″	777.1	1.8	799.0	1.8	794.5	0.9	C	790.0	1.480	0.426
9	a′	794.1	0.6	821.9	0.5	813.4	0.4				
10	a″	815.0	3.9	836.6	2.8	844.2	3.8	D	830.0	2.610	1.395
11	a′	854.7	8.0	878.1	7.3	891.5	5.6	E	874.0	5.530	1.244
12	a′	882.6	1.0	904.9	0.8	922.5	0.9				
13	a″	886.6	5.1	916.5	3.0	900.5	4.3	F	906.0	4.200	1.368
14	a″	914.0	0.5	959.2	1.1	947.4	0.3				
15	a′	914.5	1.1	938.7	1.2	956.8	0.0	G	938.0	1.400	0.435
16	a″	935.3	0.0	966.2	0.7	960.7	0.5				
17	a′	949.2	0.4	972.8	0.6	982.6	0.4				
18	a′	999.0	1.4	1038.3	1.3	1028.8	1.0	H	1022.0	1.710	0.533
19	a″	1014.9	0.7	1055.1	0.9	1033.4	0.4				
20	a′	1076.5	1.6	1116.2	1.2	1098.7	1.3	I	1098.0	1.590	0.948
21	a″	1100.5	0.3	1139.8	0.4	1121.1	0.2				
22	a′	1108.6	6.2	1148.0	4.9	1133.4	4.8	J	1126.0	5.230	2.706
23	a″	1138.8	0.2	1184.7	0.2	1171.3	0.1				
24	a′	1139.8	0.2	1188.2	0.2	1167.0	0.1				
25	a″	1191.0	0.8	1238.3	0.5	1223.2	0.6				
26	a″	1229.9	1.5	1285.8	1.7	1253.6	0.9				
27	a″	1240.5	0.4	1297.1	0.0	1267.8	0.4				
28	a″	1248.9	1.9	1301.5	1.1	1283.8	2.1	K	1270.0	2.620	3.143
29	a′	1256.2	1.4	1305.8	1.1	1296.0	1.7				
30	a′	1275.6	0.6	1329.6	0.4	1309.5	0.2				
31	a″	1313.9	10.5	1367.2	9.9	1354.7	7.2	L	1338.0	8.670	4.932
32	a′	1436.3	5.3	1494.2	4.4	1470.7	4.6	M	1454.0	5.090	4.231
33	a″	1439.6	1.0	1495.2	0.9	1473.1	0.8				
34	a′	1462.5	0.7	1517.8	0.7	1497.9	0.7				
35	a′	1578.0	3.3	1636.3	2.4	1586.3	3.2	N	1610.0	2.500	4.036
36	a′	2966.5	43.3	3040.6	41.1	3068.7	36.6				
37	a″	2969.8	29.4	3042.4	27.3	3073.7	25.9				
38	a′	2981.3	56.4	3054.8	56.5	3085.7	49.3	O	2882.0	26.41	19.54
39	a″	3015.6	4.0	3082.8	4.4	3135.1	4.1				
40	a′	3027.8	23.7	3096.8	26.0	3144.1	7.9	P_1	2958.0	67.11	
41	a″	3030.7	73.3	3100.2	76.5	3141.8	58.7	P_2	2970.0	100.0	100.0
42	a′	3032.7	55.1	3101.2	57.0	3148.6	23.5	P_3	2986.0	89.66	
43	a′	3034.8	10.7	3104.8	12.5	3152.5	45.2	P_4	2990.0	54.76	
44	a″	3109.3	10.3	3181.4	9.8	3218.6	6.9	Q	3070.0	16.73	11.72
45	a′	3134.2	18.2	3205.9	18.0	3244.6	15.6	R	3142.0	19.00	2.012

[a] Frequencies and calculated intensities are given in cm^{-1} and km/mol, respectively. [b] See ref 85. [c] Relative intensity in arbitrary unit at peak maximum. [d] Integrated absorbency in arbitrary unit.

Superficially it appears that, among the retained BP/TZVP, B3LYP/cc-pVTZ and MP2/aug-cc-pVDZ models, BP/TZVP is the one that provides the most accurate insights into the IR spectrum of norbornene. Some care is needed however before concluding that BP/TZVP is the best model for IR spectroscopy: indeed, due to the neglect of anharmonicities, theoretical frequencies obtained on the basis of the RRHO approximation are expected to overestimate the experimental ones by typically a few %, and this is precisely what is observed at the B3LYP/cc-pVTZ and MP2/aug-cc-pVDZ levels. Due to the importance of cyclic strains in the investigated cage compounds, we expect that anharmonicities should have an unusually strong influence on the frequencies. In sharp contrast with the normal expectations, the BP/TZVP frequencies in the 600 - 1700 cm^{-1} frequency range are found to systematically *underestimate* experiment by ~ 20 cm^{-1}. In line with our previous comments on the need to develop *ab initio* schemes for computing orbital momentum distributions from benchmark Dyson orbital theories, this indicates that the superiority of the BP/TZVP//RRHO model in reproducing experimental frequencies is very probably the outcome of error cancellations. This model is obviously sufficient for assigning vibrational bands with great confidence, but, clearly, further models fully coping with anharmonic effects, centrifugal distorsions, employing huge basis sets (at least aug-cc-pVTZ) and, last but not least; treating electronic correlation at an extremely high-level (CCSD[T]) will be needed before stating that the right frequencies have been obtained for the right reasons, within 20 cm^{-1} accuracy. Such calculations, however, are far too computationally expensive to be performed at present.

3.4.7 Conclusions

We have reported on the first comprehensive EMS study of the valence electronic structure of norbornene, in conjunction with DFT calculations of orbital MDs, and 1p-GF [OVGF and ADC(3)] calculations of the one-electron and shake-up ionization spectrum. Very good agreement is generally found between the experimental PES and EMS binding energies, on the one hand, and the 1p-GF results, on the other hand. Where a comparison is possible, pole strengths calculated by our 1p-GF procedures, certainly for the outer valence orbitals, were found to be largely consistent with those determined from our EMS MD data. Strong final state configuration interaction effects are predicted in our ADC(3) calculation for the inner valence $3a'$, $1a''$, $2a'$ and $1a'$ orbitals, a prediction which is consistent with the very significant band broadening observed at binding energies beyond ~ 20 eV.

Momentum Distributions for the $12a'$, $7a''$, $6a'' + 11a' + 10a' + 9a' + 5a''$, $4a'' + 8a'$, $7a'$, $6a'$, $5a' + 3a''$, $4a' + 2a''$, $3a' + 1a'' + 2a'$ and $1a'$ orbitals were measured and compared against a series of PWIA-based calculations using DFT DGauss basis sets. Our calculations, for each of the two basis sets (DZVP and TZVP), were performed using LSD and both BP and BLYP exchange correlation corrections to the DFT functional. On the basis of this comparison between the experimental and theoretical MDs, and previous experience with the series of structurally similar species of norbornadiene (NBD) and norbornane (NBA) [44, 75], we found that BP/TZVP provided an acceptable representation of the experimentally determined NBN wave function. The molecular structure of norbornene, as derived from this "optimum" BP/TZVP wave function, was seen to be in generally good agreement with the results from independent measurements. This provides compelling evidence for the utility of EMS in *a priori* evaluation of a quantum chemical wave function. In future works, with respect to the known limitations of currently available gradient corrected functionals, the quality of model wavefunctions derived from DFT computations should also be tested in detail against Dyson orbitals obtained from benchmark 1p-GF/ADC(3) calculations. The consequences of both electronic and molecular relaxation effects and nuclear dynamics within the timescale of EMS should in the future also be examined systematically in detail.

References

[1] Castro, C. R.; Dutler, R.; Rauk A.; Wieser, H. *J. Mol. Struct. (Theochem)* 1987, 152, 241.

[2] Koga, N.; Ozawa,T.; Morokuma, K. *J Phys. Org. Chem.* 1990, 3, 519.

[3] Spanget-Larsen, J.; Gleiter, R. *Tetrahedron* 1983, 39, 3345.

[4] Rondan, N. G.; Paddon-Row, M. N.; Caramella, P.; Houk, K. N. *J. Am. Chem. Soc.* 1981, 103, 2436.

[5] Spanget-Larsen, J.; R Gleiter, R. *Tetrahedron Letts.* 1982, 23, 2435.

[6] Wilsey, S.; Houk, K. N.; Zewail, A. H. *J. Am. Chem. Soc.* 1999, 121, 5772.

[7] Diels, O.; Alder, K. *Justus Liebigs Ann. Chem.* 1928, 460, 98.

[8] Dewar, M. J. S.; Jie, C. *Acc. Chem. Res.* 1992, 22, 537.

[9] Wang, F.; Brunger, M. J.; Winkler, D. A. *J. Phys. Chem. Sol.* 2004, 65, 2041.

[10] Weigold, E.; McCarthy, I. E. *Electron Momentum Spectroscopy*; Kluwer Academic/Plenum Publishers: New York, 1999.

[11] Brunger, M. J.; Adcock, W. *J. Chem. Soc. Perkin Trans.* 2002, 2, 1.

[12] Bischof, P.; Hashmall, J. A.; Heilbronner, E.; Harnung, V. *Helv. Chim. Acta* 1969, 52, 110.

[13] Demeo, D. A.; Yencha, A. J. *J. Chem. Phys.* 1970, 53, 4536.

[14] Wen, A. T.; Hitchcock, A. P.; Werstiuk, N. H.; Nguyen, N.; and Leigh, W. J. *Can. J. Chem.* 1990, 68, 1967.

[15] Bieri, G.; Burger, F.; Heilbronner, E.; Maier, J. P. *Helv. Chim. Acta.* 1977, 60, 2213.

[16] Bodor, N.; Dewar, M. J. S.; Worley, S. D. *J. Am. Chem. Soc.* 1970, 92, 19.

[17] McCarthy, I. E.; Weigold, E. *Rep. Prog. Phys.* 1991, 54, 789.

[18] Bevington, P. R.; Robinson, D. K. *Data Reduction and Error Analysis for the Physical Sciences*; McGraw-Hill Inc.: New York, 1990.

[19] McCarthy, I. E.; Weigold, E. *Rep. Prog. Phys.* 1988, 51, 299.

[20] Casida, M. *Phys. Rev. A* 1995, 51, 2005.

[21] Deleuze, M. S.; Pickup, B. T.; Delhalle, J. *Mol. Phys.* 1994, 83, 655.

[22] Szabo. A.; Ostlund, N. S. *Modern Quantum Chemistry: Introduction to Advanced Electronic Structure Theory*; McGraw-Hill: New York, 1989.

[23] Kohn, W; Sham, L. J. *Phys. Rev.* 1965, 140, A1133.

[24] Chong, D. P.; Gritsenko, O. V.; Baerends, E. J. *J. Chem. Phys.* 2002, 116, 1760.

[25] Gritsenko, O. V.; Braida, B.; Baerends, E. J. *J. Chem. Phys.* 2003, 119, 1937.

[26] Jellinek, J.; Acioli, P. H. *J. Chem. Phys.* 2003, 118, 7783.

[27] Becke, A. D. *Phys. Rev. A* 1988, 38, 3098.

[28] Becke, A. D. *J. Chem. Phys.* 1988, 88, 2547.

[29] Perdew, J. P. *Phys. Rev. B* 1986, 33, 8822.

[30] Lee, C.; Yang, W; Parr, R. G. *Phys. Rev. B* 1988, 37, 785.

[31] Liu, W.; Hong, G.; Dai, D.; Li, L.; Dolg, M. *Theor. Chem. Acc.* 1997, 96, 75.

[32] Choi, Y. J.; Lee, Y. S. *J. Chem. Phys.* 2003, 119, 2014.

[33] Duffy, P.; Chong, D. P.; Casida, M. E.; Salahub, D. R. *Phys. Rev. A* 1994, 50, 4707.

[34] Davidson, E. R. *Can. J. Phys.* 1996, 74, 757.

[35] Rolke, J.; Zheng, Y.; Brion, C. E.; Chakravorty, S. J.; Davidson, E. R.; McCarthy, I. E. *Chem. Phys.* 1997, 215, 191.

[36] Zheng, Y.; Pang, W. N.; Shang, R. C.; Chen, X J.; Brion, C. E.; Ghanty, T. K.; Davidson, E. R. *J. Chem. Phys.* 1999, 111, 9526.

[37] Pang, W. N.; Gao, J. F.; Ruan, C. J.; Shang, R. C.; Trofimov, A. B.; Deleuze, M. S. *J. Chem. Phys.* 2000, 112, 8043.

[38] Deleuze, M. S.; Pang, W. N.; Salam, A.; Shang, R. C. *J. Am. Chem. Soc.* 2001, 123, 4049.

[39] Adcock, W; Brunger, M. J.; McCarthy, I. E.; Michalewicz, M. T.; von Niessen, W.; Wang, F.; Weigold, E.; Winkler, D. A. *J. Am. Chem. Soc.* 2000, 122, 3892.

[40] Andzelm, J.; Wimmer, E. *J. Chem. Phys.* 1992, 96, 1290.

[41] Komornicki, A.; Fitzgerald, G. J. *J. Chem. Phys.* 1993, 98, 1398.

[42] Michalewicz, M. T.; Brunger, M. J.; McCarthy, I. E.; Norling, V. M. *CRAY Users Group 1995 Fall Proceedings*; Shaginaw, R., Ed.; 1995; pp 37-41.

[43] Schmidt, M. W.; Baldridge, K. K.; Boatz, J. A.; Elbert, S. T.; Gordon, M. S.; Jensen, J. J.; Koseki, S.; Matsunaga, N.; Nguyen, K. A.; Su, S.; Windus, T. L.; Dupuis, M.; Montgomery, J. A. *J. Comput. Chem.* 1993, 14, 1347.

[44] Knippenberg, S.; Nixon, K. L.; Brunger, M. J.; Maddern, T; Campbell, L.; Trout, N.; Wang, F.; Newell, W. R.; Deleuze, M. S.; Francois, J.-P.; Winkler, D. A. *J. Chem. Phys.* 2004, 121, 10525.

[45] Frost, L.; Weigold, E. *J. Phys. B* 1982, 15, 2531.

[46] Godbout, N.; Salahub, D. R.; Andzelm, J.; Wimmer, E. *Can. J. Chem.* 1992, 70, 560.

[47] Dunlap, B. I.; Conolly, J. W. D.; Sabin, J. R. *J. Chem. Phys.* 1979, 71, 4993.

[48] Becke, A. D. *J. Chem. Phys.* 1993, 98, 5648.

[49] Schirmer, J.; Cederbaum, L. S.; Walter, O. *Phys. Rev. A* 1983, 28, 1237.

[50] Schirmer, J.; Angonoa, G. *J. Chem. Phys.* 1989, 91, 1754.

[51] Weikert, H.-G.; Meyer, H.-D.; Cederbaum, L. S.; Tarantelli, F. *J. Chem. Phys.* 1996, 104, 7122.

[52] Cederbaum, L. S.; Hohlneicher, G.; Peyerimhoff, S. *Chem. Phys. Lett.* 1971, 11, 421.

[53] Pickup, B. T.; Goscinski, O. *Mol. Phys.* 1973, 26, 1013.

[54] Ohrn, Y.; Born, G. *Adv. Quantum. Chem.* 1981, 13, 1.

[55] Deleuze, M. S. *Int. J. Quantum Chem.* 2003, 93, 191.

[56] Dunning, T. H. Jr. *J. Chem. Phys.* 1989, 90, 1007.

[57] Deleuze, M. S.; Claes, L.; Kryachko, E. S.; Francois, J.-P. *J. Chem. Phys.* 2003, 119, 3106.

[58] Liu, B. in: *Numerical Algorithms in Chemistry, Algebraic Methods*, *LBL-8158*; Lawrence Berkeley Laboratory.

[59] Tarantelli, F.; Sgamellotti, A.; Cederbaum, L. S.; Schirmer, J. *J. Chem. Phys.* 1987, 86, 2201.

[60] Weikert, H.-G.; Meyer, H.-G.; Cederbaum, L. S.; Tarantelli, F. *J. Chem. Phys.* 1996, 104, 7122.

[61] Dunning, T. H. Jr. *J. Chem. Phys.* 1971, 55, 716.

[62] Martin, J. M.; El-Yazal, J.; Francois, J.-P. *Mol. Phys.* 1995, 86, 1437; See also: Koch, W.; Holthausen, M. C. A *A Chemist's Guide to Density Functional Theory*, 2nd ed.; Wiley VCH: Weinheim, Germany, 2001.

[63] Frisch, M. J.; Trucks, G. W.; Schlegel, H. B., *et al.* Gaussian98, revision A.7; Gaussian Inc, Pittsburg, PA 1998.

[64] Cederbaum, L. S.; Domcke, W. {\it Adv. Chem. Phys.} {\bf 1977}, {\it 36}, 205.

[65] Zakrewski, V. G.; von Niessen, W. {\it J. Comput. Chem.} {\bf 1993}, {\it 14}, 13.

[66] Kendall, R. A.; Dunning, T. H. Jr.; Harrison, R. J. *J. Chem. Phys.* 1992, 96, 6796.

[67] Deleuze, M. S. *J. Chem. Phys.* 2002, 116, 7012.

[68] Deleuze, M. S.; Denis, J. P.; Delhalle, J.; Pickup, B. T. *J. Phys. Chem.* 1993, 97, 5115.

[69] Deleuze, M. S.; Delhalle, J.; Pickup, B. T. *Chem. Phys.* 1993, 175, 427.

[70] Deleuze, M. S.; Delhalle, J.; Pickup, B. T. *J. Phys. Chem.* 1994, 98, 2382.

[71] Deleuze, M. S.; Cederbaum, L. S. *J. Chem. Phys.* 1996, 105, 7583.

[72] Golod, A.; Deleuze, M. S.; Cederbaum, L. S. *J. Chem. Phys.* 1999, 110, 6014.

[73] Ruhe, A. *Math. Comput.* 1979, 33, 680.

[74] Meyer, H.-D.; Pal, S. *J. Chem. Phys.* 1989, 91, 6195.

[75] Mackenzie-Ross, H.; Brunger, M. J.; Wang, F.; Adcock, W.; Maddern, T.; Campbell, L.; Newell, W. R.; Weigold, E.; Appelbe, B.; Winkler, D. A. *J. Phys. Chem. A* 2002, 106, 9573.

[76] Litvinyuk, I. V.; Zheng, Y.; Brion, C. E. *Chem. Phys.* 2000, 253, 41.

[77] Takahashi, M.; Saito, T.; Hiraka, J.; Udagawa, Y. *J. Phys. B* 2003, 36, 2539.

[78] Knippenberg, S.; Deleuze, M. S.; Cleij, T. J.; Francois, J.-P.; Cederbaum, L. S.; Eland, J. H. D. *J. Phys. Chem. A* 2005, 109, 4267.

[79] Chiang, J. F.; Chiang, R.; Lu, K. C. *J. Mol. Struct.* 1977, 41, 67.

[80] Min, J.; Benet-Buchholz, J.; Boese, R. *Chem. Comm.* 1998, 1, 2751.

[81] Brunelli, M.; Fitch, A. N.; Jouanneaux, A.; Mora, A. J. *Z. Kristallogr.* 2001, 216, 51.

[82] Holthausen, M. C.; Koch, W. *J. Phys. Chem.* 1993, 97, 10021.

[83] Yamaguchi, Y.; Frisch, M.; Gaw, J.; and Schaefer, H. F. III *J. Chem. Phys.* 1986, 84, 2262.

[84] Jenssen, F. *Introduction to Computational Chemistry*; John Wiley and Sons: Chichester, UK, 1999.

[85] NIST Mass Spec. Data Centre, Stein, S. E., director *Infrared Spectra* in *NIST Chemistry Web Book, NIST Standard Reference Database Number 69*, eds. Linstrom, P. J.; Mallard, W. G.; March 2003, National Institute of Standards and Technology: Gaithersburg MD, 20899, 2003 (http://webbook.nist.gov).

3.5 Green's function study of the one-electron and shake-up ionization spectra of unsaturated hydrocarbon cage compounds.

3.5.1 Introduction

Studies of through-bond interactions between π-bonds [1, 2] separated by a rigid σ scaffold are essential for understanding long-range electron and energy transfers between different chromophores. Several experiments have shown that the rate of electron transfer attenuates exponentially as a function of the donor-acceptor distance [3-6]. When this distance exceeds ~3 Å, the strength of the through-bond coupling also strongly depends on the molecular architecture (configuration, conformation) of the σ-spacer itself. It is known for instance that for π-bonds linked by saturated hydrocarbon chains or cages, *trans* configurations are more effective for electron transfers than other arrangements [7-9]. The strength of through-space π-interactions between double bonds, and the rate of electron transfers therefore, can also be varied by modulating the π-character of the C-C bonds in the σ-spacer [10-12] through, for instance, alterations of cyclic strains in multiply-bridged hydrocarbon cage compounds.

The method of choice to experimentally investigate [13-18] the strength of these interactions and the delocalization of the π-bonds into the adjacent σ framework is ultra-violet (He I) photoelectron spectroscopy. From an organic chemist's perspective, patterns of chemical bonding and reactivity in the outer valence electronic structure are most conveniently mapped onto familiar one-electron concepts, such as Hartree-Fock (HF) Molecular Orbital (MO) theory. The latter enables indeed easy and qualitative interpretations of photoelectron spectra and electron transfer processes, by comparison with orbital energies and with the help of Koopmans' theorem [19, 20]. At this level, initial state electron correlation and electronic relaxation effects in the final state are totally neglected, and misorderings of one-electron ionization energies therefore frequently occur. To enable more quantitative and reliable insights into photoelectron spectra, it is recommended to resort, at least, to calculations employing the Outer-Valence Green's Function scheme [21-24]. This approach is derived from one-particle Green's Function (1p-GF) (or, equivalently electron propagator) theory [25-29], on the assumption of a quasi-particle depiction of ionization (i.e. of diagonal self-energies, see [30] and references therein).

The OVGF level amounts to an expansion of the one-electron ionization energies and of the related transition moments through third-order in many-body perturbation theory, by virtue of suited renormalizations [21, 22] of the employed one-electron self-energies. The main drawback of this approach is that the dispersion of the photo- ionization intensity over shake-up states corresponding to mixtures of excited configurations in the cation is neglected. Great care is therefore needed with OVGF studies of the photoelectron spectra of compounds containing multiple π-bonds: it is known indeed [31-40] that for these molecules, both the inner- and outer-valence ionization spectra can be subject to very significant shake-up contamination. To cope with such challenging situations where the one-electron picture of ionization breaks down [31], one must resort to many-body approaches that explicitly account for initial and final-state configuration interactions. To date, the most efficient 1p-GF method for accurately studying one-electron and shake-up ionization states in large molecular systems is the so-called third-order Algebraic Diagrammatic Construction scheme [ADC(3)] [41-44].

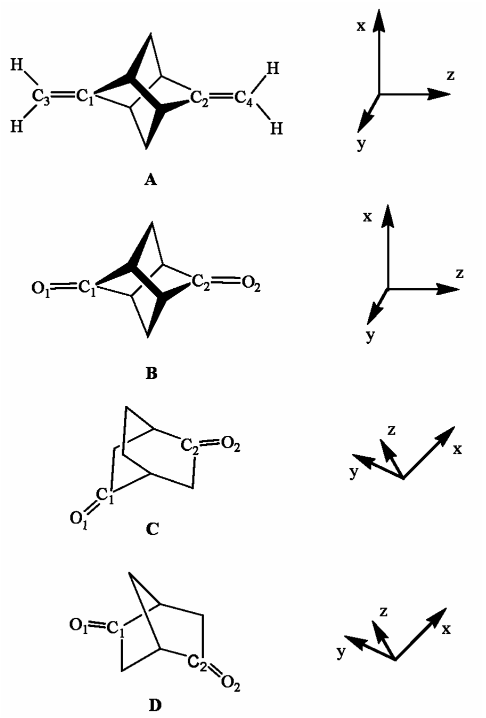

Figure 1. Molecular structures and selected orientations of the investigated compounds. (A) Stella-2,6-diene (STDE, $C_{10}H_{12}$, D_2); (B) stella-2,6-dione (STDO, $C_8H_8O_2$, D_2); (C) bicyclo-[2.2.2]-octane-2,5-dione (BCOD, $C_8H_{10}O_2$, C_2) and (D) bicyclo-[2.2.1]-hepta-2,5-dione (BCHD, $C_7H_8O_2$, C_2).

The purpose of the present work is therefore to study, both at the OVGF and ADC(3) levels, the available photoelectron spectra of a few representative cage compounds (Figure 1), within the assumption of a *vertical* depiction of ionization. As a further motivation to this study, we wish to note that hydrocarbons containing the stellane (tricyclo[3.3.0.0]octane) skeleton, such as stella-2,6-diene (STDE, Figure 1A) or stella-2,6-dione (STDO, Figure 1B), can be coupled to build much larger rigid σ-scaffolds [17]. The former compound and its congeners are known to be interesting models for studying stepwise Cope rearrangements [45, 46, 47]. The STDO compound is structurally similar to bicyclo[2.2.2]hepta-2,5-dione (BCHD, Figure 1C) and bicyclo[2.2.2]octa-2,5-dione (BCOD, Figure 1D), except for the extent of cyclic strains, which intensify in the following order: BCOD < BCHD < STDO. By studying the outer-valence electronic structure of these molecules at the OVGF and ADC(3) levels we wish to quantitatively and comparatively study the consequences of these strains on the bonding mechanisms and on the propensity towards electronic excitations within these molecules. Studies on many-body grounds of the valence one-electron and shake-up ionization spectra of compounds like BCOD and BCHD are particularly demanding, with regards to their size and limited (C_2) symmetry point group.

The interested reader is referred further to comparable OVGF and ADC(3) studies of the electronic structure of other hydrocarbon cage compounds such as norbornene [48] and norbornane [49, 50]. Extremely impressive differences around the vertical double ionization threshold have been observed between photon- and electron impact measurements of the electronic structure of the latter molecule [50], which suggests that the sudden removal of two electrons in fully saturated cages may induce ultra fast molecular dissociation processes [51] and complicated nuclear dynamic effects [52] in the ionization spectra therefore. In continuation to the work described in [49] and [50], another goal of the present work is to quantitatively evaluate the shake-off threshold of the title compounds for *sudden* double ionization events (thus, under the Born assumption of *vertical* processes, i.e. purely electronic transitions).

3.5.2 Methodology

All ADC(3) computations described in the present work have been performed upon the assumption of frozen core electrons, by means of the original 1p-GF/ADC(3) computer package [53] interfaced to GAMESS [54]. Symmetry has been exploited to the extent of the point group (D_2 or C_2) of the compounds of interest. The GAUSSIAN package of programs [55] has been employed for all other calculations.

The ADC(3) calculations have been performed using Dunning's correlation consistent polarized valence basis set of double zeta quality (cc-pVDZ) [56]. These calculations are based on geometries (Figure 1) that were optimised using Density Functional Theory in conjunction with the Becke-three-parameters-Lee-Yang-Par (B3LYP) functional [57] along with Dunning's TZVP (triple zeta valence polarized) basis set [58]. Compared with other benchmark treatments of one-electron ionization processes through third-order in electronic correlation, such as the Multi-Reference Singly and Doubly excited Configuration Interactions (MR-SDCI [59]) scheme, the superior computational efficiency of the ADC(3) procedure stems from the greater compactness of the secular matrix to diagonalize [60, 61]. As a bonus, in the latest versions [43] of the scheme derived from an order-by-order analysis of the self-energies required for expanding the one-particle Green's Function via the Dyson equation [20], the 1p-GF/ADC(3) approach incorporates [43] a band-Lanczos [62-64] "prediagonalization" of the block-matrices pertaining to the 2p-1h "shake-on" states and projection of these states onto a pseudo-electron attachment eigenspectrum of much lower dimension, prior to a block-Davidson diagonalization of the whole secular matrix [43]. This two-step strategy enables calculations, through first-order in correlation, of complex and extremely dense sets of vertical shake-up states in molecules as large as, for instance, dibenzoperylene [39], or in compounds with limited symmetry [C_2, C_s]. Unlike truncated CI treatments, ADC(3) calculations based on charge-consistent electron densities [65] are size-intensive. We wish to note that even-more promising schemes employing a non-Dyson formalism for expanding the one-particle Green's Function are currently in development [66], which enable a fully decoupled treatment of the block-matrices associated to the ionization (advanced) and electron attachment (retarded) components of the Green's Function.

For the sake of more quantitative insights into one-electron vertical ionization processes, the ADC(3)/cc-pVDZ calculations have been supplemented by OVGF calculations performed using Dunning's cc-pVXZ basis sets of double (X=D) and triple (X=T) zeta quality [56], as well as with the cc-pVDZ basis augmented by a set of diffuse *s, p* and *s, p, d* functions on hydrogen and carbon or oxygen atoms, respectively (aug-cc-pVDZ) [67, 68]. The investigated molecules are subject to extremely pronounced cyclic strains and σ-π orbital mixing therefore and the basis set is expected to have an unusually strong influence on the GF results. A methodological study of the influence of polarization and diffuse functions in the basis set on the computed ionization energies is therefore needed, in order to bracket the basis set error. Similarly, one may expect that in such strained systems the quality of the computed geometries may also significantly affect the accuracy of theoretical predictions for ionization energies. In order to bracket errors due to the employed structures, we have therefore compared OVGF results obtained upon geometries optimized using various basis sets (TZVP, cc-pVTZ, aug-cc-PVDZ) and correlation methods (B3LYP or second-order Møller-Plesset [MP2] theory [20]). For the sake of conciseness, some of these results are provided as supplementary material. OVGF results obtained using B3LYP/cc-pVTZ and B3LYP/TZVP geometries do not deviate by more than 20 meV.

The vertical double ionization potentials (VDIPs) of the title compounds have been determined through series of single-point calculations on the neutrals and dicationic species upon the B3LYP/TZVP geometry for the neutrals. These calculations have been conducted at the level of Hartree-Fock (HF), second-, third- and partial fourth-order Møller-Plesset (MP2, MP3, MP4SDQ) theories [20, 69, 70], and by means of Coupled Clusters theories [71-75] including Single and Double excitations (CCSD) as well as a perturbative estimate of connected Triple excitations [CCSD(T)].

Due to band overlaps, it is in practice difficult to assign electron- or photon-impact ionization spectra of large molecules without resorting to appropriate simulations. Therefore, as a guide to the eye, use will be made of convolutions of the ADC(3) spike spectra using as spread function a linear combination of one Gaussian and one Lorentzian of equal width (Voigt profile) and with a full width at half the maximum (FWHM) of 0.6 eV. The latter value is based on our experience with He I or He II measurements, and rather reliably accounts for the high experimental resolution in He I UPS (typically : ~0.05 eV) as well as the average natural and vibrational broadening of lines. In these simulations, line and band intensities are scaled according to the computed pole strengths.

All symmetry labels provided in the sequel for the D_2 symmetry point group are consistent with the molecular orientations displayed in Figure 1, according to the conventions described in the book by Jaffe and Orchin [76]. Core levels are not accounted for in the MO labels.

3.5.3 Results and Discussion

A. General considerations on shake-off bands

One issue that has been most commonly ignored in theoretical studies of ionization spectra so far is the relative location of the double ionization (or shake-off) threshold within the measured valence bands. On the experimental side, detection of this threshold is usually difficult and controversial. Very significant discrepancies, up to 4 eV, have been noted previously [77, 78] between the appearance potentials for double ionization in electron and photon impact experiments. The reasons for these discrepancies can be instrumental, i.e. due to inherent differences in the procedure used for determining the onset of shake-off bands, or may be ascribed to intrinsically different molecular properties as well as intrinsically different timescales for the interactions at the origin of double ionization.

Shake-up states above the vertical double ionization potential (VDIP) are quite naturally prone to decay via emission of a second-electron into the continuum. Therefore, shake-up lines computed with finite basis sets at electron binding energies above the VDIP are more correctly related to resonant states embedded into a continuum of unbound (shake-off) electronic states. From a computational viewpoint, such lines tend indeed to dilute into a continuum of states with vanishing intensities upon successive enlargements of the basis set, but without very significant alterations of the convoluted spectral envelopes. On the experimental side, the appearance of shake-off bands seems to strongly depend on the characteristic timescale of the employed spectroscopies. This timescale is defined as the interaction time of the impinging ionizing particle (photon, electron) with the molecular target. For a photon of 40 eV, it is typically of the order of ~10^{-13} s, whereas with an X-ray photon the characteristic timescale lies around 10^{-17} s. With respect to nuclear dynamical complications, X-ray Photoelectron Spectra (XPS) and Ultra-violet Photoemission Spectra (UPS) therefore intrinsically relate to vertical and adiabatic transitions, respectively.

When the characteristic timescale strongly exceeds that of electronic decays (one to a few tens *fs* [79]), as for instance with UPS, these bands take the form of very long sigmoid tails with extremely limited intensities. On the other hand, shake-off bands give rise to sharper and more easily discernible signals with spectroscopic techniques characterized by much shorter timescales (10^{-17} – 10^{-18} s), such as, typically, XPS (AlK$_\alpha$ or MgK$_\alpha$) or Electron Momentum Spectroscopy (EMS). To illustrate this point, and motivate therefore the calculation of 2h-1p shake-up states as discrete but rather reliable approximations to continuous *vertical* (i.e. non-adiabatic) shake-off bands, we refer in particular to a comparison of various theoretical ADC(3) calculations with He I, He II and EMS measurements for the innermost C_{2s} ($1a_1$) orbital of norbornane, at electron binding energies around ~28 eV [50].

In view of these recent UPS and EMS measurements on norbornane, we expect that the experimental appearance of the shake-up lines (shake-off bands) above the VDIPs calculated (Table 1) for the compounds of interest in the present work will strongly vary, depending on the employed spectroscopy. Among all four studied species, the lowest VDIP (22.1 eV at the benchmark CCSD(T) level) is, quite naturally, found for stella-2,6-diene. The two outermost levels of STDE ($7b_3$, $6b_2$) are, indeed, π-orbitals (Figures 2a and b) which merely localize on the two C=C bonds of this species, and incorporate minor contributions from the σ-spacer that account for the expected through-bond conjugation. On the other hand, for STDO (Figures 2c and d), BCOD (Figures 2e and f), and BCHD (Figures 2g and h), the canonical orbitals with the most pronounced π-character around the C=O bonds are found at much higher electron binding energies, as a result of strong inductive effects induced by the presence of oxygen atoms. These three diketones accommodate less easily one or two positive charges than stella-2,6-diene, because the two outermost orbitals dominantly relate to oxygen lone pairs. For these three species, the VDIP increases at all levels in the following order : STDO < BCOD < BCHD.

Table 1. The Vertical Double Ionization Potentials[a] for Singlet to Singlet Transitions Computed at Different Levels.

	STDE	STDO	BCOD	BCHD
HF/cc-pVDZ	22.381	25.018	26.263	26.732
HF/aug-cc-pVDZ	22.361	25.057	26.312	26.782
MP2/cc-pVDZ	21.419	21.577	22.027	22.416
MP2/aug-cc-pVDZ	21.583	21.950	22.397	22.797
MP3/cc-pVDZ	22.467	23.807	24.365	24.649
MP4SDQ/cc-pVDZ	22.825	23.616	24.393	24.832
CCSD/cc-pVDZ	22.766	23.654	24.391	24.784
CCSD(T)/cc-pVDZ	22.107	22.618	22.859	23.177
CCSD(T)/aug-cc-pVDZ[b]	22.271	22.991	23.229	23.558
B3LYP/cc-pVDZ	22.319	23.261	23.780	24.481
B3LYP/TZVP	22.404	23.604	24.130	24.831

[a]Given in electron volts.
[b]Extrapolated value.

Table 1 demonstrates the convergence, within 1.5 eV, of results obtained for singlet-singlet double ionization transitions using many-body methods which recover electronic correlation through third-order (MP3, MP4SDQ, CCSD, CCSD(T)). It is worth noting that for BCHD and BCOD the impact of the perturbative triple excitations in Coupled Cluster theory is extremely significant, therefore only the CCSD(T) level is expected to provide very quantitative insights into double ionization energies. Upon further inspection of the MP2 results in Table 1, it appears that the impact of diffuse functions on the computed double ionization energies is marginal (0.4 eV, at most). Extrapolation of the CCSD(T)/cc-pVDZ results to the benchmark CCSD(T)/aug-cc-pVDZ level is straightforward therefore. Compared with the latter level, the B3LYP/cc-pVDZ results do not deviate by more than 0.5 eV on average, which confirms the suggestion that DFT calculations employing the B3LYP functional and cc-pVDZ basis set are qualitatively suited for studying [80] the consequences of double ionization events.

B. General considerations on one-electron and shake-up ionization lines

Partly because of a lowering of the symmetry from the D_2 to C_2 point group, the MO contours displayed in Figures 2c,d (STDO), Figures 2e,f (BCOD) and Figures 2g,h (BCHD) as well as the associated orbital energies suggest an enhancement of the through-bond conjugation of C=O bonds via the σ-spacer in the following order: STDO < BCOD < BCHD, a sequence that is identical to that found (Table 1) for the VDIP, but does not entirely correlate with that expected for cyclic strains (STDO > BCHD > BCOD). In the same order (STDO, BCOD, BCHD), we note correspondingly an increase (Table 2) of the first ionization energy and of the shake-up onset. The enhancement of through-bond interactions across the σ-cage corroborates also undoubtedly a significant reduction of the distance between the C=O bonds, along with obvious departures of these two bonds from a relative coaxial location. As a result, the outermost π-levels get destabilized, whereas the frontier orbitals associated to oxygen lone-pairs get inversely stabilized. Table 2 and Figure 2 demonstrate qualitatively the strong interplay between the molecular architecture and electronic structure, more specifically the excited state properties and the chemical reactivity of cage compounds as electron donating species. Despite stronger cyclic strains, the oxygen lone pairs of the BCHD species are stabilized by ~0.2 eV compared with the oxygen lone pairs of the BCOD species, presumably as a result of the larger O_1-C_1-C_2-O_2 torsion angle (Figure 1, Table 2), which in turn enables more favourable dipole-dipole interactions between the C(δ+)=O(δ-) bonds. Cyclic strains alone are therefore not sufficient for qualitatively unravelling the electronic structure of (C, O, H) cage compounds.

Table 2. Structural and Electronic Properties of Cage Compounds.

	STDE	STDO	BCOD	BCHD
R_{12} (Å)[a]	3.176	3.148	2.908	2.851
θ_{3124} (degrees)[b]	0.000	0.000	26.923	−41.813
Bandgap (eV)[c]	13.807	13.983	14.414	14.341
First ionization energy (eV)[d]	8.738	9.007	9.551	9.692
Shake-up onset (eV)[e]	12.996	13.970	14.682	14.871

[a] Distance (R_{12}) between atoms C_1 and C_2 (B3LYP/TZVP result).

[b] Torsion angle θ_{3124} for atoms $C_3—C_1—C_2—C_4$ in STDE or atoms $O_1—C_1—C_2—O_2$ in STDO, BCOD, and BCHD (result).

[c] HOMO-LUMO bandgap (HF/cc-pVDZ result).

[d] First ionization energy (OVGF/aug-cc-pVDZ level).

[e] Shake-up onset (ADC(3)/cc-pVDZ result).

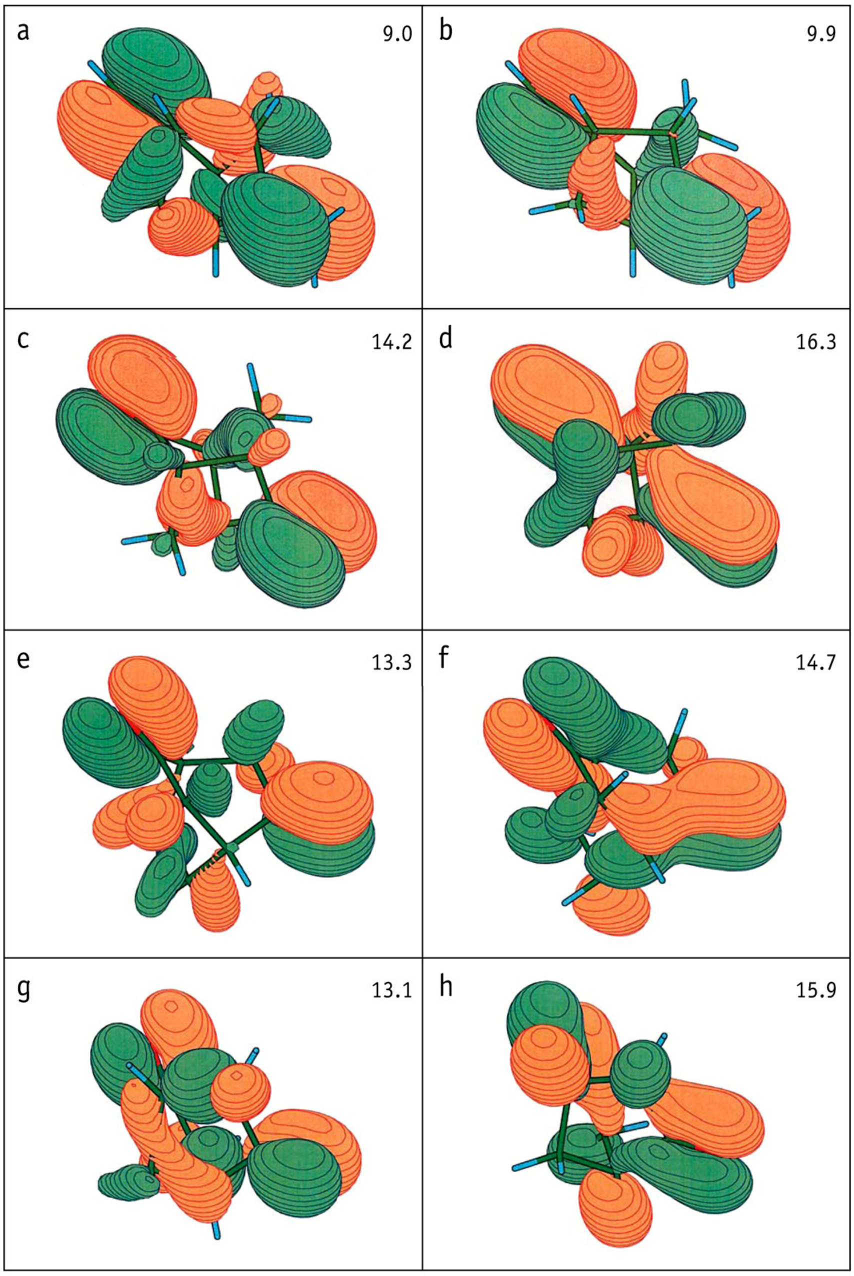

Figure 2. HF/cc-pVDZ density contours for the π-orbitals of (a-b) stella-2,6-diene, (c-d) stella-2,6-dione, (e-f) bicyclo[2.2.2]octane-2,5-dione and (g-h) bicyclo[2.2.1]hepta-2,5-dione, at contour values of 0.03 and in boxes with edges of 16.00 Å using Molden 3.8. The orbital energies, given in eV, are indicated in each upper right corner.

Table 3. ADC(3), OVGF, and Experimental UPS Results for the Ionization Spectrum of Stella-2,6-diene (STDE).*

Symbol	MO	HF/cc-pVDZ	ADC(3)/cc-pVDZ	OVGF/cc-pVDZ	OVGF/cc-pVTZ	UPS
z	$7b_2$ [π]	9.00	8.68 (0.885)	8.60 (0.902)	8.69 (0.899)	8.49
			13.20 (0.010)			
			17.31 (0.007)			
y	$6b_3$ [π]	9.93	9.55 (0.879)	9.46 (0.900)	9.54 (0.897)	9.40
			13.00 (0.008)			
			15.79 (0.017)			
x	$6b_2$ [σ]	11.28	10.32 (0.897)	10.11 (0.904)	10.20 (0.902)	10.05
w	$7a$ [σ]	11.92	10.96 (0.897)	10.76 (0.903)	10.81 (0.901)	10.9†
			19.56 (0.006)			
v	$5b_3$ [σ]	12.47	11.38 (0.896)	11.18 (0.904)	11.28 (0.901)	11.4†
u	$6b_1$ [σ]	12.75	11.70 (0.896)	11.52 (0.903)	11.59 (0.900)	
t	$6a$ [σ]	13.14	11.84 (0.893)	11.56 (0.898)	11.63 (0.895)	11.9†
s	$5b_2$ [σ]	12.96	11.95 (0.890)	11.80 (0.901)	11.86 (0.899)	
r	$4b_2$ [σ]	13.67	12.41 (0.897)	12.23 (0.904)	12.32 (0.902)	
			20.39 (0.006)			
q	$5b_1$ [σ]	14.23	12.97 (0.892)	12.90 (0.903)	13.00 (0.900)	
p	$4b_3$ [σ]	15.50	14.12 (0.847)	14.13 (0.888)	14.25 (0.884)	
			17.84 (0.008)			14.7†
o	$3b_2$ [σ]	15.72	14.31 (0.805)	14.36 (0.882)	14.49 (0.878)	
			15.03 (0.044)^{a}			
			20.10 (0.009)			
n	$3b_3$ [σ]	16.22	14.79 (0.710)	14.74 (0.890)	14.81 (0.887)	
			14.99 (0.175)^{b}			
			16.18 (0.010)			15.2†
m	$4b_1$ [σ]	16.74	15.13 (0.871)	15.04 (0.890)	15.07 (0.887)	
			19.21 (0.005)			
l	$2b_2$ [σ]	17.57	15.80 (0.078)^{c}			
			16.01 (0.549)	15.80 (0.881)	15.86 (0.877)	16.1†
			16.18 (0.252)			
k	$5a$ [σ]	18.46	16.35 (0.006)			
			16.60 (0.700)	16.57 (0.880)	16.66 (0.876)	
			17.00 (0.169)			
j	$3b_1$ [σ]	19.14	16.85 (0.108)			
			17.25 (0.736)	17.07 (0.879)	17.16 (0.875)	
			17.92 (0.011)			
i	$4a$ [σ]	19.51	17.54 (0.785)	17.41 (0.877)	17.50 (0.874)	
			17.90 (0.039)			
h	$2b_3$ [σ]	20.50	18.24 (0.718)	18.16 (0.866)	18.23 (0.861)	
			18.33 (0.040)			
			18.52 (0.060)^{d}			
g	$3a$ [σ]	22.79	19.96 (0.172)	20.16 (0.858)	20.21 (0.852)	
			20.08 (0.300)			
			20.10 (0.145)			
f	$2b_1$ [σ]	23.93	20.59 (0.179)	20.89 (0.826)‡	20.93 (0.814)‡	
			20.65 (0.075)			
			20.87 (0.076)			
			21.16 (0.080)			
e	$1b_2$ [σ]	26.08	22.46 (0.111)			
			22.52 (0.183)			
			22.59 (0.081)			
d	$2a$ [σ]	26.89	22.95 (0.140)			
c	$1b_3$ [σ]	27.68	23.89 (0.105)			
			24.29 (0.072)			

(*Continued*)

Table 3. (*Continued*)

Symbol	MO	HF/cc-pVDZ	ADC(3)/cc-pVDZ	OVGF/cc-pVDZ	OVGF/cc-pVTZ	UPS
b	$1b_1$ [σ]		25.12 (0.067) 25.14 (0.068)			
a	1a [σ]	33.05				

*Binding energies are given in electon volts, along with the ADC(3) and OVGF spectroscopic factors, which are given in parentheses. These results, obtained using the B3LYP/TZVP geometry, are compared with the UPS ionization energies of ref. 84. Only the largest ionization lines are given here; see Table 4 for further data. The molecular orientation is similar to the one used in ref. 84 and the one used for stella-2,6-dione in ref. 85.

†Our assignment.

‡Breakdown of the MO picture of ionization; see ref. 36. Dominant electronic configurations: (a) $6b_3^{-1}$ $6b_2^{-1}$ $7b_2^{+1}$ [$(\mathrm{HOMO\text{-}2})^{-1}$ $(\mathrm{HOMO\text{-}1})^{-1}$ LUMO^{+1}] and $6b_3^{-1}$ $7b_3^{-1}$ $8b_3^{+1}$ [$(\mathrm{HOMO\text{-}2})^{-1}$ HOMO^{-1} $(\mathrm{LUMO}+1)^{+1}$; (b) $7b_3^{-1}$ $6b_3^{-1}$ $7b_2^{+1}$ [HOMO^{-1} $(\mathrm{HOMO\text{-}2})^{-1}$ LUMO^{+1}]; (c) $7b_3^{-1}$ $6b_2^{-1}$ $7b_2^{+1}$ [HOMO^{-1} $(\mathrm{HOMO\text{-}1})^{-1}$ LUMO^{+1}]; (d) $7b_3^{-1}$ $6b_3^{-1}$ $7b_2^{+1}$ [HOMO^{-1} $(\mathrm{HOMO\text{-}2})^{-1}$ LUMO^{+1}].

Most of our ADC(3) and OVGF results are collected in Tables 3-10. In line with the merely saturated and unconjugated nature [81, 82] of the investigated compounds, the extent of the shake-up contamination is relatively limited (Figures 3-7), and the quasi-particle depiction embodied in the OVGF scheme remains therefore valid (Tables 3, 5, 7, 9) up to relatively high electron binding energies (18 eV for STDE, and 22 eV for STDO, BCHD and BCOD). The satellite bands are described in details through the interplay of Tables 4, 6, 8 and 10. Here again, a comparison of the ADC(3) and OVGF results for all four compounds confirms the empirical rule [36, 39] that OVGF pole strengths smaller than ~0.85 foretell a complete breakdown of the orbital picture of ionization at the ADC(3) level. This refers to situations where no clearly dominant line emerges with a pole strength (Γ) larger than ~0.5 from the ADC(3) one-electron and shake-up spectrum for a given orbital. Note that OVGF pole strengths larger than ~0.85 do not necessarily imply that the one-electron picture of ionization is fully or even partly valid [39]. As an example, the reader is advised to compare the results of OVGF (Γ=0.87) and ADC(3) (Γ<0.4) calculations for the lines derived from ionization of the 4a orbital of BCHD (Table 9). Even with weakly conjugated molecules, there is thus always a risk inherent to resorting only to OVGF or other quasi-particle calculations for interpreting photon- or electron-impact ionization spectra.

At electron binding energies below the vertical double ionization threshold, ADC(3)/cc-pVDZ or OVGF/cc-pVDZ calculations on hydrocarbon compounds with a band gap larger than 9 eV are known to reproduce experimental one-electron ionization energies or benchmark quantum chemical calculations [83] within accuracies of the order of ~0.2 eV, a statement which the present analysis of the photoelectron spectrum of STDE confirms (see Table 3). On the other hand, at the ADC(3) level, with regards to a treatment of shake-up transitions through first-order only in correlation, accuracies of ~0.6 eV only are expected on the related ionization energies.

Because of an enhanced polarization of the electronic structure and presence of localized lone pairs, a stronger influence of the basis set on the quality of the computed ionization energies is expected for compounds incorporating heteroatoms. For instance, at constant geometries, addition of diffuse functions onto the cc-pVDZ basis set results into an increase of the outermost OVGF ionization energies of STDE by ~0.15 eV, whereas an increase by 0.37 ± 0.02 eV is correspondingly observed for the ionization energies associated to the outermost oxygen lone pairs (*n*) of the diketones (STDO, BCOD, BCHD). Similar observations prevail for other levels, except that, as was noted already previously, the influence of the basis set tends also overall to slightly decrease with increasing binding energies [39]. Also, we note that comparisons of the various OVGF/cc-pVDZ results displayed as supplementary material and in Tables 3, 5, 7 and 9 indicate uncertainties of, at most, ~0.1 eV on vertical one-electron ionization energies, because of the employed molecular geometries. With regards to the extremely large band gap of the investigated species, larger than 13 eV, it is therefore not a surprise that the benchmark OVGF/aug-cc-pVDZ or OVGF/cc-pVTZ ionization energies reproduce the available UPS measurements for STDO and BCHD with average accuracies of ~0.3 eV.

Table 4. Further Ionization Lines Identified for Stella-2,6-diene[a] (B3LYP/TZVP Geometry).

Symbol	MO	ADC(3)/cc-pVDZ
h	$2b_3$ [σ]	19.04 (0.014)
g	$3a$ [σ]	20.19 (0.052), 20.30 (0.015), 20.41 (0.048), 20.66 (0.016)
f	$2b_1$ [σ]	20.25 (0.014), 20.38 (0.010), 20.71 (0.010), 20.77 (0.050), 20.89 (0.052), 20.91 (0.039), 20.93 (0.045), 21.05 (0.016), 21.22 (0.031), 21.72 (0.010)
e	$1b_2$ [σ]	22.28 (0.010), 22.33 (0.023), 22.57 (0.014), 22.63 (0.057), 22.71 (0.048), 22.77 (0.032), 22.80 (0.012), 22.87 (0.038), 23.16 (0.014)
d	$2a$ [σ]	21.93 (0.013), 22.10 (0.012), 22.22 (0.047), 22.68 (0.021), 22.73 (0.017), 22.75 (0.025), 22.76 (0.020), 22.86 (0.016), 23.02 (0.023), 23.13 (0.016), 23.45 (0.015), 23.90 (0.014), 23.96 (0.010), 23.99 (0.010), 24.04 (0.015), 24.07 (0.015), 24.12 (0.036), 24.14 (0.012), 24.30 (0.018), 24.33 (0.016)
c	$1b_3$ [σ]	23.43 (0.010), 23.45 (0.026), 23.63 (0.034), 23.72 (0.040), 23.75 (0.017), 23.85 (0.013), 23.94 (0.022), 23.97 (0.019), 24.04 (0.013), 24.05 (0.014), 24.11 (0.017), 24.14 (0.012), 24.15 (0.015), 24.16 (0.035), 24.20 (0.010), 24.22 (0.015), 24.24 (0.018), 24.27 (0.017), 24.45 (0.016), 24.56 (0.016)
b	$1b_1$ [σ]	23.31 (0.023), 23.39 (0.018), 23.45 (0.011), 24.82 (0.025), 24.89 (0.013), 25.02 (0.011), 25.08 (0.016), 25.17 (0.017), 25.21 (0.016), 25.31 (0.019), 25.32 (0.010)

[a] Binding energies are given in electron volts, along with the associated pole strengths in parentheses; only lines with pole strengths larger than 0.010 are given.

C. Ionization spectrum of stella-2,6-diene (STDE)

The only experimental sources of information on the electronic structure of stella-2,6-diene [STDE] derive from the UPS (He I) measurements by Gleiter and co-workers [84]. These are compared in Figure 3 with the results of our ADC(3)/cc-pVDZ calculations. Theoretical analysis of these measurements so far was limited to ΔSCF (HF/6-31G*//HF/6-31G*) and ΔMP2 (MP2/6-31G*//HF/6-31G*) studies of the three outermost valence bands of this compound, up to electron binding energies of 10 eV. Therefore, the present OVGF and ADC(3) study considerably improves, both qualitatively and quantitatively, our understanding of the ionization spectrum of STDE. Upon inspection of data provided as supplementary material, average and maximal discrepancies of ~0.07 and ~0.14 eV are noted between the OVGF/cc-pVDZ data obtained for STDE using B3LYP/TZVP and MP2/aug-cc-pVDZ geometries, respectively. Also, the OVGF/aug-cc-pVDZ and OVGF/cc-pVTZ data obtained using the same (B3LYP/TZVP) geometry do not differ by more than 0.10 eV (average deviation : 0.04 eV). This comparison demonstrates the robustness of our methodology.

Our calculations show (Table 3) that the orbital energy order inferred from Koopmans' theorem for one-electron ionisation lines is overall valid up to ~18 eV, except for a reversal of the energy order between orbitals $5b_2$ and 6a. They confirm in particular the assignment proposed by Gleiter for the three outermost and individually resolved ionization lines. On the experimental side, the first two lines (**z**, **y**) derived from orbitals $7b_2$ and $6b_3$ display very asymmetric and sharp profiles, with rather clearly apparent vibrational progressions, which is very typical of π-levels (see for instance the He I spectra displayed for a variety of polycyclic aromatic hydrocarbons in refs. 33, 36, 39). On the other hand, the ionization band (**x**) at 10.1 eV in the He I spectrum of STDE relates to the σ-onset (orbital $6b_3$), and as such displays a broader and more symmetric profile. Beyond this point, no line can be individually fully resolved.

Nonetheless, the theoretical ADC(3) spike spectrum displayed in Figure 3b shows that the one-electron ionization line associated to MO 7a is relatively well isolated, and leads after convolution to a rather clearly apparent shoulder (**w**) at ~10.9 eV, in good agreement with the experimental results (Figure 3a). Another minor signal (v) is discernible at ~11.4 eV, which is tentatively ascribed to the line relating to orbital $5b_2$. The next three levels (**u**, **t**, **s**) very strongly overlap, and lead to a broad and intense band (**A**) that culminates at ~11.9 eV, in quantitative agreement with the He I measurements by Gleiter. As the simulation of Figure 3b clearly demonstrates, any attempt to analyze separately the ionization intensities characterizing these three orbitals should be regarded as physically irrelevant, with regards to the limited resolution of the currently available spectrometers and the extent of vibrational broadening. Analysis of the bands recorded at binding energies around ~12.5 eV is problematic, because of the presence at these energies of a rather intense signal which Gleiter *et al.* ascribed [84] to water contamination. Without this experimental artefact, the line (**q**) related to orbital $5b_1$ should have normally been individually identified in a He I spectrum.

Two further bands (**B**, **C**) are clearly seen at electron binding energies of ~14.7 and ~15.2 eV in the UPS measurements on STDE, which, according to all ADC(3) and OVGF calculations, can be ascribed to two orbital pairs: {**p**: $4b_3$, **o**: $3b_2$} and {**n**: $3b_3$, **m**: $4b_1$}, respectively. A partial breakdown of the orbital picture of ionization is observed for orbital $2b_2$ (**l**), in the form of three lines at comparable electron binding energies in the ADC(3) spectrum, among which a dominating 1h line (Γ=0.55) at 16.0 eV. These lines are well isolated and a peak (**D**) is correspondingly observed at ~16.1 eV on the experimental side. Advocating further UPS (He I or He II) measurements, we expect that three additional peaks (**E**, **F**, **G**) relating to the {5a}, {$3b_1$+4a} and {$2b_3$} orbital sets (lines **k**, **j+i** , **h**) will be identified at ~16.6, ~17.3 and ~18.3 eV, respectively. At binding energies above ~18 eV, i.e. within the inner-valence (C_{2s}) region, the orbital picture of ionization completely breaks down. The shake-up fragmentation becomes particularly severe beyond the vertical double ionization threshold at ~22 eV, despite the finite size of the employed (cc-pVDZ) basis set. We wish to recall again that above this threshold shake-up lines are simply discrete approximations to continuous shake-off bands.

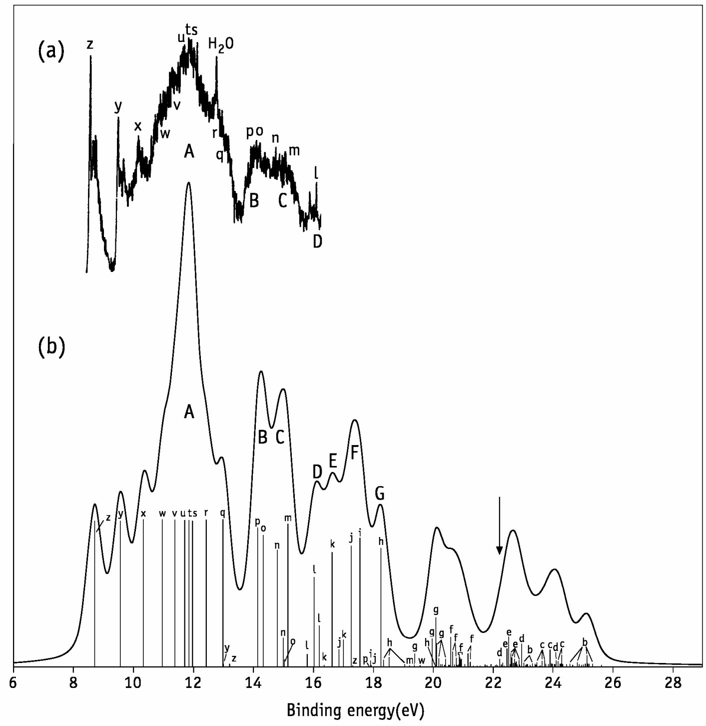

Figure 3. Comparison of the (a) UPS (He I) spectrum of stella-2,6-diene [84], with an (b) ADC(3)/cc-pVDZ simulation (FWHM=0.6 eV). The vertical arrow at 22.1 eV indicates the vertical double ionization threshold for a singlet to singlet transition.

D. Ionization spectrum of stella-2,6-dione (STDO)

Besides UPS (He I) measurements [84] up to electronic binding energies of ~16 eV, the outer-valence electronic structure of STDO has also been studied in detail using EMS [85, 86]. These UPS and EMS measurements are reproduced in Figure 4 and compared with the results of our ADC(3) calculations. The EMS measurements are reproduced together with the Gaussian fitting that was used previously [85, 86] to experimentally infer the electron momentum distributions associated to the identified ionization channels from the azimuthal angular dependence of the corresponding (e, 2e) intensities. In support to these measurements and to the assignment proposed by Nixon and Wang from modest calculations of orbital energies by means of Hartree-Fock or Density Functional Theory, these momentum distributions were compared with theoretical simulations based on Kohn-Sham orbitals derived from various DFT calculations employing standard functionals such as the Becke-Perdew (BP) or Becke, Lee, Yang, Parr (BLYP) functionals. The interested reader is referred further to a discussion [48, 87] of the shortcomings of empirical analyses of EMS experiments using Kohn-Sham orbitals and eigenenergies.

Table 5. ADC(3) and OVGF Results and Experimental UPS and EMS Data for the Ionization Spectrum of Stella-2,6-dione (STDO).*

Symbol	MO	HF/cc-pVDZ	ADC(3)/cc-pVDZ	OVGF/cc-pVDZ	OVGF/cc-pVTZ	UPS	EMS
y	$7b_2$ [n (+σ)]	10.19	8.94 (0.897)	8.65 (0.905)	8.96 (0.901)	8.84	[α] 8.84
x	$6b_3$ [n (+σ)]	11.49	10.02 (0.889)	9.80 (0.900)	10.09 (0.896)	9.90	[β] 9.90
w	7a [σ]	12.96	11.92 (0.906)	11.43 (0.911)	11.64 (0.907)		[γ] 11.58
						11.8[†]	
v	$6b_2$ [σ (+n)]	12.95	11.94 (0.883)	11.77 (0.897)	11.99 (0.894)		[δ] 11.95
u	$6b_1$ [σ]	13.72	12.62 (0.904)	12.18 (0.910)	12.40 (0.906)	12.4[†]	
t	$5b_3$ [π]	14.17	13.11 (0.854)	13.16 (0.886)	13.36 (0.882)		
			13.97 (0.011)				[ε] 12.31
							[ζ] 12.58[†]
s	$5b_2$ [σ (+n)]	14.33	13.16 (0.891)	13.00 (0.902)	13.20 (0.899)	13.1[†]	[η]12.84[†]
							[θ]13.11[†]
r	$4b_2$ [σ]	14.72	13.40 (0.893)	12.98 (0.908)	13.21 (0.904)		
q	6a [σ]	14.91	13.41 (0.894)	12.97 (0.902)	13.20 (0.898)		
p	$5b_1$ [σ]	15.20	13.89 (0.901)	13.64 (0.910)	13.85 (0.907)		[ι] 13.52[†]
						14.2[†]	
n	$4b_3$ [σ (+n)]	16.03	14.27 (0.850)	14.14 (0.891)	14.37 (0.888)		[κ] 14.20[†]
m	$3b_2$ [π]	16.26	14.28 (0.158)[a]				
			14.48 (0.669)	14.37 (0.885)	14.58 (0.882)	14.3[†]	[λ] 14.90[†]
			15.60 (0.023)[b]				
l	$3b_3$ [σ]	17.17	15.51 (0.061)				
			15.75 (0.811)	15.40 (0.897)	15.57 (0.893)		[μ]15.50[†]
						15.5[†]	[ν]15.84[†]
k	$4b_1$ [σ]	17.96	15.96 (0.867)	15.83 (0.888)	15.99 (0.883)		
j	$2b_2$ [σ (+n)]	18.78	17.00 (0.079)[c]				
			17.16 (0.761)	16.81 (0.887)	16.97 (0.883)		
i	5a [σ]	19.32	17.24 (0.828)	17.12 (0.885)	17.24 (0.880)		
h	$3b_1$ [σ]	20.05	18.02 (0.836)	17.79 (0.886)	17.96 (0.882)		
g	4a [σ]	20.49	18.41 (0.852)	18.18 (0.886)	18.36 (0.881)		
f	$2b_3$ [σ]	21.58	19.19 (0.710)	19.02 (0.874)	19.20 (0.870)		
			19.22 (0.062)				
e	3a [σ]	23.92	21.18 (0.728)	21.10 (0.869)	21.25 (0.863)		
d	$2b_1$ [σ]	26.96	23.37 (0.250)	23.26 (0.830)[‡]	23.38 (0.825)[‡]		
c	$1b_2$ [σ]	27.24	23.23 (0.106)				
			23.48 (0.098)				
			23.54 (0.111)	23.52 (0.821)[‡]	23.67 (0.800)[‡]		
b	$1b_3$ [σ]	28.64	24.71 (0.075)				
			24.81 (0.074)				
			24.86 (0.196)	24.84 (0.775)[‡]			
a	2a [σ]	33.56	28.73 (0.021)				
	$1b_1$ [σ]	38.11					
	1a [σ]	38.21					

*Binding energies are given in electron volts, along with the ADC(3) and OVGF spectroscopic factors, which are given in parentheses. These results, obtained using the B3LYP/TZVP geometry, are compared with the UPS and EMS ionization energies of refs. 84 and 85, respectively. Only the most intense ADC(3)/cc-pVDZ ionization lines are given here; see Table 6 for further data. The molecular orientation is similar to the one used in refs. 85 and 84.

[†] Our assignment.

[‡] Breakdown of the MO picture of ionization; see ref. 36. Dominant electronic configurations: (a) $7b_3^{-2}$ $8b_3^{+1}$ [HOMO^{-2} (LUMO+1)$^{+1}$]; (b) $5b_2^{-1}$ $7b_3^{-1}$ $7b_2^{+1}$ [(HOMO-5)$^{-1}$ HOMO^{-1} LUMO^{+1}]; (c) $6b_2^{-1}$ $6b_3^{-1}$ $7b_2^{+1}$ [(HOMO-1)$^{-1}$ (HOMO-2)$^{-1}$ LUMO^{+1}].

The present OVGF and ADC(3) results for STDO confirm the assignment proposed by Gleiter [84] for the two outermost one-electron ionization lines (**y**, **x**) associated to orbitals $7b_2$ and $6b_3$ under the selected molecular orientation (see Figure 1). These lines are well-isolated and their identification is straightforward. Our 1p-GF results also confirm that the σ-onset (**w**) associated to the 7a orbital lies at ~11.58 eV in the UPS and EMS measurements (band γ in Figure 4b and c). The next band (δ) in the EMS measurements was assigned to the one-electron ionization line (**v**) derived from the $6b_2$ orbital. This assignment is consistent with the results of our OVGF calculations employing the largest basis sets [Table 5]. Beyond this point, the assignment proposed by Nixon and Wang is highly questionable. Prior to a systematic discussion of this assignment, and to emphasize the robustness of our treatment, we wish to note again that, upon inspection of data provided as supplementary material, average and maximal discrepancies of ~0.05 and ~0.11 eV can be noted between the OVGF/cc-pVDZ data obtained for STDO using B3LYP/TZVP and MP2/aug-cc-pVDZ geometries, respectively. Also, the

OVGF/aug-cc-pVDZ and OVGF/cc-pVTZ electron binding energies obtained using the same (B3LYP/TZVP) geometry do not differ by more than 0.17 eV (average deviation: 0.06 eV). Similar considerations prevail for BCOD and BCHD, and will therefore not be repeated in the sequel.

Table 6. Further Ionization Lines Identified at the ADC(3)/cc-pVDZ Level for Stella-2,6-dione (B3LYP/TZVP Geometry).[a]

Symbol	MO	ADC(3)/cc-pVDZ
l	$3b_3$ [σ]	15.94 (0.016), 17.14 (0.017)
j	$2b_2$ [σ (+n)]	17.42 (0.018), 18.41 (0.024), 18.44 (0.011)
i	5a [σ]	17.39 (0.017)
h	$3b_1$ [σ]	17.75 (0.011)
f	$2b_3$ [σ]	17.85 (0.011), 19.31 (0.035), 19.84 (0.019)
e	3a [σ]	20.21 (0.025), 21.31 (0.051)
d	$2b_1$ [σ]	22.43 (0.014), 22.79 (0.015), 22.86 (0.012), 23.16 (0.012), 23.31 (0.029), 23.35 (0.050), 23.47 (0.029), 23.49 (0.012), 23.66 (0.089), 23.75 (0.021), 23.80 (0.052), 23.96 (0.018), 24.12 (0.017), 24.46 (0.015)
c	$1b_2$ [σ]	22.98 (0.016), 23.35 (0.022), 23.51 (0.060), 23.67 (0.051), 23.77 (0.010), 23.82 (0.076), 23.87 (0.024), 23.90 (0.014), 24.01 (0.019), 24.10 (0.013), 24.25 (0.015), 24.88 (0.011)
b	$1b_3$ [σ]	24.08 (0.014), 24.37 (0.017), 24.49 (0.050), 24.66 (0.010), 24.68 (0.010), 24.92 (0.027), 24.95 (0.040), 25.05 (0.012), 25.14 (0.027), 25.22 (0.039)
a	2a [σ]	28.57 (0.016), 28.58 (0.011), 28.59 (0.013), 28.73 (0.012), 28.83 (0.012), 28.84 (0.015), 28.86 (0.012), 29.02 (0.013), 29.03 (0.013)

[a] Binding energies are given in electron volts, along with the associated pole strengths in parentheses; only lines with pole strengths larger than 0.010 are given here.

With regards to their BP and BLYP analyses of spherically averaged electron momentum distributions, Nixon, Wang and co-workers located [85, 86] the one-electron ionization lines (**u**, **t**) associated to orbitals $6b_1$ and $5b_3$ at ~12.31 (band ε) and ~12.58 eV (band ζ), respectively. Compared with our best OVGF/cc-pVTZ results for the $5b_3$ electron binding energy (~13.4 eV), this would imply an error of ~0.8 eV, thus far beyond what is normally expected at this level. In view of pole strengths close to ~0.9 and of a rather uniform upward shift of one-electron ionization energies by ~0.2 eV upon enlarging the basis set from cc-pVDZ to cc-pVTZ, it is clear that so large discrepancies for the $6b_1$ and $5b_3$ electron binding energies cannot be satisfactorily explained by a weakness of the OVGF method in this highly congested region. On the contrary, combining the ADC(3) and OVGF data displayed in Table 5 yields ADC(3)/cc-pVTZ estimates of ~12.8 and ~13.3 eV for the u- and t-states, thus at 0.5 and 0.7 eV above the values inferred from the analysis by Nixon, Wang *et al.* [85, 86]. ADC(3)/aug-cc-pVDZ estimates of ~12.9 and ~13.5 eV can be similarly inferred for these two states.

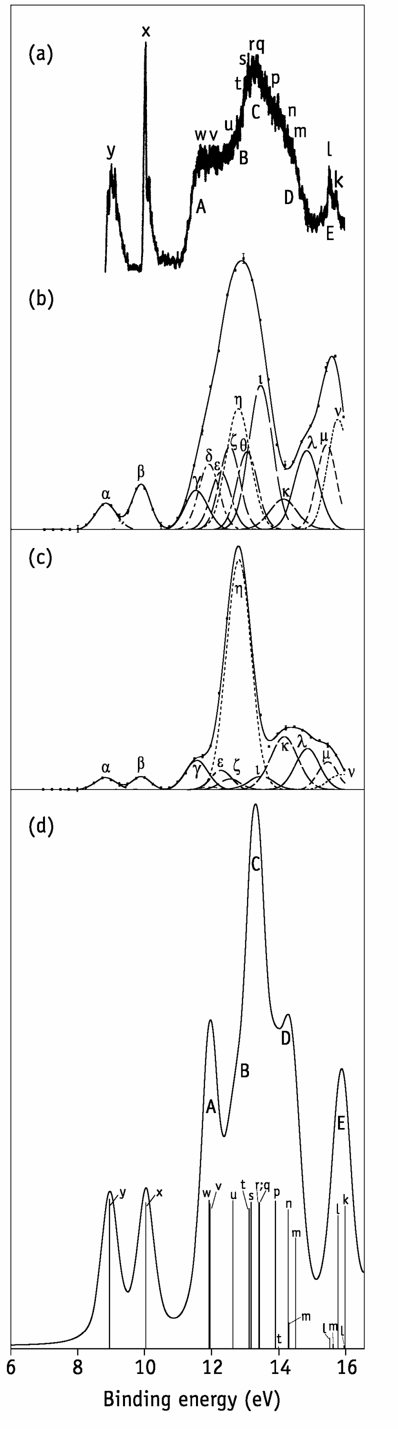

Figure 4. Comparison of the (a) UPS (He I) spectrum of stella-2,6-dione [84], and of the EMS measurements at azimuthal angles of (b) φ=10° and (c) φ=0° [85] with the results of (d) ADC(3)/cc-pVDZ calculations (FWHM=0.6 eV).

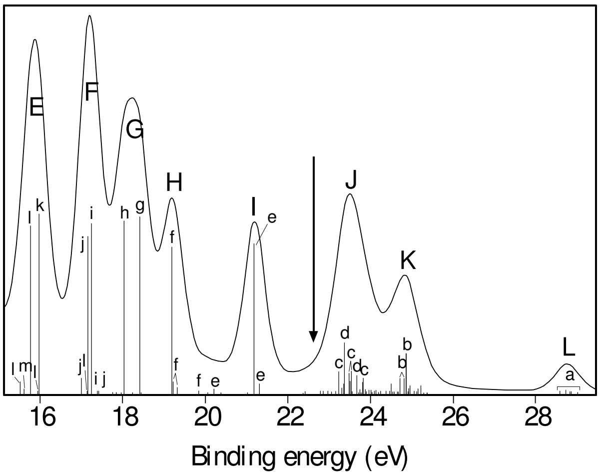

Figure 5. The theoretical spike and convoluted (FWHM=0.6 eV) ADC(3)/cc-pVDZ inner-valence ionization spectra of stella-2,6-dione. The vertical arrow at 22.6 eV pinpoints the vertical double ionization potential for a singlet to singlet transition.

Note that, according to the Gaussian fitting reproduced in Figures 2b and c, the bands ε and ζ in the (e,2e) ionization spectra very strongly overlap with two further bands (η, θ). Very clearly, a detailed analysis of these four bands on an individual basis is physically irrelevant. With regards to the limited coincidence energy resolution of the employed spectrometer (~0.52 eV), natural linewidths and vibrational broadenings (ranging from ~0.4 to 0.8 eV) of the various electronic transitions, as estimated [85] from the relevant PES measurements [84], EMS band widths comprised between ~0.9 to ~1.3 eV are normally expected. These estimated widths are much larger than the fitted resolutions of the Gaussian functions used by Nixon *et al.* for analyzing their EMS measurements on STDO, which vary [85] from 0.66 to 0.96 eV (FWHM).

In spite of severe overlaps between bands ε, ζ, η, and θ in the EMS ionization spectra, theoretical (BP/TZVP and BLYP/TZVP) electron MDs for the one-electron ionization channels (***s***, **r**, **q**) derived *solely* from the {$5b_2 + 4b_2 + 6a$} orbital set have been compared (see Figure 6 in [85]) with the experimental electron MD inferred *specifically* from the angular dependence of the (e,2e) ionization intensity of band η at 12.84 eV in the EMS measurements. In view of the results of our OVGF calculations, the contribution of line ***t*** (orbital $5b_3$) at ~0.2 eV *only* above the {$5b_2 + 4b_2 + 6a$} orbital set should have also been clearly included in a meaningful analysis of the (e, 2e) ionization intensities at electron binding energies ranging from ~12.6 to ~13.2 eV. Note that, compared with the order of electron binding energies inferred from HF orbital energies and Koopmans' theorem, a reversal of the energy order is observed between the $5b_3$, $5b_2$, $4b_2$, and 6a levels associated to the ionization lines **t**, **s**, **r**, **q**, the latter three being subject to much stronger electronic relaxation effects at the OVGF level, which is in line with their σ-nature.

Nixon *et al* assigned further (see Table 1 in [85] or Figure 3b in [86]) the band θ at 13.11 eV in the (e, 2e) ionization spectra of STDO to orbital $5b_1$ (line **p**). However, according to our best OVGF results, this line, in a vertical depiction of ionization, should be found at an electron binding energy of

13.85 eV. Exceptionally strong vibronic coupling interactions and non-adiabatic effects may occasionally induce vibrational broadening as large as ~1.0 eV, as well as shifts towards lower electron binding energies of the apparent one-electron ionization onsets (see for instance [88-90]). These shifts, however, most usually never exceed ~0.2 to ~0.3 eV. Therefore, a discrepancy of ~0.7 eV on peak positions between theory and experiment seems very abnormal. In view of the complete overlap of band θ by band η in Figures 4b and 4c, it obviously makes no sense to specifically ascribe one of these two bands to one particular orbital. It is also worth emphasizing that bands θ and ι at 13.11 and 13.52 eV exhibit very similar electron MD "p-type" profiles (compare Figs. 3c and d in [86]). Very clearly therefore, the contributions of ionization lines in this electron binding energy region cannot be non-ambiguously disentangled through a simple Gaussian fitting procedure.

According to Table 1 in [85], or Figure 3d in [86], band ι at 13.52 eV relates to orbitals $4b_3$ and $3b_2$. Upon inspection of our best OVGF results, the corresponding one-electron ionization lines (**n**, **m**) should be found at ionization energies of ~14.4 and ~14.7 eV, which implies that the assignment by Nixon *et al.* for this band was in error by, at least, 0.9 eV. Again, it is very unlikely that a so strong overestimation of the experimentally inferred electron binding energy by theoretical calculations of vertical one-electron ionization energies will be explained by vibrational effects or vibronic coupling interactions. We suggest therefore to more specifically compare the experimental electron momentum distribution of band ι with that related to line **p** (orbital $5b_1$) at ~13.85 eV. Very similar observations prevail for bands κ, λ, μ, and ν. Band κ at 14.2 eV was originally ascribed to orbital $3b_3$ (line **l**) – a line which is found at ~15.6 eV at the OVGF/aug-cc-pVDZ or OVGF/cc-pVTZ levels. In our opinion, band κ should have rather been compared with orbital $4b_3$ (line **n**) at 14.4 eV as well as with orbital $3b_2$ (line **m**) at 14.7 eV. Nixon *et al* further assigned band λ at 14.9 eV to line **k** derived from orbital $4b_1$, a line which is described at the OVGF level by an ionization energy of ~16.1 eV. We suggest to ascribe this band to orbital $3b_2$ (line **m**) at 14.7 eV in the OVGF spectra. Note also that, according to the ADC(3) results, a partial breakdown of the MO picture of ionization should slightly complicate the analysis of (e, 2e) ionization intensities and electron momentum distributions at these electron binding energies.

Last, bands μ and ν at 15.50 and 15.84 eV were originally ascribed [85, 86] to orbital $2b_2$ (line **j**) and to orbital 5a (line **i**), respectively. In the same order, these lines are found at 17.0 and 17.4 eV in our best OVGF spectra. We would rather suggest to jointly assign these two bands to orbital $3b_3$ (line **l**) at 15.6 eV and to orbital $4b_1$ (line **k**) at 16.1 eV. Again, bands μ and ν very severely overlap and any information obtained from these through a separate analysis of the associated intensities should be regarded with the greatest caution. The analyses provided in Figure 8 of [85] and in Figure 3d of [86] for the $2b_2$ and 5a orbitals, respectively, are very doubtful therefore. We wish to note that computations of spherically averaged electron momentum distributions are extremely sensitive to some input parameters in the calculations, such as the estimated momentum resolution and the step size for a spline integration of the differential (e, 2e) cross sections. Very unfortunately, these very basic input parameters have not been provided in the articles by Nixon, Wang and co-workers [85, 86] and are unobtainable from references therein.

In support to our reassignment, we wish to emphasize that the agreement between our ADC(3) and OVGF data with the He (I) UPS measurements by Gleiter is as good as it could be (see Table 3, compare also Figures 2a and d). In agreement with our simulations, four substructures *only* (**A**, **B**, **C,** **D**) are clearly discernible in UPS at binding energies comprised between 10 and 15 eV. The one-electron ionization lines **w** and **v** associated to orbitals 7a and $6b_2$ are accidentally degenerate in the ADC(3) spectrum, and result therefore in a sharp and intense peak after convolution, whereas a plateau is seen experimentally. Note that, according to the OVGF results, the one-electron lines derived from orbitals 7a and $6b_2$ exhibit an energy separation of ~0.4 eV, which appears to be more consistent with the shape of spectral bands at electron binding energies around 11.8 eV. In view of the ADC(3) results, further studies should nonetheless be necessary to determine whether these lines are subject to complicated vibronic coupling interactions that may also explain the observed broadening. Line **u** corresponding to orbital $6b_1$ at ~12.4 is relatively more isolated than other lines. It yields therefore a discernible shoulder (**B**) in the convoluted spectrum, which corroborates the appearance of the He I spectrum at this electron binding energy. Among the σ-band system, the most intense peak (**C**) in the He I spectrum culminates at ~13.1 eV, in quantitative agreement with the ADC(3) simulation and OVGF energy location of the ionization lines (lines **t**, **r, q**) associated to orbitals $5b_2$, $5b_2$ and 6a. Note that, because of the observed discrepancies between the OVGF and ADC(3) results, the relative energy location of orbital $5b_3$ (line **s**) is not entirely clear. Orbitals $4b_3$ and $3b_2$ (lines **n** and **m**) emerge in the convoluted ADC(3) spectrum (Figure 4d) in the form of a peak (**D**) at ~14.2 eV, which corroborates a pronounced shoulder in the He I spectrum (Figure 1a). Another distinctly apparent signal is peak **E** at 15.5 eV, which unambiguously relates to one-electron ionization lines (**l**, **k**) derived from orbitals $3b_3$ and $4b_1$.

The results of our ADC(3) calculations on STDO at higher electron binding energies are illustrated separately (Figure 5). They foretell four sharp and intense peaks (**F**, **G**, **H**, **I**) at ~17.2, ~18.2, ~19.2 and ~21.2 eV up to the double ionization threshold at ~23 eV (see also Table 5 for a detailed MO assignment). Beyond this point, shake-off bands are approximated by dense and complex sets of shake-up lines (see Table 6 for details). Further peaks at ~23.4, ~24.9 and ~28.7 eV are predicted assuming a vertical depiction for shake-off ionization processes.

E. Ionization spectrum of bicyclo[2.2.1]octanedione (BCOD)

In anticipation of forthcoming experimental studies of the valence electronic structure of BCOD by means of ultra-violet photoelectron spectroscopy or electron momentum spectroscopy, we refer to our ADC(3) and OVGF data in Tables 7 and 8 for detailed and quantitative predictions, within ~0.3 eV accuracy, of the valence one-electron ionization energies of this compound, up to the shake-off threshold at ~23.3 eV. Owing to the much more limited (C_2) symmetry point group of this compound, as compared with that of STDE and STDO, the ionization spectrum of BCOD is subject to a stronger shake-up fragmentation at electron binding energies above ~14.7 eV.

Again, the outermost one-electron ionization lines (**y**, **x**) relate dominantly to oxygen lone pairs. By analogy with the outermost He I valence bands of STDO (Figure 4a) or BCHD (see further), we expect that the combined 14a + 13b He I photoelectron band of BCOD will exhibit a fairly symmetric appearance and a rather limited natural and vibrational width {~0.4 eV (FWHM)}. Therefore, despite the neglect of photoelectron cross section effects, the simulation (Figure 6) drawn from our ADC(3)/cc-pVDZ results should provide a very faithful depiction of the He I spectrum of BCOD. According to this simulation, six peaks (**A**, **C**, **E**, **F**, **G**, $\mathbf{H_1}$) with possibly further minor substructures ($\mathbf{F_1}$, $\mathbf{F_2}$) will be seen in this spectrum at electron binding energies of ~9.5, ~12.3, ~14.5, ~16.8 ±0.2, ~19.0, and ~20.3 eV, respectively. In the same order, these peaks should therefore be ascribed to the following orbital subsets : **A** = {14a, 13b} (lines **y**, **x**); **C** = {13a, 12a, 11a} (lines **v**, **u, t**), **E** = {10b, 9a, 8a, 9b, 8b} (lines **q**, **p**, **n**, **m**, **l**); $\mathbf{F_1}$ = {7a, 6b} (lines **j**, **i**), $\mathbf{F_2}$ = {6a, 5b} (lines **g**, **h**), **G** = {5a} (line **f**), and $\mathbf{H_1}$ = {4b} (lines **e**). In addition, two shoulders (**B**, **D**) due to one-electron lines {**w**, or **s** + **r**} derived from the {12b} and {11b+10a} orbital subsets will be discernible at ~11.5 and ~13.7 eV, respectively.

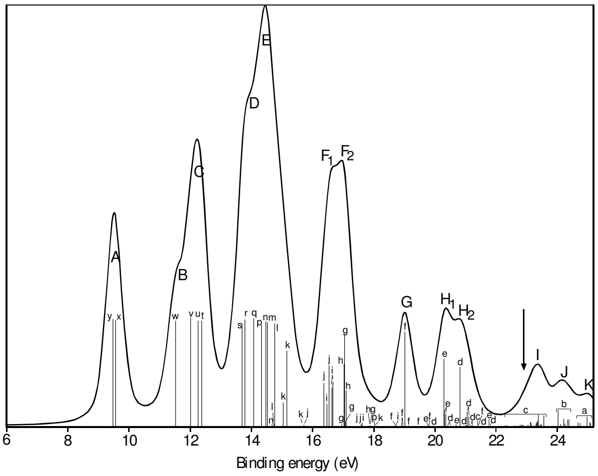

Figure 6. The ADC(3)/cc-pVDZ spike and convoluted valence ionization spectra of bicyclo[2.2.2]octane-2,5-dione (FWHM=0.6 eV). The vertical arrow at 22.9 eV marks the vertical double ionization potential for a singlet to singlet transition.

We note a rather significant breakdown of the orbital picture of ionization for orbitals 7a, 6b, and 6a (lines **j**, **i**, **h**), in the form of two or three lines with comparable intensities. Therefore, the only one-electron ionization line ($\Gamma = 0.8$) that will be individually fully resolved (band **G**) in the ionization spectrum of BCOD is line **f** derived from orbital 5a at ~19.0 eV. The two lines (**t**, **s**) which, upon a visual inspection of MO contours, dominantly belong to the π-band system of BCOD exhibit an energy separation of ~1.3 eV only (Table 7), indicating a limited through-bond conjugation of π levels via the *essentially unstrained* σ-scaffold (indeed, for this compound, all CCC bond angles are close, within deviations of a few degrees only, to the values of ~109° or ~120° that are normally expected for bond angles associated to carbon atoms in their sp^3 or sp^2 hybridization states, respectively).

For further EMS studies of BCOD, with regards to the extent of our reassignment of the (e,2e) ionization spectrum of STDO [85, 86], we recommend to follow the above orbital partitioning for fitting and interpreting the electron momentum distributions derived from an analysis of the angular dependence of the measured ionization intensities. The one-electron ($\Gamma = 0.6$) and satellite ($\Gamma = 0.2$) lines (**k**) at ~15.2 and ~15.1 eV that originate from ionization of orbital 7b are relatively well-isolated, and their intensities could therefore possibly be analysed on an individual basis. Thus, we advocate *at most* three orbital subsets {11b+10a} (lines **s**, **r**); {10b, 9a, 8a, 9b, 8b} (lines **q**, **p**, **n**, **m**, **l**); and {7b} (lines **k**) for meaningfully partitioning the (e, 2e) ionization intensities of BCOD at electron binding energies comprised between 13 and 16 eV. We similarly suggest two orbital subsets (**B**, **C**) for the band at ~12 eV, as well as two subsets (**F$_1$**, **F$_2$**) for the band at ~17 eV. In view of the limited energy resolution in EMS and the combined natural and vibrational width of spectral bands, any analysis of (e, 2e) ionization intensities that would go beyond this orbital partitioning should be regarded as improper and physically irrelevant.

Table 7. ADC(3) and OVGF Results for the Ionization Spectrum of Bicyclo-[2.2.2]-octane-2,5-dione (BCOD).*

Symbol	MO	HF/cc-pVDZ	ADC(3)/cc-pVDZ	OVGF/cc-pVDZ	OVGF/cc-pVTZ
y	14a [n (+σ)]	10.85	9.47 (0.892)	9.18 (0.905)	9.50 (0.901)
x	13b [n (+σ)]	11.03	9.56 (0.886)	9.32 (0.900)	9.65 (0.895)
w	12b [σ (+n)]	12.55	11.52 (0.888)	11.28 (0.902)	11.51 (0.898)
v	13a [σ (+n)]	13.11	12.01 (0.902)	11.70 (0.911)	11.91 (0.908)
u	11a [σ (+n)]	13.50	12.25 (0.882)	12.02 (0.907)	12.24 (0.903)
t	12a [π]	13.30	12.37 (0.880)	12.28 (0.893)	12.52 (0.888)
s	11b [π]	14.71	13.71 (0.860)	13.52 (0.895)	13.71 (0.891)
			18.92 (0.010)		
			18.94 (0.011)		
r	10a [σ]	15.08	13.79 (0.892)	13.51 (0.909)	13.71 (0.905)
q	10b [σ]	15.42	14.07 (0.898)	13.68 (0.908)	13.88 (0.905)
p	8a [n (+σ)]	16.02	14.34 (0.845)	14.13 (0.892)	14.34 (0.889)
			18.03 (0.008)		
n	9a [σ (+n)]	15.86	14.47 (0.874)	14.22 (0.899)	14.42 (0.895)
			14.68 (0.021)[a]		
m	9b [σ]	15.89	14.52 (0.870)	14.36 (0.907)	14.57 (0.903)
l	8b [σ (+n)]	16.27	14.74 (0.030)[b]		
			14.77 (0.857)	14.51 (0.902)	14.72 (0.899)
k	7b [n (+σ)]	17.02	15.05 (0.202)		
			15.16 (0.631)	15.00 (0.889)	15.09 (0.882)
j	7a [σ (+n)]	18.00	16.38 (0.364)		
			16.55 (0.511)	16.21 (0.896)	16.38 (0.891)
i	6b [n (+σ)]	18.54	16.47 (0.193)		
			16.63 (0.326)		
			16.66 (0.375)	16.43 (0.886)	16.59 (0.882)
h	6a [σ]	18.88	17.03 (0.522)	16.79 (0.890)	16.93 (0.885)
			17.10 (0.305)		
g	5b [σ]	18.72	17.05 (0.772)	16.78 (0.896)	16.95 (0.892)
			17.07 (0.047)		
f	5a [σ]	21.25	18.92 (0.037)		
			19.02 (0.784)	18.79 (0.882)	18.95 (0.877)
e	4b [σ]	22.89	20.30 (0.559)	20.24 (0.876)	20.38 (0.871)
			20.31 (0.100)		
			20.35 (0.104)		
d	4a [σ]	23.67	20.83 (0.493)	20.79 (0.862)	20.96 (0.857)
			21.06 (0.129)		
			21.10 (0.087)		
c	3b [σ]	26.72	23.38 (0.103)	23.23 (0.844)[†]	23.36 (0.838)[†]
			23.57 (0.093)		
b	3a [σ]	27.81	24.03 (0.134)		
			24.21 (0.068)		
a	2b [σ]	28.85	24.98 (0.081)		
	2a [σ]	31.91			
	1b [σ]	37.96			
	1a [σ]	38.03			

*Binding energies are given in electron volts, along with the OVGF and ADC(3) spectroscopic factors in parenthesis. Results obtained using B3LYP/TZVP geometry. Only the most intense ADC(3)/cc-pVDZ ionization lines are given here; see Table 8 for further data.

[†] Breakdown of the MO picture of ionization; see ref. 36. Dominant electronic configurations: (*a*) $14a^{-2}$ $15a^{+1}$ [HOMO^{-2} LUMO^{+1}], (*b*) $14a^{-2}$ $14b^{+1}$ [HOMO^{-2} $(\mathrm{LUMO}{+}1)^{+1}$].

F. Ionization spectrum of bicyclo[2.2.1]heptanedione (BCHD)

Owing to strong structural similarities between the two compounds, the theoretical ADC(3)/cc-pVDZ ionization spectrum (Figure 7c) of BCHD resembles that of BCOD displayed in Figure 6. This spectrum quantitatively reproduces the only He I photoelectron spectrum (Figure 7a) that is available at present for this compound [13]. For the sake of comparison, we also display in Figure 7b the results of ADC(3) calculations employing the 6-31G* basis set. It is immediately apparent that, from a qualitative point of view, the ADC(3)/6-31G* and ADC(3)/cc-pVDZ results provide consistent insights into the ionization bands of BCHD. A redistribution of the ionization intensity derived from orbitals 5b or 4a over different sets of shake-up lines (**k**, or **g**, respectively) is observed, but without any significant alteration of the computed spectral envelope. The same observation holds also above the shake-of threshold at ~23.5 eV. The reader is referred to Tables 9 and 10 for a detailed orbital assignment and comparison with further OVGF results.

Table 8. Further Ionization Lines Identified at ADC(3)/cc-pVDZ Level for Bicyclo-[2.2.2]-octane-2,5-dione (B3LYP/TZVP Geometry).[a]

Symbol	MO	ADC(3)/cc-Pvdz
k	7b [n (+σ)]	15.71 (0.016), 18.03 (0.010)
j	7a [σ (+n)]	17.59 (0.023)
i	6b [n (+σ)]	17.62 (0.032)
h	6a [σ]	17.87 (0.011)
g	5b [σ]	16.96 (0.022)
e	4b [σ]	20.70 (0.022), 21.04 (0.010)
d	4a [σ]	20.70 (0.013), 21.01 (0.017), 21.18 (0.016), 21.24 (0.017)
c	3b [σ]	22.62 (0.010), 22.75 (0.013), 22.81 (0.016), 22.86 (0.019), 22.90 (0.017), 23.02 (0.011), 23.05 (0.017), 23.13 (0.040), 23.15 (0.038), 23.18 (0.018), 23.26 (0.012), 23.31 (0.029), 23.31 (0.021), 23.34 (0.044), 23.37 (0.048), 23.44 (0.016), 23.45 (0.020), 23.49 (0.022)
b	3a [σ]	24.11 (0.022), 24.25 (0.028), 24.34 (0.054), 24.38 (0.058)
a	2b [σ]	24.68 (0.036), 24.75 (0.030), 25.06 (0.036), 25.10 (0.029), 25.11 (0.028), 25.19 (0.037)

[a] Binding energies are given in electron volts, along with the associated pole strengths in parentheses; only lines with a pole strength larger than 0.010 are given.

The two outermost levels relating to oxygen lone pairs (**y**, **x**) are quasi-degenerate. They distinctly appear therefore in the He I photoelectron spectrum (Figure 7a) in the form of a rather symmetric peak (**A**) without any apparent vibrational progression – in sharp contrast with the outermost π-levels (**z**, **y**) of STDE in Figure 3a. The next visible band (**B**) in the He I spectrum is also due to nearly degenerate one-electron ionization lines (**w**, **v**), among which one line that relates to a π-level (11a). This band is followed by a broad and composite signal extending from ~12.5 to ~15.8 eV and exhibiting two resolved peaks (**C**, **D**) at ~13.0 eV and ~14.0 eV. These relate to sets of two and four one-electron ionization lines (**u**, **t**) and (**r**, **q**, **p**, **n**) derived from the {10a, 10b} and {9a, 8a, 8b, 7b} orbitals, respectively. In this band, a shoulder (**E**) associated to orbital 6b via a one-electron ionization line (**m**) is also unambiguously observed at ~14.8 eV in the He I spectrum (Figure 7a), in good agreement (Table 9) with the ADC(3) simulations (Figures 7b and c) and OVGF/cc-pVTZ result for this line (13.1 eV). A minor shoulder at ~13.4 eV is also discernible upon scrutinizing further the He I measurements [13]. This spectral detail can be tentatively ascribed to the one-electron ionization line (**s**) at ~13.6 eV due to the σ-level 9b. We recall that He I ionization energies are essentially adiabatic in nature, and may therefore be a few tenths of an eV lower than benchmark vertical estimates (see e.g. [80]). Anticipating forthcoming EMS studies of BCHD, we correspondingly recommend to partition the (e,2e) ionization intensities obtained from this compound at electron binding energies comprised between 12.5 and 15.8 eV in, *at most*, three, or possibly four orbital subsets: **C** = {10a, 10b}; **s** = {9b}, **D** = {9a, 8a, 8b, 7b}, and **E** = {6b}. In line with our remarks for STDO, great care will be especially needed for handling the contribution from the 9b orbital (line **s**), due to very likely vibrational overlaps with the levels nearby.

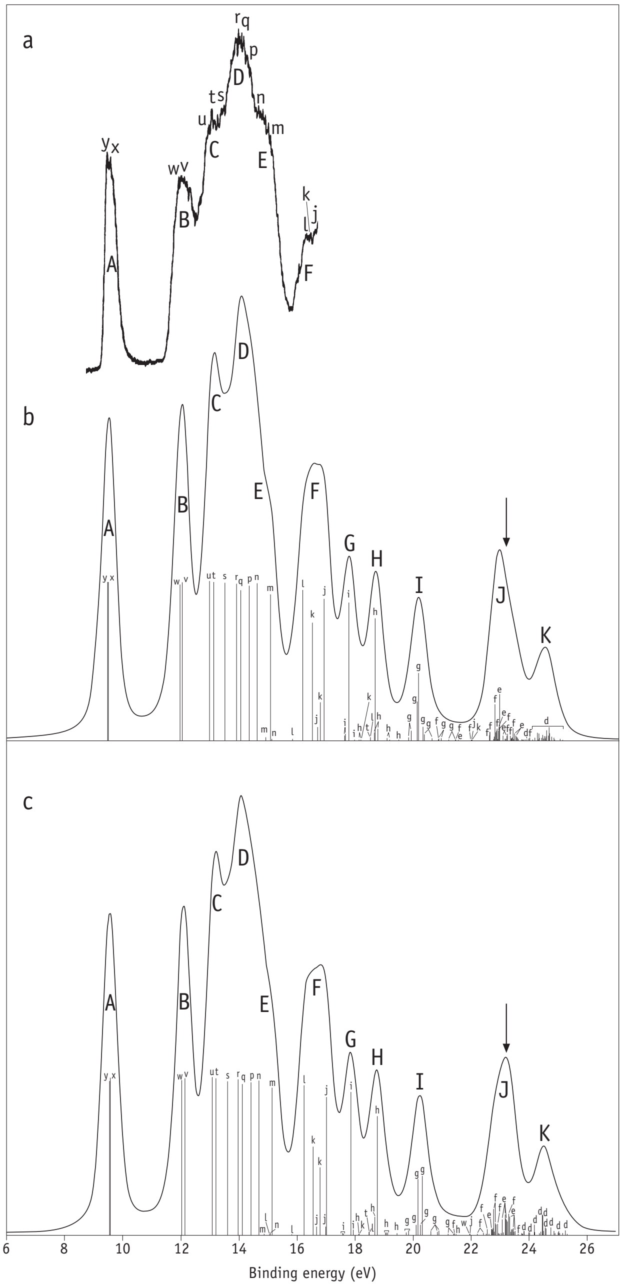

Figure 7. Comparison of the (a) UPS (He I) spectrum of bicyclo-[2.2.1]-hepta-2,5-dione [13], with (b) ADC(3)/6-31G* and (c) ADC(3)/cc-pVDZ simulations (FWHM=0.6 eV). The vertical arrows at 23.2 eV indicate the vertical double ionization potential for a singlet to singlet transition.

Proceeding further to larger electron binding energies, another composite band (**F**) is found at ~16.4 eV, which originates from one-electron and a few shake-up ionization lines (**l**, **k**, **j**) due to orbitals 7a, 5b, 6a. Two one-electron ionization lines (**i**, **h**) distinctly emerge from the ADC(3) simulations in the form of well-resolved and sharp bands (**G**, **H**) at electron binding energies of ~17.8 and ~18.8 eV. A larger width and longer tail is expected for band **I** at ~20.2 eV, because of the breakdown of the orbital picture of ionization for the 4a level, in the form of several shake-up lines (**g**) with comparable intensities.

Table 9. ADC(3), OVGF, and Experimental UPS Results for the Ionization Spectrum of Bicyclo-[2.2.1]-heptane-2,5-dione (BCHD).*

Symbol	MO	HF/cc-pVDZ	ADC(3)/cc-pVDZ	OVGF/cc-pVDZ	OVGF/cc-pVTZ	UPS[†]
y	12b [n (+σ)]	10.95	9.56 (0.893)	9.33 (0.902)	9.65 (0.898)	9.5
x	12a [n (+σ)]	10.96	9.56 (0.894)	9.31 (0.904)	9.64 (0.900)	
w	11a [π]	13.07	12.04 (0.881)	11.95 (0.897)	12.17 (0.893)	12.0
			21.95 (0.006)			
v	11b [σ (+n)]	13.14	12.14 (0.891)	11.93 (0.903)	12.15 (0.899)	
u	10a [σ (+n)]	14.21	13.08 (0.900)	12.77 (0.909)	13.00 (0.905)	13.0
t	10b [σ]	14.37	13.22 (0.893)	12.99 (0.904)	13.21 (0.900)	
			18.48 (0.018)			
			20.10 (0.008)			
s	9b [σ]	14.85	13.62 (0.889)	13.38 (0.907)	13.61 (0.903)	13.4
r	9a [σ]	15.43	13.97 (0.887)	13.66 (0.901)	13.90 (0.896)	14.0
q	8a [π]	15.90	14.12 (0.849)	14.04 (0.889)	14.27 (0.885)	
p	8b [σ (+n)]	15.79	14.42 (0.871)	14.24 (0.905)	14.46 (0.901)	
n	7b [σ]	16.11	14.69 (0.880)	14.42 (0.902)	14.64 (0.898)	
			15.07 (0.016)^{a}			
m	6b [σ]	17.03	14.87 (0.008)^{b}			
			15.14 (0.836)	15.00 (0.888)	15.09 (0.881)	14.8
l	7a [σ]	17.62	15.07 (0.005)^{c}			16.4
			15.84 (0.007)			
			16.25 (0.849)	16.03 (0.900)	16.21 (0.896)	
			18.48 (0.022)			
k	5b [σ]	18.53	16.56 (0.504)	16.43 (0.887)	16.60 (0.882)	
			16.80 (0.386)			
			18.15 (0.006)			
j	6a [σ]	19.00	16.67 (0.049)			
			17.01 (0.051)			
			17.03 (0.786)	16.86 (0.887)	17.00 (0.882)	
			21.97 (0.006)			
i	4b [σ]	19.79	17.58 (0.013)			
			17.60 (0.008)			
			17.85 (0.812)	17.64 (0.890)	17.81 (0.885)	
			17.94 (0.031)			
h	5a [σ]	20.91	18.69 (0.105)			
			18.77 (0.676)	18.56 (0.883)	18.74 (0.879)	
g	4a [σ]	22.74	20.10 (0.043)			
			20.17 (0.315)			
			20.26 (0.053)			
			20.31 (0.330)	20.10 (0.872)	20.27 (0.867)	
f	3b [σ]	26.33	22.78 (0.146)	22.84 (0.843)[‡]	22.98 (0.836)[‡]	
			22.83 (0.065)			
			22.91 (0.060)			
			23.24 (0.082)			
			23.30 (0.116)			
e	3a [σ]	26.38	22.86 (0.060)			
			23.08 (0.080)			
			23.18 (0.113)	23.12 (0.852)	23.27 (0.845)[‡]	
			23.22 (0.089)			
			23.26 (0.072)			
			23.34 (0.102)			

(*Continued*)

Table 9. (*Continued*)

Symbol	MO	HF/cc-pVDZ	ADC(3)/cc-pVDZ	OVGF/cc-pVDZ	OVGF/cc-pVTZ	UPS†
d	2b [σ]	28.24	24.18 (0.054) 24.45 (0.111) 24.47 (0.107) 24.55 (0.040) 24.75 (0.041)			
c	2a [σ]	32.58				
b	1b [σ]	38.10				
a	1a [σ]	38.18				

*Binding energies are given in electron volts, along with the ADC(3) and OVGF spectroscopic factors, which are given in parentheses. These calculations, based on B3LYP/TZVP geometries, are compared with the UPS ionization energies of ref. 13. Only the most intense ADC(3)/cc-pVDZ ionization lines are given here; see Table 10 for further data.

†Our assignment.

‡Breakdown of the MO picture of ionization; see ref. 36. Dominant electronic configurations: (a) $12a^{-1}$ $12b^{-1}$ $13a^{+1}$ [$(\text{HOMO-1})^{-1}$ HOMO^{-1} LUMO^{+1}]; (b) $12a^{-2}$ $13b^{+1}$ [$(\text{HOMO-1})^{-2}$ $(\text{LUMO+1})^{+1}$] and $12a^{-1}$ $12b^{-1}$ $13a^{+1}$ [$(\text{HOMO-1})^{-1}$ HOMO^{-1} LUMO^{+1}]; (c) $12a^{-1}$ $12b^{-1}$ $13b^{+1}$ [$(\text{HOMO-1})^{-1}$ HOMO^{-1} $(\text{LUMO+1})^{+1}$] and $12b^{-2}$ $13a^{+1}$ [HOMO^{-2} LUMO^{+1}].

Table 10. Further Ionization Lines Identified at the ADC(3)/cc-pVDZ Level for Bicyclo-[2.2.1]-heptane-2,5-dione (B3LYP/TZVP Geometry).[a]

Symbol	MO	ADC(3)/cc-pVDZ
h	5a [σ]	19.05 (0.017), 19.08 (0.018), 19.13 (0.018), 19.44 (0.011)
g	4a [σ]	19.76 (0.014), 19.85 (0.027), 20.61 (0.023), 20.83 (0.018), 20.89 (0.022)
f	3b [σ]	22.43 (0.015), 22.55 (0.021), 22.76 (0.036), 22.80 (0.017), 23.10 (0.010), 23.12 (0.011), 23.26 (0.014), 23.38 (0.017), 23.40 (0.029), 23.43 (0.030), 23.46 (0.016)
e	3a [σ]	22.70 (0.030), 22.74 (0.029), 22.78 (0.018), 22.93 (0.012), 23.07 (0.013), 23.37 (0.017), 23.39 (0.015), 23.46 (0.038), 23.51 (0.023)
d	2b [σ]	23.83 (0.020), 23.98 (0.012), 24.02 (0.014), 24.41 (0.017), 24.50 (0.020), 24.58 (0.034), 24.59 (0.022), 24.85 (0.020), 24.98 (0.011), 25.01 (0.021), 25.24 (0.024)

[a] Binding energies are given in electron volts, along with the associated pole strengths in parentheses; only lines with pole strenths larger than 0.010 are given here.

3.5. 4 Conclusions

A quantitative study of available photoelectron or electron-impact measurements of the valence electronic structure of STDE, STDO, and BCHD has been presented, with the aid of one-particle Green's Function calculations of vertical one-electron and shake-up ionization energies employing the benchmark third-order Algebraic Diagrammatic Construction [ADC(3)] scheme. These calculations are supplemented by OVGF calculations in order to determine the impact on one-electron ionization energies of possible shortcomings of the employed geometry and basis sets in strained cage compounds bearing C=C or C=O bonds. This methodological assessment as well as the confrontation against experiment lead us to conclude that, despite likely complications due to vibronic interactions in strained hydrocarbon cages, polarized valence basis sets of triple zeta quality are large enough to ensure accuracies of ~0.3 eV on one-electron ionization energies computed for diketone species. The OVGF and ADC(3) approaches have been used therefore to quantitatively predict the valence ionization spectrum of the closely related but merely unstrained BCOD species.

The present study confirms the empirical rule that OVGF pole strengths smaller than ~0.85 are indicative [36, 39] of a breakdown of the orbital picture of ionization [31] at the ADC(3) level, in the form of a dispersion of the ionization intensity over several shake-up lines with comparable strength ($\Gamma < 0.5$). Identifications of spectral fingerprints for cyclic strains in diketone cage compounds are not straightforward, due to interferences with inductive effects and dipole-dipole interactions between C=O bonds. There are nevertheless rather clear correlations between the HOMO-LUMO band gap, the first ionization energy, the shake-up onset and the shake-off threshold of all four species. With regards to these electronic properties, the investigated cage compounds can be regarded as weakly conjugated and, thus, weakly correlated species. As a result, the orbital picture of ionization remains essentially valid throughout the outer-valence region, up to electron binding energies of 18 eV for STDE, and of 22 eV for BCOD, BCHD and STDO.

The present study demonstrates that it is impossible to reliably assign complex (e, 2e) ionization spectra using Hartree-Fock or Kohn-Sham orbital energies and the related electron momentum distributions. In view of errors ranging from ~0.7 to ~1.5 eV on the electron binding energies that have been reported in recent (e,2e) investigations of the valence electronic structure of STDO, great care is recommended for further experimental studies employing EMS, because of the non-negligible extent (~0.4 eV, at least) of the natural and vibrational broadening of ionization lines as well as the limited energy resolution of the available (e,2e) spectrometers (at best, ~0.5 eV). The reported discrepancies between our benchmark OVGF/cc-pTVZ values for vertical ionization energies and electron binding energies that have been experimentally inferred from an analysis of (e, 2e) intensities using model Kohn-Sham orbital densities are much too large to be satisfactorily explained by vibronic coupling interactions. The main drawbacks of such studies stem from the inadequacy of standard Kohn-Sham orbitals to correctly describe ionization potentials as well as Dyson orbitals [87] and from the limitations of the fitting procedure used to extract experimental ionization potentials from (e,2e) ionization spectra in congested valence bands. In contrast, our analysis is based on high-level many-body treatments that enable calculations of vertical electron binding energies within accuracies of, typically, ~0.2 to ~0.3 eV [48, 49].

Considering the extent of errors in DFT assignment of recent EMS measurements on STDO, any other attempt to disentangle and individually analyse, by means of a Gaussian fitting procedure, the contributions to the measured (e,2e) ionization intensities of ionization lines exhibiting energy separations smaller than the energy resolution should be regarded as physically meaningless and proscribed. Note that shake-up fragmentation may also lead to further band broadening. Note also that, at electron impact energies of 1.5 keV, (e, 2e) ionization events have a very limited characteristic time scale (~10^{-17} s). A vertical depiction of ionization is therefore expected to prevail for EMS [50]. At last, we wish to stress that, although they account for ground state correlation in the wavefunction of the *neutrals*, KS orbitals provide only *empirical* insights into the angular dependence of (e, 2e) ionization intensities. For quantitatively interpreting EMS measurements, we therefore strongly advocate ADC(3) calculations of ionization spectra and of (e, 2e) spherically averaged electron momentum distributions using [87, 91] the related Dyson orbitals.

References

[1] Hoffmann, R. *Acc. Chem. Res.* 1971, 4, 1.

[2] Eckert-Maksic, M. in *Theoretical Models of Chemical Bonding*; Makzic, Z. B., Ed.; Springer-Verlag: Heidelberg, Germany, 1991, part 3 p. 153; and references therein.

[3] Wasiellewski, M. R. *Chem. Rev.* 1992, 92, 435.

[4] Jordan, K. D.; Paddon-Row, M. N. *Chem. Rev*. 1992, 92, 395.

[5] Paulson, B.R.; Curtiss, L. A.; Bal, B.; Closs, G. L.; Miller, J. R. *J. Am. Chem. Soc.* 1996, 118, 378.

[6] Closs, G. L.; Miller, J. R. *Science* 1988, 240, 440.

[7] Kroon, J.; Oliver, A. M.; Paddon-Row, M. N.; Verhoeven, J. W. *J. Am. Chem. Soc.* 1990, 112, 4868.

[8] Verhoeven, J. W. *Pure Appl. Chem.* 1990, 62, 1585.

[9] Paddon-Row, M. N. *Acc. Chem. Res.* 1997, 27, 18.

[10] Balaji, V.; Jordan, L. Ng. K. D.; Paddon-Row, M. N.; Partney, H. K. *J. Am. Chem. Soc.* 1987, 109, 6957.

[11] Gleiter, R.; Schäfer, W. *Acc. Chem. Res.* 1990, 23, 369.

[12] Bally, T.; Heilbronner, E. *The Chemistry of Dienes and Polyenes*; Rappoport, Z., Ed.; J. Wiley and Sons: New-York, 1997, Vol. 1 p. 173 – 261.

[13] Frost, D. C.; Westwood, N. P. C.; Werstiuk, N. H. *Can. J. Chem.* 1980, 58, 1659.

[14] Gleiter, R.; Kissler, B.; Ganter, C. *Angew. Chem.* 1987, 99, 1292.

[15] Gleiter, R.; Kissler, B.; Ganter, C. *Angew. Chem.* 1987, 26, 1252.

[16] Gleiter, R.; Kissler, B. *Tetrahedron Lett.* 1987, 28, 6151.

[17] Gleiter, R.; Gaa, B.; Sigwart, C.; Lange, K.; Borzyk, O.; Rominger, F.; Irngartinger, H.; Oeser, T. *Eur. J. Org. Chem*. 1988, 171.

[18] Altmayer, M.; Gaa, B.; Gleiter, R.; Rominger, F.; Kurzawa, J.; Schneider, S. *Eur. J. Org. Chem.* 2001, 3045.

[19] Koopmans, T. A. *Physica* (Amsterdam) 1933, 1, 104.

[20] Szabo, A.; Ostlund, N. S. *Modern Quantum Chemistry. Introduction to Advanced Electronic Structure Theory*; Dover: New York, 1996.

[21] Cederbaum, L. S.; Domcke, W. *Adv. Chem. Phys.* 1977, 36, 205.

[22] von Niessen, W.; Schirmer, J.; Cederbaum, L. S. *Comput. Phys. Rep*. 1984, 1, 57.

[23] Zakrzewski, V. G.; von Niessen, W. *J. Comp. Chem.* 1993, 14, 13.

[24] Ortiz, J. V. *Computational Chemistry: Reviews of Current Trends*; Leszczyinski, J., Ed.; World Scientific: Singapore, 1997; Vol. 2 p. 1.

[25] Linderberg, J.; Öhrn, Y. *Propagators in Quantum Chemistry*; Wiley: Hoboken, New-Jersey, 2004.

[26] Pickup, B. T.; Goscinski, O. *Mol. Phys*. 1973, 26, 1013.

[27] Cederbaum, L. S.; Hohlneicher, G.; von Niessen, W. *Mol. Phys.* 1973, 26, 1405.

[28] Herman, M. F.; Freed, K. F.; Yeager, D. L. *Adv. Chem. Phys.* 1981, 48, 1.

[29] Öhrn, Y., Born, G. *Adv. Quantum Chem.* 1981, 13, 1.

[30] Deleuze, M.; Denis, J. P.; Delhalle, J.; Pickup, B. T. *J. Phys. Chem.* 1993, 97, 5115.

[31] Cederbaum, L. S.; Schirmer, J.; Domcke, W.; von Niessen, W. *Adv. Chem. Phys.* 1986, 65, 115; and references therein.

[32] Deleuze, M. S.; Cederbaum, L. S. *Int. J. Quantum Chem.* 1997, 63, 465.

[33] Deleuze, M. S.; Trofimov, A. B.; Cederbaum, L. S. *J. Chem. Phys.* 2001, 115, 5859.

[34] Potts, A. W.; Trofimov, A. B.; Schirmer, J.; Holland, D. M. P.; Karlsson, L. *Chem. Phys.* 2001, 271, 337.

[35] Trofimov, A. B.; Schirmer, J.; Holland, D. M. P.; Karlsson, L.; Maripuu, R.; Siegbahn, K.; Potts, A. W. *Chem. Phys.* 2001, 263, 167.

[36] Deleuze, M. S. *J. Chem. Phys.* 2002, 116, 7012.

[37] Trofimov, A. B.; Schirmer, J.; Holland, D. M. P.; Potts, A. W.; Karlsson, L.; Maripuu, R.; Siegbahn, K. *J. Phys. B: At. Mol. Opt. Phys.* 2002, 35, 5051.

[38] Potts, A. W.; Holland, D. M. P.; Trofimov, A. B.; Schirmer, J.; Karlsson, L.; Siegbahn, K. *J. Phys. B: At. Mol. Opt. Phys.* 2003, 36, 3129.

[39] Deleuze, M. S. *J. Phys. Chem.* A 2004, 108, 9244.

[40] Kishimoto, N.; Hagihara, Y.; Ohno, K.; Knippenberg, S.; François, J.-P.; Deleuze, M. S. *J. Phys. Chem.* A 2005, 109, 10535.

[41] Schirmer, J.; Cederbaum, L. S.; Walter, O. *Phys. Rev. A* 1983, 28, 1237.

[42] Schirmer, J.; Angonoa, G. *J. Chem. Phys.* 1989, 91, 1754.

[43] Weikert, H. G.; Meyer, H.-D.; Cederbaum, L. S.; Tarantelli, F. *J. Chem. Phys.* 1996, 104, 7122.

[44] Deleuze, M. S.; Giuffreda, M. G.; François, J.-P.; Cederbaum, L. S. *J. Chem. Phys.* 1999, 111, 5851.

[45] Gleiter, R.; Sigwart, C. *J. Org. Chem.* 1994, 59, 1027.

[46] Roth, W. R.; Gleiter, R.; Pascmann, V.; Hacker, U. E.; Fritzsche, G.; Lange, H. *Eur. J. Org. Chem.* 1998, 961.

[47] Herb, T.; Lange, H.; Gleiter, R. *J. Chem. Soc. Perkin Trans.* 2 2000, 1155.

[48] Knippenberg, S.; Nixon, K. L.; Mackenzie-Ross, H.; Brunger, M. J.; Wang, F.; Deleuze, M. S.; François, J.-P.; Winkler, D.A. *J. Phys. Chem. A* 2005, 109, 9324.

[49] Knippenberg, S.; Nixon, K. L.; Brunger, M. J.; Maddern, T.; Campbell, L.; Trout, N.; Wang, F.; Newell, W. R.; Deleuze, M. S.; François, J.-P.; Winkler, D. A. *J. Chem. Phys.* 2004, 121, 10525.

[50] Knippenberg, S., Deleuze, M. S.; Cleij, T.J.; François, J.-P.; Cederbaum, L. S.; Eland, J. H. D. *J. Phys. Chem. A* 2005, 109, 4267.

[51] Knippenberg, S.; Hajgató, B.; François, J.-P.; Deleuze, M. S., accepted for publication in *J. Phys. Chem. A*.

[52] Köppel, H.; Cederbaum, L. S.; Domcke, W. *J. Chem. Phys.* 1988, 89, 2023.

[53] The 1p-GF/ADC(3) code originally written by Angonoa, G.; Walter, O.; Schirmer, J.; Cederbaum, L. S.; and further developed by Scheller, M. K.; Trofimov, A. B..

[54] Schmidt, M. W.; Baldridge, K. K.; Boatz, J. A.; Elbert, S. T.; Gordon M. S.; Jensen, J. H.; Koseki, S.; Matsunaga, N.; Nguyen, K. A.; Su, S. J.; Windus, T. L.; Dupuis, M.; Montgomery, J. A. *J. Comput. Chem.* 1993, 14, 1347.

[55] Frisch, M. J.; Trucks, G. W.; Schlegel, H. B., *et al.*; GAUSSIAN 98, Revision A.11; Gaussian, Inc.: Pittsburgh, PA, 1998.

[56] Dunning, T. H., Jr. *J. Chem. Phys.* 1989, 90, 1007.

[57] (a) Becke, A. D. *J. Chem. Phys.* 1993, 98, 5648; (b) Lee, C.; Yang, W.; Parr, R. G. *Phys. Rev. B* 1988, 37, 785.

[58] Dunning, T.H. Jr. *J. Chem. Phys*. 1971, 55, 716.

[59] Feller, D.; Boyle, C. M.; Davidson, E. R. *J. Chem. Phys.* 1987, 86, 3424.

[60] Schirmer, J. *Phys. Rev. A* 1991, 43, 4647.

[61] Mertins, F.; Schirmer, J. *Phys. Rev. A* 1996, 53, 2140.

[62] Ruhe, A. *Math. Comp.* 1979, 33, 680.

[63] Cullum, J. K.; Wiloughby, R.A. *Lanczos Algorithms for Large Symmetric Eigenvalue Computations*; Birkhäuser: Boston, 1985.

[64] Meyer, H.-D.; Pal, S. *J. Chem. Phys.* 1989, 91, 6195.

[65] see: Deleuze, M S *Int. J. Quantum Chem.* 2003, 93, 191; and references therein.

[66] Trofimov, A. B.; Schirmer, J. *J. Chem. Phys.* 2005, 123, 144115.

[67] Kendall, R. A.; Dunning, T. H. Jr; Harrisson, R. J. *J. Chem. Phys.* 1992, 96, 6796.

[68] Woon, D. E.; Dunning, T.H. Jr. *J. Chem. Phys.* 1993, 98, 1358.

[69] Krishnan R.; Pople, J. A. *Int. J. Quant. Chem*. 1978, 14, 91.

[70] Trucks, G. W.; Salter, E. A.; Sosa, C.; Bartlett, R. J. *Chem. Phys. Lett*. 1988, 147, 359.

[71] Purvis, G. D.; Bartlett, R. J. *J. Chem. Phys*. 1982, 76, 1910.

[72] Scuseria, G. E.; Janssen, C. L.; Schaefer III, H. F. *J. Chem. Phys*. 1988, 89, 7382.

[73] Raghavachari, K.; Trucks, G. W.; Head-Gordon, M.; Pople, J. A. *Chem. Phys. Lett*. 1989, 157, 479.

[74] Bartlett, R. J. *J. Phys. Chem.* 1989, 93, 1697.

[75] Scuseria, G. E.; Lee, T. J. *J. Chem. Phys.* 1990, 93, 5851.

[76] Jaffe, H.H.; Orchin, M. *Symmetry in Chemistry*; Wiley: New York, 1967.

[77] Rülf, E.; Price, S.D.; Leach, S. *J. Phys. Chem.* 1989, 93, 6312.

[78] Tobita, S.; Leach, S.; Jochims, H.W.; Rülh, E.; Illenberger, E.; Baumgärtel, H. *Can. J. Phys.* 2004, 72, 1060.

[79] Cederbaum, L. S.; Zobeley, J.; Tarantelli, F. *Phys. Rev. Lett.* 1997, 79, 4778.

[80] Deleuze, M.S.; François, J.-P.; Kryachko, E.G. *J. Am. Chem. Soc.* 2005, 127, 16824.

[81] Deleuze, M. S.; Cederbaum, L. S. *J. Chem. Phys.* 1996, 105, 7583.

[82] Golod, A.; Deleuze, M. S.; Cederbaum, L. S. *J. Chem. Phys.* 1999, 110, 6014.

[83] Deleuze, M. S.; Claes, L.; Kryachko, E. S.; François, J.-P. *J. Chem. Phys*. 2003, 106, 8569.

[84] Gleiter, R.; Lange, H.; Borzyk, O. *J. Am. Chem. Soc.* 1996, 118, 4889.

[85] Nixon, K. L.; Wang, F.; Campbell, L.; Maddern, T.; Winkler, D.; Gleiter, R.; Loch, P.; Loeb, P. K.; Weigold, E.; Brunger, M. J. *J. Phys. B: At. Mol. Opt. Phys.* 2003, 36, 3155.

[86] Wang, F.; Brunger, M. J.; McCarthy, I. E.; Winkler, D. A. *Chem. Phys. Lett.* 2003, 382, 217.

[87] Ning, C. G.; Ren, X. G.; Deng, J. K.; Su, G. L.; Zhang, S. F.; Knippenberg, S.; Deleuze, M. S. *Chem. Phys. Lett.* 2006, 421, 52.

[88] Köppel H.; Cederbaum, L.S.; Domcke, W. *J. Chem. Phys.* 1981, 77, 2014.

[89] Köppel H.; Cederbaum, L.S.; Domcke, W. *J. Chem. Phys.* 1988, 89, 2023.

[90] Köppel H.; Döscher, M.; Bâldea, I.; Meyer, H.-D.; Szalay, P.G. *J. Chem. Phys.* 2002, 117, 2657.

[91] Deleuze, M. S.; Knippenberg, S. *J. Chem. Phys.* 2006, 125, 104309.

Part 4: Conformationally versatile molecules

4.1 Study of the molecular structure, ionization spectrum, and electronic wave function of 1,3-butadiene using electron momentum spectroscopy and benchmark Dyson orbital theories.

4.1.1 Introduction

1,3-butadiene is the archetype of π-conjugated molecules which, by virtue of relatively easy rotations around C-C bonds with bond orders comprised between 1 and 2, are assumed to exist at ambient temperatures as equilibrium mixtures of various conformations (or conformational isomers), namely in this case the s-trans and s-cis (or gauche) conformations :

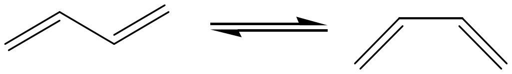

A wealth of experimental and theoretical studies on this molecule are available, many of which focus on its torsional potential [1-11]. As is well-known, the s-trans conformer has planar (C_{2h}) symmetry. A planar s-cis structure of C_{2v} symmetry would maximize conjugation of the double bonds, while a gauche structure, with a dihedral angle intermediate between 0 and 90° (C_2 symmetry) relieves steric strains between the inside hydrogens of the terminal methylene groups. It is now well-established that in the gas phase the planar (C_{2v}) s-cis conformer relates to a first order saddle point. To date, the most accurate theoretical study of the potential energy surface of 1,3 butadiene is that by A. Karpfen and V. Parasuk [11], which locates the gauche form [$\tau(C_1\text{-}C_2\text{-}C_3\text{-}C_4) = \sim 38° \pm 3°$] of this molecule at 2.90 kcal/mol (1014 cm^{-1}) above the s-trans energy minimum, according to benchmark quantum-chemical coupled cluster CCSD(T) calculations employing Dunning's correlation consistent polarized valence cc-pV5Z basis set [12]. The most recent spectroscopic determination [13] provides correspondingly enthalpy [ΔH] and entropy [ΔS] differences of 2.93 kcal mol^{-1} and 3.98 cal mol^{-1} K^{-1}, according to a principal component analysis of the temperature dependence of the ultra-violet absorption spectrum of 1,3-butadiene upon the constraint of the van't Hoff equation :

$$\ln\left(\frac{1-f}{f}\right) = -\frac{\Delta H}{RT} + \frac{\Delta S}{R}. \qquad (1)$$

In this equation, f represents the molar fraction of the s-trans conformer in the gas phase. At room temperature (298K), the gauche conformer has therefore a molar fraction of 5 % only. Note that, according to the above results, temperatures larger than ~740K and ~2400K are in principle required for observing gauche molar fractions larger than 50 and 80 %, respectively. From a kinetic viewpoint, it is also worth mentioning that the propensity of the trans-form of 1,3-butadiene to evolve towards the higher-energy lying gauche minimum is, at the end of the day, relatively limited, with regards to a conversion path characterized by an energy barrier of 6.12 kcal mol^{-1} (CCSD(T)/cc-pVDZ estimate [11]). Upon applying elementary transition state theory [14], such a barrier leads to a rate constant of the order of 10^8 s^{-1} at ambient temperatures. In other words, with respect to molecular dynamics [15] and standard thermal fluctuations, the s-trans form of 1,3-butadiene has an intrinsic lifetime of the order of ~10 *ns*. Spectroscopic techniques with a characteristic time scale much shorter than this lifetime can only provide instantaneous snapshots of the conformer equilibrium distribution that normally prevails for 1,3-butadiene.

The valence electronic structure of 1,3-butadiene has been extensively studied experimentally, using He I [16-21], He II [22, 23] and X-ray (Al Kα) [24] photoelectron spectroscopies (PES). To date, the most complete and reliable experimental study of the valence shell photoelectron spectrum of 1,3-butadiene is that by D.M.P. Holland *et al* [25]. In this latter work, synchrotron radiation has been used to study the angular dependence of the photoelectron spectrum in the 12-120 eV photon energy range, in support to high-resolution He I and He II measurements at binding energies comprised between 9 and 26 eV. Theoretical studies of the photoelectron spectra of 1,3 butadiene accounting for satellite structures due to initial and final state configuration interaction effects are comparatively very scarce. These comprise the early calculations by Cederbaum *et al* [26] employing the two-particle-one-hole Tamm-Dancoff Approximation, the calculations by Fronzoni *et al* using an homemade ab initio configuration-interaction [CI] program [27], as well as the one-particle Green's Function (1p-GF) calculations by D.M.P. Holland *et al* [25], or Deleuze *et al* [28] employing the so-called third-order Algebraic Diagrammatic Construction scheme [ADC(3)] [29-33].

All these studies indicate that the inner-valence states of 1,3-butadiene are severely split into many-states by final-state configuration-interaction effects, and somewhat more surprisingly in these early days [25 - 28], that some of the outer-valence main lines are also subject to a very significant loss, by 35% or more, of the orbital ionization intensity into satellite structures. Note that all these analyses so far were based upon the assumption of a planar (C_{2h}) structure, an assumption which always appeared to be amply sufficient for correctly and very satisfactorily unraveling all the available photoelectron measurements on 1,3-butadiene. Over the last decade, the finding that both the outer-valence σ- and π-band systems of conjugated molecules are subject to severe breakdowns of the one-electron picture of ionization [34] has been amply confirmed in studies of, for instance, large polyenes [35], carbon clusters [33, 36, 37], benzene [32, 38 and references therein], polycylic aromatic hydrocarbons [38 – 40], purine and pyrimidine [41], trans-stilbene [42], chlorobenzene [43] as well as a number of thiophene derivatives [44 - 46].

In addition to the photoelectron spectroscopy studies already cited, several studies of the ionization spectrum of 1,3-butadiene employing electron impact (e, 2e) spectroscopic techniques [47 - 51] can be mentioned. We refer in particular to an exhaustive study of the outer-valence region [52] by means of Electron Momentum Spectroscopy [53 - 55]. In straightforward relationships with an exhaustive analysis [56] of the influence of the molecular conformation on the electron momentum distributions experimentally inferred from an EMS study of *n*-butane [57], the EMS measurements by M.J. Brunger *et al* on 1,3-butadiene have been recently re-interpreted [58] by comparison with spherically-averaged distributions derived from modest Kohn-Sham orbital calculations upon s-trans- and gauche model structures. In sharp contrast with all studies so far of the valence electronic wavefunction of 1,3-butadiene, this study led to the conclusion that "four of the seven outer valence orbitals of this species are in fact engaged with the gauche form, whereas three of such orbitals receive contributions from s-trans-1,3-butadiene". In other words, according to the analysis by Saha *et al* [58], the electron momentum distributions inferred from an angular analysis of the (e, 2e) cross sections indicate that, under the prevailing experimental conditions and depending on the selected ionization channel, the gauche form of 1,3-butadiene strongly predominated in the gas phase mixtures upon which some of the (e, 2e) measurements were made.

Above all, the reader must note that, in view of a characteristic time scale of the order of 10^{-17} s for the interaction time between the molecular target and an impinging electron with a kinetic energy of 1.5 keV, the electron momentum distributions experimentally inferred by Michael J. Brunger *et al* in [52] relate to electron impact ionization events that are intrinsically vertical [59, 60] in nature. In other words, it is extremely unlikely that nuclear dynamical complications such as vibronic coupling interactions could provide some satisfactory support to the interpretations by S. Saha *et al* [58]. EMS measurements on structurally versatile molecules (see also [61] and [62]) are simply expected to straightforwardly reflect the conformer distribution, and temperature therefore, that prevail during the experiment. It seems truly impossible that the original measurements by Brunger *et al* could have been performed on molecular beams heated at temperatures above 2000K while subject to high-vacuum conditions, as the analysis and ultimate conclusion by Saha *et al* [58] implies according to our introductory discussion.

The scope of the present work is to demonstrate from benchmark theoretical data for the inner- and outer-valence ionization bands that this conclusion actually derives from several weaknesses and inconsistencies in the analysis by Saha *et al* [58], due among others to the limitations of the fitting procedure for convolving the (e, 2e) ionization spectra, the neglect of a low-energy-lying $\pi^{-2}\ \pi^{*+1}$ satellite, and, almost, the fact that the influence of the molecular conformation upon the outer-valence ionization bands of 1,3-butadiene has not been correctly accounted for, despite accurate and independent calculations [58] of one-electron binding energies by means of the Outer-Valence Green's Function approach [63, 64]. In this purpose, use will be made of Dyson orbitals [65 - 70] derived from large-scale 1p-GF/ADC(3) calculations of valence ionization spectra. Contributions from the statistically unsignificant and high-energy lying cis-conformer will be deliberately ignored, in order to identify unusual but possible experimental artefacts in [52]. In support to our analysis, the newly computed inner-and outer-valence ADC(3) ionization spectra will also be compared with the high-resolution photoelectron measurements by D.M.P. Holland *et al* [25].

4.1.2 Theory

For the theory of EMS [53-55], which is based on electron impact ionization experiments focusing on (e,2e) reactions ($M + e^{-} \rightarrow M^{+} + 2e^{-}$), we refer to Chapter 2.8. For the present refutation of the work by Saha *et al* [58], it is further essential to note that the experimentally inferred electron momentum distributions relate to (e, 2e) ionization cross sections at *fixed* ionization energies, within the usual experimental restrictions due to the limited energy resolution of the employed spectrometer. In [52], an overall coincident energy resolution of ~1.6 eV full-width-at-half-maximum (FWHM) was reported.

4.1.3 Computational details

All computations described in this work have been performed on molecular geometries that have been optimised under the constraints of C_{2h} (s-trans-1,3-butadiene) or C_2 (gauche-1,3-butadiene) symmetry point groups using Dunning's basis set of triple-ζ quality [71] with polarized valence functions (TZVP), and Density Functional Theory (DFT) in conjunction with the non-local hybrid and gradient corrected Becke three-parameter Lee-Yang-Parr functional (B3LYP) [72], an approach which is known to provide structural results of quality comparable to that achieved at the benchmark CCSD(T) theoretical level [73, 74].

The ADC(3) calculations have been carried out using the original 1p-GF/ADC(3) package of programs, interfaced to GAMESS [75]. This package incorporates a band-Lanczos [76, 77] “pre”-diagonalisation of the block matrices pertaining to the 2p-1h shake-on states into a pseudo-electron attachment spectrum, prior to a complete block-Davidson diagonalisation [78, 79] of the so-reduced ADC(3) secular matrix. With this diagonalization procedure, all eigen-values of the ADC(3) secular matrix with pole strengths equal to or larger than 0.005 could be recovered up to electron binding energies of ~30 eV. The assumption of frozen core electrons has been used throughout and the full molecular symmetry point groups have been exploited. At the self-consistent field level, the requested convergence on each of the elements of the density matrix was fixed to 10^{-10}. The ADC(3) calculations were carried out using Roos’ augmented double-ζ basis set of atomic natural orbitals (154 basis functions, shortly: aug-ANO) [80]. The corresponding contraction scheme is given by [14s 9p 4d]/(4s 3p 2d) for the C atoms and [8s 4p]/(3s 2p) for the H atoms.

For the sake of more quantitative insights into one-electron valence ionization energies, we also performed Outer-Valence Green’s Function (OVGF) calculations [63, 64] using the aug-ANO basis set as well as the extremely large (400 basis functions) Dunning’s correlation consistent polarized valence basis set of quadruple zeta quality (cc-pVQZ) [81]. These OVGF calculations were performed using the integral-driven and semi-direct routines implemented in the GAUSSIAN [82] computer package.

As a guide to the eye, the identified solutions of the secular ADC(3) eigenvalue problems are displayed in the sequel as spike spectra and in the form of convoluted densities of states. In these simulations, line intensities are scaled according to the computed ADC(3) pole strengths. These convolutions have been performed using as spread functions combinations of Gaussians and Lorenzians with equal weight and constant width (Voigt profile), taking into account the energy resolutions of the employed spectrometers (1.6 eV in EMS [52], 0.1 eV with PES), as well as a reasonable estimate of ~0.5 eV for vibrational and natural broadening. In the present work, the width of the convolution function for simulating EMS and PES measurements amounts therefore to 2.1 and 0.6 eV, respectively. For the sake of completeness, and in views of the current performances of the best (e, 2e) spectrometers, convolutions employing spread functions with a width of 1.2 eV will be also provided.

Dyson orbital momentum distributions have been generated from the output of HF calculations employing GAUSSIAN [82]. All spherically averaged Dyson orbital MDs have been obtained using an adaptation of the HEMS program by Brion and co-workers [83] and convolved [84] according to an experimental electron momentum resolution of 0.1 a.u., which is consistent with an angular resolution of $\Delta\phi = 1.2°$ in the employed (e, 2e spectrometer) [58]. The computed (e, 2e) ionization intensities have been rescaled relatively to the experimental ones.

4.1.4 Results and discussion

A. Ionization spectra

The EMS ionization spectra recorded by Brunger *et al.* at azimuthal angles of ϕ=0° and ϕ=7° are reproduced in Figures 1a and b, respectively, and readily compared with simulations drawn (dotted lines: FWHM = 1.2 eV; full lines: 2.1 eV) from the results of our ADC(3)/aug-ANO calculations on the s-trans (Figure 1c) and gauche forms (Figure 1d) of 1,3-butadiene. The 10 gaussians used by Brunger *et al.* for convolving and analyzing their (e, 2e) measurements according to a least-square-fit are also displayed in Figures 1a. and b.

It is well-known [53 - 55] that molecular orbitals with a *p*-type profile have vanishing (e, 2e) ionization cross sections at low electron momenta, i.e. when ϕ=0°. In contrast, all orbitals contribute significantly to the (e, 2e) ionization intensity at larger values of ϕ, in particular to those corresponding to electron momenta ranging from ~0.5 to ~1.0 a.u. In qualitative agreement with experiment (Figures 1a and b), the theoretical ADC(3)/aug-ANO simulation obtained using a spread function with a (FWHM) width of 2.1 eV for the s-trans-conformer exhibits a deep mimum of intensities at ~17.8 eV, which marks the border between the inner- and outer-valence regions. On the other hand, a shoulder is correspondingly seen at that electron binding energy in the spectrum calculated for the gauche form, which is due to a rather intense (Γ=0.69) one-electron ionization line originating from the inner-valence orbital 4b (θ). With regards to striking differences in the simulations obtained using narrower spread functions (FWHM = 1.2 eV), and a very limited weight of 5 % for the cis-form, it is clear that further EMS measurements with improved energy resolution would be useful for more clearly discriminating on experimental grounds the s-trans and gauche conformers of 1,3-butadiene. As shall be shown in the sequel, however, there is no need to consider the high energy-lying gauche structure for quantitatively interpreting on relative intensity scales the EMS measurements of [58], regardless of their low energy resolution and limited statistics.

The incompatibility of the ionization spectrum of the gauche conformer with gas phase determinations of the electronic structure of 1,3-butadiene through ionization experiments in high-vacuum conditions is obvious when comparing (Figure 2) the results of ADC(3)/aug-ANO simulations employing spread functions with a FWHM parameter of 0.6 eV with, for instance, the photoelectron spectrum recorded with a synchrotron radiation beam by Holland *et al.* a photon energy of 80 eV [25]. Three peaks that are predicted (Figure 2c) for the gauche form at outer-valence electron binding energies of ~12.5, ~15.0 and ~16.5 eV and originating from ionization of the 7a (γ), {5b (ε)+ 6a (ζ)} and 5a (η) orbitals are, in view of the extremely favorable energy resolution achieved in [25], clearly missing on the experimental side (Figure 2a). In the inner-valence region, according to the ADC(3)/aug-ANO results, the theoretical ionization spectrum for the gauche form (Figure 2c) is also characterized by a strikingly protruding and very well-isolated shake-up line (Γ=0.42) at 20.4 eV and relating to orbital 4a (ι). Very clearly, this line does also not correlate with any intense enough signal on the experimental side (Figure 2a). On the other hand, band **i** at 20.8 eV in the photoelectron spectrum of Figure 2a does not correlate with any significant sets of lines in the ADC(3)/aug-ANO spectrum computed for the gauche form (Figure 2c). In contrast, the ADC(3)/aug-ANO spectrum for the s-trans-conformer (Figure 2b) sustains much more favorably the comparison with the photoelectron spectrum of Figure 2a.

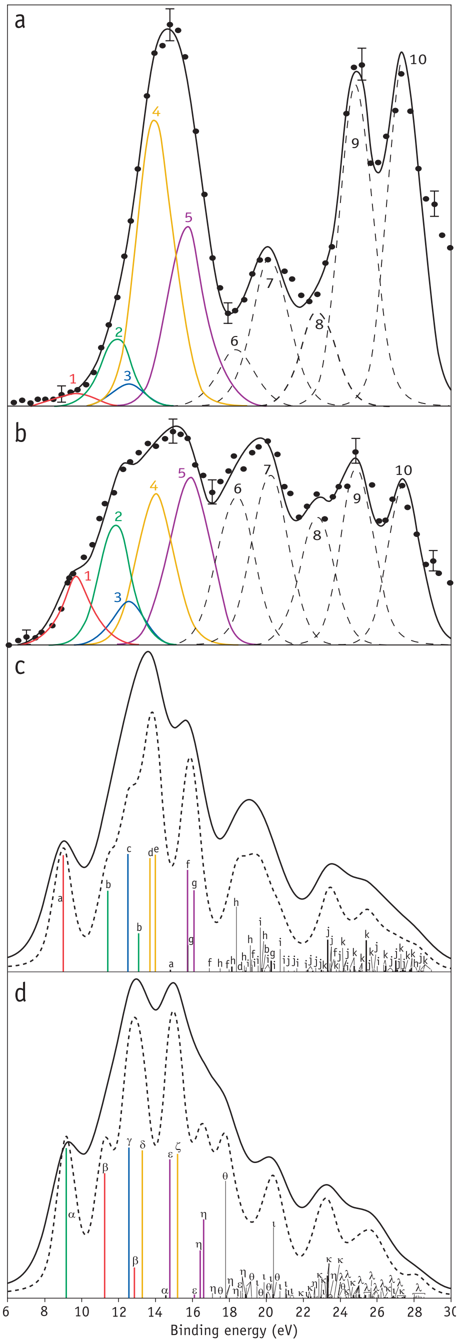

Figure 1. Comparison between experimental ionization spectra obtained through EMS measurements [52] at azimuthal angles of (a) $\phi = 0°$ and (b) $\phi = 7°$ with theoretical ADC(3)-aug-ANO spike spectra and convoluted densities of states (full lines : FWHM=2.1 eV; dotted lines : FWHM = 1.2 eV) for the s-trans (c) and gauche (d) conformational isomers of 1,3-butadiene. See tables 1 and 2 for a detailed MO labelling. Colors (red, green, blue, yellow, magenta) reflect the band assignments by Saha *et al* in [52]. See text for detailed explanations.

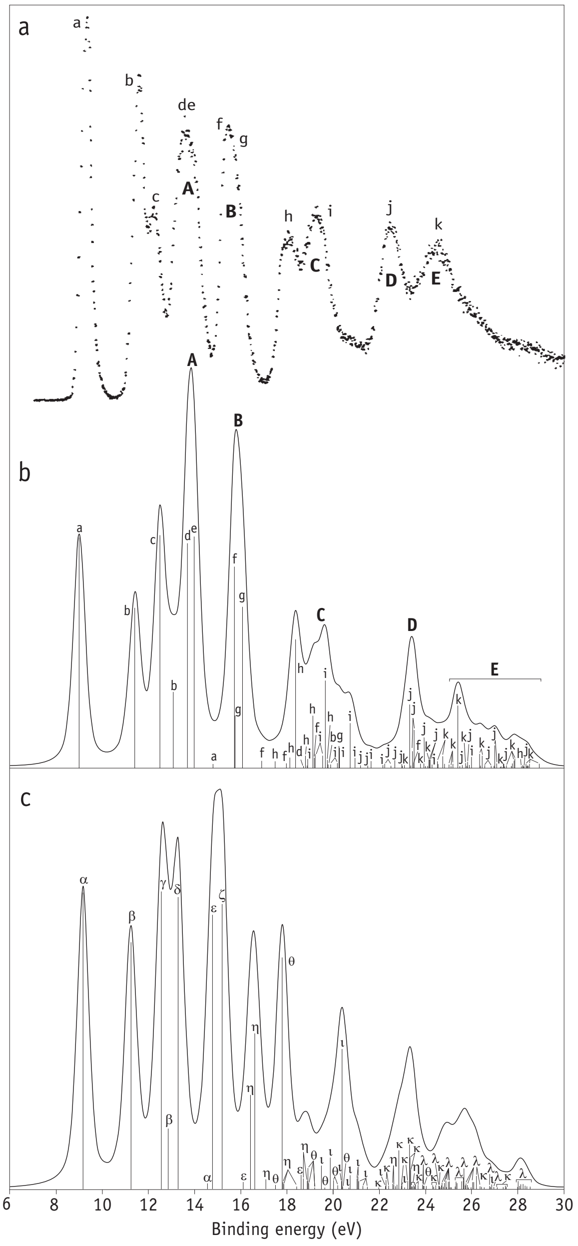

Figure 2. Comparison between (a) the experimental PES measurements at a photon energy of 80 eV as obtained by D. M. P. Holland and co-workers in ref. 25 with theoretical ADC(3)-aug-ANO spike spectra and convoluted densities of states (FWHM=0.6 eV) for the s-trans (b) and gauche (c) conformational isomers of 1,3-butadiene. See Tables 1 and 2 for a detailed MO labeling.

The reader is referred to Tables I and II for a detailed and quantitative characterization of all available theoretical data for the ionization spectrum of 1,3-butadiene with the most relevant experimental spectra. Despite differences in the employed geometries and basis sets, all ADC(3) results so far for the s-trans species indicate (Table I) that the one-electron $1a_u^{-1}$ ionization line (**b**) at ~11.4 eV possesses a rather intense satellite ($\Gamma > 0.2$) at ~13.0 eV. Similar partial breakdowns of the one-electron picture of ionization are also predicted for the $5b_u$ and $4b_u$ orbitals (**g**, **h**). At all levels, the MO picture completely breaks down when proceeding further into the inner valence region (orbitals $4a_g$, $3b_u$ and $3a_g$). For these levels (**i**, **j**, **k**), whatever the employed basis set, there is no ionized states that emerges with a pole strength larger than ~0.5 from the computed ADC(3) eigen-spectrum.

TABLE I. Theoretical and experimental characterizations of the ionization spectra of *s-trans*-1,3-butadiene (C_4H_6, C_{2h}). Binding energies are given in eV, along with the ADC(3) spectroscopic factors, which are given in parentheses. Only the ADC(3) and CI ionization lines with pole strengths larger than 0.05 are given here.

Symbol	MO	CI/DZ^{*a} (68 MOs)	ADC(3)/6-31G^{*b} (76 MOs)		ADC(3)/ANO^c (112 MOs)		ADC(3)/aug-ANO^d (154 MOs)		OVGF/aug-ANO^d (154 MOs)		OVGF/cc-pVQZ^d (400 MOs)		SAOP/TZ2P^e (150 MOs)	PES^c	EMS^f
a	$1b_g$	9.29 (0.935)	8.686	(0.891)	8.88	(0.88)	8.988	(0.833)	8.953	(0.902)	9.052	(0.902)	9.93	9.29	9.20
b	$1a_u$	12.10 (0.853)	11.160	(0.706)	11.29	(0.63)	11.402	(0.613)	11.619	(0.879)	11.670	(0.878)	12.13	11.48^g	11.50
	(S_1)	15.05 (0.064)	13.099	(0.207)	12.98	(0.27)	13.064	(0.290)^h							
							19.768	(0.013)							
c	$7a_g$	12.98 (0.881)	12.034	(0.903)	12.18	(0.89)	12.481	(0.890)	12.387	(0.900)	12.409	(0.900)	12.40	12.2^g	12.20
d	$6b_u$	14.43 (0.881)	13.374	(0.879)	13.42	(0.86)	13.688	(0.858)	13.691	(0.888)	13.723	(0.887)	13.44	13.49^g	13.40-13.90
e	$6a_g$	14.50 (0.877)	13.652	(0.897)	13.80	(0.88)	13.972	(0.885)	13.795	(0.895)	13.812	(0.893)	13.59	13.9	
f	$5a_g$	16.24 (0.821)	15.478	(0.813)	15.33	(0.79)	15.709	(0.769)	15.647	(0.860)	15.701	(0.859)	15.41	15.3^g	15.50
					19.10	(0.05)									
g	(S_2)		15.943	(0.224)	15.55	(0.28)	15.739	(0.198)^i							
	$5b_u$	16.55 (0.835)	15.634	(0.619)	15.89	(0.54)	16.065	(0.616)	15.909	(0.870)	15.965	(0.868)	15.50	15.8^g	
							20.242	(0.085)							
h	$4b_u$	19.19 (0.667)	18.245	(0.665)	17.93	(0.07)	18.358	(0.491)	···	···	18.602	(0.845)^j		18.1^g	18.10
		19.67 (0.076)	19.269	(0.108)	18.15	(0.51)	19.117	(0.197)							
			20.438	(0.064)	18.92	(0.15)									
i	$4a_g$	20.43 (0.644)	19.026	(0.057)	18.76	(0.05)	19.213	(0.051)	19.993	(0.810)^j	20.048	(0.818)^j		19.3^g	20.00
			19.475	(0.421)	19.27	(0.20)	19.649	(0.332)						20.8^{g,k}	
			19.525	(0.127)	19.35	(0.12)	20.270	(0.077)							
			19.846	(0.071)	19.54	(0.12)	20.728	(0.170)							
			20.280	(0.058)	20.13	(0.06)									
			20.888	(0.076)	20.58	(0.13)									
j	$3b_u$	24.16 (0.065)	23.390	(0.550)	22.23	(0.09)	23.307	(0.242)						22.5^g	22.60
		24.24 (0.444)	26.446	(0.050)	23.22	(0.08)	23.427	(0.063)							
		24.38 (0.098)			23.31	(0.12)	23.499	(0.144)							
					23.42	(0.17)	26.995	(0.084)							
					26.78	(0.09)									
k	$3a_g$	25.29 (0.073)	24.766	(0.058)	24.52	(0.09)	25.390	(0.235)						24.3^{g,k}	24.80
		25.54 (0.091)	25.152	(0.215)	25.18	(0.17)	26.334	(0.052)							
		26.55 (0.287)	25.744	(0.186)	25.35	(0.08)									
			27.970	(0.061)	27.78	(0.05)									

[a] G. Fronzoni *et al.* (Ref. 27).
[b] M. S. Deleuze *et al.* (Ref. 28, based on a RHF/6-31G* geometry).
[c] D. M. P. Holland *et al.* (Ref. 25 calculations based on experimental geometries).
[d] Present work, based on a B3LYP/TZVP geometry.
[e] S. Saha *et al.* (Ref. 58, based on a B3LYP/TZVP geometry).
[f] M. J. Brunger *et al.* (Ref. 52, fitted values according to the PES data of G. Bieri and L. Åsbrink, in Ref. 23).
[g] Approximate values (see discussion by Holland *et al.* in Ref. 25).
[h] Dominant electronic configuration: $1b_g^{-2}\ 2a_u^{+1}$ [HOMO^{-2} $(\text{LUMO}+5)^{+1}$].
[i] Dominant electronic configuration: $1b_g^{-1}\ 7a_g^{-1}\ 2a_u^{+1}$ [HOMO^{-1} $(\text{HOMO}-2)^{-1}$ $(\text{LUMO}+5)^{+1}$].
[j] Indicative of breakdown of the MO picture of ionization at the ADC(3) level (Refs. 39 and 40).
[k] Ascribed to satellite lines (see discussion by Holland *et al.* in Ref. 25).

A comparison of OVGF and ADC(3) results confirm the empirical rule [39, 40, 42, 85, 86] that OVGF pole strengths smaller than ~0.85 systematically foretell significant breakdowns of the MO picture of ionization at the ADC(3) level, in the form of a dispersion at this level of the ionization intensity over several shake-up lines with comparable strength ($\Gamma < 0.5$). It is nice to observe that the ADC(3)/aug-ANO and OVGF/aug-ANO results for one-electron ionization energies and pole strengths are in general almost identical. The OVGF/aug-ANO and OVGF/cc-pVQZ results for these lines do not differ by more than ~0.1 eV, which indicates near-completeness for the employed basis sets. Combining the ADC(3)/aug-ANO, OVGF/aug-ANO and OVGF/cc-pVQZ results for the main lines associated to the $1b_g$, $1a_u$, $7a_g$, $6b_u$, $6a_g$, $5a_g$, and $5b_u$ orbitals yield extrapolated ADC(3)/cc-pVQZ estimates of 9.09, 11.45, 12.50, 13.72, 13.99, 15.76, and 16.12 eV for the related vertical one-electron binding energies, to compare with experimental (PES) values of 9.29, 11.48, 12.2, 13.5, 13.9, 15.3, and 15.8 eV [25], respectively (averaged and maximal discrepancies between theory and experiment : ~0.2 and ~0.5 eV, respectively). In contrast, averaged and maximal discrepancies of ~0.3 and ~0.7 eV are noticed with estimates [58] of ionization energies derived from DFT calculations of Kohn-Sham orbital energies using the so-called SAOP model (Statistical Average of Orbital Potentials [87]). The latter approach is by construction obviously not suited for treating ionization bands subject to strong shake-up contaminations.

In contrast, our ADC(3) calculations for the s-trans conformer of 1,3-butadiene enable insights through third- and first-order in correlation, thus in practice within ~0.2 and ~0.7 eV accuracies, into the one-electron and 2h-1p shake-up ionization energies that can be experimentally inferred up to ~25 eV for 1,3-butadiene, respectively. The CI calculations by Fronzoni *et al* [27] were performed using a limited polarized double zeta basis set (68 MOs only), and were restricted to a description of the cationic wavefunction through expansions over single excited states. This amounts to a treatment of one- and 2h-1p ionized states through first-order only in correlation. Unsurprisingly therefore, the accuracy of these early CI calculations was extremely limited.

TABLE II. Present theoretical ionization spectra of *gauche*-1,3-butadiene (C_4H_6, C_2). Binding energies are given in eV, along with the ADC(3) and OVGF spectroscopic factors, which are given in parentheses (results obtained using the B3LYP/TZVP geometry). Only the ADC(3) ionization lines with pole strengths larger than 0.05 are given here.

Symbol	MO	ADC(3)/aug-ANO (154 MOs)		OVGF/cc-pVQZ (400 MOs)	
α	8*a*	9.146	(0.886)	9.198	(0.904)
β	7*b*	11.228	(0.738)	11.436	(0.891)
		12.857	(0.182)[a]		
γ	7*a*	12.546	(0.891)	12.455	(0.900)
δ	6*b*	13.269	(0.872)	13.223	(0.900)
ε	5*b*	14.767	(0.821)	14.777	(0.877)
ζ	6*a*	15.196	(0.854)	15.075	(0.885)
η	5*a*	16.430	(0.282)		
		16.609	(0.462)	16.549	(0.852)
θ	4*b*	17.790	(0.690)	17.993	(0.856)
		18.906	(0.064)		
ι	4*a*	19.492	(0.071)		
		19.876	(0.094)		
		20.387	(0.418)	20.456	(0.813)[b]
κ	3*b*	22.847	(0.117)		
		23.312	(0.134)		
		23.337	(0.094)		
		23.356	(0.057)		
λ	3*a*	25.674	(0.061)		

[a] Dominant electronic configurations: $8a^{-2}$ $10b^{+1}$ and $8a^{-2}$ $11b^{+1}$ [$HOMO^{-2}$ $(LUMO+5)^{+1}$ and $HOMO^{-2}$ $(LUMO+6)^{+1}$].

[b] Indicative of a breakdown of the MO picture of ionization at the ADC(3) level (Refs. 39 and 40).

Prior to accurately calculating the spherically averaged electron momentum distributions (MDs) of 1,3-butadiene, it is worth reconsidering the combinations of molecular orbitals that Saha *et al* have employed in their analysis [58] under the light of the newly computed ADC(3) ionization spectra. In their work (see Figure 5 of [58]), they compared the electron MD inferred from an angular analysis of the (e, 2e) ionization intensity recovered at 9.20 eV from the gaussian band **1** in Figures 1a and b with the KS orbital MDs calculated for the $1b_g$ (**a**) and 7b (**β**) levels of the s-trans and gauche conformational isomers, respectively. For the sake of clarity and reader's comfort, these bands and lines are displayed in red in Figure 1. Similarly, the experimental electron MD for band **2** at 11.5 eV (in green in Figure 1) was compared with model KS orbital MDs for the s-trans $1a_u$ (**b**) and gauche 8a (**α**) orbitals. According to the conclusions by Saha *et al*, the electron momentum distribution experimentally inferred from band **2** at 11.5 eV is "engaged" with the highest occupied molecular orbital (8a, **α**) of the gauche conformer. Note that the ADC(3)/aug-ANO ionization energy calculated for this orbital amounts to 9.1 eV. This implies that in their analysis of (e, 2e) cross sections *at 11.5 eV*, Saha *et al* neglected the fact that the (8a, **α**) orbital of this gauche conformer contributes to the ionization intensity recovered for another channel, i.e. under band **1** *at 9.2 eV*! Inversely, the outermost ionization band (**1**) at 9.2 eV was, according to Figure 5 in [58], erroneously ascribed to a one-electron ionization line ($7b^{-1}$, **β**) at an electron binding energy of 11.2 eV in the ADC(3)/aug-ANO ionization spectrum for the gauche conformer. Very unambiguously, the combinations of orbital ionization intensities that Saha *et al* have proposed for the two outermost bands in the (e, 2e) measurements are inconsistent with the corresponding ionization energies, in view of an expected accuracy of ~0.2 eV [see also ref. 88] on our best theoretical ADC(3)/aug-ANO or OVGF/cc-pVQZ estimates for vertical one-electron binding energies. Note also that the energy interval (2.4 eV) between the centroids of these two gaussian bands exceeds by 0.8 eV the energy resolution (1.6 eV) reported in [58]. It would therefore be incorrect to invoke this low energy resolution for justifying relationships between bands **1** and **2** in Figures 1a and b with the 7b (**β**) and 7a (**α**) orbitals of the gauche conformer, respectively.

Similar considerations apply for the analysis proposed in [58] for the azimuthal angular dependence of the (e, 2e) ionization intensities recovered (Figure 1) under bands **4** and **5** at electron binding energies of 13.4 and 13.9 eV, respectively. The experimental MD inferred for band **4** (in yellow) has been ascribed to the s-trans $6b_u$ (**d**) and $6a_g$ (**e**) orbitals and to the gauche 6b (**δ**) and 6a (**ζ**) orbitals. The latter orbital leads to a one-electron ionization line at 15.2 eV, implying that the assignment proposed for this orbital by Saha *et al* was in error by 1.3 eV. Inversely, the ionization lines originating from the s-trans $5a_g$ (**f**) and $5b_u$ (**g**) orbitals and from the gauche 5b (**ε**) and 5a (**η**) orbitals were ascribed to band **5** (in magenta) at 15.50 eV. According to the ADC(3)/aug-ANO results of Table II, the 5a (**η**) orbital yields essentially two ionization lines at 16.4 eV (Γ=0.28) and 16.6 eV (Γ=0.46).

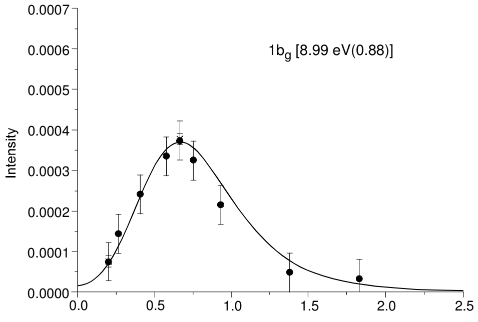

Figure 3. ADC(3)/aug-ANO Dyson orbital analysis of the angular dependence of the (e, 2e) ionization intensity recovered under band **1** at 9.2 eV in Figures 1a and b.

B. Electron momentum distributions

In view of the computed ADC(3)/aug-ANO and OVGF/cc-pVQZ spectra and expected conformer weights at ambient temperatures, we suggest to ignore contributions from the gauche conformer and compare in the present work (Figures 3 - 8) the experimentally inferred electron momentum distributions for bands **1** - **5** with spherically averaged electron momentum distributions derived from the ADC(3)/aug-ANO Dyson orbitals associated to the following sets of lines in the ionization spectrum of the s-trans conformer : (1) $1b_g^{-1}$ (at 8.99 eV [Γ=0.88]); (2) $1a_u^{-1}$ (at 11.4 eV [Γ=0.61]); (3) $7a_g^{-1}$ (at 12.48 eV [Γ=0.89]); (4) S_1 (at 13.06 eV [Γ=0.29]) + $6b_u^{-1}$ (at 13.69 eV [Γ=0.86]) + $6a_g^{-1}$ (at 13.97 eV [Γ=0.89]) and (5) $5a_g^{-1}$ (at 15.71 eV [Γ=0.77]) + $5b_u^{-1}$ (at 16.07 eV [Γ=0.62] + S_2 (at 15.74 eV [Γ=0.20]). Here, S_1 and S_2 refer to the two outermost shake-up lines with $\Gamma > 0.1$ (see Table I for a more detailed MO analysis).

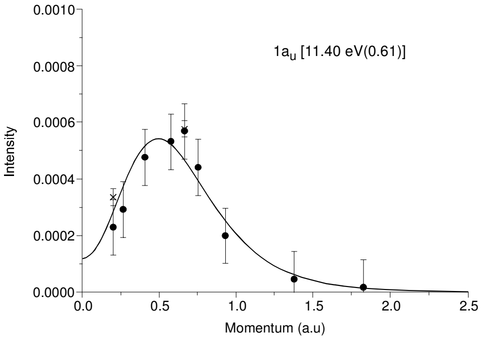

Figure 4. ADC(3)/aug-ANO Dyson orbital analysis of the angular dependence of the (e, 2e) ionization intensity recovered under band **2** at 11.5 eV in Figures. 1a and b.

Theoretical intensities have been renormalized onto the experimental ones according to the scale numbers provided in Table III. Upon inspecting this table, it is rather immediately apparent that these rescaling numbers tend to regularly decrease with increasing electron binding energies, which may first suggest that the weak-coupling approximation breaks down since, in sharp contrast with many EMS studies, band intensities do apparently not simply correlate on an absolute scale with the computed pole strengths. In our opinion, this may also more simply reflect some rather systematic experimental artefacts, such as for instance continuous and uncontrolled variations of the flux of the molecular targets or impinging electron beam currents. In support to our assertion, we refer to a fully quantitative ADC(3) Dyson orbital study [70] of better-resolved EMS measurements on a fairly pathological compound with regards to ground state correlation, namely CH_2F_2. The interested reader is also referred to some citations in a work [89] by Brunger *et al.* describing improvements made in the late nineties on the gas phase (e, 2e) apparatus at Flinders University in order to operate at higher target beam densities and achieve higher (e, 2e) count rates. Note that the original experiment on 1,3-butadiene [52] on which the present work focuses was apparently performed without resorting to these techniques and to the binning mode required [89] for "averaging non-uniform response of particle detectors and ensuring that the measured electron–binding energy spectra are free from any possible unwanted instrumental effect". Clearly, new EMS experiments on 1,3-butadiene would be very much welcome.

TABLE III. Scale number used to optimize the fits between the computed ADC(3)/aug-ANO Dyson orbital momentum distributions and the experimental ones.

Band	Line assignment (pole strengths in bracket)	Scale number
1	$1b_g$	280
2	$1a_u$	200
3	$7a_g$	280
2+3	$1a_u$[11.40 eV(0.61)]+$7a_g$[12.48 eV(0.89)]	220
4	$6b_u$[13.69 eV(0.86)]+$6a_g$[13.97 eV(0.89)]	176
	S_1[13.06 eV(0.29)]+$6b_u$[13.69 eV(0.86)] +$6a_g$[13.97 eV(0.89)]	160
5	$5a_g$[15.71 eV(0.77)]+$5b_u$[16.07 eV(0.62)] +S_2[15.74 eV(0.20)]	135
	$5a_g$[15.71 eV(0.77)]+$5b_u$[16.07 eV(0.62)]	120

Despite these experimental uncertainties, it cannot be denied that, on relative intensity scales, the computed electron momentum distributions provide accurate and consistent insights into *all* available experimental distributions, and this most generally well within the reported relative error bars on (e, 2e) ionization intensities. This observation in turn provides support to the hypothesis that the gauche conformational isomer of 1,3-butadiene has a very limited weight in the conformational mixture that normally characterizes 1,3-butadiene. Greatly improved statistics on ionization intensities will be necessary for unambiguously identifying this conformer as a very minor component from gas phase (e, 2e) or photoelectron experiments on 1,3-butadiene. At present, in any case, in view of the computed ADC(3) ionization energies and relative electron momentum distributions, the final conclusion by Saha *et al.* regarding relationships ("engagement") of four (e, 2e) ionization channels with the gauche conformer has to be called into question.

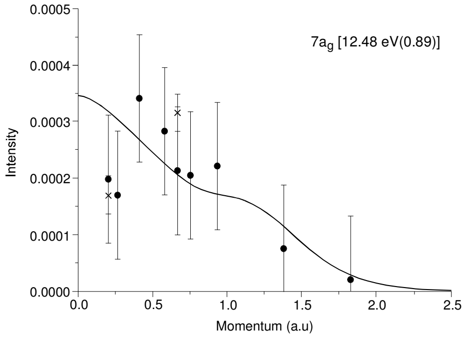

Figure 5. ADC(3)/aug-ANO Dyson orbital analysis of the angular dependence of the (e, 2e) ionization intensity recovered under band **3** at 12.2 eV in Figures. 1a and b.

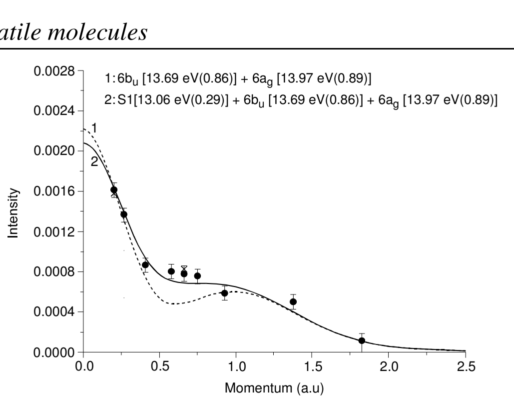

Figure 6. ADC(3)/aug-ANO Dyson orbital analysis of the angular dependence of the (e, 2e) ionization intensity recovered under band **4** at 13.4 eV (or 13.9 eV) in Figures 1a and b.

In the original work by Brunger *et al* [52], analysis of the angular dependence of the (e, 2e) intensities for band **4** at 13.40 eV led to fairly unsuccessfull speculations about some admixture from an extra 35% $1b_g$ contribution into the measured ($6b_u$ and $6a_g$) flux, a scenario which the present OVGF and ADC(3) results refute, in view of pole strengths larger than 0.90 and 0.83 for the outermost one-electron ionization line (Table I), respectively. Note that in [58], accounting for the cis-form of 1,3-butadiene did also not improve, even qualitatively, the agreement with the electron momentum distribution experimentally inferred for band **4**. Without the S_1 line, and in agreement with the empirical B3LYP/TZVP Kohn-Sham orbital calculations by Saha *et al.* [58], a clearly apparent but spurious minimum in (e, 2e) ionization intensity is observed at p~0.6 a.u (Figure 6). On the other hand, we wish to note that taking into account the contribution of the $\pi^{-2}\,\pi^{*+1}$ (S_1) shake-up line at 13.06 eV in the ionization spectrum of the s-trans conformer considerably improves (Figure 6) the quality of the prediction made for the electron distribution recovered from band **4**. On a relative intensity scale, the agreement with experiment is then almost perfect.

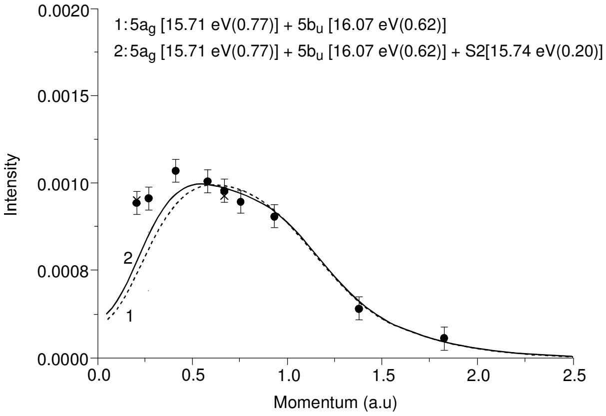

Figure 7. ADC(3)/aug-ANO Dyson orbital analysis of the angular dependence of the (e, 2e) ionization intensity recovered under band **5** at 15.5 eV in Figures 1a and b.

The S_1 line derives from a *p*-type orbital ($1a_u$) and contributes to an energy region where a *s*-type orbital ($6a_g$) dominates; it is thus expected to significantly alter the shape of the electron momentum distributions associated to that region. In contrast, the S_2 shake-up line at 15.74 eV has no significant influence on the electron momentum distribution calculated for band **5** at 15.5 eV. This satellite lies in the vicinity of the main $5b_u^{-1}$ line at 16.1 eV to which it relates, and cannot lead therefore to significant alterations of (convoluted) band intensities.

We also wish to note that the analysis of band **3** (in blue) in Figures 1a and b is rather problematic, in view of the limited energy resolution (1.6 eV) achieved in the original EMS investigation by Brunger *et al.* [52]. Very clearly, this band is totally embedded in band **2** (in green), thus band **3** at 12.2 eV can hardly be non-ambiguously ascribed to the $7a_g$ (**c**) orbital of the s-trans conformer, as was proposed in [52], and to the 7a (**γ**) orbital of the gauche conformer, as further suggested in the work by Saha *et al*. Following the guidelines by Brunger *et al* in their pioneering analysis [52], we have nonetheless been willing to individually ascribe (Figure 5) band **3** to the ionization line derived from orbital $7a_g$. Although the experimental trends for this band are, all in all, qualitatively correctly described by theory, it is rather clear that error bars on (e, 2e) intensities are in this case too large to enable a definite assignment. Therefore, in line with our remarks in [90] upon the limitations of analyses of the (e, 2e) intensities related to very strongly overlapping bands, we prefer to compare (Figure 8) summed electron momentum distributions for bands **2** and **3** with spherically averaged Dyson orbital electron momentum distributions calculated for the $1a_u$ and $7a_g$ set of one-electron ionization lines at 11.4 and 12.5 eV, respectively. This comparison is overall also very satisfactory.

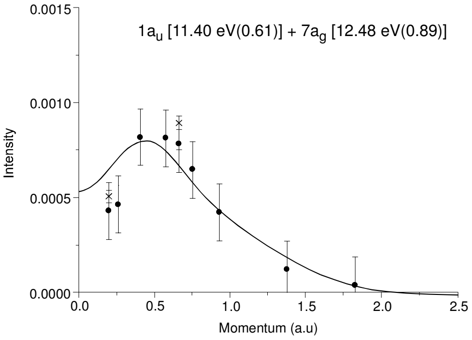

Figure 8. ADC(3)/aug-ANO Dyson orbital analysis of the angular dependence of the (e, 2e) ionization intensity recovered under bands **2** and **3** at 11.5 eV and 12.2 eV in Figures 1a and b.

4.1.5 Conclusions

One-particle Green's Function theory has been employed to analyze (e, 2e) measurements in the gas phase at high impact electron energies, and under non-coplanar symmetric kinematics, on a conjugated and structurally versatile molecule, namely 1,3-butadiene. This comparison is based on thorough calculations of the vertical ionization spectra of the s-trans and gauche conformational isomers using the benchmark ADC(3) scheme, as well as spherically averaged electron momentum distributions derived from the related Dyson orbitals, upon the assumption that the Born, binary-encounter and plane-wave impulse approximations (PWIA) are valid. For these ADC(3) calculations, use has been made of the fairly large [154 MOs] Roos' augmented double-ζ atomic natural orbital basis set. These calculations quantitatively confirm the trends observed in previous ADC(3) studies employing smaller basis sets. In addition, we present highly quantitative calculations (~0.2 accuracy) of one-electron binding energies employing the Outer Valence Green's Function (OVGF) scheme and

Dunning's correlation consistent polarized valence basis set of quadruple-zeta quality (cc-pVQZ, 400 MOs).

Comparison of the newly computed ADC(3) and OVGF ionization spectra with the results of the original (e, 2e) experiment by Brunger *et al.* [52] reconcile thermodynamics with electronic structure theory and, more specifically, Electron Momentum Spectroscopy (EMS). We call into question the conclusions drawn by Saha *et al.* [58] regarding the presence of fingerprints of the gauche conformer in the experimentally inferred electron momentum distributions of 1,3-butadiene, and ascribe specifically these conclusions to an improper description of the conformational dependence of ionization energies and an incorrect assignment of ionization bands. Further drawbacks in the analysis by Saha *et al.* [58] stem from the limitations of the fitting procedure used to extract experimental ionization potentials from (e, 2e) ionization spectra in congested valence bands and from the inadequacy of standard Kohn-Sham orbitals to correctly describe ionization potentials and possibly Dyson orbitals [70].

Because of a gauche versus s-trans energy (enthalpy) difference of ~2.9 kcal/mol, the high-lying cis-conformer has a very limited weight under standard temperatures (5 %), and is normally hardly visible in most electronic spectra. In our opinion, there is no ionization experiment so far on 1,3-butadiene which provides clear and irrefutable indications for the presence of this high-energy lying conformer in the gas-phase. On the contrary, our ADC(3) and OVGF calculations on the trans-form alone are amply sufficient to quantitatively unravel all one-electron and shake-up ionization bands, within ~0.2 and ~0.7 eV accuracy, respectively, in high-resolution photoelectron measurements employing a synchrotron radiation beam and a photon energy of 80 eV [25]. Similarly, all available EMS momentum distributions can on relative intensity scales be quantitatively reproduced using our ADC(3) Dyson orbitals for the s-trans conformer alone, on the basis of a partitioning of the (e, 2e) ionization intensity which is consistent with the computed ADC(3) ionization energies and pole strengths. A rather clear example is that of a band (**4**) at 13.40 eV, which partly relates to an intense (Γ=0.29) π^{-2} π^{*+1} shake-up line at ~13.1 eV that belongs to the $1a_u$ manifold. In contrast, the main features characterizing the theoretical ionization spectrum for the gauche conformer are clearly incompatible with the results of high-resolution photoelectron experiments.

To conclude, besides recommending ADC(3) for quantitatively deciphering ionization spectra, we advocate a systematic use of ADC(3) Dyson orbitals in analyses of the angular dependence of (e, 2e) ionization intensities in EMS experiments, in order to safely identify complications such as vibronic coupling interactions, an alteration of the molecular conformation, or a dispersion of (e, 2e) ionization intensities into shake-up processes. Whatever the correlations that prevail between the molecular orbitals of different conformers, it is clearly impossible to correctly investigate by means of EMS the electronic wavefunction of structurally flexible molecules, without first correctly identifying the influence of the molecular conformation on ionization energies. On the other hand, if the publication of mistakes should certainly not be encouraged, the present refutation of the analysis by Saha *et al* [58] on 1,3-butadiene also confirms the potential of EMS as a conformational probe [56] and for studying in details the relationships that prevail between the molecular orbitals and ionization spectra of such molecules, provided the temperature at which the (e, 2e) reactions occur in vacuum is known accurately enough [56]. The present benchmark theoretical study therefore strongly motivates further EMS experiments on 1,3-butadiene by means of (e, 2e) spectrometers with improved energy resolution and employing supersonic molecular beams with carefully monitored fluxes.

References

[1] Engeln, R.; Consalvo, D.; Reuss, J. *Chem. Phys.* 1992, 160, 427.

[2] Murcko, M. A.; Castejon, H.; Wiberg, K. B. *J. Phys. Chem.* 1996, 100, 16162.

[3] De Maré, G. R.; Pachenko, Y. N.; Vander Auwera, J. *J. Phys. Chem. A* 1997, 101, 3998.

[4] Choi, C. H.; Kertesz, M.; Karpfen, A. *Chem. Phys. Lett.* 1997, 276, 266.

[5] Karpfen, A.; Choi, C. H.; Kertesz, M. *J. Phys. Chem. A* 1997, 101, 7426.

[6] Denent, M. L. *J. Molec. Spectrosc.* 1998, 191, 265.

[7] Choi, C. H.; Kertesz, M.; Dobrin, S.; Michl, J. *Theor. Chem. Acc.* 1999, 102, 196.

[8] Sancho-Garcia, J. C.; Pérez-Jiménez, A. J.; Pérez-Jordá, J. M.; Moscardó, F. *Mol. Phys.* 2001, 99, 47.

[9] Saltiel, J.; Sears, D. F., Jr.; Turek, A. M. *J. Phys. Chem. A* 2001, 105, 7569.

[10] Sancho-Garcia, J. C.; Pérez-Jiménez, A.; Moscardó, F. *J. Phys. Chem. A* 2001, 105, 11541.

[11] Karpfen, A.; Parasuk, V. *Mol. Phys.* 2004, 102, 819.

[12] Peterson, K. A.; Kendall, R. A.; Dunning, T. H., Jr. *J. Chem. Phys.* 1993, 93, 1930.

[13] Saltiel, J.; Sear, D. F., Jr.; Turek, A. M. *J. Phys. Chem. A* 2001, 105, 7569.

[14] Gilbert, R. G.; Smith, S. C. *Theory of Unimolecular and Recombination Reactions*; Blackwell Scientific Publications: Oxford, 1990.

[15] Haile, J. M. *Molecular Dynamics Simulations*; Wiley: New-York, 1997.

[16] Eland, J. H. D. *Int. J. Mass. Spectrom. Ion. Phys.* 1969, 2, 471.

[17] Turner, D. W.; Baker, C.; Baker, A. D.; Brundle, C. R. *Molecular Photoelectron Spectroscopy*; Wiley: London, 1970.

[18] Brundle, C. R.; Robin, M. B. *J. Am. Chem. Soc.* 1970, 92, 5550.

[19] Beez, M.; Bieri, G.; Bock, H.; Heilbronner, E. *Helv. Chim. Acta* 1973, 56, 1028.

[20] White, R. M.; Carlson, T. A.; Spears, D. P. *J. Electron Spectrosc. Relat. Phenom.* 1974, 3, 59.

[21] Kimura, K.; Katsumata, S.; Achiba, Y.; Yamazaki, T.; Iwata, S. *Handbook of He I Photoelectron Spectra of Fundamental Organic Molecules*; Japan Scientific Societies Press: Tokyo, 1981.

[22] Streets, D. G.; Potts, A. W. *J. Chem. Soc. Faraday Trans. II* 1974, 70, 1505.

[23] Bieri, G.; Åsbrink, L. *J. Electron Spectrosc. Relat. Phenom.* 1980, 20, 149.

[24] Keane, M. P.; Naves de Brito, A.; Correia, N.; Svensson, S.; Karlsson, L.; Wannberg, B.; Gelius, U.; Lunell, S.; Salaneck, W. R.; Lögdlund, M.; Swanson, D. B.; MacDiarmid, A. G. *Phys. Rev. B* 1992, 45, 6390.

[25] Holland, D. M. P.; MacDonald, M. A.; Hayes, M. A.; Baltzer, P.; Wannberg, B.; Lundqvist, M.; Karlsson, L.; von Niessen, W. *J. Phys. B* 1996, 29, 3091.

[26] Cederbaum, L. S.; Domcke, W.; Schirmer, J.; von Niessen, W.; Diercksen, G. H. F.; Kraemer, W. P. *J. Chem. Phys.* 1978, 69, 1591.

[27] Fronzoni, G.; Decleva, P.; Lisini, A.; de Alti, G. *J. Electron Spectr. Relat. Phenom.* 1994, 69, 207.

[28] Deleuze, M. S.; Cederbaum, L. S. *Int. J. Quantum Chem.* 1997, 63, 465.

[29] Schirmer, J.; Cederbaum, L. S.; Walter, O. *Phys. Rev. A* 1983, 28, 1237.

[30] von Niessen, W.; Schirmer, J.; Cederbaum, L. S. *Comput. Phys. Rep.* 1984, 1, 57.

[31] Schirmer, J.; Angonoa, G. *J. Chem. Phys.* 1989, 91, 1754.

[32] Weikert, H.-G.; Meyer, H.-D.; Cederbaum, L. S.; Tarantelli, F. *J. Chem. Phys.* 1996, 104, 7122.

[33] Deleuze, M. S.; Giuffreda, M. G.; François, J.-P.; Cederbaum, L. S. *J. Chem. Phys.* 1999, 111, 5851.

[34] Cederbaum, L. S.; Domcke, W.; Schirmer, J.; von Niessen, W. *Adv. Chem. Phys.* 1986, 65, 115.

[35] Deleuze, M. S.; Cederbaum, L. S. *Adv. Quantum. Chem.* 1999, 35, 77.

[36] Deleuze, M. S.; Giuffreda, M. G.; François, J.-P.; Cederbaum, L. S. *J. Chem. Phys.* 2000, 112, 5325.

[37] Deleuze, M. S.; Giuffreda, M. G.; François, J.-P. *J. Phys. Chem. A* 2002, 106, 5626.

[38] Deleuze, M. S.; Trofimov, A. B.; Cederbaum, L. S. *J. Chem. Phys.* 2001, 115, 5859.

[39] Deleuze, M. S. *J. Chem. Phys.* 2002, 116, 7012.

[40] Deleuze, M. S. *J. Phys. Chem. A* 2004, 108, 9244.

[41] Potts, A. W.; Holland, D. M. P.; Trofimov, A. B.; Schirmer, J.; Karlsson, L.; Siegbahn, K. *J. Phys. B: At. Mol. Opt. Phys.* 2003, 36, 3129.

[42] Kishimoto, N.; Hagihara, Y.; Ohno, K.; Knippenberg, S.; François, J.-P.; Deleuze, M. S. *J. Phys. Chem. A* 2005, 109, 10535.

[43] Potts, A. W.; Edvardson, D.; Karlsson, L.; Holland, D. M. P.; MacDonald, M. A.; Hayes, M. A.; Maripuu, R.; Siegbahn, K.; von Niessen, W. *Chem. Phys.* 2000, 254, 385.

[44] Trofimov, A. B.; Schirmer, J.; Holland, D. M. P.; Karlsson, L.; Maripuu, R.; Siegbahn, K.; Potts, A. W. *Chem. Phys.* 2001, 263, 167.

[45] Potts, A. W.; Trofimov, A. B.; Schirmer, J.; Holland, D. M. P.; Karlsson, L. *Chem. Phys.* 2001, 271, 337.

[46] Trofimov, A. B.; Schirmer, J.; Holland, D. M. P.; Potts, A. W.; Karlsson, L.; Maripuu, R.; Siegbahn, K. *J. Phys. B* 2002, 35, 5051.

[47] Doering, J. P.; McDiarmid, R. *J. Chem. Phys.* 1980, 73, 3617.

[48] Mallard, W. G.; Miller, J. H.; Smyth, K. C. *J. Chem. Phys.* 1983, 79, 5900.

[49] Sodhi, R. N. S.; Brion, C. E. *J. Electron Spectroscoc. Relat. Phenom.* 1985, 37, 1.

[50] McLaren, R.; Clark, S.A.C.; Ishii, I.; Hitchcock, A. P. *Phys. Rev. A* 1987, 36, 1683.

[51] Fahr, A.; Nayak, A. K. *Chem. Phys.* 1994, 189, 725.

[52] Brunger, M. J.; Winkler, D. A.; Michalewicz, M. T.; Weigold, E. *J. Chem. Phys.* 1998, 108, 1859.

[53] McCarthy, I. E.; Weigold, E. *Rep. Prog. Phys.* 1991, 54, 789.

[54] Coplan, M. A.; Moore, J. H.; Doering, J. P. *Rev. Mod. Phys.* 1994, 66, 985.

[55] Weigold, E.; McCarthy, I. E. *Electron Momentum Spectroscopy*; Kluwer Academic Plenum Publishers: New York, 1999.

[56] Deleuze, M. S.; Pang, W. N.; Salam, A.; Shang, R. C. *J. Am. Chem. Soc.* 2001, 123, 4049.

[57] Pang, W. N.; Gao, J. F.; Ruan, C. J.; Shang, R. C.; Trofimov, A. B.; Deleuze, M. S. *J. Chem. Phys.* 2000, 112, 8043.

[58] Saha, S.; Wang, F.; Falzon, C. T.; Brunger, M. J. *J. Chem. Phys.* 2005, 123, 124315.

[59] Knippenberg, S.; Deleuze, M. S.; Cleij, T. J.; François, J.-P.; Cederbaum, L. S.; Eland, J. H. D. *J. Phys. Chem. A* 2005, 109, 4267.

[60] Tobita, S.; Leach, S.; Jochims, H. W.; Rühl, E.; Illenberger, E.; Baumgärtel, H. *Can. J. Phys.* 2004, 72, 1060.

[61] Neville, J. J.; Zheng, Y.; Brion, C. E. *J. Am. Chem. Soc.* 1996, 118, 10533.

[62] Neville, J. J.; Zheng, Y.; Hollebone, B. P.; Cann, N. M.; Brion, C. E.; Kim, C. K.; Wolfe, S. *Can. J. Phys.* 1996, 74, 773.

[63] Cederbaum, L. S.; Domcke, W. *Adv. Chem. Phys.* 1977, 36, 205.

[64] Ortiz, J. V. in *Computational Chemistry: Reviews of Current Trends*; Lezczyinski, J., ed.; World Scientific: Singapore, 1997; Vol. 2, p. 1.

[65] Mc Weeny, R.; Pickup, B. T. *Rep. Progr. Phys.* 1980, 43, 1065.

[66] Őhrn, Y.; Born, G. *Adv. Quantum Chem.* 1981, 13, 1.

[67] Pickup, B.T. *Chem. Phys.* 1977, 19, 193.

[68] Deleuze, M.; Pickup, B. T.; Delhalle, J. *Mol. Phys.* 1994, 83, 655.

[69] Seabra, G. M.; Kaplan, I. G.; Zakrzewski, V. G.; Ortiz, J. V. *J. Chem. Phys.* 2004, 121, 4142.

[70] Ning, C. G.; Ren, X. G.; Deng, J. K.; Su, G. L.; Zhang, S. F.; Knippenberg, S.; Deleuze, M. S. *Chem. Phys. Lett.* 2006, 421, 52.

[71] Dunning, T. H., Jr. *J. Chem. Phys.* 1971, 55, 716.

[72] (a) Becke, A. D. *J. Chem. Phys.* 1993, 98, 5648; (b) Lee, C.; Yang, W.; Parr, R. G. *Phys. Rev. B* 1988, 37, 785.

[73] Deleuze, M. S.; Giuffreda, M. G.; Francois, J.-P. *J. Phys. Chem. A* 2002, 106, 5626.

[74] Martin, J. M. L.; El-Yazal, J.; François, J.-P. *Mol. Phys.* 1995, 86, 1437.

[75] Schmidt, M. W.; Baldridge, K. K.; Jensen, J. H.; Koseki, S.; Gordon, M. S.; Nguyen, K. A.; Windus, T. L.; Elbert, S. T. *QCPE Bull.* 1990, 10, 52.

[76] Ruhe, A. *Math. Comput.* 1979, 33, 680.

[77] Meyer, H.-D.; Pal, S. *J. Chem. Phys.* 1989, 91, 6195.

[78] Liu, B. *Numerical Algorithms in Chemistry, Algebraic Methods*; LBL-8158, Lawrence Berkely Laboratory.

[79] Tarantelli, F.; Sgamellotti, A.; Cederbaum, L. S.; Schirmer, J. *J. Chem. Phys.* 1987, 86, 2201.

[80] Widmark, P. O.; Malmqvist, P. A.; Roos, B. O. *Theor. Chim. Acta* 1990, 77, 291.

[81] Dunning, T. H., Jr. *J. Chem. Phys.* 1989, 90, 1007.

[82] Frisch, M. J.; Trucks, G.W.; Schlegel, H.B, *et al.* Gaussian98, revision A.7; Gaussian Inc, Pittsburg, PA 1998.

[83] Hollebone, B. P.; Neville, J. J.; Zheng, Y.; Brion, C. E.; Wang, Y.; Davidson, E. R. *Chem. Phys.* 1995, 196, 13.

[84] Migdall, J. N.; Coplan, M. A.; Hench, D. S.; Moore, J. H.; Tossell, J. A.; Smith, V. H., Jr.; Liu, J. W. *Chem. Phys.* 1981, 57, 141.

[85] Knippenberg, S.; Nixon, K. L.; Mackenzie-Ross, H.; Brunger, M. J.; Wang, F.; Deleuze, M. S.; François, J.-P.; Winkler, D. A. *J. Phys. Chem. A* 2005, 109, 9324.

[86] Knippenberg, S.; Nixon, K. L.; Brunger, M. J.; Maddern, T.; Campbell, L.; Trout, N.; Wang, F.; Newell, W. R.; Deleuze, M. S.; François, J.-P.; Winkler, D. A. *J. Chem. Phys.* 2004, 121, 10525.

[87] Gritsenko, O. V.; Schipper, P. R. T.; Baerends, E. J. *Chem. Phys. Lett.* 1999, 302, 199.

[88] Deleuze, M. S.; Claes, L.; Kryachko, E. S.; François, J.-P. *J. Chem. Phys.* 2003, 119, 3106.

[89] Brunger, M. J.; Adcock, W. *J. Chem. Soc., Perkin Trans.* 2002, 2, 1.

[90] Knippenberg, S.; François, J.-P.; Deleuze, M. S. *J. Comp. Chem.* 2006, 27, 1703.

4.2 Imaging momentum orbital densities of conformationally versatile molecules: A benchmark theoretical study of the molecular and electronic structures of dimethoxymethane.

4.2.1 Introduction

Electron Momentum Spectroscopy (EMS) [1] has been extensively used for studying the valence electronic structure and wave function of small polyatomic molecules with typically one, two or three "heavy" (C, N, O,…) atoms [2], or larger but structurally rigid molecules of high and well-defined symmetry [3], such as benzene, sulphur hexafluoride, transition metal carbonyls ($X(CO)_6$ with X=Cr, Mo or W, fullerene, furane, pyrrole, norbornadiene, cubane, chlorotrifluoromethane, adamantane, amantadine, iso-butane, urotropine, pyridine, or norbornane. With this very sophisticated spectroscopic technique based on electron-impact ionization experiments at high kinetic energies, one can reliably infer electron momentum distributions associated to (in principle, carefully) selected ionization channels, from an analysis of the angular dependence of (e,2e) ionization intensities measured in coincidence at fixed electron binding energies. Because of the still limited energy resolution of the spectrometers (at best, ~0.6 eV) and of the difficulties inherent to assigning overcrowded ionization bands, interpretations of EMS experiments on large systems remain very challenging. In addition, the energies required by valence ionization processes are considerable, and most often larger than those involved in, for instance, chemical reactions (typically, a few eV). We note that many of the above listed compounds are cage compounds subject to pronounced cyclic strains, which may lead to severe vibrational complications and, in the most extreme cases, to ultrafast intramolecular rearrangements and Coulomb explosion processes at electron binding energies above the double ionization threshold [3p].

Sophisticated quantum mechanical treatments that cope, at least, with electron correlation and relaxation effects, as well as with the dispersion of the ionization intensity over shake-up states arising from configuration interaction effects in the cation [4] are therefore the most basic requirement for reliably assigning (e,2e) ionization spectra and conduct from these a safe analysis of experimental electron momentum distributions. A recent revision by our group of EMS measurements on a series of cage compounds demonstrates that it is indeed impossible to reliably assign highly congested (e,2e) ionization spectra by resorting only to standard Hartree-Fock or Kohn-Sham orbital energies and to the related electron densities [5]. Furthermore, most molecules of interest in chemistry exist in more than one stable conformation, which complicates further the analysis of the (e,2e) ionization spectra and intensities [6, 7]. The reader is referred in particular to a pioneering and very detailed analysis [8] by our group of EMS experiments [9, 10] upon a highly versatile molecule, namely, *n*-butane, employing statistical thermodynamics [11] at the level of the Rigid Rotor-Harmonic Oscillator (RRHO) approximation as well as one-electron Green's Function theory [12-16] (also referred to as electron propagator theory) along with the so-called third-order Algebraic Diagrammatic Construction scheme [ADC(3)] [15, 17].

When dealing with molecules containing one or several rotatable bonds, such as biomolecules, it is crucial to correctly assess the relative abundance of conformers and the influence of the molecular conformation upon the valence ionization spectrum. Otherwise, when failing to correctly assign the ionization bands and their relationships with one or several conformers, one may draw conclusions that lead, for instance, to obvious violations of elementary principles of thermodynamics and contradictions with an impressive number of spectroscopic evidences. A striking example has been recently discussed in details through a robust refutation [18] of an analysis by Saha *et al* [19] of EMS experiments on 1,3-butadiene [20]. The main purpose of the present work is to establish once and for all the guidelines that should systematically be followed for reliably interpreting the results of such measurements on conformationally versatile molecules. Note that it is cumbersome to *interpret a posteriori* EMS experiments from theoretical calculations. For the sake of credibility, we wish therefore to first *predict* in details the electron momentum distributions that should be experimentally amenable from EMS measurements upon dimethoxymethane, throughout the valence region of this compound.

Dimethoxymethane, the prototype of polyethers, represents one of the cornerstones of Molecular Mechanics and Conformational Analysis [21]. This compound has been extensively studied as a model of the acetal moiety in methyl pyranosides and of the glycosidic linkage in polysaccharides. Its potential energy surface is usually described [22, 23] in terms of four energy minima relating to the all-staggered (anti-anti or trans-trans, TT), trans-gauche (TG), gauche-gauche (G^+G^+) and gauche-gauche (G^+G^-) conformers (also referred to as rotamers; see Figure 1). The conformational behavior of dimethoxymethane is governed by dipole-dipole interactions and by the anomeric effect [22-29]. In a localized orbital picture, the latter is described as a through-space $n \rightarrow \sigma^*$ stabilizing frontier orbital interaction which tends to favor a co-planar alignment of one of the p-type electron lone pairs on oxygen atoms with the σ^* orbital of a vicinal C-O bond.

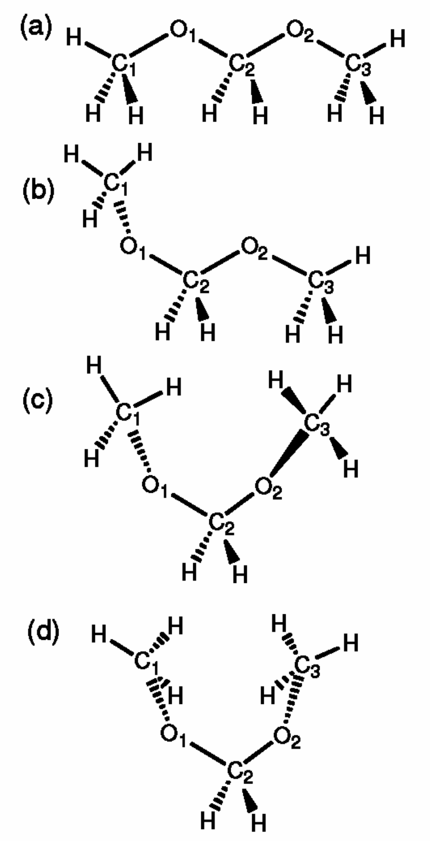

Figure 1. Geometries of the (a) TT (C_{2V} symmetry), (b) TG (C_1), (c) G^+G^+ (C_2) and (d) G^+G^- (C_s) conformers of dimethoxymethane.

Electrostatic and hyperconjugation interactions explain the overall gauche preference of substituents about C-O bonds in sugars [30, 31]. Unsurprisingly therefore, the G^+G^+ rotamer is known to be the global energy minimum form of dimethoxymethane, according to a number of experiments employing dipole moment measurements [32], electron diffraction [33], nuclear magnetic resonance [34], x-ray diffraction [35], infrared spectroscopy in argon matrices [23], or rotational spectroscopy [36]. Because of the anomeric effect, and of the usually very strong interplay between the molecular and electronic structures, dimethoxymethane could be a very ideal molecule for evaluating the so-far largely unexploited potential of Electron Momentum Spectroscopy (EMS) in experimentally "imaging" the distortions and topological changes that molecular orbitals undergo under internal rotations and variations of the molecular conformations, despite the correlation of electronic motions in many-electron systems and the fact that, even for systems containing only one electron, orbitals derived as eigenfunctions of one-electron hamiltonians do not represent true molecular observables, as very pertinently noted by Prof. Schwarz [37].

So far, experimental data about the electronic structure of dimethoxymethane are very scarce. These comprise the (He I) ultra-violet photoelectron spectrum by Jørgensen *et al* [38], and the (e,2e) ionization spectrum that Neville *et al* recorded about 10 years ago [6] at an electron impact of 1.2 keV. Note that the latter authors restricted their analysis of the related electron momentum distributions to the two outermost orbitals, presumably because accurate enough computations of the ionization spectra, relative energies and thermodynamical state functions (enthalpy, entropy, …) characterizing fairly large molecular structures with limited symmetry, or even no symmetry at all, were not achievable or even conceivable at this time. In contrast with pioneering Hartree-Fock calculations in conjunction with the standard 4-31G basis set [39], early theoretical investigations based on extended Hückel, or semi-empirical INDO or MINDO/2 calculations [40] failed to predict the correct energy minimum of dimethoxymethane, due to the inability of these schemes to describe hyperconjugation effects. The anomeric-driven G^+G^+ geometry has been thereafter confirmed at various *ab initio* levels [41, 42].

The most thorough quantum chemical studies available to date of the structures and relative energies of the various rotamers of dimethoxymethane were based on second-order Møller-Plesset calculations in conjunction with the 6-31G** basis set [22], or calculations [22, 23] employing Density Functional Theory (DFT) along with the Becke-3-parameters-Lee-Yang-Parr functional [43] and the 6-311++G** basis set. The obtained geometries are almost the same, but rather significant differences in relative energies, comprised within a range of a few kcal/mol, justify a more quantitative study of the main stationary points on the potential energy surface of DMM. Extremely accurate energy differences are indeed obviously needed for reliably evaluating, within an accuracy of a few percents, the abundances of rotamers characterized by energies that do not differ by more than ~3 kcal/mol. Relative conformer energies are thus first evaluated within the confines of nonrelativistic quantum mechanics, by means of a focal point analysis [44-47] of results obtained using *ab initio* (Hartree-Fock [48], Møller-Plesset [48, 49], Coupled Cluster [50]) methods and basis sets of improving quality. At the next step, conformer abundances at room temperature are evaluated for the gas phase from these benchmark energy differences, zero-point harmonic vibrational corrections, and from accurate Gibb's free energy corrections derived from statistical thermodynamical partition functions [11] accounting for internal hindered rotations [51]. According to these calculations, it will be found that, at room temperature, the G^+G^+ species accounts for 96% of the conformational mixture characterizing dimethoxymethane, and that the contributions from the other conformers to the measured ionization intensities is thus negligible. Therefore, in a third step, the valence one-electron and shake-up ionization spectrum of the G^+G^+ conformer alone is calculated using one-particle Green's Function [1p-GF] theory [13-16] along with the benchmark third-order algebraic diagrammatic construction [ADC(3)] scheme [15, 17]. Experimentally resolvable (e,2e) ionization bands are correspondingly identified, taking into account line broadening as well as the influence of the azimuthal angle under which the emitted electrons are collected in coincidence upon the (e,2e) intensities. At last, based on our 1p-GF/ADC(3) assignment of the ionization spectrum, accurate and spherically averaged (e,2e) electron momentum distributions at an electron impact energy of 1200 eV are computed for each resolvable bands from Dyson orbitals [52] that also readily derive from the 1p-GF/ADC(3) computations. For the sake of completeness, and to emphasize possible shortcomings of many recent theoretical analyses of EMS experiments, comparison is made with spherically averaged (e,2e) electron momentum distributions associated to Kohn-Sham orbitals deriving from DFT calculations employing the standard B3LYP functional.

4.2.2 Theory and methodology

A. Focal point analysis of energy differences

To quantitatively evaluate the relative energies and abundances, within the confines of nonrelativistic quantum mechanics, of the four known conformers of dimethoxymethane, we first analyze in detail the convergence of these energy differences upon successive and systematic improvements of the basis set and of the employed computational level. In straightforward analogy with former focal point analyses of conformational energy differences [44, 45], rotational barriers [46], or ionization energies [47], the faster convergence of the higher-order correlation corrections to the calculated energy differences is exploited in well-suited extrapolations of results obtained using CCSD(T) theory [50] (Coupled Cluster anzats including single and double electronic excitations and supplemented by a perturbative treatment of triple excitations). To be more specific, reliable estimations of CCSD(T) energy differences in the limit of an infinitely large basis set can be made by adding almost converged high-level correlation corrections, obtained at the MP3 [39], CCSD, and CCSD[T] levels with rather limited basis sets, to lower-level HF and MP2 [38] results which are calculated in conjunction with the largest basis sets, along with suited extrapolation procedures. The employed basis sets comprise the standard Pople's basis sets, namely STO-3G, 6-31G, 6-31G*, 6-31G**, 6-311G**, Dunning's correlation consistent polarized valence basis sets of double-, triple- and quadruple-zeta quality, designated as cc-pVXZ, with X = D, (T, [Q]) respectively [53], as well as an augmented version of the latter basis sets including a set of *s,p,*(*d*[*f*]) and *s,p,d,*(*f*[*g*]) diffuse functions on hydrogens, and carbons or oxygens, respectively [54a]. With the largest employed basis set (aug-cc-pVQZ), 768 basis functions were included in the calculations performed on each rotamers of dimethoxymethane. Depending on the symmetry point group, the MP3 calculations performed with this basis set required runs of 72 up to 148 hours (CPU time) on a powerful ES47 workstation (20Gb core memory, 660 Gb disk, and two dual processors of 1 GHz). Other prohibitive calculations that are presented in this work were carried out on all four species at the CCSD(T)/aug-cc-pVTZ level [414 basis functions]. On the same work station, these required runs of 19 up to 77 hours (CPU time).

Estimates of the conformer energy differences have also been calculated in the asymptotic limit of an infinitely large basis set. In this purpose, we rely on well-suited extrapolations of the HF total electronic energies obtained for the neutral molecules and their cations using Dunning's series of cc-pVXZ basis sets (with X=D, T, Q,...), and Feller's [54] exponential fit. In turn, correlated total energies are extrapolated to an asymptotically complete basis set by means of a three-point extension (named Schwartz 6(*lmn*) [55]) of Schwartz' extrapolation formula [56].

All the calculated energy differences derive from single-point calculations performed upon geometries optimized using DFT, along with the B3LYP functional and the aug-cc-pVTZ basis. At this stage, we would like to recall that, compared with experiment or benchmark theoretical results, the B3LYP predictions for bond lengths and bond angles are generally superior to the MP2 ones [57]. As such, B3LYP geometries are often retained in rigorous theoretical models aiming at chemical accuracy (see e.g. [58] for a review of the design and applications of the so-called Weizmann-1 theory). Indeed, the B3LYP approach is known to provide structural as well as harmonic vibrational frequencies of quality comparable to the CCSD(T) level (see also [59]).

B. Calculation of conformer abundances

Based on our best estimates of the relative energies of the four conformers of dimethoxymethane, the relative abundances of each species are estimated according to Boltzmann statistical thermodynamics, using the standard formula

$$n_i = \rho_i \exp(-\Delta G_i / RT) \qquad (1)$$

with ρ_i the multiplicity (or symmetry number) of the species of interest on the potential energy surface of dimethoxymethane. Here, ΔG_i denote our best estimates for the Gibbs free energy of the species of interest relative to the most stable conformer (G^+G^+). More specifically, these quantities have been obtained by adding to the benchmark quantum-mechanical energy differences, obtained from the above described Focal Point Analysis, B3LYP/aug-cc-pVTZ zero-point vibrational energy corrections as well as enthalpy and entropy corrections derived from Boltzmann statistical thermodynamics, using electronic, rotational and vibrational partition functions that were also computed at the B3LYP/aug-cc-pVTZ level, at standard temperature (298K) and pressure (1 atm). The evaluation reported here goes beyond the (uncoupled) Rigid Rotor - Harmonic Oscillator (RRHO) approximation, as hindered rotations are accounted for by means of the protocol by Ayala and Schlegel [60] for identifying and treating the internal rotation modes, using a projection of harmonic vibrational normal modes on constrained stretches, bends, and out-of-plane motions, leaving only the torsion modes, as well the rules of Mayo, Olafson, and Goddard [61] for obtaining the potential periodicity, the rotating tops' symmetry numbers, and the well-multiplicities. The protocol by Ayala and Schlegel [60] also employs an improved analytical approximation, according to a best-fit procedure, of the formula of Pitzer and Gwinn [51a] for the partition function associated to one-dimensional hindered internal rotations.

All Hartree-Fock (HF), DFT and thermodynamical calculations described so far have been performed using the GAUSSIAN 03 package of programs [62]. The Møller-Plesset (MP), and Coupled Cluster (CC) single point calculations were performed using the MOLPRO 2000.1 package of programs [63].

C. Ionization spectra

The ADC(3) calculations have been carried out using the original 1p-GF/ADC(3) package of programs, interfaced to GAMESS [64]. This package incorporates a band-Lanczos [65] "pre"-diagonalisation of the block matrices pertaining to the 2p-1h shake-on states into a pseudo-electron attachment spectrum, prior to a complete block-Davidson diagonalisation [66] of the so-reduced ADC(3) secular matrix. With this diagonalization procedure, all eigen-values of the ADC(3) secular matrix with pole strengths equal to or larger than 0.005 could be recovered up to electron binding energies of ~30 eV. The assumption of frozen core electrons has been used throughout and the full molecular symmetry point groups have been exploited. At the self-consistent field level, the requested convergence on each of the elements of the density matrix was fixed to 10^{-10}. The 1p-GF/ADC(3) calculations have been carried out using Dunning's correlation-consistent polarized valence basis set of double- ζ quality (cc-pVDZ) [53a]. To assess the effect of diffuse functions on Dyson orbital momentum distributions, an attempt to use the aug-cc-pVDZ basis with diffuse functions centered on hydrogen, carbon, as well as oxygen atoms was also made. However, severe linear dependencies resulting in divergency problems prevented us from completing successfully ADC(3) calculations with the latter basis set, which led us to drop d-type diffuse functions on carbons and oxygens atoms in the original aug-cc-pVDZ basis set, giving rise to a slightly smaller diffuse basis set referred to as the cc-pVDZ++ one.

The ionization spectra presented in the sequel have been simulated using as convolution function a combination of a Gaussian and a Lorentzian with equal weight (Voigt profile) and a constant full width at half of maximum parameter (FWHM) of 0.6 or 1.1 eV. The latter parameters have been selected in order to enable comparisons with available experimental data obtained by means of ultra-violet (He I) photoelectron spectroscopy (UPS) or Electron Momentum Spectroscopy, respectively, taking into account the energy resolutions that can be achieved for both spectroscopies nowadays, as well as natural and vibrational broadening.

D. (e,2e) Ionization intensities and spherically averaged electron momentum distributions.

The theory of electron momentum spectroscopy [1], which is based on electron impact ionization experiments focusing on (e,2e) reactions ($M + e^- \rightarrow M^+ + 2e^-$) at high kinetic energies (E_0 >> 1 keV, with E_0 the energy of the impinging electron), is discussed in Part 2 of the present thesis. In the sequel, the ADC(3) ionization energies and related Dyson orbitals have been used to simulate (e,2e) ionization spectra at specific azimuthal angles, applying the convolution procedure described in the previous section (FWHM=1.1 eV).

TABLE 1: Selected B3LYP/aug-cc-pVTZ Optimized Geometric Parameters for the Four Conformers of Dimethoxymethane[a]

TT Conformer (C_{2v}):
$C_1{-}O_1 = O_2{-}C_3 = 1.411$; $O_1{-}C_2 = C_2{-}O_2 = 1.395$
$\theta(C_1,O_1,C_2) = \theta(C_2,O_2,C_3) = 112.4$; $\theta(O_1,C_2,O_2) = 105.9$
$\varphi(C_1,O_1,C_2,O_2) = \varphi(O_1,C_2,O_2,C_3) = 180.0$

TG Conformer (C_1):
$C_1{-}O_1 = 1.423$; $O_1{-}C_2 = 1.383$; $C_2{-}O_2 = 1.415$; $O_2{-}C_3 = 1.414$
$\theta(C_1,O_1,C_2) = 114.4$; $\theta(O_1,C_2,O_2) = 110.1$; $\theta(C_2,O_2,C_3) = 112.7$
$\varphi(C_1,O_1,C_2,O_2) = 68.7$; $\varphi(O_1,C_2,O_2,C_3) = -178.5$

G^+G^+ Conformer (C_2):
$C_1{-}O_1 = O_2{-}C_3 = 1.422 = (\mathit{1.425 \pm 0.004})^b$
$O_1{-}C_2 = C_2{-}O_2 = 1.403 = (\mathit{1.400 \pm 0.004})^b$
$\theta(C_1,O_1,C_2) = \theta(C_2,O_2,C_3) = 114.0 = \mathit{112.9}^b$
$\theta(O_1,C_2,O_2) = 114.1 = \mathit{113.7}^b$
$\varphi(C_1,O_1,C_2,O_2) = \varphi(O_1,C_2,O_2,C_3) = 68.8 = \mathit{68.1}^b$

G^+G^- Conformer (C_s):
$C_1{-}O_1 = O_2{-}C_3 = 1.419$; $O_1{-}C_2 = C_2{-}O_2 = 1.403$
$\theta(C_1,O_1,C_2) = \theta(C_2,O_2,C_3) = 116.9$; $\theta(O_1,C_2,O_2) = 115.6$
$\varphi(C_1,O_1,C_2,O_2) = -\varphi(O_1,C_2,O_2,C_3) = 84.8$

[a] Bond lengths are in angstroms. Bond (θ) and dihedral (φ) angles are in degrees. [b] Experimental X-ray diffraction data.[35]

Spherically averaged orbital momentum distributions have been generated from the output of 1p-GF/ADC(3) or DFT calculations using the MOMAP program by Brion and co-workers [67] and homemade interfaces. For comparison purposes, the most accurate ADC(3)/cc-pVDZ++ Dyson orbital distributions presented in the sequel have also been convolved by means of the Gaussian weighted planar grid (GW-PG) method of Duffy *et al.* [68], according to an experimental electron momentum resolution of 0.1 a.u. (FWHM). This value is consistent with an angular resolution of $\Delta\phi = 1.2°$ at a total impact energy of 1200 eV [69].

In line with these calculations, (e,2e) ionization spectra can be easily simulated using the ADC(3) output and Dyson orbitals for all identified one-electron and shake-up lines. Specifically, in these simulations, line intensities are scaled according to (e,2e) ionization cross sections.

4.2.3. Results and discussion

A. Molecular structures and relative conformer energies

Presented in Table 1 are the main geometrical parameters characterizing the C-O-C-O-C backbone of the four conformers of dimethoxymethane, TT, TG, G^+G^+ and G^+G^-, which were optimized at the B3LYP/aug-cc-pVTZ level, under the constraints of the C_{2v}, C_1, C_2 and C_s symmetry point groups, respectively. In all four cases, vibrational analysis confirmed that these point groups are compatible with local energy minima, in line with the most thorough (B3LYP/6-31++G**) calculations available to date on this molecule [22, 23]. Note that, without diffuse functions in the basis set, the G^+G^- conformer (C_s structure) is a first order saddle point on the (B3LYP/cc-pVTZ) potential energy surface, most certainly due to an incomplete depiction of the through-space orbital interactions associated to the anomeric effect, and of the dispersion forces between the terminal methyl groups. This observation is consistent with earlier studies [29] performed with much smaller basis sets (4-31G, D95**, D95(2df,p)). For the latter species, at the B3LYP/aug-cc-pVTZ level, unusually large atomic displacements and low forces were experienced at the final stages of the geometry optimization process, which indicates that the associated energy minimum is a very shallow one. An extremely low vibrational frequency is correspondingly found for the G^+G^- conformer. Note that the TG conformer was obtained by optimizing at the same level a strongly asymmetric structure resembling the G^+G^- conformer of *n*-pentane, with in the first step C-O-C-O and O-C-O-C dihedral angles equal to 63 and -90°.

In general, end C-O bonds are slightly longer, by ~0.02 Å, than the central O-C bonds. The gauche segments of the TG, G^+G^+ and G^+G^- conformers are characterized by C-O-C bond angles ranging from 114 to 116°, as a result of unfavorable steric and electrostatic interactions between the CH_3 and CH_2 groups, and of the anomeric effect, which tends to drive the oxygen atoms towards an sp^2 state of hybridization. In straightforward analogy with *n*-pentane [45], unusually large torsion angles, around ~85°, are observed within the C-O-C-O-C backbone for the G^+G^- conformer of dimethoxymethane, as a result of particularly strong steric and electrostatic repulsion forces in this species.

TABLE 2: Focal Point Analysis of the Energy of the TG Conformer of Dimethoxymethane Relative to the G^+G^+ Species[a]

basis	3-21G[b] (61 MOs)	cc-pVDZ[b] (110 MOs)	aug-cc-pVDZ[b] (187 MOs)	cc-pVTZ[b] (262 MOs)	aug-cc-pVTZ[b] (414 MOs)	cc-pVQZ[b] (515 MOs)	aug-cc-pVQZ[b] (768 MOs)	cc-pV∞Z[c]	aug-cc-pV∞Z[c]	cc-pcVDZ[d] (130 MOs)	cc-pcVTZ[d] (327 MOs)
ΔHF	19.23	10.40	8.30	8.42	7.95	7.86	7.79	*7.673*	***7.673***		
+MP2	1.628	2.673	3.643	2.978	3.436	3.169	3.360	*3.228*	***3.341***	0.063	**−0.026**
+MP3	−1.247	−1.235	−1.208	−1.241	−1.200	−1.220	−1.221	*−1.234*	***−1.208***	−0.016	**−0.015**
+CCSD	0.843	0.675	0.553	0.570	0.535	0.528		***0.512***		0.010	**−0.006**
+CCSD(T)	0.320	0.415	0.601	0.501	**0.607**					**0.003**	
total	20.777	12.933	11.890	11.225	11.331	*10.944*[e]	*11.062*[e]	*10.786*[e]	*10.925*[e]	*10.985*	*10.881*[f]

[a] Values given in italics refer to extrapolations; energies are expressed in kilojoules per mole. [b] Calculations employing the frozen core approximation. [c] HF energies are extrapolated according to a three-point Feller extrapolation; correlation energies are extrapolated according to a three-point Schwarz extrapolation (frozen core). [d] Frozen core−full correlation energy corrections are the differences between the corresponding frozen core and the full calculations. [e] Extrapolated values, using the best values on left for the missing corrections. [f] Best estimate, obtained by summing the HF/aug-cc-pV∞Z value and all corrections in boldface.

TABLE 3: Focal Point Analysis of the Energy of the G^+G^- Conformer of Dimethoxymethane Relative to the G^+G^+ Species[a]

basis	3-21G[b] (61 MOs)	cc-pVDZ[b] (110 MOs)	aug-cc-pVDZ[b] (187 MOs)	cc-pVTZ[b] (262 MOs)	aug-cc-pVTZ[b] (414 MOs)	cc-pVQZ[b] (515 MOs)	aug-cc-pVQZ[b] (768 MOs)	cc-pV∞Z[c]	aug-cc-pV∞Z[c]	cc-pcVDZ[d] (130 MOs)	cc-pcVTZ[d] (327 MOs)
ΔHF	22.97	20.69	18.04	18.42	17.73	17.75	17.59	*17.502*	***17.527***		
+MP2	−3.201	−0.766	−1.237	−1.263	−1.106	−1.113	−1.035	*−1.068*	***−1.005***	0.110	**0.112**
+MP3	0.120	−0.447	−0.411	−0.534	−0.368	−0.443	−0.377	*−0.455*	***−0.394***	−0.013	**−0.019**
+CCSD	0.152	0.202	0.173	0.268	0.228	0.262		***0.295***		0.001	**0.011**
+CCSD(T)	−0.607	−0.432	−0.402	−0.479	**−0.445**					**−0.004**	
Total	19.438	19.243	16.166	16.412	16.041	*16.010*[e]	*15.994*[e]	*15.830*[e]	*15.979*[e]	*16.073*	*16.080*[f]

[a] Values given in italics refer to extrapolations; energies are expressed in kilojoules per mole. [b] Calculations employing the frozen core approximation. [c] HF energies are extrapolated according to a three-point Feller extrapolation; correlation energies are extrapolated according to a three-point Schwarz extrapolation (frozen core). [d] Frozen core−full correlation energy corrections are the differences between the corresponding frozen core and the full calculations. [e] Extrapolated values, using the best values on left for the missing corrections. [f] Best estimate, obtained by summing the HF/aug-cc-pV∞Z value and all corrections in boldface.

TABLE 4: Focal Point Analysis of the Energy of the TT Conformer of Dimethoxymethane Relative to the G^+G^+ Species[a]

basis	3-21G[b] (61 MOs)	cc-pVDZ[b] (110 MOs)	aug-cc-pVDZ[b] (187 MOs)	cc-pVTZ[b] (262 MOs)	aug-cc-pVTZ[b] (414 MOs)	cc-pVQZ[b] (515 MOs)	aug-cc-pVQZ[b] (768 MOs)	cc-pV∞Z[c]	aug-cc-pV∞Z[c]	cc-pcVDZ[d] (130 MOs)	cc-pcVTZ[d] (327 MOs)
ΔHF	42.57	23.55	18.72	19.27	18.04	17.98	17.79	*17.484*	***17.652***		
+MP2	0.344	4.623	6.770	5.804	6.172	5.869	6.069	*5.907*	***6.037***	0.071	**−0.050**
+MP3	−1.792	−2.438	−2.436	−2.489	−2.335	−2.389	−2.348	−2.397	***−2.336***	−0.024	**−0.027**
+CCSD	1.737	1.476	1.212	1.239	1.178	1.154		***1.168***		0.023	**−0.021**
+CCSD(T)	0.468	0.810	1.184	1.088	**1.204**					**0.007**	
Total	43.324	28.025	25.450	24.914	24.256	*23.815*[e]	*23.865*[e]	*23.365*[e]	*23.724*[e]	*23.802*	*23.635*[f]

[a] Values given in italics refer to extrapolations; energies are expressed in kilojoules per mole. [b] Calculations employing the frozen core approximation. [c] HF energies are extrapolated according to a three-point Feller extrapolation; correlation energies are extrapolated according to a three-point Schwarz extrapolation (frozen core approximation). [d] Frozen core−full correlation energy corrections are the differences between the corresponding frozen core and the full calculations. [e] Extrapolated values, using the best values on left for the missing corrections. [f] Best estimate, obtained by summing the HF/aug-cc-pV∞Z value and all corrections in boldface.

For the G^+G^+ conformer, the computed C-O-C or O-C-O bond angles (114.0º, 114.1º), as well as the dihedral (O-C-O-C or C-O-C-O) angles (68.8º), compare rather favorably with available electron diffraction data (114.6 ± 0.5º, 114.3 ± 0.7º and 63.3 ± 0.9º [33a]), or microwave rotational spectroscopic data, (111.4 º, 112.8 º and 67.6 º, respectively [36a]). See also Table 1 for a comparison of the calculated geometry for this conformer with recent X-ray diffraction data [35]. Our results are found to be in quantitative agreement with the latter data, despite possible complications due to temperature effects as well as intermolecular interactions in the solid state.

Results of the Focal Point Analysis of the conformer energies of dimethoxymethane relative to the most stable form (G^+G^+) are given in Tables 2-4, which are formed by listing theoretical methods of improving quality on one axis, and basis sets of increasing size on the other, with the best result being obviously given by the entry at the lower right corner. From these tables, extremely accurate predictions of conformer energy differences can be made by pairing different levels of theory with various basis sets. To be more specific, the values reported under the ΔHF entry correspond to the conformational energy differences at the HF level, whereas the values reported in the +MP2, +MP3, +CCSD, +CCSD(T) entries are the corrections to the conformational energy differences obtained by comparing successively the MP2 with the HF results, the MP3 with the MP2 results, the CCSD with the MP3 results, and, at last, the CCSD(T) with the CCSD results. In each column, the sum of the reported values up to a given row associated to a specific theoretical model gives thus the relative conformer energy for that model chemistry in particular.

TABLE 5: Evaluation of Relative Energy (or Enthalpy) Differences at Using the FPA Results of Tables 2−4 and the B3LYP/aug-cc-pVTZ Corrections for Zero-Point Harmonic Vibrational Energies ($\Delta H_0 = \Delta E$(FPA) + ΔZPVE)[a]

conformer	G^+G^+	TG	G^+G^-	TT
ΔE(FPA)[b]	0.000	10.881	16.080	23.635
ΔE[c]	0.000	9.459	14.763	21.132
ΔZPVE[c]	0.000	−0.934	−0.759	−2.124
ΔH_0	0.000	9.947	15.321	21.512

[a] All energy differences are given in kilojoules per mole. [b] Taken from the focal point analysis (see Tables 2−4). [c] Differences obtained from B3LYP/aug-cc-pVTZ calculations.

The key point in a focal point analysis is to determine at which basis set each of the successive corrections evaluated by the various *ab initio* methods has converged. Very clearly, the most important corrections to the ΔHF results are the MP2 ones, the convergence of which is rather slow. At the HF and MP2 levels, diffuse functions have a very substantial influence on the computed energy differences, due to the through-bond and through-space orbital interactions associated with the anomeric effect. Therefore, comparing the ΔHF results and MP2 corrections obtained using the cc-pVQZ and aug-cc-pVQZ basis sets indicates near convergence for these quantities, within 0.2 kJ/mol, with respect to further improvements of the basis set. In contrast, a comparison with energy differences obtained using the aug-cc-pVTZ and cc-pVQZ basis sets indicates an almost complete convergence, within 0.02 kJ/mol, of the CCSD correction to the MP3 result. Similarly, comparing the CCSD(T)/aug-cc-pVDZ and CCSD(T)/aug-cc-pVTZ corrections to the CCSD result obtained with the same basis sets demonstrates the convergence of the +CCSD(T) correction within ~0.04 kJ/mol.

In tables 2-4, the values displayed in italic derive either from extrapolations to the limit of asymptotically complete basis sets, using the procedures by Feller or Schwarz (see section 2), or from extrapolations employing our best estimates (in bold) of the successive contributions and corrections to the relative conformer energies. Note that the most prohibitive MP3/aug-cc-pVQZ, CCSD/cc-pVQZ and CCSD(T)/aug-cc-pVTZ calculations were so much computationally demanding that the frozen core approximation has been used almost systematically, in order to make these calculations tractable. Within the framework of this approximation, a value of 10.93 kJ/mol is thus for instance found for the extrapolated CCSD(T)/aug-cc-pv∞z energy of the TG conformer relative to the G^+G^+ global energy minimum, by adding to the ΔHF/aug-cc-pv∞z result (7.67 kJ/mol) the best estimates (+3.34, -1.21, +0.51, +0.61 kJ/mol) for the +MP2, +MP3, +CCSD and +CCSD(T) corrections. The G^+G^- and TT rotamers are similarly located at relative energies of 15.98 and 23.72 kJ/mol.

Errors made because of the frozen core approximation upon the correlation corrections to the HF energy differences were estimated separately for all employed model chemistries, using the cc-pVDZ and cc-pVTZ basis sets, by comparing results obtained for these basis sets with and without using this approximation. The core level contributions to the successive correlation corrections to the computed energy differences are listed under the two rightmost entries of Tables 2-4. As is immediately apparent, the frozen core approximation has a very marginal effect, below ~0.1 kJ/mol, on the computed energy differences. Accounting for these contributions lead to energy differences of 10.92, 15.99, and 23.64 kJ/mol between, on the one hand, the TG, G^+G^- and TT conformers, and the

G^+G^+ conformer on the other hand. The latter values define thus our best estimates, to be used in the forthcoming statistical thermodynamical study of the conformational equilibrium of dimethoxymethane, for the energy of the TG, G^+G^- and TT species relative to that of the G^+G^+ global energy minimum form. Compared with these, the B3LYP/aug-cc-PVTZ energy differences (Table 5) are in error by ~1.2 to ~2.5 kJ/mol. For the sake of completeness, we provide in Table 5 internal energy (or enthalpy) differences at 0K including B3LYP/aug-cc-pVTZ corrections for zero-point vibrational energies (ZPVEs) [$\Delta H_0=\Delta U_0=\Delta E(FPA)+\Delta ZPVE$]. Considering that, compared with the latter contributions, thermal corrections to internal energies or enthalpies at room temperature are marginal, the ΔH_0 enthalpy difference that is found (9.95 kJ/mol) between the TG and G^+G^+ species appears to be fully consistent with a reported experimental value of 10.5 ± 0.8 kJ/mol, according to temperature-dependent NMR measurements of ^{13}C-^1H coupling constants in the gas phase [34].

TABLE 6: Evaluation, Using Boltzmann Statistical Thermodynamics at the Level of the Rigid Rotor−Harmonic Oscillator and upon Accounting for Hindered Rotations, of the Abundance of the Four Conformers of Dimethoxymethane at Room Temperature ($T = 298.15$ K), Using the Best FPA Estimates (Tables 2−4) for the Energy Differences, and the B3LYP/aug-cc-pVDZ Estimates for the Zero-Point Vibrational and Thermal Contributions to the Enthalpy Differences ($\Delta\Delta H_{298} = \Delta H_{298} - \Delta E$), for the Relative Enthalpies ($\Delta H_{298} = \Delta E(\mathrm{FPA}) + \Delta\Delta H_{298}$), for Relative Entropies (ΔS_{298}), and for the Relative Gibbs Free Energies ($\Delta G_{298} = \Delta H_{298} - T\Delta S_{298}$)

	hindered rotations				RRHO			
	G^+G^+	TG	G^+G^-	TT	G^+G^+	TG	G^+G^-	TT
$\Delta E(\mathrm{FPA})^a$	0.000	10.881	16.080	23.635	0.000	10.881	16.080	23.635
$\Delta\Delta H_{298}{}^a$	0.000	−0.602	−1.343	−1.741	0.000	−0.778	−0.331	−1.527
$\Delta H_{298}{}^a$	0.000	10.279	14.737	21.894	0.000	10.103	15.749	22.108
$\Delta S_{298}{}^b$	0.000	−1.197	14.707	8.996	0.000	7.146	21.920	5.761
$\Delta G_{298}{}^a$	0.000	10.635	10.352	19.212	0.000	7.974	9.214	20.390
abundance	0.9587	0.0263	0.0147	0.0002	0.9053	0.0726	0.0220	0.0001

[a] In kJ/mol. [b] In J/(K·mol).

B. Conformational equilibrium

Along with the extremely accurate conformational energy differences derived from focal point analyses [ΔE(FPA)], we display in Table 6 the enthalpy corrections ($\Delta\Delta H_{298}$, including zero-point vibrational energies) obtained at room temperature from the B3LYP/aug-cc-pVTZ geometrical and vibrational results for each of the conformers of interest, using Boltzmann statistical thermodynamics at the elementary RRHO level, as well as upon taking into account the influence of rigid-rotor hindered rotations, using the protocol by Ayala and Schlegel [60]. We correspondingly provide in these tables our best estimates for the enthalpy, entropy and Gibb's free energy differences, with and without accounting for the hindered rotations. It is immediately apparent from this table that hindered rotations, in particular those associated to the terminal methyl groups, have quantitatively a rather significant influence, of the order of ~1.0 to ~2.5 kJ/mol, on the obtained Gibb's free energy differences, mostly via the computed entropies. The effect is particularly pronounced for the TG conformer.

In line with the respective symmetry point groups, the symmetry numbers ρ_i to retain for evaluating the conformer abundance of each species via equation (1) have been set equal to 2, 4, 2, 1 for the G^+G^+, TG, G^+G^- and TT conformers, respectively. Accounting for hindered rotations results into minor variations, by ~5%, in the computed abundances. According to our most exact model, only the G^+G^+ conformer contributes significantly, with a molar fraction approaching 0.96, to the conformational mixture characterizing a gas phase sample of dimethoxymethane at 298K. Conformer abundances have been similarly calculated at other temperatures (Table 7), using in each cases vibrational and rotational partition functions accounting for hindered rotations. It is only at temperatures above 100ºC that the molar fractions of the TG and G^+G^- conformer exceed 5%, and may then become significant from a spectroscopic viewpoint. Note that the weight of the TT conformer remains totally negligible, whatever the considered temperature, or the level of theory reached for the thermodynamical calculations. This rotamer may therefore clearly be regarded as an "electrostatically-forbidden" structure.

TABLE 7: Evalution of the Conformer Distribution as a Function of the Temperature

temp (K)	G^+G^+ (C_2)	TG (C_1)	G^+G^- (C_s)	TT (C_{2v})
198.15	0.9958	0.0034	0.0007	0.0000
223.15	0.9912	0.0068	0.0020	0.0000
248.15	0.9837	0.0117	0.0045	0.0000
273.15	0.9730	0.0183	0.0086	0.0001
298.15	0.9588	0.0263	0.0147	0.0002
323.15	0.9411	0.0356	0.0229	0.0004
348.15	0.9205	0.0458	0.0329	0.0007
373.15	0.8973	0.0567	0.0448	0.0011
398.15	0.8721	0.0679	0.0583	0.0017

Considering the results of our focal point analysis and thermodynamical calculations, as well as the still rather limited energy resolution and signal-to-noise ratio of the best (e,2e) spectrometers that are currently available, it is therefore a very reasonable choice to predict the results of EMS experiments on dimethoxymetane from calculations on the G^+G^+ conformer alone.

C. Valence electronic structure and ionization spectra.

The spike and convoluted ADC(3) spectra displayed in Figure 2 reflect the partition of the valence electronic structure of dimethoxymethane into 5 inner-valence levels (O_{2s}, C_{2s}) and 11 outer-valence levels (O_{2p}, C_{2p}, H_{1s}), at electron binding energies above and below ~19 eV, respectively. At the HF/aug-cc-pVTZ level, the most stable G^+G^+ conformer of dimethoxymethane in its (X^1A) ground state has, under the constraint of a C_2 symmetry point group, the following inner and outer valence shell electronic configurations:

inner valence shell : $(\text{core})^{10}\,\{(4a)^2\,(3b)^2\,(5a)^2\,(4b)^2\,(6a)^2\}$,
outer valence shell $\{(5b)^2\,(7a)^2\,(6b)^2\,(8a)^2\,(7b)^2\,(9a)^2\,(8b)^2\,(10a)^2\,(9b)^2\,(11a)^2\,(10b)^2\}$.

The corresponding molecular orbitals are displayed in Figure 3. The two innermost orbitals (4a, 3b) giving rise to the bands at ~32 and ~34 eV in the ADC(3)/cc-pVDZ spectrum (Figure 2c, Table 8) relate merely to bonding and anti-bonding combinations of O_{2s} atomic orbitals. Analysis of the LCAO eigenvectors indicates that the next three orbitals (5a, 4b, 6a) are dominated by C_{2s} contributions. Admixture of C_{2p} and H_{1s} contributions is nonetheless noted (Figure 3) for the orbital (6a) at the top of the inner-valence region, which through-space interactions between σ orbitals associated to C-H bonds help to slightly stabilize. The first orbital (5b) in the outer-valence region exhibits correspondingly a significant C_{2s} character. Such mixtures of C_{2s} and C_{2p}+H_{1s} contributions across the gap separating the inner- and outer-valence regions is a very typical consequence of through-space methylenic hyperconjugation effects [70].

TABLE 8: Assignment of the Experimentally Available Ionization Spectra of Dimethoxymethane, Using HF, DFT/B3LYP, and ADC(3) Ionization Energies^{a}

band^{b}	level	MO	HF/ aug-cc-pVDZ	B3LYP/ cc-pVDZ	B3LYP/ aug-cc-pVDZ	B3LYP/ aug-cc-pVTZ	ADC(3)/ cc-pVDZ	ADC(3)/ cc-pVDZ++	PES^{c}	EMS^{d}
I^{e}	1	10b	12.029	7.257	7.583	7.627	10.331 (0.906)	10.608 (0.904)	10.29	10.41
	2	11a	12.053	7.415	7.735	7.771	10.490 (0.908)	10.756 (0.905)	10.53	
II^{e}	3	9b	12.640	8.185	8.504	8.519	11.308 (0.910)	11.586 (0.906)	11.44	11.6^{h}
III^{e}	4	10a	14.203	9.616	9.897	9.905	12.942 (0.908)	13.177 (0.906)	12.98	13.2^{h}
	5	8b	14.430	10.279	10.450	10.460	13.502 (0.914)	13.657 (0.911)	13.42	
IV^{e}	6	9a	15.641	11.235	11.470	11.474	14.464 (0.907)	14.693 (0.903)	14.7^{h}	15.2^{h}
	7	7b	16.385	11.641	11.831	11.853	15.090 (0.905)	15.240 (0.902)	15.0^{h}	
	8	8a	16.603	11.848	12.050	12.062	15.312 (0.905)	15.477 (0.902)		
V^{e}	9	6b	**18.340**	13.508	13.764	13.761	**16.941** (0.894)	**17.193** (0.890)	16.9^{h}	17.2^{h}
	10	7a	**18.747**	13.453	13.699	13.698	**17.032** (0.889)	**17.250** (0.886)		
	11	5b	18.826	13.718	13.953	13.944	17.237 (0.894)	17.441 (0.890)		
VI	12	6a	22.859	16.607	16.805	16.784	20.663 (0.847)	20.807 (0.839)		20.6^{h}
VII	13	4b^{f,g}	25.369	18.744	18.941	18.902	22.778 (0.438)	22.884 (0.214)		23.5^{h}
							22.790 (0.300)	22.929 (0.500)		
VIII	14	5a^{f,g}	26.689	19.906	20.121	20.065	23.688 (0.117)	23.620 (0.026)		
							23.767 (0.137)	23.880 (0.141)		
							23.912 (0.160)	24.011 (0.120)		
								24.303 (0.101)		
IX	15	3b^{f,g}	36.589	27.375	27.697	27.605	31.718 (0.031)	31.734 (0.011)		28−36^{h}
							31.944 (0.064)	32.113 (0.011)		
X	16	4a^{f,g}	38.433	28.977	29.291	29.196	33.167 (0.029)			
							34.096 (0.028)			

[a] Spectroscopic strengths (or pole strengths Γ_n) are given in parentheses. [b] The borders of peaks are based on ADC(3)/cc-pVDZ grounds. [c] See ref 38. [d] See ref 6. [e] These peaks reproducing the PES measurements are simulated using a spread Voigt function with an fwhm parameter of 0.6 eV (see Figure 2). [f] Breakdown of the orbital picture of ionization. Additional ADC(3)/cc-pVDZ shake-up lines: 4b (**13**): 22.916 (0.012), 23.891 (0.012); 5a (**14**): 23.514 (0.012), 23.971 (0.075), 24.007 (0.093), 24.228 (0.011), 24.281 (0.039), 24.414 (0.009), 24.451 (0.037), 24.493 (0.015), 24.680 (0.011), 24.859 (0.008), 24.919 (0.015), 25.111 (0.015); 3b (**15**): 31.067 (0.009), 31.140 (0.014), 31.279 (0.010), 31.294 (0.009), 31.457 (0.016), 31.496 (0.009), 31.596 (0.013), 31.632 (0.014); 31.739 (0.029), 31.868 (0.018), 31.912 (0.009), 31.947 (0.012), 32.062 (0.010), 32.180 (0.009), 32.227 (0.010), 32.273 (0.016), 32.281 (0.020), 32.443 (0.018), 32.508 (0.012); 4a (**16**): 32.195 (0.009), 32.295 (0.009), 32.522 (0.015), 32.809 (0.013), 33.096 (0.012), 33.346 (0.009), 33.827 (0.009), 34.053 (0.021), 34.099 (0.021), 34.136 (0.009), 34.190 (0.009), 34.268 (0.009), 34.314 (0.015), 34.334 (0.010), 34.363 (0.015). Breakdown of the orbital picture of ionization. Additional ADC(3)/cc-pVDZ++ shake-up lines: 6a (**12**): 21.287 (0.006), 22.233 (0.005); 4b (**13**): 23.083 (0.022), 23.636 (0.014), 24.026 (0.008); 5a (14): 23.676 (0.007), 23.738 (0.017), 23.766 (0.005), 23.820 (0.019), 23.993 (0.010), 24.068 (0.065), 24.100 (0.086), 24.148 (0.012), 24.201 (0.023), 24.317 (0.017), 24.415 (0.017), 24.576 (0.015), 24.629 (0.007), 24.736 (0.006), 24.788 (0.016), 24.830 (0.008), 24.849 (0.006), 24.944 (0.009), 24.999 (0.025); 3b (**15**) 31.949 (0.008), 32.064 (0.010), 32.167 (0.011), 32.182 (0.008), 32.195 (0.009), 32.264 (0.008),32.267 (0.010). [g] The total fraction of ionization intensity recovered at these binding energies for the 4b orbital is, at the ADC(3)/cc-pVDZ and ADC(3)/cc-pVDZ++ levels, equal to 0.762 and 0.760, respectively. For the 5a orbital this sum is correspondingly equal to 0.754 or 0.758, respectively. A major part of the missing fraction is expected to be found at higher electron binding energies.[75] [h] Own assignment.

Running further towards lower binding energies, the next 7 orbitals that we encounter (5b, 6b, 7a, 8a, 7b, 9a, 8b) merely derive from combinations of C_{2p} and H_{1s} orbitals. Upon analyzing the LCAO eigenvectors, the molecular orbitals that dominantly relate to the four oxygen lone pairs are, clearly, the four outermost ones (10b, 11a, 9b, 10a). The two highest-lying canonical orbitals (10b and 11a) defining the HOMO (highest occupied molecular orbitals) and HOMO-1 levels derive essentially from linear combinations of two localized $n_{\pi}(2p)$-type oxygen lone pairs, with no or limited through-bond interaction via the $\pi(CH_2)$ orbitals (Figure 3). In contrast, the next two highest –lying occupied orbitals (9b, 10a) describe (Figure 3) delocalization of the two remaining $n_{\sigma}(sp^2)$-type oxygen lone-pairs over the vicinal C-O bonds and mixture with σ(C-O) and $\pi(CH_2)$ orbitals resulting into particularly favorable through-bond and through-space interactions along the C-O-C-O-C backbone. This orbital mixture can thus be typically regarded as the main outcome of the anomeric effect in a canonical (i.e. non-localized) depiction of the valence electronic structure of dimethoxymethane in its G^+G^+ conformation.

The reader is referred to Table 8 for an assignment of the He (I) photoelectron spectrum by Jørgensen *et al* (Figure 2a) [38], through a confrontation with the available HF, DFT, and ADC(3) data. It is immediately apparent that the ADC(3) calculations enable quantitative insights, within ~0.3 eV, into the experimental one-electron binding energies. In contrast, it is clear that neither HF nor KS orbital energies provide reliable estimates of the experimentally obtained one-electron binding energies. Nonetheless, the ADC(3) results confirm that the order of ionization energies predicted from the HF or KS orbital energies is correct, up to the top of the inner-valence region at ~21 eV.

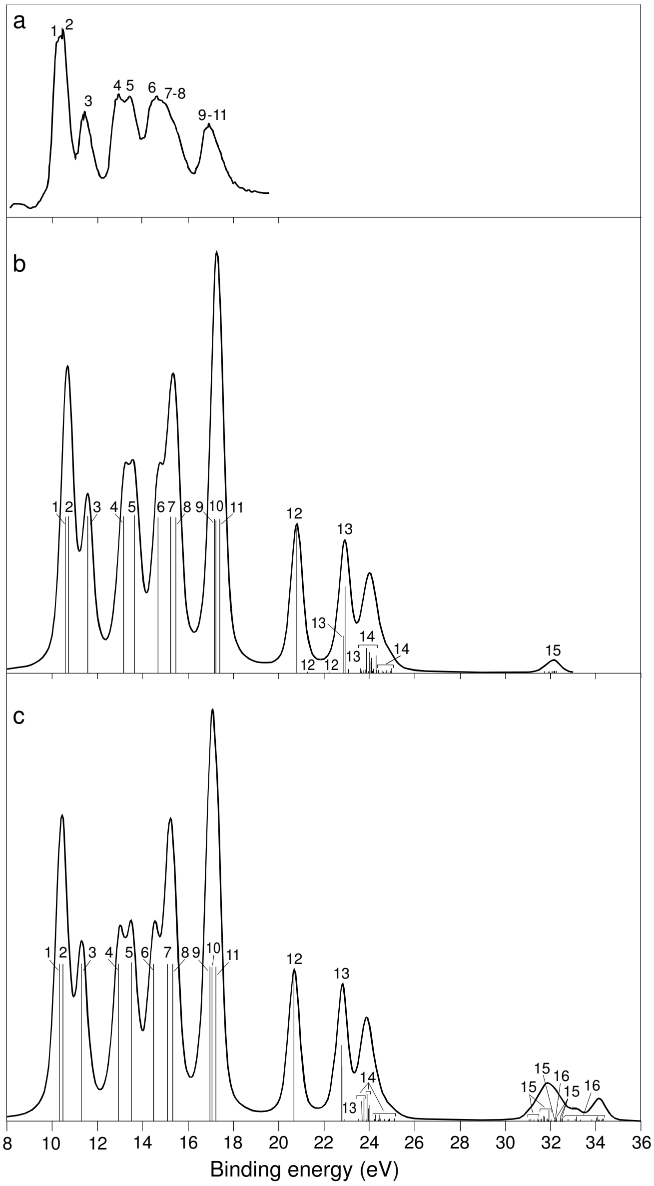

Figure 2. Comparison between the (a) He I photoelectron spectra of dimethoxymethane obtained by Jørgensen [38] and the theoretical ADC(3) spectra obtained using the (b) cc-pVDZ++ and (c) cc-pVDZ basis sets (Convolution performed using a FWHM parameter of 0.6 eV).

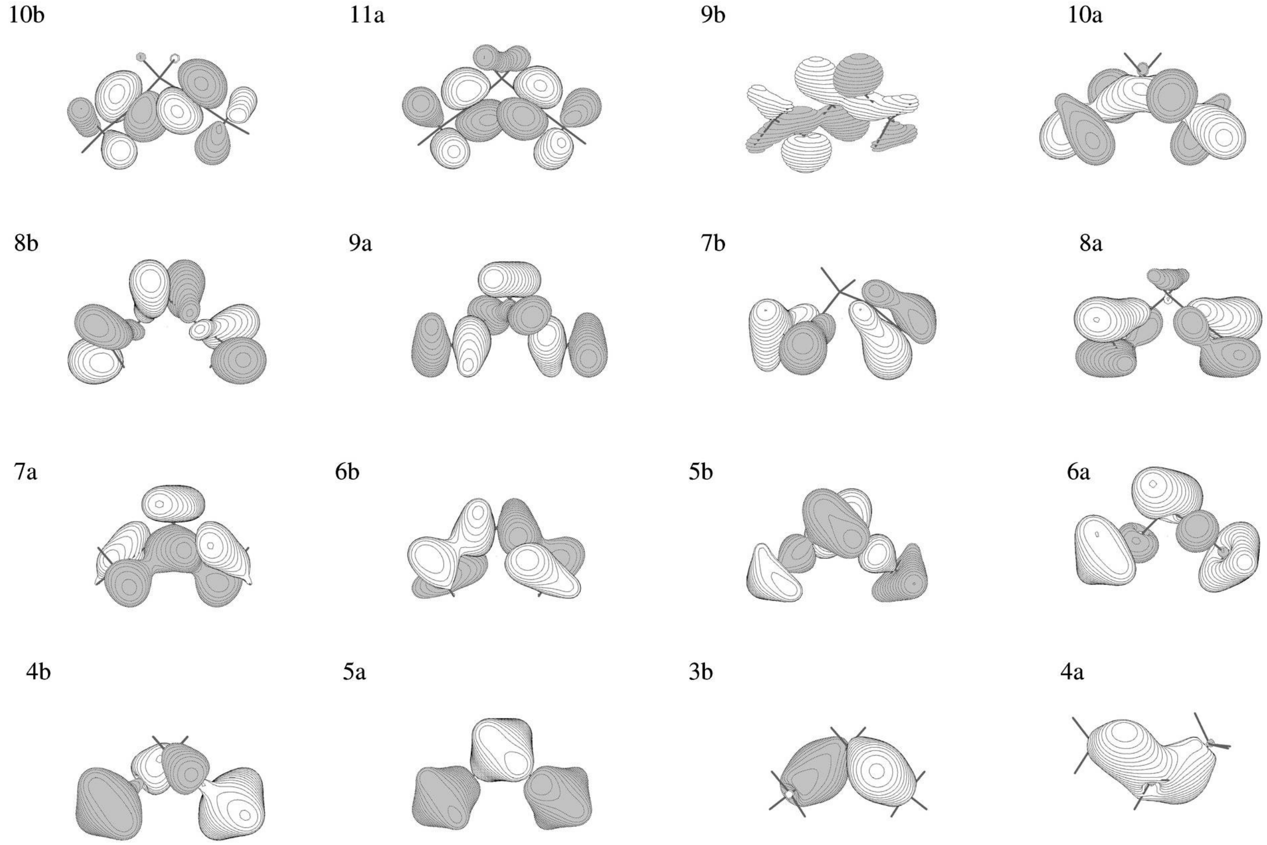

Figure 3. Valence molecular orbitals of the $G^{+}G^{+}$ conformer of dimethoxymethane (B3LYP/aug-cc-pVTZ results, using contour values equal to 0.05.

The obtained HF orbital binding energies overestimate the measured orbital ionization energies by 1.0 to 2.7 eV due to the neglect of electron relaxation and correlation effects. In line with a pioneering second-order Green's Function study of the x-ray photo-ionization spectra of finite oligomer chains converging to polyoxymethylene [70d], a comparison of the HF and ADC(3) results indicate that the relaxation effects are particularly pronounced for the two outermost orbitals (10b, 11a) relating to the two n_{π}(2p)-type oxygen lone pairs (Figure 3), and more limited for the deeper-lying $n_{\sigma}(sp^2)$-type oxygen lone-pairs, because of the greater delocalization of the latter two levels. In contrast with the HF level, all KS orbital energies calculated by the B3LYP functional underestimate the experimental ionization energies by ~3 to ~4 eV. Such severe underestimations are most common with standard exchange-correlation (XC) functionals, essentially because of the too fast decay of the electronic potential at large *r*. Also, the equivalent of Koopman's theorem in Density Functional Theory (Janak's theorem [71]) only strictly holds for the Highest Occupied Molecular Orbital (HOMO). Despite the so-called meta-Koopmans theorem [72] that relates Kohn-Sham orbital energies to *relaxed* ionization energies, we would like to remind, again, that the DFT formalism does not *explicitly* account for final-state configuration interactions leading to the dispersion of the ionization intensity into shake-up processes. At best, the DFT formalism can only *implicitly* account for electronic correlation and relaxation effects, *within the framework of a one-electron (or quasi-particle) picture of ionization*, through a *mapping of Kohn-Sham orbitals onto Dyson orbitals*. The B3LYP functional was certainly not designed to ensure such a mapping. The relationships between standard KS orbitals and ionization processes should therefore always be exploited with the greatest caution (see further).

At the 1p-GF/ADC(3) level, inclusion of diffuse functions results in shifts of the one-electron ionization energies by 0.15 eV to 0.28 eV towards higher electron binding energies (Table 8). The four lone-pair levels at binding energies comprised between 10.6 and 13.2 eV exhibit the strongest dependence to such improvements of the basis set. The most important shift is in particular observed for the line relating to orbital 9b. Similar observations can be made with the B3LYP Kohn-Sham orbital energies. It is worth noting that the calculated pole strengths remain almost constant (Γ_n ~ 0.90 ± 0.01) within the outer-valence region [10-18 eV], and indicate that ionization processes at binding energies comprised between 10 and 18 eV are qualitatively correctly described by the removal of one electron from a specific molecular orbital. In contrast with our work on 1,3-butadiene [18], for which intense shake-up lines were observed among the outermost π-ionization lines, these observations justify a comparison of the *shape* of KS orbital momentum distributions with that derived from *normalized* ADC(3) Dyson orbitals up to the upper edge of the inner-valence region, and a little beyond. The orbital picture of ionization remains indeed also essentially valid for the 6a level at ~20.8 eV [Γ_n=0.84], and to a lesser extent for the 4b level at 22.9 eV [Γ_n =0.50]. This observation provides very strong support to earlier studies [70d, 73] of conformational fingerprints at the top of the C_{2s} inner-valence bands of polyethers, due to hyperconjugation effects.

In contrast with the outer-valence region and latter two levels, both the ADC(3)/cc-pVDZ and ADC(3)/cc-pVDZ++ results point out a complete breakdown of the orbital picture of ionization for the three innermost valence orbitals (5a, 3b and 4a), in the form of a severe dispersion of the ionization intensity over many lines with extremely limited strength, from which no clearly dominant 1h state emerges. In view of the simulations displayed in Figure 2, particularly broad bands are therefore expected at binding energies around ~24, ~32 and ~34 eV.

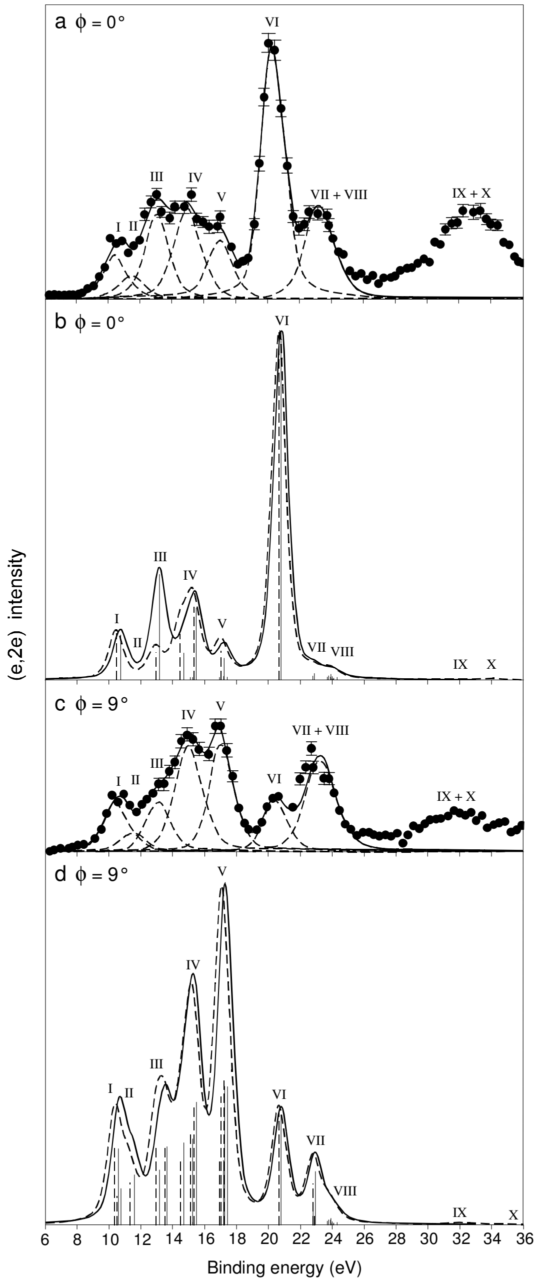

Figure 4. Comparison of the (e,2e) experimental electron binding energy spectrum recorded at azimuthal angles $\phi = 0°$ with theoretical simulations (dashed line : ADC(3)/cc-pVDZ results; solid lines: ADC(3)/cc-pVDZ++ results).

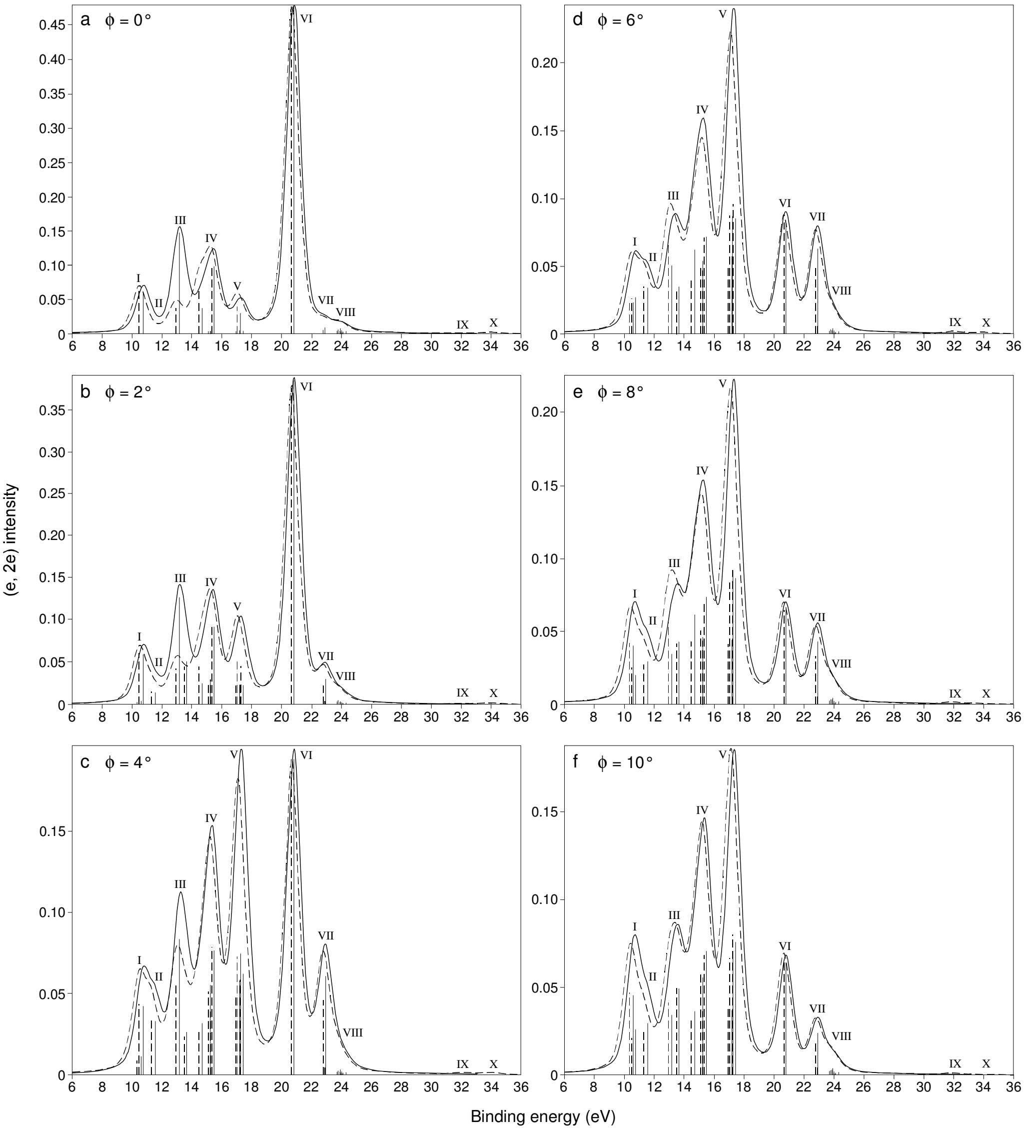

Figure 5. ADC(3) simulation of the dependence of the (e,2e) ionization spectrum of dimethoxymethane (G^+G^+ conformer only, FWHM=1.1 eV). Solid and dashed lines or curves refer to results obtained using the cc-pVDZ++ and cc-pVDZ basis set.

According to a comparison of energies obtained from single-point CCSD(T)/cc-pVDZ calculations upon the neutral and dication, the vertical double ionization threshold of dimethoxymethane in its G^+G^+ conformation lies at ~26.4 eV. All the 2h-1p shake-up states identified above that threshold should thus rather be regarded as approximations to unbound states that lie in the continuum and are thus subject to decay via emission of a second electron. In other words, the identified shake-up states above the double ionization threshold are approximations to *shake-off* resonances. Such states are extremely sensitive to improvements of the basis set, in particular to the inclusion of diffuse functions. This leads to a redistribution of the shake-up ionization intensity over many more lines, of which only a very marginal fraction can be recovered in the present work via the Block-Davidson diagonalization procedure, due to the restriction of the search to lines with a pole strength larger than 0.005. These observations, and likely vibrational complications upon the sudden removal of two electrons, explain the extremely large width (~6 eV) observed for the O_{2s} band in the x-ray-photoelectron spectra of polyoxymethylene, which HF orbital energies [73] or second-order quasi-particle Green's Function ionization energies failed to explain [70d]. A very broad O_{2s} band, extending from ~28 to ~36 eV and possibly beyond, is also seen in the EMS ionization spectra recorded by Neville *et al* [6] on dimethoxymethane (Figure 4).

Prior to proceeding to detailed calculations of electron momentum distributions, it is worth considering simulations (Figures 4, 5) of ionization spectra obtained through EMS experiments upon the G^+G^+ conformer of dimethoxymethane at various azimuthal angles, in order to reliably identify the bands that are best suited for "orbital imaging" the anomeric effect and conformational fingerprints, despite the limited energy resolution reached with such experiments. The simulations displayed for various values of the out-of-plane scattering angle indicate that, at the larger azimuthal angles, five bands (I-V) can be reliably resolved in the outer-valence region of dimethoxymethane. The 6a level (6a) fingerprinting methylenic hyperconjugation [70d] can be individually resolved at all angles, in the form of a very sharp and intense peak at the top of the inner-valence region, around 20.8 eV. The deeper-lying C_{2s} and O_{2s} levels can not be individually resolved, but rather yield broad signals in the experimental spectra, due to the shake-up fragmentation. To be more specific, the band observed at ~23.0 eV in the EMS measurements by Neville *et al.* [6] relates to a complex set of shake-up lines originating from the 4b and 5a inner-valence (C_{2s}) orbitals, whereas the very broad and intense band at binding energies comprised between 28 and 36 eV is ascribed to shake-off states associated to ionization of the innermost (O_{2s}) valence levels.

Because of unfavorable (e,2e) intensities reflecting a p-type electron momentum distribution, some bands (bands II, V and VII) tend to disappear when the azimuthal angle vanishes. These conclusions corroborate the scheme proposed by Neville *et al.* [6] for deconvolving their (e,2e) ionization spectra recorded at an impact energy of 1200 eV under an estimated experimental energy resolution of 1.4 eV (FWHM), using the He I estimates of one-electron binding energies for locating the bands, and Gaussian functions of varying width for optimizing the fit (Figures 4a and c) [68]. Based on these simulations and on the band partition by Neville *et al*, we propose to pursue the discussion of the one-electron ionization bands of dimethoxymethane through simulations of electron momentum distributions for the {10b+11a}, {9b}, {10a+8b}, {9a+7b+8a}, {6b+7a+5b} and {6a} sets of orbitals, ascribed to bands I-VI, respectively [Table 8]. Due to a rather pronounced overlap with the HOMO, the case of orbital 9b relating to band II may be considered rather problematic, since Neville *et al* might have gone beyond the limitations due to the low energy resolution (1.4 eV) of their spectrometer [6]. According to our best calculations and simulations, the 9b orbital lies indeed at ~0.8 eV below the 11a orbital. The corresponding one-electron ionization line emerges nonetheless in the form of a distinct shoulder at ~11.6 eV in the simulation of Figure 4d (FWHM = 1.1 eV), an observation that should hopefully stimulate further EMS studies of dimethoxymethane at improved energy resolutions.

The simulated (e,2e) ionization spectra derived from ADC(3)/cc-pVDZ and ADC(3)/cc-pVDZ++ calculations are displayed as dashed and solid lines, respectively (see Figures 4 and 5). Upon examining these figures in details, it is immediately apparent that our ADC(3)/cc-pVDZ++ simulations are overall in excellent agreement with the available experimental (e,2e) ionization spectra at ϕ = 0° and 9°, which confirms the high quality of the computed ionization energies and cross sections, and demonstrates the relevance of our theoretical analysis so far. It appears that, at large azimuthal angles, diffuse functions have only a moderate impact on the shape and relative intensities of bands. In sharp contrast, it is found that, at ϕ = 0°, the inclusion of diffuse functions in the basis set yields a very strong rise of the (e,2e) ionization intensity characterizing band III at ~13.2 eV encompassing the 10a and 8b ionization channels. By virtue of the confrontation with experiment, this rise may be regarded as a rather direct and irrefutable spectroscopic evidence for the through-space interactions governing the anomeric effect in dimethoxymethane, according to a canonical depiction of the valence electronic structure of this compound. Indeed, this rise is specifically ascribable to the 10a orbital, an ideally delocalized molecular orbital which describes (Figure 3) through-space and through-bond in-phase interactions between the $n_\sigma(sp^2)$-type oxygen lone-pairs via the vicinal C-O bonds. Diffuse functions are obviously required for reliably describing such interactions and orbital mixings at large molecular distances ($r \rightarrow \infty$), and, thus, vanishing electron momenta ($p \rightarrow 0$). Further detailed experimental studies of the electron momentum densities associated to the 10a ionization channel are therefore very strongly encouraged.

D. Electron momentum profiles

Electron momentum distributions for the six identified one-electron valence bands are displayed at various theoretical levels in Figures 6 - 11. The distribution of the area of peak I in the EMS ionization spectra of Neville *et al* (Figures 4a and c) yields, after a conversion of the azimuthal angles ϕ into electron momenta, the experimental momentum density profiles displayed in Figure 6a for the two outermost ionization lines. In each figures, we also display electron momentum distributions for the individual orbital levels. By analogy with atomic orbitals, these profiles can be roughly divided, depending on their symmetry, into two types of electron momentum distributions, referred to as s-type or p-type profiles. In the former case, molecular orbitals belonging to the symmetric representation (a) of the C_2 point group are all characterized by non-vanishing momentum density, i.e. (e,2e) ionization intensity at p ~ (ϕ=0°), which tends to vanish at larger electron momentum (azimuthal angles). In contrast, anti-symmetric (b-type) molecular orbitals produce p-type profiles characterized by vanishing momentum density at p ~ 0. The contribution of the latter orbitals to (e,2e) ionization intensities gradually reaches a maximum at larger azimuthal angles.

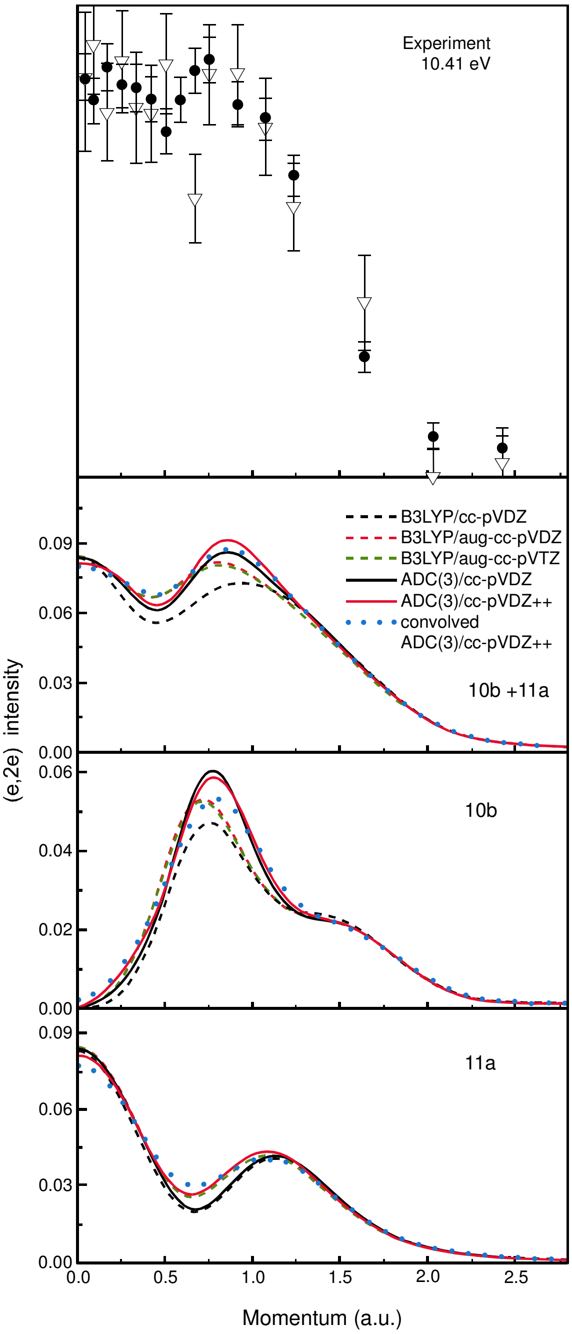

Figure 6. Experimental [6] and theoretical electron momentum distributions associated to band I at 10.41 eV. In the experimental part (top), the empty triangles and solid dots are the momentum distributions inferred from single and multiple-channel measurements by Neville *et al.* [6], respectively.

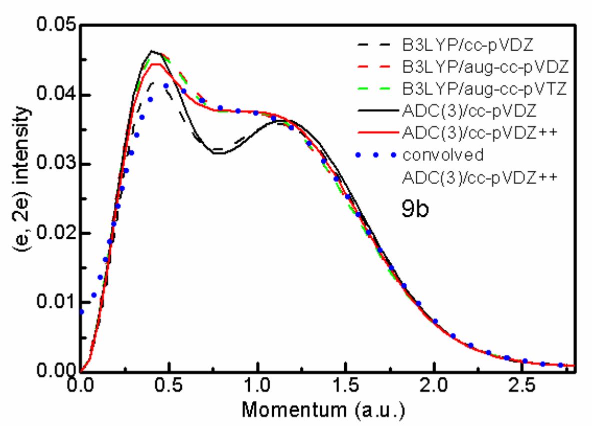

Figure 7. Dyson [ADC(3)] orbital and Kohn-Sham [B3LYP] orbital momentum distributions for orbital 9b, which resides under band II.

Upon examining Figures 6-11, one may reasonably conclude that B3LYP Kohn-Sham orbitals and normalized ADC(3) Dyson orbitals for one-electron ionization bands provide overall qualitatively similar electron momentum distributions. The match is far from being always perfect, however, which leads us to call into question the assertion [72b] that the overlap between normalized Dyson and Kohn-Sham orbitals is most generally very close to 1. The latter statement was drawn from MRSDCI (multireference single double configuration interaction) calculations of Dyson orbitals for diatomic or triatomic molecules (CO, SiO, N_2, P_2, HF, HCl, H_2O, HCN, FCN). Due to the high symmetry point group of most of these molecules, significant alterations of overlap densities due to configurations interactions in the initial and final states are very unlikely. In contrast, the structure on which the present section focuses exhibit a very limited symmetry point group (C_2) that allows many more possibilities for orbital mixing and configuration interactions in the initial and final states. Quantitatively significant differences between Kohn-Sham and normalized ADC(3) Dyson orbital distributions are in particular observed (Figures 6 - 8) for the $n_\pi(2p)$-type and $n_\sigma(sp^2)$-type oxygen lone-pair levels (10b, 10a), due to the strength of electron pair relaxation (PRX) and electron pair removal (PRM) effects [48, 70d, 74], and in the latter case, through-space hyperconjugation interactions. In line with the intricate nodal structure of the related orbitals, indicating strong AO mixing, particularly strong differences are also found within the $C_{2p}+H_{1s}$ outer-valence bands for the 9a+7b+8a levels (Figure 9) defining the fourth set of lines at electron binding energies around ~15 eV.

In many cases, and in particular at the lower electron binding energies, diffuse functions are also found to have an extremely substantial influence on the computed electron momentum profiles. It is worth noticing that the influence of diffuse functions on the calculated s-type electron momentum densities at the origin of momentum space is generally much more limited with the Kohn-Sham momentum distributions, which seems to be a rather obvious consequence of the too fast decay of the B3LYP electronic potential at large distances. Recalling that the cc-pVDZ++ basis set includes s-type and p-type diffuse functions derived from the aug-cc-pVDZ basis set, we also find that B3LYP/aug-cc-pVDZ and B3LYP/aug-cc-pVTZ momentum distributions are all almost identical, which makes us believe that the momentum distributions associated to the ADC(3)/cc-pVDZ++ Dyson orbitals should also be close to convergence with respect to further improvements of the basis set.

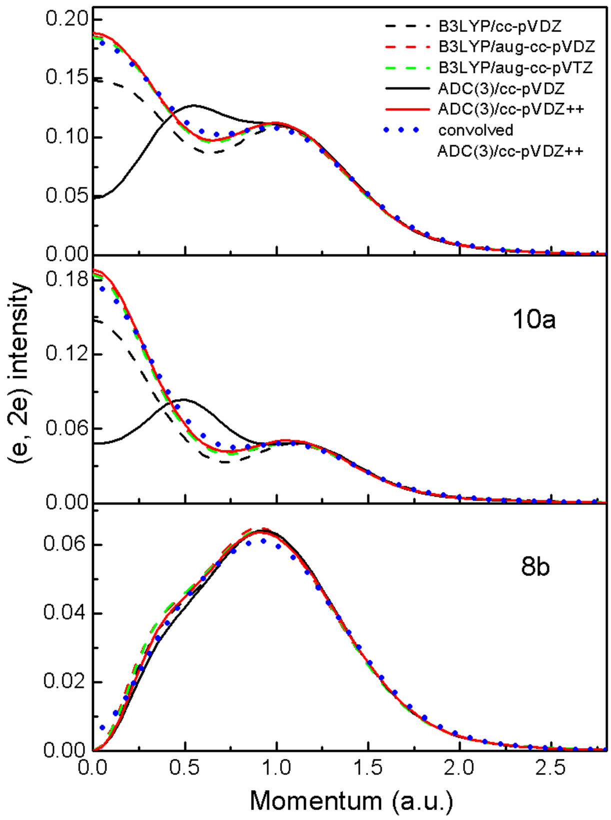

Figure 8. Dyson [ADC(3)] orbital and Kohn-Sham [B3LYP] electron momentum distributions for band III, encompassing the contributions of orbitals 10a and 8b, along with the individual orbital contributions.

Figures 6 – 11 also provide evidences for the rather substantial influence of the limited momentum resolution (0.1 a.u.) of standard (e, 2e) spectrometers on the apparent orbital shapes and spreads. The main outcome of resolution folding is overall a smoothening and flattening of the ADC(3)/cc-pVDZ++ momentum density profiles, in the form of a transfer of the (e, 2e) ionization intensity from maxima to minima in the momentum distributions. The effect is particularly pronounced for orbitals 10b, 9b, 9a, 6b (Figures 6, 7, 9, 10, respectively). For these levels, it is comparable to the influence of the basis set and/or correlation treatment.

In agreement with experiment, all model predicts a mixed s-p-type momentum profile for the outermost band (I) at ~10.4 eV (Figure 6). Such a profile is very typical of a set of lines comprising one symmetric orbital (11a) and one asymmetric orbital (10b). Compared with the B3LYP/aug-cc-pVDZ or B3LYP/aug-cc-pVTZ results, the ADC(3)/cc-pVDZ++ theoretical momentum distribution provides a slightly superior description of the relative intensity and position of the two maxima seen in the measured distribution. Indeed, at the B3LYP level, the extremum at p ~ 0 a.u. is found to exhibit the largest (e,2e) cross sections at the B3LYP level, whereas the largest (e,2e) cross sections are seen for the extremum at p ~ 0.88 a.u. and p ~ 0.73 a.u. in the ADC(3) simulations and in the most reliable (multichannel) measurements by Neville *et al*, respectively. For these levels, the KS momentum densities at non-vanishing momenta are more sensitive to the inclusion of diffuse functions than the Dyson counterpart. A shoulder at p ~ 1.49 a.u. also characterizes the 10b theoretical momentum distribution, whereas for the 11a one a maximum is found at p ~ 1.08 a.u. Taking into account the randomization of (e,2e) ionization cross sections over all molecular orientations, these additional features reflect in both cases further confinements of the electron density at small values of r by several nodal surfaces across or along the O-C(H_3) bonds, in agreement with the molecular orbital topologies of Figure 3.

The EMS momentum distribution related to band II and orbital 9b at ~11.3 eV (Figure 7) is a p-type profile characterized by two main components at p ~ 0.43 a.u. and at p ~ 1.17 a.u. Here, again, the enhancement of the electron densities at large electron momenta reflects the presence of multiple nodal surfaces across the C-O-C-O-C backbone. The effect of the confinement is more limited when diffuse functions are incorporated in the basis set. Indeed, two sharp maxima are seen in the 9b momentum distributions computed using the cc-pVDZ basis set, whereas a broad shoulder is seen at p ~ 1.0 a.u in the profiles predicted at the ADC(3)/cc-pVDZ++ or B3LYP/aug-cc-pVTZ levels.

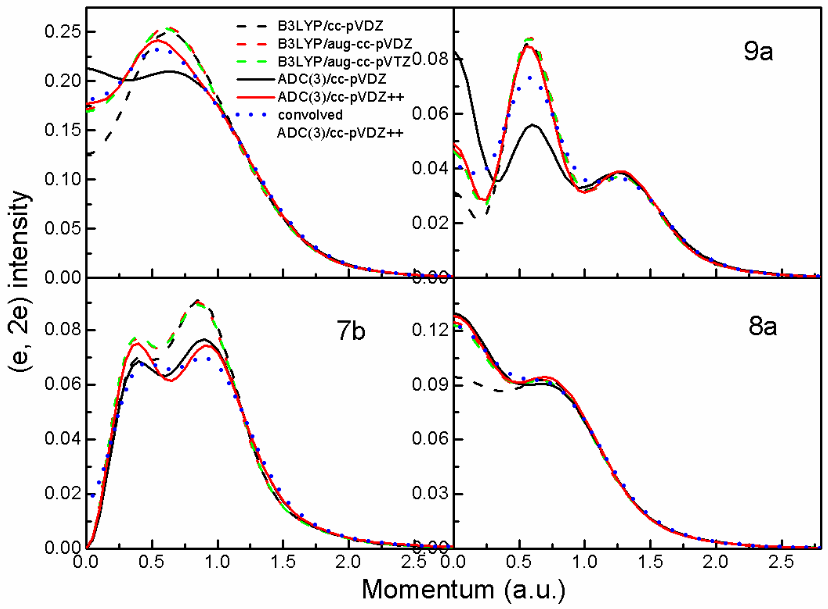

Figure 9. Dyson [ADC(3)] orbital and Kohn-Sham [B3LYP] electron momentum distributions for band IV, encompassing the contributions of orbitals 9a, 7b and 8a, along with the individual orbital contributions.

Theoretical momentum profiles for the peak (III) at ~13.3 eV that has been ascribed to the 10a and 8b orbitals are presented in Figure 8. The statement that diffuse functions play an essential role in accurate computations of orbital densities at low electron momenta is particularly true for orbital 10a (Figure 8). These computations corroborate our analysis of the intensity characterizing the $n_{\sigma}(sp^2)$ signal at ~13.2 eV in the experimental (e,2e) spectrum measured at ϕ=0°, and confirms therefore our suggestion that momentum distributions very specifically fingerprint the outcome of through-bond and through-space orbital interactions due to the anomeric effect at these electron binding energies. Whereas the ADC(3)/cc-pVDZ results clearly failed to provide reliable insights into the available (e,2e) intensities for the 10a ionization channel, the B3LYP/cc-pVDZ and ADC(3)/cc-pVDZ++ momentum distributions are rather similar. This observations provide support to our suggestion that the overall great successes of Density Functional Theory in modeling the results of EMS experiments may be due to a cancellation of errors due, among others, to basis set limitations, the too rapid decay of the electronic potential at large molecular distances and, last but not least, the neglect of electronic relaxation effects with standard functionals such as B3LYP.

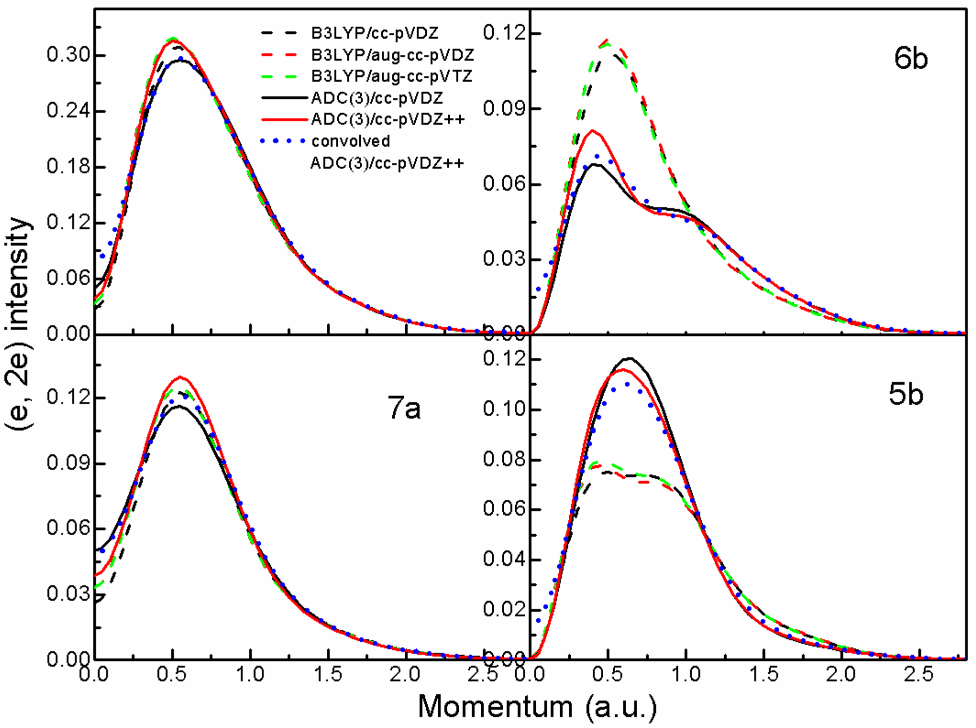

Figure 10. Dyson [ADC(3)] orbital and Kohn-Sham [B3LYP] electron momentum distributions for band V, encompassing the contributions of orbitals 6b, 7a and 5b, along with the individual orbital contributions.

The shape of the momentum distribution calculated for the band (IV) at ~15.1 eV by summing the contributions from the 9a, 7a and 8a orbitals (Figure 9) also strongly vary, depending on the presence or not of diffuse functions in the basis set. Without diffuse functions, very significant differences are observed between the total and individual B3LYP Kohn-Sham and ADC(3) Dyson orbital momentum distributions. Despite the intricate appearance of the individual orbital momentum distributions, these distributions almost converge to the same profile when diffuse functions are incorporated. This profile exhibits then a shallow minimum at p ~ 0 a.u., and a single maximum at p ~ 0.53 a.u. The 8a and 7b momentum distributions exhibit both *two* main components. Besides the maxima that are normally expected for a s-type or p-type profile, the excess component at large *p* values indicates in both cases extra confinement by *one* symmetrically non-redundant nodal surface that coincides with the O-CH_3 bonds. The individual momentum distribution for the 9a orbital consists of *three* main components at *p* ~ 0.00, ~0.56, and ~1.28 a.u., which in turn indicates also a very intricate orbital topology. By virtue of spherical averaging, the latter two maxima may here be very logically ascribed to the presence of *two* symmetrically non-redundant nodal surfaces, a first one across the O-C(H_2) bond, the second one across the O-C(H_3) bond.

Due to the more limited number of nodal surfaces, the appearance of the individual orbital momentum distributions simplifies (Figure 10) when reaching the bottom of the outer-valence region, defined by the band (V) at ~17.1 eV which finds its origin into ionization of the 6b, 7a and 5b orbitals. The predominance of b-type orbitals at these electron binding energies explains the p-type profile for the summed momentum distributions. Also, the 7a orbital is characterized by one nodal surface that follows the C-O-C-O-C backbone, which explains that the corresponding (e,2e) spherically averaged ionization cross sections almost vanish at zero momenta, despite the symmetry of the orbital. Comparison of the momentum distributions associated to the 6b and 5b orbitals seems to indicate a reversal of the energy order for the corresponding one-electron ionization channels at the B3LYP and ADC(3) levels. More specifically, due to the non-crossing rule between orbitals or wavefunctions belonging to the same irreducible representation of a given symmetry point group [74], very strong AO mixing between the two former levels is expected, with regards to an energy interval of only ~0.3 eV. Compared with the outermost momentum distributions, the differences observed among the various models for the total momentum density associated to band V are very limited.

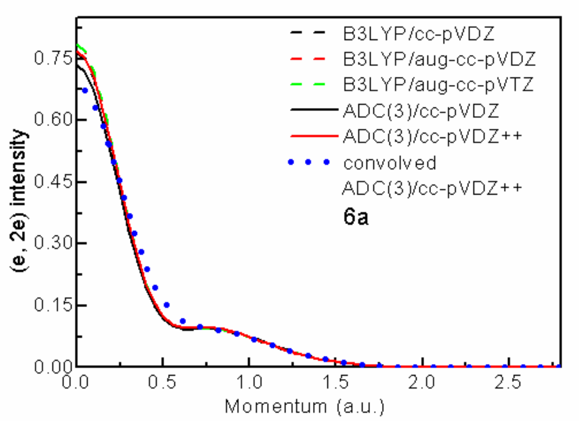

Figure 11. Dyson [ADC(3)] orbital and Kohn-Sham [B3LYP] orbital momentum distributions for orbital 6a, associated to band VI.

In line with the latter remark, we observe (Figure 11) an almost perfect agreement between the various predictions made for the 6a level marking the top of the inner-valence C_{2s} band at ~20.6 eV. Besides a maximum in the related (e,2e) ionization intensity at *p* ~ 0.00 a.u., due to the a-symmetry of the orbital, a broader component seen at *p* ~ 0.74 a.u. can be related to the confinement of the electron density by a nodal surface that approximately follows the C-O-C-O-C backbone. Beyond this point, the orbital picture of ionization is no longer strictly valid, as shake-up processes come into play.

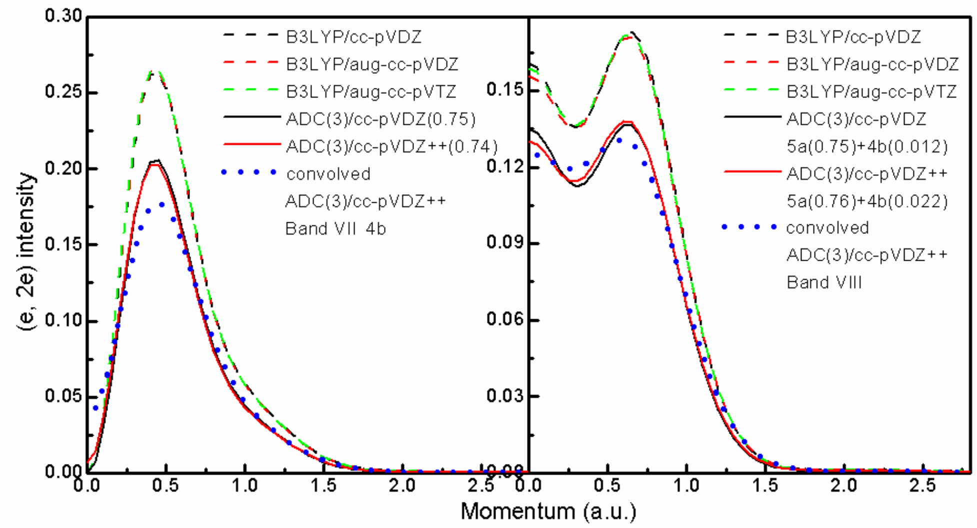

Figure 12. Unnormalized Dyson [ADC(3)] orbital and normalized Kohn-Sham [B3LYP] orbital momentum distributions for bands VII and VIII, using at the ADC(3) level the results obtained for the associated shake-up lines.

For the sake of completeness, we nonetheless provide in Figure 12 the results of our calculations for the innermost C_{2s} bands (VII, VIII) at ~22.8 and ~23.9 eV ascribed to shake-up lines from the 4b and 5a orbitals, and obtained by summing at the ADC(3) level the momentum distributions recovered from the *un-normalized* Dyson orbitals for each identified shake-up line at these binding energies (the employed total pole strength being then given in bracket). Except for the loss of ionization intensity in further unidentified shake-up processes that should contribute to a correlation tail at much higher binding energies [75], it is clear that the B3LYP Kohn-Sham orbitals and the ADC(3) Dyson orbitals lead to almost equal momentum distributions. This observation is in phase with the idea that shake-up states “borrow” their intensity to specific one-electron levels. In this energy region, diffuse functions have no influence at all on the computed electron momentum distributions, reflecting the strongly localized nature of these levels. Besides the maximum at p ~ 0.0 a.u. due to the symmetry of the 5a orbital, a second maximum at ~0.62 a.u.(ADC(3)/cc-pVDZ++ result) is seen in the momentum distribution for band VIII. This feature can be explained by the delocalization of the orbital around all three carbons and by the presence of a single nodal surface that crosses twice the C-O-C-O-C backbone. In contrast, orbital 4b merely localizes around the end methyl groups, and a simple p-type profile is correspondingly computed for band VII.

4.2.4 Conclusions

A thorough theoretical study of the molecular structure, conformational equilibrium in the gas phase, ionization spectrum and related Dyson orbital momentum distributions of dimethoxymethane has been presented, in order to establish once and for all the theoretical guidelines that should be followed for interpreting experiments on conformationally versatile molecules employing electron momentum spectroscopy. To carry out reliable enough analyses of such experiments, one should necessarily and systematically proceed through (1) a determination of relative conformer energies within an accuracy of a few tenths kJ/mol, on the basis of large scale many-body quantum mechanical treatments; (2) an evaluation of the conformer abundances within a few % accuracy, by means of statistical thermodynamics beyond the Rigid-Rotor/Harmonic-Oscillators (RRHO) approximation; (3) a simulation of the valence ionization spectrum, within an accuracy of a few tenths of an eV, and a computation of the related transition moments for the main conformers, taking into account the dispersion of the ionization intensity over secondary shake-up states; and, at last, (d) a computation of spherically averaged electron momentum distributions for each identified ionization channels or resolvable bands, taking into account the fact that the molecular conformation may have a very strong influence on the orbital energies, and ionization bands therefore [18, 70].

In the present work, these goals have been achieved by using (1) the principles of a Focal Point Analysis of energy differences computed at various [HF, MP2, MP3, CCSD and CCSD(T)] levels and supplemented by appropriate extrapolations to the limit of an asymptotically complete basis set; (2) the protocol by Ayala and Schegel [60] for treating the internal rotation modes; (3) one-particle Green's function theory along with the ADC(3) scheme for computing one-electron and 2h-1p shake-up ionization energies along with the related transition moments; and (4) an adaptation of the MOMAP methodology by Brion *et al* [67] for Fourier Transforming to momentum space and spherically averaging the related Dyson orbitals, taking into account the finite angular resolution of the (e,2e) spectrometers for convolving the momentum distributions.

The main conclusions drawn from these calculations are the following. (1) According to our best estimates, the G^+G^+, TG, G^+G^- and TT conformers of dimethoxymethane have, at 0K and regardless of zero-point vibrational effects, relative energies equal to 0.00, 10.88, 16.08 and 23.64 kJ/mol, respectively. (2) At room temperature, these energy differences and Gibb's free energy corrections yield correspondingly molar fractions equal to 0.959, 0.026, 0.015 and 0.000. (3) A confrontation with available high resolution photoelectron measurements corroborates the finding that only one conformer (G^+G^+) dominates at room temperature in the gas phase. Also, a comparison with available (e,2e) ionization spectra enables us to identify specific fingerprints of through-space orbital interactions associated with the anomeric effect, an observation which should motivate detailed experimental studies of electron momentum distributions throughout the outer-valence region and beyond. The one-electron picture of ionization remains indeed valid up to electron binding energies of ~22 eV. (4) At last, very significant differences have been noted in several cases between momentum distributions computed using the ADC(3) Dyson orbitals or the Kohn-Sham orbitals correspondingly derived from DFT calculations employing the B3LYP functional. These discrepancies and a significantly different dependence towards the presence of diffuse functions in the basis set reflect on the one hand well-known shortcomings of this functional in the asymptotic region (see refs. 4l, 4o and references therein), and on the other hand the fact that the low symmetry (C_2) of the molecule in its G^+G^+ conformation enables strong orbital mixing and opens many possibilities for configuration interactions in the ground (neutral) and final (cationic) states.

Therefore, besides recommending ADC(3) for quantitatively deciphering highly congested ionization spectra, this work advocates a systematic use of ADC(3) Dyson orbitals in further analyses of EMS experiments, in order to safely identify complications such as variations of the molecular conformation [8], distorted wave effects [76], nuclear dynamics [3p], or a dispersion of the ionization intensities into shake-up processes [4, 5, 8, 18, 77].

References

[1] (a) McCarthy, I. E.; Weigold, E. *Rep. Prog. Phys.* 1991, 54, 789. (b) Coplan, M. A.; Moore, J. H.; Doering, J. P. *Rev. Mod. Phys*. 1994, 66, 985. (c)Weigold, E.; McCarthy, I. E. *Electron Momentum Spectroscopy*; Kluwer Academic Plenum Publishers: New York, 1999. (d) McCarthy I. E.; Weigold, E. *Rep. Prog. Phys.* 1988, 51, 299.

[2] (a) Braidwood, S. W.; Brunger, M. J.; Konovalov, D. A.; Weigold, E. *J. Phys. B* 1993, 26, 1655. (b) Rolke, J.; Cann, N.; Zheng, Y.; Hollebone, B. P.; Brion, C. E.; Wang, Y. A.; Davidson, E. R. *Chem. Phys*. 1995, 201,1. (c) Duffy, P. *Can. J. Phys.* 1996, 74, 763. (d) Rolke, J.; Brion, C. E.; *Chem. Phys*. 1996, 207, 173. (e) Rolke, J.; Zheng, Y.; Brion, C. E.; Shi, Z.; Wolfe, S.; Davidson, E. R. *Chem. Phys*. 1999, 244, 1. (f) Zheng, Y.; Pang, W. N.; Shang, R. C.; Chen, X. J.; Brion, C. E.; Ghanty, T. K.; Davidson, E. R. *J. Chem. Phys*. 1999, 111, 9526.

[3] (a) Fuss, I.; McCarthy, I. E.; Minchington, A.; Weigold, E.; Larkins, F. P. *Chem. Phys*. 1981, 63, 19. (b) Weigold, E.; Zheng, Y.; von Niessen, W. *Chem. Phys*. 1991, 150, 405. (c) Rolke, J.; Brion, C. E.; Cahravorty, S. J.; Davidson, E. R.; McCarthy, I. E. *Chem. Phys.* 1997, 215, 191. (d) Vos, M.; Canney, S. A.; McCarthy, I. E.; Utteridge, S.; Michaelwicz, M. T.; Weigolf, E. *Phys. Rev. B* 1997, 56, 1309. (e) Takahashi, M.; Otsuka, K.; Udagawa, Y. *Chem. Phys*. 1998, 227, 375. (f) Takahashi, M.; Ogino, R.; Udagawa, Y. *Chem. Phys. Lett.* 1998, 288, 821. (g) Takahashi, M.; Ogino, T.; Udagawa, Y. *Chem. Phys. Lett.* 1998, 288, 714. (h) Adcock, W.; Brunger, M. J.; McCarthy, I. E.; Michlewicz, M. T.; von Niessen, W.; Wang, F.; Weigold, E.; Winkler, D. A. *J. Am. Chem. Soc.* 2000, 122, 3892. (i) Chen, X. J.; Jia, C. C.; Xu, C.K.; Ouyang, G.; Peng, L. L.; Tian, S. X.; Xu, K. Z. *Chem. Phys. Lett.* 2000, 319, 76. (j) Litvinyuk, I. V.; Zheng, Y.; Brion, C. E. *Chem. Phys.* 2000, 253, 41. (k) Litvinyuk, I. V.; Zheng, Y.; Brion, C.E.; *Chem. Phys.* 2000, 261, 289. (l) Deng, J. K.; Li, G. Q.; He, Y.; Huang, J. D.; Deng, H.; Wang, X. D.; Wang, F.; Zhang, Y. A.; Ning, C. G.; Gao, N. F.; Wang, Y.; Chen, X. J.; Zheng, Y. J. *Chem. Phys.* 2001, 114, 882. (m) Litvinyuk, I. V.; Young, J. B.; Zheng, Y.; Cooper, G.; Brion, C. E. *Chem. Phys.* 2001, 263, 195. (n) Tixier, S.; Shapley, W. A.; Zheng, Y.; Chong, D. P.; Brion, C. E.; Shi, Z.; Wolfe, S. *Chem. Phys.* 2001, 270, 263. (o) Knippenberg, S.; Nixon, K. L.; Brunger, M. J.; Maddern, T.; Campbell, L.; Trout, N.;Wang, F.; Newell, W. R.; Deleuze, M. S.; François, J.-P.; Winkler, D. A. *J. Chem. Phys.* 2004, 121, 10525. (p) Knippenberg, S.; Deleuze, M. S.; Cleij, T. J.; François, J.-P.; Cederbaum, L. S.; Eland, J. H. D. *J. Phys. Chem. A* 2005, 109, 4267.

[4] (a) Cederbaum, L. S. *J. Phys. B* 1975, 8, 290. (b) Cederbaum, L. S. *J. Chem. Phys*. 1975, 62, 2160. (c) Cederbaum, L. S.; Domcke, W.; Schirmer, J.; von Niessen, W.; Diercksen, G. H. F.; Kraemer, W. P. *J. Chem. Phys.* 1978, *69*, 1591. (d) Cederbaum, L. S.; Domcke, W.; Schirmer, J.; von Niessen, W. *Adv. Chem. Phys.* 1986, 65, 115. (e) Deleuze, M. S.; Cederbaum, L. S. *Int. J. Quantum Chem.* 1997, 63, 465. (f) Deleuze, M. S.; Giuffreda, M. G.; François, J.-P.; Cederbaum, L. S. *J. Chem. Phys.* 1999, 111, 5851. (g) Deleuze, M. S.; Cederbaum, L. S. *Adv. Quantum. Chem.* 1999, 35, 77. (h) Deleuze, M. S.; Giuffreda, M. G.; François, J.-P.; Cederbaum, L. S.; *J. Chem. Phys.* 2000, 112, 5325. (i) Deleuze, M. S.; Giuffreda, M. G.; François, J.-P. *J. Phys. Chem. A* 2002, 106, 5626. (j) Deleuze, M. S.; Trofimov, A. B.; Cederbaum, L. S. *J. Chem. Phys.* 2001, 115, 5859. (k) Deleuze, M. S. *J. Chem. Phys.* 2002, 116, 7012. (l) Deleuze, M. S. *J. Phys. Chem. A* 2004, 108, 9244. (m) Potts, A. W.; Holland, D. M. P.; Trofimov, A. B.; Schirmer, J.; Karlsson, L.; Siegbahn, K.; *J. Phys. B: At. Mol. Opt. Phys.* 2003, 36, 3129. (n) Kishimoto, N.; Hagihara, Y.; Ohno, K.; Knippenberg, S.; François, J.-P.; Deleuze, M. S.; *J. Phys. Chem. A* 2005, 109, 10535. (o) Deleuze, M. S. *Chem. Phys.* 2006, 329, 22. (p) Potts, A. W.; Edvardson, D.; Karlsson, L.; Holland, D. M. P.; MacDonald, M. A.; Hayes, M. A.; Maripuu, R.; Siegbahn. K.; von Niessen, W. *Chem. Phys.* 2000, 254, 385. (q) Trofimov, A. B.; Schirmer, J.; Holland, D. M. P.; Karlsson, L.; Maripuu, R.;

Siegbahn, K.; Potts, A. W. *Chem. Phys.* 2001, 263, 167. (r) Potts, A. W.; Trofimov, A. B.; Schirmer, J.; Holland, D. M. P.; Karlsson, L. *Chem. Phys.* 2001, 271, 337. (s) Trofimov, A. B.; Schirmer, J.; Holland, D. M. P.; Potts, A. W.; Karlsson, L.; Maripuu, R.; Siegbahn, K. *J. Phys. B* 2002, 35, 5051.

[5] Knippenberg, S.; François, J.-P.; Deleuze, M. S. *J. Comput. Chem*. 2006, 27, 1703.

[6] Neville, J. J.; Zheng, Y.; Hollebone, B. P.; Cann, N. M.; Brion, C. E.; Kim, C.-K.; Wolfe, S. *Can. J. Phys*. 1996, 74, 773.

[7] Neville, J. J.; Zheng, Y.; Brion, C. E. *J. Am. Chem. Soc*. 1996, 118, 10553.

[8] Deleuze, M. S.; Pang, W. N.; Salam, A.; Shang, R. C. *J. Am. Chem. Soc*. 2001, 123, 4049.

[9] Pang, W. N.; Gao, J. F.; Ruan, C. J.; Shang, R. C.; Trofimov, A. B.; Deleuze, M. S. *J. Chem. Phys*. 2000, 112, 8043.

[10] Pang, W. N.; Shang, R. C.; Gao, J. F.; Gao, N. F.; Chen, X. J.; Deleuze, M. S. *Chem. Phys. Lett.* 1998, 296, 605.

[11] McQuarrie, D. A. *Statistical Mechanics*; Harper and Row: New-York, 1976.

[12] Linderberg, J.; Öhrn, Y. *Propagators in Quantum Chemistry*, Wiley: Hoboken, New-Jersey, 2004.

[13] Cederbaum, L. S.; Domcke, W. *Adv. Chem. Phys.* 1977, 36, 205.

[14] Öhrn, Y.; Born, G. *Adv. Quantum Chem.* 1981, 13, 1.

[15] von Niessen, W.; Schirmer, J.; Cederbaum, L. S. *Comput. Phys. Rep.* 1984, 1, 57.

[16] Ortiz, J. V. *Computational Chemistry: Reviews of Current Trends*; Leszczynski, J., Ed.; World Scientific: Singapore, 1997; Vol. 2 p. 1.

[17] (a) Schirmer, J.; Cederbaum, L. S.;Walter, O. *Phys. Rev. A* 1983, 28, 1237. (b) Schirmer, J.; Angonoa, G. *J. Chem. Phys.* 1989, 91, 1754. (c) Weikert, H.-G.; Meyer, H.-D.; Cederbaum, L. S.; Tarantelli, F. *J. Chem. Phys*. 1996, 104, 7122.

[18] Deleuze, M. S.; Knippenberg, S. *J. Chem. Phys*. 2006, 125, 104309.

[19] Saha, S.; Wang, F.; Falzon, C. T.; Brunger, M. J. *J. Chem. Phys.* 2005, 123, 124315.

[20] Brunger, M. J.; Winkler, D. A.; Michalewicz, M.T.; Weigold, E. *J. Chem. Phys*. 1998, 108, 1859.

[21] (a) Burkert, U.; Allinger N. L., *Molecular Mechanics*, A.C.S. Monograph: Washington, DC, 1982; Vol. 177 (b) Eliel, E. L.; Allinger, N. L.; Angyal, S. J. *Conformational Analysis*; Interscience Publishers: New-York, 1967.

[22] Kneisler, J. R.; Allinger, N. L. *J. Comput. Chem*. 1996, 17, 757.

[23] Venkatesan, V.; Sundararajan, K.; Sankaran, K.; Viswanathan, K. S. *Spectrochim. Acta part A* 2002, 58, 467.

[24] Wiberg, K. B.; Murcko, M. A. *J. Am. Chem. Soc.* 1989, 111, 4821.

[25] Deslongchamps, P. *Stereoelectronic Effects in Organic Chemistr;,* Pergamon Press: Oxford, 1983.

[26] Kirby, A. J.: *The Anomeric Effects and Related Stereoelectronic Effects at Oxygen;* Springer-Verlag: Berlin, 1983.

[27] Werstiuk, N. H.; Laidig, K. E.; Ma, J. *Application of Quantum Theory of Atoms in Molecules to Study of Anomeric Effect in Dimethoxymethane*, *ACS Symp. Series* 1993, *539*, 176.

[28] Trapp, M. L.; Watts, J. K.; Weinberg, N.; Pinto, B. M. *Can. J. Chem*. 2006, 84, 692.

[29] Smith, G. D.; Jaffe, R. L.; Yoon, D. Y. *J. Phys. Chem.* 1994, 98, 9072.

[30] Lemieux, R. U. in *Molecular rearrangements*; de Mayo, P., Ed.; Wiley: New York 1964; Vol. 2, p. 709.

[31] Edward, J. T. *Chem. Ind. (London)*, 1955, 1102.

[32] Aoki, K. *J. Chem. Soc. Japan* 1953, 74, 110.

[33] (a) Astrup, E. E. *Acta Chem. Scand.* 1971, 25, 1494; (b) Astrup, E. E.; *Acta Chem. Scand.* 1973, 27, 3271.

[34] Abe, A.; Inomata, K.; Tanisawa, E.; Ando, I. *J. Mol. Struct*. 1990, 238, 315.

[35] Yokoyama, Y.; Ohashi, Y. *Bull. Chem. Soc. Japan*, 1999, 72, 2183.

[36] (a) Favero, L. B.; Caminati, W.; Velino, B. *Phys. Chem. Chem. Phys*. 2003, 5, 4776; (b) Kavitha, V.; Sundararajan, K.; Viswanathan, K. S. *J. Phys. Chem.* A 2005, 109, 9259.

[37] Schwarz, W. H. E. *Ang. Chem.* 2006, 45, 1508.

[38] Jørgensen, F. S. *J. Chem. Res. (S)* 1981, 212.

[39] Jeffrey, G. A.; Pople, J. A.; Binkley, J. S.; Vishveshwara, S. *J. Am. Chem. Soc.* 1978, 100, 373.

[40] Tvaroska, I.; Bleha, T. *J. Mol. Struct.* 1975, 24, 249.

[41] Wolfe, S.; Whangbo, M.-H.; Mitchell, D. *J. Carbohydr. Res.* 1979, 69, 1.

[42] (a) Schäfer, L.; Van Alsenoy, C.; Williams, J. O.; Scarsdale, J. N.; Geise, H. J. *THEOCHEM* 1981, 76, 349; (b) Williams, J. O.; Van Alsenoy, C.; Schäfer, L. *THEOCHEM* 1981, 76, 109.

[43] (a) Lee, C.; Yang, W.; Parr, R. G. *Phys. Rev. B* 1998, 37, 785.; (b) Becke, A. D. *J. Chem. Phys.* 1993, 98, 5648.

[44] Allinger, N. L.; Fermann, J. T.; Allen, W. D.; Schaefer III, H. F. *J. Chem. Phys.* 1997, 106, 5143.

[45] Salam A.; Deleuze, M. S. *J. Chem. Phys.* 2002, 116, 1296.

[46] Kwasniewski, S. P.; Claes, L.; François, J.-P.; Deleuze, M. S. *J. Chem. Phys.* 2003, 118, 7823.

[47] Deleuze, M. S.; Claes, L.; Kryachko, E. S.; François, J.-P. *J. Chem. Phys*. 2003, 106, 8569.

[48] Szabo, A.; Ostlund, N. S. *Modern Quantum Chemistry;* McGraw Hill: New York, 1982.

[49] Scuseria, G. E.; Lee, T. J. *J. Chem. Phys.* 1990, 93, 5851.

[50] (a) Purvis, G. D.; Bartlett, R. J. *J. Chem. Phys.* 1982, 76, 1910. (b) Scuseria, G. E.; Janssen, C. L.; Schaefer III, H. F. *J. Chem. Phys.* 1988, 89, 7382. (c) Raghavachari, K.; Trucks, G. W.; Head-Gordon, M.; Pople, J. A. *Chem. Phys. Lett.* 1989, 157, 479. (d) Bartlett, R. J. *J. Phys. Chem.* 1989, 93, 1697.

[51] (a) Pitzer, K. S.; Gwinn, W. D. *J. Chem. Phys*. 1942, 10, 428. (b) Li, C. M.; Pitzer, K. S. *J. Phys. Chem.* 1956, 60, 466. (c) Truhlar, D. G. *J. Comput. Chem.* 1991, 12, 266. (d) Chung-Philipps, A. *J. Comput. Chem.* 1992, 13, 874. (e) Hu, W. P.; Truhlar, D. G. *J. Am. Chem. Soc.* 1994, 116, 7797. (f) Corchado, J. C.; Espinogarcia, J.; Hu, W. P.; Truhlar, D.G. *J. Phys. Chem*. 1995, 99, 687. (g) Heuts, J. P. A.; Gilbert, R. G.; Radom, L. *J. Phys. Chem.* 1996, 100, 18997. (h) Hu, W. P.; Truhlar, D. G. J. *Am. Chem. Soc*. 1996, 118, 860. (i) McClurg, R. B.; Flagan, R. C.; Goddard, W. A. *J. Chem. Phys.* 1997, 106, 6675.

[52] (a) Pickup, B. T. *Chem. Phys.* 1977, 19, 193. (b) Mc Weeny, R.; Pickup, B. T. *Rep. Progr. Phys*. 1980, 43, 1065. (c) Őhrn, Y.; Born, G. *Adv. Quantum Chem*. 1981, 13, 1. (d) Deleuze, M.; Pickup, B. T.; Delhalle, *J. Mol. Phys*. 1994, 83, 655. (e) Seabra, G. M.; Kaplan, I. G.; Zakrzewski, V. G.; Ortiz, J. V. *J. Chem. Phys.* 2004, 121, 4142. (f) Ning, C. G.; Ren, X. G.; Deng, J. K.; Su, G. L.; Zhang, S. F.; Knippenberg, S. and Deleuze, M. S. *Chem. Phys. Lett.* 2006, 421, 52.

[53] (a) Dunning, T. H. Jr. *J. Chem. Phys.* 1989, 90, 1007; (b) Kendall, R. A.; Dunning, T. H.; Harrisson, R. J. *J. Chem. Phys.* 1992, 96, 6796.

[54] (a) Feller, D. *J. Chem. Phys.* 1992, 96, 6104. (b) Feller, D. *J. Chem. Phys.* 1993, 98, 7059.

[55] Martin, J. M. L.; *Ab Initio Thermochemistry Beyond Chemical Accuracy for First- and Second-Row Compounds*, in NATO ASI Symposium volume *Energetics of Stable Molecules and Reactive Intermediates*; Mirrasda Piedade, M. E. and Irikura, K. K, Eds.; Kluwer: Dordrecht, The Netherlands, 1999.

[56] Schwartz, C. *Estimating Convergence Rates of Variational Calculations,* in *Methods in Computational Physics 2*, B. J. Alder, Ed.; Academic Press: New York, 1963.

[57] (a) Van Orden, A.; Saykally, R. T. *Chem. Rev*. 1998, 98, 2313; (b) Martin, J. M. L.; Taylor, P. R. *J. Phys. Chem*. 1996, 100, 6047.

[58] (a) Martin, J. M. L.; Parthiban, S. In: *Quantum Mechanical Prediction of Thermochemical Data*, ed. Cioslowski, J. and Szareka, A.; *Understanding Chemical Reactivity Series*, Vol. 22; Kluwer: Dordrecht, The Netherlands, 2001, chapter 2, p 31-65; (b) Parthiban, S.; Martin, J. M. L. *J. Chem. Phys*. 2001, 115, 2051.

[59] (a) Martin, J. M. L.; François, J.-P.; Gijbels, R.; Almlöf, *J. Chem. Phys. Lett.* 1991, 187, 367; (b) Martin, J. M. L.; El Yazal, J.; François, J.-P. *Mol. Phys.* 1995, 86, 1437; (c) Martin, J. M. L.; El Yazal, J.; François, J.-P. *Chem. Phys. Lett.* 1995, 242, 570; (d) Martin, J. M. L.; El Yazal, J.; François, J.-P. *Chem. Phys. Lett.* 1996, 252, 9; (e) Giuffreda, M. G.; Deleuze, M. S.; François, J.-P. *J. Phys. Chem. A* 1999, 103, 5137; (f) Martin, J. M. L.; *Spectrochim. Acta* 1999, 55, 11126.

[60] Ayala, P. Y.; Schlegel, H. B. *J. Chem. Phys*. 1998, 108, 2314.

[61] Mayo, S. L.; Olafson, B. D.; Goddard, W. A. *J. Phys. Chem.* 1990, 94, 8897.

[62] Frisch, M. J.; Trucks, G. W.; Schlegel, H. B., *et al.* Gaussian 03, Revision D.01; Gaussian, Inc., Wallingford CT, 2004.

[63] (a) MOLPRO is a package of *ab initio* programs written by Werner, H.-J. and Knowles, P. J. with contributions from Amos, R. D.; Bernhardsson, A.; Berning, A., *et al.*. (b) Hampel, C.; Peterson, K.; Werner, H.-J. *Chem. Phys. Lett.* 1992, *190*, 1 and references therein. The program to compute the perturbative triples corrections has been developed by Deegan, M. J. O. and Knowles, P. J. (1992).

[64] Schmidt, M. W.; Baldridge, K. K.; Jensen, J. H.; Koseki, S.; Gordon, M. S.; Nguyen, K. A.; Windus, T. L.; Elbert, S. T. *QCPE Bull*. 1990, 10, 52.

[65] (a) Ruhe, A. *Math. Comput*. 1979, 33, 680. (b) Meyer, H.-D.; Pal, S. *J. Chem. Phys*. 1989, 91, 6195.

[66] (a) Liu, B. *Numerical Algorithms in Chemistry, Algebraic Methods, LBL-8158*; Lawrence Berkeley Laboratory: Berkeley, California. (b) Tarantelli, F.; Sgamellotti, A.; Cederbaum, L. S.; Schirmer, J. *J. Chem. Phys*. 1987, 86, 2201.

[67] See various contributions to the original HEMS program as recorded by Bawagan [A. O. Bawagan, Ph. D. Thesis, University of British Columbia (UBC), 1987]. The HEMS (now known as MOMAP) program has been extensively revised and extended at UBC by N. M. Cann and G.Cooper.

[68] Duffy, P.; Casida, M. E.; Brion, C. E.; Chong, D. P. *Chem. Phys*. 1992, 159, 347.

[69] Zheng, Y.; Neville, J. J.; Brion, C. E.; Wang, Y.; Davidson, E. R. *Chem. Phys*. 1994, 188, 109.

[70] (a) Deleuze, M. S.; Denis, J. P.; Pickup. B. T. *J. Phys. Chem.* 1993, 97, 5115. (b) Deleuze, M. S.; Delhalle, J.; Pickup, B. T.; Svensson, S. *J. Am. Chem. Soc.* 1994, 116, 10715. (c) Deleuze, M.; Delhalle, J.; Pickup, B.T. *J. Phys. Chem.* 1994, 98, 2382. (d) Deleuze, M; Delhalle J.; Mosely, D.H.; André, J.-M. *Physica Scripta* 1995, 51, 111.

[71] Janak, J.F.; *Phys. Rev. B* 1978, 18, 7165.

[72] (a) Gritsenko, O.V.; Baerends, E.J.; *J. Chem. Phys.* 2002, 117, 9154. (b) Gritsenko, O.V.; Braïda, B.; Baerends, E.J.; *J. Chem. Phys.* 2003, 110, 1937.

[73] Boulanger, P.; Riga, J.; Verbist, J.J.; Delhalle, J., *Macromolecules* 1989, 22, 173

[74] See Lowe, J.P.; *Quantum Chemistry*; Academic Press: San Diego, 1978, or any text book of quantum chemistry.

[75] Golod, A.; Deleuze, M. S.; Cederbaum, L. S. *J. Chem. Phys*. 1999, 110, 6014.

[76] (a) Takahashi, M.; Saito, T.; Hiraka, J.; Udawaga, Y. *J. Phys. B: At. Mol. Opt. Phys.* 2003, 36, 2539; (b) Takahashi, M.; Udawaga, Y. *J. Electr. Spectr. Rel. Phen.* 2004, 137, 387.

[77] Knippenberg, S.; Nixon, K. L.; Mackenzie-Ross, H.; Brunger, M. J.; Wang, F.; Deleuze, M. S.; François, J. –P.; Winkler, D. A. *J. Phys. Chem. A* 2005, 109, 9324.

4.3 Probing molecular conformations in momentum space: the case of *n*-pentane

4.3.1 Introduction

The molecular and electronic properties of *n*-alkanes and polyethylene are still worth debates with regards to conformational analysis [1-4] and the making of structurally well-defined organic surfaces [5, 6]. Small alkane chains have also played an essential role in the evolution of molecular statistical thermodynamics. The pioneering work by Pitzer in 1940 demonstrated already the need for coping with the influence of the molecular conformation in analytical derivations of the partition functions of normal paraffin molecules and associated thermodynamic functions [7]. The conformational enthalpy differences and the influence of the temperature on conformer abundances of *n*-alkane chains in the gas or liquid phase or in solution have been since then extensively investigated using Raman spectroscopy [8], statistical thermodynamics [9], electron diffraction [10], force field calculations [11], nuclear magnetic resonance spectroscopy [12], infrared spectroscopy [13] and ultrasonic absorption spectroscopy [14].

These experimental studies were supported by numerous quantum mechanical investigations of the potential energy surfaces of *n*-alkane compounds [15] at HF and post-HF levels. *n*-pentane is known to possess four conformers, namely the *trans-trans* (*tt*), *trans-gauche* (*tg*), *gauche-gauche* (g^+g^+) and *gauche-gauche'* (g^+G^-) structures exhibiting C_{2v}, C_1, C_2 and C_1 point group symmetries, respectively. With the latter nomenclature for conformers, we wish to emphasize that *G* denotes an unusually large C-C-C-C torsion angle around 90°, as a result of particularly unfavorable steric interactions between the end methyl groups, whereas *t* and *g* describe more standard dihedral angles of ~180° and ~60°, respectively. Second order Møller-Plesset (MP2) calculations along with the 6-31G* basis set led to a value of 0.67 kcal mol^{-1} for the energy difference between the *trans-trans* (*tt*) and *trans-gauche* (*tg*) conformers of *n*-pentane [15i], to compare with an experimental estimate of 0.47 kcal mol^{-1} derived from a rather tricky analysis of the temperature dependence of Raman spectra [8i]. To date, the most thorough quantum chemical study of the relative conformer energies of *n*-pentane is the benchmark Focal Point Analysis by Salam and Deleuze [16], which amounts to an extrapolation of these energy differences to the level of the Coupled Cluster ansatz involving single and double electronic excitations along with a perturbative treatment of triple excitations [CCSD(T)], and in conjunction with an exceedingly large cc-pVQZ basis set (635 atomic functions).

In sharp contrast with *n*-butane [17], the archetype of structurally versatile molecules, the most essential feature of the conformational equilibrium prevailing for *n*-pentane is that, due to the high symmetry and unfavorable entropy effects therefore, the most stable species (*tt*) is *not* the most abundant one at room temperature. Similar considerations also hold for larger *n*-alkane chains [18]. To be more specific, in a gas phase sample of *n*-pentane at 298K, the *tg*, *tt*, g^+g^+ and "sterically forbidden" g^+G^- conformers exhibit molar fractions equal to ~0.67, ~0.28, ~0.03 and ~0.01, respectively, according to the results of our Focal Point Analysis [16] and merely qualitative thermochemical calculations [16] employing Boltzmann statistical thermodynamics at the level of the Rigid Rotor / Harmonic Oscillator (RRHO) approximation [19]. Meanwhile, it has been shown by Waroquier and co-workers [20] that hindered internal rotations in *n*-alkanes strongly affect the potential energy barriers as well as the entropy differences, even in an uncoupled scheme, where all torsional potentials are considered to be one-dimensional. It is in particular known that estimates of entropy using the basic RRHO approximation tends to significantly underestimate the experimental values. With regards to further spectroscopic studies, this observation certainly justifies a more quantitative study of the conformer abundances of *n*-pentane.

In sharp contrast with structural, conformational, and statistical thermodynamical studies, experimental determinations of the electronic structure of *n*-alkanes, and of *n*-pentane in particular, are relatively scarce. The first work of relevance is a photoelectron study by Price, Potts and Streets of methane up to pentane [21], using a photon beam characterized by a wave length of 304 Å. Further works that are certainly worth a mention are the X-ray photoemission studies on a series of *n*-alkanes, starting from methane and converging to polyethylene, by Pireaux *et al.* [22], using an Al Kα (1487 eV) source. The outer-valence region of *n*-pentane has been explored in great detail by Kimura *et al.* [23], using UPS and He I (584 Å) radiation.

These studies have essentially highlighted the traditional aspects of photoelectron spectroscopy, that is, they have focused on an assignment of bands under the assumption of a one-to-one correspondence between the experimentally identified transitions and the valence one-electron (i.e. molecular orbitals) of the *most stable* conformation. The main scope of these studies was to follow at a molecular level the construction [22] of the electronic band structure of a stereoregular chain of polyethylene [24] and related paraffines such as hexatriacontane ($C_{36}H_{74}$ [25]). The most thorough calculations [26] so far on all-staggered *n*-alkane chains employed one-particle Green's Function (1*p*-GF) theory [27] and the third-order algebraic diagrammatic construction [ADC(3)] scheme [28], along with relatively small basis sets by current standards (6-31G, 6-31G*, 6-31G**). These calculations indicate that, for the largest systems, the shake-up onset in the ionization spectra lies at ~23 eV. The orbital picture of ionization is therefore suited for qualitatively analyzing conformational fingerprints in the valence photoelectron spectra of saturated hydrocarbons in the gas and solid phases, at electron binding energies below 23 eV [29].

According to calculations of cross sections using the empirical model by Gelius [30], it appears that, as a result of an estimated ratio of 13:1 for the C_{2s} versus C_{2p} atomic cross sections in (Al K_{α}) X-ray photoelectron spectroscopy (XPS), line intensities in the valence XPS ionization spectra of large enough saturated hydrocarbon chains also faithfully reflect [29] the mixture of $C_{2p} + H_{1s}$ and C_{2s} atomic contributions across the energy gap separating the inner- and outer-valence bands, as a result of an avoided crossing [29a] of molecular orbitals in all-staggered systems of C_{2v} or C_{2s} symmetry. From a chemical view point, this orbital mixing can be regarded as the outcome of long-range σ- (or hyper) conjugation interactions between optimally oriented methylene (-CH_2-) units [29, 31]. These interactions lead most specifically to a significant stabilization of the orbitals at the top of the inner-valence band, and, thus, to a stronger concentration of one-electron ionized states, yielding for large zigzag planar chains sharp and intense ionization peaks in this energy region. As shall be shown here, this cooperative effect starts to be spectroscopically detectable with *n*-pentane. This spectroscopic fingerprint has been amply exploited for characterizing the organization of various organic thin films (alkanethiols, alkyltrichlorosilanes) deposited on various substrates (gold, silica, …) and designing therefore organic surfaces suited for the making of biosensors [32].

In line with these studies of the interplay between the molecular architecture and electronic structures of structurally highly versatile systems, Deleuze and co-workers published in 2001 the first comprehensive analysis [17], throughout the valence region, of the influence of the molecular conformation on electron momentum distributions experimentally inferred from measurements on *n*-butane [32] employing Electron Momentum Spectroscopy (EMS [34]). In practice, however, because of the limited energy resolution of the spectrometers (at best, ~0.5 eV) and of the difficulties inherent to assigning overcrowded ionization bands, interpretations of EMS experiments on molecules containing one or several rotatable groups remain very challenging. Further studies are still definitely needed for assessing the potential of this spectroscopy with respect to the relationships prevailing between conformational analysis and molecular orbital theories. The relatively indirect means of inferring conformation from electron momentum spectroscopic studies requires extensive theoretical interpretation if it is to have any value at all. Indeed, a key point with EMS experiments is that the inferred electron momentum distributions relate to one or several ionization channels at well-defined and *fixed* electron binding energies. For reliably analyzing such experiments, it is therefore more than advisable to take into account the influence of the molecular conformation on the energy distribution of ionized states in the spectral bands [35], and evaluate with respect to statistical thermodynamics the contribution of each possible conformer to the measured ionization intensities [17].

The main purpose of the present work is thus to motivate further EMS studies, on reliable enough theoretical grounds that consistently account for the correct scattering potentials, for temperature effects, for electronic correlation and relaxation effects, as well as for the dispersion of the ionization intensity into shake-up processes, of the interplay between the valence electronic wave function and the conformation of structurally versatile molecules. *n*-pentane is probably one of the best suited molecules for this purpose, in view of the limited extent of the shake-up contamination in its ionization spectrum, the prevalence of the *tg* conformer at room temperature, and the appearance of methylenic hyperconjugation in the minor *tt* component. To predict the results of such experiments on *n*-pentane, we proceed through (1) an evaluation of the conformer abundances within a few % accuracy, by means of Gibbs' free energy differences obtained using statistical thermodynamics beyond the Rigid-Rotor/Harmonic-Oscillators (RRHO) approximation, as well as the best available (FPA) many-body quantum mechanical estimates for the relative conformer energies in their equilibrium geometries; (2) a simulation of the valence ionization spectra for each conformers, within an accuracy of ~0.2 eV, and a computation of the related transition moments for the main conformers, taking into account the dispersion of the ionization intensity over secondary shake-up states; and, at last, (3) a computation of spherically averaged electron momentum distributions for each identified ionization channels or resolvable bands, taking into account the fact that the molecular conformation may have a very strong influence on the orbital energies, and ionization bands therefore [17, 29, 31, 35].

4.3.2 Theory

For an introduction into 1*p*-GF theory and the ADC(3) scheme, as well as for an overview on electron momentum spectroscopy, momentum distributions and Dyson orbitals, we refer to Part 2 in the present thesis. For calibration purposes, the reader is referred to a work by Zheng *et al* on *n*-propane [36], the experimental momentum distributions of which could be almost exactly reproduced from Dyson orbitals derived from large scale MR-SDCI calculations. Since the last complete order attained in electron correlation is exactly the same (3), and since a single reference depiction clearly prevails, it is clear that the 1p-GF/ADC(3) approach will enable the same level of accuracy in studies of the electron momentum distributions of wide band-gap molecules such as *n*-alkanes. Recent applications of ADC(3) on difluoromethane [37], butadiene [35], dimethoxymethane [38] and water [39] and confrontation thereby with EMS experiments and/or large scale CI calculations indeed demonstrate the reliability of this many-body approach in highly quantitative calculations of Dyson orbitals and of the related electron momentum distributions.

4.3.3 Computational details

For the sake of consistency with our former benchmark FPA analysis of the relative conformer energies of *n*-pentane, all calculations presented in this work have been performed on geometries taken from [16]. These geometries were optimized by means of Density Functional Theory (DFT) in conjunction with the 6-311++G** basis set [40] and the Becke-three-parameters-Lee-Yang-Parr (B3LYP) functional [41]. In the present work, the relative abundances of the four conformers of *n*-pentane have been correspondingly recalculated at the B3LYP/6-311++G** level using Boltzmann statistical thermodynamics, and the standard formula:

$$n_i = \rho_i \exp(-\Delta G_i / RT) \tag{9}$$

with ΔG_i the Gibbs' free energies of the species of interest relative to the most stable conformer (*tt*), and ρ_i the corresponding multiplicities (or symmetry numbers). As in [16], the former data were obtained by incorporating in the FPA analysis B3LYP/6-311++G** estimates for zero-point vibrational energy corrections thermal corrections to the enthalpy as well as entropy corrections deriving from electronic, rotational and vibrational statistical thermodynamical partition functions.

The thermochemical analysis of conformer abundances that is presented here goes beyond the RRHO level, since the employed partition functions account for hindered rotations that were calculated using the protocol by Ayala and Schlegel [42] for identifying and treating the internal rotation modes, using a projection of harmonic vibrational normal modes on constrained stretches, bends, and out-of-plane motions, leaving only the torsion modes. In this complex procedure, use is made of the protocol of Kilpatrick and Pitzer [43] for calculating the kinetic energy matrix describing the internal rotations, as well as the rules that Mayo, Olafson, and Goddard [44] implemented in their force field DREIDING for defining the potential periodicity, the rotating tops' symmetry numbers, and the well-multiplicities of acyclic molecules. The protocol by Ayala and Schlegel [42] also employs an improved analytical approximation, according to a best-fit procedure, of the formula of Pitzer and Gwinn [45] for the partition function associated to one-dimensional hindered internal rotations. The adaptation by Ayala *et al.* [42] maintains the known good characteristics of relatively large rotational barrier heights V_0 (compared with *kT*), while improving the accuracy of the smaller ones. All DFT calculations presented in this work have been performed using the GAUSSIAN 98 package of programs [46].

The ADC(3) calculations were carried out with Dunning's cc-pVDZ basis set [47] incorporating on total 135 basis functions, by means of the original 1*p*-GF/ADC(3) computer package [48], interfaced to GAMESS [49]. At the SCF level, the requested convergence on each of the elements of the density matrix was fixed to 10^{-10}. The ionization spectra have been calculated up to electron binding energies of 30 eV, retaining all eigenvalues of the ADC(3) secular matrix with a pole strength equal to or larger than 0.005. This matrix has been diagonalized using the Block-Davidson diagonalization procedure [50] in the final diagonalization step [28c]. The assumption of frozen core electrons and the respective symmetry point groups have been exploited in order to reduce the cost of these computations. The accuracy of ADC(3)/cc-pVDZ calculations of one-electron ionization energies is typically around ~0.2 eV for saturated hydrocarbon compounds [51] and further improvements of the basis set have been comparatively shown to have only a very marginal influence on these energies [52], typically less than 0.1 eV, reflecting the near completeness of the basis set for such systems. Successive improvements of the basis set also typically result [53] into redistributions of the shake-ionization intensity over a larger number of satellites of weaker intensity, but most usually without significant alterations of the computed spectral envelope, provided the employed threshold on pole strengths is low enough.

As a guide to the eye, the ADC(3) cationic eigenstates are displayed in the sequel as spike spectra, and in the form of convoluted densities of states and of simulated (e, 2e) ionization spectra. In the former case, line intensities are simply scaled according to the computed ADC(3) pole strengths, and convoluted using a Gaussian spread function with a full width at half maximum (FWHM) of 0.6 eV, in order to account for the average effect of vibrational broadening and enable comparison with high resolution UPS (He I) measurements (in his text book [23], Kimura reports an energy resolution of 25-30 meV at FHWM). In the latter case, line intensities are proportional to (e, 2e) cross sections computed at various azimuthal angles from ADC(3) Dyson orbitals, using equations (1) and (2), and spectral bands are convoluted using a Gaussian spread function with a FWHM of 1.1 eV. The latter band width accounts for the vibrational broadening of spectral lines, as inferred from the UPS measurements, as well as for the more limited resolution of the best available (e, 2e) spectrometers (~0.5 eV). The main scope of these simulations is to identify the bands that could be reliably resolved and exploited within (e,2e) ionization spectra measured under the EMS conditions, using a standard Gaussian fitting procedure and an experimental set up identical to that available at Tsinghua University (Beijing, China) [54]. According to the characteristics of this set up, the relevant parameters (see eq. 1) amount to E_0=1200 eV, $E_1 = E_2 =$ 600 eV, $p_1 = p_2 =$ 6.64077 a.u., and p_0=0.271105 $(1200 + E_n)^{1/2}$ a.u. (1 a.u. = 1 a_0^{-1} with a_0 the Bohr radius, i.e. 0.5292 Å).

Spherically averaged Dyson orbital momentum distributions have been correspondingly generated from the output of our 1*p*-GF/ADC(3) calculations using the MOMAP program by Brion and co-workers [55] and homemade interfaces. The distributions presented in the sequel have been convolved by means of the Gaussian weighted planar grid (GW-PG) method of Duffy *et al.* [56], in order to account for an experimental resolution of 0.1 a.u. (FWHM) on electron momenta. This value is consistent with an angular resolution of $\Delta\phi = 1.2°$ at a total impact energy (E_0) of 1200 eV [57].

4.3.4 Results and discussion

A. Thermostatistical analysis

Details of our evaluation of conformer populations at room temperature are given in Table 1. In this table, the ΔE values correspond to the relative internal energies obtained from the focal point analysis published in [16] with respect to the *tt* global energy minimum, which amounts to a CCSD(T)/cc-pVQZ determination of these conformational rearrangement energies. Clearly, the g^+g^+-*tt* energy difference is less than twice the *tg*-*tt* energy difference, a phenomenon which has been referred to as the “positive pentane effect” [58] and which is due to long-range attractive dispersion interactions. The enthalpy differences (ΔH) incorporate B3LYP/6-311++G** zero-point vibrational corrections (ΔZPE) and thermal corrections, which are computed from statistical thermodynamical partition functions evaluated with the same model chemistry at the basic RRHO level and taking into account the influence of hindered rotations. ΔS and ΔG point correspondingly at entropy and Gibbs’ free energy differences (ΔG=ΔH-$T\Delta S$). From these values, and the relative conformer multiplicities (ρ), the corresponding molar fractions (x) are easy to calculate.

Despite its less favorable energy, it is immediately apparent that at room temperature, the *tg* conformer is the most abundant one, which corroborates the conclusions of our first merely qualitative RRHO analysis in [16]. Hindered rotations [42] are found nonetheless to very substantially increase the entropy of the *tg*, g^+g^+ and g^+G^- conformers relative to the *tt* one ($\Delta\Delta S$ = +1.390, +2.665 and +2.697 cal mol^{-1} K^{-1}, respectively). This decrease is mostly ascribable to non-blocked hindered rotations in the *tg*,

g^+g^+ and g^+G^- conformers, whereas all internal rotations in the *tt* conformer are energetically blocked. This observation is in line with a recent study by Vansteenkiste *et al.* [20] of the influence of the number of internal rotors on the entropy of *n*-alkane chains, and the fact that the largest discrepancy in the entropy factor between RRHO and hindered rotor analyses arises from the multiplicity of internal rotations. The final result is a decrease of the Gibbs' free energies of the *tg*, g^+g^+ and g^+G^- conformers relative to the *tt* one (at 298K : $\Delta\Delta G$ = -0.413, -0.812, -0.820 kcal mol^{-1}, respectively), when hindered rotations are accounted for. Unsurprisingly therefore, a substantial increase in the molar fractions of these conformers is correspondingly seen at room and higher temperatures. According to our most reliable results, this species dominates therefore the conformational mixture prevailing at these conditions in the gas phase, with a molar fraction of 74%, followed by the *tt*, g^+g^+ and g^+G^- conformers, which exhibit weights of 15 %, 9% and 3% only. Despite the strong entropy increase when hindered rotations are accounted for, our results confirm the suggestion that the g^+G^- species is sterically forbidden [59]. The evolution of the conformer abundances as a function of the temperature *T* is therefore provided in Table 2: note that when hindered rotations are taken into account the *tg* conformer starts to dominate the conformational mixture at temperature above 125K. Recalling that it is extremely hard to monitor the parameter in EMS experiments, it is nice to find that around 298K the dependence of the conformer populations upon the temperature is, all in all, very limited.

B. Orbital energies and ionization spectra

The influence of the conformation on inner- (C_{2s}) and outer-valence (C_{2p} + H_{1s}) orbital energies of *n*-pentane is described in details for the three most abundant conformers through the interplay of the orbital correlation diagrams of Figures 1 and 2, respectively. A further correlation diagram connecting the valence orbitals of the most abundant *tg* conformer with the highest energy-lying one (g^+G^-) is provided in an appendix at the end of this chapter. These diagrams derive from a plot of HF/cc-pVDZ orbital energies as a function of the two dihedral angles characterizing the carbon backbone of *n*-pentane, through a scan of the corresponding conformational energy map in steps of 12° on these angles. The reader is referred to Table 3 for a detailed assignment of these orbitals in all four conformers and calculation at the ADC(3)/cc-pVDZ level of the corresponding one-electron and shake-up ionization energies or related spectroscopic strengths.

It is immediately apparent that, in the inner-valence (C_{2s}) region, the molecular conformation has a marginal impact on orbital energies, except for the two levels at the top of this region. In sharp contrast, the influence of the conformation is extremely strong in the outer-valence region, where two successive accidental orbital crossings seem to occur with two levels (**12**, **13**) that belong to different irreducible representations of the C_{2v} and C_2 point groups characterizing the *tt* and g^+g^+ conformers, when the molecule evolves from the *tt* to the *tg* conformations, and from the *tg* to the g^+g^+ conformations. Note that, by virtue of the non-crossing rule for orbitals exhibiting the same symmetry [60], a true energy crossing resulting from vanishing interaction elements over the one-electron Fock operator is here ruled out. These apparent crossings are thus accidental (in the sense of J.P. Lowe in [60]) or due to the limited angular resolution of the scan. On the other hand, avoided energy crossings are for instance clearly identified at a C_2-C_3-C_4-C_5 dihedral angle (Φ) of ~150° between orbitals **9** ($7a_1$) and **10** ($8a_1$), and between orbitals **7** ($5b_2$) and **8** ($1a_2$), when the *tt* conformer transforms into the *tg* one. Another avoided energy crossing is also very apparent upon a reversing of the g^+g^+ conformer into the *tg* form for the following pairs of orbitals: **12** (8b) - **13** (10a), and **8** (8a) - **9** (6b).

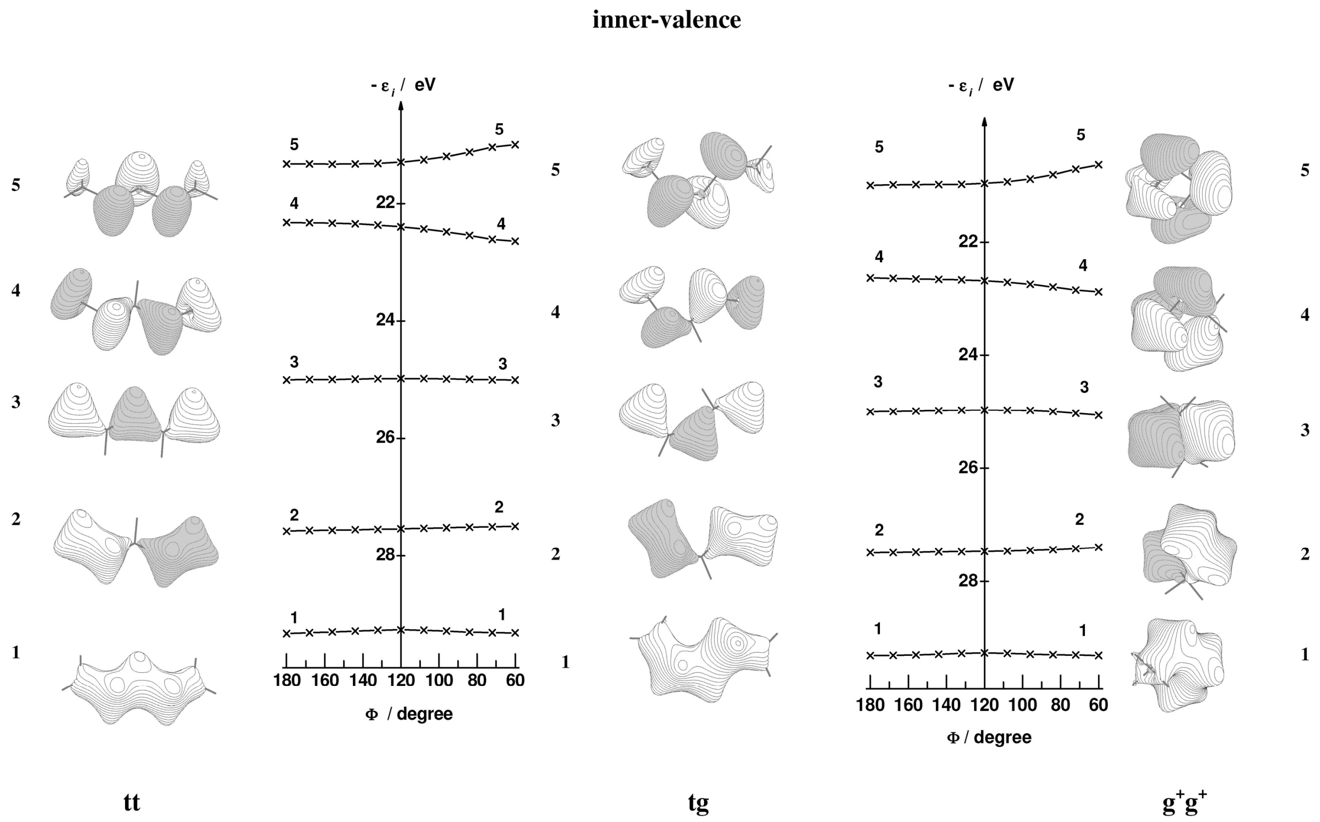

Figure 1. Inner-valence orbital correlation diagram for the *tt*, *tg* and g^+g^+ conformers of n-pentane. The energies are calculated at the HF/cc-pVDZ level as a function of the two dihedral angles characterizing the carbon backbone . Contour values of 0.05 were used, as well as edges of ~16 Å (for *tt* and *tg*) and 14 Å (for g^+g^+).

outer-valence

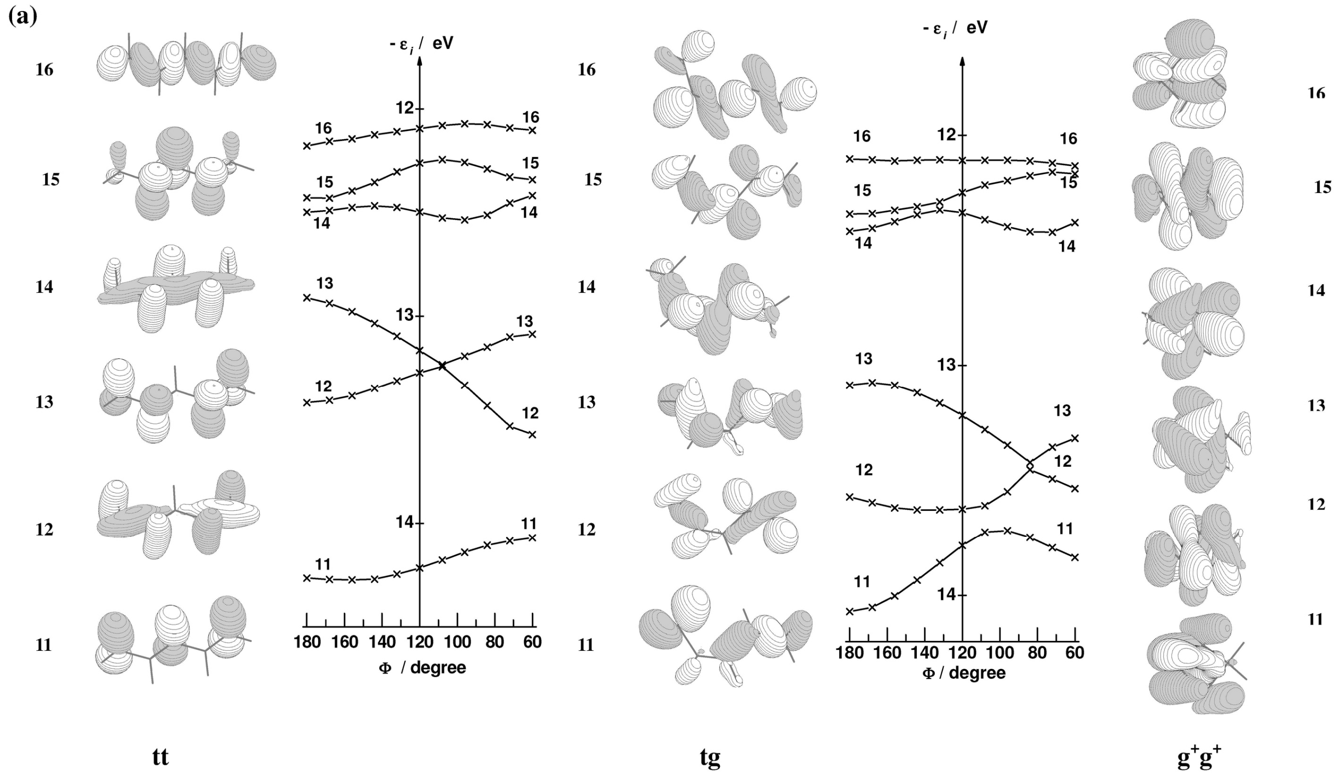

Figure 2

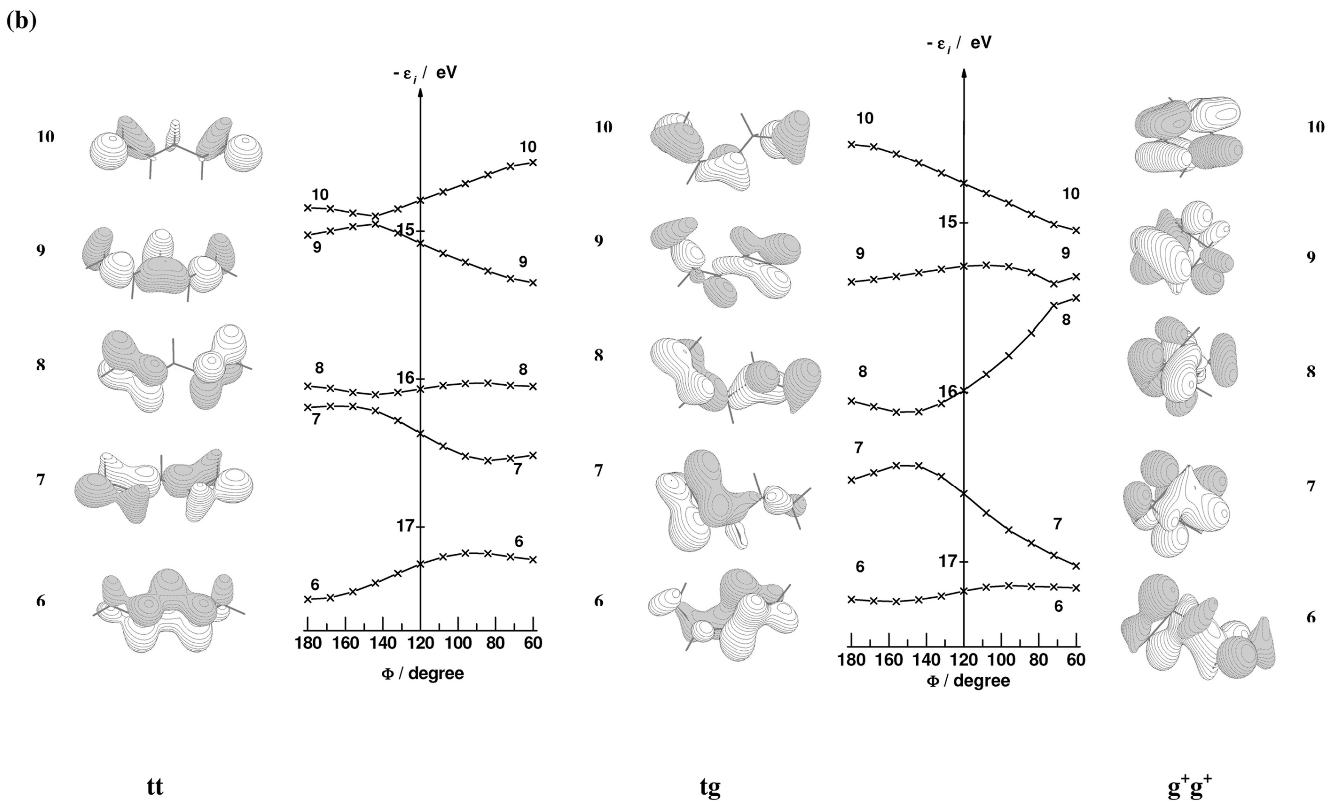

Figure 2 (continued). Outer-valence orbital correlation diagram for the *tt*, *tg* and g^+g^+ conformers of n-pentane. The energies are calculated at the HF/cc-pVDZ level as a function of the two dihedral angles characterizing the carbon backbone . Contour values of 0.05 were used, as well as edges of ~16 Å (for *tt* and *tg*) and 14 Å (for g^+g^+).

Note from Figure 1 that the $3b_2$ (**4**) and $5a_1$ (**5**) orbitals of the *tt* conformer merely localize on the C-H bonds and exhibit therefore a significant admixture of C_{2p}+H_{1s} contributions. These orbitals get stabilized and destabilized, respectively, upon a reversal of the molecular structure into the *tg* and, ultimately g^+g^+ conformations, as a result of the disruption of through-space anti-bonding and bonding methylenic hyperconjugation interactions [29, 31] between adjacent and parallel C-H bonds. Inversely, in the outer-valence region (Figure 2), the $6b_2$ (**12**) and $2a_2$ (**13**) orbitals get significantly destabilized and stabilized upon departures of the molecular architecture from an all-staggered (or zig-zag planar) conformation. A very strong destabilization is also noticed for the $1b_1$ (**6**) and $2b_1$ (**11**) orbitals, reflecting in the former case the disruption of through-space bonding interactions, and in the latter case an enhancement of anti-bonding interactions. Because of the rather intricate pattern of these correlation diagrams, it is clear that a complete and reliable assignment of the ionization spectra of *n*-pentane is impossible without reliable enough calculations of ionization energies and related spectroscopic strengths.

The results of our ADC(3)/cc-pVDZ calculations are given in Table 3, and displayed for all four conformers in the form of spike and convoluted spectra in Figure 3, using width parameters that are consistent with the modeling of UPS experiments. The ADC(3)/cc-pVDZ results confirm that the one-electron picture of ionization and energy order inferred from Koopmans' theorem are qualitatively valid theoretical concepts (Γ>0.80) throughout the outer-valence region and in the upper part of the inner-valence region, up to electron binding energies of about 23 eV. Above this energy threshold, the orbital picture of ionization completely breaks down. The results reported in Table 3 indicate very minor shifts of the identified shake-up onset, from 23.7 eV for the *tg* conformer, to 23.6, 23.5 and 23.4 eV for the *tt*, g^+g^+ and g^+G^- conformers, respectively. These variations reflect both alterations of the underlying orbital energies upon changes of the molecular conformation and an enhancement of the dispersion of the ionization intensity over shake-up states with a lowering of the molecular symmetry point group.

We wish here to remind the reader that only a fraction of the shake-up ionization intensity has been identified, due to the restriction of the search for solutions of the ADC(3) secular equation with a pole strength larger than 0.005. These fractions are reported in Table 3 and reflect the enhancement of the shake-up fragmentation upon altering the symmetry point group of *n*-pentane from C_{2v} (*tt* conformer) to C_2 (g^+g^+) or C_1 (*tg*). Compared with the latter species, the shake-up fragmentation intensifies further with the g^+G^- conformer, reflecting the destabilization of the underlying electronic wave function, and a slight closure of the energy gap between occupied and unoccupied levels. At the HF/cc-pVDZ level, this gap amounts to 17.177 eV (*tt*), 17.080 eV (*tg*), 16.938 eV (g^+g^+) and 16.893 eV (g^+G^-).

Figure 3 further confirms at a benchmark theoretical level the great dependence of the valence ionization bands throughout the outer-valence region and in the upper-part of the inner-valence region onto the molecular conformation. Whatever the conformation, and despite the extent of the shake-up fragmentation at ε_b > 23 eV, five ionization bands remain clearly resolvable in the inner-valence region. A decrease of the energy interval from 1.839 to 1.330 eV and from 1.330 to 0.755 eV is noticed between the two levels at the top of this region when *n*-pentane evolves from the g^+g^+ to the *tg* conformations, and from the *tg* to the *tt* conformations, which reflect the development of through-space and methylenic hyperconjugation interactions in all-staggered segments of the saturated hydrocarbon chain.

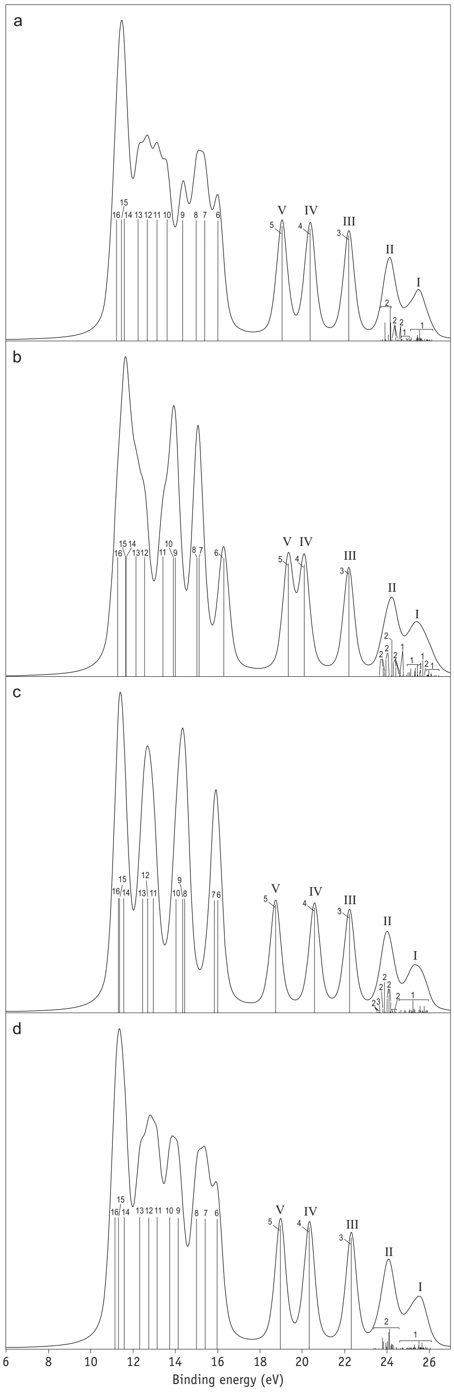

Figure 3. Theoretical ADC(3)/cc-pVDZ ionization spectra of the (a) *tg*, (b) *tt*, (c) g^+g^+ and (d) g^+G^- conformers of pentane (FWHM=0.6 eV). See table 3 for a detailed orbital assignment.

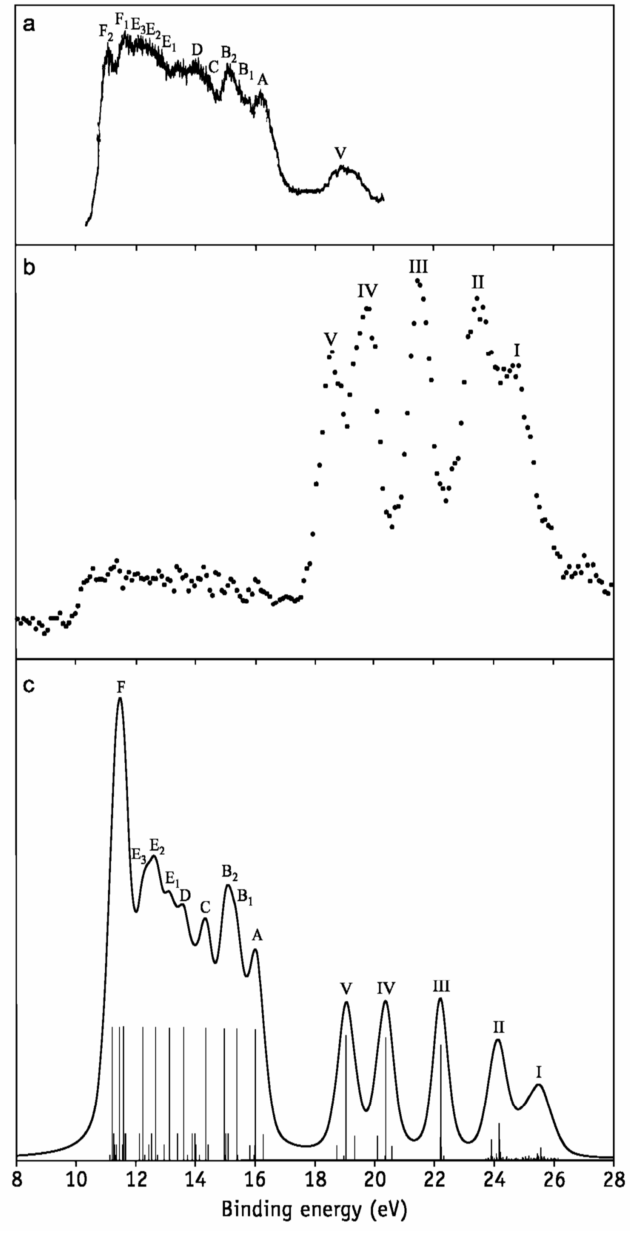

Figure 4. Comparison of the (a) UPS (He I) [23] and (b) XPS (Al Kα, hν=1486.6 eV) [29b] photoelectron spectra of *n*-pentane with (c) a thermally averaged ADC(3)/cc-pVDZ simulation (FWHM=0.6 eV).

In the outer-valence region, even the number of resolvable bands in UPS experiments vary upon changes of the conformation. In this region, the most significant variations occur around 12 and 15 eV, due to changes in the energy spreading of the one-electron ionization lines relating to the eight lowest outer-valence orbitals (**6-13**). In line with the molecular orbital correlation diagrams (Figure 2), the energy distribution of these outer-valence lines is more homogeneous for the *tg* species (Figure 3a) than for any other conformer (Figures 3b-d), yielding six or seven poorly resolved peaks at binding energies ranging from 12 to 16 eV. In contrast, considering Figure 3b, it is clear that the most stable *tt* conformer should be easy to recognize in UPS experiments from the presence of three sharp and intense peaks at 13.9, 15.1, and 16.3 eV, corresponding to the {7a$_1$, 8a$_1$, 2b$_1$ (**9-11**)}, {5b$_2$, 1a$_2$ (**7**,**8**)} and {1b$_1$ (**6**)} orbital subsets, respectively. Whatever the conformation, the three outermost one-electron ionization lines (**14-16**) tend to cluster within a narrow energy interval comprised between 10.8 and 12.0 eV, and give rise in all four cases to an intense and sharp signal in a simulation based on the depiction of vertical ionization events (Figure 3).

In line with these simulations, and despite the neglect of cross section effects, the inner-valence (e, 2e) ionization intensity used to model in the sequel the results of (e, 2e) experiments at binding energies above 18 eV on *n*-pentane can already be readily partitioned into five sets of ionization lines. More specifically, bands **V** (ranging from 17.7 to 19.7 eV), **IV** (19.7-21.2 eV) and **III** (21.2-23.4 eV) are ascribed to one-electron ionization events from the {*tg*/10a, *tt*/6a$_1$, g^+g^+/6a, g^+G^-/10a}, {*tg*/9a, *tt*/4b$_2$, g^+g^+/4b, g^+G^-/9a} and {*tg*/8a, *tt*/5a$_1$, g^+g^+/5a, g^+G^-/8a} orbital subsets, respectively. Despite the intensity spreading, the shake-up bands **II** and **I** ranging from 23.4 to 24.8 eV and from 24.8 to 27.0 eV merely derive from ionization of the {*tg*/7a, *tt*/3b$_2$, g^+g^+/3b, g^+G^-/7a} and {*tg*/6a, *tt*/4a$_1$, g^+g^+/4a, g^+G^-/6a} orbital subsets, respectively. As described above, a description of the outer-valence bands is far more intricate, because of the more strongly congested nature of these bands and the pronounced influence of the molecular conformation. (e, 2e) cross sections as well as the lower energy resolution of EMS experiments must therefore be accounted for prior to proceeding to such a partitioning of the outer-valence ionization intensity.

Before modeling EMS experiments on *n*-pentane, it is interesting to compare the thermal average (Figure 4c) of our ADC(3) ionization spectra for all four conformers, using the molar fractions computed previously by means of statistical thermodynamics, with the ultra-violet (He I) and X-ray photoelectron spectra [23, 29b] of *n*-pentane (Figures 4a and b). In view of the much sharper features predicted for the outer-valence bands of the other three conformers (Figure 3), the confrontation of theory and experiment in the outer-valence region demonstrates very clearly the dominance of the *tg* conformer in the gas phase at ~298K. In this region, the measured ionization intensities tend overall to smoothly decrease with increasing binding energies. This observation corroborates the global appearance of the thermally averaged and convolved ADC(3) spectrum in between 12 and 16 eV (Figure 4c). Several minor peaks or ridges emerge at 16.0 eV (A), {15.3 eV, 15.1 eV} ({B$_1$, B$_2$}), 14.3 eV (C), 13.6 eV (D) and {13.1 eV, 12.6 eV, 12.4 eV} ({E$_1$, E$_2$, E$_3$}) on the theoretical side, whereas comparable signals are correspondingly observed at 16.2, {15.5, 15.0}, 14.4, 13.9 and {12.8, 12.5, 12.1} eV in the He I spectrum (see Table 3 for detailed assignment). A striking discrepancy is nonetheless observed at the ionization threshold, which emerges as a sharp and intense peak at 11.5 eV according to the ADC(3)/cc-pVDZ simulation (Figure 4c), but takes the form of a strongly broadened and multiplet signal with, at least, two components at 11.5 (F$_1$) and 10.9 (F$_2$) eV on the experimental side (Figure 4a). In straightforward analogy with a recent analysis of the UPS (He I) spectrum of *n*-butane, this discrepancy can be ascribed to vibronic coupling interactions and nuclear dynamical complications that find their origin into the near-energy degeneracy of the three lowest electronic states of the *n*-pentane$^+$ radical.

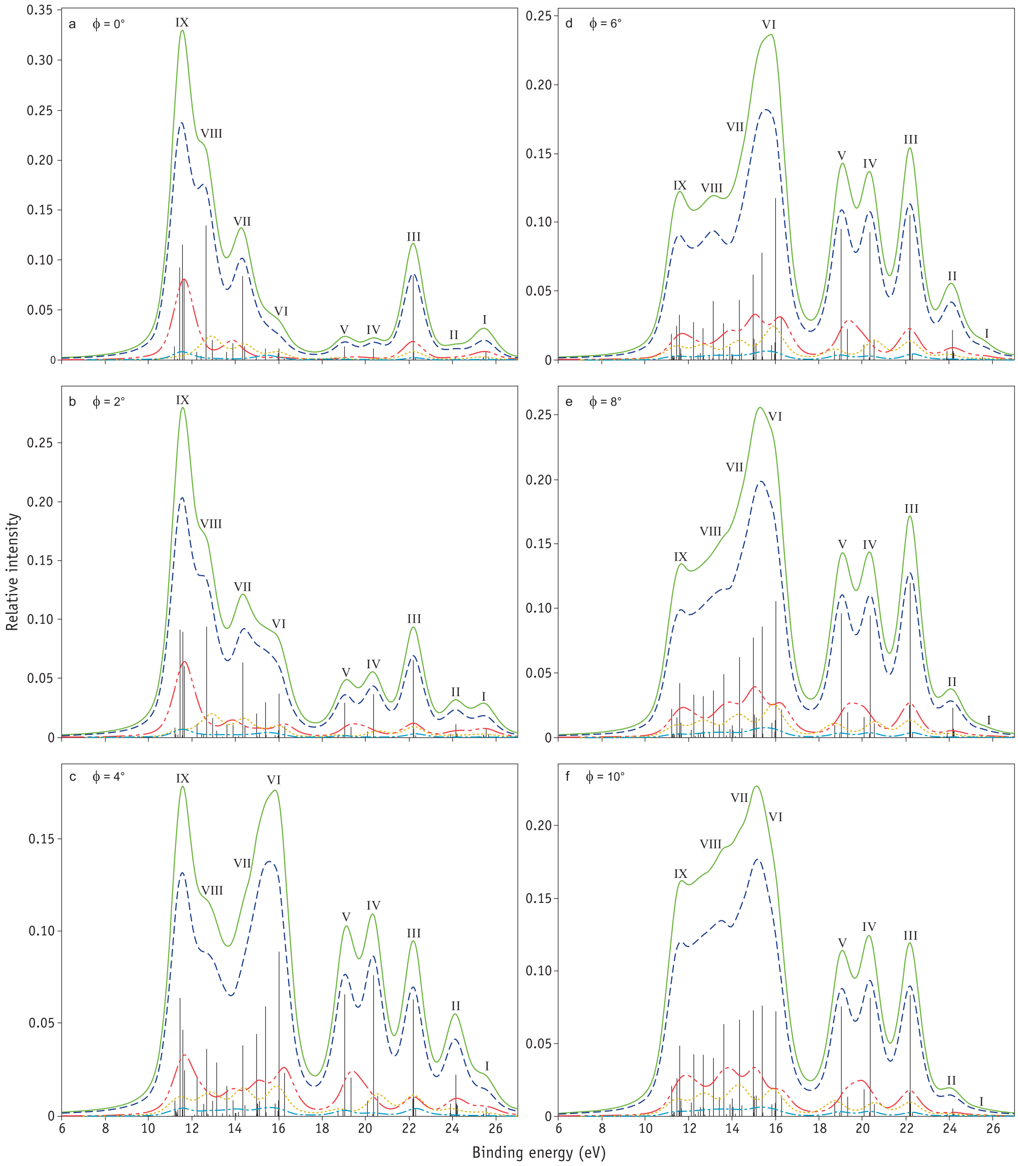

Figure 5. ADC(3)/cc-pVDZ simulation of the azimuthal angular dependence of the (e, 2e) ionization spectrum of *n*-pentane at an impact energy of 1.2 keV [FWHM=1.1 eV] and at T=298K. The thermally averaged spectrum (green —) can be compared with individual contributions from the *tg* (deep blue ---), *tt* (red ----), g^+g^+ (orange ···) and g^+G^- (light blue — - —) conformers.

In the inner-valence region, the energy spreading of the peaks **III**, **IV** and **V** in the thermodynamically averaged spectrum is almost in perfect agreement with the X-ray photoelectron spectrum: peaks **III** and **IV** lie at 3.2 and 1.3 eV above peak **V**, to compare with experimental energy intervals of 3.0 and 1.1 eV, respectively. This excellent agreement also provides strong experimental evidence for the dominance of the *tg* conformer within the gas phase mixture. In line with comparable ADC(3)/cc-pVDZ studies on saturated hydrocarbons [51], the computed inner-valence one-electron ionization energies reproduce the experimental location of bands **III**, **IV** and **V** in the XPS spectrum within 0.2 eV accuracy. In contrast, the ADC(3) results for shake-up ionization energies lead to overestimations by ~0.8 eV of the electron binding energies characterizing the innermost valence bands **I** and **II**, due to their lower-order (first-order) treatment with respect to electron correlation and relaxation. On the experimental side, a significantly enhanced band broadening [29b] corroborates the shake-up fragmentation predicted at the ADC(3) level for the two innermost C_{2s} orbitals.

In anticipation of experimental EMS studies of the valence electronic structure of *n*-pentane, we provide in Figure 5 simulations of thermally averaged (e, 2e) ionization spectra at 298K, at azimuthal scattering angles (ϕ) equal to 0, 2, 4, 6, 8 and 10° and at an electron impact energy of 1.2 keV + ε_b, within the energy (~0.5 eV) and momenta (~0.1 a.u.) resolutions that are currently achievable with the best (e, 2e) spectrometers. We thus from now on assume a spread function with a width of 1.1 eV at half maximum (FWHM). Line intensities in the spike spectra displayed in this Figure are scaled proportionally to the computed (e, 2e) cross sections as well as to our best estimates for the conformer abundances.

The bands which have a dominant contribution in (e, 2e) ionization spectra when ϕ=0° and which tends to vanish at larger azimuthal angles are traditionally referred to as orbitals of the *s*-type, whereas (e, 2e) ionization intensities that vanish at ϕ=0° and exhibit a maximum at a non-zero value of ϕ are in contrast characteristic of so-called *p*-type orbitals. This distinction is inherently based on symmetry considerations. It is hardly applicable in this case because of the lack of any symmetry element for the most abundant *tg* conformer. One exception is the angular dependence of the shake-up (e, 2e) ionization intensity related to orbitals **1** (*tg*/6a, *tt*/4a$_1$, g^+g^+/4a, g^+G^-/6a), which by virtue of the absence of nodal surface in this orbital, and thus in line with the expectations for *s*-type orbitals, smoothly decrease from a maximum at ϕ=0° and almost vanishes at ϕ=10°. In contrast, although the (e, 2e) ionization intensity for the 3b$_2$ orbital (**2**) of the most stable *tt* conformer vanishes, band **II** exhibits a limited but non-vanishing (e, 2e) ionization intensity at ϕ=0°, due to the contribution from the asymmetric and most abundant *tg* conformer. A similar observation can be made at the bottom of the outer-valence region for the 5b$_2$ orbital (**7**) of the *tt* conformer and its counterpart for the *tg* conformer, which dominantly contributes to band **VI** at values of ϕ ranging from 2 to 10°: also merely because of departures from the C_{2v} and C_2 symmetry point groups, band **VI** does not strictly vanish at ϕ=0°, but only display minimal intensities. In contrast, bands **III** and **IX** exhibit strongly dominating contributions to the (e, 2e) ionization intensities at ϕ=0°, which go through a minimum around ϕ=6°, from which they rise again relative to the other ionization bands; as such, these bands are expected to exhibit a mixed *s-p* type electron momentum profile. These considerations on the angular dependence of (e, 2e) ionization intensities prelude the identification of strong conformational fingerprints in the related electron momentum distributions (see further). Prior to studying these fingerprints in details in the outer-valence region, an identification of resolvable bands under the conditions of an EMS experiment by the best current standards is necessary.

Despite a fairly unfavorable bandwidth parameter of 1.1 eV, despite severe line overlaps and despite the intricacy of the ionization bands of a strongly versatile molecule like *n*-pentane, four bands or shoulders referred to as **VI**, **VII**, **VIII** and **IX** in Figure 5 distinctly emerge at 15.8, 14.3, 12.5 and 11.5 eV from all our simulations of the (e, 2e) ionization spectrum of this compound, respectively. In line with the usual practices, these spectral features are correspondingly ascribed to sets of one-electron ionization lines at binding energies ranging from 14.9 to 17.7 eV, from 13.6 to 14.8 eV, from 12.2 to 13.6 eV, and from 10.0 to 12.2 eV (see Table 3 for details). This partitioning accounts by construction for the transfer of the (e, 2e) ionization intensity of various individual orbital contributions from one energy region to another upon an alteration of the molecular conformation, and corresponds to one of the most critical steps in the interpretation of EMS experiments on conformationally versatile molecules (see in particular [35]). One example of a "band-to-band" shift in this case is encountered with orbital **8** (8a) of the g^+g^+ conformer: the corresponding ionization energy increases by 0.54 eV upon reversal into the *tg* conformation, and the related ionization intensity shifts therefore from band **VII** to band **VI**. Note that, in table 3, in order to account for rather severe band overlaps in the modelling of (e, 2e) experiments at the current energy resolution (0.5 eV), the ionization intensity associated to the one-electron ionization lines (**13**, Γ=0.914) at 12.24 eV in the ionization spectrum of the *tg* conformer (Figure 3a) has been distributed in equal parts to the two outermost spectral bands (**VIII** and **IX**). Similarly, the (e, 2e) ionization intensity ascribed for the same conformer to the one electron ionization line (**10**, Γ=0.910) at 13.61 eV has been equally shared between two bands **VIII** and **VII**. These lines have, rather fortunately, relatively limited (e, 2e) ionization intensity and the rather arbitrary nature of this intensity partitioning therefore is expected to have a limited influence on the momentum distributions computed for each resolvable outer-valence band. In contrast, despite the lower energy resolution, five bands (**I** - **V**) are still visible in the inner-valence region, and their assignment remains straightforward (see above and Table 3).

C. Orbital topologies and electron momentum profiles

Spherically averaged electron momentum profiles have been calculated for each of the bands that have been identified in the spectra shown in Figure 5. The results of these calculations are given in Figure 6. They should be readily comparable with profiles inferred from an analysis of the angular dependence of (e, 2e) cross sections for the selected sets of ionization channels, upon de-convolving the EMS ionization spectrum through a least square fitting of Gaussian functions with the appropriate widths and locations. We thus here wish to remind that, among the nine identified bands, only three bands (**III**, **IV**, **V**) individually relate to one-electron ionization lines. In straightforward analogy with the ionization spectra shown in Figure 5, the individual contributions from each conformer are superposed on the global profile of the channels of interest. Here also, these individual contributions are scaled according to their statistical weight at 298K.

Overall, the electron momentum profiles that are predicted for bands **I** to **V** suggest a drift of the electron densities towards higher momenta when running from the bottom to the top of the inner-valence region. This general trend is simply due to the increase for all conformers of the number of nodal surfaces within molecular orbitals upon a decrease of the corresponding electron binding energy (Figure 1), which implies a stronger confinement of the related electron densities in configuration (*r*) space.

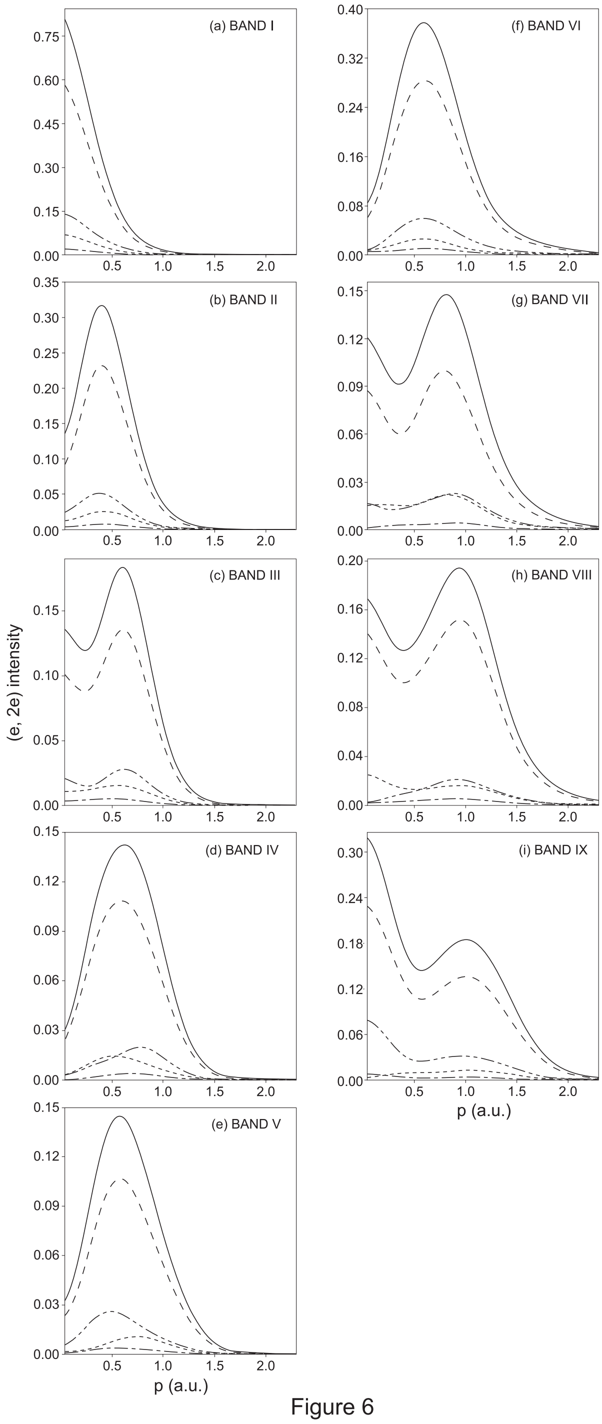
(a) BAND I
0.00
0.15
0.30
0.45
0.60
0.75
(b) BAND II
0.00
0.05
0.10
0.15
0.20
0.25
0.30
0.35
(c) BAND III
0.00
0.05
0.10
0.15
(d) BAND IV
0.00
0.03
0.06
0.09
0.12
0.15
(e) BAND V
0.00
0.03
0.06
0.09
0.12
0.15
(f) BAND VI
0.00
0.08
0.16
0.24
0.32
0.40
(g) BAND VII
0.00
0.03
0.06
0.09
0.12
0.15
(h) BAND VIII
0.00
0.04
0.08
0.12
0.16
0.20
(i) BAND IX
0.00
0.06
0.12
0.18
0.24
0.30
0.5
1.0
1.5
2.0
(e, 2e) intensity
p (a.u.)

Figure 6

Figure 6. Resolution folded ($\Delta\phi$ = 1.2°) and thermally averaged electron momentum profiles of *n*-pentane derived from ADC(3)/cc-pVDZ Dyson orbitals. The Boltzmann weighted contribution of the *trans*-*gauche* (74 %), the *trans*-*trans* (15%), the *gauche*+ *gauche*+ (9%) and the *gauche*+ *gauche*'-(3%) conformer are given with dashed (---), dashed-dotted-dotted (-··), dotted (···) and dashed-dotted (-·-·) lines, respectively. The electron momenta are given in atomic units (a.u.), while the relative spherically averaged (e,2e) cross sections are given in arbitrary units.

According to our statistical thermodynamic analysis and ADC(3)/cc-pVDZ results for the ionization spectrum of *n*-pentane (Table 3), band **I** at 25.5 eV essentially relates to shake-up lines derived from the 6a orbital (**1**) of the *tg* conformer. Despite its asymmetry, this orbital can, in view of the computed electron momentum distribution (Figure 6a), be referred to as a *s*-type orbital, which typically reflects the absence of nodal surface in the related MO contour (Figure 1). Like the related orbital energy (Figure 1) or convolved shake-up band (Figure 3), this momentum distribution is almost insensitive to the molecular conformation (Figure 6a). This was expected since orbital **1** is strongly localized in the area associated with C-C chemical bonds and does not exhibit nodal surfaces. As shall be seen, the influence of the molecular conformation on the computed electron momentum distributions increases progressively with decreasing electron binding energies, due to the larger numbers of nodal surfaces in the related molecular orbitals, the topology of which is likely to be strongly affected by a torsion of the carbon backbone.

An influence of the molecular conformation is already discernable (Figure 6b) with the electron momentum distribution characterizing band **II** at 24.1 eV (ADC(3)/cc-pVDZ result). In line with the presence of one nodal surface in the associated orbital, this momentum distribution resembles a *p*-type profile (Figure 6b). Note nonetheless that, because of the asymmetry of the most abundant conformer, this momentum distribution is far from vanishing at p = 0 a.u. Also, a shift in the position of the maximum, from p = 0.38 a.u. to 0.41 a.u. and 0.43 a.u. is observed upon twisting the *tt* carbon backbone into the *tg* and g^+g^+ forms, respectively. This shift towards larger momenta typically reflects the enhancement of through-space anti-bonding interactions and, thus, a stronger confinement of the orbital electron density in configuration space.

Rather remarkable conformational fingerprints are inferred from theory for band **III** at 22.2 eV, in the form of a mixed *s*-*p* type profile for the momentum distribution characterizing $5a_1$ and 8a orbitals (**3**) of the *tt* and *tg* conformers, which exhibit a minimum and maximum of the (e, 2e) ionization intensity at 0.26 and 0.61 a.u., whereas the corresponding orbitals (5a and 8a) for the g^+g^+ and g^+G^- conformers yield a *p*-type profile with maxima located at p=0.58 and 0.50 a.u., respectively. These variations in momentum space are consistent with the changes in spread and topology that these molecular orbitals undergo in configuration space. Indeed, the $5a_1$ and 8a orbitals (**3**) of the *tt* and *tg* conformers exhibit two distinct and approximately parallel nodal surfaces across the carbon backbone, for only one nodal surface in the g^+g^+/5a and g^+G^-/8a orbitals. The removal of one minimum in the predicted (e, 2e) ionization intensities for band **III** at non-vanishing electron momenta upon twisting the carbon backbone of *n*-pentane into a *gauche* - *gauche* conformation thus nicely images the loss of one nodal surface in the corresponding molecular orbital. In the outlook of forthcoming EMS experiments on *n*-pentane, it must nonetheless be reminded that the g^+g^+ and g^+G^- conformers have very limited weight at 298K, and would thus be very hard to detect at standard conditions. EMS measurements at higher temperatures (Table 2) would be needed for unambiguously observing their fingerprint. Such experiments are possible nowadays on molecular supersonic beams and would clearly be extremely useful for investigating the electronic structure of structurally versatile molecules, and their dependence towards the molecular conformation.

The momentum distributions predicted for bands **IV** and **V** at 20.4 eV and 19.0 eV for the *tg* and *tt* conformers are shown in Figures 6d and 6e, respectively. In line with the presence of an odd number of nodal surfaces in the related MO contours (3 and 1, respectively), both distributions resemble a *p*-type profile. Upon considering the pronounced influence of the molecular conformation on the spread and shape of the individual contributions, it is legitimate to conclude that both electron momentum profiles straightforwardly image the dominance of the *tg* conformer at 298K. These conformational fingerprints are in both cases ascribable to alterations of the pattern of through-space bonding methylenic hyperconjugation interactions that prevail at the top of the inner-valence region of zig-zag planar (all-staggered) hydrocarbon chains.

For band **IV**, the maximum of the envelope is predicted at *p*= 0.63 a.u., a value to compare with the maximum location at *p*= 0.59 a.u. for the MD related to the *tg*/9a orbital (**4**). The shift by 0.04 a.u. towards larger electron momenta corroborates the energy increase observed for orbital **4** upon conversion into the *tt*/4b$_2$ one (Figure 1). These variations in energies and momenta both correlate with a significant enhancement of anti-bonding interactions between adjacent C-H bonds, and, thus, a stronger confinement of the electron density in the *tt*/4b$_2$ orbital (Figure 1). The latter orbital yields vanishing and maximal electron densities distribution at p = 0 and at *p*= 0.78 a.u., respectively. In contrast, a shift towards lower electron momenta of the electron density distribution associated to band **IV** is predicted with a slight increase (Table 2) at higher temperatures of the molar fraction of the g^+g^+ conformer, due to the enhancement of through-space bonding interactions between end-methyl groups, and, thus, the reduced electron confinement in *r*-space that underlie (Figure 1) the stabilization of the g^+g^+/4b orbital relative to *tt*/9a level (**4**).

Precisely the opposite trends are found for the various conformer contributions to the momentum profile associated to band **V**, which this time consistently reflects the destabilization of the g^+g^+/6a orbital (**5**) relative to the *tg*/10a and *tt*/6a$_1$ levels (Figure 1), due to the progressive disruption of through-space bonding methylenic hyperconjugation interactions between adjacent C-H bonds. In line with the orbital destabilization, a shift towards larger electron momenta in the position of the maximum is observed when successively comparing the *tt*/6a$_1$ to the *tg*/10a orbital densities and the *tg*/10a to the g^+g^+/6a orbital densities: the g^+g^+/6a, *tg*/10a and *tt*/6a$_1$ orbital momentum distributions have their maxima located at *p*=0.75, 0.59, and 0.51 a.u., to compare with a value of p=0.59 a.u. for the momentum profile characterizing band **V** as a whole. A shift towards larger electron momenta of the electron density distribution associated to band **V** is therefore predicted with an increase at higher temperatures of the molar fraction of the g^+g^+ conformer.

Analyses of conformational fingerprints in the outer valence region are more challenging, due to the congested nature of the underlying ionization bands. With band **VI** at 15.8 eV, the main difference between the individual conformer distributions is observed at the origin of momentum space (Figure 6f). A minimal but clearly non-vanishing (e,2e) cross section is found at p = 0 a.u. for the asymmetric and most abundant conformer (*tg*). In contrast, and in agreement with symmetry considerations, the (e, 2e) cross sections computed at p = 0 a.u. for that band and for the *tt* conformer almost vanish, indicating overall a *p*-type symmetry under the limitations due to the finite resolution on electron momenta. This vanishing finds its root into the topology of the related 1b$_1$, 5b$_2$, 1a$_2$ orbitals, which exhibit (Figure 1) one (1b$_1$, 5b$_2$) or two nodal planes (1a$_2$) along the main C$_2$ rotation axis, with in the latter case an essentially non-bonding interaction across the mirror symmetry plane that is perpendicular to the *tt* carbon backbone. Another minor conformational fingerprint with band **VI** pertains to the position of the maximum in the related momentum profile, which shifts from p = 0.54 a.u. with the *tt* conformer to p = 0.60 a.u. or p = 0.57 a.u. for the *tg* or g^+g^+ conformers, respectively, and again merely reflects an enhanced confinement of the electron density in *r*-space upon progressive departures of the carbon backbone from an *all-staggered* conformation.

The electron momentum distributions related to the bands **VII**, **VIII** and **IX** at 14.3, 12.5, and 11.5 eV have all clearly dominantly a mixed *s-p* character (Figures 6g, 6h and 6i). Exploitable conformational fingerprints are identified for the momentum profiles derived from all three bands. Here also, successive twists of an *all-staggered* (*tt*) carbon backbone into an *all-gauche* (g^+g^+) conformation are found overall to result into shifts towards larger electron momenta of the maximum characterizing the *p*-lobes of the individual conformer contributions, due to enhanced anti-bonding interactions and electron confinement in *r*-space.

For band **VII** (Figure 6g), the most striking clue of the presence of the minor *tt* and g^+g^+ conformers in a gas phase sample of *n*-pentane pertains to the relative intensity of the two peaks that emerge in the corresponding electron momentum distribution. The related 14a and 15a orbitals from the *tg* conformer have both a topology characterized by two distinct and approximately parallel nodal planes, yielding a momentum profile with two maxima at p = 0 a.u. and p = 0.80 a.u. and with an intensity ratio equal to 0.87. In the global envelope, the intensity ratio between the peaks at p = 0.00 a.u. and at 0.82 a.u. reduces to 0.82. This change in relative (e, 2e) intensities is clearly ascribable to the non-negligible influence of the minor *tt* and g^+g^+ conformer fractions at these electron momenta and binding energies. Indeed, at this range of electron binding energies, the individual *tt* and g^+g^+ contributions to the global momentum profile exhibit a maximum at p = 0.91 a.u. and p = 0.84 a.u., respectively. The intensity ratio between the maximum at p = 0 a.u. and latter maximum correspondingly amount to 0.64 and 0.74. The momentum distribution related to the *tt* conformer also exhibits a well-marked minimum at 0.25 a.u., whereas the g^+g^+ conformer has only a shallow minimum at p=0.49 a.u.

With band **VIII** (Figure 6h), the most significant differences between the individual conformer contributions to the global momentum distribution are again seen at the origin of momentum space. With the *tt* conformer, the (e, 2e) cross section associated to the peak at p = 0 a.u. in the summed momentum distribution for the $2b_1$ and $6b_2$ orbitals (**11**, **12**) identically vanishes. In contrast, this peak exhibits an approximately equal or larger intensity relative to that of the peak at p = 0.92 a.u. in the global momentum distributions derived from the (15a, 16a, 17a,18a) set of orbitals (**10-13**) for the *tg* conformer, and from the (9a, 8b, 10a) orbital set (**11-13**) for the g^+g^+ conformer, respectively. More specifically, the corresponding intensity ratios are equal to 0.92 and 1.40, and typically reflect an enhancement of through-space bonding interactions upon successive twists of the *tt* carbon backbone (Figure 2), and enhanced delocalization of the electron density at remote distances in *r*-space or close to the origin of momentum space therefore.

The intensity ratio between the two peaks that characterize the momentum distributions pertaining to the outermost valence band **IX** at 11.5 eV is strongly on the relative weight of the three most abundant conformers, and defines therefore a strong conformational fingerprint. The largest component to the individual contribution from the *tt* conformer to the electron momentum distribution pertaining to this band is ascribable to the $9a_1$ orbital (**14**). The latter orbital is very similar to the $6a_g$ orbital of *n*-butane (see Figure 3 in [17]), which gave rise to a very similar momentum distribution characterized by an intense rise of the (e, 2e) cross sections at vanishing electron momenta (see Figure 5f in [17]), due to enhanced electron delocalization at large distances in *r*-space. In both cases, this rise is indeed ascribable to the rather peculiar underlying orbital topologies, which both exhibit one closed prolate ellipsoidal nodal surface separating a σ-bonding core which nicely delocalizes along the carbon backbone from in-phase contributions that delocalize externally on all C-H bonds (compare Figure 2 with Figure 3 in [17]). The latter through-space bonding alterations are unfavorably altered upon twisting C-C-C-C torsion angles in the *tt* structure, which explains a global increase of the energy of this orbital in the *tg* and g^+g^+ conformers, which in turn foretells overall a decrease of the relative (e, 2e) ionization intensity from the latter two species at 11.5 eV and at vanishing momenta. More quantitatively, the maximum of the p-lobe in the momentum distribution for the *tt*, *tg*, and g^+g^+ conformers, and for their thermal average at 298K, is located at p = 0.97, 1.02, 1.05, and 1.02 a.u., respectively. The intensity ratios at p = 0.00 a.u. and at the latter values of momenta correspondingly amount to 2.46, 1.69, 0.20, and 1.75. In contrast with band **VIII**, the latter global ratio is therefore expected to significantly decrease at higher temperatures, due to the changes in the relative abundances of the g^+g^+, *tg* and *tt* conformers. Also, the influence of the minor *tt* and g^+g^+ conformer fractions on this intensity ratio is evident at room temperature, and should be rather easily detectable with standard EMS experiments.

4.3.5 Conclusions

A thorough theoretical study of conformational equilibrium in the gas phase, ionization spectrum and related Dyson orbital momentum distributions of *n*-pentane has been presented, following benchmark theoretical guidelines for interpreting experiments on conformationally versatile molecules employing Electron Momentum Spectroscopy. To carry out reliable enough analyses of such experiments, one should necessarily and systematically proceed through (1) an evaluation of the conformer abundances, within a few % accuracy, by means of statistical thermodynamics beyond the Rigid-Rotor/Harmonic-Oscillators (RRHO) approximation, along with a determination of relative conformer energies, within an accuracy of ~0.05 to 0.1 kcal mol^{-1}, on the basis of calculations at the confines of non-relativistic many-body quantum mechanics; (2) a simulation for each conformers of the valence one-electron and shake-up ionization spectrum, within an accuracy of ~0.2 eV on the computed one-electron binding energies; and, at last, (3) a computation of spherically averaged electron momentum distributions for all resolvable bands, taking into account the fact that the molecular conformation may have a very strong influence on the orbital energy order.

In the present work, these goals have been achieved by using (1) the results of a recent Focal Point Analysis of the conformational energy differences of *n*-pentane computed at various [HF, MP2, MP3, CCSD and CCSD(T)] levels and supplemented by appropriate extrapolations to the limit of an asymptotically complete basis set, as well as the protocol by Ayala and Schegel [42] for treating the internal rotation modes; (2) one-particle Green's function theory of ionization along with the ADC(3) scheme [28]; and (3) an adaptation of the MOMAP methodology by Brion *et al* [55] for Fourier Transforming to momentum space and spherically averaging the Dyson orbitals associated to all identified poles of the ADC(3) one-particle Green's Function, taking into account the finite angular resolution of the (e,2e) spectrometers for convolving the momentum distributions.

The main conclusions drawn from these calculations are the following. According to our best estimates, the *tg*, *tt*, g^+g^+ and g^+G^- conformers of *n*-pentane have, at 298K, molar fractions equal to 0.741, 0.147, 0.086, and 0.026, respectively. Compared with the standard RRHO depiction of internal nuclear motions, hindered rotations were correspondingly found to lower by more than 50% the abundance of the most stable conformer (*tt*). Comparison with available X-ray and ultra-violet (He I) photoelectron measurements clearly confirms the suggestion that, due to entropy effects, the *trans-gauche* (*tg*) conformer strongly dominates the conformational mixture characterizing *n*-pentane at room temperature. Our simulations demonstrate further that, despite the still rather limited energy and momentum resolution that is achievable nowadays, experimental measurements of (e, 2e) valence ionization spectra and electron momentum distributions would very consistently and straightforwardly image the topological changes and energy variations that molecular orbitals undergo due to torsion of the carbon backbone of *n*-pentane. The most clearly discernible fingerprints for the most stable conformer (*tt*) in momentum space have been identified for the electron momentum distributions associated to ionization channels at the top of the inner-valence region, which sensitively image the development of methylenic hyperconjugation in all-staggered *n*-alkane chains. These conformational fingerprints are significant enough to be experimentally amenable using the available (e, 2e) spectrometers. We therefore very much advocate detailed EMS studies of the electronic structure and wavefunction of *n*-pentane, the simplest paraffine compound which at 298K dominantly deviates in the gas phase from its most stable *all-staggered* conformation, because of entropy effects.

References

[1] Eliel, E. L.; Allinger, N. L.; Angyal, S. J.; Morrison, G. A. *Conformational Analysis*; Wiley: New York, 1965.

[2] Lipton, M.; Still, W. C. *J. Comput. Chem.* 1988, 9, 343.

[3] Nair, N.; Goodman, J. M. *J. Chem. Inf. Comput. Sci.* 1998, 38, 317.

[4] Fraser, G. T.; Suenram, R. D.; Lugez, C. L. *J. Phys. Chem. A* 2000, 104, 1141.

[5] Friedrich, J.; Kühn, G.; Mix, R.; Unger, W. *Plasma Process. Polym.* 2004, 1, 28.

[6] Zhao, H. C.; Yang, P.; Deng, J. P.; Liu, L. Y.; Zhu, J. W.; Sui, Y. A.; Lu, J. M.; Yang, W. T. *Langmuir* 2007, 23, 1810.

[7] Pitzer, K. S. *J. Chem. Phys.* 1940, 8, 711.

[8] (a) Szasz, G. J.; Sheppard, N.; Rank, D. H. *J. Chem. Phys.* 1948, 16, 704. (b) Sheppard, N.; Szasz, G. J. *J. Chem. Phys.* 1949, 17, 86. (c) Verma, A. L.; Murphy, W. F.; Bernstein, H. J. *J. Chem. Phys.* 1974, 60, 1540. (d) Compton, D. A. C.; Montero, S.; Murphy, W. F. *J. Phys. Chem.* 1980, 84, 3587. (e) Durig, J. R.; Compton, D. A. C. *J. Phys. Chem.* 1979, 83, 265. (f) Devaure, J.; Lascombe, J. *Nouv. J. Chim.* 1979, 3, 579. (g) Kint, S.; Scherer, J. R.; Snyder, R. G. *J. Chem. Phys.* 1980, 73, 2599. (h) Rosenthal, L.; Rabolt, J. F.; Hummel, J. *J. Chem. Phys.* 1982, 76, 817. (i) Kanesaka, I.; Snyder, R. G.; Strauss, H. L. *J. Chem. Phys.* 1986, 84, 395.

[9] Ito, K. *J. Am. Chem. Soc.* 1953, 75, 2430.

[10] Bartell, L. S.; Kohl, D. A. *J. Chem. Phys.* 1963, 39, 3097.

[11] (a) Bradford, W. F.; Fitzwater, S.; Bartell, L. S. *J. Mol. Struct.* 1977, 38, 185. (b) Schachtschneider, J. H.; Snyder, R.G. *Spectrochim. Acta* 1963, 19, 117. (c) Murphy, W. F.; Fernández-Sáchez, J. M.; Raghavachari, K. *J. Phys. Chem.* 1991, 95, 1124.

[12] Woller, P. B.; Garbisch, E. W., Jr. *J. Am. Chem. Soc.* 1972, 94, 5310.

[13] (a) Stidham, H. D.; Durig, J. R. *Spectrochimica Acta* 1986, 42A, 105. (b) Herrebout, W. A.; van der Veken, B. J.; Wang, A.; Durig, J. R. *J. Phys. Chem.* 1995, 99, 578.

[14] Piercy, J. E.; Seshagiri Rao, M. G. *J. Chem. Phys.* 1967, 46, 3951.

[15] (a) Radom, L.; Lathan, W. A.; Hehre, W. J.; Pople, J. A. *J. Am. Chem. Soc.* 1973, 95, 693. (b) Hoyland, J. R. *J. Chem. Phys.* 1968, 49, 2563. (c) Peterson, M. R.; Csizmadia, I. G. *J. Am. Chem. Soc.* 1978, 22, 6912. (d) Van-Catledge, F. A.; Allinger, N. L. *J. Am. Chem. Soc.* 1982, 104, 6272. (e) Steele, D. *J. Chem. Soc., Faraday Trans. 2* 1985, 81, 1077. (f) Raghavachari, K. *J. Chem. Phys.* 1984, 81, 1383. (g) Wiberg, K. B.; Murcko, M. A. *J. Am. Chem. Soc.* 1988, 110, 8029. (h) Allinger, N. L.; Grev, R. S.; Yates, B. F.; Schaefer III, H. F. *J. Am. Chem. Soc.* 1990, 112, 114. (i) Mirkin, N. G.; Krimm, S. *J. Phys. Chem.* 1993, 97, 13887. (j) Murcko, M. A.; Castejon, H.; Wiberg, K. B. *J. Phys. Chem.* 1996, 100, 16162. (k) Smith, G. D.; Jaffe, R. L. *J. Phys. Chem.* 1996, 100, 18718. (l) Allinger, N. L.; Fermann, J. T.; Allen, W. D.; Schaefer III, H. F.; *J. Chem. Phys.* 1997, 106, 5143.

[16] Salam, A.; Deleuze, M. S. *J. Chem. Phys.* 2002, 116, 1296.

[17] Deleuze, M. S.; Pang, W. N.; Salam, A.; Shang, R. C. *J. Am. Chem. Soc.* 2001, 123, 4049.

[18] Asheko, A. A.; Ivanova, O. I. *Russ. J. Phys. Chem.* 1989, 63, 1588.

[19] McQuarrie, D. A. *Statistical Thermodynamics*; Harper and Row: New York, 1976.

[20] Vansteenkiste, P.; Van Speybroeck, V.; Marin, G. B.; Waroquier, M. *J. Phys. Chem.* 2003, 107, 3139.

[21] Price, W. C.; Potts, A. W.; Streets, D. G. in *Electron Spectroscopy*; Shirley, D. A., ed.; North Holland: Amsterdam, 1972; p. 187.

[22] (a) Pireaux, J. J.; Caudano, R. *Am. J. Phys.* 1984, 52, 821. (b) Pireaux, J. J.; Svensson, S.; Basilier, E.; Malmqvist, P-A.; Gelius, U.; Caudano, R.; Siegbahn, K. *Phys. Rev. A* 1976, 14, 2133. (c) Pireaux, J.-J.; Svensson, S.; Basilier, E.; Malmqvist, P.-A.; Gelius, U.; Caudano, R.; Siegbahn, K. *J. Phys.* (in French) 1977, 38, 1213. (d) Pireaux, J.-J.; Caudano, R. *Phys. Rev. B* 1977, 15, 2242. (e) Pireaux, J.-J.; Svensson, S.; Basilier, E.; Malmqvist, P.-A.; Gelius, U.; Caudano, R.; Siegbahn, K. *J. Phys.* (in French) 1977, 38, 1221.

[23] Kimura, K.; Katsumata, S.; Achiba, Y.; Yamazaki, T.; Iwata, S. *Handbook of HeI Photoelectron Spectra of Fundamental Organic Molecules*; Japan Scientific Society: Tokyo, 1981.

[24] For a review, see e.g. Karpfen, A. *J. Chem. Phys.* 1981, 75, 238.

[25] (a) Delhalle, J.; André, J.-M.; Delhalle, S.; Pireaux, J. J.; Caudano, R.; Verbist, J. J. *J. Chem. Phys.* 1974, 60, 595. (b) Seki, K.; Karlsson, U.; Engelhardt, R.; Koch, E. E. *Chem. Phys. Lett.* 1984, 103, 343. (c) Seki, K.; Ueno, N.; Karlsson, U. O.; Engelhardt, R.; Koch, E. E. *Chem. Phys.* 1986, 105, 247. (d) Fujimoto, H.; Mori, T.; Inokuchi, H.; Ueno, N.; Sugita, K.; Seki, K. *Chem. Phys. Lett.* 1987, 141, 485. (e) Ueno, N.; Seki, K.; Sato, N.; Fujimoto, H.; Kuramochi, T.; Sugita, K.; Inokuchi, H. *Phys. Rev. B* 1990, 41, 1176.

[26] (a) Deleuze, M. S.; Cederbaum, L. S. *J. Chem. Phys.* 1996, 105, 7583. (b) Golod, A.; Deleuze, M. S.; Cederbaum, L. S. *J. Chem. Phys*. 1999, 110, 6014.

[27] (a) Linderberg, J.; Öhrn, Y. *Propagators in Quantum Chemistry*; Academic Press, London, 1973. (b) Pickup, B. T.; Goscinski, O. *Mol. Phys.* 1973, 26, 1013. (c) Cederbaum, L. S.; Hohlneicher, G.; von Niessen, W. *Mol. Phys.* 1973, 26, 1405. (d) Cederbaum, L. S.; Domcke, W. *Adv. Chem. Phys.* 1977, 36, 205. (e) Herman, M. F.; Freed, K. F.; Yeager, D. L. *Adv. Chem. Phys.* 1981, 48, 1. (f) Őhrn, Y.; Born, G. *Adv. Quantum Chem.* 1981, 13, 1. (g) von Niessen, W.; Schirmer, J.; Cederbaum, L. S. *Comput. Phys. Rep.* 1984, 1, 57. (h) Ortiz, J. V. *Computational Chemistry: Reviews of Current Trends*; Leszczynski, J., Ed.; World Scientific: Singapore, 1997; Vol. 2 p. 1.

[28] (a) Schirmer, J.; Cederbaum, L. S.; Walter, O. *Phys. Rev. A* 1983, 28, 1237. (b) Schirmer, J.; Angonoa, G. *J. Chem. Phys.* 1989, 91, 1754. (c) Weikert, H. G.; Meyer, H.-D.; Cederbaum, L. S.; Tarantelli, F. *J. Chem. Phys.* 1996, 104, 7122. (d) Deleuze, M. S.; Giuffreda, M. G.; François, J.-P.; Cederbaum, L. S. *J. Chem. Phys.* 1999, 111, 5851.

[29] Deleuze, M.; Denis, J.-P.; Delhalle, J.; Pickup, B. T. *J. Phys. Chem.* 1993, 97, 5115. (b) Deleuze, M.; Delhalle, J.; Pickup, B. T.; Svensson, S. *J. Am. Chem. Soc.* 1994, 116, 10715. (c) Deleuze, M.; Delhalle, J.; Pickup, B. T. *J. Phys. Chem.* 1994, 98, 2382.

[30] Gelius, U. *J. Electron Spectrosc. Rel. Phenom.* 1974, 5, 985.

[31] (a) Deleuze, M.; Delhalle, J.; Mosely, D. H.; André, J.-M. *Physica Scripta* 1995, 51, 111. (b) Duwez, A. S.; Di Paolo, S.; Ghijsen, J.; Riga, J.; Deleuze, M. S.; Delhalle, J. *J. Phys. Chem. B* 1997, 101, 884. (c) Deleuze, M. S.; Delhalle, J. *J. Phys. Chem. A* 2001, 105, 6695.

[32] (a) Salomon, A.; Cahen, D.; Lindsay, S.; Tomfohr, J.; Engelkes, V. B.; Frisbie, C. D. *Adv. Mat.* 2003, 15, 1881. (b) Lindsay, S. M.; Ratner, M. A. *Adv. Mat.* 2007, 19, 23.

[33] Pang, W. N.; Gao, J. F.; Ruan, C. J.; Shang, R. C.; Trofimov, A. B.; Deleuze, M. S. *J. Chem. Phys.* 2000, 112, 8043.

[34] (a) McCarthy, I. E.; Weigold, E. *Rep. Prog. Phys.* 1991, 54, 789. (b) Leung, K. T. in *Theoretical models of chemical bonding*; Z. B. Maksic, ed.; Springer-Verlag: Berlin, 1991; Vol. 3, p. 339. (c) Weigold, E.; McCarthy, I. E. *Electron Momentum Spectroscopy*; Kluwer Academic Plenum Publishers: New York, 1999. (d) Coplan, M. A.; Moore, J. H.; Doering, J. P. *Rev. Mod. Phys.* 1994, 66, 985.

[35] Deleuze, M. S.; Knippenberg, S. *J. Chem. Phys.* 2006, 125, 104309.

[36] Zheng, Y.; Pang, W. N.; Shang, R. C.; Chen, X. J.; Brion, C. E.; Ghanty, T. K.; Davidson, E. R. *J. Chem. Phys*. 1999, 111, 9526.

[37] Ning, C. G.; Ren, X. G.; Deng, J. K.; Su, G. L.; Zhang, S. F.; Knippenberg, S.; Deleuze, M. S. *Chem. Phys. Lett.* 2006, 421, 52.

[38] Huang, Y. R.; Knippenberg, S.; Hajgato, B.; François, J.-P.; Deng, J. K.; Deleuze, M. S. *J. Phys. Chem. A* 2007, 111, 5879.

[39] Ning, C. G.; Hajgato, B.; Zhang, S. F.; Liu, K.; Luo, Z. H.; Knippenberg, S.; Deng, J.-K.; Deleuze, M. S.; accepted with minor revisions in *Chem. Phys.*

[40] Frisch, M. J.; Pople, J. A.; Binkley, J. S. *J. Chem. Phys.* 1984, 80, 3265.

[41] (a) Becke, A. D. *J. Chem. Phys.* 1993, 98, 5648. (b) Lee, C.; Yang, W.; Parr, R. G. *Phys. Rev. B* 1988, 37, 785.

[42] Ayala, P. Y.; Schlegel, H. B. *J. Chem. Phys.* 1998, 108, 2314.

[43] Kilpatrick, J. E.; Pitzer, K. S. *J. Chem. Phys.* 1949, 17, 1064.

[44] Mayo, S. L.; Olafson, B. D.; Goddard, W. A. *J. Phys. Chem.* 1990, 94, 8897.

[45] Pitzer, K. S.; Gwinn, W. D. *J. Chem. Phys.* 1942, 10, 428.

[46] Frisch, M. J.; Trucks, G.W.; Schlegel, H.B, *et al.* Gaussian98, revision A.7; Gaussian Inc, Pittsburg, PA 1998.

[47] Dunning, T. H., Jr. *J. Chem. Phys.* 1989, 90, 1007.

[48] The 1*p*-GF/ADC(3) code originally written by Angonoa, G.; Walter, O.; Schirmer, J.; Cederbaum, L. S. and further developed by Scheller, M. K. and Trofimov, A. B.

[49] Schmidt, M. W.; Baldridge, K. K.; Boatz, J. A.; Elbert, S. T.; Gordon, M. S.; Jensen, J. H.; Koseki, S.; Matsunaga, N.; Nguyen, K. A.; Su, S. J.; Windus, T. L.; Dupuis, M.; Montgomery, J. A. *J. Comput. Chem.* 1993, 14, 1347.

[50] (a) Liu, B. *Numerical Algorithms in Chemistry, Algebraic Methods*; LBL-8158; Lawrence Berkely Laboratory; (b) Tarantelli, F.; Sgamellotti, A.; Cederbaum, L. S.; Schirmer, J. *J. Chem. Phys.* 1987, 86, 2201.

[51] Knippenberg, S.; Nixon, K. L.; Brunger, M. J.; Maddern, T.; Campbell, L.; Trout, N.; Wang, F.; Newell, W. R.; Deleuze, M. S.; François, J.-P.; Winkler, D. A. *J. Chem. Phys.* 2004, 121, 10525.

[52] Knippenberg, S.; Deleuze, M. S.; Cleij, T. J.; François, J.-P.; Cederbaum, L. S.; Eland, J. H. D. *J. Phys. Chem. A* 2005, 109, 4267.

[53] (a) Deleuze, M. S.; Trofimov, A. B.; Cederbaum, L. S. *J. Chem. Phys.* 2001, 115, 5859. (b) Kishimoto, N.; Hagihara, Y.; Ohno, K.; Knippenberg, S.; François, J.-P.; Deleuze, M. S. *J. Phys. Chem. A* 2005, 198, 10535; and references therein.

[54] (a) Ren, X. G.; Ning, C. G.; Deng, J. K.; Zhang, S.; Sum, G.; Huang, F.; Li, G. *Chem. Phys. Lett.* 2005, 404, 279. (b) Su, G. L.; Ren, X. G.; Su, G. L.; Ning, C. G. *J. Chem. Phys.* 2005, 122, 054301. (c) Zhang, S. F.; Ren, X. G.; Su, G. L.; Ning, C. G.; Zhou, H.; Li, B.; Li, G. Q.; Deng, J. K. *Chem. Phys.* 2006, 327, 269.

[55] See various contributions to the original HEMS program as recorded by Bawagan [Bawagan, A. O.; Ph. D. Thesis; University of British Columbia (UBC), 1987]. The HEMS (now known as MOMAP) program has been extensively revised and extended at UBC by Cann, N. M.; and Cooper, G.

[56] Duffy, P.; Casida, M. E.; Brion, C. E.; Chong, D. P. *Chem. Phys.* 1992, 159, 347.

[57] Zheng, Y.; Neville, J. J.; Brion, C. E.; Wang, Y.; Davidson, E. R. *Chem. Phys.* 1994, 188, 109.

[58] (a) Klauda, J. B.; Brooks, B. R.; MacKerell, A. D., Jr.; Venable, R. M.; Pastor, R. W. *J. Phys. Chem. B* 2005, 109, 5300. (b) Klauda, J. B.; Pastor, R. W.; Brooks, B. R. *J. Phys. Chem. Lett. B* 2005, 109, 15684.

[59] Mencarelli, P. *J. Chem. Educ.* 1993, 72, 13887.

[60] Lowe, J. P. *Quantum Chemistry*; Academic Press: San Diego, 1978.

Table 1. Evaluation, using Boltzmann statistical thermodynamics at the level of the Rigid-Rotor Harmonic Oscillator and upon accounting for hindered rotations, of the abundance of the four conformers of dimethoxymethane at room temperature (T=298.15 K), using the best FPA estimates (ΔE) for the energy differences, and the B3LYP/6-311++G** estimates for the zero-point vibrational and thermal contributions to the enthalpy differences ($\Delta\Delta H_{298}$=ΔH_{298}-ΔE), for the relative enthalpies (ΔH_{298}= ΔE(FPA) + $\Delta\Delta H_{298}$), for the relative entropies (ΔS_{298}) and for the relative Gibbs free energies (ΔG_{298}= ΔH_{298} - $T\cdot\Delta S_{298}$). ρ denotes the relative multiplicities of the conformer on the potential energy surface of *n*-pentane. Energies (enthalpies) and entropies are in kcal mol^{-1} and cal mol^{-1} K^{-1}, respectively.

	With hindered rotations				Without hindered rotations			
	tg (C_1)	*tt* (C_{2v})	g^+g^+ (C_2)	g^+G^- (C_1)	*tg* (C_1)	*tt* (C_{2v})	g^+g^+ (C_2)	g^+G^- (C_1)
ρ	4	1	2	4	4	1	2	4
ΔE	0.621	0.000	1.065	2.917	0.621	0.000	1.065	2.917
ΔZPE	0.068	0.000	0.377	0.195	0.068	0.000	0.377	0.195
ΔH	0.649	0.000	1.279	3.024	0.648	0.000	1.296	3.040
ΔS_{Vib}	-0.775	0.000	-0.982	-0.699	-0.218	0.000	-0.882	-0.204
ΔS_{Rot}	3.407	0.000	2.820	4.654	1.462	0.000	0.055	1.463
ΔS_{Tot}	2.634	0.000	1.838	3.956	1.244	0.000	-0.827	1.259
ΔG	-0.136	0.000	0.731	1.845	0.277	0.000	1.543	2.665
x	0.741	0.147	0.086	0.026	0.678	0.271	0.040	0.012

Table 2. – Evolution of the conformer abundances as a function of the temperature, using a Boltzmann thermostatistical analysis, corrected for hindered rotations.

Temperature[a]	*tg* (C_1)	*tt* (C_{2v})	g^+g^+ (C_2)	g^+G^- (C_1)
100	0.348	0.648	0.004	0.000
125	0.509	0.479	0.012	0.000
150	0.611	0.366	0.023	0.000
175	0.672	0.292	0.035	0.001
200	0.707	0.242	0.047	0.003
225	0.727	0.207	0.059	0.007
250	0.738	0.181	0.069	0.012
275	0.742	0.162	0.078	0.019
300	0.741	0.146	0.086	0.027
325	0.737	0.134	0.093	0.036
350	0.731	0.124	0.099	0.047
375	0.724	0.115	0.104	0.058
400	0.715	0.108	0.108	0.070
425	0.706	0.101	0.111	0.082
450	0.696	0.096	0.114	0.094
475	0.686	0.091	0.116	0.106
500	0.676	0.087	0.118	0.119

[a] in Kelvin

Table 3. The ADC(3)/cc-pVDZ ionization spectra of the four conformers of pentane.[a]

Band	MO	*tg* [C_1]			*tt* [C_{2v}]			g^+g^+ [C_2]			g^+G^- [C_1]			UPS[b]
IX	**16**	21a	11.213	(0.910)	$7b_2$	11.255	(0.905)	10b	11.292	(0.910)	21a	11.131	(0.912)	F_2-F_1, 10.9-11.5
	15	20a	11.451	(0.911)	$3b_1$	11.644	(0.915)	11a	11.346	(0.911)	20a	11.308	(0.911)	
	14	19a	11.581	(0.916)	$9a_1$	11.655	(0.911)	9b	11.554	(0.911)	19a	11.578	(0.915)	
	13	18a	12.237	(0.457)	$2a_2$	12.123	(0.913)							
VIII	**13**	18a	12.237	(0.457)				10a	12.443	(0.909)	18a	12.302	(0.914)	E_3, 12.1
	12	17a	12.670	(0.911)	$6b_2$	12.537	(0.908)	8b	12.681	(0.911)	17a	12.739	(0.908)	E_2, 12.5
	11	16a	13.133	(0.910)	$2b_1$	13.401	(0.910)	9a	12.953	(0.910)	16a	13.125	(0.911)	E_1, 12.8
	10	15a	13.605	(0.405)										
VII	**10**	15a	13.605	(0.405)	$8a_1$	13.894	(0.904)	7b	14.031	(0.904)	15a	13.737	(0.910)	D, 13.9
	9	14a	14.347	(0.907)	$7a_1$	13.992	(0.904)	6b	14.348	(0.905)	14a	14.143	(0.907)	C, 14.4
	8							8a	14.439	(0.906)				
VI	**8**	13a	14.978	(0.904)	$1a_2$	15.023	(0.904)				13a	14.991	(0.904)	B_2, 15.0
	7	12a	15.389	(0.902)	$5b_2$	15.106	(0.901)	5b	15.826	(0.897)	12a	15.416	(0.900)	B_1, 15.5
	6	11a	16.014	(0.899)	$1b_1$	16.265	(0.896)	7a	15.980	(0.897)	11a	15.962	(0.899)	A, 16.2
V	**5**	10a	19.036	(0.861)	$6a_1$	19.327	(0.856)	6a	18.724	(0.862)	10a	18.960	(0.861)	

IV	**4**	9a	20.366	(0.842)	$4b_2$	20.082	(0.845)	4b	20.563	(0.837)	9a	20.327	(0.841)	
III	**3**	8a	22.201	(0.795)	$5a_1$	22.185	(0.796)	5a	22.220	(0.788)	8a	22.311	(0.774)	
II	**2**	7a	23.909	(0.141)	$3b_2$	23.805	(0.067)	3b	23.807	(0.029)	7a	23.803	(0.082)	
			24.076	(0.047)		23.872	(0.032)		23.882	(0.244)		23.847	(0.056)	
			24.161	(0.255)		23.936	(0.126)		23.997	(0.113)		23.962	(0.048)	
			24.191	(0.140)		24.221	(0.276)		24.093	(0.144)		23.999	(0.022)	
			24.416	(0.029)		24.293	(0.103)		24.176	(0.086)		24.034	(0.057)	
				(0.707)^c		24.407	(0.068)		24.265	(0.020)		24.101	(0.122)	
							(0.700)^c		24.360	(0.025)		24.126	(0.144)	
										(0.720)^c		24.197	(0.029)	
												24.236	(0.041)	
												24.264	(0.036)	
												24.322	(0.030)	
													(0.738)^c	
	1				$4a_1$	24.767	(0.040)	4a	24.655	(0.022)				
									24.838	(0.023)				
I	**1**	6a	24.930	(0.022)	$4a_1$	24.982	(0.031)	4a	25.068	(0.028)	6a	25.305	(0.034)	
			25.043	(0.024)		25.053	(0.034)		25.137	(0.024)		25.483	(0.022)	
			25.153	(0.030)		25.109	(0.060)		25.220	(0.099)		25.523	(0.056)	
			25.421	(0.023)		25.296	(0.040)		25.267	(0.033)		25.666	(0.048)	
			25.436	(0.045)		25.321	(0.065)		25.306	(0.026)			**(0.522)**^{c}	
			25.469	(0.030)		25.419	(0.087)		25.506	(0.023)				
			25.485	(0.020)		25.682	(0.123)		25.553	(0.054)				
			25.548	(0.082)		25.966	(0.046)		25.679	(0.020)				
			25.585	(0.024)		26.061	(0.022)		25.754	(0.054)				
			25.648	(0.020)		26.097	(0.020)		25.866	(0.021)				
				(0.539)^c			**(0.639)**^{c}			**(0.543)**^{c}				

[a] Binding energies are given in eV, along with the ADC(3) spectroscopic factors, which are given in parentheses. The first column relates to the labels used in the visualizations of the ADC(3) spectra. Only the ADC(3) ionization lines with pole strengths larger than 0.020 are given here.

[b] Our assignment of the He (I) spectrum by Kimura *et al.* [32] (Figure 4).

[c] Identified fraction of the shake-up ionization intensity for each orbital within the band under investigation. The recovered fractions of ionization intensity amount to {0.713 (7a), 0.568 (6a)} for the *tg* conformer, {0.729 ($3b_2$), 0.697 ($4a_1$)} for the *tt*, {0.720 (3b), 0.602 (4a)} for the g^+g^+ and {0.738 (7a), 0.577 (6a)} for the g^+G^- ones. These fractions were obtained by summing the pole strengths of all lines identified under bands **II** and **I**.

Appendix: Correlation diagrams connecting the valence orbitals of the most abundant *tg* conformer with the highest energy-lying g^+G^- one.

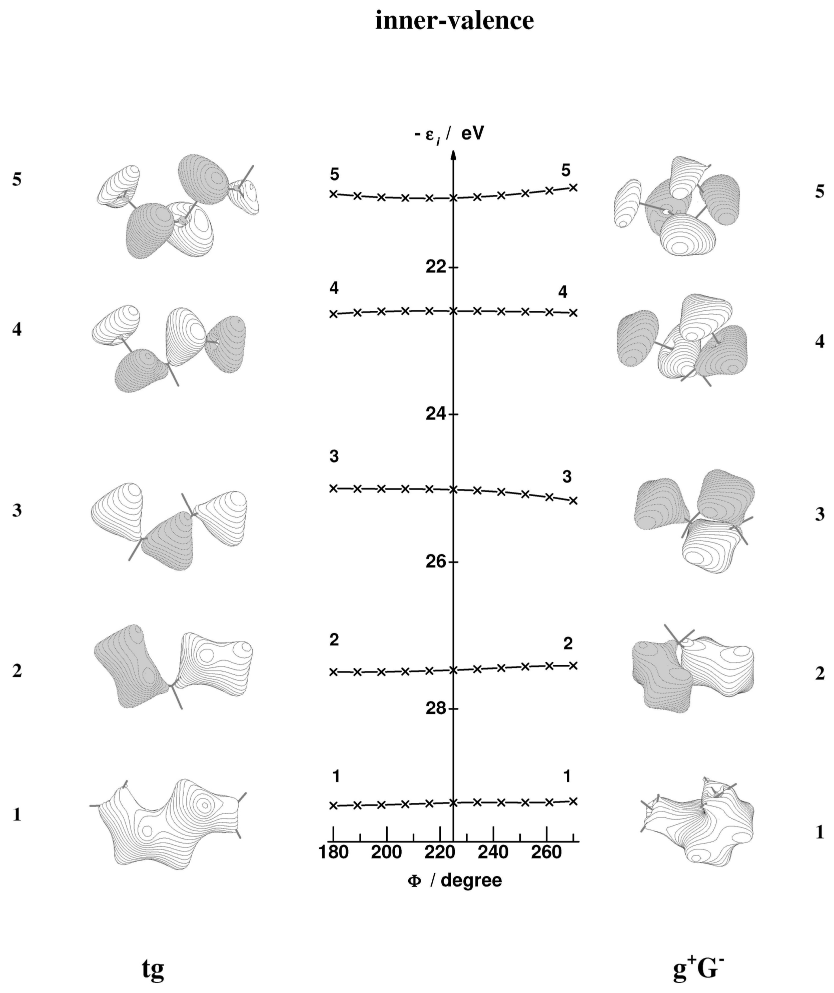

Figure A1. Orbital correlation in inner-valence region of pentane for the *tg* and g^+G^- conformers. The energies are calculated at HF/cc-pVDZ level as a function of the two dihedral angles characterizing the carbon backbone of *n*-pentane. Contour values of 0.05 were used, as well as edges of ~16 Å.

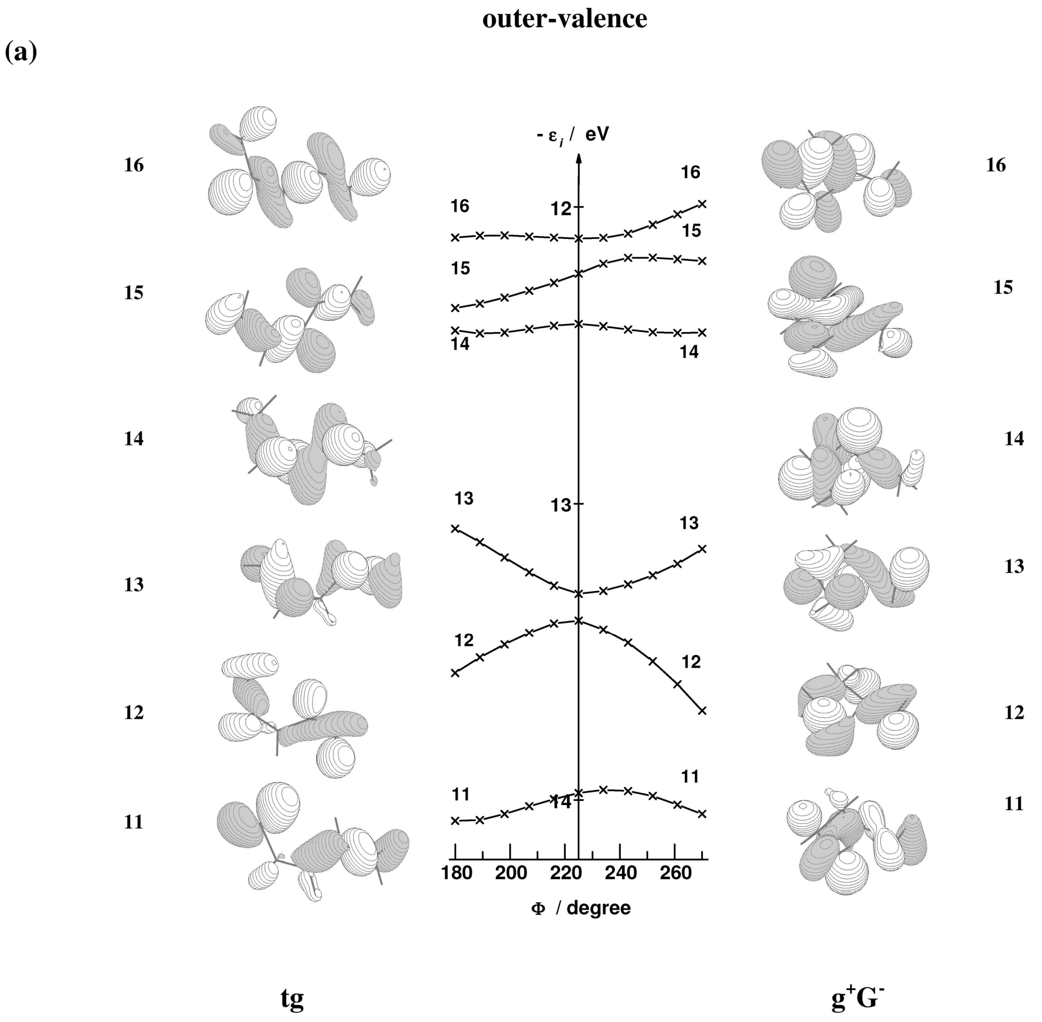
outer-valence
(a)
16
15
14
13
12
11
- ε_i / eV
12
13
14
180
200
220
240
260
Φ / degree
tg
g+G-

Figure A2

(b)

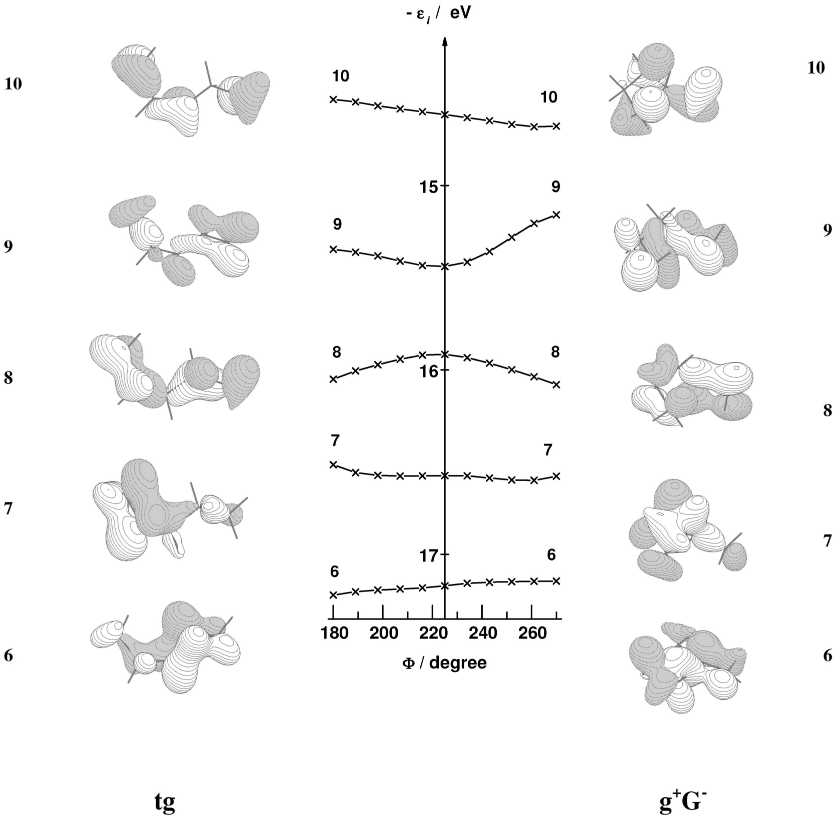

Figure A2 (continued)

Figure A2. Orbital correlation in outer-valence region of pentane for the *tg* and g^+G^- conformers. The energies are calculated at HF/cc-pVDZ level as a function of the two dihedral angles characterizing the carbon backbone of *n*-pentane. Contour values of 0.05 were used, as well as edges of ~16 Å.

4.4 Probing the shape and stereochemistry of molecular orbitals in locally flexible aromatic chains: A Penning ionization electron spectroscopy and Green's function study of the electronic structure of biphenyl.

4.4.1 Introduction

Biphenyl ($C_{12}H_{10}$) is composed of two phenyl rings connected by a single C-C bond. Although π conjugation tends to enforce coplanarity between these two rings, biphenyl is known to be a markedly non-planar structure in the gas phase [1-4], due to the steric repulsion of hydrogen atoms in *ortho* positions. Compared with many other conjugated aromatic hydrocarbons such as benzene, trans-stilbene and larger oligo-phenylene-vinylenes, or polycyclic aromatic hydrocarbons, the departure from planarity must obviously strongly influence the energy distribution and shape of molecular orbitals, since σ- and π- orbitals are allowed to directly interact, as a result of the release of mirror symmetry. Biphenyl is the simplest molecule which reproduces the main structural properties of poly(*p*-phenylene) (PPP), a conjugated polymer that shows conductivity after exposure to oxidizing or reducing agents [5]. Many studies suggest that the conductivity of polymers is closely related to ionization, electron attachment, and charge-transfer excitation processes, namely to the injection of electrons and holes into the material, and the propagation of charge-carriers described as electrically charged and partly localized structural distortions (polarons, bipolarons) along the polymer lattice [5, 6]. Understanding in details the relationships that prevail between the electronic structure and molecular architecture is therefore an essential prerequisite for monitoring the properties of electronic devices (field effect transistors, electroluminescent diodes, solar cells) manufactured from such materials. The radical cations of biphenyls can be regarded as models of single-charge defects in PPP. In that respect, it is worth noting that, in the case of PPP, single-charge polarons specifically take the form of structural transitions from an aromatic to a quinoidal bonding pattern. Correspondingly, ionization of, or electron attachment on biphenyl drive the molecule towards planarity in the gas phase (twist angles of 40.1, 18.9 and 0.0° between the phenyl rings have been reported at the B3LYP/6-311+G(2d,2p) level for the neutral molecule, and for its radical cation and anion, respectively) [7].

A further motivation for studying the electronic structure of biphenyl stems from the fact that this molecule is the base compound for polychlorinated biphenyls (PCBs) [8], which, despite their high toxicity, have served in many industrial applications, as lubricating fluids, fire retardants, and insulating agents. From the impact of the location of Cl substituents onto the toxicity of PCBs, it appears that the latter directly relates to the structural and dynamical properties of biphenyl, namely the relatively limited barrier to rotation about the central C-C bond (4-8 kJ mol^{-1}) [1, 9]. At last, from Fukui's frontier orbital theory [10], it is clear that the topological characteristics of the HOMO and LUMO are of great significance for understanding the chemical properties and reactivity of biphenyl and similar molecules towards electrophilic or nucleophilic agents. The structural, dynamical, electronic and chemical properties of π-conjugated systems are thus intimately related, a consideration which makes us believe that shape- and orbital-imaging techniques such as electron momentum spectroscopy [11] or Penning ionization electron spectroscopy [12] can play an essential role in the context of materials science.

The torsional potential around the central C-C bond of a non rigid but conjugated molecule such as biphenyl has raised considerable interest on the experimental side as an important problem in structural chemistry [7, 13]. For instance, various measurements (by means of Raman spectroscopy [1], IR spectroscopy [9], and X-Ray diffraction [14]) indicate that biphenyl adopts a coplanar conformation in the solid state, which enlightens the importance of packing forces in such an environment. On the other hand, twist angles of 42-44° between the two phenyl rings have been found from electron diffraction experiments in the gas phase [15]. Besides the already reported studies of biphenyl in the gas phase by means of ultra-violet photoelectron spectroscopy [16, 17] He I ultraviolet photoelectron spectra (UPS) and Ne*($^3P_{0,2}$) Penning ionization electron spectra (PIES) measurements of major relevance for the present study are those performed by Kubota and co-workers on films of biphenyl deposited at various temperatures on copper [17]. Irreversible changes in band intensities and energy locations were observed both in UPS and PIES upon annealing at 170 K the films obtained at a lower temperature (109 K). These intensity variations and band shifts have been interpreted as the outcome of a phase transition and realignment of the orientation of the biphenyl molecules on the metal substrate. Kubota *et al.* [17], however, could not discard the possibility that these band shifts might also be due to a change in the molecular conformation [17]. Besides studying in details the anisotropy of the interaction potentials pertaining to each ionization channel of biphenyl through detailed measurements of the collision energy dependence of the related Penning ionization cross sections upon collision with He(2^3S), a specific goal of the present work is therefore to evaluate the influence of an enforcement of the planarity of this molecule on its Penning electron ionization and ultra-violet photoelectron spectra. As explained in Part 2 of the present thesis, Penning ionization electron spectra (PIES) are obtained by measuring the kinetic energy distribution of electrons that are ejected upon collision between a molecular target, M, and a rare gas atom in a metastable excited state, A*, as a result of chemi-ionization processes for various ionization channels ($A^* + M \rightarrow A + M_i^+ + e^-$) [12].

At last, EMS measurements of orbital momentum densities have recently confirmed on experimental grounds that the spread and topology of canonical molecular orbitals is very sensitive to the torsional characteristics of small molecules, such as *n*-butane [18]. In support to the newly reported gas phase PIES and UPS measurements, another purpose of the present work is therefore to present a detailed theoretical study of the one-electron and shake-up ionization bands of biphenyl both in twisted and planar configurations accounting for the structures that prevail in the gas phase and within the bulk of highly-ordered (crystalline) layers, respectively.

4.4.2 Theory and methodological details

A. Ionization cross sections

Electron density contours and EED values for the relative Penning ionization cross sections have been obtained from Hartree-Fock (HF) self-consistent field (SCF) calculations performed using the 6-31++G basis set. In the contour maps shown in the sequel, thick solid curves indicate the repulsive molecular surface that has been used for evaluating the PIES cross sections upon the EED model and which is defined by atomic spheres of van der Waals radii [19].

B. Interaction potentials and collision-energy dependence of partial ionization cross sections.

The interaction potentials between the molecular target and the incoming He*(2^3S) atom have been calculated in this work using a model Li(2^2S) probe, at the level of second-order Møller-Plesset perturbation theory (MP2) [20], in conjunction with the 6-31G basis set [20].

C. Ionization spectra

The valence one-electron and 2h-1p (two-hole, one-particle) shake-up ionization bands of biphenyl in model twisted and planar configurations have been calculated using the so-called third-order algebraic diagrammatic construction scheme [ADC(3)] [21-23] derived within the framework of one-particle Green's Function (or one-electron propagator) theory [24-27]. In contrast with CI treatments of the same-order in correlation, ADC(3) offers the key advantage of size-consistency in the dissociation limit [28]. The size-intensivity of the computed ionization energies follows readily for large (extended) systems, provided that static self-energies are obtained from charge-consistent one-electron densities [28, 29].

At the ADC(3) level, the one-electron (1h) and shake-up (2h-1p) ionization energies are recovered through third- and first-order in correlation, respectively. Except for the outermost ionization lines which appear to be extremely sensitive to the quality of the basis set [30], ADC(3) calculations in conjunction with Dunning's correlation consistent polarized valence basis set of double zeta quality (cc-pVDZ) [31] are sufficient to ensure accuracies of about 0.2 eV on *vertical* one-electron ionization energies, provided that the employed geometries also account for the effect of electronic correlation [30, 32a].

The ADC(3) computations described in this work have therefore been performed on molecular geometries that have been optimised under the constraints of D_2 and D_{2h} symmetry point groups, using the cc-pVDZ basis set, and Density Functional Theory (DFT) in conjunction with the non-local hybrid and gradient corrected Becke three-parameter Lee-Yang-Parr functional (B3LYP) [33] (an approach which is known to provide structural results of quality comparable to that achieved at the benchmark CCSD(T) theoretical level [34c, 35]).

All the ADC(3) calculations have been carried out using the original 1p-GF/ADC(3) package of programs, interfaced to GAMESS [36]. In the present work, a threshold on pole strengths of 0.005 has been retained in the final diagonalization step, which has been performed using the block-diagonalization procedure [37]. The assumption of frozen core electrons has been used throughout and the full molecular symmetry point group has been exploited. The convergence of the ADC(3) ionization spectra with regards to further improvements of the cc-pVDZ basis set has been rechecked by comparison with results and simulations obtained using the 6-31G and 6-31G* standard basis sets. This comparison fully confirms the conclusions drawn in [32a,b] about the influence of the basis set in ADC(3) calculations on relatively large and strongly conjugated molecules such as naphthalene and azulene, and will therefore not be repeated here.

For the sake of comparison, these computations will be supplemented by Outer-Valence Green's Function (OVGF) [38] calculations of one-electron ionisation energies, also in conjunction with the cc-pVDZ basis set. These OVGF calculations have been completed by means of the semi-direct and integral-driven algorithms implemented within the GAUSSIAN98 package of programs [39].

In the sequel, the ultra-violet photoelectron and Penning ionisation electron measurements are compared with convolutions drawn from the ADC(3) ionisation spectra, using as spread function a combination of a Lorentzian and Gaussian with equal weight and width (FWHM = 0.5 eV). For UPS, cross section effects are neglected, i.e. the line intensities are simply scaled according to the pole strengths (Γ_i) computed from the 1h and 1p components of the ADC(3) eigenvectors. In contrast, line intensities in the simulated PIES have been rescaled according to the computed EED values.

4.4.3 Experimental section

The experimental apparatus for He*(2^3S) PIES and He I UPS has been reported previously [40-42]. In our experimental set up, beams of metastable and electronically excited He*(2^1S, 2^3S) atoms were produced by a discharge nozzle source with a tantalum hollow cathode. The He*(2^1S) component was quenched by a water-cooled helium discharge lamp, and the He*(2^3S) (E_A=19.82 eV) beam was introduced into the reaction cell. He I UPS were measured by using the He I resonance photons (584 Å, 21.22 eV) produced by a discharge in pure helium gas. The background pressure in a reaction chamber was of the order of 10^{-7} Torr. The solid sample molecules were put into a small container under the reaction cell in the vacuum chamber at room temperature. The kinetic energy of ejected electrons was measured by a hemispherical electrostatic deflection type analyzer using an electron collection angle of 90° relative to the incident He*(2^3S) or photon beam. Measurement of the full width at half-maximum (fwhm) of the $Ar^+(^2P_{3/2})$ peak in the He I UPS led to an estimate of 60 meV for the energy resolution of the electron energy analyzer. The transmission efficiency curve of the electron energy analyzer was determined by comparing our UPS data of some molecules with those by Gardner and Samson [43] and Kimura *et al.* [44]. Calibration of the electron energy scale was made by reference to the lowest ionic state of N_2 mixed with the sample molecule.

The collisional reaction dynamics of Penning ionization processes and details of the interaction potential between He* probes and target molecules can be experimentally studied by ionic counts as a function of the collision energy (E_c) [12b]. For atomic targets characterized by isotropic interaction potentials, measurements of the collision energy dependence of total ionization cross sections are amply sufficient for analyzing the dynamics of the Penning ionization process [45]. In contrast, with molecular targets, the interaction potentials with the approaching probe is obviously anisotropic, and only an average potential can be deduced from the collision energy dependence of the total ionization cross section [46]. In this case, to obtain more specific information on the angular dependence of the interaction potentials within the MO region where the electron exchange Penning ionization process occurs, one must resort to ionic-state-selected measurements of the collision energy dependence of partial Penning ionization cross sections (CEDPICS) [40]. Two-dimensional (collision energy / electron-energy-resolved) mapping of the Penning ionization electron spectrum (2D-PIES) [41] can be achieved by combining a kinetic analysis of the ionized electrons with CEDPICS measurements employing the cross-correlation time-of-flight method [47] in order to select and monitor the velocity of the He* beam. The collision energy dependence of PIES can strongly vary depending on the ionization channel, and enables therefore rather straightforward assignments of the involved orbitals in many situations, among which in studies of five-membered (pyrrole, furan, thiophene, and bromothiophenes) [48, 49] and six-membered (benzene [42, 50, 51] and azabenzenes [52]) conjugated cyclic compounds. For such systems, π-π^* shake-up bands are known to have relatively large cross sections in PIES [42, 48-53]. Their origin has been confirmed by the dependency of the related partial ionization cross section upon the collision energy, which is very similar to that of the π one-electron ionization bands to which they borrow their intensity [42, 48-52].

In the experimental set-up for the collision-energy-resolved Penning ionization measurements, the metastable atom beam was modulated by a pseudorandom chopper [47], and then introduced into a reaction cell located at 504 mm downstream from the chopper disk. For reducing the resonance in chopper rotation, we attached two chopper plates to the motor and rotated these at 400 Hz. The measured Penning ionization spectra $I_e(E_e, t)$ were stored as a function of the electron kinetic energy (E_e) and time (t). The resolution of the analyzer was lowered to 250 meV in order to obtain higher counting rates of Penning electrons. Analysis of the time-dependent Penning ionization spectra $I_e(E_e, t)$ by means of the Hadamard transformation [47], normalized by the velocity distribution of the He* beam, can lead to a two-dimensional mapping of the Penning ionization cross section as functions [$\sigma(E_e, E_c)$] of the electron energies, E_e, and collision energies, E_c. The velocity distribution in the metastable atom beam was determined by monitoring secondary electrons emitted from a stainless steel plate inserted in the reaction cell.

4.4.4 Results and discussion

A. ADC(3) analysis of the He I UPS and He* (2^3S) PIES gas-phase measurements

The gas-phase ultra-violet (He I) photoelectron and He*(2^3S) Penning ionization spectra of biphenyl in the gas phase are displayed in Figure 1, together with a simulation of the PIES records drawn from the ADC(3)/cc-pVDZ ionization spectrum computed for the B3LYP/cc-pVDZ energy minimum form of biphenyl and model EED cross sections. Despite the rather approximate nature of the EED model, the shape and relative intensities of bands in the Penning ionization electron spectrum are overall very satisfactorily reproduced by the simulation, an observation which confirms the ability of this technique to probe the spread, i.e. the σ-like or π-like character, and nucleophilicity of the molecular orbitals of large conjugated molecules, even when these exhibit significant departures from planarity. Despite the release of mirror symmetry, and a twist angle of about 40 degrees between the two phenyl rings, six of the nine outermost orbitals of the D_2 form of biphenyl (**1** : $9b_2$, **2** : 12a, **3** : $11b_1$, **4** : $9b_3$, **7** : $8b_2$, **9** : $7b_3$) exhibit markedly larger EED values, all above 4.6. These orbitals display a nodal surface that approximately follows the planes of the phenyl rings, and correlate with the $2b_{2g}$, $1a_{1u}$, $1b_{1g}$, $2b_{3u}$, $1b_{2g}$, and $1b_{3u}$ π-levels, respectively, of the 1st-order saddle-point and strictly planar form (D_{2h}) of biphenyl (Figure 2). In contrast, the remaining orbitals in the D_2 form all have EED values smaller than 2.5 and are merely localized around the C-C or C-H bonds. It can thus be concluded that these orbitals are of σ-like nature, in full agreement with the MO correlation diagram of Figure 2.

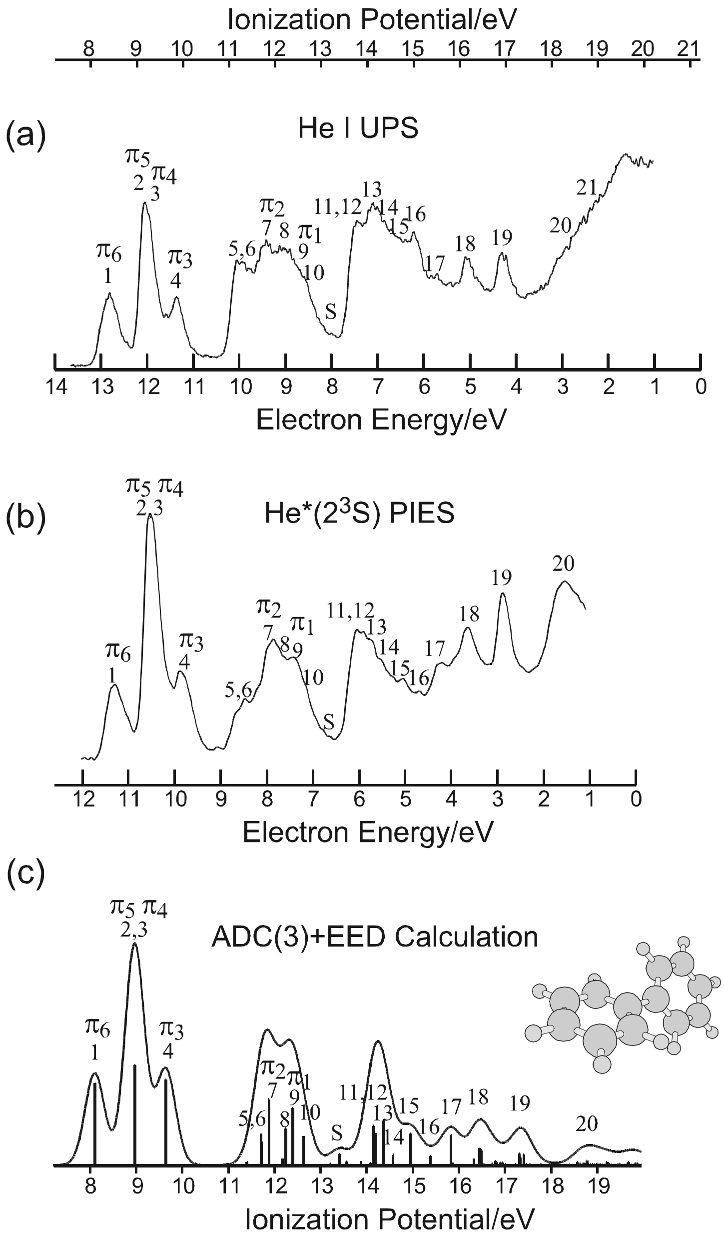

Figure 1. Comparison of the He I ultraviolet photoelectron and He*(2^3S) Penning ionization spectra of biphenyl with a simulation drawn from the theoretical ADC(3) eigenspectra and model EED cross sections calculated for the twisted (D_2) form.

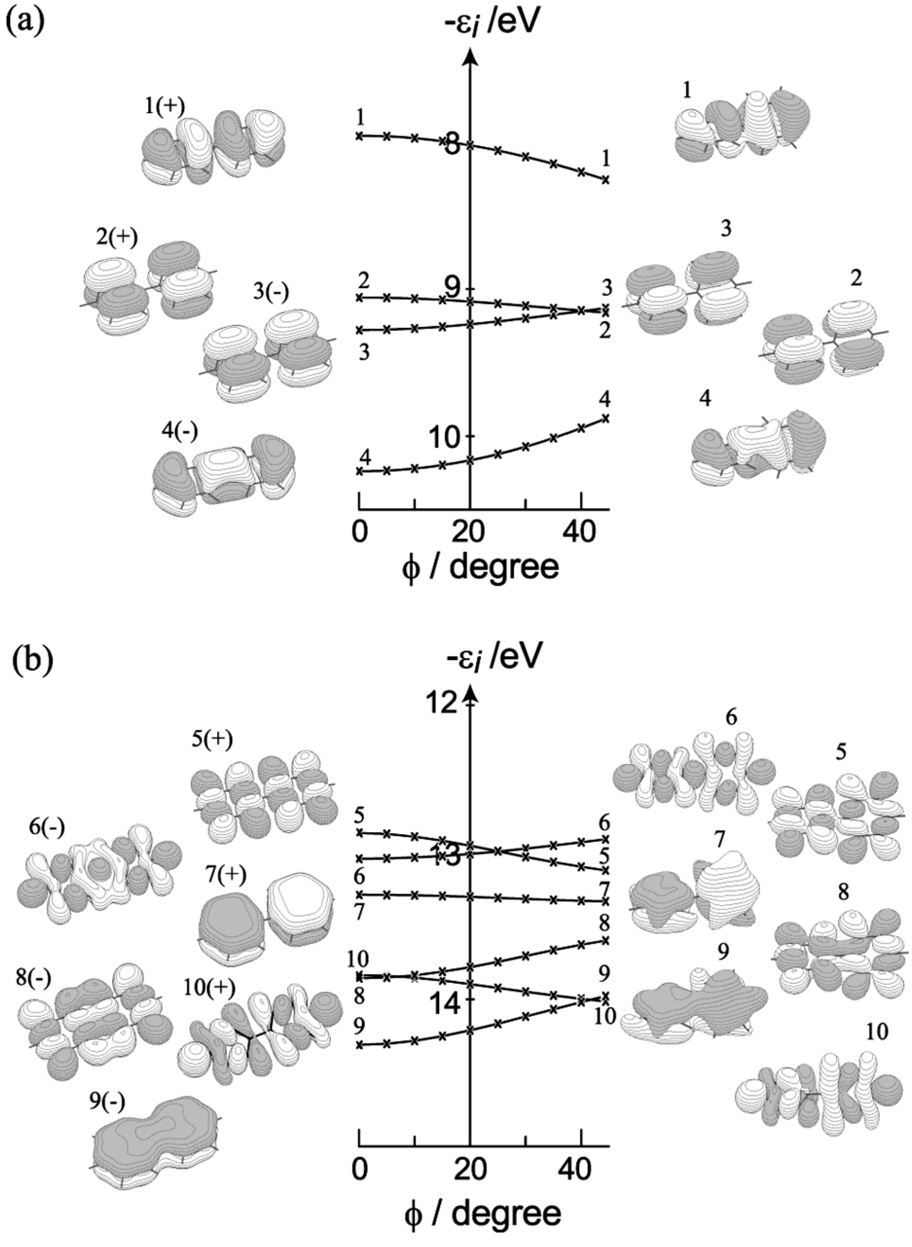

Figure 2. HF/cc-pVDZ energies of the outer-valence molecular orbitals of biphenyl, as a function of the twist angles between the two phenyl rings. The provided labels are consistent with the MO assignment of Tables 1 and 2, with the spike spectra displayed in Figures 3 and 8, and with the detailed ADC(3) data provided as supplementary material. On the left hand-side (D_{2h} form), all levels with a_u, b_{1u}, b_{2g}, b_{3g} symmetry labels are marked by (+), whereas all orbitals with a (-) sign relate to levels with a_g, b_{1g}, b_{2u} and b_{3u} symmetry labels.

For the sake of simplicity and conciseness, and although such a partition is clearly abusive from a formal symmetry view point, we will therefore discuss the electronic structure and ionization spectra of the energy minimum form (D_2) of biphenyl in terms of π- and σ-levels, according to the EED values displayed in Table 1 (included at the end of this chapter) and the MO correlations of Figure 2. It can further be noticed from Figure 2 that all orbitals belonging to the a_u, b_{1u}, b_{2g}, b_{3g} irreducible representations of the D_{2h} point group get stabilized by a few tenths of an eV as the twist angle between the two phenyl rings increases from 0 to 42 degrees, whereas all levels with a_g, b_{1g}, b_{2u} and b_{3u} symmetry labels are inversely destabilized (The two groups of orbitals are differentiated in Figure 2 by adding a (+) or (-) to the MO label, respectively). These energy variations obviously relate to an enhancement of through-space bonding and anti-bonding interactions, respectively, between the two phenyl rings, and reflects the rather pronounced aromatic nature of the biphenyl molecule.

The reader is referred to Table 1 for a detailed assignment of the experimental records on the basis of OVGF one-electron ionization energies and of the most important ADC(3)/cc-pVDZ results. This table confirms the empirical rule [32b, 32c, 54] that OVGF pole strengths smaller than 0.85 systematically corroborate a breakdown of the orbital picture of ionization at the ADC(3) level. As in previous studies of benzene and polycyclic aromatic hydrocarbons [32], we note that the ionization bands belonging to the π-band system are subject to shake-up fragmentation at low binding energies. For biphenyl, the shake-up onset relating to the HOMO^{-2} LUMO^{+1} ($9b_2^{-2}$ $10b_3^{+1}$) excited configuration of the cation is a satellite at 11.42 eV (Γ=0.03) of the $9b_3^{-1}$ (**4**) one-electron ionization line. The orbital picture of ionization partly breaks down for the two lowest π-orbitals, $8b_2$ and $7b_3$ (see lines with labels **7** and **9,** respectively, in the theoretical simulations of Figures 1 and 3). In contrast, the orbital picture holds to a much greater extent within the σ-band system (namely, in this case, up to binding energies around 16 eV). The UPS measurements of Figure 1a can be readily compared with the ADC(3)/cc-pVDZ spike ionization spectrum and convoluted density of states calculated for that structure, which are presented in Figure 3. Overall, this convolution rather nicely matches the UPS record up to binding energies of 18 eV.

The orbital picture of ionization completely breaks down at binding energies above 18 eV. On the theoretical side, one broad peak is observed at a binding energy around 18.7 eV, in qualitative agreement with the PIES measurements. It is worth noting that at the MP2/aug-cc-pVDZ level, the vertical and adiabatic double ionization potentials of biphenyl amount to 21.4 and 20.8 eV, respectively. Therefore all computed shake-up states at binding energies above 20.8 eV are subject to decay via ionization of a second-electron, and should rather be regarded as resonances in a continuum of shake-off states.

The three outermost bands in the UPS and PIES measurements are to be ascribed to four π orbitals (π_6-π_3) originating from the highest occupied MOs ($1e_{1g}$) of benzene. These energy levels display large intensities in PIES. Intensities and band widths in UPS and PIES also readily image the near-energy degeneracy of the π_4 and π_5 orbitals [12a (**2**) and $11b_1$ (**3**)]. In line with the EED values, this pair of lines has extremely large intensity in PIES. In contrast, although the one-hole states produced by ionization of orbitals **5** ($8b_3$) and **6** (11a) are also quasi-degenerate, their signal emerges with much less intensity in PIES, which undoubtedly demonstrates that these orbitals belong to the σ-band system. In straightforward analogy with the $^2E_{1g}$ (σ) and $^2A_{2u}$ (π) electronic states of the benzene radical cation, whose vibronic couplings led to a particularly complicated vibronic structure at electron binding energies ranging from 11.4 to 12.5 eV in the UPS spectrum of this compound [see in particular refs. 55], severe vibronic coupling interactions for ionization of an electron of the σ-orbitals **5** ($8b_3$) and **6** (11a) are also expected, due to the very nearby presence of a π-one-electron ionization line for orbital

$8b_2$ (**7**). These probably explain the poorer agreement between theory and experiment, in particular UPS, at ionization energies around 11.5 eV. This π-state directly derives from the $1a_{2u}$ π- orbital of benzene and can be distinctly identified both in the gas phase UPS and PIES measurements (Figures 1a and 1b). In line with its belonging to the π-band system, this state is more strikingly apparent in the latter case (Figure 1b).

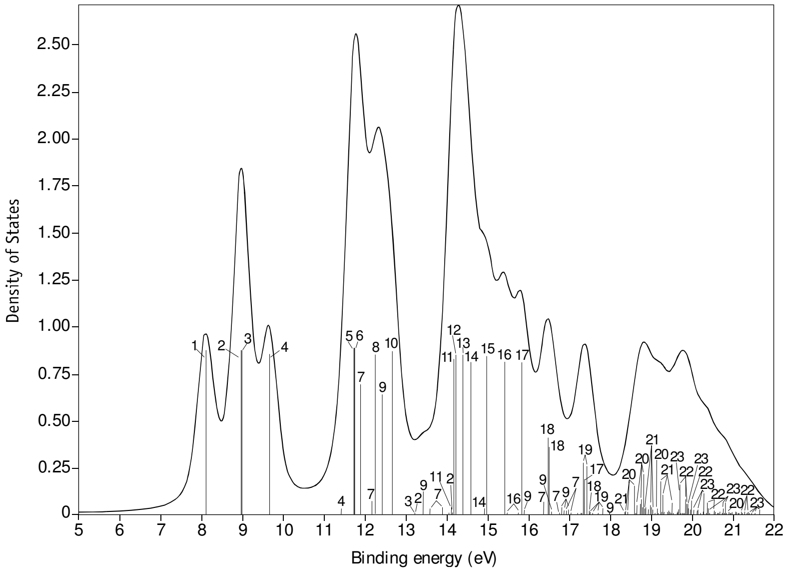

Figure 3. ADC(3)/cc-pVDZ ionization spectrum of the twisted energy minimum form (D_2) of biphenyl (spike spectra and convoluted densities of states as a function of binding energies). $21=4b_3$, $22=4b_2$, $23=7a$. See Table 1 for a detailed orbital assignment.

The same consideration applies for the most intense line produced by ionization of the innermost π-orbital [$7b_3$ (**9**), IP= 12.4 eV, Γ=0.63] : this line undoubtedly relates to the peak that can be distinctly observed at an electron energy of 7.48 eV [i.e. at an ionization energy of 12.34 eV in the gas-phase PIE spectrum (Figure 1b)].. A shoulder (S) with relatively limited intensity can be discerned at an electron binding energy of about 13.4 eV both in UPS and PIES measurements of Figures 1a and 1b, and may at first glance be ascribed to the vibrational tail of the π- and σ- orbitals **9** ($7b_3$) and **10** ($10b_1$). The EED simulation for the twisted (D_2) form of biphenyl in Figure 2b suggests that this shoulder might also relate to a rather weak $\pi^{-2}\,\pi^{*+1}$ satellite (S) with a pole strength of Γ = 0.12 only.

The next spectral feature predicted in the simulations given in Figure 3 is a sharp and narrow peak around 14.1 eV. This peak is produced by the overlap of four one-electron σ-ionization lines (**11-14**), among which a quasi-degenerate pair (within 0.06 eV) of cationic states (**11**, **12** : $6b_3^{-1}$, $10a^{-1}$). With regards to these energy degeneracies, strong vibronic coupling effects can again be expected. Quite naturally therefore, the bands from the σ-ionization lines (**11-14**) display a somewhat different appearance on the experimental side, in particular with UPS, a spectroscopy which by virtue of its relatively large time scale (~10^{-12} s) is particularly sensitive to such effects. Lower PIE intensities relative to the UPS ones suggest that bands **14** and **16** relate to one-electron ionization lines derived from σ-orbitals ($5b_3$ and $5b_2$), which are merely localized around C-C bonds. Such orbitals are not easily accessible to an incoming He* probe and are therefore characterized by very limited EED values, smaller than 0.65. A very considerable decrease of intensity is correspondingly noted at electron energies around 5.0 eV in He*(2^3S) PIES (Figure 1b), compared with the intensity measured at ionization energies of about 14.8 eV in UPS (Figure 1a). On the other hand, orbitals **15**, **17**, **18** ($9b_1$, 9a, $8b_1$) are merely localized around C-H bonds. These orbitals are intrinsically more easily reachable and larger relative EED cross sections (around 2) have been therefore calculated. This is in qualitative agreement with the PIES measurements, taking into account the presence of an intense background signal at electron energies lower than *ca.* 5 eV. It is worth noting that MO **17** (9a) relates exclusively to C-H contributions (see the MO plot of Figure 2). Ionization of this orbital is thought therefore to result into very substantial excitations of C-H stretching vibrations, which explains the very significant broadening observed experimentally for this level, both in UPS and PIES.

The last feature that the EED simulation of Figure 1c shows is a band (**19**), at an electron energy of ca. 3.0 eV, which, according to the ADC(3)/cc-pVDZ results, dominantly relates to shake-up lines produced by ionization of an orbital (8a) which extends fully in-phase outside the molecular surface (Figure 2). It is known that the EED model tends to underestimate the relative PIES of ionization bands derived from such orbitals [42, 48, 50, 51], a fact which a comparison of Figures 1b and 1c confirms.

B. Experimental and theoretical characterization of the anisotropies of the interaction potential of He* (2^3S) around biphenyl.

The slope parameters (*m*) characterizing the collision energy dependence of partial ionization cross sections (CEDPICS) obtained from the 2D-PIES measurements on biphenyl in the gas phase have also been reported in Table 1. These slope parameters have been obtained by means of a least-squares method for collision energies ranging from 90 to 235 meV. He*(2^3S) collision-energy-resolved Penning ionization electron spectra (CERPIES) of biphenyl are correspondingly shown in Figure 4, for collision energies of ~90 meV (dashed curve), ~120 meV (solid curve), ~150 meV (broken curve) and ~200 meV (dotted curve). The CEDPICS of biphenyl are further displayed as log E_c vs. log σ plots in Figure 5. These CEDPICS plots have been obtained from 2D-PIES measurements within an appropriate range of electron energies, typically in electron energy intervals equal to the resolution of the spectrometer, i.e. ~250 meV, in order to avoid a contamination from neighboring bands. Electron density contour maps of σ orbitals are also shown on a plane including a phenyl group. For π orbitals, electron density maps have been plotted on a plane at a height of 1.7 Å above the plane including the phenyl group, along with the 3D plots visualized by MOLDEN [56]. In these plots, thick solid curves indicate the repulsive molecular surface approximated by van der Waals radii. At last, figure 6 provides the interaction potential energy curves $V^*(R)$ calculated at the MP2/6-31G level as functions of the distance *R* between the model Li probe and selected target points in the molecule, along various direction approaches.

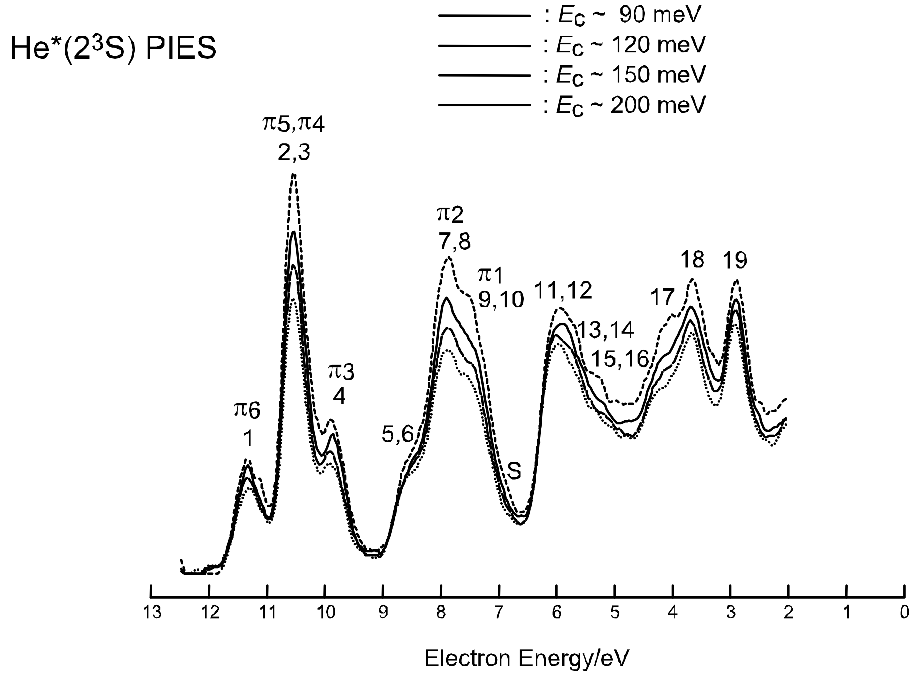

Figure 4. Collision-energy-resolved Penning ionization electron spectra of biphenyl with He*(2^3S) metastable atoms (dashed curve : E_c = 90 (±7) meV; solid curve : E_c = 120 (±12) meV; broken curve : E_c = 150 (±16) meV; dotted curve : E_c = 200 (±25) meV).

The partial ionization cross sections of the π-ionization channels are characterized by strongly negative collision energy dependencies (Figure 5), which demonstrate on experimental grounds that the potential energy surface describing the interaction between the molecule and the approaching He* probe is strongly attractive around the π orbital region. The slope values (m = -0.34 ~ -0.45) obtained from the collision energy dependence of the Penning π-ionization cross sections of biphenyl are similar to those previously inferred for the π-levels of benzene (m = -0.32 or -0.34) [50, 51, 57]. In agreement with these observations, strongly attractive potential wells are found from our potential calculations (Figure 6) when the Li(2^2S) model probe approaches the π orbital region of biphenyl along axes that are perpendicular to the plane of one of the two phenyl rings. Among these model interaction curves, the deepest well is found when the approach follows an axis that intersects the center of one of these rings.

In contrast with the π-levels, a much more limited collision energy dependence is observed in CERPIES and CEDPICS for $\sigma_{C\text{-}H}$ ionization bands such as bands **5**,**6** (m = -0.03). Therefore, the very limited slope parameter characterizing the CEDPICS of bands **4**,**5** indicates that the interaction potential that prevails around the $\sigma_{C\text{-}H}$ bond region of aromatic hydrocarbons is more strongly repulsive. For the sake of comparison, it is worth recalling that slope parameters (m) ranging from +0.10 to –0.02 have been previously inferred for the CEDPICS of σ bands of benzene in effusive condition [50, 51, 57]. In contrast, the present 2D-PIES measurements on biphenyl yield CEDPICS slopes m around –0.10 for σ bands (bands **5**,**6** and **11**,**12**, Figures 5 and 7).

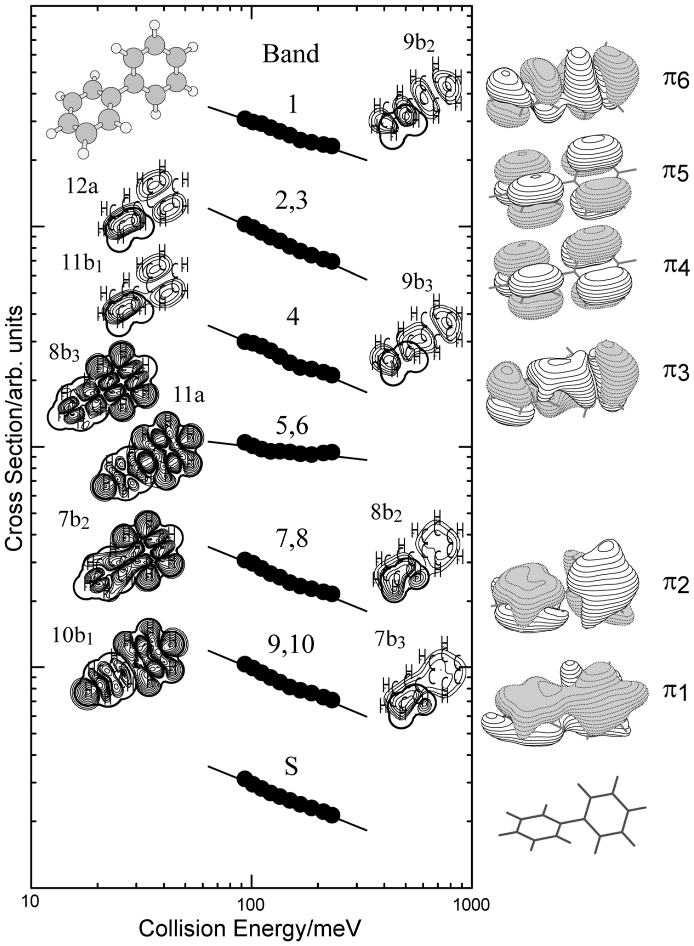

Figure 5. Collision energy dependence of partial ionization cross sections of biphenyl with He*(2^3S) metastable atoms for bands 1-10 and band S.

Since the ADC(3) calcula-tions demonstrate that the contribution of shake-up lines in the π ionization band system is overall extremely limited at binding energies larger than 13 eV, the more strongly negative collision energy dependence of σ-cross sections can be ascribed to a stronger deflection of He* trajectories by enhanced attractive interactions at larger distances around the phenyl groups. Indeed, slope parameters around –0.1 have also previously been found for the CEDPICS characterizing the σ-ionization bands of naphthalene ($C_{10}H_8$) [58]. For the sake of comparison, slope parameters around –0.2 have been inferred from the CEDPICS measured for the σ-ionization bands of anthracene ($C_{14}H_{10}$) [58]. Considering all results obtained so far for benzene, naphthalene, anthracene and biphenyl, these variations in the collision energy dependence of Penning ionization cross sections indicate that the affinity of large π-conjugated molecules towards an impinging electrophilic species such as He*(2^3S) increases with system size, as a result of an enhancement of the polarizability and electron donating (metallic) nature of these aromatic systems, an observation which can ultimately be related to the closure of the HOMO-LUMO band gap and significant enhancements of electron correlation effects [see ref. 30 in particular]. In line with this, a previous comparative PIES study of ethylene derivatives have also shown that the strength of the attraction forces between the molecular target and the He*(2^3S) probe very substantially increases as the ionization energy of an electron in the HOMO decreases [59].

The π_6-π_3 and π_2-π_1 orbitals of biphenyl can be regarded as in-phase or out-of-phase combinations of the $1e_{1g}$ and $1a_{2u}$ orbitals of benzene, respectively. Since biphenyl has a non-planar structure in the gas phase, the electron density distributions of π orbitals are spatially rather intricate. In addition, the calculated potential curves show that, due to enhanced steric interactions, the central C-C bond is much less easily accessible than the centers of the phenyl rings (Figure 6). Some subtle differences in the CEDPICS characteristics of the three outermost π-bands (**1**-**4**) are worth therefore a more detailed analysis. On the other hand, the ionization bands relating to the $8b_2$ (**7**, π_2) and $7b_3$ (**9**, π_1) orbitals overlap with σ-ionization bands and are therefore less easy to characterize. The CEDPICS of the 12a and $11b_1$ (**2**,**3**) ionization channels (π_4, π_5) have a slope parameter m = -0.45, to compare with values of m = -0.34 and m = -0.42 for the slopes characterizing the CEDPICS of the $9b_2$ (**1**, π_6) and $9b_3$ (**4**, π_3) ionization bands, respectively.

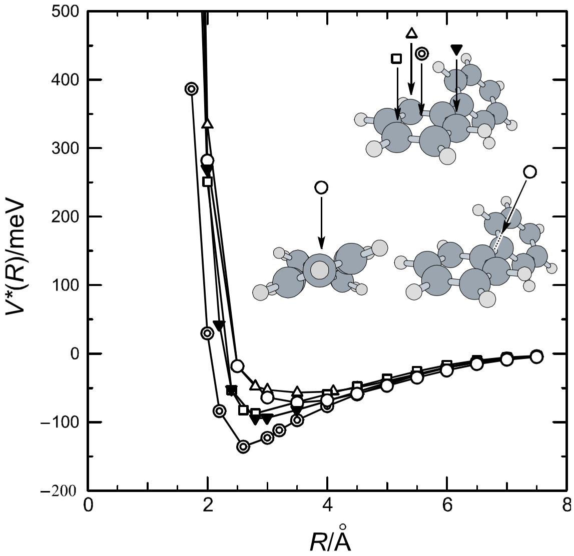

Figure 6. Interaction potential curves $V^*(R)$ for the biphenyl and Li along various direction approaches. R is the distance between Li and C atoms or the center of phenyl ring or the C-C single bond.

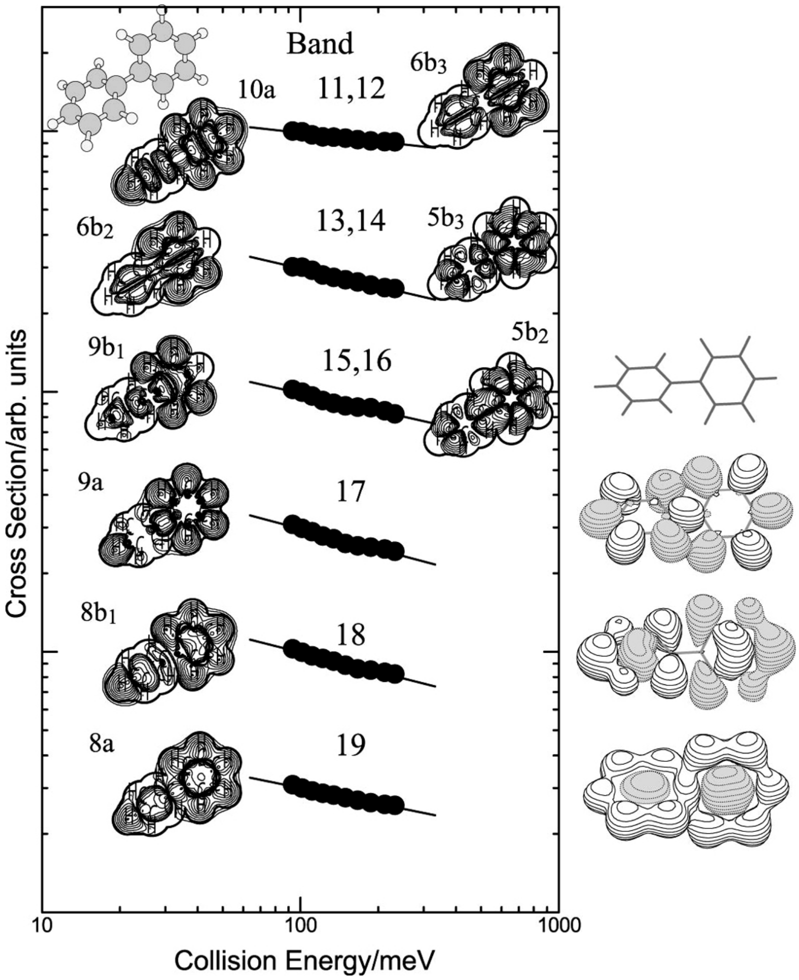

Figure 7. Collision energy dependence of partial ionization cross sections of biphenyl with He*(2^3S) metastable atoms for bands 11-19.

In Figure 5, we separately display the collision energy dependence of the partial ionization cross sections (CEDPICS) of the shoulder (**S**) observed at an ionization energy around 13.2 eV in the He*(2^3S) PIES spectrum of Figure 1. The dependence of the cross sections is markedly negative (*m* = -0.40), which seems to confirm that this shoulder relate to the π-band system, as a $\pi^{-2}\ \pi^{*+1}$ satellite of orbital $7b_3$ (**9**, π_1) (Table 1, Figure 3), rather than to the vibrational tail of the nearest and σ-one-electron ionization line derived from orbital $10b_1$ (**10**), at ~12.7 eV.

C. Conformational fingerprints in the UPS and PIES measurements on biphenyl

The ADC(3)/cc-pVDZ result obtained for the planar 1st-order saddle point form of biphenyl is displayed as a spike spectrum and convoluted densities of states in Figure 8. In Figure 9 we provide the He I ultra-violet and Ne* PIES photoelectron spectra which Kubota *et al.* [17] have obtained from polycrystalline and amorphous thin films of biphenyl of about 10 nm thickness and deposited at temperatures of 170K and 109K on a copper substrate, respectively. A simulation of PIES measurements on the planar form of biphenyl with gas phase resolution is provided further in Figure 10 for the sake of comparison. The reader is referred to Table 2 (included at the end of this chapter) for a quantitative assignment of these spectra and a comparison with ADC(3) and OVGF results. Most of the observations that have been previously made regarding the accuracy of the computed one-electron ionization energies, as well as the significance of OVGF pole strengths smaller than 0.85, are still valid and will not be repeated here.

A comparison with the theoretical simulations in Figure 3 indicates that many bands in the gas phase ionization spectrum of biphenyl are rather sensitive to an alteration of the twist angle between the two phenyl rings. According to these simulations, one of the most significant structural fingerprints for the planar 1st-order saddle-point form versus the twisted energy minimum form pertains to the relative energy location of the ionization bands relating to the σ-orbitals **17**, **18**, and **19**. Very clearly, the UPS and PIES gas phase measurements at electron binding energies ranging from 15 to 18 eV are completely incompatible with the simulations drawn from a planar structure.

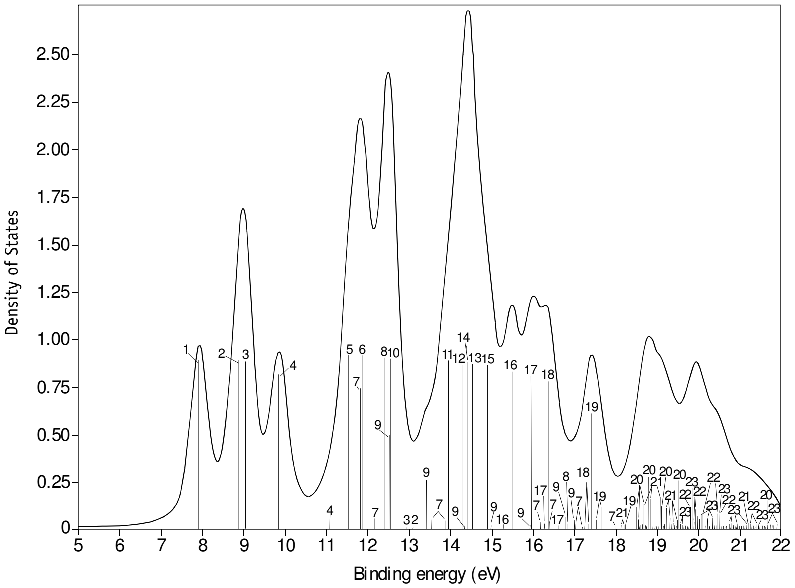

Figure 8. ADC(3)/cc-pVDZ ionization spectrum of the planar (1st-order saddle-point) form (D_{2h}) of biphenyl (spike spectra and convoluted densities of states as a function of binding energies). See Table 2 for a detailed orbital assignment.

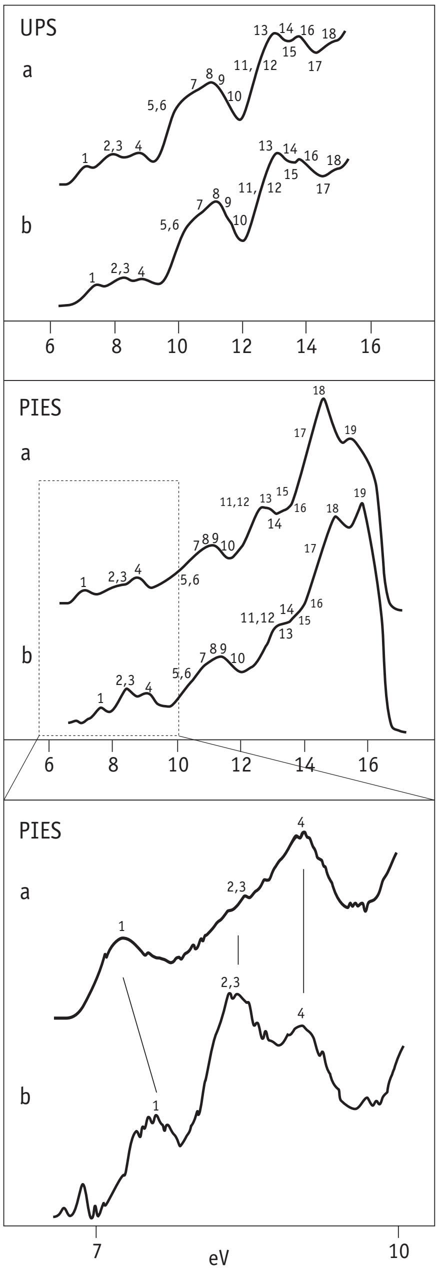

Figure 9. Assignment of the UPS and Ne* PIES measurements by Kubota *et al* [17] on (a) polycrystalline and (b) amorphous layers of biphenyl deposited on copper at temperatures of 170 and 107K.

Compared with the situation that prevails in the gas phase, at least one structural fingerprint of the planar form is clearly apparent in the UPS and Ne* (PIES) (Figure 9) measurements performed on the polycrystalline thin films of biphenyl deposited (or annealed) at 170K [17]. The ADC(3) and OVGF results indicate that, by comparison with the twisted energy minimum form, planarity induces a significant increase, by about 0.4 eV, of the energy spreading of the four outermost π-bands (see also Figure 2a), an observation which fully matches the experimental data for these layers [17]. These results demonstrate therefore on further spectroscopic grounds that the thermodynamically most stable configuration of biphenyl in an optimally relaxed crystalline network is planar at room temperature. In contrast, upon both UPS and Ne* (PIES) measurements, it appears that the energy spreading of the four outermost π-bands obtained from the film deposited at 109K is very similar to that found in the gas phase and from the ADC(3)/cc-pVDZ calculations on the twisted (D_2) form of biphenyl. This obviously corroborates the amorphous, i.e. disordered, nature of this film, and indicates that within the very top layers that are effectively probe by means of UPS and Ne* PIES, biphenyl dominantly lie within a twisted configuration.

Such views are consistent with the conclusions drawn from Kubota *et al.* [17] upon considering the very limited intensity of the Ne* PIES intensities measured from the sample annealed at 170 K for the π_4 and π_5 orbitals (**2**,**3**) compared with that found for the film originally deposited at 109K (see Figure 9). Considering the topology of these orbitals (see Figure 2), these intensity variations indicate that the longitudinal axes of the molecules of biphenyl are all (approximately) aligned perpendicularly to the surface of the polycrystalline layers, whereas the molecules at the surface of the amorphous film are merely randomly oriented [17].

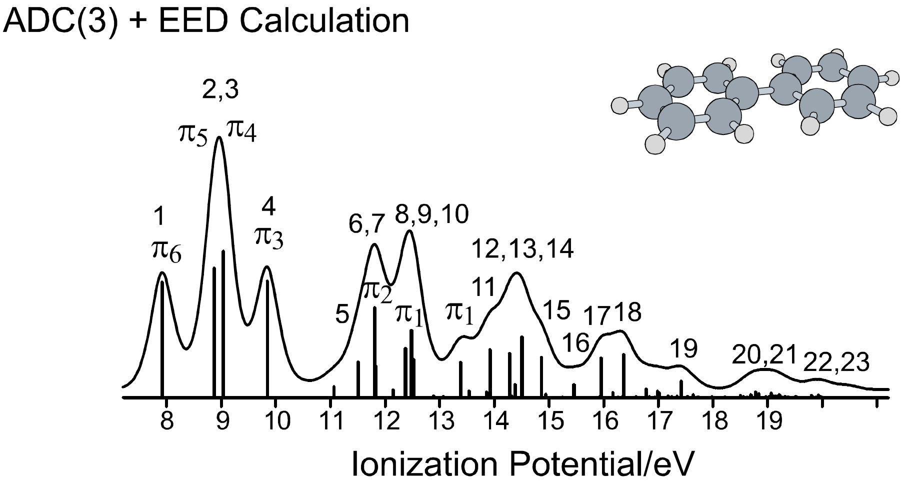

Figure 10. He*(2^3S) Penning ionization spectra simulated upon EED model cross sections and the ADC(3)/cc-pVDZ results for the planar (D_{2h}) 1st-order saddle-point form of biphenyl.

Identification of conformation fingerprints at higher ionization energies is more difficult for the thin films, because of the lower experimental resolution and extremely strong inelastic scattering background, or solid phase effects such as relatively strong π-stack intermolecular interactions, long-range electronic and geometrical relaxations, phonon broadenings, ... etc. For a comparison of ionization energies with simulations on an absolute energy scale, one would also need to know the work function of the sample. The latter being unknown, bands in these measurements are therefore assigned (Figure 9) from their relative location. Despite the complications inherent to the solid phase, we would like to note nonetheless that, in line with the simulations displayed in Figures 1c and 10, significant differences for bands **18**-**19** in the PIES spectra (Figure 9) of the thin films prepared at 170K and 109K are observed. More specifically, a significant lowering of the intensity of band **19** relative to that of band **18** from the 170K (polycrystalline) to the 109K (amorphous) samples corroborates the suggestion that within the outermost layers of these samples biphenyl molecules adopt merely a planar (D_{2h}) and twisted (D_2) conformations, respectively.

4.4.5 Conclusions

We have reported on the PIES and CERPIES study of the valence electronic structure of biphenyl in gas phase, up to electron binding energies of 20 eV, in conjunction with Exterior Electron Density (EED) calculations of partial cross sections in Penning ionization experiments and one-particle Green's Function (1p-GF) [OVGF and ADC(3)] calculations of the one-electron and shake-up ionization spectra of model twisted and planar conformations. In the present work, Penning ionization intensities have been analyzed by means of the EED model and comparison with UPS measurements in the gas phase. The agreement between theory and experiment is satisfactory overall up to electron binding energies of ~18 eV, despite the extremely challenging nature of this compound, namely its high torsional flexibility around the central C-C bond, a strongly conjugated character and a propensity therefore to undergo electronic as well as vibrational excitation processes upon ionization. Due to near energy-degeneracies between a number of states, likely complications due to vibronic coupling transitions are expected at ionization energies around 12 and 14 eV. It would be worth studying explicitly the bands measured at these energies using multistate nuclear dynamics [55].

Compared with the lines originating from σ-orbitals, ionization lines belonging to the π-band system, including shake-up lines, have much larger Penning ionization cross sections, due to their greater extent outside the molecular vdW surface. Due to the neglect of phase factors, the EED model tends nonetheless to underestimate the relative intensity of fully bonding orbitals compared with orbitals characterized by a rich nodal structure. It would be worth therefore to improve on this model by explicitly accounting for the overlaps between the 1s orbitals of the impinging He* atoms and the target molecular orbitals within a model employing thermostatistical mechanics or classical dynamical simulations [60, 61] on quantum-chemical potential energy surfaces for computing and integrating the results of different collision pathways rather than using rigid van der Waals boundary surfaces.

As a byproduct of the present study, a comparison of ADC(3) simulations with the PIES and UPS measurements performed by Kubota and co-workers [17] on thin films of biphenyl deposited at 170 and 109 K on copper demonstrates that biphenyl molecules lying at the surface of polycrystalline layers adopt predominantly a planar configuration, whereas within an amorphous sample most molecules have twisted structures similar to that prevailing in the gas phase. These conclusions have been drawn on the very reasonable assumption that, although they may change the ionization threshold of biphenyl by a few tenths of an eV (see a previous study of the ionization threshold of oligoacenes at the confines of non-relativistic quantummechanics [30]), geometrical relaxation effects and further improvements of the quality of the basis set should influence the outermost electron binding energies of the twisted and planar forms in very similar ways, considering that these forms have comparable HOMO-LUMO band gaps (at the HF/cc-pVDZ level, these amount to 10.8 and 10.3 eV, respectively).

References

[1] (a) Carreira, L. A.; Towns; T. G. *J. Mol. Struct.* 1977, 41, 1. (b) Bree, A.; Edelson, M. *Chem. Phys. Lett.*, 1977, *46*, 500.

[2] Bastiansen, O.; Samdal, S. *J. Mol. Struct.* 1985*,* 128, 115.

[3] Im, H.; Bernstein, E. R. *J. Chem. Phys.* 1988, 88, 7337.

[4] Takei, Y.; Yamaguchi, T.; Osamura, Y.; Fuke, K.; Kaya, K. *J. Phys. Chem.* 1988, 92, 577.

[5] In *Conjugated Polymers: The Novel Science and Technology of Highly Conducting and Nonlinear Optically Active Materials*, Brédas J. L.; Sillbey R.; eds.; Kluwer, Dordrecht, The Netherlands, 1991.

[6] André, J. M.; Delhalle, J.; Brédas, J.-L. *Quantum Chemistry Aided Design of Organic Polymers – An Introduction to the Quantum Chemistry of Organic polymers and its applications*; World Scientific Publishing Co. Pte. Ltd.: London, 1991.

[7] Arulmozhiraja, S.; Fujii, T. *J. Chem. Phys.* 2001**,** 115, 10589.

[8] (a) Erickson; M.D. *Analytical Chemistry of PCBs*; Butterworth: Boston, 1986. (b) Safe, S. *Polychlorinated Biphenyls - PCBs : Mammalian and Environmental Toxicology*; Springer-Verlag: Berlin, 1987.

[9] Keaton, T. E.; Lippincott, E. R.; *Spectrochimica Acta* 1959, 15, 627.

[10] Fukui, K. *Theory of Orientation and Stereoselection*; Springer-Verlag: Berlin, 1975.

[11] Weigold, E.; McCarthy, I. E. *Electron Momentum Spectroscopy*; Kluwer Academic/Plenum Publishers: New York, 1999.

[12] (a) Čermák, V. *J. Chem. Phys.* 1966, 44, 3781. (b) Niehaus, A. *Adv. Chem. Phys.* 1981**,** 45, 399. (c) Yencha, A. J. *Electron Spectroscopy: Theory, Technique, and Applications*, Vol. 5, Brundle, C. R.; Baker, A. D.; Eds.; Academic, New York, 1984.

[13] (a) Suzuki, H. *Bull. Chem. Soc. Jpn.* 1959, 32, 1340. (b) Lim, E. C.; Li, Y. H. *J. Chem. Phys.* 1970, 52, 6416. (c) Eaton V. J.; Steele, D. *J. Chem. Soc. Faraday Trans. 2,* 1973, 69, 1601. (d) Murakami, J.; Ito, M.; Kaya, K. *J. Chem. Phys.* 1981, 74, 6505. (e) Tsuzuki, S.; Uchimaru, T.; Matsumura, K.; Mikami M.; Tanabe, K. *J. Chem. Phys.* 1999**,** 110, 2858.

[14] (a) Hargreaves, A.; Rizvi, S. H. *Acta Crystallogr.* 1962, 15, 365. (b) Charbonneau, G. -P.; Delugeard, Y. *Acta Crystallogr., Sect. B: Struct. Crystallogr. Cryst. Chem.* 1977, *B33*, 1586. (c) Cailleau, H.; Baudour, J. L.; Zeyen, C. M. E. *Acta Crystallogr., Sect. B: Struct. Crystallogr. Cryst. Chem.* 1979**,** B35, 426.

[15] Almenningen, A.; Bastiansen, O.; Fernholt, L.; Cyvin, B. N.; Cyvin, S. J.; Samdal, S. *J. Mol. Struct.* 1985, 128, 59.

[16] (a) Pignataro, S.; Mancini, V.; Ridyard J. N. A.; Lempka, H. J. *Chem. Commun.* 1971**,** 142. (b) Maier, J.P.; Turner, D.W. *Faraday Discussions Chem. Soc.* 1972, 54, 149.

[17] Kubota, H.; Munakata, T.; Hirooka, T.; Kuchitsu, K.; Harada, Y. *Chem. Phys. Lett.* 1980, 74, 409.

[18] Deleuze, M. S.; Pang, W. N.; Salam, A.; Shang, R.C. *J. Am. Chem. Soc.* 2001**,** 123, 4049.

[19] Pauling, L. *The Nature of the Chemical Bond*, Cornell University: Ithaca, New York, 1960.

[20] See e.g. Szabo, A.; Ostlund, N. S. *Modern Quantum Chemistry: Introduction to Advanced Electronic Structure Theory*; Macmillan Publishing Co., Inc., 1982.

[21] Schirmer, J.; Cederbaum, L. S.; Walter, O. *Phys. Rev. A* 1983, 28, 1237.

[22] Schirmer, J.; Angonoa, G. *J. Chem. Phys.* 1989, 91, 1754.

[23] Weikert, H.-G.; Meyer, H.-D.; Cederbaum, L. S.; Tarantelli, F. *J. Chem. Phys.* 1996, 104, 7122.

[24] Cederbaum, L. S.; Hohlneicher, G.; Peyerimhoff, S. *Chem. Phys. Lett.* 1971, 11, 421.

[25] Pickup, B. T.; Goscinski, O. *Mol. Phys.* 1973, 26, 1013.

[26] Ohrn, Y.; Born, G. *Adv. Quantum Chem.* 1981, 13, 1.

[27] Ortiz, J. V. in *Computational Chemistry : Reviews of Current Trends*, Leszczyinski, J.; Ed.; World Scientific: Singapore, 1997; Vol.2, p.1.

[28] Deleuze, M. S. *Int. J. Quantum Chem.* 2003, 93, 191.

[29] Deleuze, M. S.; Scheller, M. K.; Cederbaum, *J. Chem. Phys.* 1995, 103, 3578.

[30] Deleuze, M. S.; Claes, L.; Kryachko, E.G.; Francois, J.-P. *J. Chem. Phys.* 2003, 119, 3106.

[31] (a) Dunning, T. H. *J. Chem. Phys.* 1989, 90, 1007. (b) Kendall, R. A.; Dunning, T. H.; Harrison, R. J. *J. Chem. Phys.* 1992, 96, 6796.

[32] (a) Deleuze, M. S.; Trofimov, A. B.; Cederbaum, L. S. *J. Chem. Phys.* 2001, 115, 5859. (b) Deleuze, M. S. *J. Chem. Phys.* 2002, 116, 7012. (c) Deleuze, M. S. *J. Phys. Chem. A* 2004, 108, 9244.

[33] (a) Becke, A. D. *J. Chem. Phys.* 1993, 98, 5648. (b) Lee, C.; Yang, W.; Parr, R. G. *Phys. Rev. B* 1988, 37, 785.

[34] (a) Deleuze, M. S.; Giuffreda, M. G.; Francois, J.-P.; Cederbaum, L. S. *J. Chem. Phys.* 1999, 111, 5851. (b) Deleuze, M. S.; Giuffreda, M.G.; Francois, J.-P.; Cederbaum, L. S.; *J. Chem. Phys.* 2000, 112, 5325. (c) Deleuze, M. S.; Giuffreda, M. G.; Francois, J.-P. *J. Phys. Chem. A* 2002, 106, 5626.

[35] Martin, J. M. L.; El-Yazal, J.; François, J.-P. *Mol. Phys.* 1995**,** 86, 1437.

[36] Schmidt, M. W.; Baldridge, K. K.; Jensen, J. H.; Koseki, S.; Gordon, M. S.; Nguyen, K. A.; Windus T. L.; Elbert, S. T. *QCPE Bull.* 1990, 10, 52.

[37] (a) Liu, B.; in *Numerical Algorithms in Chemistry, Algebraic Methods,* LBL-8158; Lawrence Berkely Laboratory. (b) Tarantelli, F.; Sgamellotti, A.; Cederbaum, L. S.; Schirmer, J. *J. Chem. Phys.* 1987, 86, 2201.

[38] (a) Cederbaum, L. S.; Domcke, W. *Adv. Chem. Phys.* 1977**,** 36, 205. (b) von Niessen, W.; Schirmer, J.; Cederbaum, L. S. *Comp. Phys. Rep.* 1984, 1, 57. (c) Ortiz, J. V. *J. Chem. Phys.* 1988**,** 89, 6348. (d) Zakrzewski, V. G.; von Niessen, W. *J. Comp. Chem.* 1993**,** 14, 13.

[39] Frisch, M. J.; et al. *GAUSSIAN 98* (Revision A.7); Gaussian Inc., Pittsburgh, PA, 1998.

[40] Mitsuke, K.; Takami, T.; Ohno, K. *J. Chem. Phys.* 1989, 91, 1618.

[41] Ohno, K.; Yamakado, H.; Ogawa, T.; Yamata, T. *J. Chem. Phys.* 1996, 105, 7536.

[42] Takami, T.; Ohno, K. *J. Chem. Phys.* 1992**,** 96, 6523.

[43] Gardner, J.L.; Samson, J.A.R. *J. Electron Spectrosc. Relat. Phenom.* 1976, 8, 469.

[44] Kimura, K.; Katsumata, S.; Achiba, Y.; Yamazaki, T.; Iwata, S. *Handbook of He I Photoelectron Spectra of Fundamental Organic Molecules*; Japan Scientific Press, Tokyo, 1981.

[45] (a) Illenberger, E.; Niehaus, A. *Z. Phys. B* 1975, 20, 33. (b) Woodard, M.R.; Sharp, R.C.; Seely, M.; Muschlitz Jr., E.E. *J. Chem. Phys.* 1978, 69, 2978. (c) Parr, T.; Parr, D.M.; Martin, R.M. *J. Chem. Phys.* 1982, 76, 316. (d) Appolloni, L.; Brunetti, B.; Hermanussen, J.; Vecchiocattivi, F.; Volpi, G.G. *J. Chem. Phys.* 1987, 87, 3804.

[46] Haberland, H.; Lee, Y. T.; Siska, P. E. *Adv. Chem. Phys.* 1981, 45, 487.

[47] Kishimoto, N.; Aizawa, J.; Yamakado, H.; Ohno, K. *J. Phys. Chem. A*, 1997, 101, 5038.

[48] Kishimoto, N.; Yamakado, H.; Ohno, K. *J. Phys. Chem.* 1996, 100, 8204.

[49] Tian, S.X.; Kishimoto, N.; Ohno, K. *J. Phys. Chem. A* 2002, 106, 7714.

[50] Yamakita, Y.; Yamauchi, M.; Ohno, K. *Chem. Phys. Lett.* 2000, 322, 189.

[51] Yamazaki, M.; Maeda, S.; Kishimoto, N.; Ohno, K. *J. Chem. Phys.* 2005, 122, 044303.

[52] Kishimoto, N.; Ohno, K. *J. Phys. Chem. A* 2000, 104, 6940.

[53] Masuda, S.; Aoyama, M.; Ohno, K.; Harada, Y. *Phys. Rev. Lett.* 1990, 65, 3257.

[54] Knippenberg, S.; Nixon, K. L.; Brunger, M. J.; Maddern, T.; Campbell, L.; Trout, N.; Wang, F.; Newell, W. R.; Deleuze, M. S.; Francois, J.-P.; Winkler, D. A. *J. Chem. Phys.* 2004, 121, 10525.

[55] (a) Köppel, H.; Cederbaum, L. S.; Domcke, W. *J. Chem. Phys.*, 1988, 89, 2023, (b) Döscher, M.; Köppel, H.; Szalay, P. G. *J. Chem. Phys.*, 2002, 117, 2645, (c) Köppel, H.; Döscher, M.; Bâldea, I.; Meyer, H.-D.; Szalay, P.G. *J. Chem. Phys.*, 2002, 117, 2657.

[56] Schaftenaar, G.; CAOS/CAMM Center, the Netherlands, 1991.

[57] Horio, T.; Maruyama, R.; Kishimoto, N.; Ohno, K. *Chem. Phys. Lett.* 2004, 384, 73.

[58] Yamauchi, M.; Yamakita, Y.; Yamakado, H.; Ohno, K. *J. Electron Spectrosc. Relat. Phenom.* 1998, 88-91, 155.

[59] Yamakado, H.; Okamura, K.; Ohshimo, K.; Kishimoto, N.; Ohno, K. *Chem. Lett.* 1997, 269.

[60] (a) Ogawa, T.; Ohno, K. *J. Chem. Phys.* 1999, 110, 3773. (b) Ohno, K. *Bull. Chem. Soc. Jpn.* 2004, 77, 887.

[61] Ohno, K.; Harada, Y. *Penning Ionization : the Outer Shape of Molecule,* pp-199-233 in *Theoretical Models of Chemical Bonding* (*Vol. Part 3)*; Z.B. Maksić, Ed.; Springer-Verlag, Berlin, 1991.

Table 1. Assignment of the Penning ionization electron spectrum of biphenyl, from EED values (%), CEDPICS slope parameters (*m*), and by comparison with the ultraviolet photoelectron spectrum (UPS) and theoretical [ADC(3), OVGF, and Koopmans] ionization energies (ADC(3) and OVGF pole strengths are given in parentheses).[a]

Band	IP_{UPS}	MO	$IP_{ADC(3)/cc\text{-}pVDZ}$[b]	$IP_{OVGF/cc\text{-}pVDZ}$	$IP_{HF/cc\text{-}pVDZ}$	EED	*m*
1	8.41	$9b_2$ (π_6)	8.12 (0.873)	8.02 (0.890)	8.12	4.85	-0.34
2,3	9.16	12a (π_5)	8.98 (0.867)	8.80 (0.888)	9.11	5.77	-0.45
		$11b_1$ (π_4)	8.99 (0.868)	8.88 (0.887)	9.08	5.95	
4	9.87	$9b_3$ (π_3)	9.66 (0.847)	9.41 (0.886)	9.88	5.22	-0.42
5,6	11.25	$8b_3$	11.72 (0.881)	11.55 (0.893)	13.08	1.85	-0.12
		11a	11.73 (0.886)	11.40 (0.892)	13.10	1.35	
7	11.80	$8b_2$ (π_2)	11.89 (0.687)	11.78 (0.824)	13.18	4.95	-0.41
			12.18 (0.070)				
			16.34 (0.067)				
8	12.18	$7b_2$	12.26 (0.847)	12.08 (0.889)	13.62	2.25	
9	12.4	$7b_3$ (π_1)	12.41 (0.638)	12.31 (0.818)	13.86	4.63	-0.42
10	12.7	$10b_1$	12.65 (0.870)	12.46 (0.887)	14.08	1.75	
S	(~13.2)	$7b_3$ (π_1)	13.42 (0.121)	-	-	4.63	-0.40
11,12	13.8	$6b_3$	14.16 (0.830)	14.01 (0.878)	15.74	2.43	-0.11
		10a	14.21 (0.852)	13.94 (0.877)	15.79	1.94	
13	14.11	$6b_2$	14.38 (0.851)	14.21 (0.879)	15.96	2.71	-0.23
14	14.5	$5b_3$	14.58 (0.812)	14.20 (0.864)	16.36	0.65	
15	14.7	$9b_1$	14.97 (0.843)	14.92 (0.871)	16.69	1.94	-0.22
16	15.02	$5b_2$	15.40 (0.814)	14.99 (0.861)	17.21	0.58	
17	15.53	9a	15.84 (0.810)	15.76 (0.857)	17.78	1.92	-0.26
18	16.15	$8b_1$	16.46 (0.414)	16.32 (0.849)	18.37	2.09	-0.25
			16.50 (0.360)				
19	16.90	8a	17.33 (0.278)	17.13 (0.840)	19.33	2.09	-0.20
			17.35 (0.190)				
			17.42 (0.258)				

[a] Ionization energies are in eV. [b] Further ionization lines with pole strengths larger than 0.050 have been identified as follows : $7b_1$: 18.58 (0.152), 18.71 (0.054), 18.74 (0.084), 18.79 (0.214). $4b_3$: 19.22 (0.181), 19.26 (0.107), 19.50 (0.061). $4b_2$: 19.69 (0.159), 19.83 (0.081), 19.86 (0.058), 19.98 (0.075), 20.36 (0.063). 7a: 19.69 (0.091),19.89 (0.060), 20.28 (0.111), 20.80 (0.061).

Table 2. Theoretical EED values (%) and [ADC(3), OVGF, and Koopmans] ionization spectra computed for the first-order planar form of biphenyl. [a]

Band	MO	$IP_{ADC(3)/cc\text{-}pVDZ}$	$IP_{OVGF/cc\text{-}pVDZ}$	$IP_{HF/cc\text{-}pVDZ}$	EED
1	$2b_{2g}$ (π_6)	7.93 (0.871)	7.86 (0.890)	7.92	4.87
2	$1a_{1u}$ (π_5)	8.89 (0.862)	8.74 (0.887)	9.05	5.51
3	$1b_{1g}$ (π_4)	9.05 (0.860)	8.92 (0.887)	9.24	6.25
4	$2b_{3u}$ (π_3)	9.86 (0.796)	9.75 (0.882)	10.26	5.37
		11.08 (0.074)			
5	$7b_{3g}$	11.52 (0.889)	11.31 (0.896)	12.85	1.46
6	$11a_{1g}$	11.84 (0.885)	11.55 (0.892)	13.25	1.31
7	$1b_{2g}$ (π_2)	11.82 (0.645)	11.86 (0.818)	13.26	5.11
		12.16 (0.056)			
		13.55 (0.050)			
8	$7b_{2u}$	12.39 (0.880)	12.20 (0.891)	13.77	2.06
9	$1b_{3u}$ (π_1)	12.49 (0.484)	12.65 (0.808)	14.25	5.10
		13.40 (0.254)			
		16.79 (0.062)			
10	$10b_{1u}$	12.53 (0.872)	12.35 (0.886)	13.98	1.62
11	$6b_{3g}$	13.93 (0.861)	13.79 (0.879)	15.54	2.06
12	$10a_{1g}$	14.29 (0.845)	14.10 (0.874)	15.96	1.92
13	$6b_{2u}$	14.52 (0.846)	14.39 (0.877)	16.17	2.64
14	$5b_{3g}$	14.39 (0.854)	14.04 (0.870)	16.19	0.57
15	$9b_{1u}$	14.88 (0.843)	14.83 (0.871)	16.59	1.76
16	$5b_{2u}$	15.47 (0.808)	15.09 (0.854)	17.40	0.59
17	$9a_{1g}$	15.96 (0.781)	15.88 (0.856)	17.92	1.86
18	$8b_{1u}$	16.38 (0.757)	16.29 (0.849)	18.35	2.10
19	$8a_{1g}$	17.43 (0.587)	17.34 (0.837)	19.57	1.03
		17.65 (0.110)			
20	$7b_{1u}$	18.52 (0.112)	18.74 (0.822)	21.50	0.82
		18.70 (0.128)			
		18.79 (0.265)			
		19.12 (0.082)			

21	$4b_{3g}$	18.71 (0.098)	18.99 (0.820)	21.82	0.99
		18.85 (0.148)			
		19.08 (0.166)			
		19.23 (0.105)			
		19.33 (0.051)			
22	$4b_{2u}$	19.82 (0.109)	20.00 (0.798)	22.96	0.83
		19.94 (0.115)			
		20.11 (0.061)			
		20.48 (0.078)			
		20.52 (0.059)			
23	$7a_{1g}$	19.84 (0.081)	20.06 (0.815)	23.19	0.52
		19.99 (0.058)			
		20.07 (0.071)			
		20.36 (0.051)			
		20.52 (0.076)			

[a] Ionization energies are in eV. Only the lines with a pole strength larger than 0.05 (in parentheses) are reported.

Part 5: Electron momentum spectroscopy studies on small test systems

5.1 Probing Dyson orbitals with Green's function theory and electron momentum spectroscopy.

5.1.1 Introduction

The main scope of this work is to demonstrate that one-particle Green's function theory (1p-GF) [1, 2, 3], in conjunction with the third-order algebraic diagrammatic construction [ADC(3)] scheme [4, 5], not only provides quantitatively insight into ionization spectra [6, 7, 8], but also enables straightforwardly accurate computations of Dyson orbitals [1, 9] in momentum space. With this in view, a study of the valence electronic structure of difluoromethane (CH_2F_2) is presented here by resorting to high resolution electron momentum spectroscopy (EMS) [9]. The quality of Hartree-Fock (HF) and Kohn-Sham (KS) orbitals is comparatively assessed.

5.1.2 Computational details

To assess the influence of the basis set in computations of orbital MDs, we compare Hartree-Fock or density functional theory (DFT) results obtained using Dunning's correlation consistent polarized valence basis sets of double [or triple] zeta quality (aug-cc-pVXZ, X=D[T]) and augmented by a set of *s,p,*[*d*] and *s,p,d,*[*f*] diffuse functions on hydrogens, and carbons or fluorines, respectively [10]; as well as Dunning's cc-pVTZ basis [10] augmented by a set of *s,p* and *s,p,d* diffuse functions only on hydrogens, and carbons or fluorines, respectively (cc-pVTZ++). The ADC(3) calculations have been completed by means of the original code interfaced to the GAMESS92 package of programs [11]. KS and HF orbital MDs have been generated from DFT or HF calculations employing GAUSSIAN98 [12]. The DFT calculations have been performed using the standard gradient-corrected Becke-Perdew (BP86) functional, and its extension, the hybrid Becke-Perdew-3-parameters- Lee-Yang-Parr (B3LYP) functional [12]. All spherically averaged orbital MDs have been obtained using the HEMS program [13] and convolved according to the experimental momentum resolution [14].

5.1.3 Experiment

The employed EMS spectrometer has been described in detail elsewhere [15]. This spectrometer employs a symmetric non-coplanar geometrical set up, and a kinematics which ensures therefore clean ''knockout'' collision events. A double toroidal analyzer equipped with a series of conical retarding lenses is used for electron energy and angle analyzing, and the electron position detection and data acquisition are realized by using a pair of wedge strip anode position sensitive detectors with a Universal Serial Bus multiparameter data-acquisition system [16]. According to tests on argon and helium, the energy and time resolutions are around 1.2 eV and 2 ns, respectively. Improvements of the employed multi-angle and multi-energy detection techniques greatly increased the detection rate of (e,2e) events in coincidence, by two orders of magnitude higher compared with our previous spectrometer [17]. In order to identify possible failures of the PWIA approximation, the electron MDs of CH_2F_2 have been measured at impact energies (E_i) of 600, 1200 and 1600 eV (+ electron binding energy). At these energies, the resolution on momenta correspondingly amounts to 0.11, 0.17 and 0.20 a.u. (1 a.u. = $\hbar\, a_0^{-1}$ with a_0 the Bohr radius).

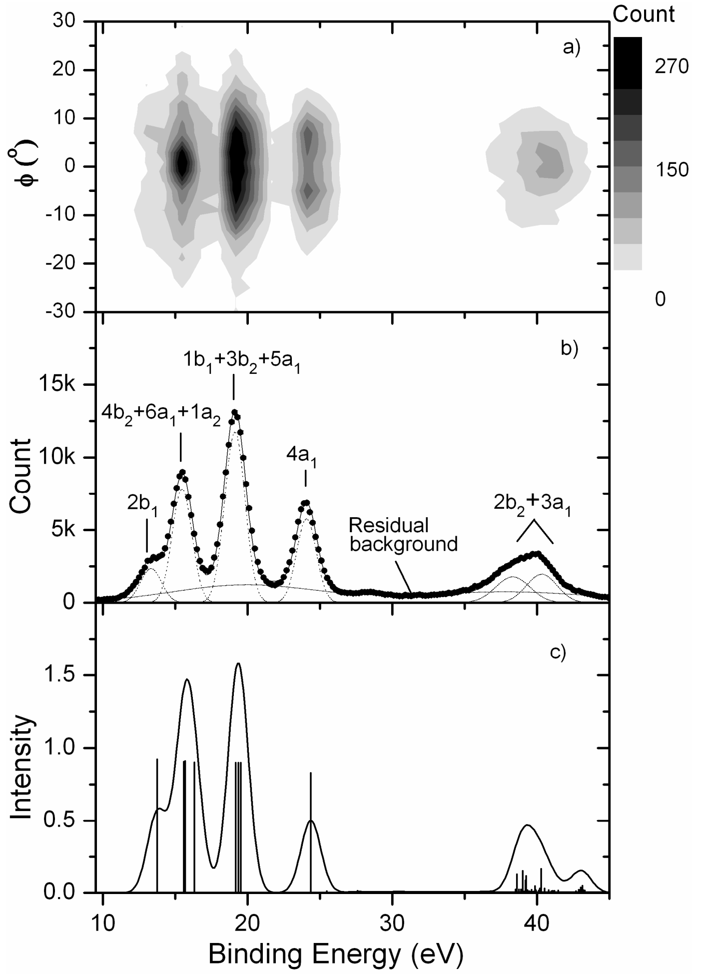

Figure 1. (a) Angular resolved and (b) summed experimental ionization spectra of CH_2F_2 (E_i = 1600 eV). The dashed and full lines represent Gaussian fits and their sum, respectively. (c) ADC(3)/cc-pVTZ++ spike and convolved ionization spectra (FWHM=1.6 eV).

5.1.4 Results and discussion

The experimental electron density distribution map of CH_2F_2 at E_i = 1600 eV is illustrated in Figure 1a. An average ionization spectrum is obtained from this map (Figure 1b) by summing measurements over all ϕ angles. This spectrum is assigned by comparison with a simulation drawn from our best ADC(3)/cc-pVTZ++ theoretical results (Figure 1c; averaged accuracy on one-electron ionization energies: ~0.2 eV, to compare with errors of ~3 to ~4 eV for B3LYP or BP86 orbital estimates). Only 1h states ($\Gamma_f > 0.8$) produced by the removal of an electron from the $2b_1$ or $4a_1$ orbitals can be individually resolved at ~13.3 and ~24.9 eV, respectively. In the outer-valence region, two further bands at ~15.4 and 19.1 eV relate to unresolved 1h states associated to the {$4b_2$, $6a_1$, $1a_2$ } and {$1b_1$, $3b_2$, $5a_1$} sets of orbitals, respectively. A severe breakdown of the orbital picture of ionization is noticed at the ADC(3)/cc-pVTZ++ level for the innermost $2b_2$ and $3a_1$ levels, in the form (Figure 1c) of a dispersion of the related ionization intensity over many shake-up lines with very limited intensity ($\Gamma_f < 0.17$). More specifically, at this level, 77 (71) % of the $2b_2$ ($3a_1$) ionization intensity is recovered at binding energies comprised between 36 and 43 eV in the form of 27 (33) lines with $\Gamma_f > 0.005$. Very significant band broadening is correspondingly observed on the experimental side (Figure 1b).

Analysis of the angular dependence of the (e, 2e) intensities for the identified ionization channels provide straightforward access to the related MDs. We refer to [16] for a description of the procedure used for extracting the experimental MDs. These are compared in Figures 2 and 3 with theoretical HF, KS, or ADC(3) Dyson orbital MDs. These theoretical MDs are overall similar and in general very faithfully reproduce the experimental measurements. Noteworthy differences are nonetheless observed at electron momenta smaller than 1 a.u. – with the ADC(3) results enabling overall the best description of experiment. Note that the BP86 and B3LYP functionals produce also excellent and essentially identical results for CH_2F_2.

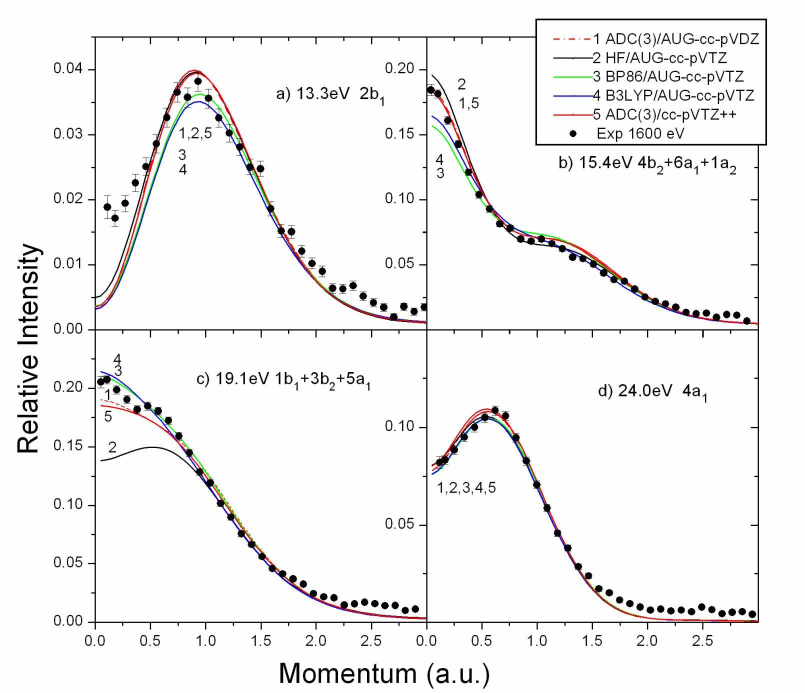

Figure 2. Measured and calculated momentum distribution for the resolved $2b_1$, {$4b_2$+$6a_1$+$1a_2$}, {$1b_1$+$3b_2$+$5a_1$} and $4a_1$ sets of orbitals (E_i=1600 eV).

The HF/aug-cc-pVTZ level fails to qualitatively describe the MD associated to the {1b$_1$, 3b$_2$, 5a$_1$} set (Figure 2c), a failure which reflects very significant *electronic correlation and relaxation effects*. Indeed, in contrast, the ADC(3) MDs very correctly reproduce the experimental results for this orbital set. Such a difference between the HF and ADC(3) results for momentum distributions demonstrates that, although the corresponding ADC(3) eigenvectors have one dominant 1h component relating to the 1b$_1$, 3b$_2$, or 5a$_1$ HF orbitals, the contributions of many other and individually small 1h or 1p components, due to electronic relaxation in the final state or ground state correlation, respectively, may altogether significantly alter the shape of the associated Dyson orbitals. A comparison of ADC(3) results obtained using the aug-cc-pVDZ and cc-pVTZ++ basis sets confirms that the latter is large enough to ensure the convergence of the computed MDs with respect to incorporations of further atomic orbitals.

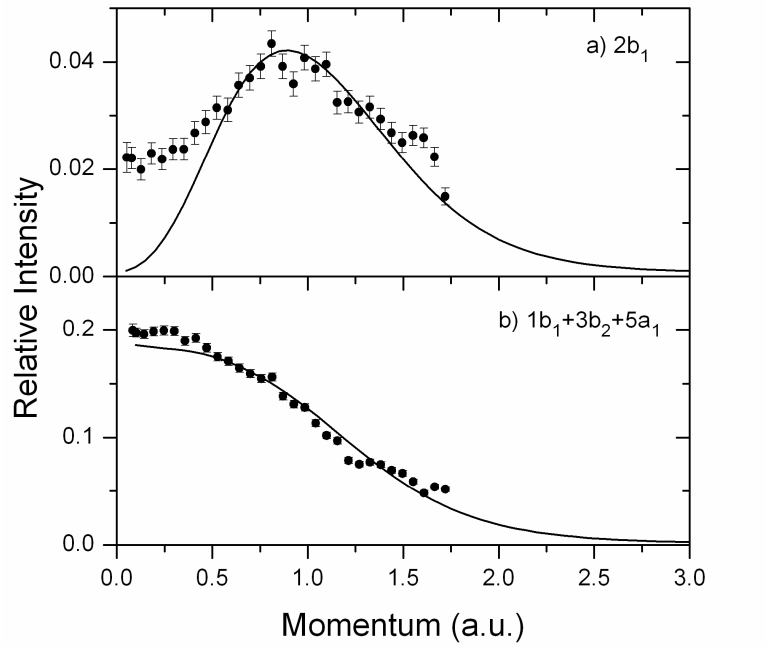

Figure 3. Measured and ADC(3)/cc-pVTZ++ momentum distirbutions for the 2b$_1$ and {1b$_1$+3b$_2$+5a$_1$} orbital sets (E_i=600 eV).

All employed models fail to reproduce the "turn up" of the experimental MD at low electron momenta for the 2b$_1$ orbital. With regards to the π^*-like topology of this orbital, which exhibits two perpendicular nodal planes (Figure 4), this discrepancy is typically due to distorted wave effects [18, 19]: indeed, its extent strongly increases upon a lowering of E_i down to 1200 and 600 eV (compare Figure 2a (1600 eV) with Figure 3a (600 eV)). For all other orbitals the related experimental MDs are insensitive to E_i (compare e.g. Figure 2c with Figure 3b for the {1b$_1$, 3b$_2$, 5a$_1$} set), and the plane wave impulse approximation seems therefore valid. Note that, according to He(II) measurements [20], vibrational broadening of the 2b$_1$ ionization line does not exceed 0.68 eV (FWHM).

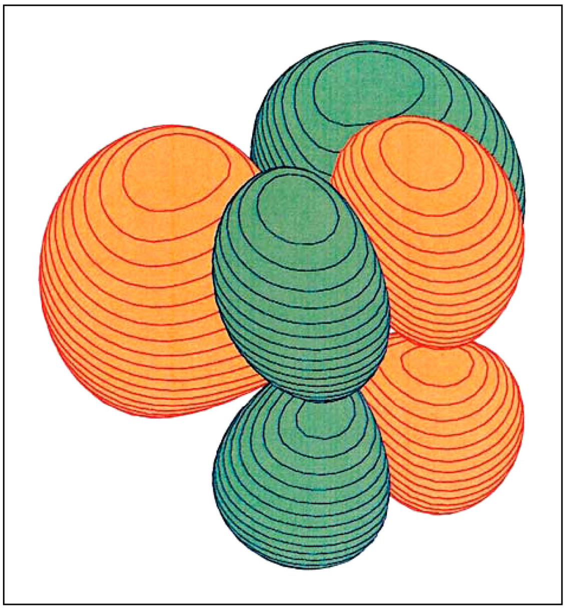

Figure 4. Contour plot for the $2b_1$ orbital of CH_2F_2.

The summed ADC(3) MDs for the $\{1b_1, 3b_2, 5a_1\}$ set slightly underestimate the experimental ones at low momenta: since this set corresponds to localized (F_{2p}) lone pairs, this underestimation may be ascribed to nuclear dynamical complications. With regards to the phase relationships between their AO (atomic orbital) components, a stretching of the CF bonds, or a strong increase of the FCF bond angles are indeed expected upon ionization of an electron from orbital $3b_2$, and from orbitals $1b_1$ or $5a_1$, respectively. Since in all three cases the distance between fluorine atoms increases, these distortions will result into an enhancement of the related orbital densities at large r (low p). Thus, it appears that the excellent agreement that is most usually reported between KS and experimental MDs may partly stem from a cancellation of errors (a too rapid decay of the employed exchange-correlation potentials at large distances versus the neglect of the relaxation of the electron density and of the molecular geometry).

The MD displayed at the ADC(3)/cc-pVTZ++ level for the innermost $2b_2$ and $3a_1$ valence bands (Figure 5) has been calculated by summing the contributions from the 60 shake-up lines found at binding energies between 36 and 43 eV. For these bands, the agreement between the total ADC(3) and experimentally measured MDs is remarkable, as is the agreement of the ADC(3) MDs with the HF and KS results. This, as well as further inserts in Figure 5 providing on an individual basis the Dyson orbital MDs associated to the 10 most intense shake-up lines, reflect the fact that Dyson orbitals for satellites related to the same electronic level have the same composition in a MO or AO basis.

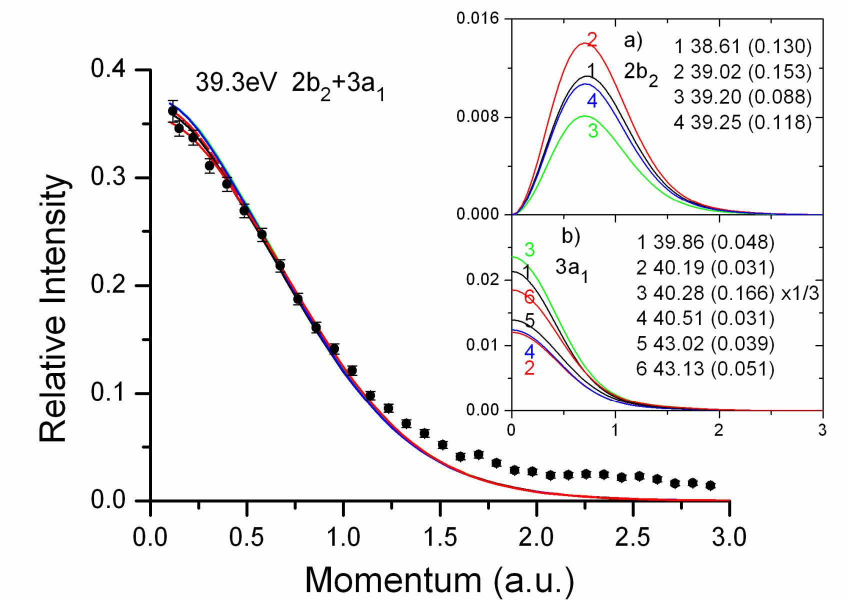

Figure 5. Measured and calculated momentum distributions for the $2b_2 + 3a_1$ shake-up bands (E_i=1600 eV), along with (insert) the ADC(3)/cc-pVTZ++ Dyson orbital momentum distirbutions for the 10 most intense shake-up lines (ionization energies in eV; pole strengths in parenthesis).

5.1.5 Conclusions

A link between one-particle Green's Function theory and Electron Momentum Spectroscopy has been established using Dyson orbitals derived from the ADC(3) scheme. This formalism has been applied for the first time to study the electron momentum distributions associated to the one-electron and shake-up ionization channels of difluoromethane. A comparison of ADC(3) Dyson orbital MDs with experimental or HF and KS results demonstrate the importance of static and dynamic correlation effects in (e, 2e) processes, and the advantages of a treatment of these effects by means of a *many-body* scattering potential that has the right asymptotic behavior. Besides recommending ADC(3) for quantitatively deciphering ionization spectra, this work advocates therefore a systematic use of ADC(3) Dyson orbitals in analyses of EMS experiments, in order to safely identify complications such as distorted wave effects, nuclear dynamics, or a dispersion of the ionization intensities into shake-up processes.

References

[1] Deleuze, M. S.; Pickup, B.T.; Delhalle, J. *Mol. Phys.* 1994, 83, 655.

[2] Cederbaum, L. S.; Domcke, W. *Adv. Chem. Phys.* 1977, 36, 205.

[3] Öhrn, Y.; Born, G. *Adv. Quantum Chem.* 1981, 13, 1.

[4] Schirmer, J.; Cederbaum, L. S.; Walter, O. *Phys. Rev. A* 1983, 28, 1237.

[5] Weikert, H. G.; Meyer, H.-D.; Cederbaum, L. S.; Tarantelli, F. *J. Chem. Phys.* 1996, 104, 7122.

[6] Knippenberg, S.; Nixon, K. L.; Mackenzie-Ross, H.; Brunger, M. J.; Wang, F.; Deleuze, M. S.; François, J.-P.; Winkler, D. A. *J. Phys. Chem. A* 2005, 109, 9324.

[7] Knippenberg, S.; Nixon, K. L.; Brunger, M. J.; Maddern, T.; Campbell, L.; Trout, N.; Wang, F.; Newell, W. R.; Deleuze, M. S.; François, J.-P.; Winkler, D. A. *J. Chem. Phys.* 2004, 121, 10525.

[8] Adcock, W.; Brunger, M. J.; McCarthy, I. E.; Michaelewicz, M.T.; von Niessen, W.; Wang, F.; Winkler, D. A. *J. Am. Chem. Soc.* 2000, 122, 3892.

[9] Weigold, E.; McCarthy, I. E. *Electron Momentum Spectroscopy*; Kluwer Academic/ Plenum Publishers, New York, 1999.

[10] Dunning, T. J., Jr. *J. Chem. Phys.* 1989, 90, 1007.

[11] Schmidt, M. W. *et al.*, *J. Comput. Chem.* 1993, 14, 1347.

[12] Frisch, M. J. *et al.*, Gaussian98, revision A.7; Gaussian Inc, Pittsburg, PA 1998.

[13] Hollebone, B. P.; Neville, J. J.; Zheng, Y.; Brion, C. E.; Wang, Y.; Davidson, E. R. *Chem. Phys.* 1995, 196, 13.

[14] Migdall, J. N.; Coplan, M. A.; Hench, D. S. *et al.*, *Chem. Phys.* 1981, 57, 141.

[15] Ren, X. G.; Ning, C. G.; Deng, J. K.; Zhang, S. F.; Su, G. L.; Huang, F.; Li, G. Q. *Rev. Sci. Instrum.* 2005, 76, 063103.

[16] Ning, C. G.; Deng, J. K.; Su, G. L.; Zhou, H.; Ren, X. G. *Rev. Sci. Instrum.* 2004, 75, 3062.

[17] Deng, J. K.; Li, G. Q.; He, Y., *et al.*, *J. Chem. Phys.* 2001, 114, 882.

[18] Braidwood, S. W.; Brunger, M. J.; Konovalov, D. A.; Weigold, E. *J. Phys. B* 1993, 26, 1655.

[19] Ren, X. G.; Ning, C. G.; Deng, J. K. *et al.*, *Phys. Rev. Lett.* 2005, 94, 163201.

[20] Bieri, G.; Asbrink, L.; von Niessen, W. *J. Electron Spectrosc. Relat. Phenom.* 1981, 23, 281.

5.2 High resolution electron momentum spectroscopy of the valence orbitals of water.

5.2.1 Introduction

Electron momentum spectroscopy (EMS), also known as (e, 2e) spectroscopy, is a powerful tool for investigating the electronic structure of matter [1-4]. The basic principle of EMS is a kinematically complete study of electron impact ionization events inducing (e, 2e) reactions. The differential cross sections at sufficiently high energies are very sensitive to the energy-momentum densities. The observed momentum distributions (MD) are most usually analyzed through comparisons with theoretical calculations performed under the assumptions of the Born-Oppenheimer, binary encounter, and plane wave impulse approximations (PWIA). Under the so-called EMS conditions associated with electron impact ionization events at high kinetic energies ($E_0 >> 1$ keV), these approximations enable indeed a rather straightforward mapping between the experimentally obtained momentum distributions and the calculated orbital electron densities. EMS is therefore most commonly regarded as a powerful "orbital imaging" technique.

It is justifiable to some extent to employ this technique for evaluating the reliability of theoretical wave functions with regards to the usual limitations encountered in molecular quantum mechanics, namely the size of the employed basis set, and the level achieved in treating electronic correlation within the neutral ground state. However, the available EMS spectrometers still badly need improvement with regards to energy and momentum resolution for probing on more quantitative grounds the outcome of the dynamical correlation and relaxation effects induced by (e, 2e) ionization processes on the effective shape and spread of the orbitals involved in these processes. In an exact theory of ionization at the limit of high kinetic energies for the impinging electrons, the measured electron momentum distributions relate to Dyson orbitals [5-12], measuring partial overlaps between the neutral ground state and the corresponding cationic states of the target.

Various experimental and theoretical investigations have been reported to date on the electronic states of water, and interest in this tremendously important molecule in chemistry, biology, physics, geology, hydrology,… remains unabated [13-27]. The first reported studies using EMS were early works by Dixon *et al.* [28] and Hood *et al.* [29]. Subsequent works by Bawagan *et al.* [30-31] have extensively investigated the electronic states of water using EMS methods. In these works, a comparison with results obtained from Configuration Interaction (CI) calculations has enlightened the importance of the electron correlation effects in describing the low momentum parts of outer valence electron distributions.

However, a major drawback in these early experimental studies is the low statistical accuracy and poor energy resolution, which impeded the identification of weak satellite states at experimental ionization energies around 27 eV. Also, these states were not recovered by the theoretical calculations presented in the work by Bawagan *et al.* [31] with an even tempered set of 109 Gaussian Type Orbital (GTO's) basis functions. However, shake-up states with exceedingly limited strength and with the appropriate symmetry could be recovered nearly four decades ago at ~27 eV from very simple Green's Function calculations of the ionization spectrum of water [32], using an expansion of the self-energy that is correct through second-order and incorporates partial infinite series of higher-order terms by virtue of a renormalization of the energy denominators. Although of weak intensity, a shake-up band was also very clearly discernable at 27 eV in the valence ESCA spectrum of water recorded by K.

Siegbahn and his co-workers, also more than four decades ago [33]. This exceedingly challenging issue was nonetheless most commonly elusive in later theoretical investigations of the ionization spectrum of water [34-51]. The existence of these shake-up states has received recently strong support, both experimentally and theoretically, from high resolution synchrotron radiation PES measurements [52], and calculations employing the Symmetry Adapted Cluster Configuration Interaction (SAC-CI) scheme at the level of the general-R approximation [53]. It is thus now almost 20 years that the pioneering EMS work by Bawagan *et al.* [31] on water is awaiting a confirmation on more robust experimental grounds of the momentum profiles associated to the shake-up ionization channels of water.

In the present work, we report therefore a new experimental EMS investigation, at much higher resolution and statistical accuracy than any study so far, of the momentum distributions asociated to all valence orbitals of water, throughout the valence region, up to electron binding energies of ~45 eV. This study has been made possible by the development of an electron momentum spectrometer of the third generation at Tsinghua University, the characteristics of which are very superior to former spectrometers. The azimuthal and polar angular resolutions, and energy resolutions that are achieved at present under (e, 2e) non-coplanar symmetric kinematics are $\Delta\phi = \pm 0.84°$, $\Delta\theta = \pm 0.53$, and ΔE = 0.45-0.68 eV (depending on the electron beam current), respectively. Further theoretical calculations employing a variety of single-reference and multi-reference quantum mechanical methods are performed for elucidating the origin of the shake-up band at 27 eV.

5.2.2 Theory and computational details

EMS is a binary (e, 2e) experiment in which an incident electron with high enough energy E_0 induces ionization of a molecular target. The scattered and ionized electrons are subsequently detected in coincidence at equal kinetic energies and equal polar angles. Under the assumptions of the Born (sudden or vertical), binary encounter, and plane wave impulse approximations (PWIA), the triple differential EMS cross-section for randomly oriented molecules is then given by

$$\sigma_{EMS} \propto \int d\Omega \left| \left\langle \upsilon_{\vec{p}} \Psi_f^{N-1} \middle| \Psi_i^N \right\rangle \right|^2 . \tag{1}$$

where $\upsilon_{\vec{p}}$ represents a plane wave function $e^{i\,\vec{p}\bullet\vec{r}}$. The overlap of the ion and neutral wavefunctions in Eq. (1) is referred to as a Dyson orbital [5-12]. Dyson orbitals are straightforwardly obtained from CI [31] or Green's Function (GF) calculations [11, 54, 9-10]. Assuming a depiction of ionization events at the level of Koopmans' theorem, Dyson orbitals most naturally reduce to Hartree-Fock orbitals (Target Hartree-Fock Approximation, THFA) with a spectoscopic strength equal to 1. Most EMS experiments nowadays are interpreted using the empirical Target Kohn-Sham Approximation (TKSA), which amounts to substituting Dyson orbitals by the most relevant Kohn-Sham orbitals. With the THFA or TKSA, and upon accounting for the dispersion of the ionization intensity over shake-up and shake-off satellites, Eq. (1) then simply becomes [55-56]

$$\sigma_{EMS} \propto S_i^f \int d\Omega \left| \psi_i(p) \right|^2 , \tag{2}$$

where $\psi_i(p)$ represents the momentum space representation, i.e. Fourier transform, of a canonical HF or KS orbital, and S_i^f denotes the associated pole strength. Neutral ground state correlation is by construction included in the Kohn-Sham orbital through the exchange-correlation potential [56]. In contrast, many-body effects in the final state are very obviously not accounted for by these orbitals in standard applications of Density Functional Theory. In the present work, we therefore comparatively study the outcome of DFT calculations using the standard hybrid Becke-Perdew-3-parameters-Lee-

Yang-Parr (B3LYP) functional [57] with more reliable Dyson orbital calculations of electron momentum distributions. To investigate further the influence of the basis set, a new program (NEMS) has been implemented for computing HF and KS momentum distributions using an almost complete basis set, namely d-aug-cc-pV6Z [58]. The neutral molecular equilibrium geometry (R_{OH} = 0.9572 Å, θ_{HOH} = 104.52°) was used for generating the calculated wave functions [31].

As EMS, one-particle Green's function (1p-GF) theory enables a direct mapping, and this within an exact many-body framework, of vertical ionization energies and Dyson orbitals. For more information on 1p-GF [12] theory, the Algebraic Diagrammatic Construction scheme of third order [ADC(3)], Dyson orbitals and their pole strengths [59], we refer to Chapter 2.7 in the present thesis. Briefly, at the ADC(3) level, one-electron and shake-up ionization energies are obtained as eigenvalues (E) of a secular matrix (**H**) cast over the one-hole (1h) and two-hole/one-particle (2h-1p) excited (shake-up) configurations of the radical cation M^+, as well as 1p and 2p-1h (shake-on) anionic configurations produced by electron attachment processes on *M* [60-62]. The sets of Feynman-Dyson transition amplitudes (X) required to expand Dyson orbitals derive [12, 63] from the 1h and 1p components of the associated eigenvectors ($\mathbf{HX = XE}$, $\mathbf{X^{\dagger}X = 1}$). By virtue of its treatment of static and dynamic self-energies, through fourth- and third-order in correlation [54], respectively, the 1p-GF/ADC(3) approach predicts vertical one-electron ionization energies within accuracies of ~0.2 eV [64-65]. In contrast with comparable MR-SDCI (Multi-Reference Single and Double CI) treatments, the 1p-GF/ADC(3) scheme is size-consistent [66] and applicable therefore to extremely large systems [67]. At last, unlike DFT calculations employing standard functionals, a charge-consistent ADC(3) scheme guarantees that the associated scattering potentials have the correct scaling in the asymptotic region [66].

A drawback of the ADC(3) scheme is the limited order attained in correlation for the shake-up energies. Whereas one-electron ionization energies are treated through third-order, singly-excited 2h-1p shake-up states are of first-order only, and higher-rank (double, triple, …) electronic excitations are neglected. An ADC(3) treatment of shake-up states is therefore comparable with a CIS calculation of excited states in molecular radical cations. Nonetheless, in most applications of the ADC(3) approach, the achieved accuracy on 2h-1p shake-up ionization energies ranges usually from ~0.5 to ~1 eV, depending on the energy of the ionized orbital (see [9] and references therein).

Recent SAC-CI general-R calculations using a cc-pVTZ basis set augmented by α_s = 0.059, 0.017, 0.0066; α_p = 0.059, 0.015, 0.0054; α_d = 0.059, 0.016, 0.0032 Rydberg functions [68] on the oxygen atom (from now on abbreviated to rTZ) appeared to be required for reproducing the $2a_1$ shake-up states of water at ~27.1 eV [53] The symmetry adapted cluster configuration interaction (SAC-CI) general-R method [69] is designed to describe multiple-electron processes with extremely high accuracy because it involves single, double, and higher excitation operators up to sextuple excitations. The SAC-CI general-R approach has also been amply used for studying congested ionization spectra and is especially powerful for shake-up states [69-71]. Remembering that most theoretical works so far on the ionization spectrum of water failed to reproduce the shake-up states at ~27.1 eV, we believe that a comparison of further improved SAC-CI calculations with other many-body quantum mechanical calculations might be useful.

One may indeed wonder whether the failure of many previous theoretical studies in describing the $2a_1$ shake-up states of water at ~27.1 eV is ascribable to the lack of Rydberg atomic functions in the employed basis sets, which are most reasonably expected to be essential for calculating shake-up states when these states fall in energy ranges similar to the valence electron binding energies. In the present work, the ionization spectrum of water is therefore investigated further using a variety of methods employing an even larger basis set than the one used by Ehara *et al.* [53] More specifically, in our work, use was made of a Rydberg augmented Triple Zeta (raTZ) basis set derived from Dunning's aug-cc-pVTZ basis set [72], which has been augmented with s-, p-, and d-type Rydberg functions for O atom: α_s = 0.017, 0.0066; α_p = 0.015, 0.0054; α_d = 0.059, 0.016, 0.0032 [68]. Our raTZ basis set therefore incorporates in total 115 basis functions, compared with the 85 functions in the basis set used by Ehara *et al.* [53]. For comparison purposes, besides these SAC-CI general R/raTZ calculations, we also provide the results of ADC(3)/raTZ calculations. In the present work, all single reference calculations were performed at Hasselt University using the Gaussian03 [73] program package [SAC-CI], except the ADC(3) calculations that were carried out using the original package of programs by Schirmer and co-workers. In the latter calculations, the retained threshold on pole strengths in the final block-Davidson diagonalization procedure was 0.001.

Comparison is further made with the results of calculations of the excited states of the water radical cation (H_2O^+) employing multi-reference single and double configuration interaction theory (MR-SDCI) [74-76]. In our work, these calculations are based on CAS reference wave functions employing an active space constructed by distributing the 7 valence electrons over 11 orbitals, among which there are 6, 3, and 2 orbitals with a_1, b_1 and b_2 symmetry labels, respectively [CAS(7,11)]. The same wavefunction was used to carry our further multi-reference calculations in conjunction with second and third order Rayleigh Schrödinger perturbation theory (MR-RSPT2; MR-RSPT3 [77]). All these multi-reference calculations have been performed at Hasselt University using the Molpro2000 package [78].

5.2.3 Experimental set-up

Recently, a high sensitivity EMS spectrometer was constructed at Tsinghua University, which features a high coincidental count rate [79]. It takes symmetric noncoplanar conditions and uses a double toroidal energy analyzer and position sensitive detectors to achieve the energy and angle multi-channel detection. Although its coincidental count rate is about two orders of magnitude higher than that of our previous spectrometer, the resolution has not been improved yet. To achieve higher resolutions, significant modifications have been implemented on this spectrometer. Briefly, an electron gun equipped with the oxide cathode, which worked at a much lower temperature than the generic filament cathodes, is used to generate the electron beam with low energy spread and low divergence angle. The electron beam size is constrained to 0.3 mm in diameter by a molybdenum aperture and the pass energy is set to 50 eV for improving the momentum resolution and energy resolution. Since the oxide cathode is easily poisoned by active gas, an additional vacuum chamber has been designed to mount the electron gun, which is evacuated to a base pressure 10^{-7} Pa by a 600 L/s molecular turbopump, which has a 2 mm diameter hole connect to the main chamber for electron beam passing through.

With these measures and optimization of electron optics using the Monte Carlo simulation, the angle resolutions which were $\Delta\phi = \pm 0.84°$, $\Delta\theta = \pm 0.53°$, respectively, were obtained by standard calibration run for argon. The peak to valley ratio for the argon 3p momentum distribution reached 8:5:1 at an impact energy of 1200 eV plus binding energy. The energy resolution is highly dependent on the emitting current of the cathode due to space charge effects. The energy resolution ΔE = 0.45 eV (FWHM) is obtained with an emitting current of 1 μA at an impact energy 1200 eV. This resolution deteriorates to ΔE = 0.68 eV (FWHM) with an emitting current of 6 μA. Compared with the resolution

ΔE = 1.6 eV FWHM achieved previously by Bawagan *et al.* [31] such an improved energy resolution ΔE = 0.68 eV (FWHM) seems good enough for improving in details the experimental EMS characterization of water. The electron gun has therefore been operated at a constant emitting current of 6 μA for shortening the measuring period. The collected current in the Faraday cup, which is placed after the reaction region is only about 16% of the cathodic current, due to an aperture of 0.3 mm. Despite this loss of intensity for the impinging electron beam, the typical coincidental count rate is ~12 per second at an impact energy of 1200 eV in EMS experiments on an argon sample.

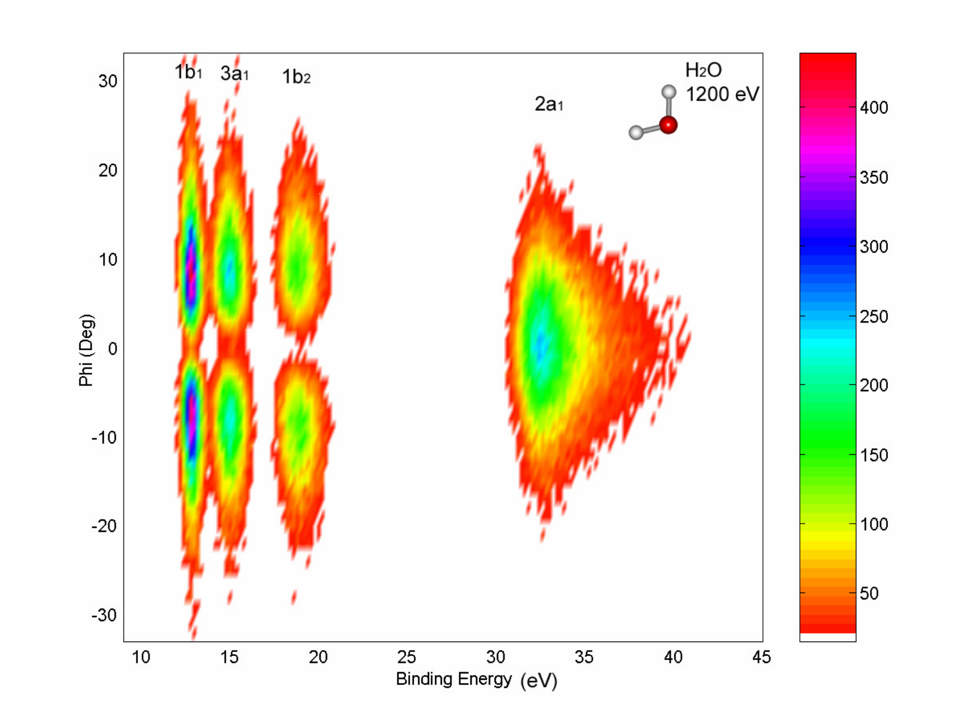

Figure 1. Valence momentum-energy density distribution of water.

5.2.4 Results and discussion

A. Density map

Figure 1 shows the momentum-energy density map of H_2O at an electron impact energy of 1200 eV plus binding energy. In this map, the three outermost one-electron ionization states relating to the $1b_1$, $3a_1$, $1b_2$ orbitals are clearly resolved and appear as sharp peaks characterized by a p-type electron momentum distribution, which is qualitatively in line with the presence of one nodal plane in the corresponding canonical orbitals. For each of these three states, this profile implies thus a vanishing (e, 2e) ionization intensity at momentum origin, and goes through a maximum at a non-vanishing electron momentum (or azimuthal angle). In contrast, the ionization band derived from the inner-valence $2a_1$ orbital extends over almost 10 eV at ϕ = 0°, and exhibits maximal (e, 2e) ionization intensities at the origin of momentum space. The corresponding momentum distribution therefore indicates a s-type canonical orbital, which consistently reflects the lack of a nodal plane.

Electron binding energy spectra can be inferred from this density map for each azimuthal angle defining the momentum of the ionized electron prior to ionization. Inversely, the angular dependence of ionization intensities can be used to reconstruct the experimental electron momentum distributions associated to specific ionization channels.

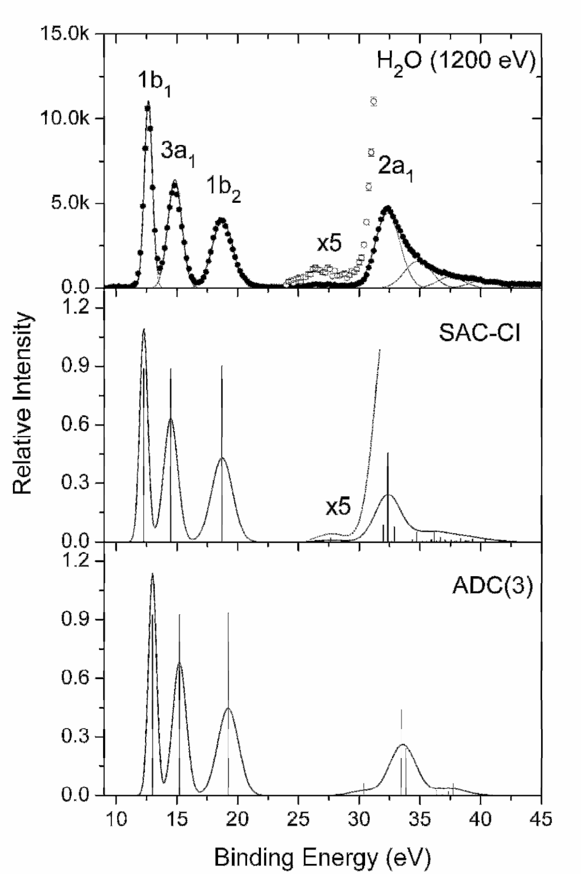

Figure 2. Experimental binding energy spectrum summed over all ϕ angles (top) compared with SAC-CI (middle) and ADC(3) (bottom) theoretical simulations. See text for details.

B. Electron binding energy spectra

Figure 2 shows the (e, 2e) ionization spectrum of H_2O at electron binding energies ranging from 9 to 45 eV and at an impact energy of 1200 eV plus binding energies. This spectrum was obtained by integrating the electron density map of Figure 1 over all azimuthal angles. Gaussian functions have been fitted to the most important bands in this spectrum, using vertical ionization potentials and Franck-Condon widths (folded with the EMS instrument energy resolution 0.68 eV FWHM) estimated from photoelectron spectroscopy measurements [80]. The relative energy spacings of the Gaussian peaks were estimated from experimental estimates for the vertical ionization potentials, with small adjustments to compensate the asymmetries in the shape of the Franck-Condon envelopes. The absolute binding energy scale was set by assigning the energy of the $1b_1$ peak to the vertical ionization potential, as measured by high resolution PES [80]. The centers and widths of these Gaussian bands are listed in Table 1 (included at the end of this chapter). The simulations displayed in Figure 2 were obtained by convoluting the contributions from each identified ionization line by a Gaussian spread function with a width fitted to the EMS experiment, and by scaling line intensities proportionally to the computed ADC(3) pole strengths. Magnification of the experimental (e, 2e) ionization spectrum reveals a shallow peak at ~27.1 eV, which defines the shake-up onset for the $2a_1$ orbital. This peak is certainly not ascribable to a shake-off band, the double ionization threshold being located at 41.3 eV, according to benchmark CCSD(T)/arTZ calculations. At the same level, the vertical ionization threshold related to the $1b_1$ orbital lies at 12.67 eV.

Agreement between theory and experiment for the outer-valence bands at electron binding energies below 20 eV is quantitatively satisfactory enough (~0.3 eV accuracy). The ADC(3) vertical one-electron binding energies slightly overestimate the experimental ones by ~0.4 eV, whereas SAC-CI underestimate the experimental values by ~0.3 eV. All the reported theoretical calculations (Figure 2, Table 1) indicate a severe breakdown of the orbital picture of ionization for the innermost $2a_1$ orbital, in the form of a dispersion of the ionization intensity into shake-up lines ranging from 30 to 40 eV, which explains the intensity spreading over almost 10 eV in the experimental spectrum. In this electron binding energy region, the ADC(3) results for shake-up ionization energies are at best qualitative with respect to the distribution of intensity, due to the limitation of the excitation subspace to the manifold of singly excited 2h-1p states in the radical cation, and treatment therefore of the 2h-1p states at first order only in the correlation potential. Whatever the employed basis set, the ADC(3) calculations locate the $2a_1$ shake-up onset at ~ 30.2 to ~ 30.4 eV, thus at 3 eV above experiment. One can nonetheless not entirely rule out the possibility that the employed block-Davidson diagonalization approach was not powerful enough for recovering at the ADC(3)/raTZ level Rydberg-like shake-up ionization lines with particularly low spectroscopic strengths, lower than the considered threshold ($\Gamma<0.001$). In contrast, the SAC-CI calculations locate this threshold at ~27.6 eV, thus in almost perfect agreement with experiment. This shift is thus probably ascribable to its greatest extent to the role played by double electronic excitations due to electronic relaxation effects induced by ionization of a strongly localized, and almost atomic-like, O_{2s} level. Indeed further CIS and CIS(D) calculations of the excitation energies of the water radical cation employing the aug-cc-pVTZ indicate a shift of the shake-up $2a_1$ excitation onset towards lower energies by 1 to 1.5 eV when double electronic excitations are included. At the ADC(3)/raTZ and SAC-CI general R/raTZ levels, the location of the most intense shake-up bands are reproduced within an accuracy of ~1 eV and ~0.2 eV, respectively.

In order to assess more in details the role of multiple electronic excitations on the location of the $2a_1$ shake-up onset, we display in Table 2 (included at the end of this chapter) estimates of ionization energies that were obtained by adding to the experimental value (12.62 eV) [81] for the first ionization energy of water the excitation energies computed at the MR-SDCI or MR-RSPT2/3 levels for the water radical cation in its $^2B_1$ ground state. The role of the basis set in these calculations is investigated in details. Whatever the employed basis set, these calculations locate the $2a_1$ shake-up onset at 27.1 to 27.4 eV, thus in quantitative agreement with experiment. The same procedure applied to the best MR-SDCI/raTZ results for excitation energies in H_2O^+ locates the $1a_1$ and $1b_2$ ionization lines at 14.87 eV and 19.00 eV, to compare with experimental values of 14.8 and 18.7 eV, respectively. With this indirect approach for estimating electron binding energies, pole strengths are unfortunately not readily accessible.

C. Momentum distributions

Figure 3 shows the experimental momentum distributions for the outer valence orbitals of H_2O compared with the results of our theoretical calculations. In the present work, the theoretical spherically averaged momentum distributions have been convoluted with the experimental momentum resolution using Monte Carlo methods [82]. The CI theoretical curves are taken from [56], and convolved according to our experimental momentum resolution. The theoretical calculations for the $1b_2$ orbital with HF, DFT, ADC(3) and CI methods all give almost the same momentum distributions. Following the procedure by Bawagan *et al.* [31] the measured (e, 2e) intensities were therefore systematically rescaled according to the normalization factor ensuring the best fit between theory and experiment for the $1b_2$ orbital. For this orbital, the agreement between theory and experiment is truly optimal throughout the investigated range of electron momenta, except at momenta below 0.2 a.u. where a slight but clearly discernible rise of the measured electron density may reflect a symmetry breaking that is possibly ascribable to vibration effects [83]. This slight discrepancy between experimental distributions and theoretical calculations for the $1b_2$ orbital is also possibly due to distorted wave effects. Indeed, a comparison of Figures 3 and 4 demonstrates that this discrepancy almost vanishes at impact energy of 2400 eV plus binding energies. The shape and spread of the momentum distributions derived from the other bands remain on the contrary unaffected by an increase of the kinetic energy of the impinging electron.

In general, theoretical calculations reliably reproduce the measured momentum distribution, except when a very limited basis set such as 6-31G is employed [73]. Even with a basis set as large as the aug-cc-pVTZ one, the HF calculations rather obviously fail to quantitatively reproduce the $1b_1$ and $3a_1$ experimental momentum distributions. In contrast, the agreement with the experimental curves is much better with this basis set when using B3LYP Kohn-Sham orbitals, or Dyson orbitals derived from CI or ADC(3) calculations. The latter theoretical orbital momentum distributions are found again to almost coincide.

The experimental momentum distribution inferred in Figure 3 from an angular analysis of the (e, 2e) ionization intensity ascribed to the peak at 32.4 eV is compared in Figure 3 with the Dyson orbital momentum distribution characterizing the closest shake-up line in the ADC(3) spectrum, namely the satellite line at 33.5 eV with a pole strength of 0.44. All theoretical distributions for this orbital are normalized. It appears that the CI/109GTO's calculations by Bawagan *et al.* [31] slightly overestimate the $2a_1$ orbital density that is experimentally observed at low momenta.

The experimental momentum distribution of the satellite peak at 27.1 eV is compared with DFT calculations at the B3LYP/aug-cc-pVTZ level for the $2a_1$ momentum distribution in Figure 5. A slight difference between the theoretical curves for the momentum densities computed at an impact energy of 1200 eV (dashed line) and 2400 eV (solid line) is simply due to convolutions with slightly different momentum resolutions. The estimated experimental pole strength for this band amounts to 0.021 at both impact energies. The shape of the experimental distribution compared with the theoretical one confirms the relationship of this shake-up band with the $2a_1$ orbital, in agreement with the theoretical SAC-CI, MR-SDCI or MR-RSPT2/3 calculations described in the previous section, or assignment by Ehara *et al.* [53].

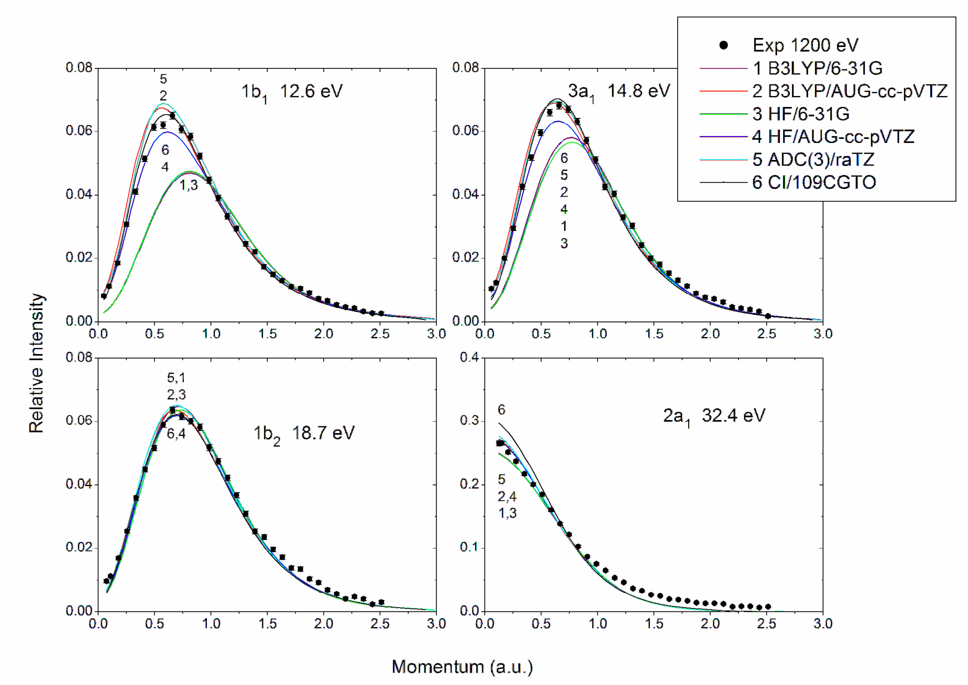

Figure 3. Convolved and spherically averaged momentum distributions of the 1b$_1$, 3a$_1$, 1b$_2$, 2a$_1$ orbitals at an impact energy of 1200 eV plus binding energy.

It thus experimentally appears that the intensity of the 2a$_1$ shake-up onset at 27.1 eV does not show any dynamical dependence on the impact energy, at kinetic energies above 1200 eV. In contrast, it is interesting to note that in synchrotron experiments the intensity of this band was found to vary in a remarkable way with the photon energy [52]. One obvious explanation is that with photoelectron experiments at photon energies of 100 eV, residual interactions between the molecular radical cation and the outgoing electron remain strong, which results in severe alterations of the continuum wave function, the shape of which is strongly dependent on the kinetic energy of the ionized electron. This is not the case with ionization events induced by electron impact at high kinetic energies: under the so-called EMS conditions, the impinging and outgoing electrons are on the contrary reliably described by plane waves.

D. Basis set effects

Figures 6 and 7 confirm the rather strong influence of the basis set on the theoretical momentum distributions associated to the 1b$_1$ and 3a$_1$ orbitals. Although Bawagan *et al.* have discussed these effects [31], it is still instructive, with regards to software and hardware developments over the last 20 years, to investigate further the influence of the basis. The original HEMS program developed at the University of British Columbia (UBC) [31], which is now widely used to calculate electron momentum distributions, cannot handle basis sets containing *g*-type polarization functions and beyond.

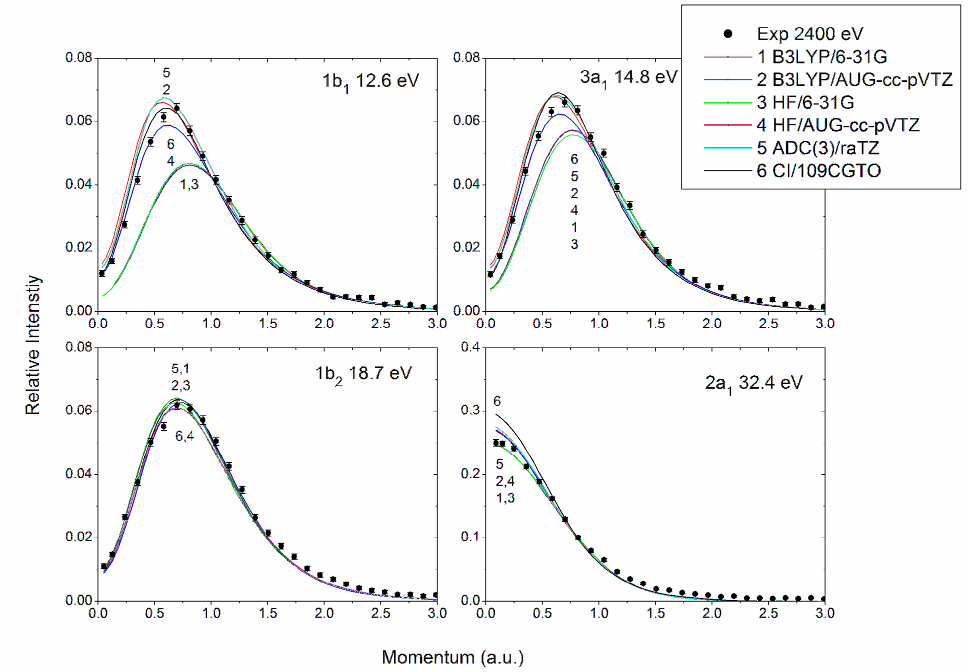

Figure 4. Convolved and spherically averaged momentum distributions of the $1b_1$, $3a_1$, $1b_2$, $2a_1$ orbitals at an impact energy of 2400 eV plus binding energy.

A new program for computing momentum distributions was therefore developed for this purpose at Tsinghua University. This program, named NEMS, was coded using FORTRAN90. It makes use of general analytic formula [84] for handling basis functions, whatever their angular momentum quantum number. The fast algorithm of continual fractions [85] was used for numerically computing spherical harmonical functions $j_l(x)$. This algorithm is considered to be the best strategy for calculating high order spherical harmonical functions $j_l(x)$ near space origin (x~0) and in the asymptotic region (x>>1). This new program enabled us to compute momentum distributions using a much larger basis set (d-aug-cc-pV6Z), which includes *g*-, *h*-, and *i*-type basis functions that could not be handled so far with the HEMS program.

Table 3 (included at the end of this chapter) gives the calculated dipole moment and total energy of water molecule using HF and DFT methods with various basis sets. The slight difference in total energies, as well as in dipole moments, between the aug-cc-pVTZ and d-aug-cc-pV6Z basis sets indicates that these basic ground state properties, and the underlying wavefunction therefore, are almost almost effectively converged with the aug-cc-pVTZ basis set. The excellent agreement between the calculated dipole moment at the B3LYP/d-aug-cc-pV6Z level and the experimental values [86-87], as well as for the total energy and momentum distributions, confirms that DFT calculations incorporating ground state correlation effects are superior to the HF approach for studying molecular properties related to the ground state electron density. Note nonetheless that DFT is semi-empirical in nature, and does not obey therefore the variational principle regarding the total energy. Indeed, in this case, it is found that close to the limit of a complete basis set, the B3LYP total energy is obviously lower than the experimental value found for the total non-relativistic energy at equilibrium [31]. It is thus here worth remembering that the electron densities measured in EMS relate to transition amplitudes between the neutral ground state and cationic states - they do not therefore simply relate to ground state electron densities for specific sets of orbitals, as was so commonly assumed so far in DFT studies of EMS experiments.

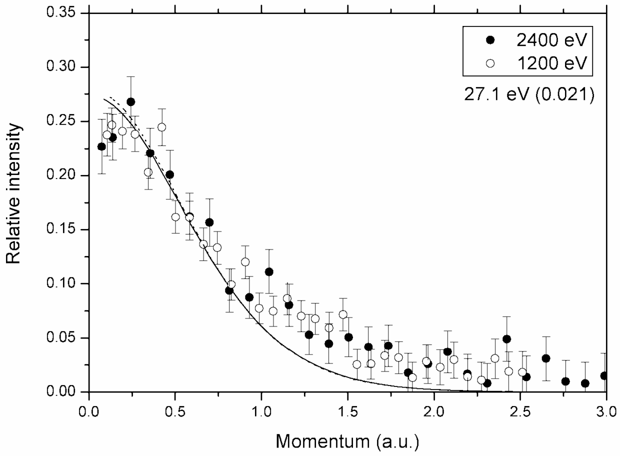

Figure 5. Convolved and spherically averaged momentum distribution inferred for the shake-up peak at 27.1 eV at impact energies of 1200 eV and 2400 eV plus binding energy.

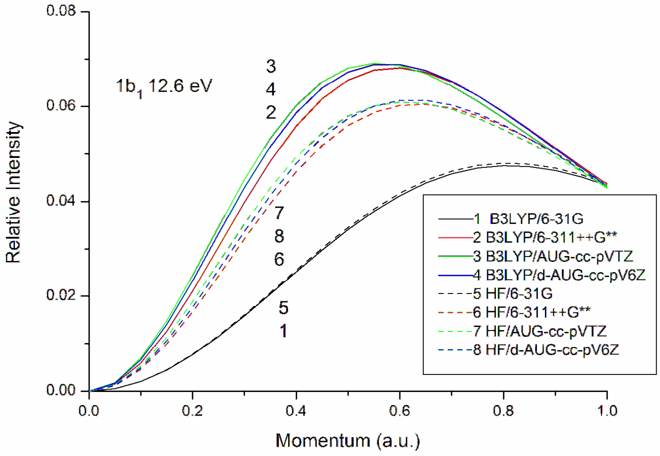

Figure 6. Momentum distributions of the $1b_1$ orbital at various theoretical levels (the experimental resolution is not accounted for).

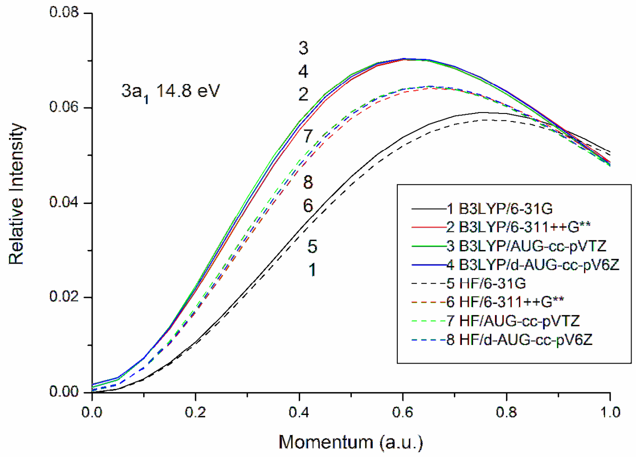

Figure 7. Momentum distributions of the 3a$_1$ orbital at various theoretical levels (the experimental resolution is not accounted for).

As is clearly seen from Figure 6, the momentum distribution computed for the 1b$_1$ orbital at low electron momenta tends to increase with the number of diffuse functions in the basis sets (see the progression of curve 1,2,3 for DFT, and 5, 6, 7 for HF). Beyond the aug-cc-pVTZ basis set, a slight reversal in this trend is seen when considering the results obtained with the largest basis set considered in this study, namely d-aug-cc-pV6Z (see curve 4 and 8). It is interesting to note that, in the saturation limit, the same trends are observed both with GTO and STO basis sets [31]. Therefore, this variation in the influence of the basis set might be due to the fact that the d-aug-cc-pV6Z basis set contains more split-valence components. All the theoretical momentum distributions are generated using the newly developed NEMS program, which can handle arbitrary type basis functions.

5.2.5 Conclusions

In this paper, we report the results of an exhaustive reinvestigation, throughout the valence region, of the electronic structure of water using a new (e, 2e) spectrometer, which enables a much improved energy resolution of ΔE = 0.45-0.68 eV, as well as azimuthal and polar angle resolutions of $\Delta\phi = \pm 0.84°$ and $\Delta\theta = \pm 0.53°$, respectively. The measured electron impact (e, 2e) ionization spectra were compared with a variety of calculations of one-electron and shake-up ionization spectra employing the 1p-GF/ADC(3) and SAC-CI general approaches, and of excitation energies in the water radical cation employing multi-reference theories (MR-SDCI, MR-RSPT2, MR-RSPT3). The high accuracy experimental momentum distributions derived from an angular analysis of (e, 2e) ionization intensities were compared with spherically averaged momentum distributions derived from HF orbitals, B3LYP Kohn-Sham orbitals, and ADC(3) Dyson orbitals. A weakly discernible peak at 27.1 eV defining the experimental shake-up onset of water was confirmed to relate to a complex set of shake-up states produced by ionization of the 2a$_1$ orbital. The influence of Rydberg-type basis functions on the energies of these states is rather limited. In contrast, the 2a$_1$ shake-up onset is strongly dependent on the inclusion of double electronic excitations in the shake-up excitation operator manifold, possibly because of the almost atomic-like O_{2s} nature of the ionized orbital, which may result in unusually strong electronic relaxation effects.

A new algorithm has been developed for calculating electron momentum distributions using almost complete basis sets, such as d-aug-cc-pV6Z. A comparison with results obtained with smaller basis sets indicate near saturation at the HF/aug-cc-pVTZ and B3LYP/aug-cc-pVTZ levels.

References

[1] McCarthy, I.E.; Weigold, E. *Rep. Prog. Phys.* 1991, 91, 789 (1991).

[2] Weigold, E.; McCarthy, I. E. *Electron Momentum Spectroscopy*; Kulwer/Plenum: New York, 1999.

[3] Brion, C. E. *Int. J. Quantum Chem.* 1986, 29, 1397.

[4] Coplan, M.A.; Moore, J. H.; Doering, J. P. *Rev. Mod. Phys.* 1994, 66, 985.

[5] McWeeny, R.; Pickup, B. T. *Rep. Progr. Phys.* 1980, 43, 1065.

[6] Őhrn, Y.; Born, G. *Adv. Quantum Chem.* 1981, 13, 1.

[7] Pickup, B.T. *Chem. Phys.* 1977, 19, 193.

[8] Seabra, G. M.; Kaplan, I. G.; Zakrzewski, V. G.; Ortiz, J. V. *J. Chem. Phys.* 2004, 121, 4142.

[9] Deleuze, M. S.; Knippenberg, S. *J. Chem. Phys.* 2006, 125, 104309.

[10] Huang, Y. R.; Knippenberg, S.; Hajgato, B.; Francois, J.-P.; Deng, J. K.; Deleuze, M. S. *J. Phys. Chem. A* 2007, 111, 5879.

[11] Ning, C. G.; Ren, X. G.; Deng, J. K.; Su, G. L.; Zhang, S. F.; Knippenberg, S.; Deleuze, M. S. *Chem. Phys. Lett.* 2006, 421, 52.

[12] Deleuze, M. S.; Pickup, B. T.; Delhalle, J. *Mol. Phys.* 1994, 83, 655.

[13] Hafied, H.; Eschenbrenner, A.; Champion, C.; Ruiz-López, M. F.; Dal Cappello, C.; Charpentier, I.; Hervieux, P.A. *Chem. Phys. Lett.* 2007, 439, 55.

[14] Page, R. H.; Larkin, R. J.; Yhen, Y. R.; Lee, Y. T. *J. Chem. Phys.* 1987, 88, 2249.

[15] Reutt, J. E.; Wang, L. S.; Lee, Y. T.; Shirley, D. A. *J. Chem. Phys.* 1986, 85, 6928.

[16] Lefaivre, D.; Marmet, P. *Can. J. Phys.* 1978, 56, 1549.

[17] Botter, R.; Carlier, J. *J. Electron Spectrosc. Relat. Phenom.* 1977, 12, 55.

[18] Dixon, R. N.; Duxbury, G.; Rabalais, J. W.; Asbrink, L. *Mol. Phys.* 1976, 31, 423.

[19] Karlsson, L.; Mattson, L.; Jadrny, R.; Albridge, R. G.; Pinchas, S.; Bergmark, T.; Siegbahn, K. *J. Chem. Phys.* 1975, 62, 4745.

[20] Debies, T. P.; Rabalais, J. W. *J. Am. Chem. Soc.* 1975, 97, 487.

[21] Rabalais, J. W.; Debies, T. P.; Berkosky, J. L.; Huang, J.-T. J.; Ellison, F. O. *J. Chem. Phys.* 1974, 61, 516.

[22] Bermark, T.; Karlsson, L.; Jadrny, R.; Mattsson, L.; Albridge, R. G.; Siegbahn, K. *J. Electron Spectrosc. Relat. Phenom.* 1974, 4, 85.

[23] Katayama, D. H.; Huffman, R. E.; O'Bryan, C. L. *J. Chem. Phys.* 1973, 59, 4309.

[24] Asbrink, L.; Rabalais, J. W. *Chem. Phys. Lett.* 1971, 12, 182.

[25] Brundle, C. R.; Turner, D. W. *Proc. Roy. Soc. (London)* 1968, A307, 27.

[26] Campbell, M. J.; Liesegang, J.; Riley, J. D.; Leckey, R. C. G.; Jenkin, J. G.; Poole, R. T. *J. Electron Spectrosc. Relat. Phenom.* 1979, 15, 83.

[27] McCulloh, K. E. *Int. J. Mass. Spectrom. Ion. Phys.* 1976, 21, 333.

[28] Dixon, A. J.; Dey, S.; McCharthy, I. E.; Weigold, E.; Williams, G. R. *Chem. Phys.* 1977, 21, 81.

[29] Hood, S. T.; Hamnett, A.; Brion, C. E. *J. Electron Spectrosc. Relat. Phenom.* 1977, 11, 205.

[30] Bawagan, A. O.; Lee, L. Y.; Leung, K. T.; Brion, C. E. *Chem. Phys.* 1985, 99, 367.

[31] Bawagan, A. O.; Brion, C. E.; Davison, E. R.; Feller, D. *Chem. Phys.* 1987, 113, 19.

[32] Cederbaum, L. S. *Mol. Phys.* 1974, 28, 479.

[33] Siegbahn, K.; Nordling, C.; Johansson, G.; Hedman, J.; Heden, P. F.; Hamrin, K.; Gelius, U.; Berkmark, T.; Werme, L. O.; Manne, R.; Baer, Y. *ESCA Applied to Free Molecules*; North-Holland: Amsterdam, 1969.

[34] Pickup, B. T.; Goscinski, O. *Mol. Phys.* 1973, 26, 1013.

[35] Chong, D. P.; Herring, F. G.; Mc Williams, D. *J. Chem. Phys.* 1974, 61, 3567.

[36] Jorgensen, P.; Simons, J. *J. Chem. Phys.* 1975, 63, 5302.

[37] Davidson, E. R. *J. Comput. Phys.* 1975, 17, 87.

[38] Hubac, I.; Urban, M. *Theor. Chim. Acta* 1977, 45, 195.

[39] von Niessen, W.; Diercksen, G. H. F.; Cederbaum, L. S. *J. Chem. Phys.* 1977, 67, 4124.

[40] Hermann, M. F.; Yeager, D. L.; Freed, K. F. *Chem. Phys.* 1978, 29, 77.

[41] Carravetta, V.; Moccia, R. *Mol. Phys.* 1978, 35, 129.

[42] Kurtz, H. A.; Öhrn, Y. *J. Chem. Phys.* 1978, 69, 1162.

[43] Born, G.; Öhrn, Y. *Physica Scripta* 1980, 21, 378.

[44] Cacelli, I.; Moccia, R.; Carravetta, V. *Chem. Phys.* 1982, 71, 199.

[45] Baker, J.; Pickup, B. T. *Mol. Phys.* 1983, 49, 651.

[46] Baker, J. *Chem. Phys.* 1983, 79, 117.

[47] Ortiz, J. V.; Basu, R.; Öhrn, Y. *Chem. Phys. Lett.* 1983, 103, 29.

[48] Yeager, D. L. *J. Chem. Phys.* 1996, 105, 8170.

[49] Heryadi, D.; Yeager, D. L.; Golab, J. T.; Nichols, J. A. *Theor. Chim. Acta* 1995, 90, 273.

[50] Nooijen, M.; Snijders, J. G. *Int. J. Quantum Chem.* 1993, 48, 15.

[51] Morrison, R. C.; Liu, G. H. *J. Comp. Chem.* 1992, 13, 1004.

[52] Banna, M. S.; McQuaide, B. H.; Malutzki, R.; Schmidt, V. *J. Chem. Phys.* 1986, 84, 4739.

[53] Ehara, M.; Ishida, M.; Nakatsuji, H. *J. Chem. Phys.* 2001, 114, 8990.

[54] Deleuze, M. S.; Giuffreda, M. G.; François, J.-P.; Cederbaum, L. S. *J. Chem. Phys.* 1999, 111, 5851.

[55] Zheng, Y.; Brion, C. E.; Brunger, M. J.; Zhao, K.; Grisogono, A. M.; Braidwood, S.; Weigold, E.; Chakravorty, S. J.; Davidson, E. R.; Sgamellotti, A.; von Niessen, W. *Chem. Phys.* 1996, 212, 269.

[56] Duffy, P.; Chong, D. P.; Casida, M. E.; Salahub, D. R. *Phys. Rev. A* 1994, 50, 4704.

[57] Lee, C.; Yang, W.; Parr, R. G. *Phys. Rev. B* 1988, 37, 785.

[58] This basis set was obtained from the Extensible Computational Chemistry Environment Basis Set Database, Version 02/02/06, as developed and distributed by the Molecular Science Computing Facility, Environmental and Molecular Sciences Laboratory which is part of the Pacific Northwest Laboratory, and funded by the U.S. Department of Energy. Also see reference : Wilson, A. K.; Mourik, T. V.; Dunning, T. H., Jr. *J. Mol. Struct. (THEOCHEM)* 1997, 388, 339.

[59] Cederbaum, L. S.; Domcke, W. *Adv. Chem. Phys.* 1977, 36, 205.

[60] Schirmer, J.; Cederbaum, L. S.; Walter, O. *Phys. Rev. A* 1983, 28, 1237.

[61] Schirmer, J.; Angonoa, G. *J. Chem. Phys.* 1989, 91, 1754.

[62] Weikert, H. G.; Meyer, H.-D.; Cederbaum, L. S.; Tarantelli, F. *J. Chem. Phys.* 1996, 104, 7122.

[63] Knippenberg, S.; Nixon, K. L.; Mackenzie-Ross, H.; Brunger, M. J.; Wang, F.; Deleuze, M. S.; François, J.-P.; Winkler, D.A. *J. Phys. Chem. A* 2005, 109, 9324.

[64] Knippenberg, S.; Nixon, K. L.; Brunger, M. J.; Maddern, T.; Campbell, L.; Trout, N.; Wang, F.; Newell, W. R.; Deleuze, M. S.; François, J.-P.; Winkler, D. A. *J. Chem. Phys.* 2004, 121, 10525.

[65] Adcock, W.; Brunger, M. J.; McCarthy, I. E.; Michaelewicz, M. T.; von Niessen, W.; Wang, F.; Winkler, D. A. *J. Am. Chem. Soc.* 2000, 122, 3892.

[66] Deleuze, M. S. *Int. J. Quantum Chem.* 2003, 93, 191.

[67] Deleuze, M. S. *J. Phys. Chem. A* 2004, 108, 9244.

[68] Dunning, T. H.; Hay, P. J., Jr. *Methods of Electronic Structure Theory*; Schaefer III, H. F., ed.; New York: Plenum, 1977.

[69] Nakatsuji, H. *Chem. Phys. Lett.* 1991, 177, 331.

[70] Ehara, M.; Ohtsuka, Y.; Nakatsuji, H.; Takahashi, M.; Udagawa, Y. *J. Chem. Phys.* 2005, 122, 234319.

[71] Ehara, M.; Ishida, M.; Nakatsuji, H. *J. Chem. Phys.* 2002, 117, 3248.

[72] Dunning, T. J., Jr. *J. Chem. Phys.* 1989, 90, 1007.

[73] Frisch, M. J. *et al.*, Gaussian03, revision D02; Gaussian Inc; Pittsburgh, PA (2003).

[74] Werner, H. J.; Knowles, P. J. *J. Chem. Phys.* 1988, 89, 5803.

[75] Knowles, P. J.; Werner, H.-J. *Chem. Phys. Lett.* 1988, 145, 514.

[76] Knowles, P. J.; Werner, H.-J. *Theor. Chim. Acta.* 1992, 84, 95.

[77] Werner, H.-J. *Mol. Phys.* 1996, 89, 645.

[78] MOLPRO is a package of ab initio programs written by Werner, H.-J.; Knowles, P. J. with contributions from Amos, R. D.; Bernhardsson, A.; Berning, A. *et al.*

[79] Ren, X. G.; Ning, C. G.; Deng, J. K.; Zhang, S. F.; Su, G. L.; Huang, F.; Li, G. Q. *Rev. Sci. Instrum.* 2005, 76, 063103.

[80] Kimura, K.; Katsuwata, S.; Achiba, Y.; Yamazaki, T.; Iwata, S. *Handbook of HeI Photoelectron Spectra of Fundamental Organic Molecules*; Halsted Press: New York, 1981.

[81] Potts, A. W.; Price, W. C. *Proc. R. Soc. Lond. A* 1972, 326, 181.

[82] Duffy, P.; Casida, M. E.; Brion, C. E.; Chong, D. P. *Chem. Phys.* 1992, 159, 347.

[83] Hollebone, B. P.; Neville, J. J.; Zheng, Y.; Brion, C. E.; Wang, Y.; Davidson, E. R. *Chem. Phys.* 1996, 196, 13.

[84] Mathar, R. J. *Int. J. Quantum Chem.* 2002, 90, 227.

[85] Lentz, W. J. *Appl. Opt.* 1976, 15, 668.

[86] Clough, S. A.; Beers, Y.; Klein, G. P.; Rothman, L. S. *J. Chem. Phys.* 1973, 59, 2254.

[87] Rosenberg, B. J.; Shavitt, I. *J. Chem. Phys.* 1975, 63, 2162.

Table 1. Ionization energies (eV), intensities (pole strengths) and assignments for H_2O.

EMS			SAC-CI			ADC(3)		
Assign.	IP(FWHM)	Ps^a	IP	Ps	State	IP	Ps	Assign.
$1b_1$	12.6 (0.78)	1.00	12.272	0.888	$^2B_1$	12.990	0.925	$1b_1$
$3a_1$	14.8 (1.35)	1.00	14.496	0.888	$^2A_1$	15.214	0.925	$3a_1$
$1b_2$	18.7 (2.0)	1.00	18.723	0.900	$^2B_2$	19.217	0.932	$1b_2$
$2a_1$	27.1 (2.6)	0.021	27.641	0.020	$^2A_1$	30.388	0.065	$2a_1$
			27.932	0.001	$^2B_1$			
			29.269	0.002	$^2B_1$			
			29.694	0.001	$^2B_2$			
			32.013	0.086	$^2A_1$			
			32.244	0.001	$^2B_1$	32.028	0.001	$1b_1$
$2a_1$	32.4 (2.4)	0.495	32.357	0.455	$^2A_1$	33.469	0.440	$2a_1$
			32.712	0.002	$^2B_1$			
			32.898	0.076	$^2A_1$			
			33.229	0.001	$^2B_2$			
			33.444	0.001	$^2B_1$			
			34.216	0.001	$^2B_2$			
			34.377	0.008	$^2A_1$			
$2a_1$	34.8 (2.6)	0.186	34.717	0.048	$^2A_1$	33.864	0.239	$2a_1$
			34.864	0.000	$^2B_2$			
			35.101	0.001	$^2B_1$			
			35.224	0.003	$^2A_1$			
			35.560	0.002	$^2B_1$			
			35.912	0.011	$^2A_1$			
			35.981	0.012	$^2B_1$			
			36.175	0.001	$^2B_1$			
$2a_1$	37.5 (2.6)	0.072	36.177	0.049	$^2A_1$	36.369	0.024	$2a_1$
			36.382	0.004	$^2A_1$	36.859	0.004	$2a_1$
			36.569	0.002	$^2B_2$	37.339	0.018	$2a_1$
			36.691	0.021	$^2A_1$	37.726	0.062	$2a_1$
			37.055	0.008	$^2A_1$			
			37.113	0.004	$^2B_1$			
			37.203	0.001	$^2B_1$			
			37.596	0.009	$^2A_1$			
			37.812	0.003	$^2B_1$			
			37.888	0.003	$^2B_2$			
			37.909	0.001	$^2B_1$			
			38.005	0.003	$^2B_1$			
			38.098	0.002	$^2A_1$			
			38.346	0.017	$^2A_1$			
			38.686	0.001	$^2B_1$			
			38.720	0.005	$^2A_1$			
			38.728	0.004	$^2B_2$			
			38.767	0.001	$^2B_1$			

$2a_1$	40.1 (2.6)	0.047	38.820	0.006	$^2A_1$	39.307	0.010	$2a_1$
			38.896	0.002	$^2A_1$			
			38.981	0.002	$^2A_1$			
			39.058	0.003	$^2A_1$			
			39.201	0.001	$^2B_1$			
			39.290	0.001	$^2B_1$			
			39.321	0.013	$^2A_1$			
			39.524	0.001	$^2A_1$			
			40.227	0.001	$^2A_1$			
			40.342	0.001	$^2B_1$			
			40.393	0.012	$^2A_1$			
			40.839	0.001	$^2A_1$			
			41.066	0.001	$^2A_1$			
			41.517	0.006	$^2A_1$			

[a] Relative to the $1b_2$ orbital – the normalization procedure takes the experimental pole strength of $1b_2$ as one unit.

Table 2. Multi-reference calculations of ionization energies of water.

State	MR-RSPT2/ cc-pVDZ	MR-RSPT2/ cc-Pvtz	MR-RSPT2/ aug-cc-pVDZ	MR-RSPT2/ rTZ	MR-RSPT3/ cc-pVDZ	MR-RSPT3/ cc-pVTZ	MR-RSPT3/ aug-cc-pVDZ	MR-SDCI/ cc-pVDZ	MR-SDCI/ cc-pVTZ	MR-SDCI/ aug-cc-pVDZ	MR-SDCI/ rTZ
$^2B_2$	33.04	32.82	32.80	33.48	33.13	32.96	33.13	33.14	32.93	32.89	32.87
$^2A_1$	33.05	32.37	32.05	33.32	33.22	33.00	32.91	33.14	32.78	32.84	32.62
$^2B_1$	32.69	32.33	32.46	32.50	32.93	33.07	32.48	32.86	32.67	31.92	31.84
$^2A_1$	32.07	31.94	31.94	32.00	32.11	32.00	32.08	32.04	31.95	31.89	32.12
$^2B_2$	29.34	29.17	29.28	33.81	29.48	29.44	30.16	29.47	29.37	29.32	29.32
$^2B_1$	28.90	28.81	28.83	28.87	28.94	28.88	28.87	28.93	28.84	28.79	28.80
$^2B_1$	27.26	27.21	27.10	27.20	27.30	27.28	27.14	27.29	27.26	27.09	27.18
$^2A_1$	27.17	27.18	27.13	27.19	27.24	27.27	27.21	27.18	27.23	27.16	27.41
$^2B_2$	19.13	18.94	19.04	18.95	19.17	18.99	19.08	19.21	19.03	19.09	19.00
$^2A_1$	14.88	14.81	14.86	14.81	14.91	14.83	14.89	14.88	14.87	14.91	14.87
$^2B_1$	12.62	12.62	12.62	12.62	12.62	12.62	12.62	12.62	12.62	12.62	12.62

Table 3. Basis-set dependence of the total energy and dipole moment of H_2O.

Method/Basis set	Size	Dipole Moment (D)	Total energy (Hartree)
B3LYP/6-31G	13	2.463	-76.3849
B3LYP/6-311++G**	37	2.1625	-76.4592
B3LYP/aug-cc-pVTZ	105	1.8409	-76.4671
B3LYP/d-aug-cc-pV6Z	551	1.8548	-76.4742
HF/6-31G	13	2.6299	-75.9834
HF /6-311++G**	37	2.2392	-76.0529
HF /aug-cc-pVTZ	105	1.9757	-76.0611
HF /d-aug-cc-pV6Z	551	1.9815	-76.0674
Experimental		1.8546 ± 0.0006^a	76.4376 ± 0.0004^b

[a] taken from [86].

[b] taken from [31, 87]. It is the non-relativistic, non-vibrating total energy.

Part 6: General conclusions and outlook for the future

The main purpose of the present work was to assess the potential of advanced "orbital imaging" spectroscopic methods like Electron Momentum Spectroscopy (EMS) and Penning Ionization Electron Spectroscopy (PIES) in probing the shape, spread, and stereochemistry of molecular orbitals in challenging situations such as those encountered when studying cyclically strained molecules (part 3) subject to severe structural distortions upon ionization, or conformationally versatile molecules (part 4), including the case of conjugated systems subject to electronic excitation processes that may easily lead to a breakdown of the one-electron picture of ionization.

Despite these difficulties, our work confirms the intimate relationships of ionization with canonical, i. e., delocalized orbitals, and the ability of ionization spectroscopies therefore to probe the molecular structure as a whole (bonding characteristic, cyclic strain, conformation). Numerous spectral fingerprints of the finest details of the molecular architecture can indeed be identified in the valence ionization bands and related properties such as spherically averaged electron momentum distributions in EMS and the collision energy dependence of partial ionization cross sections in PIES. As shown through ample enough examples, the interpretation of these experiments is subject to many complications like the usually very strong influence of the molecular conformation on the ionization energies, electronic correlation and relaxation effects, a dispersion of the ionization intensity over secondary structures such as shake-up lines and shake-off bands, vibronic coupling interactions and ultra-fast nuclear dynamical effects, or a breakdown of the plane wave impulse approximation. Therefore, interpretation of EMS or PIES experiments, even with the assistance of more standard Photo-Electron Spectroscopy (PES) measurements, requires extensive theoretical work if it has to have any value at all. To achieve this goal, we have resorted to the benchmark theoretical approaches described in part 2 for coping with many-body effects (Configuration Interaction, Many-Body Perturbation Theory, Coupled Cluster theory, one-particle Green's Function theory along with the third order Algebraic Diagrammatic Construction [ADC(3)] scheme) and for calculating statistical thermo-dynamical partition functions and the related state functions beyond the Rigid Rotor Harmonic Oscillator approximation.

A link between one-particle Green's Function (1p-GF) theory and EMS has been established, through the interplay of Dyson orbitals [1], defined as partial overlaps between the initial neutral ground state and final ionized states. With regards to electronic correlation and relaxation, these orbitals enable a formally exact description of electronic momentum distributions inferred from the angular dependence of (e,2e) ionization cross sections in EMS experiments, within the framework of the binary encounter approximation for electronic scattering, the Born assumption of a sudden (vertical) ionization event, and the plane wave impulse approximation for describing the ingoing and outgoing electrons.

Our first analyses of EMS experiments were performed on cage compounds (norbornane, norbornene) following the prevailing views in the field, thus under the tacit and empirical assumption that, despite the fact that they provide very poor estimates of one-electron ionization energies and fail to describe shake-up processes, Kohn-Sham orbitals strongly resemble Dyson orbitals. With this assumption, it was thus at first glance most tempting to use Electron Momentum Spectroscopy for identifying the "best" electronic wavefunction and make use of it for computing various grounds state molecular properties (molecular structures, dipole moments, infra-red spectra, NMR shifts,… etc). One should not forget however that the calculations of such properties using standard procedures are also subject to approximations that may lead to a somehow too good agreement with experiment. One example we early discussed in Chapter 3.4 on norbornene is the neglect of anharmonic effects in Density Functional Theory (DFT) calculations of infra-red frequencies, which are nowadays most often implicitely accounted for through empirical scaling factors. One of our later works demonstrated that, due to the neglect of many-electron effects (relaxation, configuration interactions) in the final state, Kohn-Sham orbitals obtained with standard functionals may strongly deviate from Dyson orbitals, in particular when tackling molecules with low symmetry.

The works performed during the four years of this philosophical degree reflect therefore a rather significant evolution in our views on the theory behind "orbital imaging". Spectroscopies like EMS or PIES are unquestionably suited for probing the shape, spread and stereochemistry of molecular orbitals and their interplay with the molecular architecture, under the numerous constraints and limitations inherent to the interpretation of highly challenging ionization experiments. The EMS studies described in the preceding chapters have been performed in collaboration with the experimental research groups of Prof M. J. Brunger at Flinders University in Adelaide (Australia) for the cage compounds and of Prof. J.K. Deng at Tsinghua University in Beijing (China) for the conformationally versatile molecules. For norbornane we could also rely on new photoelectron measurements by Prof. J.H.D Eland at Oxford University (United Kingdom) and stimulating discussions with Prof. L.S. Cederbaum from Heidelberg University (Germany). The PIES study on biphenyl was the result of a collaboration with the group of Prof. K. Ohno and Dr. N. Kishimoto at Tohoku University in Sendai (Japan). The main results of these works can be summarized as follows:

In Chapter 3.1, we have reported on results of an exhaustive study of the valence electronic structure of norbornane (C_7H_{12}), up to binding energies of 29 eV. Experimental EMS and theoretical 1p-GF and DFT approaches were all utilized in this investigation. A stringent comparison between the electron momentum spectroscopy and theoretical orbital momentum distributions found that, among all the tested models, the combination of the Becke-Perdew functional and a polarized valence basis set of triple-ς quality provides the best representation of the electron momentum distributions for all of the 20 valence orbitals of norbornane. This experimentally validated quantum chemistry model was then used to extract some chemically important properties of norbornane. When these calculated properties are compared to corresponding results from other independent measurements, generally good agreement is found. The 1p-GF calculations at the ADC(3) level indicate that the orbital picture of ionization breaks down at binding energies larger than 22.5 eV. Despite this complication, they enable insights within 0.2 eV accuracy into the available ultra-violet photoemission and newly presented (e,2e) ionization spectra, except for the band associated with the $1a^{-1}_2$ one-hole state, which is probably subject to rather significant geometry relaxation and vibrational effects, and a band at ~ 25 eV characterized by a momentum distribution of "*s*-type" symmetry, which the Green's Function calculations fail to reproduce. We note the vicinity of the vertical double ionization threshold at ~ 26 eV.

In Chapter 3.2, we have presented 1p-GF calculations of the ionization spectrum of norbornane at the ADC(3) level using basis sets of varying quality, along with accurate evaluations at the CCSD(T) level of the vertical (26.5 eV) and adiabatic (22.1 eV) double ionization thresholds under C_{2v} symmetry. The obtained results have been compared with newly recorded Ultraviolet Photoemission Spectra (UPS), up to binding energies of 40 eV. The theoretical predictions are entirely consistent with experiment and indicate that, in a vertical depiction of ionization, shake-up states at binding energies larger than ~26.5 eV tend to decay via emission of a second electron in the continuum. A band of *s*-type symmetry that has been previously seen at ~25 eV in the electron impact ionization spectra of norbornane was found to be entirely missing in the UPS measurements and theoretical ADC(3) spectra.

With regard to the low fraction of the recovered $1a_1$ ionization intensity, it might be worth recalculating the shake-up ionization spectrum using more sophisticated diagonalization approaches, such as the block- or band-Lanczos procedures [2]. Further 1p-GF calculations incorporating very diffuse functions, as well as Coulomb and distorted plane waves in the basis set might also be probably useful, as well as two-particle Green's function calculations of doubly ionized states, for investigating that part of the spectrum. Nonetheless, in view of the very usual basis set dependence of the $1a_1$ shake-up band at 28 eV, and of the exceedingly large (e,2e) ionization intensity at 25 eV, we are confident that this band does not relate to standard shake-up or shake-off processes.

With regard to our obtained results and to the time scales characterizing electron-electron interactions in EMS (10^{-17} s) as compared with that (10^{-13} s) of photon-electron interactions in UPS, and considering the *p*-type symmetry of the electron momentum distributions for the nearest $1b_1$ and $1b_2$ orbitals, band 12 can certainly not simply be due to adiabatic double ionization processes starting from the ground electronic state of norbornane, or to exceptionally strong vibronic coupling interactions between cationic states derived from ionization of the latter orbitals. It has therefore been tentatively ascribed to auto-ionization processes via electronically excited and possibly dissociating states. To investigate this experimentally, it would be worth considering EMS measurements on norbornane with varying impact energies. Furthermore, measurements of electron energy loss spectra at large deflection angles would be welcome, as well as mass spectra at varying electron kinetic energies.

In order to confirm this fairly daring scenario of auto-ionization of a second electron via an intramolecular Coulomb decay mechanism and dissociation of a doubly ionized cage, we have investigated in Chapter 3.3 the potential energy surface of norbornane in its dicationic singlet ground state using DFT along with the non-local hybrid and gradient corrected Becke three-parameter Lee-Yang-Parr functional (B3LYP) and the cc-pVDZ basis set. For the sake of more quantitative insights in the chemical reactions induced by double ionization of norbornane, this study has been supplemented by a calculation of thermodynamical state functions coupled to a focal point analysis of energy differences obtained using correlation treatments and basis sets of improving quality, enabling an extrapolation of these energy differences at the CCSD(T) level in the limit of an asymptotically complete (cc-pV∞Z) basis set. Our results demonstrate the likelyhood of an ultra-fast intramolecular rearrangement of the saturated hydrocarbon cage after a sudden removal of two electrons into a kinetically metastable five-membered cyclic $C_5H_8^+$-CH^+-CH_3 intermediate, prior to a Coulomb explosion into $C_5H_7^+$=CH_2 and CH_3^+ fragments, which may explain the huge rise of (e,2e) intensities at electron binding energies around the double ionization threshold. The first step is straightforward and strongly exothermic (ΔH_{298} = - 114.0 kcal mol^{-1}). The second step is also exothermic (ΔH_{298} = - 10.2 kcal mol^{-1}) but requires an activation enthalpy ($\Delta H^{\dagger}_{298}$) of 39.7 kcal/mol. The various factors governing the structure of this intermediate, such as electrostatic interactions, inductive effects, cyclic strains, and methylenic hyperconjugation interactions, have been discussed in details. Further studies employing nuclear dynamics or wave packet dynamics around conical intersections might be necessary, in order to quantitatively evaluate the influence of intra-molecular rearrangement and charge dissociation processes on the innermost valence ionization spectrum of norbornane, and the corresponding electron distributions in the configuration and momentum spaces.

In Chapter 3.4, results of a study of the valence electronic structure of norbornene (C_7H_{10}), up to binding energies of 30 eV have been reported in a discussion based on experimental EMS and theoretical 1p-GF and DFT data. In analogy with the study on norbornane, the Becke-Perdew functional and a polarized valence basis set of triple-ς quality provides the best representation of the electron momentum distributions for all 19 valence orbitals of norbornene. This experimentally validated model has then been used with reasonable success to extract other molecular properties of the latter cage compound (geometry, infrared spectrum). It appeared that, due to the improved energy resolution, EMS is now at a stage to very finely image the effective topology of molecular orbitals at varying distances from the molecular center, and the way the individual atomic components interact with each other, often in excellent agreement with theory. 1p-GF calculations employing the ADC(3) scheme indicate that, for norbornene, the orbital picture of ionization breaks down at binding energies larger than about 22 eV. Despite this complication, they enable insights within 0.2 eV accuracy into the available ultraviolet emission and newly presented (e,2e) ionization spectra. Finally, limitations inherent to calculations of momentum distributions based on Kohn-Sham orbitals and employing the vertical depiction of ionization processes were emphasized, in a formal discussion of EMS cross sections employing Dyson orbitals.

At last, the valence one-electron and shake-up ionization spectra of stella-2,6-diene, stella-2,6-dione, bicyclo-[2.2.2]-octane-2,5-dione, and bicyclo-[2.2.1]-heptane-2,5-dione have been exhaustively studied in Chapter 3.5, up to the double ionization threshold and beyond, by means of 1p-GF theory. This study was based on calculations employing the Outer-Valence Green's Function (OVGF) and the ADC(3) schemes, along with a variety of basis sets. A comparison is made with available ultraviolet (He I) photoelectron and (e, 2e) electron impact ionization spectra, with main focus on the identification of spectral fingerprints for cyclic strains and through bond π-conjugation. As a byproduct, our results demonstrated that it is impossible to reliably assign complex (e, 2e) ionization spectra by resorting only to Hartree–Fock (HF) or Kohn–Sham (KS) orbital energies and to the related electron momentum distributions. Limitations of the fitting procedure used in the EMS community to extract experimental ionization potentials from (e,2e) electron binding energy spectra were exposed in details. This fitting is typically based on a set of Gaussians whose number and position are taken from available UPS spectra. With regards to the errors to which such a procedure may lead, we strongly advocate to use ADC(3) data instead.

With part 4, we shift from rigid systems to highly flexible structures, namely conformationally versatile molecules. The scope of Chapter 4.1 was to reconcile EMS with elementary thermodynamics, and refute surprising conclusions drawn by Saha *et al.* in [3] regarding fingerprints of the *gauche* conformational isomer of 1,3-butadiene in electron momentum distributions that were experimentally inferred from gas phase (e,2e) measurements on this compound [4]. This refutation demonstrates how easy it is to misunderstand conformational fingerprints due to erroneous band assignments in electron momentum spectra. Our analysis and reassignment was based on thorough calculations of one-electron and shake-up ionization spectra employing 1p-GF theory along with the benchmark ADC(3) scheme. Accurate spherically averaged electron momentum distributions have been correspondingly computed from the related Dyson orbitals. The ionization spectra and Dyson orbital momentum distributions that were computed for the *trans*-conformer of 1,3-butadiene alone are amply sufficient to quantitatively unravel the shape of all available experimental (e,2e) electron momentum distributions. A comparison of theoretical ADC(3) spectra for the *s-trans* and *gauche* energy minima with inner- and outer-valence high-resolution photoelectron measurements employing a synchrotron radiation beam [5] demonstrates that the *gauche* structure is incompatible with ionization experiments in high-vacuum conditions and at standard temperatures. On the other hand, it turned out that outer-valence Green's function calculations on the *s-trans* energy minimum form and approaching basis set completeness provide highly quantitative insights, within ~0.2 eV accuracy, into the available experimental one-electron ionization energies. At last, analysis of the angular dependence of relative (e,2e) ionization intensities has nicely confirmed the presence of one rather intense $\pi^{-2}\,\pi^{*+1}$ satellite at ~13.1 eV in the ionization spectrum of the *s-trans* conformer.

In line with this first work on butadiene, the main purpose of Chapter 4.2 was to predict from benchmark many-body quantum mechanical calculations the results of experimental studies of the valence electronic structure of dimethoxymethane employing EMS, and establish once and for all the guidelines that should systematically be followed in order to reliably interpret the results of such experiments on conformationally versatile molecules. In a first step, accurate calculations of the energy differences between stationary points on the potential energy surface of this molecule have been performed using Hartree-Fock [HF] theory and post-HF treatments of improving quality [MP2, MP3, CCSD, CCSD(T)], along with basis sets of increasing size. In this study, we focused on the four conformers of this molecule, namely the *trans-trans* (TT), *trans-gauche* (TG), *gauche-gauche* (G^+G^+) and *gauche-gauche* (G^+G^-) structures. A focal point analysis supplemented by suited extrapolations to the limit of asymptotically complete basis sets has been carried out to determine how the conformational energy differences at 0K approach the full CI limit. In a second step, statistical thermodynamics accounting for hindered rotations was used to calculate Gibb's free energy corrections to the above energy differences, and evaluate the abundance of each conformer in the gas phase. It was found that, at room temperature, the G^+G^+ species accounts for 96% of the conformational mixture characterizing dimethoxymethane. In a third step, the valence one-electron and shake-up ionization spectrum of dimethoxymethane has been analyzed according to calculations upon the G^+G^+ conformer alone by means of 1p-GF theory along with the benchmark ADC(3) scheme. A complete breakdown of the orbital picture of ionization was noted at electron binding energies above 22 eV. A comparison with available (e,2e) ionization spectra has enabled us to identify specific fingerprints of through-space orbital interactions associated with the anomeric effect. At last, based on our 1p-GF/ADC(3) assignment of spectral bands, accurate and spherically averaged (e,2e) electron momentum distributions at an electron impact energy of 1200 eV have been computed from the related Dyson orbitals. Very significant discrepancies were observed with momentum distributions obtained for several outer-valence levels using standard Kohn-Sham orbitals.

A comprehensive study, throughout the valence region, of the electronic structure and electron momentum density distributions of the four conformational isomers of *n*-pentane, has been presented in Chapter 4.3. Theoretical (e, 2e) valence ionization spectra at high electron impact energies (1200 eV + electron binding energy) and at azimuthal angles ranging from 0° to 10° in a non-coplanar symmetric kinematical set up were generated according to the results of large scale 1p-GF function calculations of Dyson orbitals and related electron binding energies, using the ADC(3) scheme. The results of a focal point analysis of relative conformer energies [6] and improved thermodynamical calculations accounting for hindered rotations were also employed in order to quantitatively evaluate the abundance of each conformer in the gas phase at room temperature and reliably predict the outcome of experiments on *n*-pentane employing high resolution EMS. Comparison with available photoelectron measurements confirmed the suggestion that, due to entropy effects, the *trans-gauche* (*tg*) conformer strongly dominates the conformational mixture characterizing *n*-pentane at room temperature. Our simulations have demonstrated therefore that experimental measurements of (e, 2e) valence ionization spectra and electron momentum distributions would very consistently and straightforwardly image the topological changes and energy variations that molecular orbitals undergo due to torsion of the carbon backbone. The strongest fingerprints for the most stable conformer (*tt*) were found for the electron momentum distributions associated to ionization channels at the top of the inner-valence region, which sensitively image the development of methylenic hyperconjugation in all-staggered *n*-alkane chains.

In straightforward extension of the latter works on electron momentum spectra, we reported in Chapter 4.4 on the results of an exhaustive study of the interplay between the valence electronic structure, the topology and reactivity of orbitals, and the molecular structure of biphenyl by means of Penning ionization electron spectroscopy in the gas phase upon collision with metastable He*(2^3S) atoms. These measurements have been compared with 1p-GF calculations of one-electron and shake-up valence ionization spectra employing the ADC(3) scheme. Penning ionization intensities were also analyzed by means of the exterior electron-density model and comparison with photoelectron spectra: in contrast with the lines originating from σ-orbitals, ionization lines belonging to the π-band system have large Penning ionization cross sections due to their greater extent outside the molecular van der Waals surface. The involved chemi-ionization processes were further experimentally investigated using the Collision Energy Dependence of Partial Ionization Cross sections (CEDPICS). The cross sections of π-ionization bands exhibit a markedly negative collision-energy dependence and indicate that the interaction potential that prevails between the molecule and the He*(2^3S) atom is strongly attractive in the π-orbital region. On the other hand, the partial ionization cross sections pertaining to σ-ionization channels are characterized by more limited collision energy dependencies, as a consequence of rather repulsive interactions within the σ-orbital region. A comparison of ADC(3) simulations with the Penning ionization electron spectra and ultra-violet photoelectron spectra measured by Kubota *et al.* [7] on thin films of biphenyl deposited at 170 and 109 K on copper demonstrated further that biphenyl molecules lying at the surface of polycrystalline layers adopt predominantly a planar configuration, whereas within an amorphous sample most molecules have twisted structures similar to those prevailing in the gas phase. At last, in comparison with the UPS measurements of biphenyl in the gas phase, complications due to vibronic coupling transitions are expected at ionization energies around 12 and 14 eV in line with near energy degeneracies between a number of states. These bands would be worth further specific studies using nuclear multistate dynamics [8]. It would be worth improving on the use of rigid van der Waals surfaces for the overlap between the 1*s* orbitals of the impinging He* atoms and the target molecular orbitals within a model employing thermostatistical mechanics or classical dynamical calculations based on quantum-chemical potential-energy surfaces for computing and integrating the results of different collision pathways rather than using rigid van der Waals boundary surfaces. Dyson orbitals would be here also very much advocated. As a result of interactions with our research group, very recent studies of the CEDPICS characteristics of a simple test molecule like N_2 demonstrate indeed again the superiority over Kohn-Sham and HF orbitals in modeling ionization-based experiments [9].

In support to the points discussed so far, EMS studies on small test systems were at last reported in part 5 of the present thesis. In Chapter 5.1, we analyzed the results of an experimental study of the valence electronic structure of difluoromethane employing high-resolution EMS with various impact energies. Accurate spherically averaged electron momentum distributions were derived from Dyson orbitals obtained using the ADC(3) scheme. The corresponding eigen-energies were found to accurately reproduce the (e, 2e) ionization spectrum. Shortcomings of empirical analyses of (e, 2e) experiments based on Kohn–Sham orbitals and eigen-energies have been comparatively discussed. A failure of the target Hartree-Fock approximation was noted for the momentum distribution pertaining to the $1b_1 + 3b_2 + 5a_1$ levels. Since all employed models fail to reproduce the “turn up” of the experimental MD at low electron momenta for the HOMO of this compound, it has been concluded that distorted wave effects must play an important role in describing the experimental momentum distribution of this π^* like orbital. For such situations, it is highly desirable to improve on the theoretical description of (e,2e) reaction mechanisms by developing a distorted wave scheme for molecular applications.

In Chapter 5.2, the development of a third-generation electron momentum spectrometer with very significantly improved energy and momentum resolutions at Tsinghua University (ΔE=0.45-0.68 eV, $\Delta\theta$=±0.53° and $\Delta\phi$=±0.84°) has enabled a reinvestigation of the valence orbital electron momentum distributions of water with improved statistical accuracy. The measurements have been conducted at impact energies of 1200 eV and 2400 eV in order to check the validity of the plane wave impulse approximation. The obtained ionization spectra and electron momentum distributions have been compared with the results of computations carried out with Hartree-Fock theory, DFT along with the standard B3LYP functional, 1p-GF theory along with the ADC(3) scheme, Symmetry Adapted Cluster Configuration Interaction (SAC-CI) theory [10], and a variety of Multi-Reference (MR-SDCI, MR-RSPT2, MR-RSPT3) theories (see e.g. [11]). The influence of the basis set on the computed momentum distributions has been investigated further, using a variety of basis sets ranging from the 6-31G basis to the almost complete d-aug-cc-pV6Z. With this work, we have been willing to emphasize limitations of the 1p-GF/ADC(3) approach in quantitative studies of singly-excited shake-up states, as these are calculated at first-order in correlation only, which implies the neglect of double, triple and higher-order electronic excitations. A main issue in this discussion of improved EMS experiments on water pertained to a shake-up band of very weak intensity at 27.1 eV, of which the related momentum distribution was analyzed for the first time. The experimental evidences and the most thorough theoretical calculations demonstrate that this band borrows its ionization intensity to the $2a_1$ orbital and is strongly dependent on the inclusion of double electronic excitations in the shake-up excitation operator manifold. An extension of the ADC-scheme *through* fourth order is required for quantitatively unravelling this shake-up band within the framework of one-particle Green's function theory.

Clearly, science is a never ending construction…

References

[1] (a) McWeeny, R.; Pickup, B. T. *Rep. Prog. Phys.* 1980, 43, 1065. (b) Öhrn, Y.; Born, G. *Adv. Quantum Chem.* 1981, 13, 1. (c) Pickup, B. T. *Chem. Phys.* 1977, 19, 193. (d) Deleuze, M.; Pickup, B. T.; Delhalle, J. *Mol. Phys.* 1994, 83, 655.

[2] See: Golod, A.; Deleuze, M. S.; Cederbaum, L. S. *J. Chem. Phys.* 1999, 110, 6014; and references therein.

[3] Saha, S.; Wang, F.; Falzon, C. T.; Brunger, M. J. *J. Chem. Phys.* 2005, 123, 124315.

[4] Brunger, M. J.; Winkler, D. A.; Michalewicz, M. T.; Weigold, E. *J. Chem. Phys.* 1998, 108, 1859.

[5] Holland, D. M. P.; MacDonald, M. A.; Hayes, M. A.; Baltzer, P.; Wannberg, B.; Lundqvist, M.; Karlsson, L.; von Niessen, W. *J. Phys. B* 1996, 29, 3091.

[6] Salam, A.; Deleuze, M. S. *J. Chem. Phys.* 2002, 116, 1296.

[7] Kubota, H.; Munakata, T.; Hirooka, T.; Kuchitsu, K.; Harada, Y. *Chem. Phys. Lett.* 1980, 74, 409.

[8] (a) Köppel, H.; Cederbaum, L. S.; Domcke, W. *J. Chem. Phys.* 1988, 89, 2023. (b) Döscher, M.; Köppel, H.; Szalay, P. G. *J. Chem. Phys.* 2002, 117, 2645. (c) Köppel, H.; Döscher, M.; Bâldea, I.; Meyer, H.-D.; Szalay, P. G. *J. Chem. Phys.* 2002, 117, 2657.

[9] (a) Yamazaki, M.; Horio, T.; Kishimoto, N.; Ohno, K. *Phys. Rev. A* 2007, 75, 03272. (b) Kishimoto, N.; Ohno, K. *Int. Rev. Phys. Chem.* 2007, 26, 93.

[10] See: Nakatsuji, H. *Chem. Phys. Lett.* 1991, 177, 331; and references therein.

[11] Szabo, A.; Ostlund, N. S. *Modern Quantum Chemistry. Introduction to Advanced Electronic Structure Theory*; Dover: New York, 1996.

Part 7: Algemene conclusies en vooruitzichten

Het hoofddoel van het huidige werk was het nagaan van de mogelijkheden van geavanceerde “orbitaal visualiserende” methoden zoals Elektronen Impuls Spectroscopie (Eng. *Electron Momentum Spectroscopy*, EMS) en Penning Ionisatie Electronen Spectroscopie (PIES) bij het peilen naar de vorm, uitgebreidheid en stereochemie van moleculaire orbitalen in uitdagende situaties zoals bij cyclische, aan spanning onderhevige moleculen (deel 3) die ernstige structurele vervormingen na ionisatie ondergaan, of flexibele moleculen (deel 4), waaronder het geval van geconjugeerde systemen onderworpen aan elektronische excitatieprocessen die gemakkelijk kunnen leiden tot het wegvallen van het één-elektronen beeld voor ionisatie.

Ondanks deze moeilijkheden, bevestigt ons werk de diepliggende relaties van ionisatie met kanonische, i.e. gedelokaliseerde, orbitalen, en de mogelijkheid hierbij van ionisatie spectroscopische technieken om naar de moleculaire structuur in zijn geheel te peilen (bindingskarakteristieken, cyclische spanning, conformatie). Talloze spectrale vingerafdrukken van de kleinste details van de moleculaire architectuur kunnen inderdaad geïdentificeerd worden binnen de valentie ionisatiebanden en gerelateerde eigenschappen zoals sferisch gemiddelde elektronen impuls verdelingen (Eng. *Momentum Distribution*, MD) in EMS en de botsingsenergie afhankelijkheid van gedeeltelijke ionisatie werkzame doorsneden in EMS. Zoals in ruim voldoende voorbeelden aangegeven, is de interpretatie van deze experimenten vatbaar voor vele complicaties zoals de meestal zeer sterke invloed van de molecularie conformatie op ionisatie energieën, elektronische correlatie- en relaxatie-effecten, een dispersie van de ionisatie-intensiteit over secundaire structuren zoals shake-up lijnen en shake-off banden, vibronische koppeling interacties en ultra-snelle nuclearie dynamische effecten, of een instorten van de vlakke golf puls benadering. Daarom vereist de interpreatie van EMS of PIES experimenten, zelfs met de assistentie van meer algemene foto-elektron spectroscopische metingen (Eng. *Photo-Electron Spectroscopy*, PES), extensief theoretisch werk, als deze enige waarde kan hebben. Om dit doel te bereiken hebben we ons gewend tot referentie theoretische benaderingen, beschreven in deel 2 om veel-deeltjes effecten (configuratie interactie, veel-deeltjes storingstheorie, coupled cluster theorie, één-deeltje Greense functie theorie samen met het Algebraïsche Diagrammatische Constructie schema van de derde orde [ADC(3)]) te behandelen en om statistische thermodynamische partitiefuncties en de gerelateerde toestandsfuncties voorbij de Rigide Rotor-Harmonische Oscillator (RRHO) benadering te berekenen.

Een link tussen één-deeltje Greense functie (1p-GF) theorie en EMS wordt gevormd door de wisselwerking van Dyson orbitalen [1], gedefinieerd als gedeeltelijke overlappingen tussen de initiële neutrale grondtoestand en finale geïoniseerde toestanden. Met betrekking tot elektronen correlatie en relaxatie, laten deze orbitalen een formeel exacte beschrijving toe van elektronen impuls verdelingen, opgebouwd uit de hoek afhankelijkheid van (e,2e) ionisatie werkzame doorsneden in EMS experimenten, binnen het kader van de tweevoudige botsingsbenadering (Eng. *binary encounter approximation*) voor elektronen verstrooiing, de Born aanname voor een plotse (vertikale) ionisatie gebeurtenis, en de vlakke golf puls benadering om inkomende en uitgaande elektronen te beschrijven.

Onze eerste analyses van EMS experimenten werden uitgevoerd op kooimoleculen (norbornaan, norborneen) volgens de heersende zienswijzen in het veld, dus onder de stilzwijgende en empirische aanname dat, ondanks het feit dat zij erg magere schattingen leveren voor één-elektronen ionisatie energieën en falen bij het beschrijven van shake-up processen, Kohn-Sham orbitalen sterk gelijken op Dyson orbitalen. Met deze aanname was het dus op het eerste zicht enorm verleidelijk om electronen impuls spectroscopie te gebruiken om de “beste” elektronen golffunctie te identificeren en ervan gebruik te maken om verschillende moleculaire eigenschappen van de grondtoestand (molecularie structuren, dipoolmomenten, infra-rood spectra, NMR shifts,...) te berekenen. Men zou echter niet mogen vergeten dat de berekeningen van zulke eigenschappen bij gebruik van standaard procedures ook onderworpen zijn aan benaderingen die kunnen leiden tot een enigszins tè goede overeenkomst met het experiment. Een voorbeeld, voorheen behandeld in Hoofdstuk 3.4 over noborneen, is de verwaarlozing van anharmonische effecten in DichtheidsFunctionaal Theorie (DFT) berekeningen van infra-rood frequenties, die tegenwoordig meestal impliciet in rekening worden gebracht door empirische schalingsfactoren. Eén van onze laatste werken toonde aan dat, omwille van de verwaarlozing van veel-elektronen effecten (relaxatie, configuratie interacties) in de eindtoestand, Kohn-Sham orbitalen verkregen door standaard functionalen sterk kunnen afwijken van Dyson orbitalen, in het bijzonder bij het aanpakken van moleculen met lage symmetrie.

De werken die gedurende de vier jaren voor het behalen van de graad van doctor in de wetenschappen uitgevoerd werden, reflecteren daarom een nogal belangrijke evolutie in onze zienswijzen op de theorie achter “orbitaal visualisatie”. Spectroscopische technieken, zoals EMS of PIES, zijn ontegensprekelijk geschikt voor het peilen naar de vorm, spreiding en stereochemie van moleculaire orbitalen en hun interactie met de moleculaire architectuur, onder de vele voorwaarden en limieten die inherent zijn aan de interpretatie van bijzonder uitdagende ionisatie-experimenten. De EMS studies beschreven in de voorbije hoofdstukken werden uitgevoerd in samenwerking met de experimentele onderzoeksgroepen van Prof. M. J. Brunger aan de Flinders University te Adelaide (Australië) voor de kooimoleculen en van Prof. J. K. Deng aan de Tsinghua Unversity te Beijing (P. R. China) voor de flexibele moleculen. Voor norbornaan konden we ook bouwen op nieuwe foto-elektron metingen van Prof. J. H. D. Eland aan de Oxford University (Verenigd Koninkrijk) en stimulerende discussies met Prof. L. S. Cederbaum van de Universität Heidelberg (Duitsland). De PIES studie op bifenyl was het resultaat van een samenwerking met de groep van Prof. K. Ohno en Dr. N. Kishimoto aan de Tohoku University in Sendai (Japan). De belangrijkste resultaten van dit werk kunnen als volgt samengevat worden:

In Hoofdstuk 3.1 hebben we de resultaten naar voren gebracht van een uitvoerige studie over de valentie elektronenstructuur van norbornaan (C_7H_{12}) tot op bindingsenergieën van 29 eV. Experimentele EMS en theoretische 1p-GF en DFT benaderingen werden gezamenlijk binnen dit onderzoek gebruikt. Een strenge vergelijking tussen de elektronen impuls spectroscopie en theoretische orbitaal impuls verdelingen vond dat, onder alle geteste modellen, de combinatie van de Becke-Perdew functionaal en een gepolariseerde valentie basisset van drievoudige ς kwaliteit de beste voorstelling geven van de elektronen impulsverdelingen voor alle 20 valentie orbitalen van norbornaan. Dit experimenteel naar waarde geschatte kwantum chemisch model werd dan gebruikt om bepaalde chemisch belangrijke eigenschappen van norbornaan na te gaan. Wanneer deze berekende eigenschappen vergeleken worden met corresponderende resultaten van andere onafhankelijke metingen, wordt doorgaans een goede overeenkomst gevonden. De 1p-GF berekeningen op ADC(3) niveau duiden aan dat het orbitaal beeld voor ionisatie wegvalt bij bindingsenergieën hoger dan 22,5 eV. Ondanks deze complicatie, laten zij toch inzichten toe binnen 0,2 eV nauwkeurigheid in de beschikbare ultra-violet foto-emissie en nieuwe (e,2e) ionisatiespectra, behalve voor de band geassocieerd met de $1a^{-1}_2$ één-gat toestand, die waarschijnlijk onderworpen is aan nogal belangrijke geometrische relaxatie en vibratrionele effecten, en een band bij ~25 eV gekarakteriseerd door een impuls verdeling met een “*s*-type” symmetrie, welke de Greense functie berekeningen niet kunnen reproduceren. Wij noteren de nabijheid van de vertikale dubbele ionisatiedrempel op ~26 eV.

In Hoofdstuk 3.2 hebben we 1p-GF berekeningen gepresenteerd van het ionisatiespectrum van norbornaan op ADC(3) niveau gebruik makend van basissets van variërende kwaliteit, samen met accurate evaluaties op CCSD(T) niveau van de vertikale (26,5 eV) en adiabatische (22,1 eV) dubbele ionisatiedrempels onder C_{2v} symmetrie. De behaalde resultaten werden vergeleken met nieuw gemeten Ultraviolet foto-emissie spectra (Eng. *Ultraviolet Photo-emission Spectra*, UPS), tot op bindingsenergieën van 40 eV. De theoretische voorspellingen zijn geheel consistent met het experiment en duiden aan dat, in een vertikaal beeld voor ionisatie, shake-up toestanden bij bindingsenergieën hoger dan ~26,5 eV trachten te vervallen via emissie van een tweede elektron in het continuüm. Een band van *s*-type symmetrie die voorheen gezien werd bij ~25 eV in de elektronen impact ionisatiespectra van norbornaan, bleek totaal afwezig te zijn in de UPS metingen en de theoretische ADC(3) spectra. Met betrekking tot de lage fractie van gevonden $1a_1$ ionisatie intensiteit, kan het waard zijn het shake-up ionisatie spectrum te herberekenen gebruik makend van meer gesofisticeerde diagonalisatie methoden, zoals de “Block-” of “Band-Lanczos procedures” [2]. Verdere 1p-GF berekeningen met zeer diffuse functies, Coulomb en verstoorde vlakke golven in de basisset kunnen mogelijks ook bruikbaar zijn, zowel als twee-deeltje Greense functie berekeningen van dubbele ionisatietoestanden, om dat deel van het spectrum te onderzoeken. Niettemin, met betrekking tot de zeer gebruikelijke basisset afhankelijkheid van de $1a_1$ shake-up band bij 28 eV, en van de bijzonder sterke (e,2e) ionisatie-intensiteit bij 25 eV, zijn we overtuigd dat deze band niet te maken heeft met standaard shake-up of shake-off processen.

Met betrekking tot onze behaalde resultaten en tot de tijdsschalen die elektron-elektron interacties in EMS (10^{-17} s) karakteriseren na een vergelijking met deze (10^{-13} s) van foton-elektron interacties in UPS, en bij het beschouwen van de *p*-type symmetrie van de elektronen impuls verdeling voor de naburige $1b_1$ en $1b_2$ orbitalen, kan band 12 zeker niet eenvoudig te wijten zijn aan adiabatische dubbele ionisatieprocessen startend van de elektronen grondtoestand van norbornaan, of aan uitzonderlijk sterke vibronische koppelingsinteracties tussen kationische toestanden afgeleid van ionisatie van de laatste orbitalen. Band 12 werd daarom eerst tentatief toegeschreven aan auto-ionisatie processen via elektronisch geëxciteerde en mogelijkerwijze dissociërende toestanden. Om dit experimenteel te onderzoeken, is het waard EMS metingen op norbornaan te beschouwen met variërende impact energieën. Vervolgens zouden metingen van elektronen energie-verlies spectra (Eng. *Electron Energy Loss Spectra*, EELS) op grote afbuigingshoeken welkom zijn, zowel als massaspectra met variërende kinetische elektronen energieën.

Om dit nogal gedurfde scenario te bevestigen van auto-ionisatie van een tweede elektron via een intramoleculair Coulomb verval mechanisme en dissociatie van een dubbel geïoniseerde kooi, hebben we in Hoofdstuk 3.3 het potentiaal energie oppervlak van norbornaan onderzocht in zijn dikationische singlet grondtoestand gebruik makend van DFT samen met de niet-lokale hybride en gradiënt gecorrigeerde Becke drie-parameter Lee-Yang-Parr functionaal (B3LYP) en de cc-pVDZ basisset. Omwille van meer kwantitatieve inzichten in de chemische reacties geïnduceerd door dubbele ionisatie van norbornaan, werd deze studie aangevuld met een berekening van thermodynamische toestandsfuncties gekoppeld aan een focale puntsanalyse van energieverschillen bepaald door gebruik te maken van correlatie behandelingen en basissets van toenemende kwaliteit. Dit laat een extrapolatie toe van deze energie-verschillen op CCSD(T) niveau in de limiet van een asymptotisch volledige (cc-pV∞Z) basis set. Onze resultaten tonen de waarschijnlijkheid aan van een ultra-snelle intramoleculaire herschikking van de verzadigde koolwaterstof kooi na een plotse verwijdering van twee elektronen in een kinetisch metastabiel vijf-ledig cyclisch $C_5H_8^+$-CH^+-CH_3 intermediar, vooraf gaand aan een Coulomb explosie in $C_5H_7^+$=CH_2 en CH_3^+ fragmenten, die de kolossale stijging van de (e,2e) intensiteiten op elektronen bindingsenergieën rond de dubbele ionisatiedrempel kan uitleggen. De eerste stap is rechtdoor en sterk exotherm (ΔH_{298} = - 114,0 kcal mol^{-1}). De tweede stap is ook exotherm

(ΔH_{298} = - 10,2 kcal mol^{-1}) maar vereist een activatie enthalpie ($\Delta H^{\ddagger}_{298}$) van 39,7 kcal mol^{-1}. De verschillende factoren die de structuur van dit intermediair drijven, zoals elektrostatische interacties, inductieve effecten, cyclische spanningen en methyleen hyperconjugatie-interacties, werden in detail bediscussieerd. Verdere studies gebruik makend van nucleaire dynamica of golfpakket dynamica rond konische intersecties kunnen nodig zijn, om kwantitatief de invloed te evalueren van intra-moleculaire herschikking en ladingsdissociatie processen in het binnen valentie ionisatie spectrum van norbornaan, en de corresponderende elektronen verdelingen in de configuratie- en impulsruimten.

In Hoofstuk 3.4 werden de resultaten van een studie van de valentie elektronenstructuur van norborneen (C_7H_{10}) gerapporteerd tot op bindingsenergieën van 30 eV in een discussie gebaseerd op experimentele EMS en theoretische 1p-GF en DFT gegevens. In analogie met de studie op norbornaan geeft de Becke-Perdew functionaal en een gepolariseerde valentie basisset van drievoudige ς kwaliteit de beste voorstelling van de elektronen impulsverdelingen voor alle 19 valentie orbitalen van norborneen. Dit experimenteel gevalideerde model werd dan met redelijk succes gebruikt om andere eigenschappen te bepalen van het laatst genoemd kooimolecule (geometrie, intrarood spectrum). Het bleek dat, omwille van de verhoogde energieresolutie, EMS nu op een niveau staat om zeer nauwkeurig de effectieve topologie van moleculaire orbitalen af te beelden op verschillende afstanden van het moleculaire centrum, alsook de manier waarop de individuele atomaire componenten met elkaar interageren, wat vaak gebeurt bij een uitmuntende overeenkomst met theorie. 1p-GF berekeningen gebruik makend van het ADC(3) schema duiden aan dat, voor norborneen, het orbitaal beeld van ionisatie weg valt bij bindingsenergieën hoger dan ongeveer 22 eV. Ondanks deze moeilijkheid laten ze inzichten toe tot op 0.2 eV nauwkeurigheid in de beschikbare ultraviolet emissie en nieuw gepresenteerde (e,2e) ionisatiespectra. In een formele discussie over EMS werkzame doorsneden gebruik makend van Dyson orbitalen werden uiteindelijk beperkingen benadrukt die inherent zijn aan berekeningen van impulsverdelingen gebaseerd op Kohn-Sham orbitalen en gebruik makend van het vertikale beeld van ionisatieprocessen.

Ten slotte werden de valentie één-elektron en shake-up ionisatie spectra van stella-2,6-dieen, stella-2,6-dioon, bicyclo-[2.2.2]-octaan-2,5-dioon, and bicyclo-[2.2.1]-heptaan-2,5-dioon uitvoerig bestudeerd in Hoofdstuk 3.5 met behulp van 1p-GF theorie tot op de dubbele ionisatiedrempel en erboven. Deze studie was gebaseerd op berekeningen gebruik makend van de buiten-valentie Greense functie (Eng. *Outer-Valence Green's Function*, OVGF) en ADC(3) schema's, samen met een veelheid aan basissets. Een vergelijking werd gemaakt met beschikbare ultraviolet (He I) foto-elektron en (e,2e) elektronen impact ionisatiespectra, met als hoofddoel de identificatie van spectrale vingerafdrukken voor cyclische spanningen en "through bond" π-conjugatie. Als een bijproduct illustreren onze resultaten dat het onmogelijk is betrouwbaar ingewikkelde (e,2e) ionisatiespectra te assigneren door enkel maar gebruik te maken van Hartree-Fock (HF) of Kohn-Sham (KS) orbitaal energieën en van de gerelateerde elektronen impulsverdelingen. Beperkingen van de fittingsprocedure, die in de EMS gemeenschap gebruikt worden om experimentele ionisatiepotentialen te halen uit (e,2e) elektronen bindings energiespectra werden in het detail bloot gelegd. Deze fitting is typisch gebaseerd op een set van Gaussische functies wiens aantal en positie genomen worden uit de beschikbare UPS spectra. Met betrekking tot de fouten waartoe zulke procedure kan leiden, bevelen we sterk het gebruik aan van ADC(3) gegevens.

Met deel 4, schakelen we van rigide systemen over naar sterk flexibele moleculen. Het doel van Hoofdstuk 4.1 was om EMS opnieuw te verzoenen met elementaire thermodynamica en verrassende resultaten van Saha *et al.* [3] te weerleggen wat betreft vingerafdrukken van het *gauche* conformationele isomeer van 1,3-butadieen in elektronen impulsverdelingen die experimenteel bepaald werden uit gasfase (e,2e) metingen op deze verbinding [4]. Deze weerlegging laat op zien hoe gemakkelijk het is conformationele vingerafdrukken omwille van foutieve band toekenningen verkeerd te begrijpen in elektronen impulsverdelingen. Onze analyse en hertoekenning was gebaseerd op degelijke berekeningen van één-elektron en shake-up ionisatiespectra gebruik makend van 1p-GF theorie samen met het referentie ADC(3) schema. Accurate sferisch gemiddelde elektronen impulsverdelingen werden overeenkomstig berekend vanuit de gerelateerde Dyson orbitalen. De ionisatiespectra en Dyson orbitaal impuls verdelingen die berekend werden voor het *trans*-conformeer van 1,3-butadieen zijn alleen zeker voldoende om kwantitatief de vorm van alle aanwezige experimentele (e,2e) elektronen impulsverdelingen te ontrafelen. Een vergelijking van theoretische ADC(3) spectra voor de *s-trans* en *gauche* energie-minima met binnen en buiten valentie hoge resolutie foto-elektron metingen gebruik makend van een synchrotron stralings bundel [5] toont aan dat de *gauche* structuur niet compatibel is met ionisatie experimenten in hoog-vacuüm condities en bij standaard temperaturen. Aan de andere kant werd het duidelijk dat buiten-valentie Greense functie berekeningen op de *s-trans* energieminimum vorm in de basisset limiet hoog kwantitatieve inzichten geven, tot op ~0,2 eV nauwkeurigheid, in de beschikbare experimentele één-elektron ionisatie-energieën. Ten slotte bevestigde de analyse van de hoek afhankelijkheid van relatieve (e,2e) ionisatie-intensiteiten de aanwezigheid van een tamelijk intense $\pi^{-2}\,\pi^{*+1}$ satelliet op 13,1 eV in het ionisatiespectrum van het *s-trans* conformeer.

In overeenstemming met dit eerste werk op butadieen werd het hoofddoel van Hoofdstuk 4.2 gevormd door het voorspellen van resultaten van experimentele studies van de valentie elektronen structuur van dimethoxymethaan gebruik makend van EMS op basis van referentie veel-deeltjes kwantum mechanische berekeningen, waarbij voor eens en altijd de richtlijnen vastgelegd werden die systematisch dienen gevolgd te worden om betrouwbaar de resultaten van zulke experimenten op flexibele moleculen te interpreteren. In een eerste stap werden acurate berekeningen van de energieverschillen tussen stationaire punten op het potentiaal energie oppervlak van dit molecule uitgevoerd gebruik makend van Hartree-Fock [HF] theorie and post-HF behandelingen van stijgende kwaliteit [MP2, MP3, CCSD, CCSD(T)], samen met basissets met stijgende grootte. In deze studie concentreerden we ons op de vier conformeren van deze molecule, namelijk de *trans-trans* (TT), *trans-gauche* (TG), *gauche-gauche* (G^+G^+) en *gauche-gauche* (G^+G^-) structuren. Een focale puntsanalyse uitgebreid met geschikte extrapolaties naar de limiet van asymptotisch volledige basissets werd uitgevoerd om te bepalen hoe de conformationele energieverschillen bij 0 K de *full CI* limiet benaderen. In een tweede stap werd statistische thermodynamica met inachtname van gehinderde rotaties gebruikt om Gibbs' vrije energie correcties te berekenen voor de hoger genoemde energieverschillen en het evalueren van het voorkomen van ieder conformeer in de gasfase. Er werd gevonden dat, bij kamertemperatuur, de G^+G^+ species voor 96% deelneemt aan het conformationele mengsel dat dimethoxymethaan karakteriseert. In een derde stap werd het valentie één-elektron en shake-up ionisatiespectrum van dimethoxymethaan geanalyseerd voor uitsluitend het G^+G^+ conformeer door middel van 1p-GF theorie samen met het referentie ADC(3) schema. Een volledig wegvallen van het orbitaal beeld van ionisatie werd genoteerd bij elektronen bindingsenergieën boven 22 eV. Een vergelijking met beschikbare (e,2e) ionisatiespectra heeft ons in staat gesteld specifieke vingerafdrukken te identificeren van orbitaal interacties doorheen de ruimte, geassocieerd met het anomerisch effect. Uiteindelijk, gebaseerd op onze 1p-GF/ADC(3) assignering van spectrale banden, werden accurate en sferisch gemiddelde (e,2e) elektronen impuls verdelingen berekend voor een elektronen impactenergie van 1200 eV vanuit de gerelateerde Dyson orbitalen. Grote significante discrepanties werden vastgesteld bij impulsverdelingen bepaald voor vele buiten-valentie niveaus gebruik makend van standaard Kohn-Sham orbitalen.

Een begrijpbare studie, doorheen de valentie zone, van de elektronen structuur en elektronen impuls dichtheidsverdelingen van de vier conformationele isomeren van *n*-pentaan werd gepresenteerd in Hoofdstuk 4.3. Theoretische (e,2e) valentie ionisatiespectra bij hoge elektronen impact energieën (1200 eV + elektronen bindingsenergie) en op azimuthale hoeken variërend van 0° tot 10° in een niet-coplanaire symmetrische kinematische set-up werden gegenereerd overeenkomstig met de resultaten van grootschalige 1p-GF berekeningen van Dyson orbitalen en gerelateerde elektronen bindingsenergieën, gebruik makend van het ADC(3) schema. De resultaten van een focale puntsanalyse van relatieve conformeer energieën [6] en verbeterde thermodynamische berekeningen rekening houdend met gehinderde rotaties werden ook aangewend om kwantitatief het voorkomen te evalueren van ieder conformeer in de gasfase bij kamertemperatuur en om betrouwvol de uitkomst van experimenten op *n*-pentaan te voorspellen gebruik makend van hoge resolutie EMS. Een vergelijking met beschikbare foto-elektron metingen bevestigde de suggestie dat, omwille van entropieeffecten, het *trans-gauche* (*tg*) conformeer sterk domineert binnen het conformationele mengsel dat *n*-pentaan karakteriseert bij kamertemperatuur. Onze simulaties hebben daarom aangetoond dat experimentele metingen van (e,2e) valentie ionisatiespectra en elektronen impulsverdelingen zeer degelijk en rechtstreeks de topologische veranderingen en energie variaties visualiseren die moleculaire orbitalen ondergaan onder invloed van een torsie van het koolstof skelet. De sterkste vingerafdrukken voor het meest stabiele conformeer (*tt*) werd gevonden voor de elektronen impulsverdelingen geassocieerd met ionisatiekanalen aan de top van de binnen-valentie zone, die een gevoelig beeld geeft van de ontwikkeling van methyleen hyperconjugatie in "*all-staggered*" *n*-alkaan kettingen.

In een verdere uitbreiding van de laatste werken rond elektronen impulsspectra, rapporteerden we in Hoofdstuk 4.4 de resultaten van een uitvoerige studie van de interactie tussen de valentie elektronenstructuur, de topologie en reactiviteit van orbitalen, en de moleculaire structuur van bifenyl door middel van Penning ionisatie elektronen spectroscopie in de gasfase door botsing met metastabiele $He^*(2^3S)$ atomen. Deze metingen werden vergeleken met 1p-GF berekeningen van één-elektron en shake-up valentie ionisatiespectra gebruik makend van het ADC(3) schema. Penning ionisatie intensiteiten werden ook geanalyseerd door middel van het uitwendige elektronen dichtheidsmodel (Eng. *exterior electron-density model*) en door vergelijking met foto-elektron spectra: in tegenstelling tot de lijnen die afkomstig zijn van σ-orbitalen, hebben ionisatielijnen die toehoren aan het π-band system grote Penning ionisatie werkzame doorsneden te wijten aan hun grote uitgebreidheid buiten het moleculaire van der Waals oppervlak. De betrokken chemi-ionisatieprocessen werden verder experimenteel onderzocht gebruik makend van de botsingsenergie afhankelijkheid van partiële ionisatie werkzame doorsneden (*Eng.* Collision Energy Dependence of Partial Ionization Cross sections, CEDPICS). De werkzame doorsneden van π-ionisatie banden vertonen een opmerkelijke negatieve botsingsenergie afhankelijkheid en geven aan dat de interactie potentiaal, die zich tussen de molecule en het $He^*(2^3S)$ atom handhaaft, sterk aantrekkend is in de π-orbitaal zone. Aan de andere kant worden de partiële ionisatie werkzame doorsneden, behorend bij de σ-ionisatie kanalen, gekarakteriseerd door meer gelimiteerde botsingsenergie afhankelijkheden als een consequentie van nogal afstotende interacties in het σ-orbitaal gebied. Een vergelijking van ADC(3) simulaties met de Penning ionisatie elektronen spectra en ultraviolet foto-elektron spectra gemeten door Kubota *et al.* [7] op dunne filmen van bifenyl afgezet op koper bij 170 and 109 K toonde verder aan dat bifenyl moleculen die aan het oppervlak liggen van polykristallijne lagen overwegend een planaire configuratie aannemen, terwijl binnen in een amorf monster de meeste moleculen getwiste structuren hebben, gelijkend op deze die in de gasfase voorkomen. Ten slotte, in vergelijking met de UPS metingen op bifenyl in de gasfase, worden complicaties te wijten aan vibronische koppelingstransities verwacht bij ionisatie-energieën rond 12 en 14 eV samen met nabije energetische ontaardingen tussen een aantal toestanden. Deze banden zouden verder specifieke studies waard zijn gebruik makend van nucleaire multi-toestandsdynamica [8]. Het zou waard zijn het gebruik van rigide van der Waals oppervlakken te verbeteren voor de overlap tussen de 1*s* orbitalen van de inslaande He* atomen en de doel moleculaire orbitalen binnen een model dat rekening houdt met statistische thermodynamica of klassieke dynamische berekeningen gebaseerd op kwantum chemische potentiaal oppervlakken voor het berekenen en integreren van de resultaten van verschillende botsingspaden eerder dan gebruik te maken van rigide van der Waals grensvlakken. Dyson orbitalen zouden hierbij ook zeer aan te raden zijn. Als een resultaat van interacties met onze onderzoeksgroep tonen uiterst recente studies van de CEDPICS karakteristieken van een eenvoudig test molecule zoals N_2 inderdaad opnieuw de superioriteit aan boven Kohn-Sham en HF orbitalen bij het modeleren van ionisatie-gebaseerde experimenten [9].

Als ondersteuning voor de tot dusver besproken punten, werden EMS studies op kleine test systemen als laatste gerapporteerd in deel 5. In Hoofdstuk 5.1 analyseerden we de resultaten van een experimentele studie van de valentie elektronenstructuur van difluoromethaan door gebruik te maken van hoge resolutie EMS met verschillende impactenergieën. Accurate sferisch gemiddelde elektronen impulsverdelingen werden afgeleid van Dyson orbitalen verkregen via het ADC(3) schema. De corresponderende eigen-energieën bleken het (e,2e) ionisatiespectrum accuraat te reproduceren. Tekorten van de empirische analyses van (e,2e) experimenten gebaseerd op Kohn-Sham orbitalen en eigen-energieën werden vergelijkend besproken. Het falen van de target Hartree-Fock benadering werd waargenomen voor de impulsverdeling horend bij de $1b_1 + 3b_2 + 5a_1$ niveaus. Omdat alle aangewende methodes falen bij het reproduceren van de “bocht omhoog” van de experimentele impulsverdeling bij lage elektronen impuls voor de HOMO van dit molecule, werd er geconcludeerd dat geperturbeerde golfeffecten een belangrijke rol moesten spelen in het beschrijven van de experimentele impulsverdeling van deze π*-achtige orbitaal. Voor zulke situaties is het hoogst wenselijk de theoretische beschrijving van (e,2e) reactie-mechanismen te verbeteren door ontwikkeling van een schema voor geperturbeerde golven voor moleculaire toepassingen.

In Hoofdstuk 5.2 liet de ontwikkeling van een derde generatie elektronen impuls spectrometer met zeer significante verbeterde energie- en impulsresoluties in de Tsinghua University (ΔE=0,45-0,68 eV, $\Delta\theta$=±0,53° and $\Delta\phi$=±0,84°) een vernieuwd onderzoek toe van de valentie orbitaal elektronen impulsverdelingen van water met een verhoogde statistische accuraatheid. De metingen werden uitgevoerd bij impact energieën van 1200 eV en 2400 eV om in staat te zijn de geldigheid van de vlakke golf impulsbenadering na te gaan. De verkregen ionisatiespectra en elektronen impulsverdelingen werden vergeleken met de resultaten van berekeningen uitgevoerd met Hartree-Fock theorie, DFT met de standaard B3LYP functionaal, 1p-GF theorie met het ADC(3) schema, symmetrisch aangepaste cluster configuratie interactie (Eng. *Symmetry Adapted Cluster Configuration Interaction*, SAC-CI) theorie [10], en een veelheid aan Multi-Referentie (MR-SDCI, MR-RSPT2, MR-RSPT3) theorieën (zie bijvoorbeeld [11]). De invloed van de basisset op de berekende impulsverdelingen werden verder onderzocht, gebruik makend van basis sets gaande van 6-31G tot de bijna volledige d-aug-cc-pV6Z. Met dit werk hebben we de beperkingen van de 1p-GF/ADC(3) benadering willen aantonen in kwantitatieve studies van enkelvoudig geëxciteerde shake-up toestanden, vermits deze enkel berekend worden tot op eerste orde in correlatie, wat het verwaarlozen impliceert van dubbele, drievoudige en hogere orde elektronen excitaties. Een hoofd item in deze discussie betreffende verbeterde EMS experimenten op water had te maken met een shake-up band met een zeer zwakke intensiteit op 27,1 eV, waarvan de gerelateerde impulsverdeling voor de eerste keer geanalyseerd werd. De experimentele evidenties en de meest degelijke theoretische berekeningen tonen aan dat deze band zijn ionisatie-intensiteit ontleent aan de $2a_1$ orbitaal en sterk afhankelijk is van het meenemen van dubbele elektronen excitaties in de manifold der shake-up excitatie operatoren. Een uitbreiding van het ADC-schema minstens tot op vierde orde is vereist om kwantitatief deze shake-up band te ontrafelen binnen het kaderwerk van de één-deeltje Greense functie theorie.

Referenties

[1] (a) McWeeny, R.; Pickup, B. T. *Rep. Prog. Phys.* 1980, 43, 1065. (b) Öhrn, Y.; Born, G. *Adv. Quantum Chem.* 1981, 13, 1. (c) Pickup, B. T. *Chem. Phys.* 1977, 19, 193. (d) Deleuze, M.; Pickup, B. T.; Delhalle, J. *Mol. Phys.* 1994, 83, 655.

[2] See: Golod, A.; Deleuze, M. S.; Cederbaum, L. S. *J. Chem. Phys.* 1999, 110, 6014; and references therein.

[3] Saha, S.; Wang, F.; Falzon, C. T.; Brunger, M. J. *J. Chem. Phys.* 2005, 123, 124315

[4] Brunger, M. J.; Winkler, D. A.; Michalewicz, M. T.; Weigold, E. *J. Chem. Phys.* 1998, 108, 1859.

[5] Holland, D. M. P.; MacDonald, M. A.; Hayes, M. A.; Baltzer, P.; Wannberg, B.; Lundqvist, M.; Karlsson, L.; von Niessen, W. *J. Phys. B* 1996, 29, 3091.

[6] Salam, A.; Deleuze, M. S. *J. Chem. Phys.* 2002, 116, 1296.

[7] Kubota, H.; Munakata, T.; Hirooka, T.; Kuchitsu, K.; Harada, Y. *Chem. Phys. Lett.* 1980, 74, 409.

[8] (a) Köppel, H.; Cederbaum, L. S.; Domcke, W. *J. Chem. Phys*. 1988, 89, 2023. (b) Döscher, M.; Köppel, H.; Szalay, P. G. *J. Chem. Phys.* 2002, 117, 2645. (c) Köppel, H.; Döscher, M.; Bâldea, I.; Meyer, H.-D.; Szalay, P. G. *J. Chem. Phys.* 2002, 117, 2657.

[9] (a) Yamazaki, M.; Horio, T.; Kishimoto, N.; Ohno, K. *Phys. Rev. A* 2007, 75, 03272. (b) Kishimoto, N.; Ohno, K. *Int. Rev. Phys. Chem.* 2007, 26, 93.

[10] See: Nakatsuji, H. *Chem. Phys. Lett.* 1991, 177, 331; and references therein.

[11] Szabo, A.; Ostlund, N. S. *Modern Quantum Chemistry. Introduction to Advanced Electronic Structure Theory*; Dover: New York, 1996.

List of publications

1. S. Knippenberg, K. L. Nixon, M. J. Brunger, T. Maddern, L. Campbell, N. Trout, F. Wang, W. R. Newell, M. S. Deleuze, J.-P. François, D. A. Winkler, "Norbornane: An investigation into its valence electronic structure using electron momentum spectroscopy, and density functional and Green's function theories.", *J. Chem. Phys.* 2004, 121, 10525.

2. S. Knippenberg, M. S. Deleuze, T. J. Cleij, J.-P. François, L. S. Cederbaum, J. H. D. Eland, "The band 12 issue in the electron momentum spectra of norbornane: A comparison with further Green's function calculations and ultra-violet photoemission measurements.", *J. Phys. Chem. A* 2005, 109, 4267.

3. S. Knippenberg, K. L. Nixon, H. Mackenzie-Ross, M. J. Brunger, F. Wang, M. S. Deleuze, J.-P. François and D. A. Winkler, "Investigation into the valence electronic structure of norbornene using electron momentum spectroscopy, Green's function and density functional theories.", *J. Phys. Chem. A* 2005, 109, 9324.

4. N. Kishimoto, Y. Hagihara, K. Ohno, S. Knippenberg, J.-P. François, M. S. Deleuze, "Probing the shape and stereochemistry of molecular orbitals in locally flexible aromatic chains: a Penning ionization electron spectroscopy and Green's function study of the electronic structure of biphenyl.", *J. Phys. Chem. A* 2005, 109, 10535.

5. C. G. Ning, X. G. Ren, J. K. Deng, G. L. Su, S. F. Zhang, S. Knippenberg, M. S. Deleuze, "Probing Dyson orbitals with Green's function theory and electron momentum spectroscopy", *Chem. Phys. Lett.* 2006, 421, 52.

6. S. Knippenberg, J.-P. François, M. S. Deleuze, "Green's function study of the one-electron and shake-up ionisation spectra of unsaturated hydrocarbon cage compounds", *J. Comp. Chem.* 2006, 27, 1703.

7. M. S. Deleuze and S. Knippenberg, "Study of the molecular structure, ionization spectrum and electronic wave function of 1,3-butadiene using electron momentum spectroscopy and benchmark Dyson orbital theories", *J. Chem. Phys.* 2006, 124, 104309.

8. Y. R. Huang, S. Knippenberg, B. Hajgató, J.-P. François, J. K. Deng, M. S. Deleuze, "Imaging momentum orbital densities of conformationally versatile molecules: a benchmark theoretical study of the molecular and electronic structures of dimethoxymethane.", *J. Phys. Chem. A* 2007, 111, 5879.

9. S. Knippenberg, B. Hajgató, J.-P. François, M. S. Deleuze, "Theoretical study of the fragmentation pathways of norbornane in its doubly ionized ground state", accepted for publication in *J. Phys. Chem A*.

10. S. Knippenberg, Y. R. Huang, B. Hajgató, J.-P. François, M. S. Deleuze, "Probing molecular conformations in momentum space: the case of *n*-pentane", accepted for publication in *J. Chem. Phys.*

11. C. G. Ning, B. Hajgató, Y. R. Huang, S. F. Zhang, K. Liu, Z. H. Luo, S. Knippenberg, J. K. Deng, M. S. Deleuze, "High resolution electron momentum spectroscopy of the valence orbitals of water", accepted with minor revisions in *Chem. Phys.*

List of attended conferences

- 5-7 April 2006: "International conference on the theoretical aspects of chemical reactivity", Vrije Universiteit Brussel (Belgium), poster presentations.
- 27 January 2006: "Quantum chemistry in Belgium, 7th edition", Université de Mons-Hainaut (Belgium), poster presentations.
- 16-21 January 2005: "7th Congress of the World Association of Theoretically Oriented Chemists", Cape Town (South Africa), poster presentation.
- 19-23 September 2004: "40th Symposium for theoretical chemistry", Sühl – Philipps Universität Marburg (Germany), poster presentation.
- 1-3 July 2004: "International conference on Electron and photon impact ionization and related topics", Université Catholique de Louvain (Belgium), poster presentation.
- 21 November 2003: "Quantum chemistry in Belgium, 6th edition", Universiteit Gent (Belgium).

List of oral presentations

- Invited talks: 10 July 2007 (Universiteit Gent, Belgium), 20 March 2007 (Johann Wolfgang Goethe-Universität, Frankfurt am Main, Germany), 30 January 2007 (Technische Universität München, Germany), 18 July 2006 (Facultés Universitaires Notre Dame de la Paix, Namur, Belgium), 18 May 2006 (Tsinghua University, Beijing, China).
- 9 April 2006 (Vlaams Jongerencongres van de Chemie – achtste editie, Leuven, Belgium).